702979

BNWL-36

AEC RESEARCH AND DEVELOPMENT REPORT

HANFORD RADIOLOGICAL SCIENCES RESEARCH AND DEVELOPMENT ANNUAL REPORT FOR 1974

REPOSITORY PNL
COLLECTION General Human Subjects
BOX No. N/A
FOLDER N/A

0028130

BNWL-36
UC-48, Biology and Medicine

HANFORD RADIOLOGICAL SCIENCES RESEARCH AND DEVELOPMENT ANNUAL REPORT FOR 1964

By
Staff Members of
Physics and Instruments Department
Chemistry Department

Edited by
D. W. Pearce and J. K. Green

January 1965

FIRST UNRESTRICTED DISTRIBUTION MADE AUG 25 '65

PACIFIC NORTHWEST LABORATORY
RICHLAND, WASHINGTON

0028131

Printed in the USA. Charge $8.71. Available from the U.S. Atomic Energy Commission, Division of Technical Information Extension, P. O. Box 1001, Oak Ridge, Tennessee. Please direct to the same address inquiries covering the procurement of other classified AEC reports.

0028132

TABLE OF CONTENTS

Page

ATMOSPHERIC PHYSICS 1.1

A Model of Diffusion and Transport for a Continuous Release in a Stable Atmosphere - C. L. Simpson 1.1

Measurements of Dispersion from a Continuous Elevated Point Source in an Unstable Atmosphere - C. E. Elderkin and W. T. Hinds 1.7

Atmospheric Turbulence Measurements - C. E. Elderkin . 1.27

Area Dosage Relationships Downwind of a Point Source - P. W. Nickola and Naydene E. Nutley 1.33

Precipitation Scavenging Studies - R. J. Engelmann . . 1.54

A Sampler for Recording the Concentration of Airborne Zinc Sulfide on a Real Time Scale - P. W. Nickola . . . 1.59

Field Testing of a Fluorescein-Zinc Sulfide Dual Atmospheric Tracer Technique - P. W. Nickola 1.65

Improvements in Micrometeorological Instrumentation - P. W. Nickola 1.78

References . . . . . .

RADIOLOGICAL PHYSICS 2.1

Radioactivity Measured in Alaskan Natives, 1962-1964 - H. E. Palmer, W. C. Hanson, B. I. Griffin, and L. A. Braby 2.1

Seasonal Variations of Cs^{137} in Alaskan Eskimos - H. E. Palmer, W. C. Hanson, L. A. Braby, and B. I. Griffin 2.2

Urinalysis for Cs^{137} - H. E. Palmer 2.4

0028133

TABLE OF CONTENTS (Contd.)

Page

Na^{22} in People and Food - H. E. Palmer 2.8

Fe^{55} in Humans and Their Foods - H. E. Palmer and T. M. Beasley 2.9

Radioactivity in an Individual Eskimo - H. E. Palmer . . 2.13

Simplified Whole Body Counting - H. E. Palmer . . . 2.16

Cs^{137} in Trappist Monks - R. A. Jalbert and H. E. Palmer . 2.19

Humans Exposed to Uranium Mine Atmospheres - H. E. Palmer, R. W. Perkins and B. O. Stuart 2.20

Standardization of Whole Body Counters - R. A. Jalbert and W. C. Roesch 2.21

Progress in Plutonium Whole Body Counting - K. L. Swinth and B. I. Griffin 2.24

Counting Plutonium in Animals and in Excreta - K. L. Swinth and B. I. Griffin 2.27

Low Energy Fast Neutron Spectroscopy - W. A. Glass . . 2.32

The Secular Change of Pu-Be Neutron Sources - L. L. Nichols 2.36

Fast Neutron Medical Research Facility - K. L. Swinth . . 2.38

Instrumentation for Local Dose Measurement - W. A. Glass, L. L. Nichols, and D. N. Samsky 2.39

A Helium Ion Separator for the Positive Ion Accelerator - L. W. Seagondollar and L. L. Nichols. 2.43

Pulse Reader for Ion Chambers - L. A. Braby 2.46

Fast-Pulse Averaging - W. C. Roesch 2.47

An Alpha- and Beta-Ray Calorimeter - D. M. Fleming . . 2.49

0028134

TABLE OF CONTENTS (Contd.)

Page

Calorimetric Determination of the Mean Beta Energy and Half-Life of Pm^{147} - E. J. Wheelwright, D. M. Fleming, and F. P. Roberts 2.51

A Pulsed X-Ray Machine - D. M. Fleming and N. E. Mutka . 2.52

Stopping Power Ratios for Radiation Nonequilibrium - K. G. Pailthorp 2.52

References 2.55

RADIOLOGICAL CHEMISTRY 3.1

Radiation Chemistry 3.1

Radiation-Induced Swelling and Hemolysis of Red Blood Cells - D. R. Kalkwarf and W. D. Felix 3.1

Radiation Protection of Aqueous Jellies - D. R. Kalkwarf . 3.4

Radiation Chemistry of Erioglaucine in Frozen Aqueous Solution - D. R. Kalkwarf 3.7

Yield of p-Nitroaniline Radicals Formed in Irradiated Aqueous Solutions - R. N. Diebel and D. R. Kalkwarf 3.10

Comparison of Radicals Formed by Gamma Irradiation and Dithionite Reduction of Aromatic Nitro-Compounds in Water - D. R. Kalkwarf and R. N. Diebel 3.12

Kinetics of Diffusion Through Human Erythrocyte Membranes - W. D. Felix 3.21

Development of Apparatus and Techniques for Pulsed Radiolysis - W. D. Felix 3.31

Radioanalytical Methods 3.35

Cs^{137} in Alaskan Eskimo Hair - T. M. Beasley and H. E. Palmer 3.35

0028135

TABLE OF CONTENTS (Contd.)

Page

Separation of Sr^{90} from Hair - T. M. Beasley 3.36

The Radiochemical Determination of Plutonium in Soil - W. B. Silker 3.37

A Rapid Method for the Determination of Plutonium in Urine - W. B. Silker 3.39

Application of Tertiary Amine Extraction to the Determination of Uranium in Biological Materials - T. M. Beasley . . . 3.40

The Direct Measurement of Radionuclides in Bioassay Samples by Multidimensional Gamma-Ray Spectrometry - R. W. Perkins 3.41

The Determination of Rare Earth and Yttrium Radionuclides in Reactor Effluent Water by Use of Multidimensional Gamma-Ray Spectrometry - D. E. Robertson 3.41

Evaluation of Radiochemical Methods for Radiological Purposes - W. B. Silker, D. E. Robertson, C. W. Thomas, and R. W. Perkins 3.43

Reactor Studies 3.44

The Effect of Water Treatment Chemicals and pH on Reactor Effluent Radioisotope Concentrations - W. B. Silker and C. W. Thomas 3.44

Removal of Fission Products from Contaminated Water by Flocculation Methods - W. B. Silker 3.47

Counting Studies 3.50

Anticoincidence Shielded-Multidimensional Gamma-Ray Spectrometry for High Sensitivity Analysis of Radionuclide Mixtures - R. W. Perkins 3.50

0028136

TABLE OF CONTENTS (Contd.)

Page

An Anticoincidence Shielded-Multidimensional Gamma-Ray Spectrometer - R. W. Perkins 3.50

A High-Resolution Lithium-Drifted Germanium Gamma-Ray Spectrometer - M. W. Hill 3.51

Large Area Alpha Ray Spectrometry - T. M. Beasley . . 3.55

Environmental Studies 3.58

Airborne-Radionuclide Measurements and Physical Characteristics Determinations - R. W. Perkins, C. W. Thomas, and J. M. Nielsen 3.58

Physical and Chemical Characteristics of Various Fallout Radionuclides - C. W. Thomas 3.58

Air Concentrations of Short-Lived Radionuclides Resulting from 1964 Chinese Detonation - C. W. Thomas. 3.62

Measurement of Airborne Radionuclides in Alaska - R. W. Perkins and H. G. Rieck 3.65

Na^{22} and Cs^{134} in Fallout, Foods, and People - R. W. Perkins and J. M. Nielsen. 3.67

Air Concentrations of 12 Radionuclides from 1962 Through Mid-1964 - R. W. Perkins, J. M. Nielsen, and C. W. Thomas 3.68

Ag^{110m} in the Atmosphere - R. W. Perkins 3.68

Determination of Columbia River Flow Times Using Radioactive Tracers Introduced by the Hanford Reactors - J. L. Nelson, R. W. Perkins, and W. L. Haushild . . 3.70

Behavior and Transport of Radionuclides in the Columbia River Between Hanford and the Ocean - R. W. Perkins, J. L. Nelson, and W. L. Haushild 3.70

0028137

TABLE OF CONTENTS (Contd.)

Page

Scouring of Radionuclides Deposited with Columbia River Sediments During the Spring Freshet - J. L. Nelson . . 3.71

Studies of Radionuclides in Columbia River Sediments - J. L. Nelson, R. W. Perkins, and J. M. Nielsen . . . 3.74

Studies of the Mechanism of Retention of Radionuclides in Columbia River Sediments - J. L. Nelson and N. H. Cutshall 3.75

Distribution of Sediments and Associated Radionuclides in the Columbia River Below Hanford - J. L. Nelson 3.80

Measurement of a Large Group of Radionuclides in Columbia River Aquatic Organisms - R. W. Perkins. 3.88

I^{131} Measurements in Large Volumes of Columbia River Water - R. W. Perkins 3.90

Collection of Radioisotopes from River and Sea Water by Various Materials - W. B. Silker. 3.93

A Comparison of the Ratios of Cs^{136} to Cs^{137} and Ba-La^{140} to Cs^{136} from U^{235} and Pu^{239} Fission - C. W. Thomas. . 3.95

Cl^{38} and S^{38} Produced by Cosmic Radiation - R. W. Perkins, C. W. Thomas, M. W. Hill, and J. M. Nielsen . . . 3.97

Washout Studies Using Natural Tracers from Radiochemical Separations Plant Stacks - R. W. Perkins 3.99

Fluorescein as a Dual Atmospheric Tracer - J. D. Ludwick . 3.101

Investigation of Inert Atmospheric Tracers; Xe^{133} - J. D. Ludwick 3.104

References 3.115

0028138

TABLE OF CONTENTS (Contd.)

Page

CHEMICAL EFFLUENTS TECHNOLOGY 4.1

Soil Chemistry and Geochemistry 4.1

Some Adsorption, Diffusion and Dispersion Characteristics of Anions in Soils - B. F. Hajek 4.1

Clay Mineral Composition of Two Hanford Soils - B. F. Hajek

Self-Diffusion Coefficients of Some Cations in Open Zeolites - L. L. Ames, Jr. 4.6

Linde 13X Equilibria with Trivalent Cerium and Yttrium Cations - L. L. Ames, Jr. 4.8

Zeolite Cation Selectivity - L. L. Ames, Jr. 4.12

Soil Physics 4.14

The Movement of Ground Waters in Confined Aquifers Beneath the Hanford Project - R. E. Brown 4.14

A Sequence for Predicting Waste Transport by Ground Water - R. W. Nelson 4.16

The Permeability Integral: A Key to Measurement in Heterogeneous Porous Media - R. W. Nelson 4.27

Earth Material Sampling by Coring Techniques - J. R. Raymond 4.29

Use of a Neutron Well Probe - J. R. Raymond 4.36

Analytical Description of Soil Characteristics for Partially Saturated Flow - L. G. King 4.39

Measurement of Soil Characteristics for Partially Saturated Flow - L. G. King 4.47

Prediction of One-Dimensional, Transient, Partially Saturated Imbibition - L. G. King. 4.50

0028139

TABLE OF CONTENTS (Contd.)

Page

Iterative Calculation of One-Dimensional, Transient, Partially Saturated Flow - A. E. Reisenauer 4.53

Comparison of Approximate Solution for Flow in Heterogeneous Soil with an Exact Solution - A. E. Reisenauer 4.56

Atmospheric Radioactivity and Fallout, Aerosol Studies . . 4.58

Analysis of Particle Size Frequency Distributions - G. A. Sehmel 4.58

Theoretical Expressions for the Motion of Particles in a Temperature Gradient - A. K. Postma 4.61

Electrical Charges on Particles Produced by a Spinning Disc - A. K. Postma 4.65

Particle Deposition and Retention in Vertical Conduits - G. A. Sehmel 4.67

Improved Aerosol Generators and Applications - A. K. Postma 4.70

References 4.73

INSTRUMENTATION 5.1

Radiological Measurement Methods and Instrumentation . . 5.1

Alpha Energy Analysis Plutonium Air Monitoring - D. P. Brown and N. S. Porter 5.1

Detection of Low Energy Beta Particles - C. A. Ratcliffe and E. M. Sheen 5.7

Method for Beta-Gamma Hand and Shoe Counting Under Varying Background Conditions - W. G. Spear 5.14

0028140

TABLE OF CONTENTS (Contd.)

Page

Advanced Alpha-Beta-Gamma Hand and Shoe Contamination Monitor - C. A. Ratcliffe and E. M. Sheen. 5.14

Detection and Measurement of Airborne Plutonium - W. G. Spear 5.20

Compact Solid State High Voltage Supply - E. M. Sheen and C. A. Ratcliffe 5.29

Integrator for a Portable Neutron Dose Rate Meter - E. M. Sheen and C. A. Ratcliffe 5.33

Neutron Soil Moisture Monitor - E. M. Sheen, W. L. Bunch, and M. R. Wood 5.39

Biological and Biomedical Instrumentation 5.39

Instrument for the Automatic Regulation of Inhaled Aerosols - D. P. Brown and N. S. Porter 5.39

Animal Physiological Function and Radionuclide Uptake Measurement and Telemetry Development - N. C. Hoitink and N. S. Porter 5.42

Detection of Pu^{239} in Human Wounds - D. P. Brown and N. S. Porter 5.48

Improvements to the Biology Animal Scanning Counter - N. S. Porter and D. P. Brown 5.52

Biological Spectrometer and Analyzer - N. S. Porter and E. M. Sheen 5.55

Dosimetery and Atmospheric Physics Instrumentation. . . . 5.59

Peak Pulse Measuring Instrumentation for Use with Ion Chamber Dosimeters - N. C. Hoitink 5.59

0028141

TABLE OF CONTENTS (Contd.)

Page

Gamma Spectrometer for Use in Whole Body Counting - E. M. Sheen 5.67

Signaling Radiation Dosemeters - D. P. Brown. 5.80

Wind Component Analyzer Development - C. A. Ratcliffe and E. M. Sheen 5.89

Automatic Data Collection System for Meteorological Tower Investigations - C. A. Ratcliffe and E. M. Sheen 5.95

References 5.101

0028142

ATMOSPHERIC PHYSICS

A Model of Diffusion and Transport for a Continuous Release in a Stable Atmosphere - C. L. Simpson

The Hanford diffusion model expresses the exposure distribution resulting from a release to the atmosphere as bivariate normal. Relationships for the plume growth parameters, σ_z and σ_y, were derived from experimental data and are dependent on the time of plume travel. The vertical deviation of exposure σ_z, is related to the stability of the atmosphere. The horizontal growth parameter, σ_y, depends only on the standard deviation of the wind direction during the period of release and the mean wind speed.

Experiments successfully completed during 1964 with release heights of 23 and 185 ft show that:

- Ground exposures from elevated releases initially were less than those that were observed from releases near the ground, but approached the ground source values at longer travel times.
- Increasing the height of release reduces the maximum exposure.
- The time to the maximum exposure is linearly related to atmospheric stability.

Hanford has for years sustained a program to investigate the diffusive capacity of the atmosphere. Results obtained in field experiments provided guidance to those responsible for plant operation and contributed knowledge in a relatively new discipline. Early experiments were necessarily limited to gathering data within a few hundred meters from the point of tracer release because of the inadequacy of sampling equipment that was available. In 1959, as a result of successful experiments with the particulate tracer, zinc sulfide, and the development of detection and assaying systems, 28 experiments were completed. In those tests, air samples were obtained 16 mi from the source. The results which followed from the analysis of the data were factored into the solution of many practical problems, and they led to the formulation of several new concepts in diffusion theory.

0028143

Analysis of the 28 mesoscale experiments showed that the relationships between cloud growth and distance were not significantly different than those that had been deduced from the early small scale tests. Specifically, the standard deviation of the crosswind mass distribution, σ_y, was directly proportional to the distance raised to the 0.8 power. The air exposure was inversely proportional to the distance raised to the 1.7 power. It was noted, however, that even though the power functions fitted the average data reasonably well, further refinement could be made with other mathematical formulations.

There were also other challenges. Of immediate practical importance was the desire to specify the diffusive capability of the atmosphere at any given time to the meteorological conditions that prevailed at that time. Generalizations were made, but many of the differences observed from test to test were not explained. Data were gathered at Hanford; at Cape Kennedy, Florida; and at Vandenberg Air Force Base, California. By 1962, there was a sufficient number of field experiments conducted under a wide range of atmospheric conditions to examine in detail those variations that were not understood.

Diffusion data obtained in the mountain-valley regime (Hanford) and land-sea regime (Cape Kennedy and Vandenberg) could be compared. The details of these analyses are included in the 1962 and 1963 issues of this report.* It was shown that cloud growth depended on wind variability during the release, analogous to a mathematical model derived for Brownian motion by the classic theorist, G. I. Taylor, in 1921. The unexplained differences in diffusion data became ordered with respect to specific meteorological variables when plotted as a function of travel time, not travel distance. Independent confirmation of this fact was obtained, and a procedure for predicting the exposure distributions that are observed in prolonged releases (several hours) was evolved. Details on the concepts are given in Reference (1.1).

---

* HW-77609 and HW-81746, HAPO, General Electric, Richland, Washington.

0028144

These results led to the significant improvement of the Hanford diffusion model, first by enabling more precise definition of the diffusion in relation to the existing meteorological state and, second, by permitting solutions to more complex problems than had previously been possible. The model accounted for meteorological parameters significant in diffusion processes, yet it was direct, simple, and adaptable for operational use. In a planned release of trace quantities of radioiodine, predictions of the exposure distribution made while the 40 min release was in progress agreed extremely well with the exposures computed from air samples taken within 2 mi of the source.

Discussion of the model, its parameters, and its application was given in the 1963 issue of this report.* An example of obtaining problematical exposure estimates by introducing climatological data into the model is shown in Reference (1.2).

In the formulation, the distribution of air exposure (g-sec/m^3) is represented as bivariate normal:

$$E = \frac{Q}{\pi \sigma_y \sigma_z \overline{U}_h} \exp\left[-1/2\left(\frac{y^2}{\sigma_y^2} + \frac{h^2}{\sigma_z^2}\right)\right] . \qquad (1)$$

E is the air exposure, Q is the total amount of material released, h is the height of the release, $\overline{U}_h$ is the average wind speed during the release at the height of release, and y is the cross-wind coordinate. These quantities are usually easily determined and pose no problem. The variances of the distribution, σ_y^2 and σ_z^2, are the statistics that have stimulated activities in diffusion research and that must be related to the variable properties of the atmosphere. It has not been an easy task to find the relation between the geometry of a plume and the controlling meteorological properties. Inadequacies in theoretical development and absence of ability to measure turbulence in sufficient detail contributed to the dilemma. Empirical generalizations formulated from experimental data served to guide industrial

* HW-81746, HAPO, General Electric, Richland, Washington.

decisions. Average growth curves (σ_y and σ_z versus X) for representative atmospheric conditions define the diffusivity for ranges of atmospheric states and are still being effectively applied to many problems.

From an analysis of Hanford experiments a more specific relationship between plume growth and the controlling meteorological parameters was derived. This result is important because it permits the evaluation of the consequences of any release using direct meteorological measurements obtained during the release. From experimental data, the lateral growth of the plume was found to depend directly on the variations in the wind direction and the mean wind speed. The specification of the σ_y parameter resulted in the capability of quantitatively specifying the exposure in terms of the wind direction, speed, and stability. Furthermore, the consequences of prolonging the release over periods of hours are automatically accounted for in the wind variability parameter. The Hanford relationship between σ_y and the properties of the wind permits a more precise delineation of the results of diffusion and can be more simply and readily applied to industrial problems than can older methods. The expression for lateral growth, σ_y, is

$$\sigma_y^2 = At + \frac{A^2}{2(\sigma_\theta \overline{U})^2} \left[\exp\left(-\frac{2t\,(\sigma_\theta \overline{U})^2}{A} \right) - 1 \right], \tag{2}$$

where

$$A = B + 232\,\sigma_\theta \overline{U}\ .$$

The term σ_y^2 (m^2) is the variance of the mass distribution, t is the travel time (sec), σ_θ (rad) is the standard deviation of the wind direction over the release period, and $\overline{U}$ (m/sec) is the average wind speed at release height. The variance for the vertical exposure distribution has been empirically determined from data collected during stable atmospheric tests. The variance (σ_z^2) is related to the travel time, t, as

$$\sigma_z^2 = a[1 - \exp(-k^2 t^2)] + bt, \tag{3}$$

where a, b, and k^2 are functions of the degree of stability. Values of these parameters are given in Table 1.1.

TABLE 1.1

VALUES OF STABLE ATMOSPHERIC DISPERSION PARAMETERS

Parameter	Degree of Stability: Moderate	Degree of Stability: High
a	$97\ m^2$	$34\ m^2$
b	$0.33\ m^2\ sec^{-1}$	$0.025\ m^2\ sec^{-1}$
k^2	$2.5 \times 10^{-4}\ sec^{-2}$	$8.8 \times 10^{-4}\ sec^{-2}$

The exposure for a given release can be determined from Equation (1) by substituting the growth parameters derived from Equations (2) and (3). Values of the growth parameters are dictated by existing meteorological conditions. This is the Hanford diffusion model, the parameters derived from experimental data.

From 1959 through 1962, the release of the zinc sulfide tracer was made near the ground surface. In 1963, some releases were made from a 23 ft stack in stable atmospheres, but no detailed analysis was made. In 1964, other releases were made from 185 ft on the Hanford Meteorology Tower and all the exposure data gathered from the elevated releases for stable atmospheres were compared with those values obtained for ground releases.

Figure 1.1 is a summary of the results of the experimental tests. On the ordinate is represented the centerline exposure normalized for the mean wind speed, $\bar{U}$, and the source strength, Q. The travel-time is plotted on the abscissa. The shaded areas, therefore, show the manner in which exposure was observed to vary with the travel time for releases at several heights in stable conditions. With increasing time, the ground exposure values for the elevated releases generally approach the values that would be expected for a ground release. This characteristic is predicted by Equation (1), for with large travel-times σ_z^2 becomes large, h^2/σ_z^2 approaches zero, and the exposure value approaches that which would occur from a ground release.

0028147

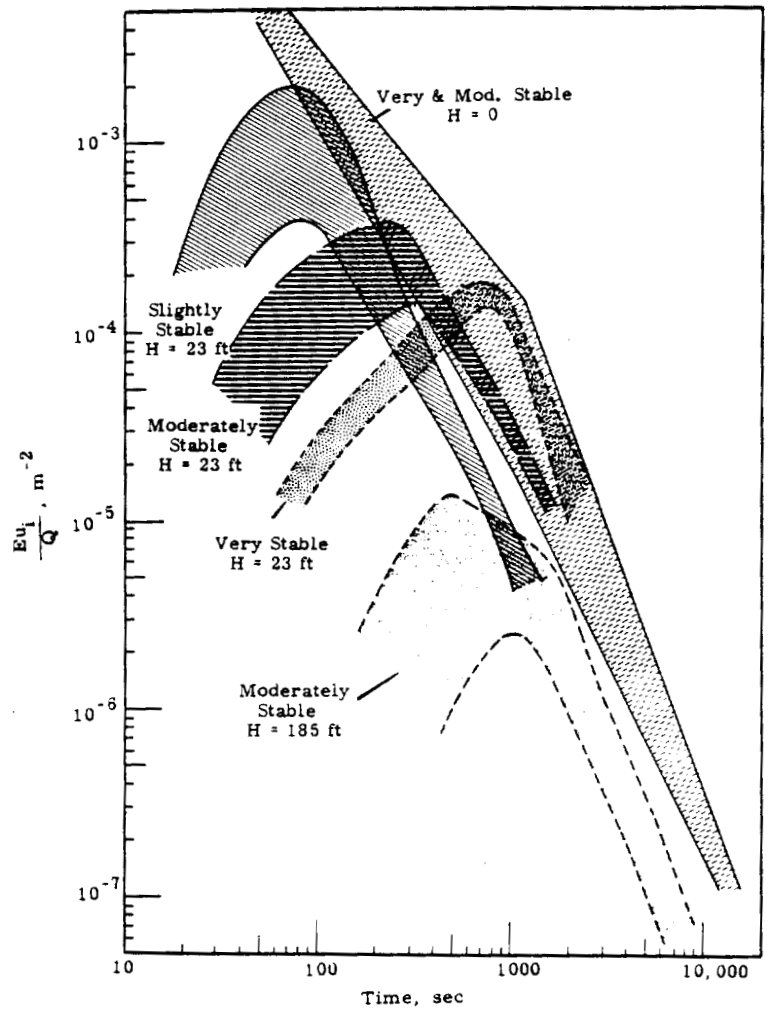

FIGURE 1.1

Normalized Exposure Versus Travel Time
for Stable Hanford Tests

The quality of the 12 tests with 23 ft source height was very good, so the stratification of the data shown in the graph is considered to have physical significance rather than to reflect random errors in sampling. It is noted that with increased stability, the time of maximum exposure becomes greater. Also, with increasing stability, the maximum value of the exposure decreases, again consistent with expectations derived

Neg. No. 0650288-3

0026148

from theory. Empirically, the time to maximum exposure was found to depend directly on the standard measure of atmospheric stability, the Richardson Number, Ri,

$$T_{max} = 1750 \text{ Ri}. \tag{4}$$

Data from tests of release height, 185 ft, appeared to behave in a similar manner but were too few in number to justify quantitative analysis.

There are several major problems associated with the analysis and interpretation of diffusion data that have been identified for some time; yet little progress has been made in their solution. Equation (1) relates the exposure to the wind speed, commonly taken by the experimentalist to be the wind speed at the release height. In stable conditions, however, a particle diffusing vertically will move through zones of large wind shear and will be affected by the change in speed. For the release heights in this analysis, the problem arises immediately as to what is the "representative speed" in the layer through which the particle fell. The mean wind speed shown on the ordinate was arbitrarily defined here to be the speed at the Geometric Mean Height. The difficulty is introduced initially by the necessity of having to assume the speed constant to integrate the basic diffusion equation.

The results presented in Figure 1.1 pertain to zinc sulfide particles of mean diameter 2.5 μ which have a finite fall velocity. These particles are also carried to the ground and vegetation by turbulent eddies where some fraction is retained. The deposition velocity—or the ratio of the total deposited (per unit area) to the exposure—is about 1 cm/sec. This value is the same as that determined for radioiodine.

Measurements of Dispersion from a Continuous Elevated Point Source in an Unstable Atmosphere - C. E. Elderkin and W. T. Hinds

Seventeen elevated continuous source diffusion tests were conducted at Hanford in unstable and neutral atmospheric conditions over a range of wind speeds. Tracer releases were made from 185 ft and samples were taken

0028149

at the surface on 9 arcs out to 1 mi from the source. In general, the horizontal turbulence was similar to that of other areas where turbulence studies have been made. Of particular importance to continuous source diffusion are low frequency "mesoscale" eddies containing a significant share of the turbulent energy. These spread the plume laterally at a nearly linear rate of increase out to the 1 mi limit of measurements. The near linear growth permits organization of the data as a function of distance, proportional to x and $\sigma_v/\overline{U}$, or as a function of time, proportional to t and σ_v. The plume width grows more closely proportional to $t^{0.9}$; this slight deviation from a linear growth is shown by the Hay-Pasquill prediction technique, which estimates all lateral plume standard deviation measurements quite well with a simple assumption of $\beta = 1$. The widths can be more closely estimated by taking β ranging from 3 to about 1.5 for the smallest σ_v to the largest σ_v cases, respectively.

Estimates of the standard deviation of vertical velocity were calculated from the measured wind speeds and stabilities using the similarity theory relationships. If a linear rate of increase in vertical plume spread, proportional to σ_w, is assumed, the bivariate normal model for an elevated source gives exposure estimates comparing quite well with measured exposures.

Experimental Procedures

The diffusion experiments described here were performed at Hanford, Washington, and consist of a group of 17 tests with tracer releases made from a height of 185 ft for periods generally of 1 hr but ranging down to 17 min. The tests were conducted in neutral to very unstable atmospheric conditions and over a wide range of wind speeds. Surface exposures (time integrated concentrations) were measured at a height of 1.5 m along 9 arcs, covering more than 120° of azimuth and extending to a radial distance of 1600 m. The tracer release, sampling, and assaying techniques are described fully elsewhere.[1.3]

Accompanying wind and temperature measurements were taken from a meteorology tower, equipped with aerovane anemometers and thermohm temperature sensors at 8 levels from the surface up to 400 ft. Mean temperatures were determined for the duration of each test from the samples taken sequentially every 4 min throughout the experiments. The mean wind

speeds and directions were computed from 20-sec average readings of the wind records. Also, the horizontal Cartesian components for each basic 20 sec period were determined, and the lateral and logitudinal wind variances during the periods of release were calculated for the 50 and 200-ft levels, as were spectral estimates for each of the tests. It is recognized that the 20-sec basic wind readings will reduce the variances somewhat; but, in unstable conditions, the error should be small, particularly in view of the large contribution at low frequencies permitted by the long records.

Table 1.2 lists the 200 and 50-ft mean wind speeds calculated for the period of generation for each test. Richardson Numbers are also listed for the 12.3 ft level calculated from the 50 and 3 ft wind speeds and temperatures. An attempt to calculate the Richardson Number for a higher level proved fruitless, since the wind speed differences were too small and were comparable in magnitude to errors in measurement.

The Richardson Number is not directly proportional to height, but the Monin-Obukov stability parameter, z/L', can be obtained for unstable conditions from the expression

$$\frac{z}{L'} = \frac{Ri}{(1 - 18\ Ri)^{1/4}} \tag{1}$$

so that a measure of the stability at any height, z, can easily be determined (assuming that the wind and temperature profiles are similar). From the measured values of the Richardson Number at 12.3 ft, z/L' was determined and projected to the 50 ft level. These values are listed in Table 1.2. The 50-ft wind measurements were considered to be most representative of the turbulence and transport characteristics responsible for carrying the plume from the 185 ft release height to the 5 ft sampling height.

Turbulence Measurements

The lateral spread of a diffusing plume is, of course, intimately related to the characteristics of the lateral wind velocity fluctuations. The

TABLE 1.2

WIND SPEEDS, STABILITY, AND TURBULENCE PARAMETERS

Test	$\bar{U}_{50}$, m/sec	$\bar{U}_{200}$, m/sec	Ri at z = 12.3 ft	z/L' at z = 50 ft	σ_{v50} m/sec	σ_{v200}, m/sec	$\frac{\sigma_{v50}}{\bar{U}_{50}}$	σ_{u50}, m/sec	σ_{u200}, m/sec	$\frac{\sigma_{u50}}{\bar{U}_{50}}$	σ_{uHi50}	$\frac{\sigma_{uHi50}}{\bar{U}_{50}}$	Calculated σ_{w50}, m/sec	Calculated $\frac{\sigma_{w50}}{\bar{U}_{50}}$
10	3.4	4.0	-0.539	-1.21	1.2	1.3	0.36	0.86	0.93	0.25	0.69	0.20	0.56	0.166
11	2.2	2.5	-0.650	-1.40	0.78	0.80	0.35	1.1	1.0	0.48	0.66	0.30	0.39	0.178
12	3.0	3.6	-0.281	-0.629	1.3	1.1	0.43	1.7	1.6	0.57	0.90	0.20	0.37	0.124
13	10.9	12.9	-0.0275	-0.102	1.2	1.4	0.11	1.4	1.3	0.12	1.08	0.10	0.82	0.075
14	5.9	7.0	-0.0221	-0.083	0.92	1.0	0.16	1.5	1.5	0.25	0.98	0.17	0.43	0.073
15	7.7	9.5	0	0	1.2	1.3	0.16	1.4	1.3	0.18	0.78	0.10	0.52	0.067
16	6.8	8.4	0	0	1.2	1.4	0.18	1.5	1.6	0.22	0.86	0.13	0.46	0.067
17	7.9	8.9	-0.0289	-0.106	0.86	1.0	0.11	1.2	1.1	0.14	1.02	0.13	0.59	0.075
18	7.4	8.4	-0.0291	-0.107	1.1	1.1	0.15	1.1	1.2	0.15	0.84	0.11	0.56	0.076
21	6.9	8.3	-0.0412	-0.146	0.87	1.0	0.13	1.1	0.90	0.15	0.87	0.13	0.55	0.080
22	4.3	4.8	-0.314	-0.797	1.2	1.2	0.28	1.2	1.2	0.28	0.76	0.18	0.59	0.137
24	6.8	8.0	-0.238	-0.641	2.3	2.3	0.34	2.0	2.0	0.30	1.26	0.19	0.85	0.125
26	4.4	4.8	-0.327	-0.825	1.9	1.8	0.43	1.4	1.4	0.32	0.91	0.21	0.61	0.139
27	2.7	3.3	-0.818	-1.68	1.2	1.5	0.45	1.5	1.5	0.55	0.83	0.31	0.53	0.195
28	7.4	8.4	-0.0915	-0.292	1.3	1.4	0.19	1.2	1.3	0.16	0.77	0.10	0.69	0.093
30	8.4	9.6	-0.0190	-0.072	1.0	1.1	0.13	1.3	1.2	0.15	0.91	0.11	0.60	0.072
33	7.6	8.0	-0.115	-0.356	1.6	1.6	0.21	1.6	1.5	0.21	1.08	0.14	0.75	0.099

0028152

standard deviation of the lateral velocity component, σ_v, measured at a fixed point has been found, at many locations, to be roughly proportional to wind speed in neutral conditions. However, a dependence on conventional roughness length, which might be expected, has not been found, so constants of proportionality relating σ_v with friction velocity, u^*, for neutral conditions differ at various sites, ranging from 1.3 at Brookhaven, Long Island, to 2.6 at Round Hill, Massachusetts. Also, the lateral wind variance has been found to increase with increasing instability, but remains relatively constant with change in height, contrary to expectations from similarity theory. A complete discussion of the findings on turbulence structure is given by Lumley and Panofsky.[1.4]

Similarly at Hanford, measurements of lateral wind component fluctuations at 50 ft taken during the diffusion tests show an increase in lateral intensity of turbulence, $\sigma_v/\overline{U}$, with increasing instability as shown in Figure 1.2. However, the correlation between wind speed and stability is responsible to a large degree for this dependence. With a value of $\sigma_v/\overline{U} = 0.15$ taken for near neutral stability (for $-z/L' < 0.3$) and with a roughness length of about 3 cm for the Hanford site, the proportionality constant between σ_v and u^* is 2.3, a value within the range found at other sites. Table 1.2 shows, for the most part, only slightly larger values of σ_v at 200 ft than at 50 ft, again, a result not at variance with that found elsewhere. Low frequency horizontal eddies, produced by mesoscale features, contain a large share of the variance, resulting in the observed turbulence characteristics, not expected from similarity theory. Of course, for diffusion problems involving release and travel times on the order of 1/2 hr and greater, the mesoscale turbulence plays a dominant role.

Variance of the longitudinal wind component, σ_u^2, likewise is much the same as measured elsewhere. Contrary to similarity theory, but in agreement with other observations, σ_u is relatively constant with height as shown in Table 1.2; and, when divided by wind speed, σ_u increases with instability.

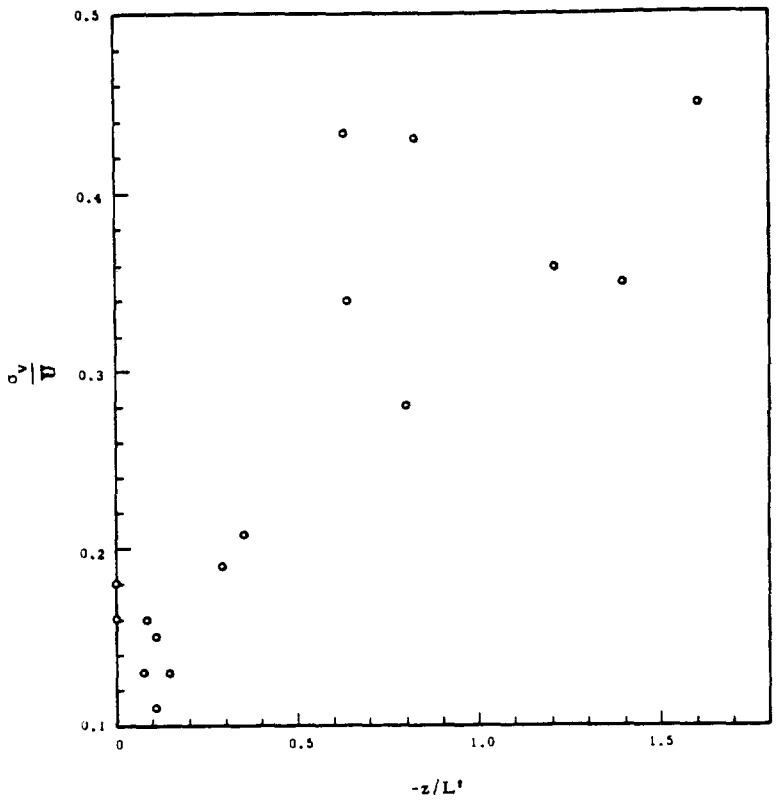

FIGURE 1.2

Lateral Turbulence Intensity Versus Stability

Diffusion from a continuous source has no direct relation to the longitudinal velocity variance, but the gustiness or turbulent intensity of the longitudinal component may be a good indicator of the turbulent intensity of the vertical wind component for which there were no measurements in this test series. This might be particularly true if the variance contributed at low frequencies, due to mesoscale influences, was filtered out. A running average numerical filter with an averaging time of 160 sec was used to separate the variance for frequencies effectively above 10 cycles/hr from those below. As described by Pasquill [in Reference (1.5) see his Figure 15] the separation is not sharp and a fraction of the energy in the range from about 2 to 22 cycles/hr is contained in each group. However, this isolates fairly well the micrometeorological σ_u^2 from the mesometeorological contribution. The filtered values, σ_{uHi}, are listed in Table 1.2.

Neg. No. 0650409-10

In neutral conditions, σ_w is simply proportional to friction velocity,

$$\sigma_w = Au^* = \frac{Ak\overline{U}}{\ln(z/z_o)} \tag{2}$$

with the universal constant, A, equal to about 1.05. For unstable conditions, σ_w can be found from

$$\sigma_w = A\, u^*\, h'(z/L') \tag{3}$$

where the friction velocity is given by

$$u^* = \frac{k\,\overline{U}}{[\ln(z/z_o) - \Psi(z/L')]} \quad . \tag{4}$$

The stability dependent functions $h'(z/L')$ and $\Psi(z/L')$ are discussed by Lumley and Panofsky.[1.4] The values for these functions were determined for the stabilities listed in Table 1.2. Then, using a value of 3 cm for the roughness length, and with the measured wind speeds at 50 ft, estimates of σ_w and $\sigma_w/\overline{U}$ for the 50 ft level were calculated for each test. These are also entered in Table 1.2.

Dispersion Measurements

The spread of the elevated source plumes as observed at the surface shows a nearly linear increase in width with increasing distance or travel time indicating the dominant role play by the large variance at low frequencies. According to Taylor's theory, the Lagrangian autocorrelation for the lateral wind component remains near unity and the plume width equals the product of the standard deviation of the lateral wind component and the travel time. As long as the growth remains linear, i.e., while the travel distance remains small compared to the scale of lateral turbulence, the plume width can be considered proportional to turbulence intensity, $\sigma_v/\overline{U}$, and travel distance. That is,

$$\sigma_y = \sigma_v t = \frac{\sigma_v}{\overline{U}}\, x \tag{5}$$

where the wind speed and lateral component standard deviation are determined at the transport level, 50 ft. The averaged plume standard deviations for each of the two stability groups shown in Figure 1.3, with the

envelope for each group also shown, agree well with the simple linear relations

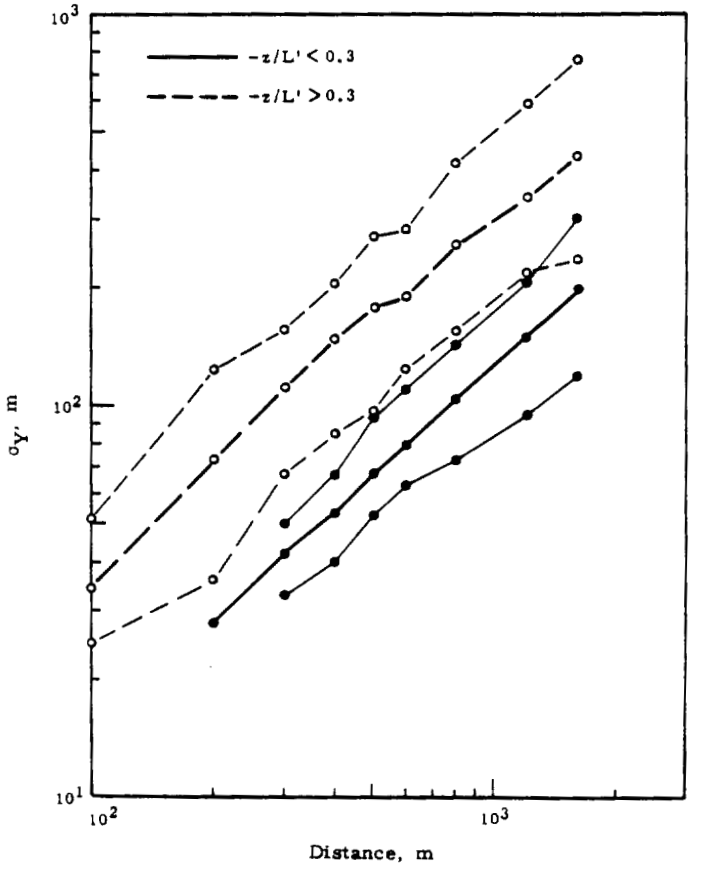

FIGURE 1.3
Averaged Standard Deviation of Crosswind Exposure Distribution Versus Distance

$$\sigma_y = 0.137\ x \qquad \text{for } -z/L' < 0.3 \qquad (5a)$$

and

$$\sigma_y = 0.325\ x \qquad \text{for } -z/L' > 0.3 \qquad (5b)$$

where the coefficients in Equation (5) are the average $\sigma_v / \overline{U}$ values for each of the stability groups. Equation (5a) agrees to within 10% of averaged measured σ_y values at each arc for $-z/L' < 0.3$. Equation (5b) agrees to within 20% of the averaged measured σ_y values for $-z/L' > 0.3$. Plume widths for each of the individual tests can also be related to the measured $\sigma_v / \overline{U}$ for each test with fair agreement. The ratios of measured σ_y, at the point of maximum crosswind integrated exposure, to the value calculated

Neg. No. 0650491-2

from Equation (5), range from 0.71 to 1.15. The average ratio is 0.86, apparently less than unity due to the slight drop off in the Lagrangian autocorrelation and the resulting slightly less than linear increase of σ_y with distance.

Since the lateral wind component variance is related to the stability as shown in Figure 1.2 for the Hanford site, the lateral plume spread could be further related to stability through a strictly empirical expression,

$$\sigma_y = \frac{\sigma_v}{\overline{U}} x = [0.13 + 0.35(1/L')] x \quad . \tag{6}$$

However, there is no basis for assuming a linear relationship for the data of Figure 1.2, and there is no assurance that the data are characteristic of the stability dependence of lateral turbulence intensity for any site other than Hanford. In addition, the scatter of the data in Figure 1.2 is considerable. Consequently, reliance on measured wind variances is more dependable for estimating lateral plume width than a model relating plume spread directly to the stability even though a definite stability dependence is indicated.

These findings agree with those of Islitzer,[1.6] whose elevated source experiments likewise show σ_y increasing nearly linearly with distance and proportional to the standard deviation of horizontal wind direction, a good estimate of $\sigma_v / \overline{U}$.

Islitzer's tests also considered a similar relation for the vertical dispersion, proportional, through the constant 0.81, to distance and the measured standard deviation of the vertical angle of the wind. These were compared with the standard deviation of the vertical plume concentration distribution, σ_z, at the point of maximum surface concentration, determined to be $\sigma_{zPk} = H/\sqrt{2}$ from the bivariate normal model (the continuity equation with assumed Gaussian horizontal and vertical concentration distributions). Here, H is the release height. The comparison showed good agreement, supporting the use of a bivariate normal elevated source dispersion model with both horizontal and vertical plume distribution standard deviations proportional to distance from the source and to

measured wind direction standard deviations in the horizontal and vertical, respectively, with a proportionality constant of 0.81 in both cases.

As mentioned previously, no measurements of the vertical angle of the wind were made during the Hanford elevated releases, but through the stability parameter z/L' for the 50 ft level, similarity theory predicts the vertical wind component standard deviation, σ_w, listed in Table 1.2. As with the horizontal plume growth, if we take

$$\sigma_z = \sigma_w t = \frac{\sigma_w}{\overline{U}} x, \tag{7}$$

the bivariate normal model gives at the point of maximum crosswind integrated exposure,

$$\sigma_{zm} = H \tag{8}$$

and

$$\frac{\sigma_w}{\overline{U}} = \frac{\sigma_{zm}}{x_m} = \frac{H}{x_m} \tag{9}$$

where H is the release height and x_m is the distance to the point of maximum. Figure 1.4 shows the values of H/x_m for each test plotted against the measured stability. The dashed curve shows the calculated $\sigma_w/\overline{U}$ as a function of stability, which is generally slightly higher than the observed H/x_m but which verifies Equation (9) quite well. The outstanding exception is Test 12, which was carried out the same day as Tests 10 and 11. The meteorological conditions changed very little through the day, with only a slightly increased instability expected through the series of three tests. However, the calculations gave a smaller value of $-z/L'$ for Test 12, so it is questioned that, in this case, the meteorological measurements in the lowest 50 ft used for calculating stability, were representative of the entire layer through which the plume was diffusing. The average ratio of H/x_m to $\sigma_w/\overline{U}$, excluding Test 12, is 0.88, agreeing quite well with Islitzer's ratio of 0.81 and with the average ratio of σ_{ym}/x_m to $\sigma_v/\overline{U}$ for the Hanford data shown previously to be 0.86. Thus, a simple relationship such as

Equation (5), with possibly a proportionality constant of 0.87 included, for the lateral plume spread and a similar expression for the vertical dispersion, will serve well to predict maximum exposures when used in the bivariate normal model.

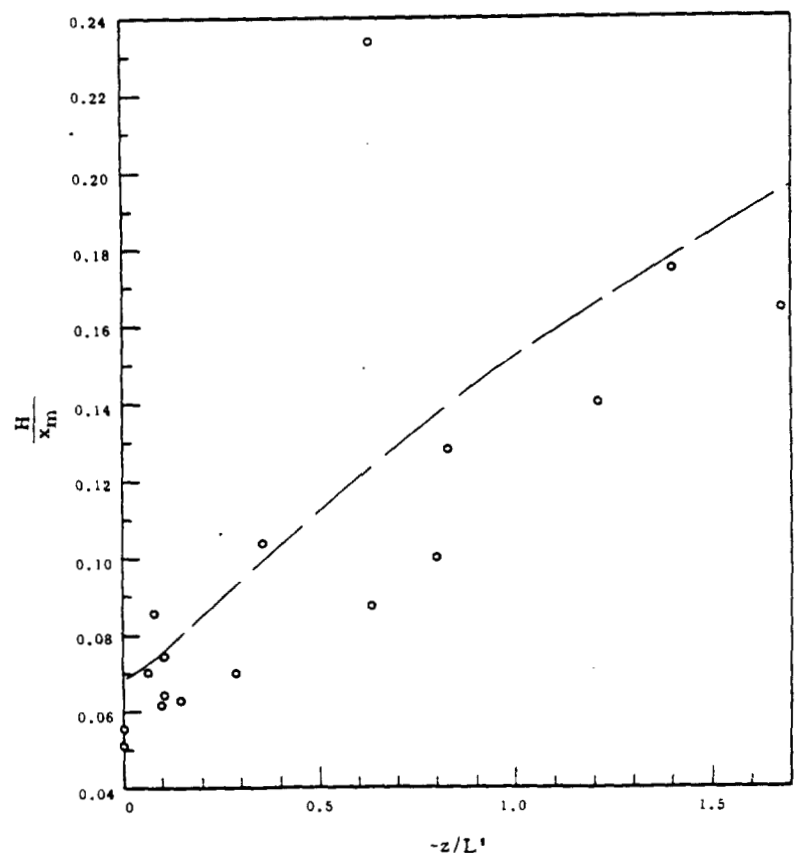

FIGURE 1.4

Distance to Maximum Normalized Crosswind Integrated Exposure as a Function of Stability

The curves for the crosswind integrated exposure, normalized to unit source strength and wind speed, versus distance, separate into the two stability groups: $-z/L' < 0.3$ and $-z/L' > 0.3$ as did the σ_y versus distance curves. The average values for these two groups and the data envelope for each group are shown in Figure 1.5. Though the two groups are distinctly separate, the averaging has flattened the curves so that they are not representative of the true shape of the normalized crosswind integrated

Neg. No. 0650409-4

exposure curves. Consequently, it is not surprising that while the assumption of σ_z proportional to x, works well in the bivariate normal model at the point of maximum for individual tests, this assumption does not give comparable results over the entire range of averaged measurements when used in the normalized crosswind integrated form of the bivariate normal model,

$$\frac{CIE\ \overline{U}}{Q_T} = \sqrt{\frac{2}{\pi \sigma_z^2}} \exp\left(-1/2 \frac{H^2}{\sigma_z^2}\right) \quad . \tag{10}$$

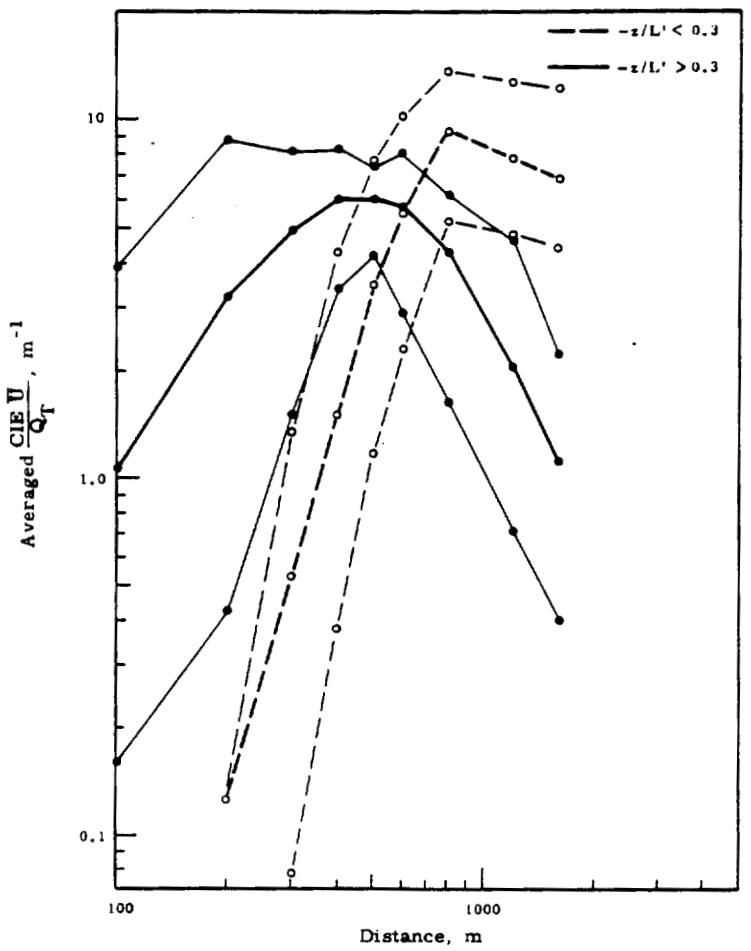

FIGURE 1.5

Average Normalized Crosswind Integrated Exposure Versus Distance

Neg. No. 0650409-17

Similarly, the curves of normalized peak exposure, $E_P\overline{U}/Q_T$, versus distance separate into two groups for $-z/L' < 0.3$ and $-z/L' > 0.3$. The averaged values for each of these groups are shown in Figure 1.6 with the data envelope for each group. Again, the averaged curves are flattened because of the data spread within each group, and the shape of these curves is not representative of the true shape of the peak exposure versus distance curves.

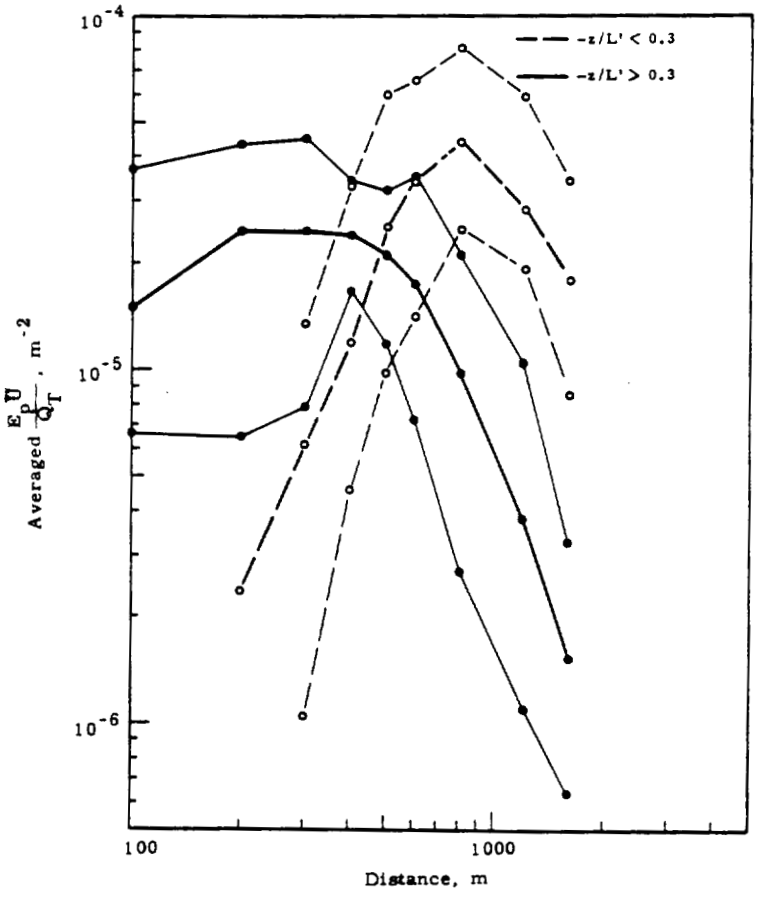

FIGURE 1.6

Averaged Normalized Peak Exposure Versus Distance

When plotted, versus time, the diffusion results present some clear advantages. The exposure measurements give a more unified picture when plotted together against travel time than appeared with the

Neg. No. 0650409-12

exposure plots versus distance even with the stability separation noted. The normalized crosswind integrated exposures and the normalized peak exposures for all tests are shown in Figures 1.7 and 1.8 as functions of the travel time determined from the wind speed at the 50 ft transport height.

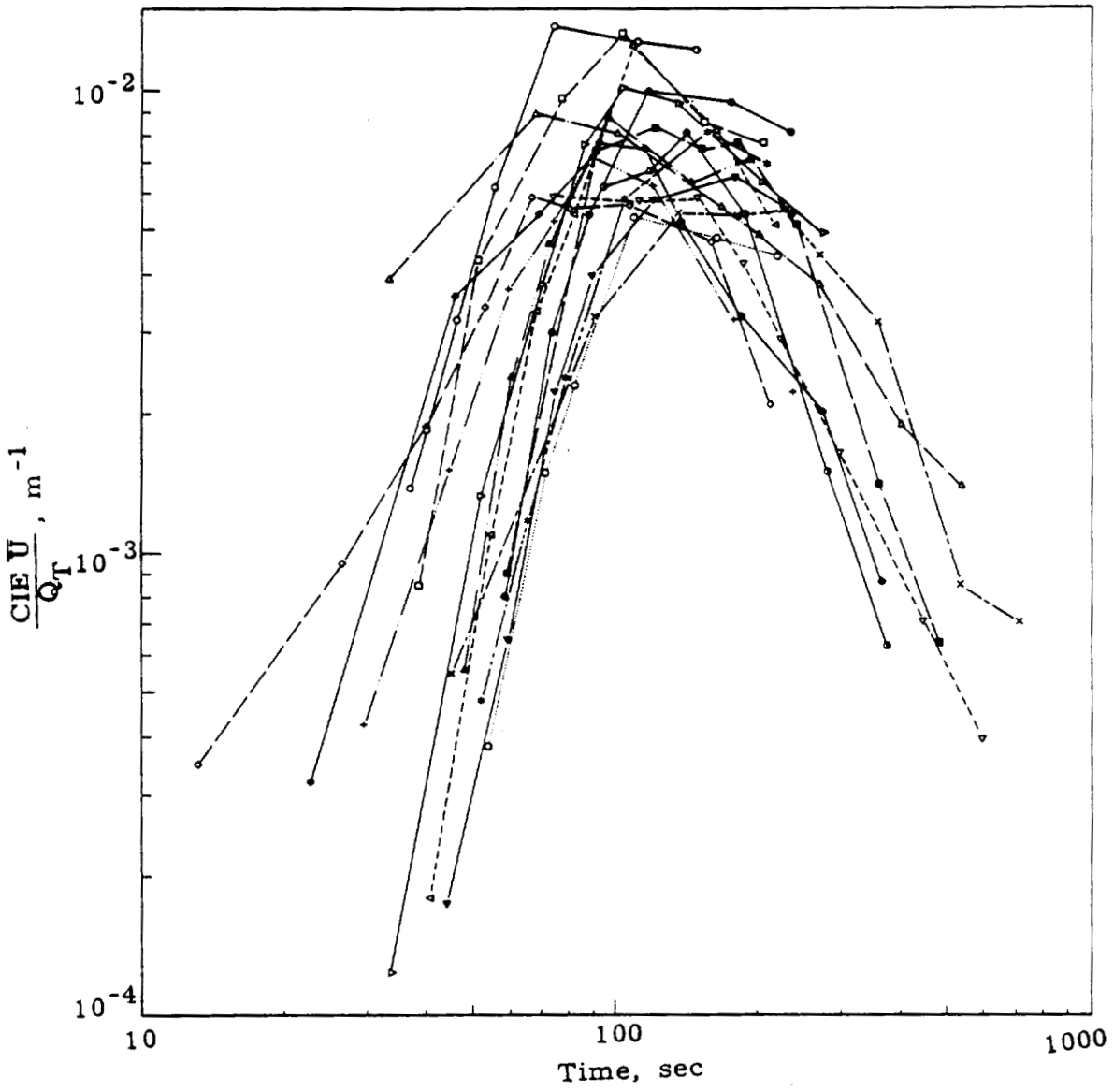

FIGURE 1.7

Normalized Crosswind Integrated Exposure
Versus Travel Time

Neg. No. 0650409-9

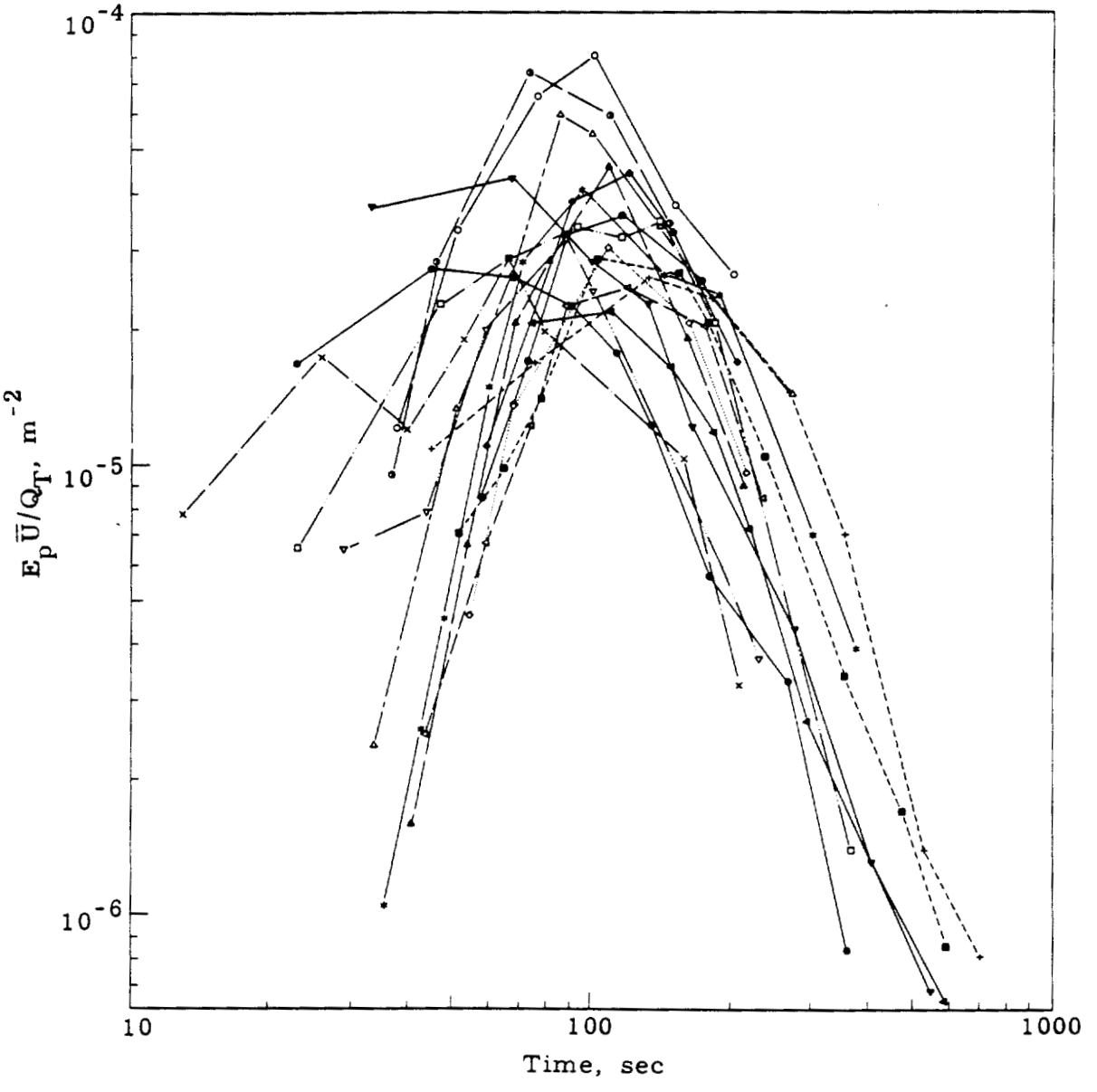

FIGURE 1.8

Normalized Peak Exposure
Versus Travel Time

It was mentioned previously that from Taylor's theory we would expect σ_y to increase as a function of time, proportional to σ_v. Only with a nearly linear increase of σ_y with time would it be advisable to organize

Neg. No. 0650409-6

σ_y measurements as a function of distance, proportional to σ_v. Such is the case for the distance range out to 1 mi covered in these tests. However, σ_y increases more closely proportional to $t^{0.9}$ so that, for the distance dependence plot, discrepancies increase as distance increases. Furthermore, there is nothing to assure us that the exponent of time will not soon decrease to a value of 0.5 eventually expected from the Taylor theory.

The lateral standard deviation of the plume, σ_y, organized as a function of travel time, can be separated into 3 groups for $\sigma_v < 1.0$ m/sec, 1.0 m/sec $\leq \sigma_v \leq 1.3$ m/sec, and $\sigma_v \geq 1.3$ m/sec (including Test 12) with average σ_v values of 0.86, 1.2, and 1.8 m/sec, respectively.

The averaged σ_y versus time curves and their envelopes are shown in Figure 1.9. The middle group contains the bulk of the data while each of the extreme groups contains four tests. Estimates of σ_y given by the Hay-Pasquill technique for computing lateral plume width from lateral wind component fluctuation data were compared with σ_y measurements. This technique, described in Reference (1.5), requires an assumed value of β, the ratio of the Lagrangian to the Eulerian scales. A value of $\beta = 1$ was first used to calculate σ_y. Then σ_y, predicted from the Hay-Pasquill technique was plotted against each measured σ_y in Figure 1.10. The bulk of the data falls only slightly below the dashed line, where perfect agreement would be indicated, so that generally σ_y is just slightly underestimated with $\beta = 1$ for this group of tests in unstable conditions. The averaged σ_y values predicted by the Hay-Pasquill technique are also plotted in Figure 1.9 for of the three σ_v groups. These would be shifted into almost perfect agreement with the observed $\overline{\sigma}_y$ versus t curves if, for the $\overline{\sigma}_v = 0.86$ m/sec group, $\beta = 3$, while for the $\overline{\sigma}_v = 1.2$ m/sec group, $\beta = 2$, and for the $\overline{\sigma}_v = 1.8$ m/sec group, $\beta = 1.2$ to 1.5 so that β decreases with increasing σ_v. The predicted σ_y curves would then show essentially the same dependence on $t^{0.9}$ over the range of coincidence; but, beyond the observed data, a continued slight reduction in the exponent of time is indicated for most of the tests.

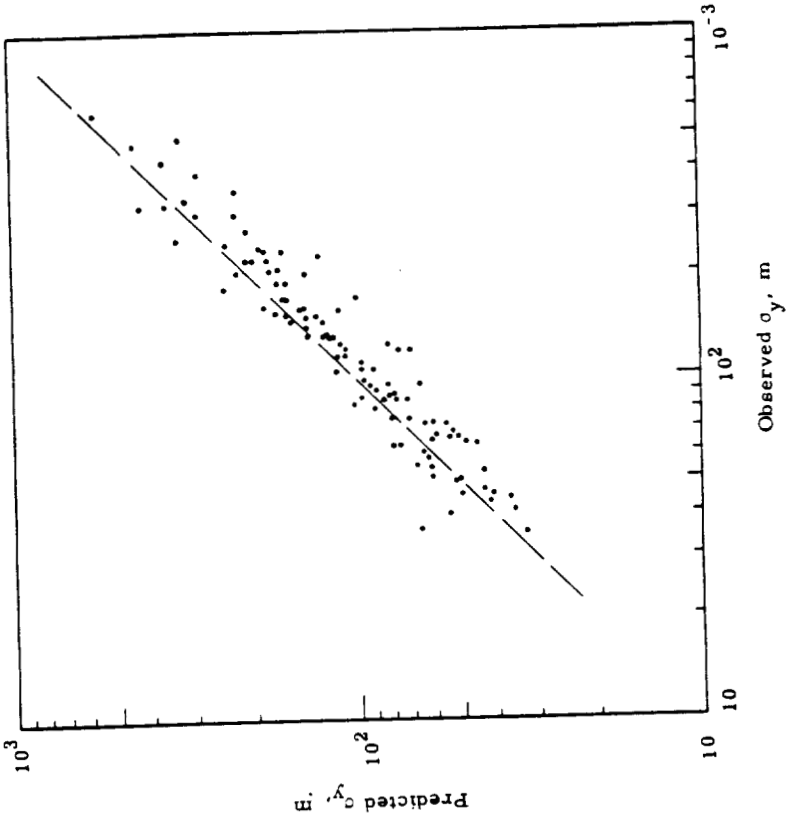

FIGURE 1.10
Comparison of Observed Lateral Plume Width to Plume Width Calculated from Smoothed Lateral Wind Fluctuation Data

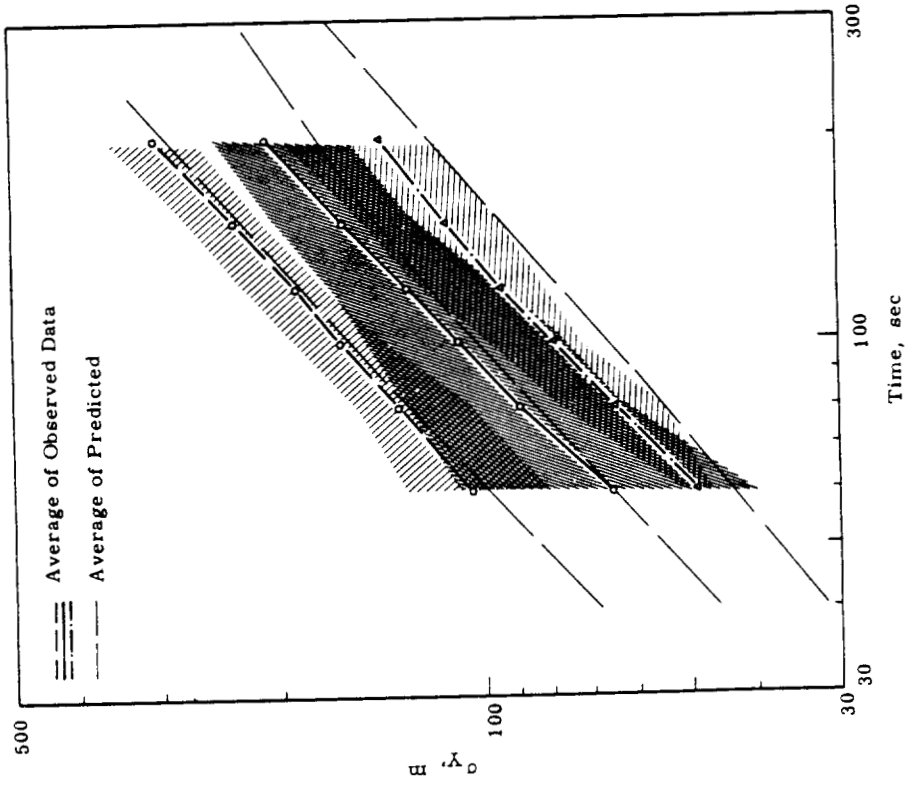

FIGURE 1.9
Averaged Standard Deviation of Crosswind Exposure Distribution Versus Travel Time

Neg. No. 065049-1; 0640409-11

0028165

The bivariate normal model shows the normalized crosswind integrated exposure CIE $\overline{U}/Q_T$ to be a function of σ_z only, so that the vertical plume spread can be investigated even though direct measurements of σ_z were not made. Again, the model gives at the point of maximum, $\sigma_z = H$ and with σ_z assumed proportional to travel time and σ_w, the unity of the CIE $\overline{U}/Q_T$ versus time curves demonstrates a rather small variation of σ_w for neutral through very unstable conditions. It was suggested earlier that the filtered longitudinal wind component standard deviation might be an easily measured good indicator of the vertical dispersion. In spite of the narrow range of σ_w, Figure 1.11 (showing H/t_m versus σ_{uHi} where t_m is the travel time to the point of maximum) supports the use of σ_{uHi} as an indicator for σ_w since $H/t_m = \sigma_w$ with the above assumptions.

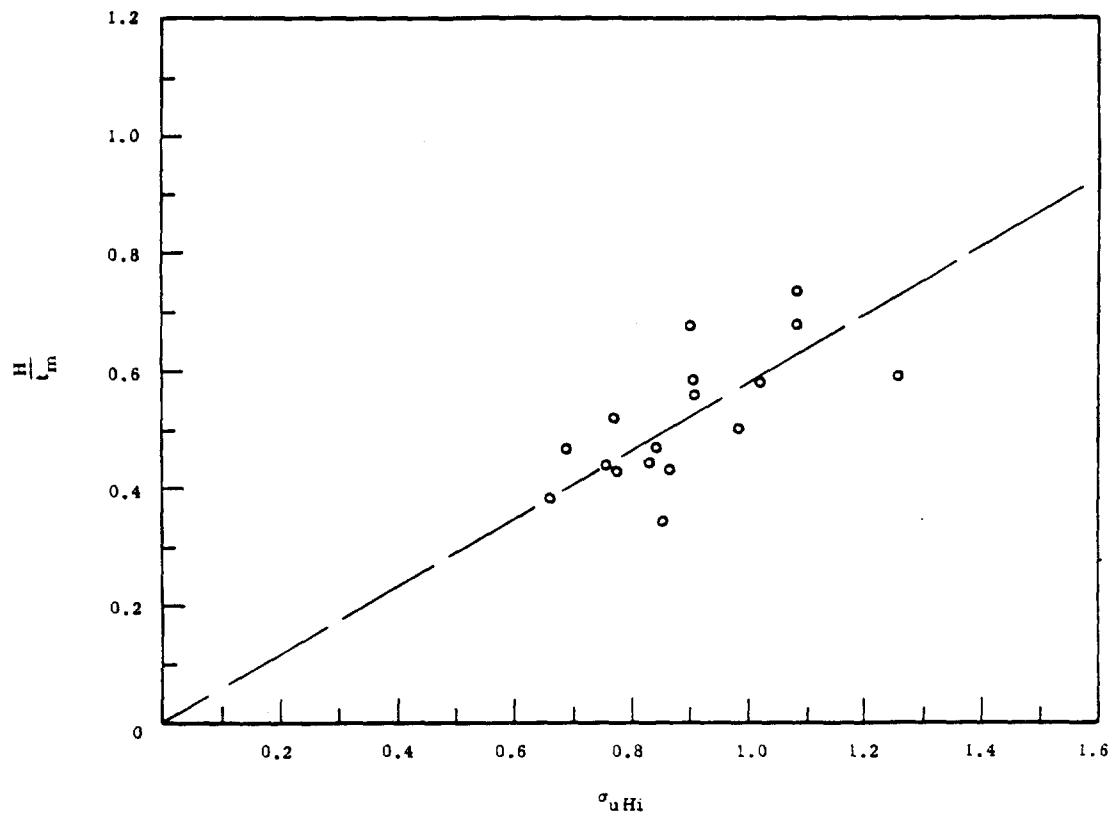

FIGURE 1.11

Travel Time to the Maximum Normalized Crosswind Integrated Exposure as a Function of the Standard Deviation of Longitudinal Wind Fluctuations with Low Frequency Oscillations Excluded

Neg. No. 0650409-16

Separating the CIE $\overline{U}/Q_T$ curves into two groups, for $\sigma_{uHi} < 0.88$ and $\sigma_{uHi} > 0.88$, the averages for each groups as well as the average for the entire series of tests is plotted against travel time in Figure 1.12. The average for the entire series had to be broken into two curves because only six of the curves extended to 350 sec and these were, on the average, slightly lower in normalized crosswind integrated exposure than the entire series of tests. The maximum values of the curves deviate by as much as 20% from the bivariate normal model maximum CIE $\overline{U}/Q_T$ value of 8.6×10^{-3}. However, the normalized crosswind integrated exposure expression from the bivariate normal model with an assumed linear increase of σ_z with time, when matched at the peaks of each of the three average curves of Figure 1.12, shows essentially the same shape as the experimental

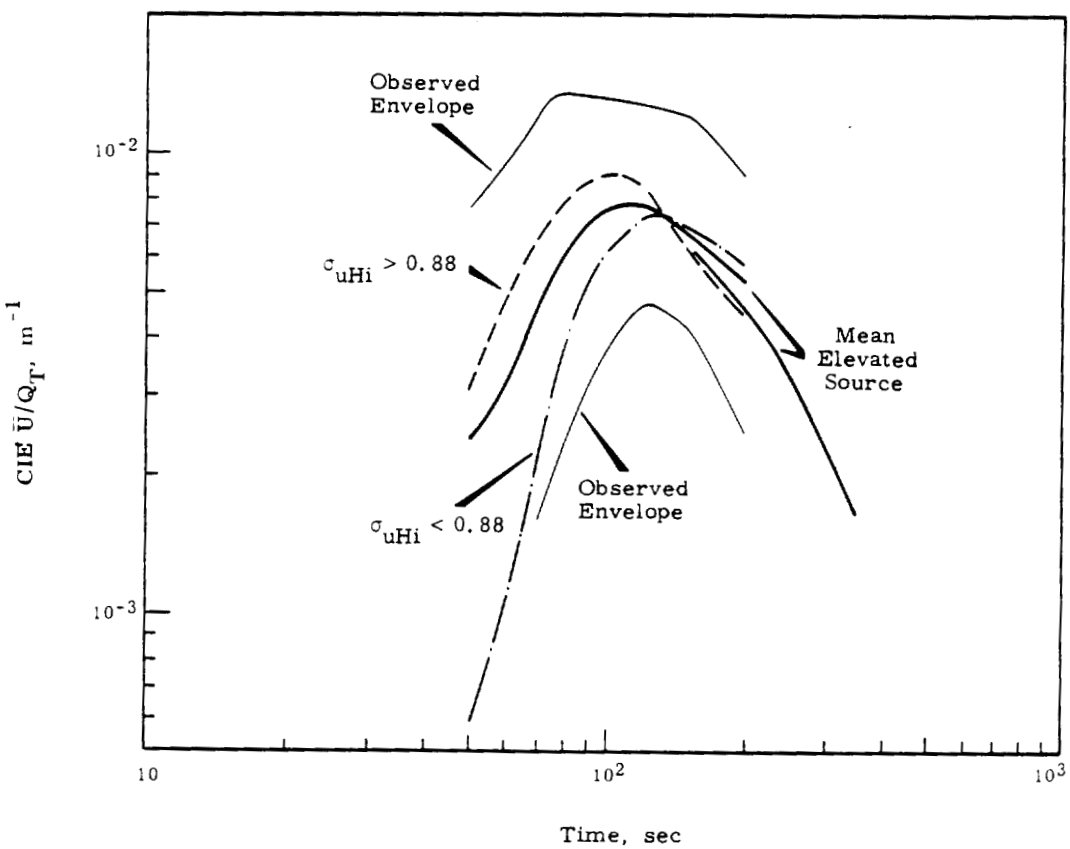

FIGURE 1.12

Averaged Normalized Crosswind Integrated Exposure Versus Travel Time

Neg. No. 0650491-4

0028167

values over much of the time range. For the curve representing the average of the entire series and that for the tests with $\sigma_{uHi} < 0.88$, the agreement is to within 10% over the range from about 65 to 200 sec travel time. For the $\sigma_{uHi} > 0.88$ curve, agreement is better than 10% from 65 sec out to 110 sec, just beyond the maximum. This confirms the use of the bivariate normal model and the assumption of σ_z proportional to time for elevated source diffusion in unstable conditions over a considerable range of travel time. Beyond the maximum, the experimental curves begin to show increasingly faster drop off in exposure than the bivariate normal model. This could possibly be due to the increasing interaction of the plume with the surface and the deviation from the form of the continuity equation used in the bivariate normal model, which does not account for tracer material deposited on the surface.

Summary

Measurement of the horizontal turbulence components at Hanford in neutral and unstable atmospheric conditions demonstrates features similar to those found at other sites. It is expected that diffusion results presented here are likewise not unrepresentative. For the short range diffusion tests performed, the lateral plume width increases nearly linearly with increasing travel time, proportional to the standard deviation of the lateral wind component fluctuations. The linear relation allows the data to be well organized as a function of distance with a stability separation noted primarily due to the correlation between wind speed and stability. Prediction of plume width is best accomplished through measurement of lateral wind fluctuations. The Hay-Pasquill running average technique works well in this respect, with best agreement indicated for an assumed β varying from 3 to 1.5 with increasing lateral turbulence.

Similarly, a linear increase in vertical plume width with increasing time, proportional to σ_w, allows the bivariate normal model to predict the occurrence of the maximum surface exposure quite well. The vertical wind variance, when not directly measured, can be adequately calculated for this

purpose from stability, wind speed, and roughness length. Alternatively, the vertical plume spread can be adequately indicated by easily measured longitudinal wind component variances about a running mean. This parameter stratifies the normalized crosswind integrated exposure versus time curves even though the data are well unified due to the relatively small variation of σ_w in neutral and unstable conditions. The exposure results, when plotted versus distance are widely spread, but separate according to stability, again primarily due to the correlation between wind speed and stability.

Atmospheric Turbulence Measurements - C. E. Elderkin

> A fast response turbulence sensor measuring the three components of the wind was used with a magnetic tape recorder to collect turbulence data at heights of 3 and 6 m. Measurements were made in both daytime and nighttime for periods of up to 1 hr. Analysis is being performed on an analog computer to obtain Reynolds' stresses as well as power-spectral estimates and cross-spectral estimates over frequencies from about 0.01 to 5 cps.

For atmospheric diffusion and transport processes to be understood adequately, there must be a clear understanding of the turbulence responsible for the diffusion and transport. Experimental turbulence studies have been undertaken at Hanford in the hope of eventually establishing diffusion models more firmly based on turbulence characteristics.

A turbulence instrument, originally designed by J. J. Fuquay has, in the last 2 yr, been improved by the Nucleonic Instrumentation Unit of Battelle-Northwest, and made compatible with a magnetic tape recording system for convenient acquisition and storage of large quantities of detailed turbulence data.

The turbulence sensor, termed the wind component meter, senses the three components of the wind at a given single point and produces continuous voltage signals related to the three spherical wind components. The speed signal, V, is a fluctuating dc signal resulting from a bridge, two legs of which are thermocouple wires heated by 610 cps current impressed across

0028169

the thermocouple wires at a very constant, controlled voltage. The thermocouples are suspended in and cooled by the air stream while the reference junctions formed at the mounting studs are maintained at ambient temperature. Another unheated thermocouple removes the fluctuations in the signal due to ambient temperature variation. The emf produced by this thermocouple arrangement is filtered to remove residual heating current and extraneous noise, amplified, and recorded on the tape recorder.

The inclination or vertical angle signal, φ, is also derived from heated thermocouple wires. These are inclined at 45° angles to the horizontal, forming a "V" in the vertical plane. The thermocouple output is zero for horizontal winds and varies positively and negatively for downward and upward gusts, respectively. This signal is also filtered to remove noise, then amplified and recorded.

The sensor head is continuously driven to remain oriented in the direction of the horizontal wind, keeping the wind normal to the speed sensing thermocouple wires at all times and keeping the wind in the plane of the vertical angle sensing "V"-shaped thermocouple arrangement. A second "V"-shaped arrangement of platinum wires in the horizontal plane provides an error signal to a servo amplifier and motor, which continually drives the probe to the null position, orienting the head into the instantaneous wind. A potentiometer is also connected to the shaft of the servo motor so a signal proportional to the horizontal angle, θ, is produced to be amplified and recorded with the other two spherical wind components.

Calibration of the wind component meter was accomplished first by comparing the speed signal with the standard cup anemometer at the Department of Atmospheric Sciences, the University of Washington, in their wind tunnel. The calibration curve gave a nonlinear relation between the instrument output and the true wind speed. Later, when the instrument was improved, a change in the probe heating current changed the wind speed signal from the previous signal level by a constant factor for all wind speeds. The new calibration was made by comparing wind component meter signals with those from recently installed Beckman and Whitley anemometers on the Hanford Portable Mast in near-laminar flow conditions.

0028170

Calibration of the vertical angle signal was performed in a small wind tunnel at Hanford made from a 6 in. diam plastic tube. The thermocouple head, which can be removed from the shaft of the wind component meter, was inserted into the tunnel and inclined at various angles to the air stream. The calibration tunnel is shown with the wind component meter probe in Figure 1.13. The resulting calibration curve again provided a nonlinear relation between the signal and the true vertical angle. The vertical angle calibration is a function of wind speed, and this dependence was also determined in the small wind tunnel.

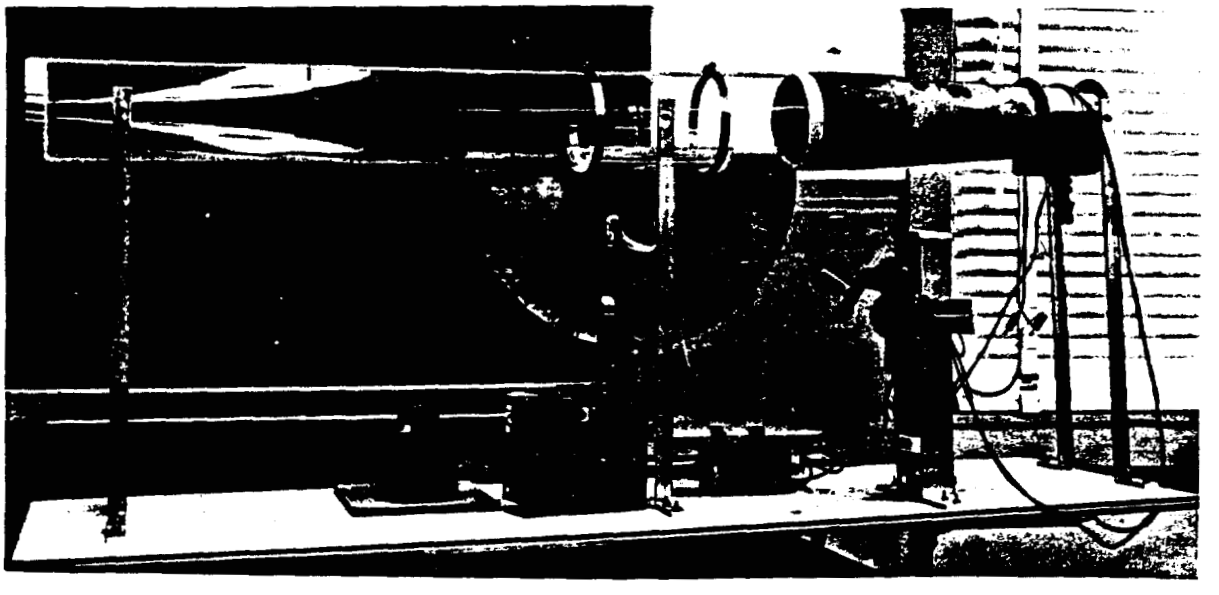

FIGURE 1.13
Calibration Tunnel
with Wind Component Meter Probe Inserted

The horizontal angle signal is linearly related to the true angle, and the constant of proportionality is established by the known voltage across the potentiometer providing the horizontal angle signal.

The response of the instrument has been tested by oscillating the probe head at known frequencies in the constant velocity air stream of the small calibration tunnel. The decrease in instrument outputs below the static calibration values as the frequency of oscillation was increased

provided the frequency response characteristics of the instrument. Fluctuations at frequencies below 3 cps altered the signals very little from calibration curve values, and correction for attenuation of power spectral estimates should be possible to frequencies at least as high as 5 cps.

The wind component meter is mounted on the Hanford portable micrometeorological mast so that simultaneous, mean wind and temperature profiles can be obtained to be related to the turbulence results. Figure 1.14 shows the wind component meter mounted on the portable mast with accompanying meteorological instrumentation. The wind component meter is to the right of the conventional wind vane.

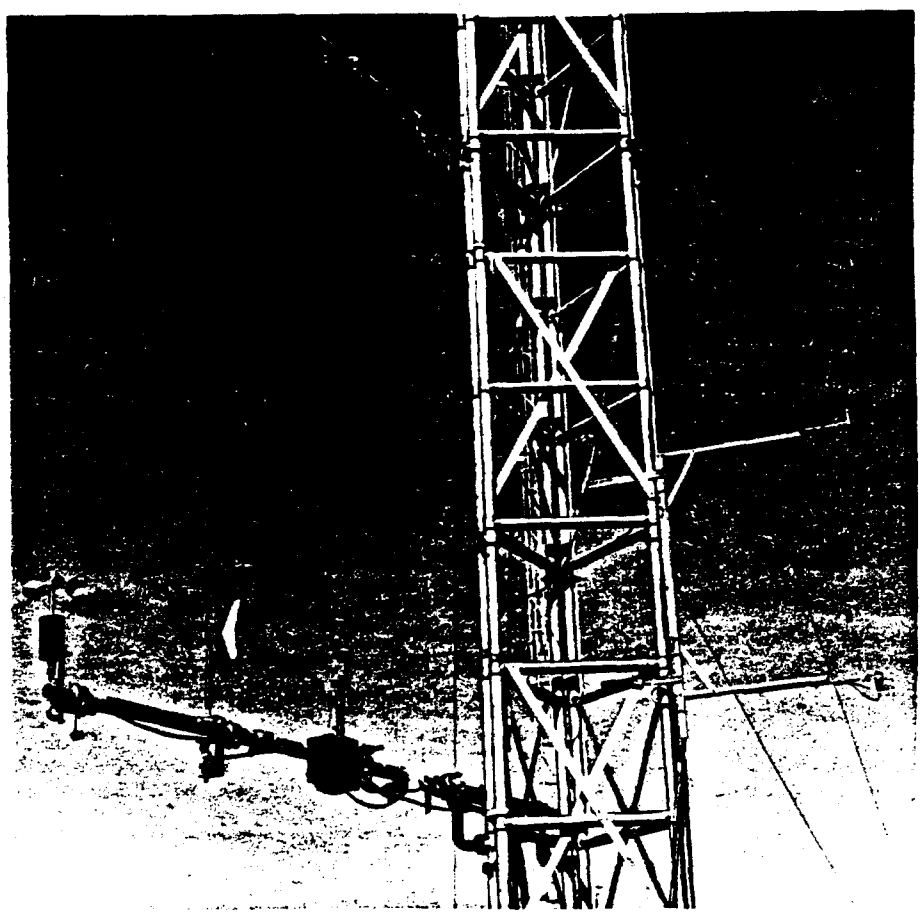

FIGURE 1.14

Wind Component Meter
Mounted on Portable Mast

A series of measurements was taken in July, 1964, in cooperation with the Department of Atmospheric Sciences, the University of Washington, who brought to Hanford instruments to measure turbulence and wind and temperature profiles. Measurements were taken with the wind component meter from the 3- and 6-m levels on the portable mast. Tests ranging from about 15 min to 1 hr were made in both daytime and nighttime. The data were recorded and stored on magnetic tape for later analysis on an analog computer.

The analog computation technique was chosen to allow analysis of the high frequency contribution to the turbulence while avoiding the tremendous sampling and data storage problem involved in the digital approach. In addition, the variations in the turbulence characteristics with time can be observed during the analysis, providing some insight into the effects of quasistationary turbulence and the representativeness of the final results.

The analog computer was first programmed to obtain from the tape recorded signals, voltages proportional to the turbulent fluctuation components in a Cartesian coordinate system oriented along the mean wind. The program provided for function generators, set up with the instrument calibration curves, to give voltages directly proportional to the spherical wind components. Resolvers then transformed the spherical coordinate components to Cartesian coordinates. These were integrated to give the average vector wind speed and direction for each test. The test was then reanalyzed, subtracting the mean direction from the incoming direction signal off the tape recorder so the coordinate system was reoriented along the mean wind direction. A constant voltage equal to the mean wind speed was then subtracted from the final longitudinal to component signal and the three continuous turbulence component signals, u', v', and w', where u' is in the direction of the mean wind and the others normal to it, were recorded on a second tape recorder. The analysis was performed at a faster tape playback speed than the original recording speed so that the data were compressed into 1/16 of the original time interval. Thus, the five-tape reels of raw data recorded during the field tests were analyzed to give the three

turbulence components recorded on less than 1/2-reel of magnetic tape. The speed-up compression of the data also serves to increase the frequencies of interest in the atmosphere to a range high enough for spectral analysis with filters on the analog computer.

The filter program provides power spectral estimates by filtering the data with band pass filters at 18 center frequencies, logarithmically spaced, squaring the filtered continuous signals and integrating. The data are played from the tape recorder into the filtering program at a number of speeds so that the same filters are used to obtain spectral estimates over a number of frequency ranges. The program has been tested and is expected to analyze wind component power spectra over a frequency range from about 0.01 to 5 cps. The transformed wind component meter data are presently being analyzed on this program.

Another program to calculate the total variance and covariance for the recorded wind components has been used to obtain the Reynolds' stresses for the tests conducted last summer. In this program, the wind component signals are first passed through a high-pass filter to remove residual dc levels in the signals and to filter trends and very low frequency oscillations which sometimes appear in the u' and v' data. The selection of the optimum filter for this function is somewhat subjective since the separation of the power in micrometeorological scale fluctuations from that due to mesoscale oscillations is not always clear cut. However, after a number of filters were tested on the data, one was selected to be included in the program which effectively removes the variance and covariance contributions due to oscillations with periods greater than about 9 min. The filtered wind component signals are then squared and integrated or cross-multipled and integrated. The final integrated values, divided by the time of integration, give the desired variances and covariances.

In addition to the analog computer analysis already tested and in use, another program to obtain cospectral, quadrature spectral, and power spectral estimates is planned, using a Fourier transform technique.

0028174

It should be possible to relate the Reynolds' stresses, obtained from the fluctuation data, to calculations made using the mean wind and temperature profiles. This study is planned for the near future as well as a second series of wind component meter measurements to extend the turbulence investigation to heights above the 3- and 6-m levels of the last series.

Area Dosage Relationships Downwind of a Point Source - P. W. Nickola and Naydene E. Nutley*

A relationship is developed between the value of a dosage isopleth downwind of a point source and the area enclosed by that isopleth. Equations describing this relationship are presented for stable, slightly stable, and unstable atmospheres. These equations for estimating area are improved by the inclusion of a wind speed in the dosage term. The choice of a representative wind speed is discussed.

These empirical equations are compared to similar equations previously developed, and implications of the differences are presented.

Introduction

The ability to predict the areal extent of specified dosages downwind of a pollutant source has important practical application, for example, to those who design, operate, or insure chemical or radiological installations in which routine or accidental discharges of noxious material must be considered.

Two previous attempts to define the area-dosage relationship will be reviewed. Modification of some of the previous data as well as presentation of some new data will be made in an effort to refine and extend the former results. Although the equations and conclusions developed offer no contradiction to theory, they are the result of empirical techniques.

Prairie Grass and Green Glow Experiments

Elliott[1.7] and then Elliott, Engelmann, and Nickola[1.8, 1.9] developed empirical relationships between area and dosage based on two series

* Department of Atmospheric Sciences, University of Washington.

of diffusion experiments conducted in 1956 and in 1959. The "pollutant" source in these studies was a point source located near ground level. The 1956 experiments, referred to as the Prairie Grass experiments,[1.10] were conducted near O'Neill, Nebraska over a flat grassy surface. Sulfur dioxide tracer was released from a source 0.5 m above ground level and was collected on an array of samplers located 1.5 m above the ground. The sampling network was laid out in five concentric semicircles whose radial distances from the source were 50, 100, 200, 400 and 800 m.

The 1959 diffusion experiments, nicknamed Green Glow,[1.11] were conducted at Hanford. Here the primary vegetation is sagebrush, 1 to 2 m high. The area is relatively flat but is not so smooth as the Prairie Grass site. The tracer used was fluorescent zinc sulfide particles with a geometric mean particle diameter of about 2.3 μ. A network of samplers, 1.5 m above ground level, was laid out in six arcs concentric about the source. Arc radii were 200, 800, 1600, 3200, 12,800 and 25,600 m from the source. Inasmuch as this present paper deals primarily with results of experiments made at Hanford, further details on the field course layout and sampling techniques will be presented later in the discussion.

Definition of Terms

Dosage (D) is defined in this paper as the mass of tracer collected divided by the flow rate through the collector. The units of dosage are gram-seconds per cubic meter. The term exposure is sometimes used instead of dosage. In this paper, the term dosage is used to maintain continuity from the previously referenced area-dosage studies.[1.7, 1.8, 1.9] Multiplication of dosage by a sampling rate gives the units of mass. For example, dosage times inhalation rate gives the mass of material to which a subject respiratory system would be exposed.

Ohe physical parameter of concern in diffusion studies is the atmospheric stability. Under relatively stable conditions, the atmosphere tends to dampen out vertical motions, and thus inhibits mixing. Under relatively unstable conditions, the atmosphere tends to augment vertical motions, and thus enhances mixing.

Two factors indicative of the relative stability of the atmosphere are the vertical temperature gradient and the vertical wind speed gradient. Other conditions being held constant, the greater the temperature decrease with height, the more unstable the atmosphere (lapse condition). Conversely, the smaller the temperature decrease or the greater the temperature increase with height (inversion condition) the greater stability. If one considers the vertical wind speed gradient alone, diffusion will occur more rapidly when the wind speed changes rapidly with height than when it changes slowly.

These two factors can be combined in many different ways, resulting in numbers which are measures of relative atmospheric stability. One of these combinations is the Richardson number,[1.12] Ri. Ri is defined as

$$Ri = \frac{2g\, z_{1.2}(\theta_2 - \theta_1) \ln n}{T_2(u_2 - u_1)^2}$$

g = acceleration of gravity, cm-sec^{-2}

$z_{1.2}$ = geometric mean height of levels z_1 and z_2, cm

θ = potential temperature, K

$n = \sqrt{\frac{Z_2}{Z_1}}$

T = temperature, K

u = wind speed, cm-sec^{-1}.

Ri is a measure of convective stability and is zero for adiabatic or thermally neutral stratification, negative for unstable thermal stratification (lapse), and positive for stable thermal stratification (inversion). Values for z_1 and z_2 were 2.1 and 15.2 m, respectively, in the present study.

Elliott, in his Prairie Grass Analysis, and Elliott and Nickola, in their analysis of Hanford Green Glow data, used the stability ratio, instead of Richardson number in their division of the data into stability groups. The stability ratio is defined as

0028177

$$\text{Stability Ratio} = \frac{T_3 - T_1}{u_2^{\,2}}$$

where T is temperature, u is wind speed and the subscripts refer to elevations in units of meters. As with Ri, increasing values indicate increasing stability and vice versa. The chief appeal of the stability ratio is its ease of calculation. One of its main drawbacks is its great sensitivity to the level chosen for measuring the wind speed.

Field Design and Procedure

With the exception of the Prairie Grass data, all other data considered in this and the referenced area-dosage studies were generated from field experiments on the Hanford sampling grid. The grid is laid out in a direction which takes advantage of high wind direction frequency. The sampling grid is superimposed on a relief map of the Hanford area in Figure 1.15. The area is relatively flat, dropping about 300 ft in the 16 mi from the source to the most distant sampling arc.

The tracer employed in Hanford field diffusion experiments is a fluorescent zinc sulfide powder. The powder is designated as Pigment No 2210 by the manufacturer, U. S. Radium Corporation. The pigment size distribution is log-normal with a geometric mean diameter of 2.3 μ.

The dispersal of the tracer to the atmosphere entails the suspension of insoluble zinc sulfide particles in a tank of water and subsequent regulated dispersal of the atomized tracer slurry by a conventional insecticide spraying apparatus. The water droplets evaporate to leave individual tracer particles suspended in the atmosphere. To assist in this evaporation, hot gases from a combustion chamber are mixed with the water droplets at release.

To minimize impaction of the droplets on sagebrush near the generators, the exit nozzles are pointed slightly upward. The result is an effective source height of about 4 m. During the subject experiments, tracer generation generally lasted 30 min. The duration increased to as long as 1 hr on some occasions when favorable meteorological conditions persisted.

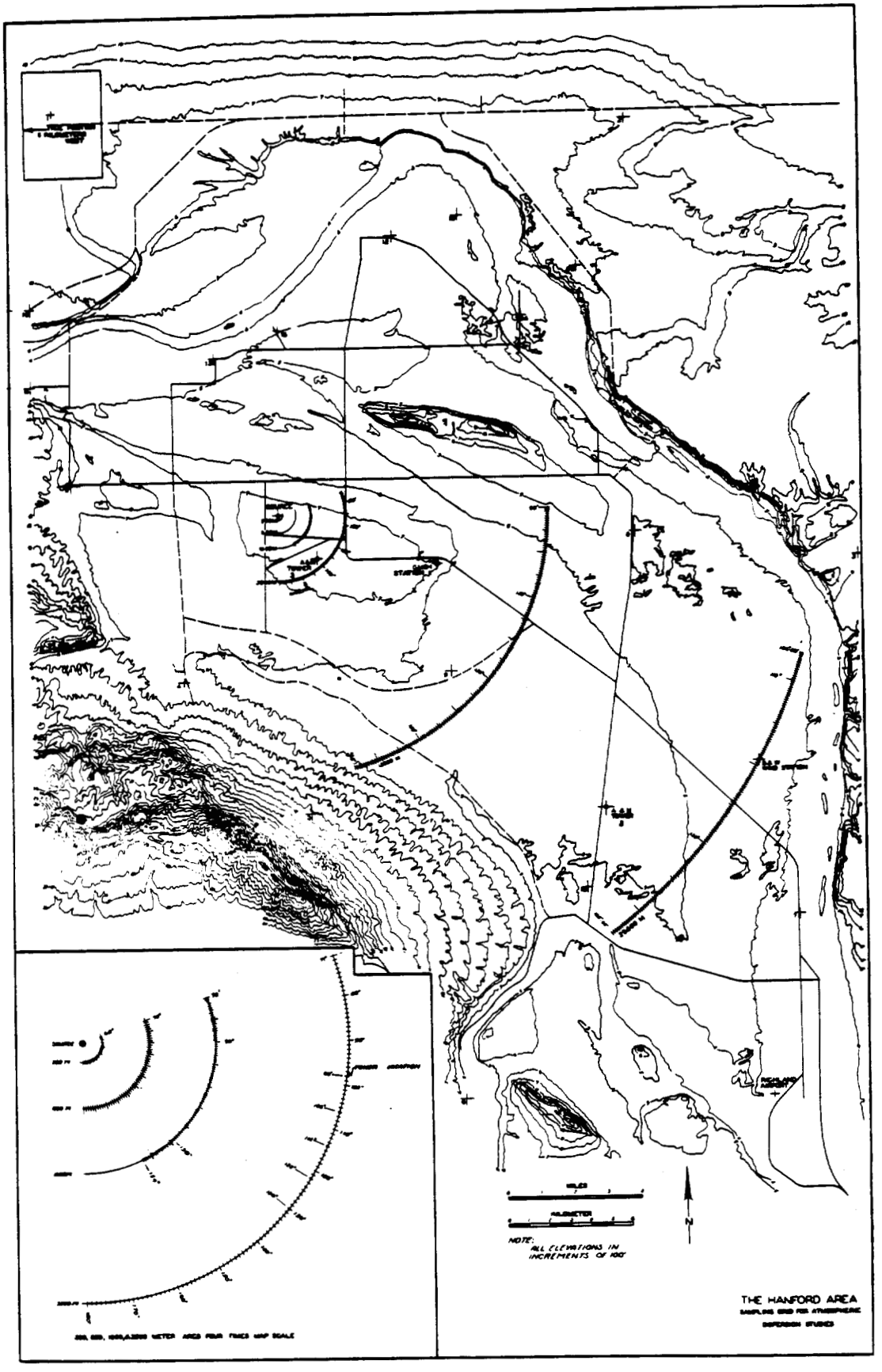

FIGURE 1.15

Hanford Area and Sampling Grid

Neg. No. 0650288-1

0028119

The pigment was collected on membrane filters of 47 mm diam. These filters were exposed at an elevation of 1.5 m along 6 arcs concentric about the tracer source. Characteristics of the sampling network are listed in Table 1.3. Spacing of samples varies with distance from the source to permit a detailed crosswind structure at each sampling arc. To offset partially the effect of decreasing concentrations with distance, flow rates are markedly increased at the outer arcs.

TABLE 1.3

CHARACTERISTICS OF SAMPLING NETWORK

Arc	Distance from Source		Sampler Spacing		Arc Length, degrees	Flow Rate, liters/sec
	Kilometers	Miles	Degrees	Meters		
1	0.2	0.12	2	7	90	0.148
2	0.8	0.50	2	28	90	0.153
3	1.6	0.99	1	28	48 to 84[a]	0.232
4	3.2	1.99	1	56	90	0.513
5	12.8	7.95	0.5	112	75	1.963
6	25.6	15.91	0.25	112	37.25	1.980

(a) Arc length increased during field experiment series.

Although of small consequence in the collection of data for this study, a vertical array of samplers also was exposed on a network of 20 towers. Towers ranged in height from 27 m on Arc 1 to 62 m on Arc 4. No vertical sampling was attempted on Arcs 5 and 6.

Assay of Field Samples

The great majority of field sample filters were assayed by the "Rankin counting method."[1.11] This method employs an alpha emitter to excite the fluorescent particles and the resulting photon emissions are counted by a multiplier phototube. The technique is that of scintillation counting except that the strength of the radiation source remains constant and the amount of scintillator (zinc sulfide tracer) varies. Rankin counters have been calibrated in terms of scintillations versus mass of zinc sulfide. Standard error at low counting rates is 10%; at higher counting rates it diminishes to 3%.

In some instance the high flow rates at the 12.8 and 25.6 km arcs resulted in significant amounts of foreign matter from the atmosphere being deposited on the membrane filters. The foreign matter partially obscured

any zinc sulfide from alpha bombardment in the Rankin counters. Assay of these "dirty" filters was accomplished by dissolving the membrane filter, exposing the suspended tracer and dirt to white light, and then measuring the resulting phosphorescence in a liquid scintillation counter. The measured phosphorescence was corrected by a factor determined from turbidity measurements with a colorimeter. Calibration procedures gave curves necessary to convert the resultant corrected phosphorescence to mass of the tracer. Assay of filters by this modified liquid scintillation technique entails a standard error of about 20%.

Method of Analysis

For each field experiment, values of dosage were plotted for each field filter. Plotting was done on grids identical (except in size) to those in Figure 1.15. The maximum value of dosage (D) on each arc was selected, and isopleths were drawn with the aid of corresponding dosage values on arcs closer to the source. The area (A) within each isopleth was determined by use of a planimeter.

Since differing amounts of tracer were released during different field runs, observed values of peak dosage were divided by the total amount of pigment emitted (E). It had been demonstrated in the previous area-dosage work, and from examination of theoretical equations developed by Sutton,[1.13] that the prediction technique could be significantly improved if a wind speed factor were included. Thus, the values of D/E were multiplied by a mean wind speed (U). (The choice of elevation and location of wind speed to be used are discussed later.) The resulting values of normalized dosage (DU/E) were then plotted on logarithmic paper against the isoplethed area enclosed by the selected dosage value.

In plotting, the data were grouped into three stability classes according to Richardson number. Field runs during which $Ri > 0.08$ were considered stable; if $0.08 > Ri > 0$, runs were considered slightly stable; and if $0 > Ri$, runs were considered unstable. Winds and temperatures used in the calculation of Ri were averaged over the release time for each run. Heights of 2.1 and 15.2 m were used for z_1 and z_2, respectively. The data were

taken from a 400 ft instrumented tower located 100 m from the source. The choice of stability class limits was consistent with limits used in previous Hanford studies.[1.14]

Data used in formulating area-dosage relationships for this paper were generated during 50 field experiments carried out between July, 1959, and August, 1962. Of this total, 20 runs were carried out during the Green Glow program. All data employed for arcs at 12.8 and 25.6 km originated during the Green Glow series (1959). All runs in the unstable category were carried out in the post Green Glow period, and as such are completely new data. The stable and slightly stable results reported come from a mixture of Green Glow and post Green Glow experiments. As will be discussed shortly, all data–including those generated during the Green Glow program–have been reanalyzed.

Comparision of Isoplething Differences

Inasmuch as there is a distinct element of subjectivity involved in the isoplething procedure, it was decided to compare the areas isoplethed and planimetered by Nutley in the present case with those previously reported by Elliott and Nickola in their analysis of Green Glow data. Although Elliott and Nickola based their results on isopleths dictated by peak dosages at distances of 1.6, 3.2, 12.8, and 25.6 km from the source, the raw data for the 1.6 km distance were not located. Thus, isopleth comparison was necessarily limited to three distances. Considerable disagreement between the two sets of areas was found as is shown in Table 1.4.

TABLE 1.4

RATIO OF ISOPLETHED AREAS FOR 14 GREEN GLOW RUNS
(Nutley to Elliott-Nickola)

Isoplethed Distance, km	Mean Ratio	Mean ± Standard Error
3.2	1.14	0.90 to 1.44
12.8	1.40	1.11 to 1.78
25.6	1.25	0.88 to 1.67

The figures in the table show, for instance, that Nutley's values for isopleths to 3.2 km average 1.14 of Elliott-Nickola's, and approximately two-thirds of the time they fall between ratios of 0.90 and 1.44. Except for 3.2 km, the average discrepancy is greater than the "within 20%" reported previously by Elliott and Nickola.

Since the disagreement in the comparison was so large, a further check of Nutley's isopleths seemed in order. The two Green Glow field runs in which the Nutley to Elliott-Nickola area ratios were the lowest (Run 5) and highest (Run 13) were selected and independently isoplethed by four other members of the Hanford Meteorology research team. They were not instructed as to how to isopleth, nor were they told beforehand of the mentioned Nutley to Elliott-Nickola area ratios. Table 1.5 presents the results of this comparison.

TABLE 1.5

RATIO OF ISOPLETHED AREAS FOR GREEN GLOW RUNS 5 AND 13
(Nutley to Mean of "Others")

Isoplethed Distances, km	Ratio	
	Run 5	Run 13
0.2	(1.35)	1.15
0.8	0.96	1.05
1.6	0.92	1.07
3.2	1.02	1.00
12.8	0.99	1.20
25.6	(0.78)	0.95

With but the two exceptions indicated by the parentheses, the Nutley to "others" ratios are within 20% of perfect agreement. Since only two ratios for each distance were made, no standard errors were computed. In any event, for these two cases in which Nutley might have been expected to be at her worst (suggested by the disagreement with Elliott-Nickola) she is not generally in serious disagreement with the other isoplethers.

A better indication of the subjectivity involved in isoplething to the peak value at specific distances can be obtained. This estimate is given

by the standard error of area for the five analyses (Nutley and the four "others") for each arc and run. These values are given in Table 1.6.

TABLE 1.6

STANDARD ERROR OF ISOPLETHED AREAS FOR GREEN GLOW RUNS 5 AND 13

Isoplethed Distance, km	Standard Error, % Run 5	Run 13
0.2	35	24
0.8	9	8
1.6	10	6
3.2	4	8
12.8	6	20
25.6	23	15

The greatest disagreement among analysts is for the 0.2 km distance. This is understandable inasmuch as this area is isoplethed from only two data points: the source and peak dosage value at the 0.2 km sampling arc. This procedure is not as absurd as it may seem at first glance, since considerable guidance is given by the shape and gradient of isopleths drawn to the more distant sampling arcs. But again on the debit side, the scale of grid used in the isoplething resulted in planimetering of areas of less than 1 in.^{2} for the 0.2 km distance. Therefore, small differences in planimetering contribute greater differences in computed areas.

Isoplething to distances of 0.8, 1.6, and 3.2 km was relatively straightforward because of the density of dosage values to which to isopleth and since the experimental technique here gave data points in which high confidence could be placed. Additionally, consistent meteorological conditions generally prevailed during the time interval required for the tracer to traverse through these distances. The result is a smooth series of isopleths. Nutley and Elliott-Nickola as well as Nutley and "others" find their best agreement at these distances.

At the relatively great distances of 12.8 and 25.6 km there is frequently a change in meteorology during the time the tracer is in transit. Terrain effects, known or unknown, have more space and time to disrupt the idealized smooth isopleths. The low concentration of tracer at these greater distances results in more difficulty in determining dosages. The lack of a 6.4 km sampling arc from the radial logarithmic space of the sampling arcs leaves a "hole" in the plotted dosages. All of the preceding factors tend to degrade one's ability to precisely isopleth at the two most distant sampling arcs.

Nutley is in considerably better agreement with the areas determined by the "other" Hanford meteorologists than she is with the areas previously reported by Elliott and Nickola. It is felt that the Nutley areas are more representative of the true areas. One reason for the difference in areas may be that Elliott and Nickola drew smoothed idealized ellipses, while Nutley tried to draw more closely to the plotted data points. Despite the drawbacks mentioned in the preceding paragraph, Nutley placed more confidence in the individual dosage values reported at the 12.8 and 25.6 km arcs than was assumed in the previous papers. It was felt that continued success of the Hanford fluorescent tracer technique for several years since the previous papers justified the added confidence in the data. In addition, as will be described later, detailed consideration of the meteorology at these greater distances during the time the tracer was in transport showed that the dosage data appear reasonable.

Wind Speed Variability

As mentioned, the empirical formulas used for estimating the areas within dosage isopleths are improved by the inclusion of the wind speed in the dosage term. In previous analyses of the area-dosage relationship, wind speeds have been taken from measurements made at the source. Winds measured near source heights have generally been used except for Elliott and Nickola's 1961 analysis in which they used winds at a height of 16 m with an effective source height of about 4 m. In the present study,

winds measured at the 2 m level near the source were first used in computing DU/E. A discontinuity in the plotted DU/E versus A values resulted. The authors feel that this same sort of discontinuity is suggested by an examination of points generated in the previous Green Glow area-dosage studies.

It seemed possible to the authors that a more sophisticated choice of mean wind speed (U) could be made. If U is to be used in the calculations, an attempt should be made to use a wind speed that comes as close as possible to representing the wind that actually is responsible for the observed distribution of the pigment.

Several attempts were made to find more representative values of U. The variability of wind speed with height was taken into consideration in the first attempt. When the pigment is released at the source, some of it diffuses upward and thus is transported downwind at a higher level than the source height. Since the wind usually increases with height, this would indicate that the pigment should arrive at distances down course before it would have had it been transported by the source-level wind only. Experiment has shown this to be true.[1.8] Engelmann predicts that on the average a wind speed at an elevation somewhere between 50 and 100 ft is necessary to specify the time of arrival on the 12.8 km arc. Could this choice of U apply to a plume centroid as well as to time of arrival? Wind measured on a 400 ft tower near the source offered such a choice.

Inasmuch as a smoothing of the discontinuity in the plotted data required a lessening of the DU/E values, the effect of a choice of a higher value for U at 12.8 km was the opposite to that which seemed reasonable. From a total of 19 Green Glow runs in which 12.8 km data were available, only three found improvement in the "straightness" of plotted data by substituting the 100 ft wind for the 2 m source wind. Thus, it was concluded that the 100 ft wind speeds are generally too high to represent the average wind responsible for the distribution of the tracer.

0028186

Before choosing another set of U's to run through the exposure calculations, the authors decided to look in detail at wind patterns for the Green Glow runs. To get an idea of the spatial as well as time variability of the wind, U versus time graphs for the 2 m winds were plotted for the source and for A&M Towers 1 and 2 (see Figure 1.15 for location of A&M Towers). Generally, there appeared to be a good correlation among the different stations in the variation of wind speed with time. In the stable cases considered, the wind speed remained relatively constant with time, while in seven out of the nine slightly stable cases, there was a marked decrease.

Also, there is a relationship between stability and wind speed variability. We can look at this in a more quantitative manner by comparing the constancies (c) of the wind for the runs in question. Constancy of the wind is defined by Engelmann as the maximum number of successive 20-sec intervals in a 20 min period in which the mean wind speed did not change as much as 1 mi/hr. c, Ri, and field run numbers are listed in Table 1.7. Except for Run 21, we find values of c of 6 or below for the slightly stable cases. For the stable runs, we find values of c greater than 8 with the exception of Run 8. Thus, we can see that generally the stable runs are associated with periods of more constant winds.

An investigation was then made of the spatial variation of wind speed. Table 1.7 compares the average 2 m wind speed taken near the source with that from A&M Tower 2. The comparison was drawn between the source and A&M Tower 2 winds to isolate the spatial effect as much as possible. If A&M Tower 3 wind speeds had been used, other factors such as the choice of time periods would have become important. Evidence in Table 1.7 shows that the wind speed usually decreases downwind in slightly stable cases and remains essentially unchanged in the stable cases.

In summary, all of the above data on time and spatial variation give a general impression of what the overall wind patterns were and how they differed between the stable and the slightly stable cases. In stable cases, we find only small wind speed variation in time and space. In most of the slightly stable cases, we find a marked decrease in the wind speed down course.

0028187

TABLE 1.7

WIND CONSTANCY DURING GREEN GLOW FIELD RUNS AND WINDS AT 2 m AVERAGED OVER THE HOUR FOLLOWING ONSET OF RELEASE

	Ri	c	Run	(A) Source, m/sec	(B) A&M Tower 2, m/sec	(B)-(A)
	0.011	6	19	5.3	5.2	-0.1
	0.028	4	25	4.9	4.4	-0.5
	0.031	3	22	4.9	4.3	-0.6
Slightly Stable	0.031	6	18	4.4	2.7	-1.7
	0.032	3	17	3.9	4.4	0.5
	0.037	5	10	5.9	4.9	-1.0
	0.049	4	6	4.2	2.7	-1.5
	0.067	9	21	4.1	3.3	-0.8
	0.078	3	13	3.6	4.8	1.2
					Mean	-0.5
	0.083	6	8	2.6	2.9	0.3
	0.097	24	5	1.9	1.8	-0.1
	0.112	12	9	2.7	2.6	-0.1
Stable	0.119	18	7	1.5	1.5	0
	0.121	17	12	2.0	2.3	0.3
	0.198	9	11	1.4	1.6	0.2
	0.247	11	15	1.8	1.8	0
	0.289	26	14	1.4	1.6	0.2
					Mean	0.1

In view of the observed variations, it was decided that the best choice of U would be one that took into account both the time and space variability of the wind. To allow for spatial variations, the source 2 m winds were used for the arcs at 0.2, 0.8, 1.6, and 3.2 km while the A&M Tower 3 wind at 2 m elevation were used for arcs at 12.8 and 25.6 km.

To make allowances for the time variation of wind speed, three different time periods for averaging the wind speed data were chosen. Wind speed data were averaged over the hour following the release time of the pigment for the inner four arcs. For arcs at 12.8 and 25.6 km, the beginning of the time period was chosen by adding the travel time (to the arc under consideration) to the time of first release of the tracer. A&M Tower 3 wind speed data were then averaged for 1 hr following that time. The tracer travel time was computed by Engelmann[1.15] based on a network of wind stations located in the Hanford area.[1.11] These wind station locations are indicated by a plus sign (+) and an adjacent number on Figure 1.15.

Table 1.8 lists field run numbers, Engelmann's travel times, the time periods used, and the average wind at 2 m for that time period as reported by A&M Tower 3.

TABLE 1.8

TRAVEL TIMES, TIMES PERIODS, AND WIND SPEEDS FOR ARCS AT 12.8 AND 25.6 km

	12.8 km Arc				25.6 km Arc			
Run	Travel Time, min	Time Period, From	To	U_{2m}, m/sec	Travel Time, min	Time Period, From	To	U_{2m}, m/sec
5	105	2305	0005	2.11	211	0051	0151	1.93
6	48	2305	0005	2.05	111	0008	0108	1.68
7	96	2337	0037	1.14	166	0047	0147	0.86
8	68	2308	0008	1.61	154	0034	0134	0.97
9	71	0035	0135	2.61	140	0144	0244	2.19
10	32	2233	2333	3.14	84	2325	0025	1.51
11	123	0003	0103	1.20	No travel time data			
12	91	0146	0246	1.14	No exposure data			
13	63	2333	0033	1.22	131	0041	0141	1.33
14	113	0158	0258	1.30	No wind speed data			
15	82	0132	0232	2.45	169	0259	0359	2.74
17	42	2212	2312	2.93	107	2317	0017	2.30
18	49	2234	2334	2.16	119	2344	0044	1.04
19	37	2222	2322	3.01	87	2312	0012	3.12
21	47	2155	2255	1.52	121	2309	0009	2.58
22	39	2129	2229	3.45	85	2215	2315	2.87
23	No exposure data				No exposure data			
24	No travel time or exposure data				No travel time or exposure data			
25	45	2255	2355	4.73	78	2328	0028	4.84
26	No exposure data				No exposure data			

Using the values in Table 1.8 for U, the "straightness" of the regression lines for individual runs was improved for 14 out of the 17 cases at the 12.8 km arc. The three cases in which U's from Table 1.8 did not help were all stable. Locations for the 25.6 km points were "improved" in 12 out of 14 cases. The two locations not improved occurred in stable cases.

Admittedly, this technique of "improving the straightness" of the plotted lines involves subjectivity. Perfectly straight lines can be based on completely erroneous data. However, there are two main reasons that

the technique is appealing. First, the recomputed U's do rid the plotted data of the unlikely discontinuity. Second, and more important, the recomputed U's are felt to be much more representative of the winds which physically transported the tracer to the greater sampling distances.

Perhaps, a bit more confidence in the technique can be gained through comparision of the resulting regression line with Elliott's Prairie Grass results. Using U's observed at 2 m for "only those points for nighttime gas releases at Prairie Grass,[1.8] the area-dosage relationship was found to be

$$A = 33.1 \left(\frac{DU}{E}\right)^{-0.91} . \tag{1}$$

The equation for Green Glow data including U's taken from Table 1.8 is

$$A = 27.0 \left(\frac{DU}{E}\right)^{-0.90} . \tag{2}$$

The equation for Green Glow data using 2-m source winds for all arcs is

$$A = 13.9 \left(\frac{DU}{E}\right)^{-0.98} . \tag{3}$$

That Equations (1) and (2) are in such excellent agreement is no doubt to some extent fortuitous, even though they do both include only field experiments conducted under similar nighttime stabilities. However, the better agreement of Equation (2) with Equation (1) than of Equation (3) with Equation (1) does offer encouragement.

In any event, the authors have concluded that improvements in results can be obtained by taking into consideration time and space variations in choosing a representative U.

Now, having developed an area predictor based on a varying wind, what are the implications in terms of choice of wind in using the predictor? Bear in mind that the reason for using a varying wind in plotting points for a given emission, was to specify the wind actually affecting the diffusing tracer. Thus, if, in using the predictor, one had no reason to suspect a

change in wind speed during the period of interest, one would use a constant U. Since E is also a constant, the choice of values of D would specify a single set of DU/E parameters with which to enter the equation or graph and forecast associated A's.

If one anticipated or measured a significant change in wind speed during the period of interest, likely the best technique would be to make two sets of predictions of A based on the changing U. The resulting forecasts would be the limits of predicted A's.

Judicial subjectivity could further refine the prediction. For instance, if winds were expected to change from U_1 during a pollutant emission to U_2 after emission, two areas could be derived for each selected value of D. U_1 would be used in predicting the smaller A's, i.e., the areas generated almost entirely during the period of emission. For larger areas, i.e., the areas generated both during and after actual pollutant emission, the values of A predicted would be biased more and more toward the limits of A predicted by use of U_2.

Results

Figure 1.16 gives least squares regression lines for the area-dosage relationships based on the analysis of data from the 50 field experiments. For the stable curve, data from 19 runs were used; for the slightly stable, 21; and for the unstable, 10. The equations of these lines are as follows:

Stable (Ri > 0.08) $$A = 31\left(\frac{DU}{E}\right)^{-0.91} \quad (4)$$

Slightly Stable (0 < Ri < 0.08) $$A = 28\left(\frac{DU}{E}\right)^{-0.89} \quad (5)$$

Unstable (Ri < 0) $$A = 82\left(\frac{DU}{E}\right)^{-0.75} \quad (6)$$

The standard error of estimate of the regression line is suggested by the sample shaded areas on Figure 1.16. The range of standard error is from 65 to 153% of the predicted A for the stable case. Similarly, standard error ranges for the slightly stable and unstable curves are 69 to 145% and 66 to 152%, respectively.

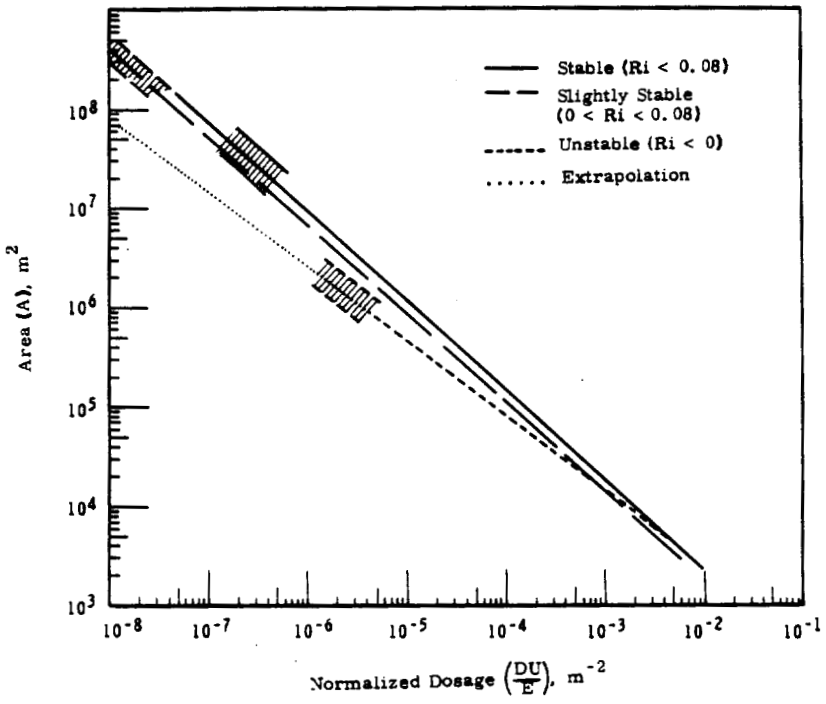

FIGURE 1.16

Area-Dosage Relationship Based on Data from 0.2 km Arc to 25.6 km Arc

Data from which these curves were generated extended through a range of A's from 4×10^3 to 1.5×10^8 m^2 for the stable and slightly stable cases. For the unstable case (since no 12.8 or 25.6 km data were available), the extent was from 8×10^3 to 7×10^5 m^2.

The authors feel that the equations discussed in the preceding three paragraphs represent the best estimates of the area-dosage relationship which can be gleaned from the subject field runs. However, at the risk of diluting this conclusion, three more curves are presented in Figure 1.17. These curves were generated from the same 50 field runs. The only differences are that no data from arcs at 12.8 and 25.8 m are included, and that, therefore, all U's employed in the computation of DU/E come from the source winds at the 2 m elevation. Equations for these curves based on a reduced volume of data are:

Neg. No. 0650288-4

Stable (Ri > 0.08) $$A = 15\left(\frac{DU}{E}\right)^{-0.99} \quad (7)$$

Slightly Stable (0 < Ri < 0.08) $$A = 28\left(\frac{DU}{E}\right)^{-0.89} \quad (8)$$

Unstable (Ri < 0) $$A = 82\left(\frac{DU}{E}\right)^{-0.75} . \quad (9)$$

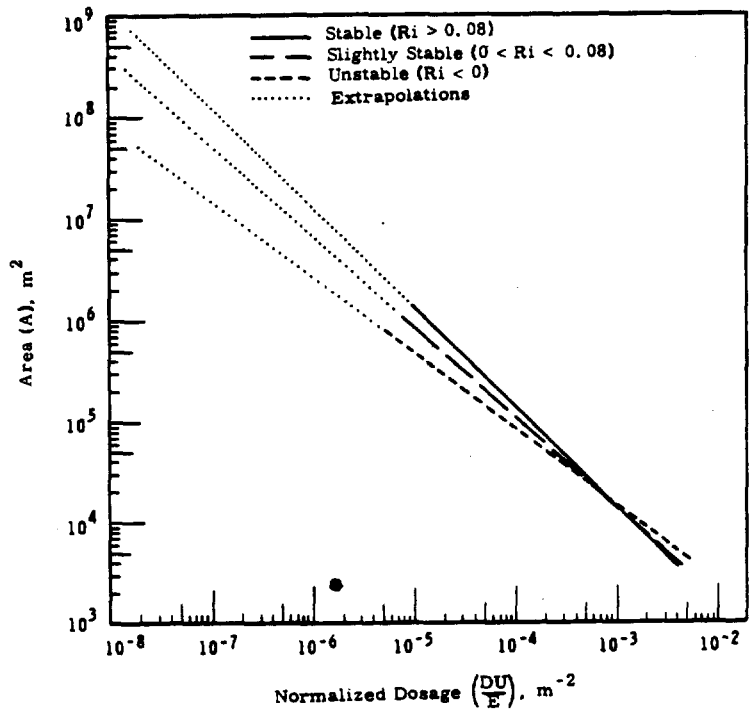

FIGURE 1.17

Area-Dosage Relationship Based on Data from 0.2 km Arc to 3.2 km Arc

The range of A's from which the stable and slightly stable data were generated was from 4×10^3 to 8×10^5 m^2. There is no change in data for the unstable stability class since no data were available for the outer two arcs in either computation.

Thus, Equations (6) and (9) are identical because they contain identical input data. However, slightly stable Equations (5) and (8) are identical (to significant figures) despite the inclusion of 18 additional data points in Equation (5).

Neg. No. 0650288-4

Equations (4) and (7) for the stable case are different. At a DU/E value of 10^{-7} m^{-2}, the value of A predicted by extrapolation of the Figure 1.17 stable curve is 40% greater than that obtained by using the stable curve of Figure 1.16. This figure is still within the standard error of estimate Equation (4).

Admittedly, Equation (7) has a certain appeal over Equation (4) when comparing the family of stable, slightly stable, and stable equations. There is a better separation of the data as indicated by the larger exponent. Also the intercept values (82, 28, 15) are ordered. But Equation (4) includes data points more than two orders of magnitude beyond those included in Equation (7), plus including all of those embraced in Equation (7). The authors feel more confident when predicting with the curve based on experimental data over the larger range, especially in the larger area, smaller dosage range.

Both families of Equations, (4, 5, 6) and (7, 8, 9), display similar characteristics. Slopes decrease with increasing stability. The curves diverge at larger areas, indicating that stability becomes a more important factor at greater distances. The curves converge at relatively small areas. This has basis in logic since the areas are all zero at the source.

Elliott and Nickola[1.9] presented results from Prairie Grass and Green Glow which were stratified according to "most" and "least" stable. No unstable data were available. As mentioned earlier, the stability ratio was used in place of Ri for defining stability classes. Also, a wind speed elevation of 16 m was used for U, instead of 2 m. Although the equations cannot be compared directlv, it is of interest to compare the exponents in these equations and their implications. The equations are:

Prairie Grass most stable $$A = 91\left(\frac{DU}{E}\right)^{-0.92} \quad (10)$$

Prairie Grass least stable $$A = 25\left(\frac{DU}{E}\right)^{-0.98} \quad (11)$$

Green Glow most stable $$A = 75\left(\frac{DU}{E}\right)^{-0.88} \quad (12)$$

Green Glow least stable $$A = 4.0\left(\frac{DU}{E}\right)^{-1.09} . \quad (13)$$

In both sets of equations, slopes increase with increasing stability. The curves thus converge at larger areas, indicating that stability becomes less important at greater distances. This is the opposite conclusion to that reached in the present study.

The Elliott-Nickola results are similar to those developed in this paper in that throughout the range of observational points, the data layers according to stability class, with larger areas for the same dosage as stability increases.

Conclusions

This study reveals that an estimate of the areal extent of a chosen dosage value can be made if one is given or can forecast the mean wind speed and the total mass of pollutant emitted from a point ground source. A significant improvement in predicting the area can be made if one has the information at hand to compute the Richardson number, a measure of atmospheric stability. Further refinements in the estimate of area can be made if spatial and time variation in wind speed are known or can be reasonably estimated.

Strictly speaking, the results are applicable only for predicting in the Hanford environs, where terrain is relatively flat and vegetation is sagebrush interspersed with desert grasses. Considering the magnitude of the errors involved in this and previous similar studies, one can still accept with fair confidence the conclusion that present results could be extended to transport over flat, grassy terrain. However, extrapolation to uneven terrain where extreme channeling could take place would be hazardous at best. Similarly, effects of great deviation in surface roughness, such as forested or urban areas, have not been evaluated.

Precipitation Scavenging Studies - R. J. Engelmann

Experiments are described which measure washout coefficients in rains and snow using stack gases released during normal plant operations. A value of 4.5×10^{-5} sec^{-1} was measured in snowfall of 1.0 mm/hr for inorganic gaseous iodine. Coefficients for inorganic iodine are higher than for the organic form.

Washout coefficients for large particulates are calculated using measured rain spectra with those collection efficiencies measured by Kinzer and Cobb and those predicted by Mason. The coefficient varies with the 0.75 and 0.8 power of rainfall rate for the respective cases. The rain spectra are approximated by log-normal distributions.

Introduction

In a previous report,[1.16] we have described experiments measuring the washout by rain of particulates from the air. The use of a water sensitive paper to determine raindrop sizes was described, and two of the measured rain spectra were combined with the measured rain scavenging efficiencies to provide washout coefficients in light rain.

It was noted that anisokinetic errors of filter samples, and difficulties in determining particulate source strength, made this experimental design a laborious if rewarding approach. It was also noted that scavenging by snow was not treated in the literature, either experimentally or theoretically, and this was regarded as a serious omission.

Washout Tests in Snow

Experiments to determine the washout coefficients of rain and snow, similar to those of May,[1.17] have been successfully conducted this past year using the stack gases released during operation of one of the Hanford plants. The development of the multidimensional gamma ray spectrometry system by the Battelle-Northwest Radiological Chemistry group[1.18] has provided the sensitivity needed to measure the trace quantities of inorganic and organic iodine. The radiological chemistry group measures the radioiodine released from the stack and determines the inorganic and organic iodine scavenged from the stack gas plume by the rain or snow.

The quantity washed out is then used to determine the washout coefficient for that rain or snowfall using one of the following formulas:

$$\lambda = \frac{V \, \Delta y \, \Sigma c}{Q \, t \, A} \tag{1}$$

$$\lambda = \frac{V \, \Delta y \, R \, \Sigma k}{Q} \quad , \tag{2}$$

where

λ = washout coefficient
V = wind speed at plume height
Δy = distance between samplers
Σc = total material collected in all samples, less background
Q = source release rate
t = sampling time
A = area of one sampler
R = precipitation rate
k = material collected per volume of water, less background.

The samplers are 1 m^2 saucer-like dishes formed by attaching polyethylene sheets to large hoops made of plastic hose. Fifty to seventy of these are exposed on a line or arc transverse to the stack plume overhead. The collected rain or snow is gathered after a few hundredths of an inch has fallen and provides the data needed in Equation (1). As yet, there appears to be no splash or residue problem with these simple basins.

In the event a heavy snowfall occurs when the hoops are not positioned, the snow can be gathered from the ground or older snow beneath, and either Equations (1) or (2) used to calculate the washout. Of course, the source, Q, must be measured or estimated.

It is possible to sample the precipitation along two lines or concentric arcs, spaced 5 to 20 mi downwind, and determine the washout coefficient (but in the absence of dry deposition) independent of knowledge of Q. We have not used this design as yet, but its versatility is obvious,

especially when the tracer is particulate. If the washout coefficient is independently measured, using Equation (1), the two arcs may be used to determine the dry deposition between them.

Four washout tests were conducted in 1964. The first, which we call PUREX-1, was conducted November 3 in a light rain. The sampling arc of hoops was limited by other field activities to the south, so the wind at stack height occasionally carried the Hanford PUREX stack plume past the end of the arc. We can only estimate what fraction of the time the plume was not sampled, perhaps a third, and, therefore, can only estimate the washout coefficient for inorganic gaseous iodine. The value (2.8×10^{-5} sec^{-1}) was not significantly different from that theoretically predicted by Chamberlain[1.19] for the same rainfall rate of 0.37 mm/hr. We found that organic iodine was washed out with a distinctly lower coefficient, but there was an insufficient amount scavenged to provide a quantitative result.

Tests PUREX-2 and PUREX-3 were actually the successive samples in a single snowfall of December 14. This snow consisted of spatial dendrites, much of it in agglomerates up to 3/4 in. diam. It was a "wet" snow, following a short rain at the start of the sampling. The source strength changed by nearly a factor of 2 during the test, as determined by two consecutive stack gas samples. The washout for the entire snowfall of 1.0 mm/hr (water equivalent) was 4.5×10^{-5} sec^{-1} for inorganic gaseous iodine. This was the result of a coefficient of 4.2×10^{-5} in the first part of the snow, and 4.7×10^{-5} in the last of the snow, at precipitation rates of 1.2 and 0.79 mm/hr, respectively.

It is interesting that the higher coefficient was measured with the lighter snow. This may well be due to sampling errors in these first tests, but the author instead feels that it is due to the smaller fall velocity of the flakes in the lighter snow. Whereas, for rain, one may assume that the washout coefficient for gases varies with about the 0.6 power of the precipitation rate, for snow, one must consider the type and size of flake.

Test REDOX-1 was conducted during "heavy" (2.7 mm/hr) nighttime snow of December 21. This snow was unpredicted, and a washout coefficient

had to be calculated using Equation (2) and a REDOX plant stack sample taken the next day. The calculated washout coefficient for inorganic gaseous iodine was 1.8×10^{-5} sec^{-1}, which is lower than that of PUREX-2 and -3. These samples were gathered too close to the stack, however, for the 23 mi/hr wind which had occurred during the snow, and it is almost certain that only the larger agglomerates of the snow reached the sampling site after falling through the plume. This coefficient may, therefore, be regarded as a minimum value, subject in addition to whatever error was introduced by the noncoincident stack sampling.

Rain Spectra

In the early morning of March 21, 1964, a large isolated rain shower very slowly moved over Sunnyside, Washington. Winds were very light so that winnowing of the drops as they fell should have been minimized. Sixteen spectra were measured during 2 hr and 40 min, the first probably 1/2 hr after the rain began.

The washout coefficients for these 16 spectra and all other Hanford spectra have been calculated using Kinzer and Cobb's[1.20] efficiencies for the parameter $a^2\rho = 42$, where a is the particle radius in microns, and ρ is the particle density. The coefficients for Kelkar's[1.21] average spectra were also calculated.

These show considerable deviation about any line of fit (Figure 1.18), but indicate that λ varies with about the 0.75 power of rainfall rate. Also entered on the figure is the line of prediction using Mason's[1.22] efficiencies. This line has a slope of 0.8.

Kinzer and Cobb's efficiencies are much larger than Mason's for the more numerous small raindrops. Nevertheless, Mason's efficiencies give higher washout coefficients. This is because the greatest contribution to the cross-sectional scavenging area is still made by the larger drop sizes where Mason's efficiencies are greater than Kinzer and Cobb's.

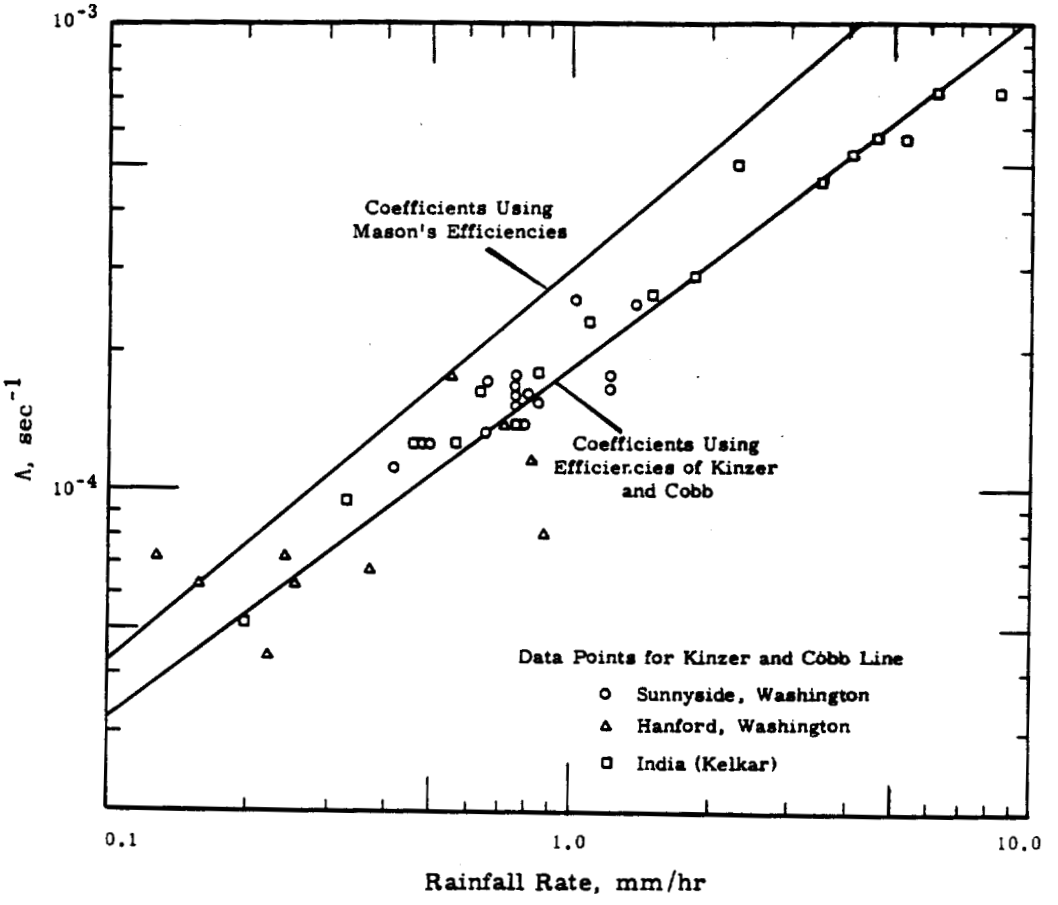

FIGURE 1.18

Washout Coefficients for $a^2\rho = 42$, Calculated Using Rain Spectra Measured at Sunnyside and Hanford, Washington, and by Kelkar in India

Most empirical raindrop size distributions cannot fit a bell-shaped curve, and yet most rain spectra show a peak frequency at a diameter between 0.5 and 1.0 mm. Levin[1.23] has shown that several empirical "space density" formulas for rain spectra (drops per volume of space per diameter interval) are approximated by portions of a logarithmic-normal distribution. This distribution can fit a peak and can be argued to have a theoretical basis. The additional convenience of logarithmic-normal probability paper makes it an attractive distribution. It approximates the rains sampled by Kelkar in India, and the 0.76 mm/hr Sunnyside, Washington shower of March 21 (but after somewhat arbitrary allowance for evaporation

Neg. No. 0650586-8

of the falling drops). The uncorrected Sunnyside shower is shown in Figure 1.19 with Kelkar's averaged spectra for several precipitation rates.

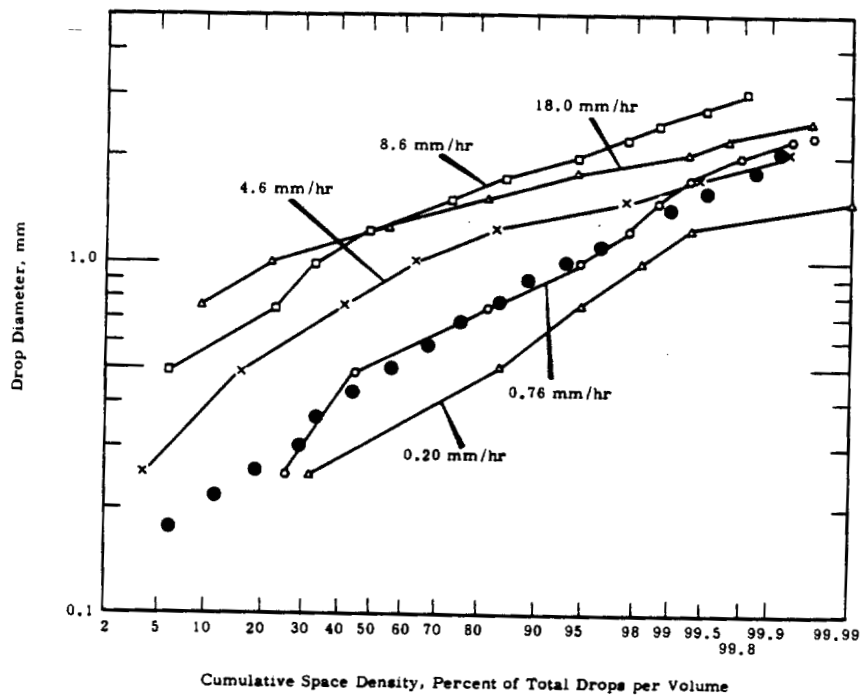

FIGURE 1.19

Rain Spectra in India for Selected Precipitation Rates, and a 0.76 mm/hr Shower at Sunnyside, Washington (The latter is shown as solid circles.)

A Sampler for Recording the Concentration of Airborne Zinc Sulfide on a Real Time Scale - P. W. Nickola

An instrument system that records the concentration of a fluorescent atmospheric tracer on a real time scale has been developed. Techniques of primary and field calibration are described, and calibration curves are given. The instrument has a sensitivity of about 3×10^{-8} g/m^3 for each minor recorder chart unit, and a detection limit of about 2.5×10^{-7} g/m^3.

The great majority of samples taken during atmospheric diffusion studies are of the bulk variety. The pollutant or tracer in the atmosphere is collected over some period of minutes, hours, or days on or in a

0028201

collecting device that has time resolution only to the extent that it is known when the sampler is turned on and off. Thus, an increasing volume of experimental results is being published with regard to mean concentrations or dosages that can be expected from continuous sources. However, minimal data are available concerning the time history of concentration contributing to the means.

A device capable of monitoring and recording air concentrations of a phosphorescing tracer (U. S. Radium Corporation zinc sulfide pigment No. 2210) on a real time scale has been developed at Battelle-Northwest. Within the technical limitations of the sampler, parameters such as source height, meteorological conditions, terrain, vegetation, and distance from the pollutant source can be related to time-dependent variables such as arrival and departure of the contaminant, percent of time the contaminant is detectable, or peak-to-mean air concentration ratios.

Figure 1.20 shows the real time sampler set up for field use. Component parts of the field sampling system, with the exception of portable vacuum and 110 V ac power supplies, are shown in Figure 1.21.

FIGURE 1.20
Real Time Sampler Set up for Field Use

0028202

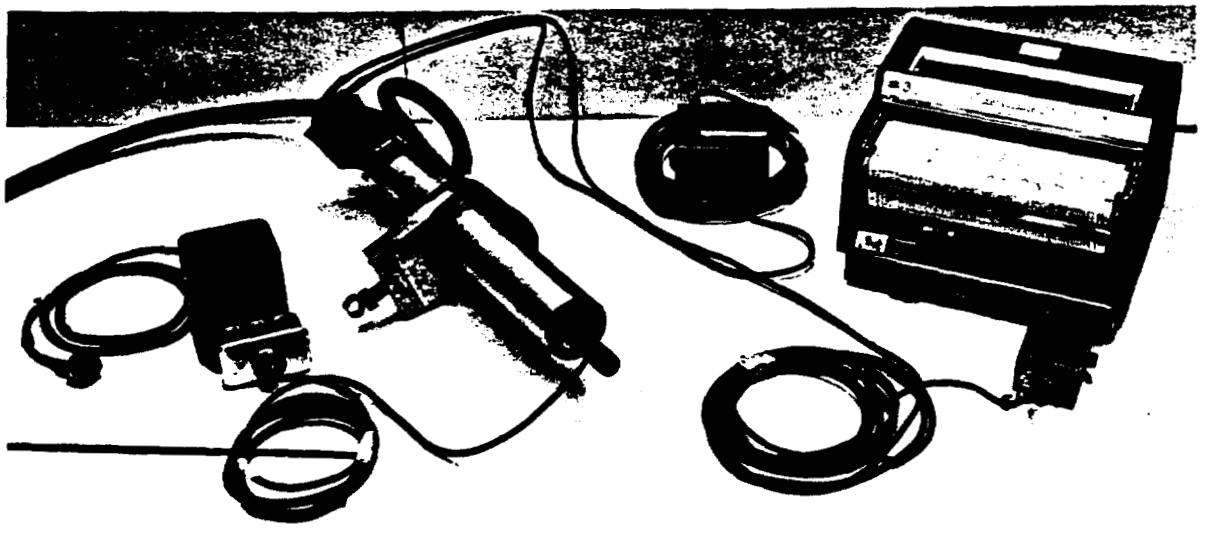

FIGURE 1.21
Components of the Real Time Sampler

In the sampling head (second from the left in Figure 1.21, the phosphorescent tracer is drawn into a chamber where it is irradiated with ultraviolet radiation, and is then passed through a light trap to a viewing chamber. In the viewing chamber, the phosphorescent particles are observed by a multiplier phototube. The anode current of the phototube, which is monitored by the strip chart recorder, is proportional to the tracer concentration. The transformer at the left in Figure 1.21 powers the ultraviolet lamp in the sampler head. Between the head and recorder in Figure 1.21 is the battery-operated, corona-regulated power supply for the photomultiplier.

A range selector that plugs into the input of the recorder permits the choice of over three orders of magnitude in sensitivity of the recorder. This feature makes possible recording at meaningful recorder chart levels for a wide range of tracer concentrations.

Field calibration of the system is accomplished by the insertion of a light source in front of the phototube. This source employs Pm^{147} activated self-luminous paint. With the source in the "calibrate" position, the high voltage to the photomultiplier is adjusted until the signal delivered

to the recorder is of the desired magnitude. The source is withdrawn from the viewing chamber during tracer sampling. In Figures 1.20 and 1.21 the source is in place in the viewing chamber. It is removed by merely pulling the ring to which it is attached (note near the bottom of the sensor head) to the "out" position. Field calibration checks, then, are readily performed.

This real time sampler has been mentioned in previous reports,[1.24-1.27] but the rather tedious calibration of the sampler in terms of concentration had not been completed.

Calibration in units of tracer concentration versus recorder signal level was accomplished by first exposing the sampler within a few inches of a filter which is of a type routinely used in collection and assay of the tracer.[1.27-1.29] The tracer was emitted in routine fashion at upwind distances varying from 0.2 to 12.8 km. The filter was replaced after each "puff" of tracer passed, as was indicated by the real time record. A knowledge of the flow rates through the sampler (4 ft^3/min) and the adjacent routine filter, the timer interval over which the tracer was collected, and the mass of tracer passing through the equipment (as estimated from the adjacent filter) permitted a calibration of the real time sampler in terms of mass per unit volume.

Air concentrations during calibration ranged from 10^{-7} to approximately 6×10^{-4} g/m^3. Since there are approximately 10^{10} particles per gram, concentrations thus ranged from 1000 to 6×10^6 particles per cubic meter. Concentration computations were made for 62 "puffs" of from 10 sec to 5 min duration, and the mean recorder signal level during each puff was noted. Fitting a least squares regression line to the logarithms of the resultant points gave the equation

$$C = 2.90 \times 10^{-8} R^{0.965}$$

where C is concentration in g/m^3, and R is the recorder chart reading normalized to the most sensitive range setting. This curve is the dotted line in Figure 1.22. The standard error of this regression line is indicated by the shaded area. This error embraces the range of C - 0.31 C to C + 0.44 C. The error includes variance due to actual differences in concentration observed between the real time samplers and the nearby calibration filters.

The hypothesis that the computed exponent 0.965 is really 1.000 is readily acceptable on statistical as well as theoretical grounds. If this hypothesis is accepted, and the curve drawn through the mean of the logarithms of the data points, the equation becomes

$$C = 2.35 \times 10^{-8} R.$$

This equation, which is considered the most representative, is shown as the solid line on Figure 1.22.

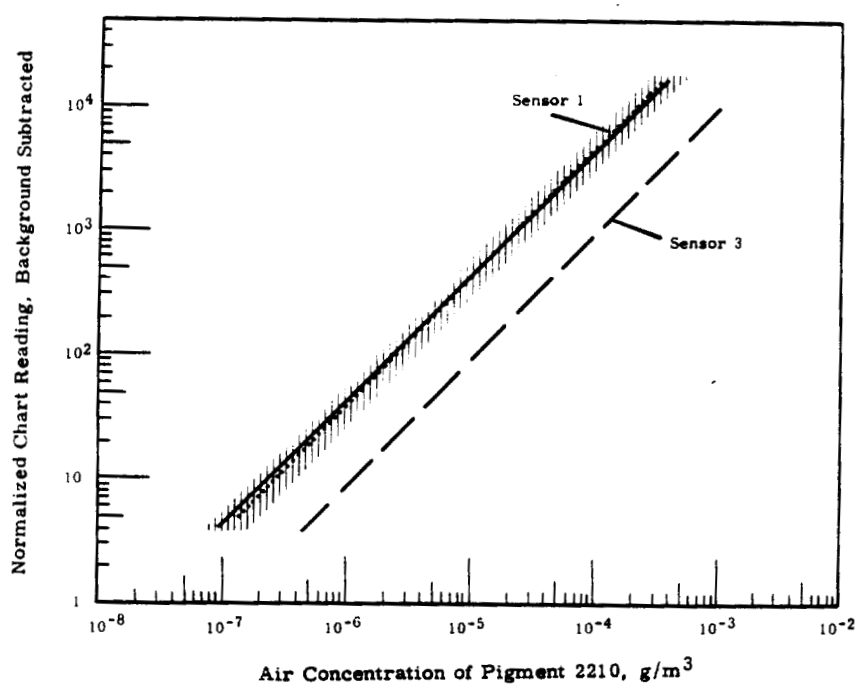

FIGURE 1.22

Calibration Curves of Zinc Sulfide Real Time Samplers

The sensitivity and detection limit were also considered. At the most sensitive setting, one recorder chart unit equates to about 3×10^{-8} g/m^3 of tracer (300 particles/m^3). An atmospheric concentration of this amount results in about one particle passing into the sampler each 1.7 sec. It is felt that these individual particles register on the recorder; and, therefore, the system can be said to have the ultimate detection limit of a single particle.

However, it is inherent in the instrument that some particles, during sampling at higher concentrations, impact in the ultraviolet irradiation

Neg. No. 0650341

chamber. These particles are sporadically knocked loose from the chamber to give an increase in background noise signal which is indistinguishable from true low-level atmospheric concentrations. Thus, a more realistic estimate of detection limit of the instrument is subjectively set at 2.5×10^{-7} g/m^3 (2500 particles/m^3).

The impaction problem described in the preceding paragraph results in the sampler being more reliable in indicating the arrival of the leading edge of a tracer puff than in indicating the passing of the trailing edge.

Two real time sampler units have been calibrated. The computed regression curve for the second sampler is

$$C = 1.28 \times 10^{-7} R^{0.974}.$$

The computed standard error on this line was almost identical to that of the other, with the applicable figures being C - 0.31 C to C + 0.45 C. As before, theory and reasonable statistics permit the acceptance of the hypothesis that the equation is

$$C = 1.12 \times 10^{-7} R.$$

This curve is the broken line at the right on Figure 1.22.

Use of a portable ac power supply for the recorder, ultraviolet lamp, and vacuum pump allows the system to be installed on a mobile unit. The size of the intake pipe can be altered to better approximate isokinetic sampling conditions for different wind speeds (or relative wind speeds for a moving unit).

The sampler has been mounted on pickup trucks and the short term crosswind concentration distribution of a continuously emitted plume observed. This measurement is accomplished by driving crosswind through the plume.

Additional versatility is being gained by the installation of a real time sampler unit in an airplane. Samples at a wide variety of elevations and in areas inaccessible to ground-based sampling will be possible. At the present time, the calibration process for the airplane real time sampler is underway.

Field Testing of a Fluorescein-Zinc Sulfide Dual Atmospheric Tracer Technique - P. W. Nickola

Four field experiments were conducted in investigation of the compatibility of fluorescein and fluorescent zinc sulfide as dual atmospheric tracers. The two tracers were emitted simultaneously from a common source and collected on common field filters. Qualitative and quantitative comparisions of the sampled tracer distributions are presented. The agreement is good.

The dual tracer technique has application in the investigation of the effects of differences in pollutant source type or location.

Introduction

Inasmuch as one cannot duplicate atmospheric conditions existing during any given field diffusion experiment, efforts have been directed toward simultaneous dispersion and collection of two different tracers. Successful application of such a dual tracer technique would lead to elimination of many variations in results stemming from differences in many meteorological parameters during separate field experiments. Differences in tracer concentrations could be more clearly related to such parameters as source height; size distribution of particulate contaminants; and reactive, adsorptive, or deposition phenomena occurring between the effluent tracers and the vegetation and terrain.

One of the most pressing of the areas demanding investigation is that of source height effects. If the dual tracer technique is to be used in this investigation, it is desirable to use tracers which have identical aerodynamic properties, even if these identical properties are not ideal.

Procedures

The primary field tracer used by Battelle-Northwest at Hanford is U. S. Radium Corporation's Pigment 2210, a fluorescing zinc sulfide with a log normal size distribution. The geometric mean diameter of the particulates is about 2.3 μ. Computed terminal fall velocity is on the order of centimeters to a few meters during the time interval the tracer traverses the few miles on the primary Hanford diffusion grids. Simple assaying

techniques have been developed for this tracer.[1.30] It was appropriate to search for a second tracer compatible with the existing Pigment 2210.

One candidate for use as a second tracer was the water-soluble dye fluorescein. This dye has been used as an atmospheric tracer by other investigators.[1.31] J. D. Ludwick[1.32] demonstrated the feasibility of laboratory separation and quantitative analysis of Pigment 2210 and fluorescein which had been simultaneously collected on a membrane filter. A modification[1.33] of the original technique was used in fluorescein determinations reported in this paper.

In December, 1962, a field experiment, designated MT-1, was conducted in which fluorescein and Pigment 2210 were simultaneously dispersed from adjacent generators. Results of this test, described in the 1962 issue of this report[1.33] were not encouraging. Although analysis of field samples showed qualitative agreement, the generation of approximately equal masses of fluorescein and 2210 resulted in an average of about 1.7 times as much fluorescein as 2210 on field filters. The variance in the fluorescein-to-2210 mass ratios from filter to filter was large. Unfortunately, a change in wind direction near the beginning of the field experiment resulted in significant samples being collected on only 30 filters.

Microscopic examination of several field filters from MT-1 showed the 2210 particles to be larger than the fluorescein. In the generation of insoluble Pigment 2210, the particle size is predetermined; the dissolving of the soluble fluorescein and subsequent spraying of a mist produce a variation in the size of particulates left in the atmosphere. The fluorescein particle size distribution is a function of the concentration of dissolved fluorescein fed to the generator and of the size distribution of the droplets being generated. An effort was made to increase the size of fluorescein particles in the atmosphere in multitracer tests conducted after MT-1. This was done by increasing the concentration of the fluorescein formulation solution.

Table 1.9 lists information pertinent to generation during multitracer tests to date. The "Particle Size Setting" is a nomenclature marked on the

generator which qualitatively controls the size of the emitted spray droplets. Larger settings indicate larger spray droplets. Under "Formulation" is listed the concentration of the source tracer solution (fluorescein) or suspension (2210). Also noted is the liquid used in preparation of the solution or suspension for the generation. Trichloroethane was used as the carrier for 2210 in tests MT-2, MT-3, and MT-4. The generation technique involves atomizing the "formulation," heating it, and spraying it into the atmosphere where the liquid carrier evaporates leaving the dry tracer particulate. Since trichloroethane is more volatile than water, greater quantities of "formulation" could be emitted without having droplets fall to the surface before evaporation.

TABLE 1.9

GENERATOR DATA FOR MULTITRACER FIELD EXPERIMENTS

		Fluorescein				Pigment 2210				
Experiment	Date	Formulation, g/liter	Generator	Particle Size Setting	Mass Generated, g	Formulation, g/liter	Generator	Particle Size Setting	Mass Generated, g	Generated Ratio, 2210/Fluorescein
MT-1	12/3/62	9.09 (water)	Unknown	7	527	9.09 (water)	Unknown	7	509[a]	1.04
MT-2	5/19/64	50.0 (water)	POO 1029	7[b]	1050	20.0 (trichloroethane)	78-19096	16[c]	340	0.32
MT-3	6/12/64	31.2 (water)	78-19095	7	750	16.7 (trichloroethane)	78-19096	16	2000	2.67
MT-4	6/25/64	31.2 (water)	78-19096	7	906	16.7 (trichloroethane)	78-19095	16	2000	2.21

(a) Approximate; estimated 3 liters of formulation leaked through bad packing in generator.
(b) May have been 16.
(c) May have been 7.

Run MT-2 was a failure from several standpoints. During the generation, the Pigment 2210 generator faltered and finally failed. Despite the fact that the fluorescein generator was turned off a few seconds after the 2210 generator stopped, there is considerable doubt about the constancy of rate of generation of 2210 during this run. The expectation, then, that the ratio of masses of tracer on each filter should be the same as the ratio of masses emitted would no longer be true. Additionally, the generator operator felt uncertain as to whether he had set the fluorescein "particle size setting" at 7 and the 2210 at 16, or vice or versa. Dispersal of the

0028209

fluorescein-water solution at a 16 setting would have resulted in considerable droplet deposition near the generator. In any event, Run MT-2 is listed in the table primarily to retain continuity in experiment nomenclature.

Experiments MT-3 and MT-4 provided hundreds of field filters upon which significant amounts of both tracers were collected. There was no apparent malfunction of any of the generation equipment and a minimum of missing or questionable field samples.

The diffusion sampling grid on which the dual tracers were released consists of four arcs of about 90°, which are concentric about the generation point. (See Table 1.3 and Figure 1.15 in Area-Dosage Relationships Downwind of a Point Source, p. 1.33.) "Ground" samples are collected at an elevation of 1.5 m at 268 sampling positions on these arcs. Distances of the arcs from the source are 0.2, 0.8, 1.6, and 3.2 km. Additionally, five towers on each arc permit vertical sampling to heights of 27, 42, 62, and 62 m on arcs at 0.2, 0.8, 1.6, and 3.2 km, respectively. Towers are located at azimuths of 98, 106, 114, 122, and 130° with respect to the source.

Experiment MT-4 was more successful than MT-3. During test MT-3, the mean wind direction was such that the northernmost tail of the tracer distribution was off course. This is illustrated in Figure 1.23 and 1.24. The entire crosswind distribution of the tracer was sampled during MT-4, as can be seen in Figures 1.27 and 1.28. Also, distribution of tracer on the tower samplers was ideal during Run MT-4 (the maximum masses being collected at the middle radial row of towers, with decreasing masses on the towers at both sides). During Experiment MT-3, the peak tower masses were collected on towers at 98°, an end radial row of towers. Thus, the crosswind distribution of tracer above the ground level is not well defined for Run MT-3.

For ease in comparison of the masses of tracer collected on each filter, the determined mass of fluorescein was multiplied by the ratio of tracer masses emitted. This ratio is listed in Table 1.9. Henceforth, in this report, then, perfect agreement of samples will be indicated by identical masses of fluorescein and 2210.

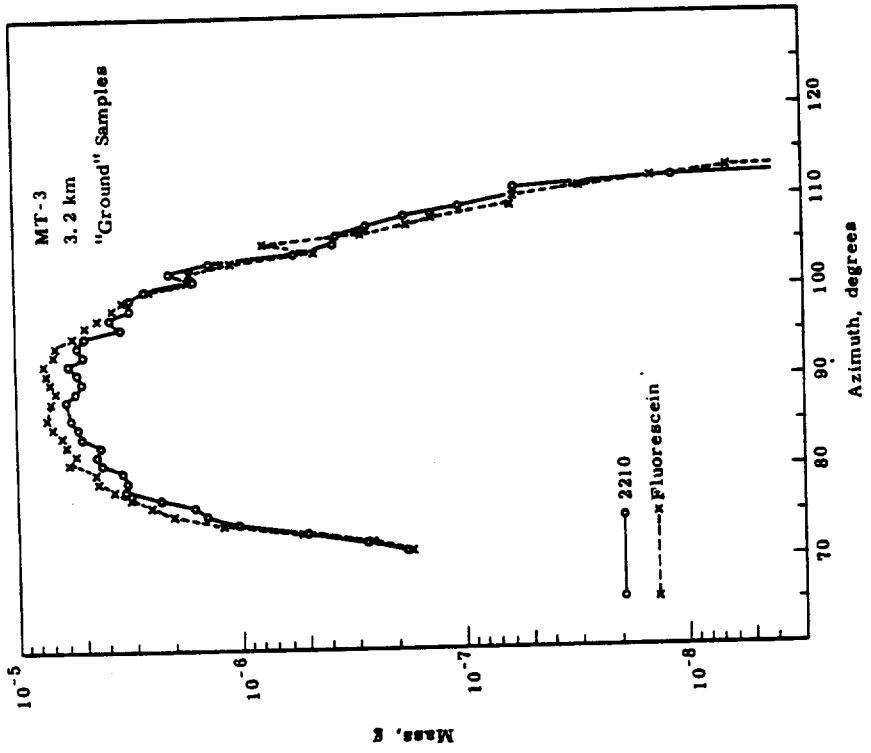

FIGURE 1.24
Horizontal Mass Distribution, 3.2 km, MT-3

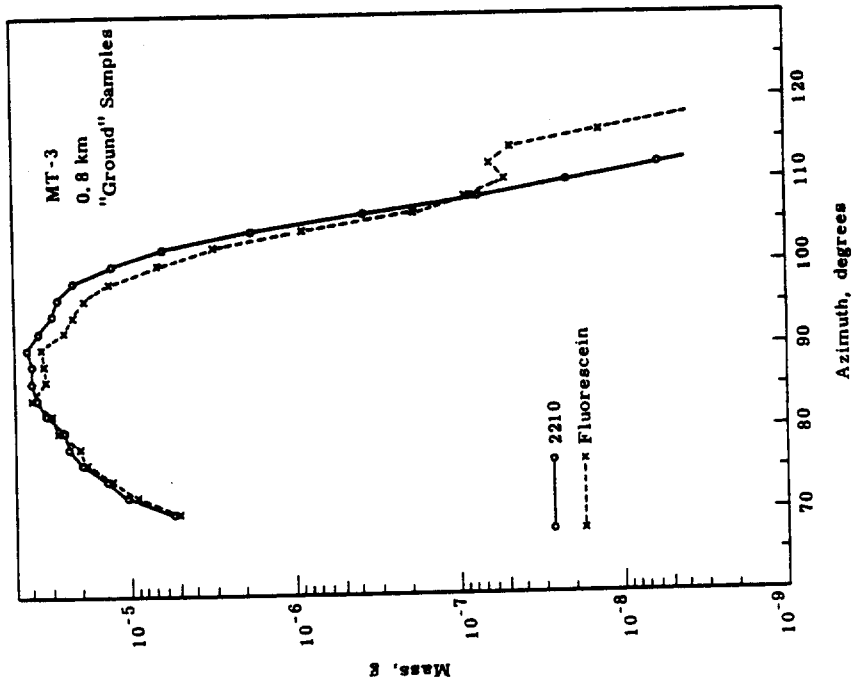

FIGURE 1.23
Horizontal Mass Distribution, 0.8 km, MT-3

Neg. No. 0650574-5; 0650574-1

Analysis

There is no single obvious way to make an investigation of the compatibility of these two tracers. One may qualitatively look at the horizontal or vertical crosswind distributions and compare them. Figures 1.23 through 1.30 give examples of such comparisons. There is certainly agreement in the general character of the distributions.

The ratio of masses of tracers on each filter could be examined. For instance, on Figure 1.24 the ratio of mass of fluorescein to that of 2210 varies from the extreme highs of 2.10 at 105° and 1.44 at 96° to the extreme lows of 0.50 at 111° and 0.59 at 109°. The modal ratio for the illustrated arc is 1.16.

One might attempt to smooth out some errors in assay or sampling by summing crosswind the mass of tracer collected on all "ground" samplers. This procedure leads to the conclusion that at ground level, the worst agreement on all arcs for Runs MT-3 and MT-4 is observed at the 3.2 km arc during Test MT-3, the arc just discussed in the preceding paragraph, and shown on Figure 1.24. The appropriate mass sums are 1.40×10^{-4} and 1.13×10^{-4} g with a resulting fluorescein-to-2210 mass ratio of 1.24. Conversely, the best agreement by this technique is found on the 0.8 km arc during Run MT-4, shown on Figure 1.27. Fluorescein and 2210 masses here were 4.81×10^{-5} and 4.77×10^{-5} g, for a ratio of 1.01. Table 1.10 summarizes for both field tests the ratio of sums of fluorescein mass to 2210 mass for ground samples.

TABLE 1.10

RATIO OF CROSSWIND SUMS OF FLUORESCEIN MASS TO PIGMENT 2210 MASS FOR "GROUND" SAMPLES

	Arc			
Experiment	0.2 km	0.8 km	1.6 km	3.2 km
MT-3	0.94	0.83	1.04	1.24
MT-4	0.83	1.01	1.05	1.10

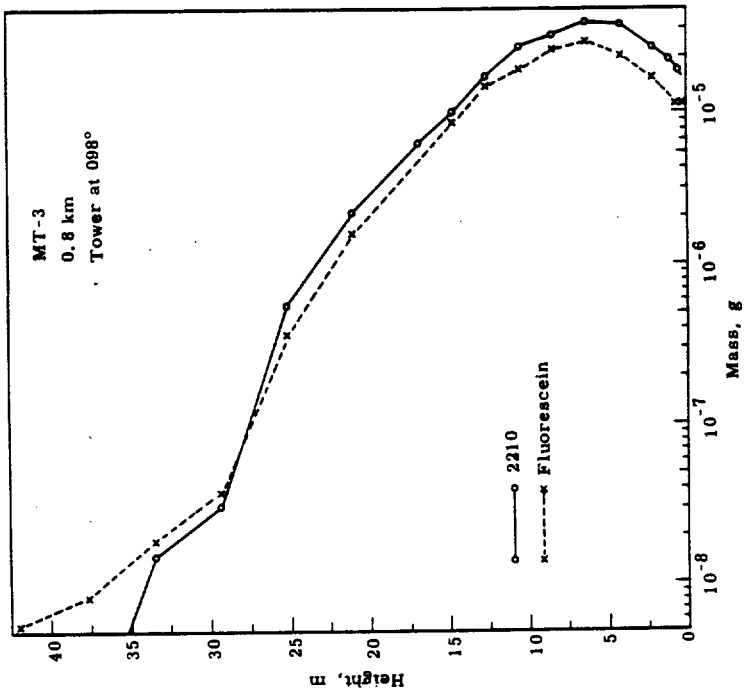

FIGURE 1.25
Vertical Mass Distribution, 0.8 km, MT-3

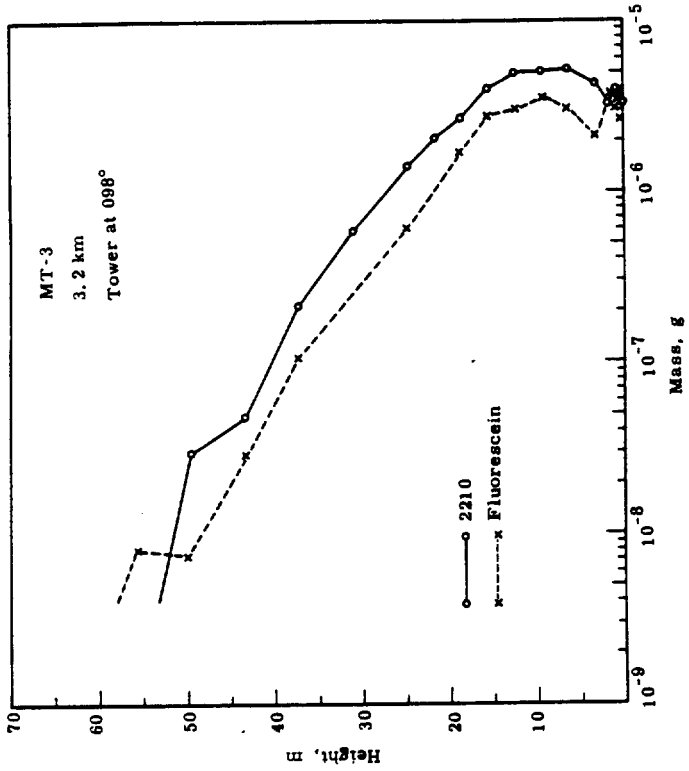

FIGURE 1.26
Vertical Mass Distribution, 3.2 km, MT-3

Neg. No. 0650574-9; 0650574-6

0028213

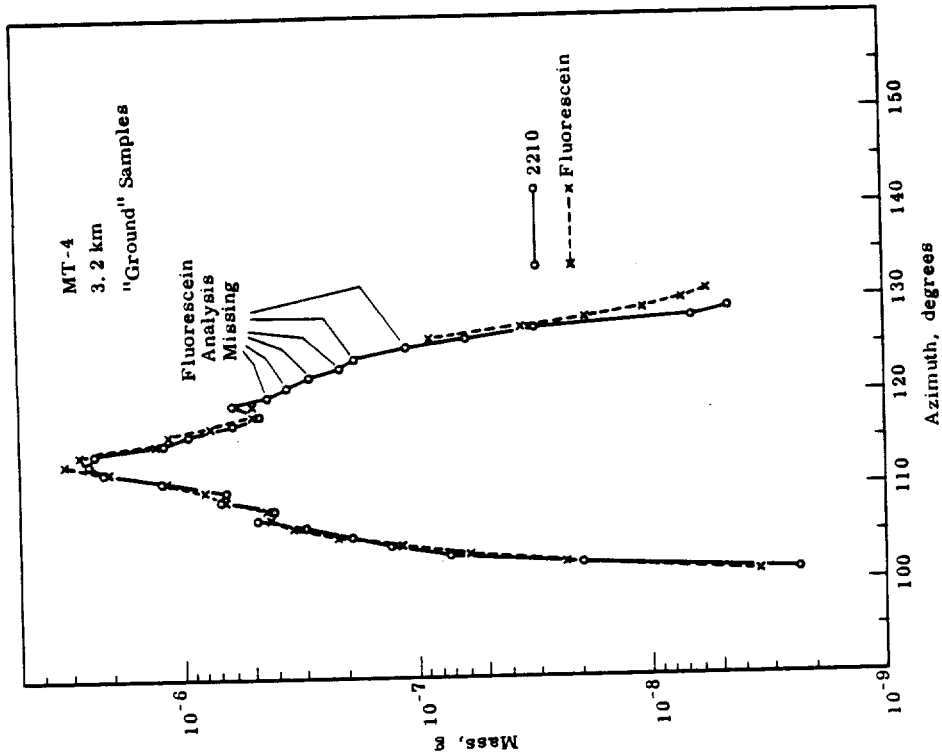

FIGURE 1.28
Horizontal Mass Distribution,
3.2 km, MT-4

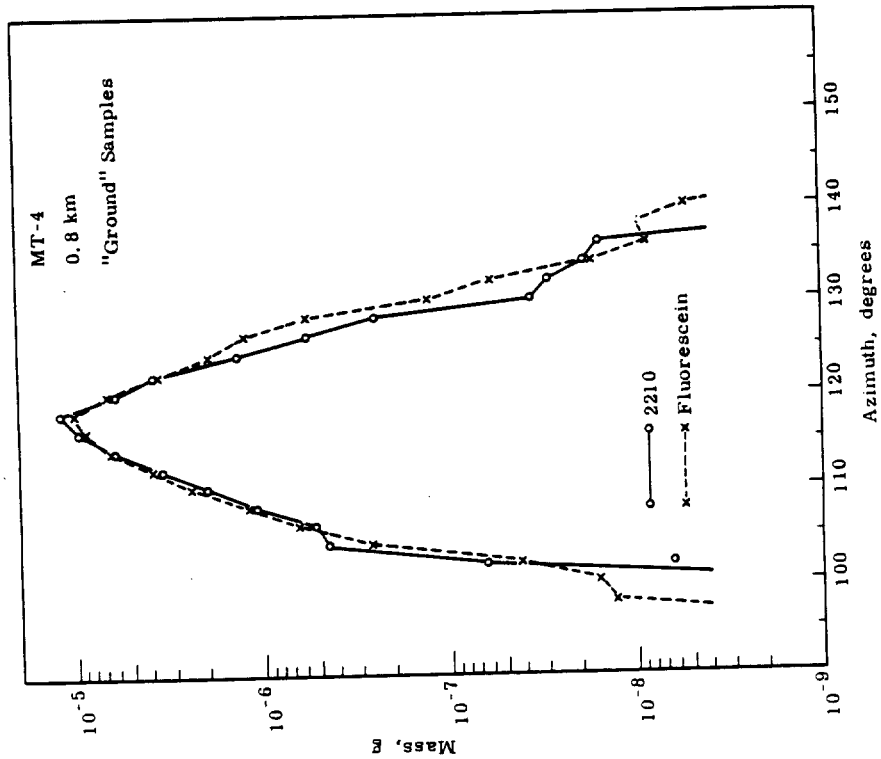

FIGURE 1.27
Horizontal Mass Distribution,
0.8 km, MT-4

Neg. No. 0650574-2; 0650574-4

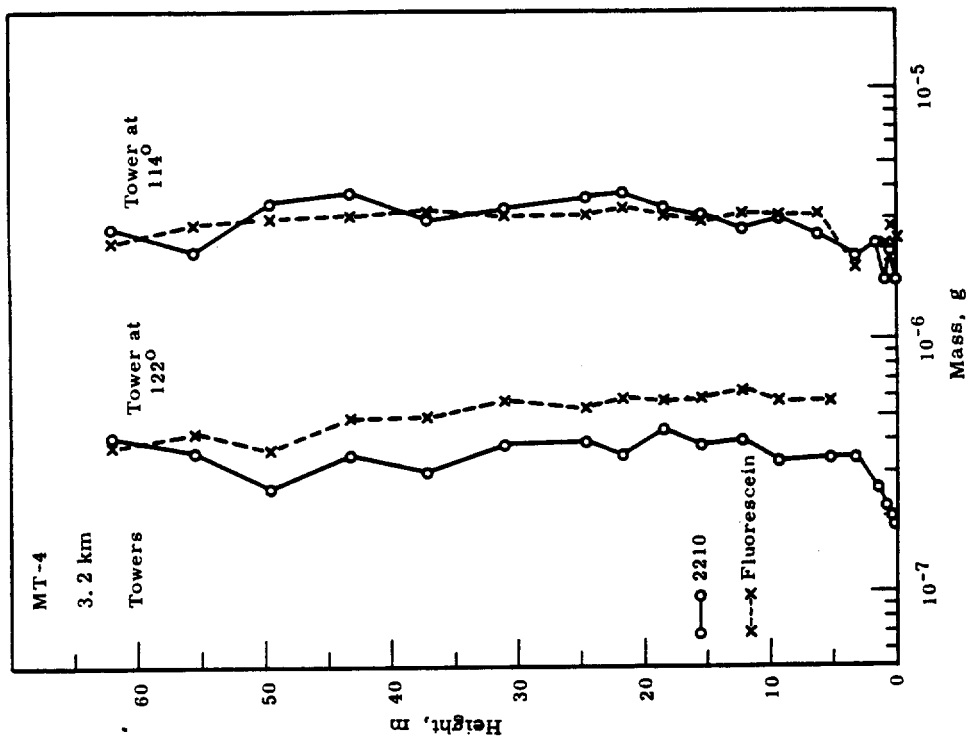

FIGURE 1.30
Vertical Mass Distribution, 3.2 km, MT-4

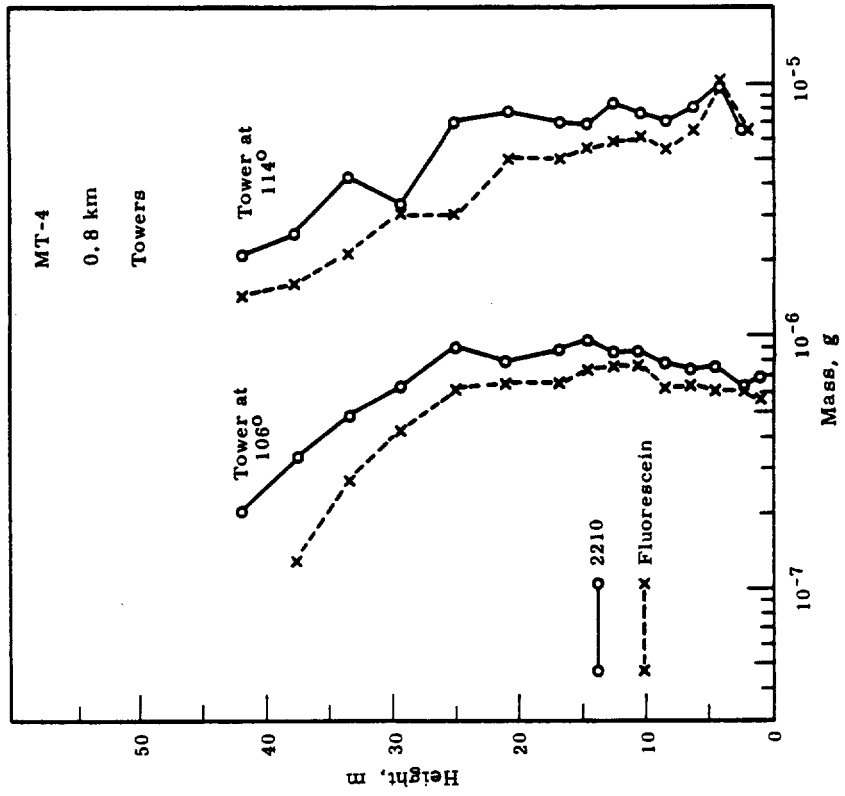

FIGURE 1.29
Vertical Mass Distribution, 0.8 km, MT-4

Neg. No. 0650574-3; 0650574-7

A technique similar to that described in the preceding paragraph can be applied at levels above the 1.5 m "ground" level if sufficient tower samples are available, as is the case in Test MT-4. But, whereas the sums from which the ratios of Table 1.10 were computed were the result from 15 to 46 individual samples, a maximum of 5 samples is available for summing at each aloft level, i.e., only one mass at each tower azimuth. If, for instance, one is summing across the 0.8 km arc at the 20 m level (see Figure 1.29), masses of 7.5×10^{-6} and 5.0×10^{-6} g for 2210 and fluorescein, respectively, would be employed at the 114° tower. These figures would be added to similarly determined masses at other towers on the 0.8 km arc. The ratios resulting from these sums are presented in Table 1.11.

TABLE 1.11

CROSSWIND SUMS OF EXPOSURES AND THE RATIO OF THESE SUMS (FLUORESCEIN TO 2210) FOR ALOFT LEVELS DURING EXPERIMENT MT-4

(Multiply each mass sum by 10^{-6} for true mass sum in grams.)

	0.2 km Arc			0.8 km Arc			1.6 km Arc			3.2 km Arc		
Level, m	2210	Fluorescein	Ratio	2210	Fluorescein	Ratio	2210[a]	Fluorescein	Ratio	2210[a]	Fluorescein	Ratio
1.5	136	122	0.90	10.8	10.8	1.00	2.24	2.45	1.11	0.745	0.852	1.14
5	115	104	0.90	12.5	12.1	0.97	2.84	2.72	0.96	0.830	M	M
10	87.4	68.7	0.79	13.0	11.2	0.86	2.93	2.81	0.96	0.983	1.08	1.10
15	72.8	M	M	12.2	10.4	0.85	3.18	3.13	0.98	1.00	1.07	1.07
20	30.7	M	M	13.3	9.8	0.74	2.65	2.43	0.92	1.17	1.11	0.95
25	12.3	M	M	14.1	7.35	0.52	2.38	2.11	0.88	1.13	1.07	0.94
30				9.45	7.59	0.80	2.33	2.18	0.94	1.04	1.06	1.02
35				7.66	5.90	0.77	2.04	1.85	0.91	0.966	1.05	1.08
40				5.15	4.40	0.85	1.94	1.64	0.84	1.04	1.03	0.99
45							1.86	1.49	0.80	1.14	1.01	0.89
50							1.46	1.36	0.93	0.994	0.975	0.98
55							1.58	M	M	0.753	M	M
62							1.24	M	M	0.925	0.876	0.95

(a) Collected mass normalized to flow rate of arcs at 0.2 and 0.8 km.

M = missing

Table 1.11 also presents the sum of the cross wind samples for both tracers. The figures reported for arcs at 0.2 and 0.8 km are those actually collected at the flow rate employed on these arcs—0.15 liter/sec. For purposes of comparing masses collected at different arcs, masses reported for the 1.2 and 3.2 km arcs have been normalized to the flow rate observed at the inner two arcs. Thus, we are in effect comparing exposures or dosages, a mass divided by a flow rate. It is somewhat unfortunate that the flow rate

to which the masses were normalized to obtain exposure was 0.15 liter/sec. The resulting units of gram-sec/0.15 liter is a bit unconventional, but does not alter the validity of the data. At this writing, it is questionable in the mind of the author whether the hundred or so calculations avoided by using 0.15 flow rate is not more than offset by the extra words of explanation required.

The exposure values in Table 1.11 can be used to construct the profile of the sums of crosswind exposure shown on Figure 1.31. A line separates the level above which there is an excess of 2210 and below which there is an excess of fluorescein. One finds the greatest disagreement in isopleths in the vicinity of 1 km from the source.

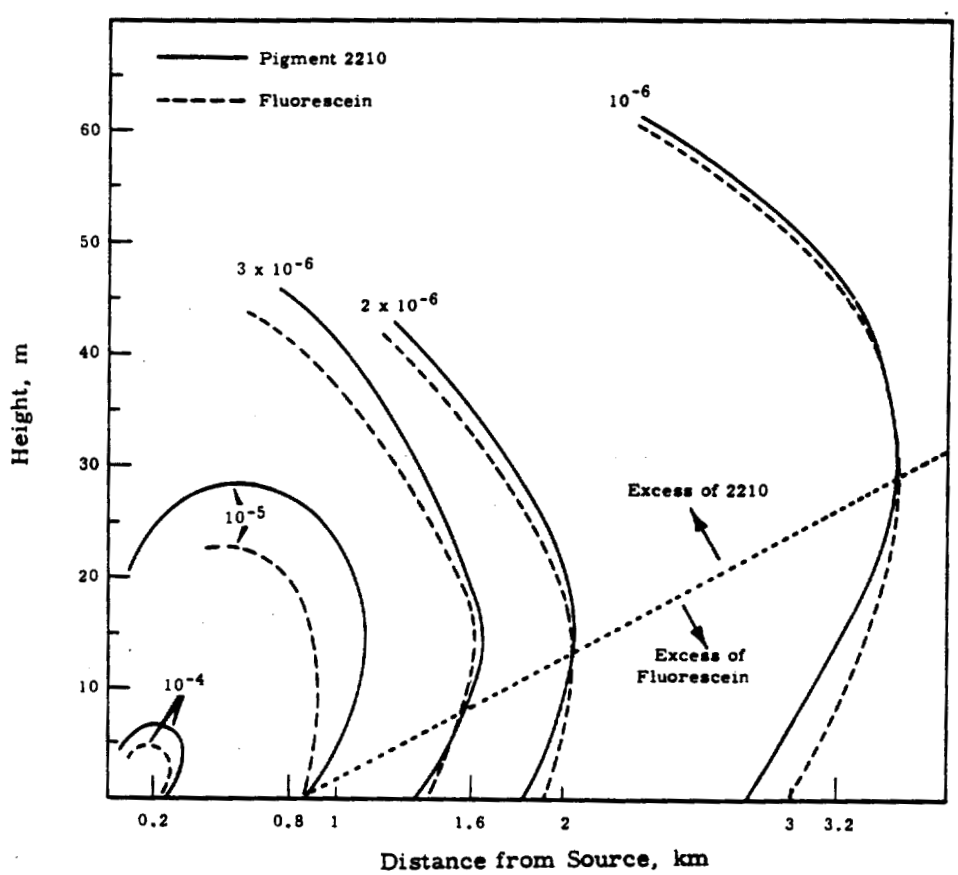

FIGURE 1.31

Sum of Crosswind Exposures (g-sec/0.15 liter) at Tower Locations for Test MT-4

Neg. No. 0650584-8

Conclusions and Conjectures

One can observe many facts and make many conjectures from the tables and figures presented. Only a few are mentioned in the following paragraphs.

On Run MT-3, there is a tendency for the fluorescein masses to be relatively high on the more northerly end of the arc while the 2210 is relatively high on the southern end of the distribution. Although no such tendency is obvious for the ground samples on Run MT-4, just the opposite effect is suggested by examination of tower data, as seen on Figure 1.30. Here fluorescein is greater on the south end. The generation of tracers took place within 5 ft of each other and the nozzles were aimed at a common point about 15 ft downwind. Thus, source location was likely not a factor.

From Tables 1.10 and 1.11, one might conclude that the fluorescein-to-2210 ratio increases with distance from the source. However, the ratios for the 0.2 and 0.8 km arcs during MT-3 show the reverse trend. And, as has been pointed out previously, a ratio from Table 1.10 is more reliable than one from Table 1.11 because of the much greater amount of data used in computing each ratio.

There is another difference between the inner two arcs and the outer two which could have a bearing on these ratios. Flow rate through the filters at 0.2 and 0.8 km is 0.15 liter/sec; at 1.6 km, it is 0.23 liter/sec; and at 3.2 km, it is 0.51 liter/sec. Diameter of the filter face used results in all these flow rates being less than isokinetic. However, the deviation from isokinetic is less at the higher two flow rates. If we hypothesize that the 2210 particles were larger than the fluorescein, the error due to impaction would have been greater on the inner two arcs, and the fluorescein-to-2210 ratios would have been less. The hypothesis concerning smaller fluorescein particles is supported in situations where vacuum pump failure resulted in pure impaction samples. Nearly all the fluorescein to 2210 ratios were less than 1.00. In one instance, the ratio was 1/30.

The microscopic sizing of particulates is a tedious, time-consuming, and eye-straining job. The author confesses that for the preceding reasons,

only a few filters from the multitracer tests were microscopically examined—and these only qualitatively. Unfortunately, the fluorescein analysis is a destructive assaying technique. On the basis of the filters examined, it was not obvious that the Pigment 2210 particles were larger.

One can further speculate on particle size effects on the basis of Figure 1.31. For example, is the deficiency of fluorescein near the source due to an excess of large particles which immediately fall out of the plume? The better and better agreement with distance could be attributed to the slower depletion of the "not quite so large" particles of Pigment 2210, which finally leaves only the particles of both tracers which have negligible fall velocities. But how, then, does one explain the excess of fluorescein which develops near the ground?

Perhaps, speculation of this nature is entirely idle. Perhaps, any reasonably small particulates of fluorescein would be compatible with Pigment 2210. The best estimates of fall velocities of 2210 particulates indicate that the bulk of this pigment would fall less than 5 m during a 1/2 hr transit to the 3.2 km arc. Other factors, such as a nonlinear error in mass calibration or an error in determining masses emitted could significantly affect the conclusions drawn concerning particle fall characteristics.

Let us recall that the purpose of the experiments was to demonstrate, if possible, that fluorescein and 2210 are compatible atmospheric tracers—even if they are not the ultimate. The discrepancies in the present technique generally fall within the generous limits usually allowed to date in studies involving atmospheric diffusion. It is further felt that errors involved in use of the fluorescein-2210 dual tracer technique would not significantly limit its use in the investigation of pollutant source height effects.

One drawback of the technique could be the dependence of the fluorescein dispersal on the specific generator used. The generators used at Hanford are commercially available insecticide sprayers. Their control settings are not expected to be precise in the scientific sense. Thus, settings which would result in a satisfactory size distribution of fluorescein in one generator might not apply to another. A minimal effort to investigate this

possibility was made in the switching of generators for Tests MT-3 and MT-4 (Table 1.9). In this instance, it appears that no extreme differences resulted. This may have been fortuitous.

It is quite possible that continuance of field experiments in the MT-series would result in better combinations of fluorescein formulation concentration and/or generator control settings. It might also be demonstrated that generator-to-generator difference and moderately different control settings are of minor significance. In any event, field experiments MT-3 and MT-4 do demonstrate that generator settings exist which result in a reasonably compatible fluorescein-2210 technique.

Before the technique is put into further field use, it is necessary that the fluorescein analysis be set up as a routine procedure. Analysis of the samples for the tests described in this paper was directed, and to a considerable extent performed, by J. D. Ludwick, a research chemist. The [illegible] for his cooperation in "retooling" for a

A knowledge of the vertical profiles of wind and temperature is a necessity in any detailed investigation of atmospheric diffusion, transport, and deposition. The availability of wind and temperature data from a 400 ft meteorological tower gave great aid in the first relatively crude diffusion studies carried out at Hanford. But the sensors used were physically large and of a rugged construction. Their response characteristics were relatively slow. The anemometers had relatively high wind speed thresholds (up to about 3 mi/hr). Additionally, they were spaced at 50 ft intervals on a tower whose location was fixed.

Efforts at refining diffusion models and associated prediction capabilities led to a desire for more detailed profiles of wind and temperature, especially in the lowest layers of the atmosphere where gradients change most rapidly. Short term variations in wind and temperature became important. The ability to investigate spatial variations in wind and temperature and to be able to take vertical measurements near any desired pollutant source led to the desire for a mobile unit.

In 1953, the meteorology group initiated use of its "portable meteorological mast."[1.34] This 80 ft tower, of aluminum tubular construction, could be disassembled, moved, and reassembled at another location in a day or two. Wind speed, wind direction, and air temperature were monitored by sensors mounted on six booms which protruded approximately 3 ft from the mast. The sensor output was then telemetered to a mobile van, which could be located up to 500 ft from the mast, and the signals were sequentially recorded on a single strip-chart recorder. Under normal circumstances, a period of 1.8 min was required to sample the six wind speeds, four wind directions, and six temperatures.

Chart readings were listed manually and the listings were used to keypunch data processing cards. These cards were the input for an electronic computer program which resulted in summaries of the originally measured parameters.

Obsolescence plus the desirability of a shorter scanning period resulted in the design of a new data collection system for use on the 80 ft

0028221

mast. A description of the system design was presented in the 1963 issue of this report.[1.35] Components and circuit details of the system were described by Ratcliffe and Sheen in a subsequent document.[1.36]

The portable mast, as the system is still called, went into field operation in July, 1964. The original 80 ft tower with six booms is still employed for the mounting of the sensors. Essentially every other portion of the system is new.

As before, signals from the sensors are telemetered from the mast to the translating and recording equipment located up to 500 ft away. The analog signals are digitized and recorded sequentially on a punched paper tape. The six wind speed signals, the six wind direction signals, and one temperature signal are punched during a given 5 sec interval. During the subsequent 5 sec interval, the same wind sensors are monitored, but a different temperature sensor is scanned. Thus, wind speed and direction are recorded 21.6 times during a 1.8 min period—a period in which they would have been recorded just once under the original portable mast system. Similarly, temperatures are recorded 3.6 times as often.

In addition to the punched paper tape record, an optional printed paper tape output permits an immediate visual review of the data.

The input supplied for electronic data processing is the punched paper tape. The output parameters computed in the present program are end-to-end means and standard deviations. Up to 10 different increments of averaging may be specified for each run. In addition, the six basic speeds, six directions, and one temperature for each 5 sec interval are printed (primarily as an aid in checking for errors).

At the present time, the portable mast is used routinely during field diffusion tests. A minimum of difficulty is being experienced in keeping the system operating properly. The automated recording system results in having the data summarized and available for analysis within a few days after its generation.

0028222

REFERENCES

1.1 J. J. Fuquay, C. L. Simpson, and W. T. Hinds. "Prediction of Environmental Sources Near the Ground, Based on Hanford Experimental Data," Hanford Radiological Sciences Research and Development Annual Report for 1963, HW-81746. 1964.

1.2 J. J. Fuquay, C. L. Simpson, and W. T. Hinds. Estimates of Ground-Level Air Exposures Resulting from Protracted Emissions from 70-Meter Stacks at Hanford, HW-80204. January, 1964.

1.3 "The Green Glow Diffusion Program," Geophysical Research Papers No. 73, edited by M. L. Barad and J. J. Fuquay, Air Force Cambridge Research Laboratories, Bedford, Massachusetts. HW-71400 VOL1. 1962.

1.4 J. L. Lumley and H. A. Panofsky. The Structure of Atmospheric Turbulence, Interscience Publishers, New York. 1964.

1.5 F. Pasquill. Atmospheric Diffusion, Van Nostrand, London. 1962.

1.6 N. F. Islitzer. "Short-Range Atmospheric Dispersion Measurements from an Elevated Source," J. Meteorol., vol. 18, pp. 443-450. 1961.

1.7 W. P. Elliott. "The Areas Within Concentration Isopleths Downwind of Continuous Point Source," Intern. J. Air Pollution, vol. 2, pp. 115-126. October, 1959.

1.8 W. P. Elliott, R. J. Engelmann, and P. W. Nickola. "Area-Dosage Relationships and Time of Tracer Arrival in the Green Glow Program," Air Force Surveys in Geophysics No. 134, Air Force Cambridge Research Center, Bedford, Mass. May, 1961.

1.9 W. P. Elliott and P. W. Nickola. "The Estimation of Areas Within Isopleths of Dosage Downwind of a Point Source," Am. Ind. Hyg. Assoc. J., vol. 22, pp. 238-244. August, 1961.

0028223

REFERENCES (Contd.)

1.10 "Project Prairie Grass, A Field Program in Diffusion," Geophysical Research Paper No. 59, edited by M. L. Barad, Air Force Cambridge Research Laboratories, Bedford, Massachusetts, AD-152572 VOL1. 1958.

1.11 "The Green Glow Diffusion Program," Geophysical Research Papers No. 73, edited by M. L. Barad and J. J. Fuquay, Air Force Cambridge Research Laboratories, Bedford, Massachusetts. HW-71400 VOL1, pp. 9-26. 1962.

1.12 H. H. Lettau. "Computation of Richardson Numbers, Classification of Wind Profiles and Determination of Roughness Parameters," Exploring the Atmosphere's First Mile, edited by H. H. Lettau and B. Davidson, Pergamon Press, New York, vol. I.

1.13 O. G. Sutton. Micrometeorology, McGraw-Hill, New York. 1953.

1.14 J. J. Fuquay, C. L. Simpson, and W. T. Hinds. "Prediction of Environmental Exposures from Sources Near the Ground, Based on Hanford Experimental Data," Hanford Radiological Sciences Research and Development Annual Report for 1963, HW-81746. 1964.

1.15 R. J. Engelmann. Unpublished Data, Battelle-Northwest, Richland, Washington. 1960.

1.16 R. J. Engelmann. "Precipitation Scavenging Processes," Hanford Radiological Sciences Research and Development Annual Report for 1963, HW-81746, pp. 1.36-1.43. 1964.

1.17 F. G. May. The Washout by Rain of Lycopodium Spores, AERE HP/R 2198. 1958.

1.18 R. W. Perkins. "Application of Multidimensional Gamma Ray Spectrometry," Hanford Radiological Sciences Research and Development Report for 1963, HW-81746, pp. 3.1-3.12. 1964.

REFERENCES (Contd.)

1.19 A. C. Chamberlain. Aspects of Travel and Deposition of Aerosol and Vapour Clouds, AERE HP/R 1261. 1953.

1.20 G. D. Kinzer and W. E. Cobb. "Laboratory Measurements and Analysis of the Growth and Collection Efficiency of Cloud Droplets," J. Meteorol., vol. 15, pp. 138-148. 1958.

1.21 V. N. Kelkar. "Size Distribution of Raindrops - Part I," Ind. J. Meteorol. Geophys., vol. 10, pp. 125-136. 1959

1.22 B. J. Mason. The Physics of Clouds, Oxford University Press. 1957.

1.23 L. M. Levin. "Size Distribution Function for Cloud Droplets and Raindrops," Dok. Akad. Nauk., vol. 94, pp. 1045-1048. 1954. (Translation available from Directorate of Scientific Information Service, DRB, Canada.)

1.24 P. W. Nickola and J. J. Fuquay. "Advances in Atmospheric Tracer Technology," Hanford Radiological Sciences Research and Development Annual Report for 1962, HW-77609, pp. 1.30-1.34. 1963.

1.25 P. W. Nickola, M. O. Rankin, M. F. Scoggins, and E. M. Sheen. A Device for Recording Air Concentrations of Zinc Sulfide Fluorescent Pigment on a Real Time Scale, HW-SA-3317. January 10, 1964.

1.26 P. W. Nickola and M. F. Scoggins. "Atmospheric Tracer Technology," Hanford Radiological Sciences Research and Development Annual Report for 1963, HW-81746, pp. 1.47-1.48. 1964.

1.27 J. J. Fuquay. Progress in Atmospheric Physics: A Summary of Hanford Laboratories Work on This Program under General Electric, 1959-1964, HW-83602, pp. 6-10. 1964.

1.28 "The Green Glow Diffusion Program," Geophysical Research Papers No. 73, edited by M. L. Barad and J. J. Fuquay, Air Force Cambridge Research Laboratories, Bedford, Massachusetts. HW-71400 VOL1, pp. 48-50. 1962.

REFERENCES (Contd.)

1.29 P. W. Nickola and M. F. Scoggins. "Atmospheric Tracer Technology," Hanford Radiological Sciences Research and Development Annual Report for 1963, HW-81746, p. 143. 1964.

1.30 J. J. Fuquay. Progress in Atmospheric Physics: A Summary of Hanford Laboratories Work on this Program under General Electric, 1959-1964, HW-83602. 1964.

1.31 E. Robinson, J. A. Macleod, and C. E. Lapple. "A Meteorological Tracer Technique Using Uranine Dye," J. Meteorol., vol. 16, pp. 63-67. 1959.

1.32 J. D. Ludwick. Dual Atmospheric Tracer Techniques for Diffusion Studies Using Phosphorescence-Fluorescence Analysis, HW-70892. March, 1961.

1.33 J. D. Ludwick and P. W. Nickola. "A Fluorescein Analysis Technique for Use in Atmospheric Diffusion Studies," Hanford Radiological Sciences Research and Development Annual Report for 1962, HW-77609, pp. 3.15-3.19. 1963.

1.34 R. G. Clark and P. W. Nickola. A Portable Meteorological Mast, HW-29478. September 30, 1953.

1.35 E. M. Sheen and C. A. Ratcliffe. "Automatic Data System for Atmospheric Physics Studies," Hanford Radiological Sciences Research and Development Annual Report for 1963, HW-81746, pp. 5.6-5.10. 1964.

1.36 C. A. Ratcliffe and E. M. Sheen. Automatic Data Collection System for Meteorological Tower Instrumentation, HW-84213. October 20, 1964.

002822b

RADIOLOGICAL PHYSICS

Radioactivity Measured in Alaskan Natives, 1962-1964* - H. E. Palmer, W. C. Hanson,** B. I. Griffin, and L. A. Braby

We have made periodic measurements of Cs^{137} in northern Alaskan natives since the summer of 1962.(2.1, 2.2)

Whole body counting measurements of total Cs^{137} content were made on northern Alaskan natives during the summer of 1964. Table 2.1 gives the results obtained. The adults of the interior village of Anaktuvuk Pass, Alaska, showed the highest average body burden: 1280 nCi of Cs^{137}. This is an increase of 200% over the average in the summer of 1962 and 100% over the average in the summer of 1963. The maximum burden found in a native in 1964 was 2.4 μCi, but the highest Cs^{137} body burden, 3.0 μCi, was measured in a nonnative living on a diet consisting mostly of caribou meat. Na^{22} was found in Eskimo urine samples and subsequently in the Eskimos and reindeer and caribou meat.

TABLE 2.1

Cs^{137} IN ADULT (Over 14 yr) ESKIMOS AND INDIANS OF ALASKAN VILLAGES ESTIMATED BY WHOLE BODY COUNTING, nCi

	Summer 1962		Summer 1963		Summer 1964	
	Average	Maximum	Average	Maximum	Average	Maximum
Anaktuvuk Pass	421	790	628	1240	1280	2400
Kotzebue	138	518	140	732	321	929
Barrow	52	166	60	177	- -	- -
Point Hope	17	119	39	88	50	92
Fort Yukon	- -	- -	34	181	- -	- -
Arctic Village	- -	- -	- -	- -	614	1156

* Science, vol. 147, p. 620. 1965.

** Biology Department

0028227

Seasonal Variations of Cs^{137} in Alaskan Eskimos - H. E. Palmer, W. C. Hanson,* L. A. Braby, and B. I. Griffin

Residents of two Eskimo villages show marked and quite different changes of Cs^{137} body burdens during the year.

To study the seasonal variation of Cs^{137} body burdens in Eskimos, we have made whole body counts at intervals of about 3 mo since January, 1964, at Anaktuvuk Pass, Alaska. In addition, we obtained monthly urine samples from Point Hope from which we estimated the average body burden.[2.3] Figure 2.1 shows the average body burden during the year for these two villages. The people of Anaktuvuk reach a maximum during the summer months while the people of Point Hope do so in the winter.

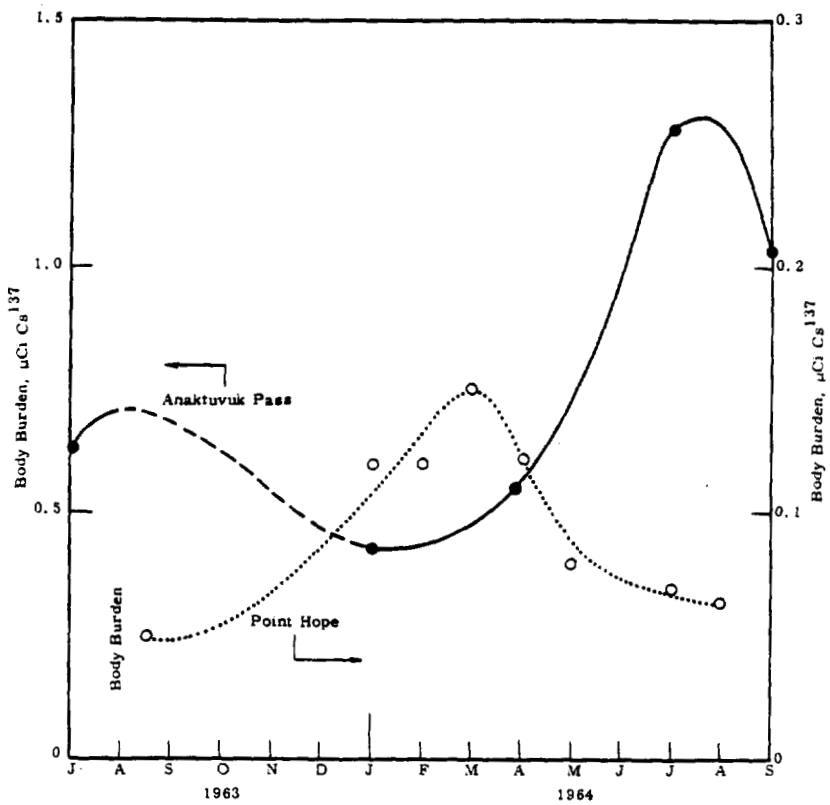

FIGURE 2.1
Seasonal Variation of Cs^{137} in Eskimos of Two Villages

* Biology Department

These changes and the differences between villages can be explained by food habits of the Eskimos and the caribou. At Anaktuvuk Pass most of the caribou are killed in the spring (about April) and in the fall (about September). The fresh meat is stored in underground caches dug vertically into the permafrost which permits frozen storage and an abundance of meat until the next killing season. Caribou that are killed in the spring have been feeding largely on lichens during the winter and the meat in the animals is relatively high in Cs^{137}. The body burdens of Eskimos eating this meat will increase until an equilibrium is reached with the diet. Caribou killed in the fall have been feeding largely on grass and plant life other than lichens that have been growing during the summer, and the meat in these animals is much lower in Cs^{137} than those killed in the spring. The body burdens of the Eskimos eating this meat will decrease until an equilibrium is again reached with the diet. The time between seasons is such that the body burden is almost in equilibrium with the diet, then the Cs^{137} content in the diet changes again. Because of these factors, the residents of Anaktuvuk Pass have maximum body burdens in July or August and minimum body burdens in about January or February. On the other hand, the residents of Point Hope have minimum body burdens in August and September and maximum body burdens in March because they kill most of their caribou during the winter. They do not store meat extensively, and have very little caribou to eat during the summer.

The fluctuation of the average body burden of Anaktuvuk Pass residents due to seasonal differences and to increasing Cs^{137} levels since July, 1962, is shown in Figure 2.2. The general increase in body burdens is due to the fallout from the 1961-1962 nuclear testing.

0028229

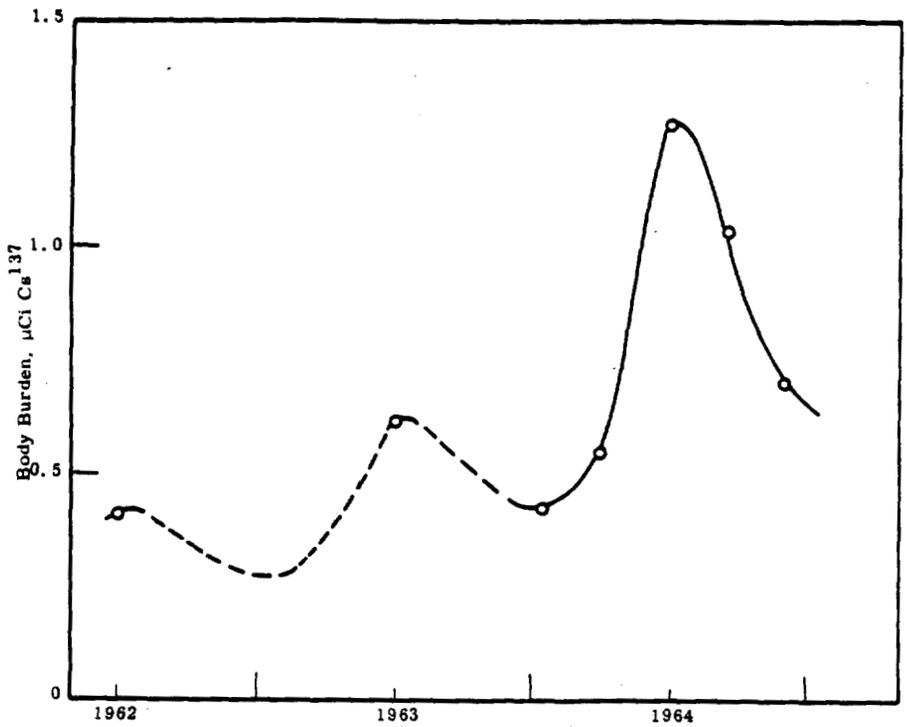

FIGURE 2.2
Cs^{137} Body Burdens of Adult Eskimos
of Anaktuvuk Pass, Alaska, Since July, 1962

Urinalysis for Cs^{137} - H. E. Palmer

Measurement of Cs^{137} in urine by gamma ray spectrometry was used to measure burdens in Alaskan natives and in residents of Richland, Washington.

Along with our first whole body counting studies of Cs^{137} in the Eskimos we collected urine samples from some of those counted and correlated the amounts in the urine with those in the body.[2.4] This was done by two methods. One used the Cs^{137} content of the 24 hr collection of urine and the other used the ratio of Cs^{137} to grams of potassium in the urine.

Starting in January, 1964, monthly urine samples were collected from 16 men at each of three different Alaskan villages to further test these methods for usefulness in estimating average body burdens at a village.

It was also a test to see if urine samples could be routinely obtained from the native villages. One man in each village was paid to collect and ship the samples, and each man was paid a small sum for a monthly sample of 2 liters of urine. These samples were analyzed at our laboratory for the Cs^{137} and potassium content.

The urine sampling in one of the villages, Fort Yukon, was not successful because regular samples were not received. The samples from the other two villages, Point Hope and Anaktuvuk Pass, have been obtained regularly since January, 1964. The urinalysis results for Anaktuvuk Pass are shown in Figure 2.3 where they are compared to whole body counting data taken over the same period. The measured counts were normalized to what would have been received from 1500 ml, an average 24 hr sample. The body burdens estimated from the Cs^{137} in the urine agree quite well with the whole body counting results, although on the average they are slightly lower than the whole body counting results. The body burden estimates made from the Cs^{137} per gram of potassium were very poor. This was surprising since all of the previous comparisons had been good. These comparisons had all been made in the months of either January or July. The poor agreement seems to be due to a decrease in the amount of potassium excreted rather than a change in the Cs^{137} excretion. During April and May the average potassium excretion was only about two thirds that during the other months, and low potassium content would give a high estimate of body burden. The results from Point Hope were similar, and, although no interim whole body counts were made, the estimates made using the Cs^{137}-potassium ratio were too high judged by the counts made before and after this period. The same low excretion of potassium during the spring months was evident. The cause of this reduced potassium excretion is unknown but may be due to a change in their diet.

At Richland, Washington, the average body burden as estimated from the Cs^{137}-potassium ratio for the urine agreed quite well with whole body counting data. A monthly composite urine sample from about 150 people was collected at the Kadlec Methodist Hospital. The potassium

content of a 2 liter sample was quite constant at 2.34 g/liter ± 7%. The potassium and Cs^{137} concentrations and the estimated body burden are shown in Table 2.2. The average body burden was estimated from a calibration curve obtained by carefully measuring the Cs^{137} body burden and Cs^{137} and potassium excretion of 20 adult males living in the vicinity of Richland. These data are shown in Figure 2.4. The slope is significantly greater than that obtained from the Eskimo data, which indicates they either have a more rapid Cs^{137} excretion or less potassium in their total diet. The latter may be true since the average potassium content of Eskimo urine samples was only about 2/3 that of the Richlanders.

TABLE 2.2

ANALYSIS OF COMPOSITE URINE SAMPLES FROM RICHLAND, WASHINGTON

	K, g[a]	Cs^{137}, nCi[a]	nCi/g	Body Burden, nCi[b]
February	4.49	0.137	0.031	18
March	4.42	0.132	0.030	17.5
April	4.42	0.151	0.034	20
May	4.69	0.146	0.031	18
June	5.04	0.176	0.034	20
July	4.73	0.183	0.038	23
August	4.49	0.159	0.035	21
September	4.82	0.139	0.029	17
October	4.55	0.156	0.034	20
November	4.73	0.176	0.037	21.5
December	4.76	0.166	0.035	21

(a) In 2 liters of urine.

(b) Using the non-Eskimo calibration data.

From these results it is apparent that it is better to use the Cs^{137} content of the urine per unit volume rather than the Cs^{137}-potassium ratio for estimating body burdens of the Eskimos. For people with a diet with a more constant potassium intake the Cs^{137}-potassium ratio works quite well.

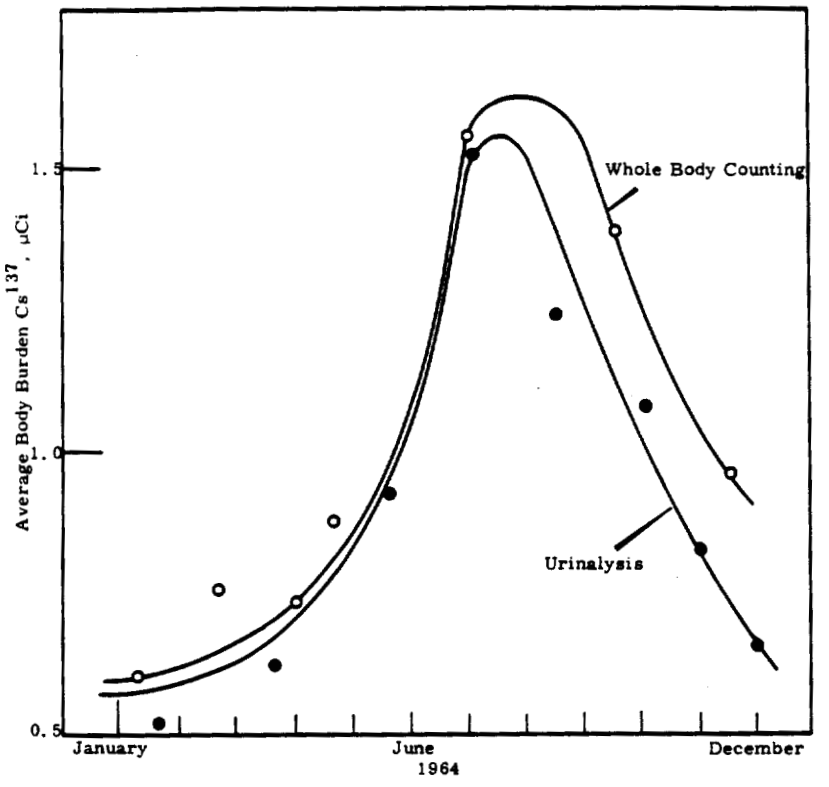

FIGURE 2.3

Comparision of Urinalysis with Whole Body Counting for Cs^{137} in 16 Eskimos at Anaktuvuk Pass, Alaska

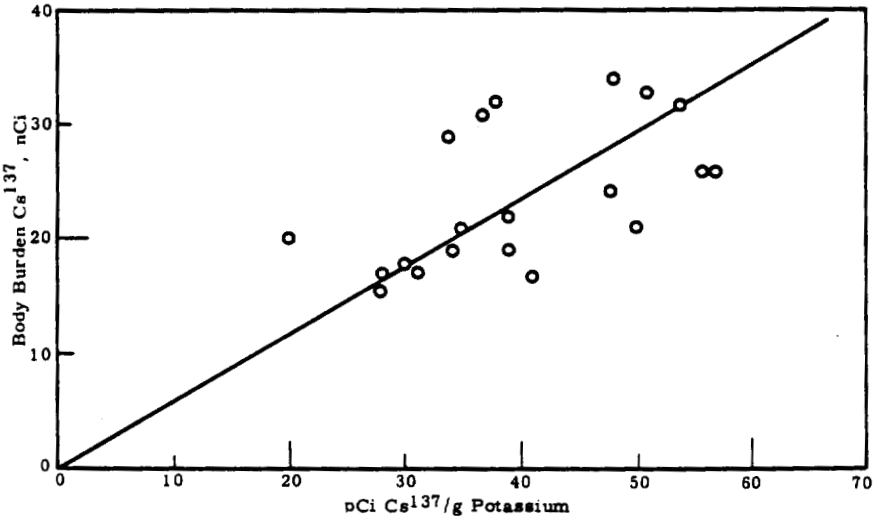

FIGURE 2.4

Correlation of Urinalysis and Whole Body Counting for 20 Adult Males Living Near Richland, Washington

Na^{22} in People and Food - H. E. Palmer

The 1961 bomb tests introduced enough Na^{22} into fall-out to be readily measureable in urine of Alaskans and Richlanders and in food. It can also be detected by whole body counting in Eskimos.

In about February, 1964, some unusual gamma-ray peaks began to appear in counts of urine samples from Eskimos of Anaktuvuk Pass, Alaska. These were identified as Na^{22}. Figure 2.5 shows a spectrum of a 2 liter sample counted between two 4 by 9 3/8 in. NaI crystals connected in parallel. The Na^{22} produces peaks or sum peaks at 0.51, 1.02, 1.28, 1.79, and 2.36 MeV. The amount of Na^{22} present became enough to interfere with potassium determinations of K^{40} counting.* It became necessary to determine potassium by flame photometry.

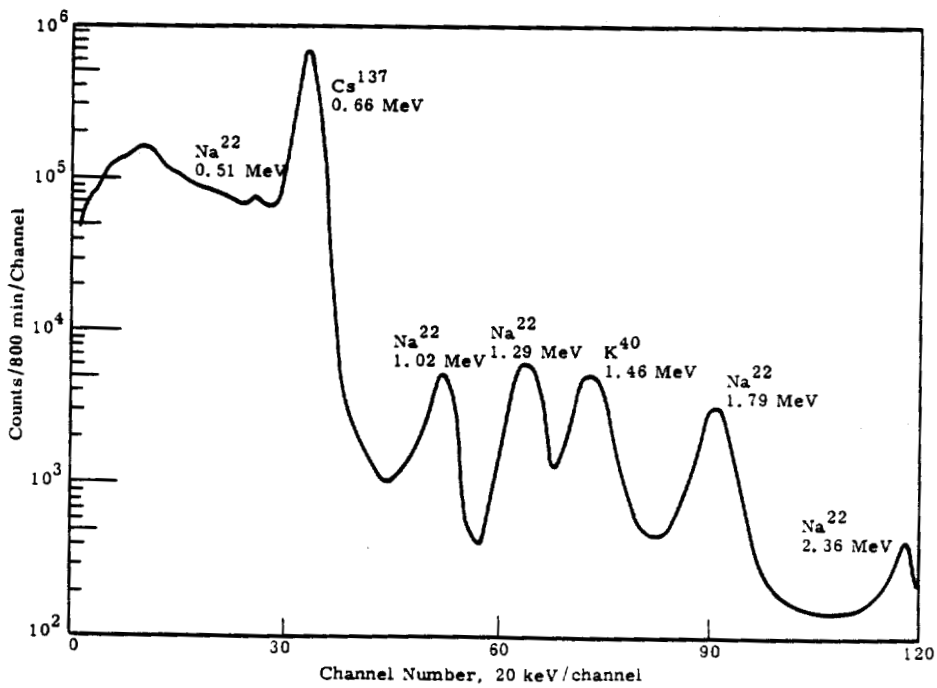

FIGURE 2.5

Typical Gamma-ray Spectrum of Eskimo Urine Sample from Anaktuvuk Pass, Alaska

---

* See "Urinalysis for Cs^{137}," p. 2.4.

The amount of Na^{22} increased in the March and April urine specimens and then leveled off. The maximum concentration measured was 0.97 nCi/liter. For a normal urine excretion rate and a 10 day biological half-life, this concentration indicates a body burden of 17 nCi. For comparison, the Na^{22} concentration in urine from Richland, Washington, was about 0.01 nCi/liter in April, 1964.

During July, 1964, we attempted to detect the Na^{22} in several Eskimos by whole body counting. The attempts were not directly successful because the counting times were so short (10 min) that poor statistics prevented peaks being recognizable. However, when the spectra of the ten Eskimos having the highest Cs^{137} body burdens were added, a peak was plainly visible at 1.28 MeV. The sum spectrum is shown in Figure 2.6. The area under the peak indicates an average body burden of about 12 nCi.

Samples of caribou meat obtained during 1964 were counted and showed enough Na^{22} to account for the amounts in the urine. Caribou and reindeer meat obtained before the summer of 1963 showed very little Na^{22}. This indicates that the Na^{22} in the fallout from the latest nuclear tests is much higher than that in tests prior to 1961. The incidence of the Na^{22} in the Eskimos coincided with the spring kill of caribou at Anaktuvuk. These caribou had been eating quantities of lichens during the winter. The lichens had probably accumulated considerable Na^{22} just as they had Cs^{137}.

<u>Fe^{55} in Humans and Their Foods</u> - H. E. Palmer and T. M. Beasley*

> Fe^{55} is present in people, animals, and food. It is measured by counting prepared samples on a proportional counter with anticoincidence shielding.

Fe^{55} is one of several activation products that have been found in relative abundance in fallout.[2.5] This summer we looked for and found Fe^{55}, first in caribou blood; then in blood of Alaskan Eskimos and of residents of Richland, Washington; and in their food.

Fe^{55} is an electron capture nuclide. The only easily detectable radiation it emits is a 5.9 keV X-ray in 28% of the disintegrations. To

---

* Chemistry Department

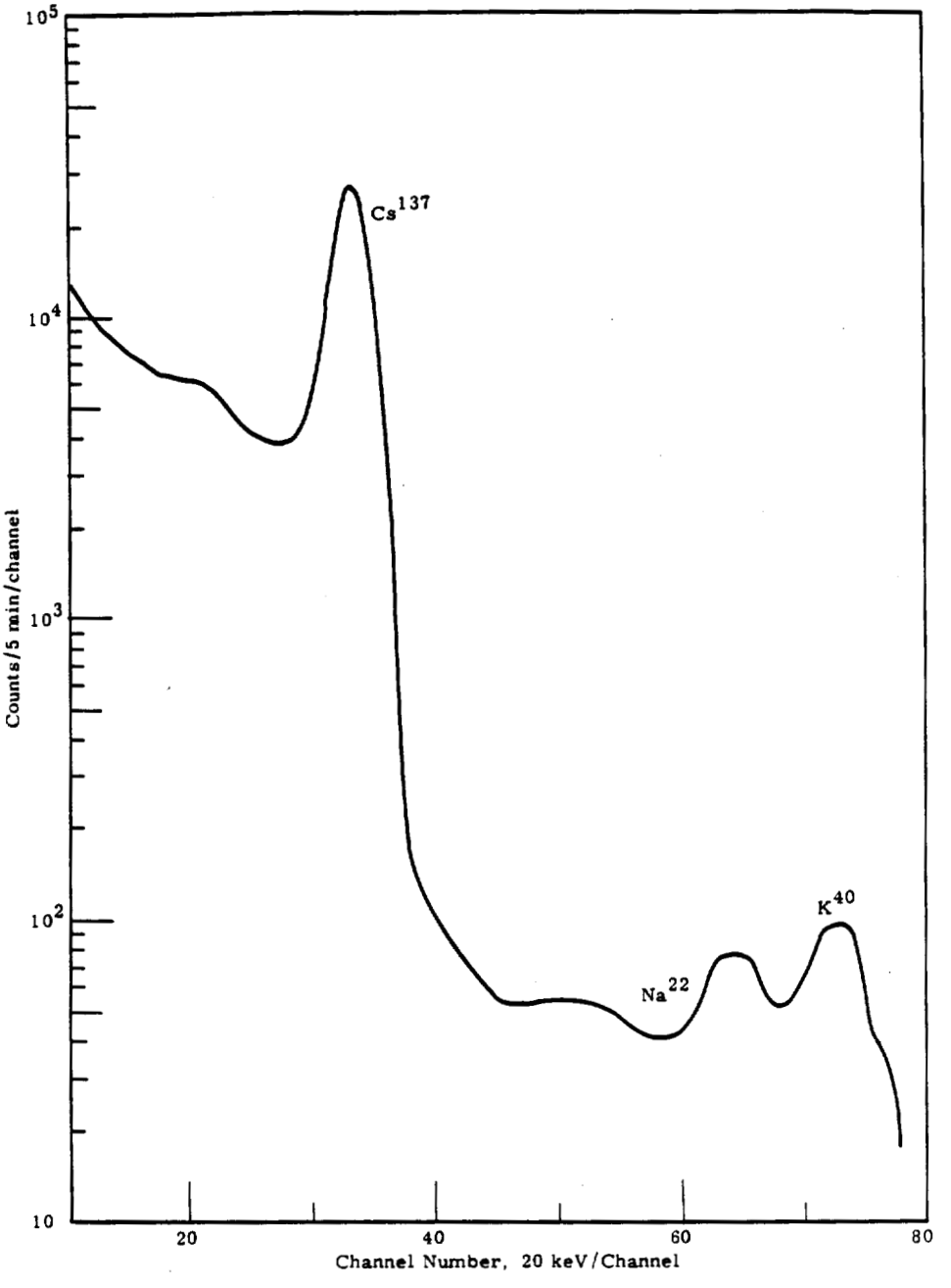

FIGURE 2.6

Sum Spectrum for the 10 Eskimos from Anaktuvuk Pass, Alaska, with the Highest Cs^{137} Body Burdens

0028236

The procedure currently in use for determining Sr^{90} in hair in this laboratory consists of:

(1) Acid dissolution of the hair in concentrated nitric, perchloric, and sulfuric acids containing 30 mg of strontium carrier
(2) Fusion of the mixed calcium and strontium sulfate with sodium carbonate
(3) Dissolution of the carbonate precipitate followed by an iron hydroxide scavenging step to remove traces of radium and its daughter products
(4) Precipitation of calcium and strontium carbonate
(5) Acid dissolution of the carbonate precipitate followed by two successive fuming nitric acid precipitations of strontium as the nitrate
(6) Water dissolution of the final strontium nitrate precipitate and a final carbonate precipitation to isolate the strontium in a form suitable for beta counting.

The chemical procedure as outlined has also been used with success in analyzing 10-g human hair samples containing inert strontium and Sr^{85} and in the analysis of pig hair containing metabolized Sr^{85}. In some samples a slight positive bias has been observed with respect to gravimetric yields versus radiometric yields, but in all cases the bias has not exceeded 6%. Normal recovery of carrier strontium has ranged between 82 and 86%. The procedure is currently being used in the analysis of Alaskan Eskimo hair for Sr^{90}.

The Radiochemical Determination of Plutonium in Soil - W. B. Silker

A procedure is described for the determination of plutonium in soil. The procedure is based on isolation of plutonium by anion exchange methods and electrodeposition. Recoveries of 55 to 65% are reported.

Plutonium contained by soil can be adsorbed on the surface of the soil particles; or, for debris from a nuclear detonation, it can be incorporated within the matrix of refractory compounds. Various methods involving leaching the sample can be highly efficient in removing surface-bound plutonium. Complete dissolution of the sample is required, however,

when plutonium is incorporated in particulates as would be the case in fall-out from either a tower or ground-level nuclear explosion.

The radiochemical procedure outlined below involves fusion of 2-g samples of finely divided soil with sodium carbonate. The melt is reduced to a powder by grinding and is leached by stirring for 1 hr in hot water to remove soluble salts. The insoluble material is removed by filtration, washed with water, and dissolved in 200 ml of 7.2N HNO_3. The sample is heated to 80 C and equilibrated by stirring for 5 min with two 10 g portions of air dried anion exchange resin (Dowex 1 x 2, 50-100 mesh, nitrate form). The resin is transferred to a glass column, washed with additional 7.2N HNO_3, 75 ml of an 8N HCl–0.3N HNO_3 mixture, and plutonium is finally eluted with 100 ml of 0.36N HCl–0.01N HF. The eluate is further acidified with 10 ml of concentrated HNO_3 and 3 ml of concentrated $HClO_4$ and is evaporated just to dryness. The residue is dissolved with 5 ml of 0.5N HNO_3 and the the plutonium is electrodeposited on stainless steel from oxalate solution by the method of Ko.[3.54]

Application of the procedure to spiked soil samples yielded the results shown in Table 3.1. The recovery through the ion exchange separation was determined from an aliquot of the solution taken before electrodeposition.

TABLE 3.1

RECOVERY OF PLUTONIUM FROM SPIKED SOIL

Sample	Recovery After Ion Exchange, %	Recovery After Electrodeposition, %
1	70.3	53.2
2	79.9	58.1
3	89.2	64.7
4	78.2	63.7

Plutonium recoveries of 70.3 and 85.0% were obtained from two samples of contaminated soil from the Nevada Test Site. These samples contained sufficient plutonium to permit its measurement by X-ray counting with a thin NaI(Tl) crystal, which allowed evaluation of plutonium losses

through the procedure. The major loss of plutonium, exclusive of that in the electrodeposition, occurred during the ion exchange adsorption step and the first acid wash. This was believed to result from formation of a plutonium complex with some inorganic constituent, possibly phosphate ion. The final product was free of americium isotopes.

Formation of an inorganic gel would occur if the acid solution was permitted to cool during the ion exchange adsorption step. This was untenable because of plutonium retention in the gel and also fouling of the ion exchange resin. This problem was circumvented by maintaining the temperature of the solution at 80 C and by allowing no delay between sample dissolution and the exchange separation.

The high plutonium recoveries obtainable make this procedure attractive as a method for determination of plutonium in soil. Addition of a known amount of a tracer, such as Pu^{236}, would permit determination of individual sample yield by alpha energy analysis of the final product. If this refinement is not employed, the plutonium levels could still be determined within a deviation of ± 5 to 10%.

A Rapid Method for the Determination of Plutonium in Urine* -
W. B. Silker

In cases of known or suspected exposure of individuals to plutonium it is necessary to obtain rapid estimation of the quantity taken into the body to determine proper therapy. The following method can be used to determine the body burden of an exposed individual within 2 hr after receipt of a urine sample. The method involves retention of plutonium on anion exchange resin by batch contact with digested urine which is 7.2N in HNO_3. After transfer of the resin to a glass column, interfering materials are removed with successive washes of 100 ml of 7.2N HNO_3 and 100 ml of an 8N HCl-0.3N HNO_3 mixture. The plutonium is eluted with 125 ml of a 0.3N HCl-0.01N HF mixture, which is evaporated onto a planchet and measured by alpha counting. Recovery of 84.5 ± 3.3% was obtained from six urine samples containing metabolized plutonium. The deviation was calculated at the 95% confidence limits. Negligible carry-through of the isotopes of uranium, americium, or curium

* Accepted for publication in Health Physics.

occurred; however, 13% of added thorium and 37% of neptunium were found in the plutonium product. The procedure would be capable of detecting 2.0 disintegrations/min/sample with a counting time of 10 min. If a 500 ml sample of the first urine voided following an exposure incident were available, this would correspond to approximately 1% of a plutonium body burden.

Application of Tertiary Amine Extraction to the Determination of Uranium in Biological Materials* - T. M. Beasley

Liquid anion exchange using long chain tertiary amines has been shown to be an effective means of separating actinides from various mineral acid solutions. This technique has been successfully applied to the determination of uranium in tissue and urine. The radiochemical procedures developed are suitable for the analysis of urinary excreta from personnel involved in the processing of irradiated thorium, or from individuals engaged in the investigation of U^{232} as a possible power source.

Table 3.2 shows the extraction limits of the major inorganic elements present in both tissue and urine.

TABLE 3.2

RECOVERY OF MAJOR ELEMENTS PRESENT IN TISSUE AND URINE USING STANDARD EXTRACTION PROCEDURE

Element	Tracer Recovered, %[a]
Calcium	0
Copper	<0.01
Iron	<0.01
Zirconium	<0.02

(a) Each element was examined at both tracer and milligram levels. No difference was observed in the percent recovered.

Uranium recoveries using both spiked and metabolized urine and tissue are 93 ± 2% with excellent decontamination from the uranium daughter products. Uranium can be determined either by alpha counting or by fluorometric methods.

* Accepted for publication in Health Physics.

0028240

The Direct Measurement of Radionuclides in Bioassay Samples by Multidimensional Gamma-Ray Spectrometry - R. W. Perkins

The direct measurement of radionuclides in either whole or ashed bioassay samples has had limited application because of both the relatively large amounts of natural K^{40} present and the overall low radioactivity levels of the samples. The applibility of multidimensional gamma-ray spectrometry to bioassay measurements is evaluated and the concentrations of several radionuclides which are normally present, but which have not previously been observed in bioassay samples, are discussed. The method of measurement, the concentration factors of the radionuclides, and the routes to man of some of these radionuclides are discussed.(3.55)

The Determination of Rare Earth and Yttrium Radionuclides in Reactor Effluent Water by Use of Multidimensional Gamma-Ray Spectrometry - D. E. Robertson

Individual rare earth and yttrium radionuclides in reactor effluent water have been measured, without performing chemical separations, by use of multidimensional gamma-ray spectrometry. After an initial rare earth group separation and removal of lanthanum, the following radionuclides can be measured: Y^{92}, Y^{93}, La^{140}, Ce^{143}, Sm^{153}, Eu^{152m}, Eu^{152}, Eu^{154}, Eu^{156}, and Tb^{160}.

The recent application of multidimensional gamma-ray spectrometry to radioanalytical problems has led to the resolution of complex gamma-ray spectra, involving mixtures of many radionuclides, without performing chemical separations.(3.56, 3.57) The rare earth group of radionuclides present in reactor effluent water is a typical example of such a complex mixture. The present procedure for the determination of individual rare earth and yttrium radionuclides in reactor effluent water involves a group separation followed by a lengthy and intricate ion exchange chromatographic separation.(3.58) This procedure could be greatly simplified if the ion exchange chromatography step could be eliminated. This work is an attempt to measure individual rare earth and yttrium radionuclides from a group separation by the use of multidimensional gamma-ray spectrometry.

0028241

The rare earth and yttrium radionuclides from 2 gal of fresh reactor effluent water containing 5 mg of added cerium carrier were concentrated by a ferric hydroxide scavenge followed by a standard rare earth group separation.[3.58] Since a large concentration of La^{140} is present in fresh reactor effluent water and since its decay scheme would undoubtedly interfere with the measurement of other rare earth radionuclides, the La^{140} was removed from the rest of the rare earth group. This was accomplished by sorbing the total mixture on a small column of Bio-Rad AG-50w (20 to 30 μ) cation exchange resin in the ammonium form and then rapidly eluting the rare earths with 1M lactic acid-ammonium lactate at pH 3.25 and 75 C. The eluant was collected in a small volume of saturated oxalic acid solution, and the elution was discontinued when the cerium had completely eluted, as determined by the absence of the cerium oxalate precipitate formation. Since lanthanum is the last rare earth to elute and is preceded in the elution by cerium and since, under the conditions of this procedure, there is a gap of several milliliters between the cerium and lanthanum factions, the lanthanum could be quantitatively held on the ion exchange resin after all other rare earths and yttrium had been eluted. The oxalate precipitate was mounted on a 1 in. stainless steel dish for coincidence gamma-ray counting with a multidimensional gamma-ray spectrometer, and the La^{140} was measured by gamma counting the resin on a 3 by 5 in. NaI(Tl) crystal coupled to a 400 channel analyzer.

The oxalate precipitate containing the rare earth group, except lanthanum, was counted 8 hr, 2 days, 5 days, and 23 days after sampling of the effluent water. The short half-life radionuclides Y^{92} (3.5 hr), Y^{93} (10 hr), and Eu^{152m} (9.3 hr) could readily be measured from the first count. The longer lived radionuclides Ce^{143} (33 hr), Sm^{153} (47 hr), Eu^{156} (15 days), Eu^{152} (12.5 yr), Eu^{154} (16 yr), and Tb^{160} (73 days) could be measured from the counts taken 2 and 5 days after sampling. The count taken 23 days after sampling showed only those long-living radionuclides listed above, except Sm^{153}.

Standard spectra of all of the above radionuclides must be prepared before Compton corrections and counting efficiencies can be determined.

0028242

Where standard spectra may be difficult to prepare, the counting efficiency can be estimated from an efficiency versus energy curve.[3.56]

A new multidimensional analyzer has been purchased which can perform spectrum stripping. With this technique, lanthanum need not be separated by chemical means, since its contribution can readily be stripped from the spectrum, leaving a residual rare earth coincidence gamma-ray spectrum. The large contributions from the europium radionuclides can also be stripped from the spectrum in a similar manner, yielding a less complex spectrum where possibly other rare earths may be identified and measured.

Many rare earth radionuclides found in reactor effluent water have X-rays or gamma rays of less than 100 keV in coincidence with higher energy gamma-rays. A 1 mm thick by 9 in. diam NaI(Tl) crystal for measuring X-rays and low energy gamma rays has been purchased. This may be used in coincidence with a 5 in. thick by 9 in. diam NaI(Tl) crystal to measure these coincidence events. In this manner additional rare earth radionuclides, other than those mentioned previously, could be measured.

Selective Tissue Accumulation of Uranium and Thorium in Rats After Inhalation of Uranium Ore Dust* - B. O. Stuart** and T. M. Beasley

Evaluation of Radiochemical Methods for Radiological Purposes - W. B. Silker, D. E. Robertson, C. W. Thomas, and R. W. Perkins

Procedures for determining the following radionuclides in the matrices given were evaluated in a program to provide procedures which had been critically evaluated by a laboratory not responsible for the original method development. Americium in water and urine; cerium in water, urine, and soil; P^{32} in urine; plutonium in water, urine, and feces; plutonium in urine and water; polonium in water and urine; ruthenium in soil, water, and urine; Sr^{90} in water and urine; uranium in water and urine by fluorimetry; and uranium in water and urine (radiochemical).

---

* This paper is presented in the Hanford Biology Research Annual Report for 1964.

** Biology Department

Humans Exposed to Uranium Mine Atmospheres* - H. E. Palmer,** R. W. Perkins, and B. O. Stuart***

Fe^{55} in Humans and Their Foods† - H. E. Palmer** and T. M. Beasley

Reactor Studies

The Effect of Water Treatment Chemicals and pH on Reactor Effluent Radioisotope Concentrations†† - W. B. Silker and C. W. Thomas

This paper describes a study designed to evaluate the effect of water treatment flocculating agents and pH on the concentration of radioisotopes in reactor effluent water. Results are reported for periods of water treatment with an aluminum sulfate and sulfuric acid mixture and with an aluminum nitrate and nitric acid mixture, both at pH 6.6 and 7.0.

Experimentation on the effects of water treatment variables on reactor effluent radioisotopes was facilitated upon completion of the Water Treatment Pilot Plant (WTPP). With this unit, sufficient water was treated to cool two reactor process tubes, one aluminum and one zirconium. Both tubes contained aluminum-clad fuel elements throughout these experiments.

The coolant was initially treated with aluminum sulfate as the coagulant and sulfuric acid to maintain pH 6.6 in the finished water. After a suitable period, the pH was increased to 7.0 to evaluate the effect of this variable on reactor effluent activity. Subsequent to the evaluation of steady state concentrations of the effluent radioisotopes under these conditions, aluminum nitrate was substituted as the coagulant, and nitric acid was employed for pH adjustment. The effects of this nitrate system were also evaluated at pH 6.6 and 7.0. During both tests the coagulant feed rate was maintained to provide a coagulum with a zeta potential of 0 to -5 mV, which according to laboratory findings should result in maximum removal of anions from solution.

---

* This paper is presented in Section II, Radiological Physics, on page 2.20. Published in Health Physics, vol. 10, pp. 1129-1135. 1964.

** Physics and Instruments Department

*** Biology Department

† This paper is presented in Section II, Radiological Physics, on page 2.9.

†† Not funded by the Division of Biology and Medicine.

0028244

The concentrations of several radioisotopes in the effluent from the two tubes were measured and compared with values concurrently obtained from the effluent of another aluminum process tube that was cooled with normal process water. The average ratios obtained during the period of water treatment with aluminum sulfate and sulfuric acid are presented in Table 3.3.

TABLE 3.3

AVERAGE RATIOS OF RADIOISOTOPE CONCENTRATIONS DURING FLOCCULATION WITH ALUMINUM SULFATE

	$\left(\frac{\text{Aluminum Tube}}{\text{Control Tube}}\right)$		$\left(\frac{\text{Zirconium Tube}}{\text{Control Tube}}\right)$	
Isotope	pH 6.6	pH 7.0	pH 6.6	pH 7.0
P^{32}	1.36	1.17	0.95	0.82
As^{76}	0.86	1.24	0.55	0.81
Zn^{65}	1.48	1.96	1.00	1.31
Cu^{64}	0.87	1.60	0.45	0.89
Mn^{56}	0.58	1.45	0.31	0.82
Np^{239}	1.23	1.22	0.99	1.06

Only the P^{32} ratio decreased when the pH was changed from 6.6 to 7.0, and the percentage decrease was identical in both the aluminum and zirconium tubes. This is attributed to the decreased sulfuric acid requirement, which reduced the amount of parent sulfur available for the $S^{32}(n, p)$ P^{32} reaction. The Np^{239} ratios were unaffected by change in pH; however, the remaining isotopes were found in lower concentrations at the reduced pH. It was previously shown that removal of parent isotopes by the water treatment process was equally efficient at pH 6.6 and 7.0; therefore, the change in concentration should not be attributable to the water treatment. The lower radioisotope concentrations probably resulted from the decreased aluminum corrosion rate at the lower pH. With reduced corrosion, fewer sites would be available for retention of parent isotopes on the corrosion film, with a resultant decrease in the daughter radioisotope production. The lower concentrations of radioisotopes found in the effluent from the zirconium tube reflect the relative incapability of a zirconium surface to provide sites for parent isotope retention.

The radioisotope ratios observed during water treatment with aluminum nitrate and nitric acid are shown in Table 3.4.

TABLE 3.4

AVERAGE RATIOS OF RADIOISOTOPE CONCENTRATIONS DURING FLOCCULATION WITH ALUMINUM NITRATE

	$\left(\frac{\text{Aluminum Tube}}{\text{Control Tube}}\right)$		$\left(\frac{\text{Zirconium Tube}}{\text{Control Tube}}\right)$	
Isotope	pH 6.6	pH 7.0	pH 6.6	pH 7.0
P^{32}	0.53	0.49	0.56	0.56
As^{76}	0.37	0.46	0.74	0.97
Zn^{65}	1.38	0.85	0.51	0.63
Cu^{64}	0.62	0.81	0.86	1.43
Mn^{56}	0.18	0.31	0.65	0.82
Np^{239}	0.48	0.48	0.40	0.44

The ratios of P^{32} and Np^{239} were nearly constant at the two acidities and were essentially the same for both the aluminum and zirconium tubes. The amount of sulfur present in the cooling water was minimized by treatment with the nitrate system and was constant for both periods of operation. The sources from which the observed P^{32} was derived were the natural sulfur in river water, that amount of phosphate not removed by the water treatment process, and the combined amounts of these two materials present in the reactor components. The concentration of P^{32} in the effluent from the experimental tubes may well represent the minimum attainable under idealized water treatment conditions.

With the exception of Zn^{65} in the aluminum tube, the concentration ratios of the other isotopes were again diminished at the lower pH. The concentrations of the radioisotopes in the effluent from the aluminum tube, however, were significantly lower than in the zirconium tube effluent. In a previous report[3.59] it was shown that the total aluminum corrosion in the experimental aluminum tube was much lower than that in the control tube. Corrosion of the aluminum fuel jackets in the zirconium tube, however, was nearly twice as high as that in the control tube, and as much as three times higher than the cladding corrosion measured in the experimental

0028246

aluminum tube. Thus, it appears that use of the nitrate system for water treatment provided a beneficial effect in the aluminum tube but may have been detrimental with respect to fuel element corrosion in the zirconium tube.

Throughout the period of flocculation with aluminum nitrate, operation of the WTPP was most satisfactory and water of excellent quality was produced. Numerous process perturbations occurred during the period that aluminum sulfate was used as the flocculating agent, due primarily to equipment failures and the initial unfamiliarity of the operators with the problems involved in water treatment processes.

Because of unknown influences due to differences in water quality between these two periods, comparison of the analytical data was not attempted. The data presented in this report, however, indicate that use of the nitrate system at pH 6.6 in the water treatment process will provide minimum effluent activity from both aluminum and zirconium process tubes. Although the benefits were most pronounced in the aluminum tube, reduction in concentrations of the four isotopes of major biological significance, P^{32}, As^{76}, Zn^{65}, and Np^{239}, also occurred under these conditions in the zirconium tube. Reduction of radiophosphorus was noted in each instance that a reduction in sulfate ion was made, which emphasizes the desirability of eliminating sulfuric acid and sulfate salts from the water treatment process.

Removal of Fission Products from Contaminated Water by Flocculation Methods - W. B. Silker

The feasibility of reducing the surface dose rates of a swamp contaminated with fission products by application of flocculant precipitates was determined. The relative effectiveness of three flocculating agents is reported.

Disposal of waste streams containing low levels of radioactive contamination can be made by diverting the water to low lying sections of land. This common practice creates an open swamp from which the water leaves

by percolation through the soil and decontamination is obtained by fixation of the radioisotopes on the bottom sediments. An accidental discharge of curie amounts of fission products to such a swamp created a situation in which decontamination of a shallow body of water with a surface area of about 10 acres was desired. Although decontamination by the natural processes of percolation and bottom fixation of the fission product nuclides was eventually employed, several alternate approaches were considered. This paper presents the results of the study undertaken at that time to determine the feasibility of removing soluble nuclides by flocculation processes.

One liter aliquots of a sample of the contaminated swamp water were treated by each of four methods each employing various concentrations of the reagents. Iron and aluminum were added as $Fe_2(SO_4)_3 \cdot 7H_2O$ and $Al_2(SO_4)_3 \cdot 18H_2O$. Stoichiometric amounts of $KMnO_4$ and $FeSO_4$ were added to a third set of samples resulting in Fe^{+++} and MnO_2 as the products of the redox reaction. Potassium permanganate, the sole additive to the final set of samples, underwent partial biological reduction resulting in the formation of MnO_2. The hydrolysis products of these additives formed a matrix incorporating various amounts of the dissolved fission products. Fission product removal was then achieved by coagulation and settling. The additives were introduced without stirring, with one exception, in an attempt to simulate potential application to the swamp. The efficiency of the various agents in removing fission products was determined by periodic removal of a small sample from 1/2 in. below the liquid surface. After evaporation, the quantity of radioisotopes in the sample was measured by gamma spectrometry. The results are shown in Tables 3.5 through 3.8.

TABLE 3.5

REMOVAL OF FISSION PRODUCTS FROM WATER BY TREATMENT WITH FERRIC SULFATE

Settling Time, hr	Percent Removal								
	20 ppm Iron			50 ppm Iron			100 ppm Iron		
	Cerium	Ruthenium	Zr-Nb	Cerium	Ruthenium	Zr-Nb	Cerium	Ruthenium	Zr-Nb
1	0	1.2	1.4	48	43	52	58	63	68
5	50	29	42	92	74	91	88	85	94
26							95	91	99
45							>98	92	>99
120							>98	92	>99

TABLE 3.6

REMOVAL OF FISSION PRODUCTS FROM WATER BY TREATMENT WITH ALUMINUM SULFATE

Settling Time, hr	Percent Removal											
	10 ppm Aluminum			20 ppm Aluminum			50 ppm Aluminum			100 ppm Aluminum		
	Cerium	Ruthenium	Zr-Nb	Cerium	Ruthenium	Zr-Nb	Cerium	Ruthenium	Zr-Nb	Cerium	Ruthenium	Zr-Nb
1	15	0	0	0	0	2.0	0	9	4	73	60	87
6	5	0	0	5	0	3.2	71	48	70	95	76	95
23										>98	78	98
27										>98	79	99
100										>98	79	99
120										>98	78	99

TABLE 3.7

REMOVAL OF FISSION PRODUCTS FROM WATER BY TREATMENT WITH $KMnO_4$ AND $FeSO_4$

Settling Time, hr	Percent Removal											
	10 ppm $KMnO_4$ 29 ppm $FeSO_4$			50 ppm $KMnO_4$ 144 ppm $FeSO_4$			50 ppm $KMnO_4$ 144 ppm $FeSO_4$ [a]			100 ppm $KMnO_4$ 283 ppm $FeSO_4$		
	Cerium	Ruthenium	Zr-Nb	Cerium	Ruthenium	Zr-Nb	Cerium	Ruthenium	Zr-Nb	Cerium	Ruthenium	Zr-Nb
1	0	3.3	6.3	88	58	93	75	75	86	72	78	92
6	81	62	82	96	62	98	>98	88	98	79	84	98
24	97	73	97	>98	67	>99	>98	91	>99	>98	87	>99
29				>98	67	>99						
47				>98	67	>99						
120				>98	67	>99						

(a) Stirred after reagent addition.

TABLE 3.8

REMOVAL OF FISSION PRODUCTS BY TREATMENT WITH $KMnO_4$

Settling Time, hr	Percent Removal								
	10 ppm $KMnO_4$			30 ppm $KMnO_4$			50 ppm $KMnO_4$		
	Cerium	Ruthenium	Zr-Nb	Cerium	Ruthenium	Zr-Nb	Cerium	Ruthenium	Zr-Nb
17	10	7	8	41	35	59	71	42	68
89	94	66	89	>98	66	95	>98	65	95

With the exception of aluminum sulfate in low concentrations, all of the chemicals tested were successful to varying degrees in removing Ce^{141}, Ru^{103}, and $Zr\text{-}Nb^{95}$. The degree of removal was a function of the additive concentration. Aluminum sulfate at a concentration of 100 ppm and the mixture of potassium permanganate and ferrous sulfate at respective concentrations of 50 and 144 ppm were equally efficient, each providing near quantitative removal of Ce^{141} and $Zr\text{-}Nb^{95}$ and a 70 to 80% reduction in Ru^{103}. The use of 100 ppm of ferric sulfate provided the best decontamination of any of the reagents tested. Essentially no removal of Cs^{137} was obtained with any of these processes. The chemistry of these processes was such that most of the strontium contamination would also remain in solution.

It was concluded that treatment of highly contaminated waters with any of these chemicals could provide a significant decrease in the surface dose rate by coprecipitation of many of the fission products. No removal of cesium or strontium isotopes would be anticipated.

Counting Studies

Anticoincidence Shielded-Multidimensional Gamma-Ray Spectrometry for High Sensitivity Analysis of Radionuclide Mixtures* - R. W. Perkins

This paper presents a summary of the method and numerous applications of multidimensional gamma-ray spectrometry. The operation, counting efficiency and sensitivity of the instrument is considered along with applications including the direct measurement of numerous radionuclides in complex radionuclide mixtures which have previously required extensive chemical separations plus extremely sensitive counting methods. Applications of this direct instrumental method of analysis which are demonstrated include the measurements of 12 radionuclides on air filters, of 15 radionuclides in Hanford reactor effluent water, of the distribution of cosmic-ray produced Na^{22} through the biosphere, of several radionuclides in bioassay samples, of cosmic-ray produced Na^{24} in rain water, and of the discovery of cosmic-ray produced Cl^{38} and S^{38} in the atmosphere.

An Anticoincidence Shielded-Multidimensional Gamma-Ray Spectrometer** - R. W. Perkins

A three-crystal detector system has been fabricated and evaluated in conjunction with a 4096 channel multiparameter analyzer for multidimensional gamma-ray spectrometry. The detector system consists of two 4 in. thick by 6 in. diam NaI(Tl) crystals that are contained in the center hole of an annular NaI(Tl) crystal of 11 1/2 in. diam by 12 in. thick. The spectrometer utilizes the gamma-ray decay characteristics of each radionuclide for its identification and measurement by viewing the sample with two detectors and canceling those events not totally absorbed in these principal detectors with a third detector which serves as an anticoincidence annulus. Coincidence counts are stored according to the photon energies responsible for the event in the energy-energy plane of the memory while noncoincidence events are

---

* International Conference on Radiochemical Methods of Analysis, Salzburg, Austria, October 19-23, 1964, paper SM-55/53, IAEA Proceedings.

** Accepted for publication in Nuclear Instruments and Methods.

stored in the normal manner. For triple coincidence spectrometry the three detectors view the source, and the coincidence spectrum of any two can be recorded while the third detector serves as the coincidence monitor. Measurements of the system's counting efficiency, and of factors affecting its background, Compton, and backscatter response are discussed along with some applications of the instrument.

A High-Resolution Lithium-Drifted Germanium Gamma-Ray Spectrometer-

M. W. Hill

A gamma-ray spectrometer has been constructed which uses a lithium-drifted germanium diode as the detector. Typical spectra which compare the high resolution of this detector system with that of a conventional sodium iodide spectrometer are presented along with a brief description of the system and proposed modifications.

The development of lithium-drifted germanium detectors has received world-wide attention during recent months and promises to revolutionize the field of gamma-ray spectrometry.[3.60] To become familiar with the use of these detectors and to explore potential areas of application, we constructed such a spectrometer. The spectrometer consists of a source holder and vacuum chamber,* a cryostat* for cooling the detector* to liquid nitrogen temperatures, a lithium-drifted germanium diode, a power supply and preamplifier, and a 400-channel pulse-height analyzer.

The detector used has an active area of 1.0 cm^2 and a depletion depth of 1 mm. It has a resolution of 8.7 keV (FWHM) at 662 keV and 6.3 keV (FWHM) at 60 keV. The door of the vacuum chamber was replaced with one having a recessed shelf which permits samples to be placed directly beneath the detector but outside the vacuum chamber itself. The vacuum is provided by an 8.0 liter/sec Vac Ion pump. Cooling was attempted initially with a Joule-Thompson effect cryostat utilizing a high-pressure source of prepurified nitrogen gas. This proved to be unsatisfactory, however, as water vapor and CO_2 invariably solidified in the cryostat, causing it to clog and fail. Cooling was later provided by liquid nitrogen, which unfortunately required constant attention because of the small size of the Dewar. An Ortec Model 101 preamplifier is used in conjunction with the amplifiers built into the 400-channel pulse-height analyzer.

---

* Solid State Radiations, Inc., Los Angeles

0028251

Spectra of standard sources of Am^{241}, Hg^{203}, Ce^{144}, Be^{7}, Cs^{137}, Cs^{134}, Sc^{46}, Co^{58}, Y^{88}, and Sb^{125} have been accumulated along with spectra of gross fission products of various ages and chemically separated fission products such as Pm^{148}, Eu^{154}, Eu^{155}, and Cs^{136}. The high resolution provided by the lithium-drifted germanium detector reveals features in these spectra that cannot be seen with a conventional sodium iodide spectrometer. Spectra of a 13 mo old fission product sample are reproduced in Figures 3.18 and 3.19 to illustrate this point. It is obvious that the detail provided by the Ge(Li) counter will enable many studies to be made which were previously thought to be impossible. The system should be particularly useful in studies of fission products, where the high resolving power of the detector may be conveniently utilized with the intensely radioactive sources which are available. Although the photoelectric counting efficiency of the detector is low, particularly for high energy gamma rays, its high resolution offsets this disadvantage in many other studies.

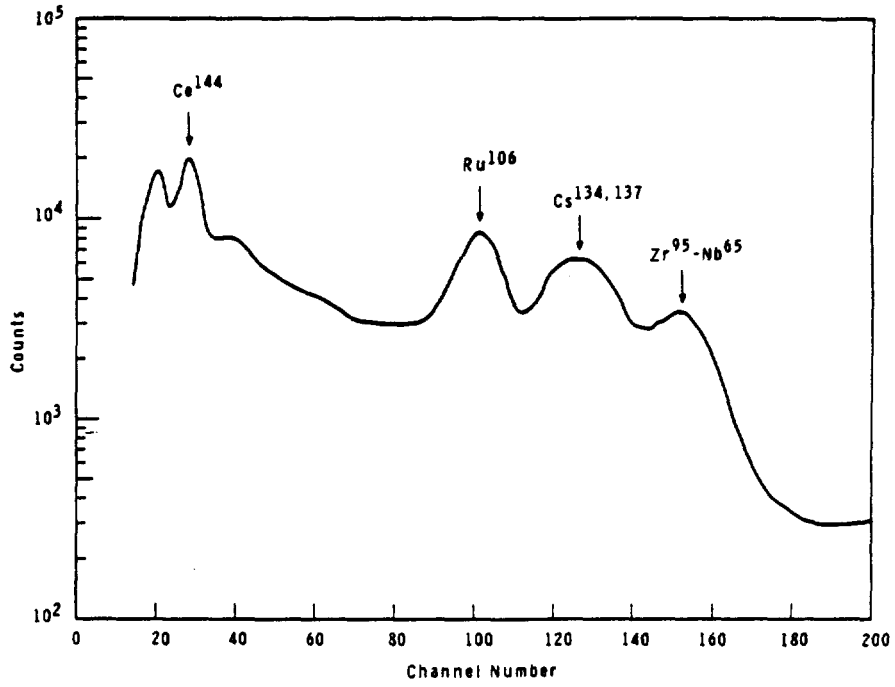

FIGURE 3.18

Gamma-Ray Spectrum of 13 mo Old Fission Products Taken with 3 by 5 in. NaI Detector

Neg. No. 0643396-3

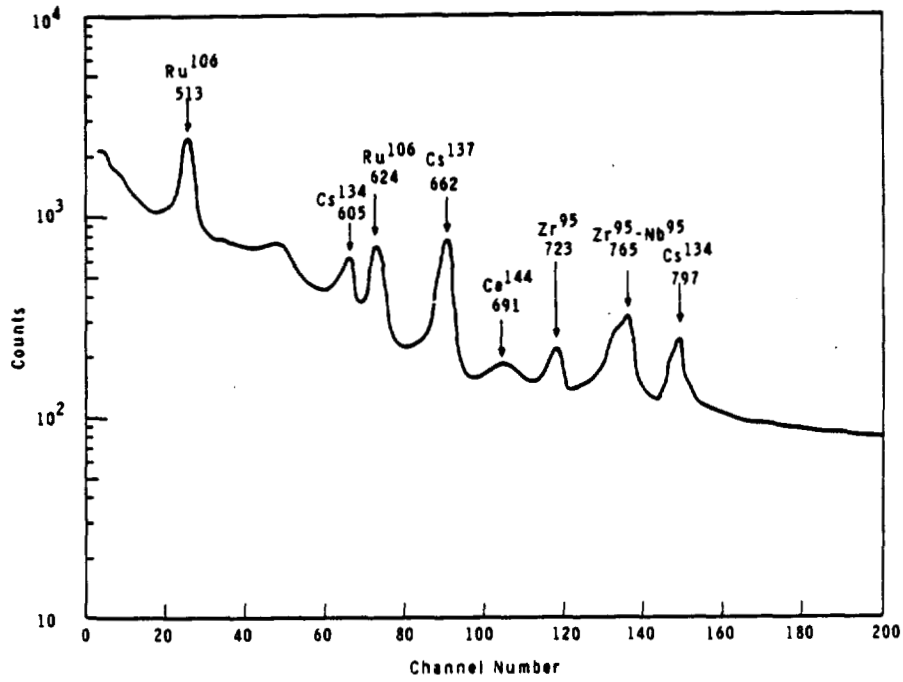

FIGURE 3.19

Gamma-Ray Spectrum of 13 mo Old Fission Products Taken with Lithium-Drifted Germanium Detector

The photoelectric counting efficiency of the detector has been determined by calibration with several standard sources. The efficiency curve is shown in Figure 3.20. The efficiencies shown are for disc sources placed on the top shelf of the spectrometer and are given as the number of counts per gamma ray emitted by the source. For low energy gamma rays the efficiency is high and the resolution is much better than that obtained with proportional counters. Resolutions of just over 2 keV have been obtained by other groups using Ge(Li) counters. For higher energy gamma rays the efficiency is low but good counting statistics may still be obtained with millicurie sources in a matter of minutes. For high energy gamma rays (greater than about 1.7 MeV) the cross-section for pair-production becomes larger than that for the photoelectric effect, and intrinsic efficiencies of 0.3% at 2.614 MeV and 0.2% at 7.639 MeV have been reported for the "double-escape" peaks produced.[3.61]

Neg. No. 0643396-4

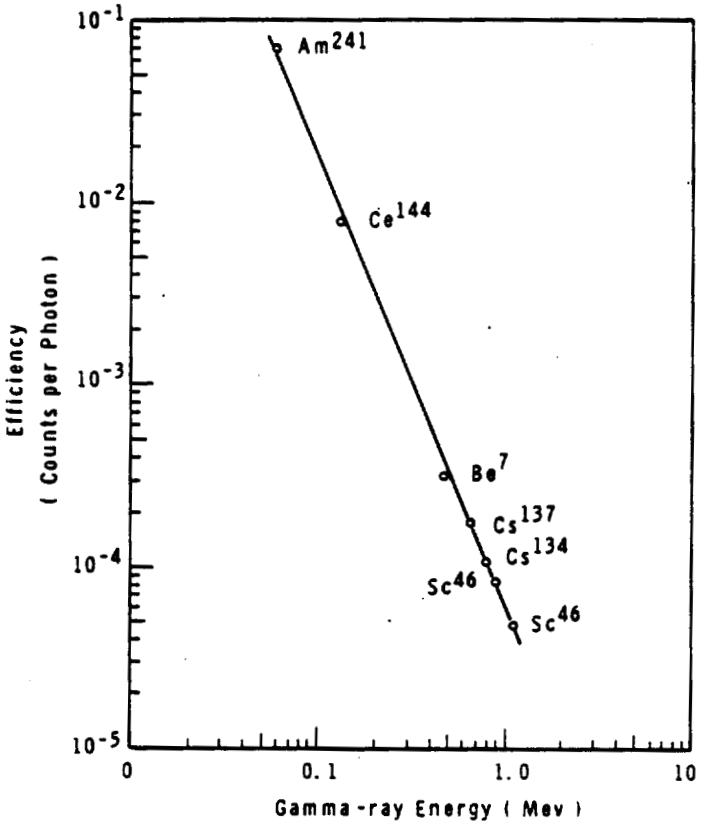

FIGURE 3.20

Counting Efficiency Curve
for Lithium-Drifted Germanium Detector

One of the undesirable features of the present system is the method of cooling. Because of the small size of the Dewar it must be refilled every 10 min and requires almost constant supervision. The detector is therefore removed from the system whenever it is not being used, placed in an air-tight container, and stored in dry ice. A chamber is now being built which will accommodate a 10 liter liquid nitrogen reservoir. This should require filling no oftener than 2 to 3 days and will enable the detector to be kept indefinitely in the chamber at -196 C.

Another undesirable feature of the present system is the large Compton distribution produced by gamma rays scattered into and away from the detector. This Compton background will be reduced in the near future by utilizing a 26 in. diam plastic scintillator as an anti-coincidence shield.

Neg. No. 0643396-6

A reduction in the Compton background will enable measurements to be made of low energy gamma rays in the presence of more intense higher energy gamma rays.

Large Area Alpha Ray Spectrometry - T. M. Beasley

The development of large area alpha spectrometers capable of measuring alpha-emitting radionuclides in the natural environment is described. Preliminary tests and applications are reported.

The need to measure and identify alpha emitting radionuclides at extremely low specific activities has led to the development of large area alpha spectrometers capable of measuring radioactivity of near a picocurie per gram of material.[3.62-3.65] The present discussion describes two spectrometers that are currently being developed for use in measuring naturally occurring alpha emitting radionuclides and also for tracing the translocation of uranium daughter products following inhalation by experimental animals.

The instruments under development at this laboratory are essentially those described by Hill.[3.62-3.64] Briefly, the spectrometers consist of cylindrical chambers capable of accommodating source areas of 1200 cm^2 and 15,000 cm^2. The large source areas are requisite in that high resolution alpha spectroscopy requires surface densities no greater than 100 $\mu g/cm^2$. The counting gas used in the pulse ionization chambers is a 90:10 argon-methane mixture maintained at atmospheric pressure and circulated at a rate of about 2 liters/min through the chamber and purification train. The latter consists of a heated (350 C) calcium bed to remove oxygen, followed by an activated charcoal bed maintained at -78 C for removing radon contamination, and finally a charcoal and Drierite bed to remove traces of moisture. Before entering the chamber the counting gas passes through a final thermostated bed to maintain the gas at a constant temperature. The pulses from the ionization chamber are fed to a 400 channel pulse height analyzer for alpha energy analysis.

The smaller of the two chambers makes use of a Frisch grid to reduce the "positive ion effect" and thus increase the resolution of the instrument. The larger chamber employs a thin metal rod passing through the center of the chamber as the collecting electrode. Each chamber has guard rings at the ends which establish a graded potential thus providing similar field conditions all through the chamber.

Source preparation is undoubtedly the limiting factor in large area alpha spectrometry. The technique most commonly employed consists of grinding the sample to particle sizes of 1μ or less, slurrying the residue with water, and aspirating the suspension onto a previously wetted aluminized cellulose acetate sheet which serves as the source holder. Alpha peaks with half widths at full maximum of 150 to 200 keV have been obtained using this technique. Another approach for biological samples is to oxidize the sample in an atomic oxygen furnace thus removing the organic material, then to grind the resultant ash and aspirate the slurry onto the source holder. The latter approach has the advantage of using larger initial samples.

The measurement of alpha emitting radionuclides in water can be accomplished by reducing large volumes through boiling and aspirating the small residue onto the sample holders. There is a risk however of losing some radionuclides through hydrolysis (notably polonium, thorium, and plutonium). A technique employed at this laboratory has been to acidify the water solutions to prevent hydrolysis and then to carry the alpha emitting radionuclides from a basic solution using a nominal iron hydroxide precipitate (normally using 20 mg iron carrier). The precipitate is then dissolved in dilute acetic acid (0.1M) and aspirated onto the sample holder. Virtually all actinides and heavy metal elements are carried by the precipitate. The exceptions to the method are the alkaline earths, including radium, which are not carried quantitatively. The technique is useful, however, in that it avoids the long times necessary for boiling solutions to low volumes with the attendant risk of loss through spattering. No loss of resolution occurs; in some instances source quality has improved.

Figure 3.21 shows a test spectrum of a solution of thorium nitrate salt. Although the activity is high, it serves to indicate the type of information one can obtain using the instruments described. The background counting rate in the chambers is such that 0.5 pCi of a monoenergetic alpha emitter can be easily detected and identified. Instrument stability is good (less than 1% drift in 8 hr) which enables one to count for periods of up to 1000 min.

The use of large-area alpha spectrometry should permit the measurement of alpha-emitting isotopes in the natural environment, in various organs of experimental animals following administration of tracers, in sediments from rivers whose waters are used for cooling nuclear reactors, and in the measurement of fallout debris resulting from both subterranean and atmospheric nuclear tests.

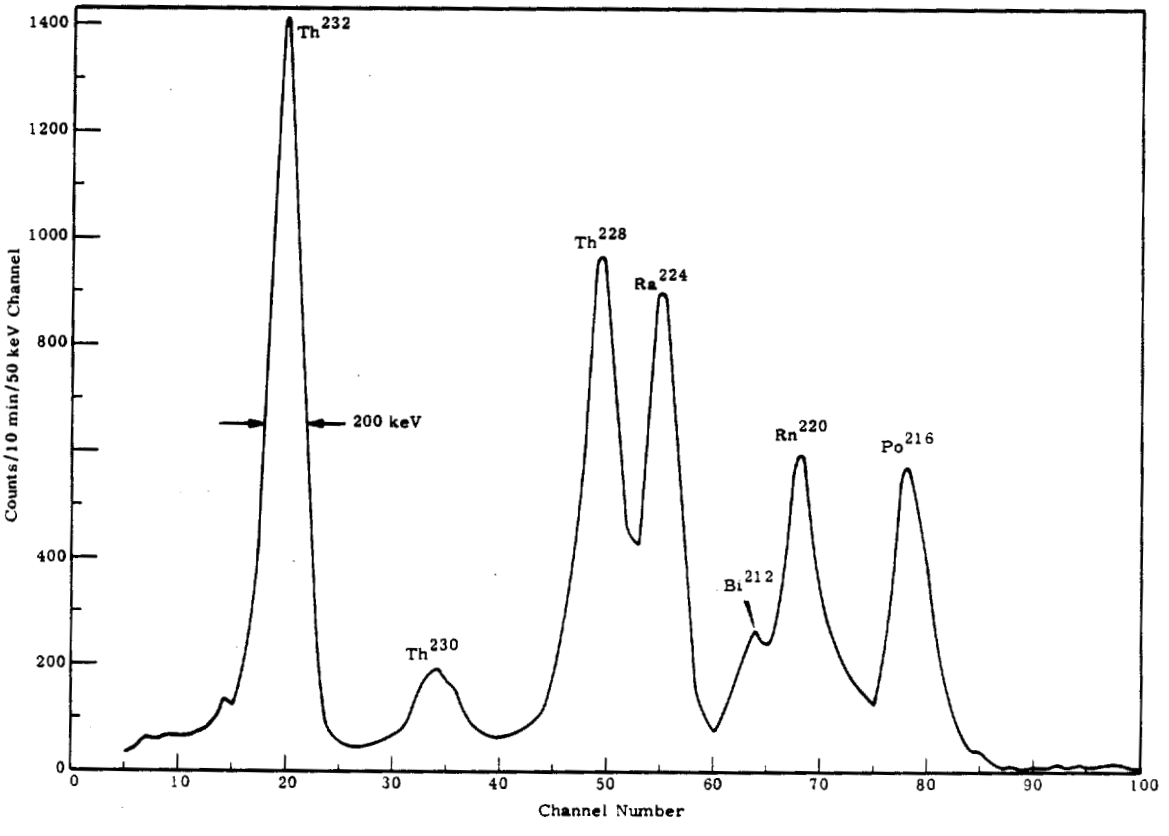

FIGURE 3.21

Alpha Energy Spectrum of $Th(NO_3)_4$ Salt
(Source Area = 1200 cm^2)

Environmental Studies

Airborne-Radionuclide Measurements and Physical Characteristics Determinations* - R. W. Perkins, C. W. Thomas, and J. M. Nielsen

The measurement, distribution in the atmosphere, and the physical and chemical behavior of the 13 radionuclides Be^7, Na^{22}, Mn^{54}, Co^{60}, Y^{88}, Zr^{95}-Nb^{95}, Ru^{106}, Sb^{124}, Sb^{125}, Cs^{134}, Cs^{137}, Ce^{144}, and Pu^{239} are described. With the exception of Pu^{239} all of the radionuclides were measured directly by multidimensional gamma-ray spectrometry and the concentrations of the radionuclides for the period 1962 through September 1964 at Richland, Washington, are included. The stratospheric distribution of this large group of radionuclides is covered along with their measured solubility and their deposition rates as both wet and dry fallout. The stratospheric distribution and fallout rates of the tracer radionuclides Y^{88} and Sb^{124} are discussed.

Physical and Chemical Characteristics of Various Fallout Radionuclides - C. W. Thomas

Dry fallout and rain samples were filtered and the filtrate passed through anion and cation exchangers to investigate some of the physical and chemical characteristics of the fallout radionuclides. Similarities and differences are reported in the behavior of the 11 radionuclides studied.

In June, 1964, a study of the physical and chemical characteristics of fallout radionuclides was started. Plexiglas trays covering a 78.7 ft^2 area and containing 1 in. of water were used to collect "dry" fallout. Concurrently, plastic coated metal trays covering 90 ft^2 were used to collect rain samples. The rain trays were tilted so that any precipitation would drain from a spigot to be collected directly into large plastic carboys or passed through filter and ion exchange columns before collection. The rain trays were washed daily to rid them of any "dry" fallout collected during the day. A standard U. S. Weather Bureau Rain Gage was used to measure the amount of precipitation which fell. With these trays, a comparison of radionuclides associated with dry and rain fallout was made. Also, with filtered water from the dry fallout collectors an indication was obtained of different solubilities of radionuclides.

---

* Proceedings of the Second AEC Fallout Conference, November 3-6, 1964. Washington, D. C.

0028258

Since the annual precipitation in this area is only 8 in., rainfall is not the major mechanism for fallout deposition. The contribution due to rain during the summer of 1964 is shown in Figure 3.22. Rain-out and wash-out of the atmosphere as compared to the dry deposition should be influenced by any difference in size and mass of the particles associated with the radionuclides with the larger and heavier particles favoring the dry fallout mechanism. If such is the case the data then indicate that Sb^{124}, Cs^{137}, and Y^{88} were associated with larger particles than Ru^{106}, Na^{22}, and Mn^{54}.

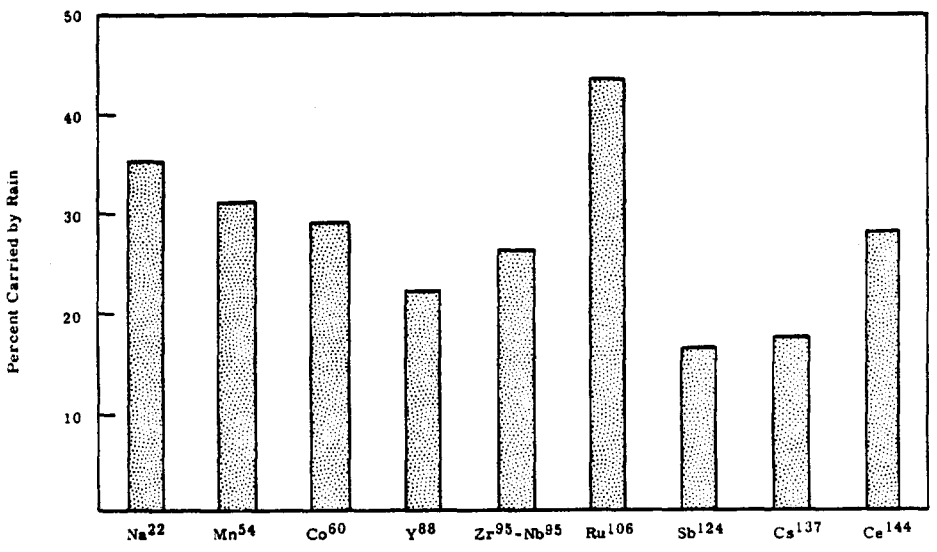

FIGURE 3.22

Comparison of the Radionuclide Concentrations of Rain and Dry Fallout

The amount of radionuclides found in solution from the dry fallout and in rain samples as presented in Figure 3.23 were obtained by filtering each sample through a 5 μ pore size membrane filter. The fraction which penetrated the filter was considered "in solution." Two periods of approximately 2 wk duration were selected: a period in which 0.2 in. of rain fell and another in which no precipitation occurred. The major fraction of the radionuclides associated with rain-out and wash-out of the atmosphere

Neg. No. 0642840-12

passed through the filter. These same radionuclides from dry fallout were retained on the filter indicating either a larger particle size, or sorption of the radionuclide onto larger foreign particulates in the water of the dry fallout collectors, or agglomeration of the fallout particles. Since in most cases the more soluble species in rain were also the more soluble species in dry fallout, these results would indicate that agglomeration of particles was appreciable in the dry fallout collectors.

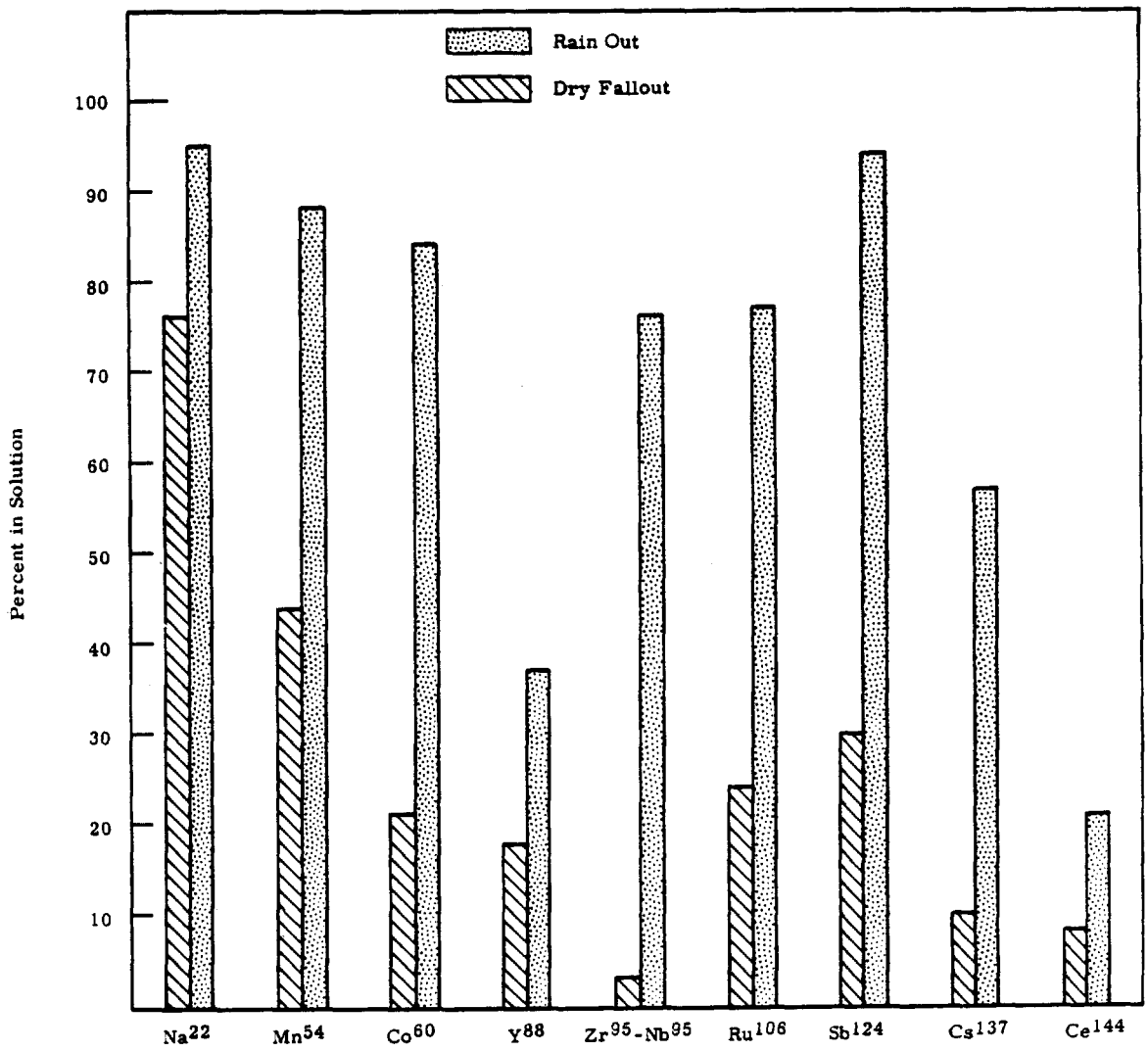

FIGURE 3.23

Solubilities of Fallout Isotopes

Neg. No. 0642840-13

These results indicate that immediate filtering is essential. This was possible only with rain samples where the activity density was sufficiently high to measure short term collections. A system was built which incorporated a filter and two fast flow ion exchange cartridges. As the rain was collected it was filtered, passed through the ion exchangers and the effluent collected in a carboy. The results from the first rain using a 5 μ filter followed by an anion exchanger and a cation exchanger are presented in Table 3.9.

TABLE 3.9

FORMS OF RADIONUCLIDES IN RAINWATER OBTAINED FROM FILTER AND ION EXCHANGE STUDIES

	Total Activity, %			
Isotope	5 μ Filter	Anion Resin	Cation Resin	Effluent
Ru^{106}	18	57	7	18
Sb^{124}	15	68	2	15
$Zr\text{-}Nb^{95}$	36	55	2	7
Sb^{125}	25	58	2	15
Na^{22}	2	10	85	3
Cs^{134}	25	2	70	3
Mn^{54}	20	2	75	3
Co^{60}	60	7	30	3
Cs^{137}	65	6	25	4
Y^{88}	75	16	6	5
Ce^{144}	87	10	1	2

The distribution of the fallout radionuclides on the 5 μ filter was in general agreement with previous data with the exception of Co^{60} which was found at a much higher extent on the filter. The majority of Ru^{103}, Sb^{124}, $Zr\text{-}Nb^{95}$, and Sb^{125} were collected on the anion column, with small amounts collecting on the filter, and any remaining radionuclides passed through the cation column to be collected in the effluent. Since the anion column immediately followed the filter, the removal of radionuclides by this column could be due to filtration of particles less than 5 μ diam as well as to anion exchange. The radionuclides Na^{22}, Cs^{134}, and Mn^{54} were retained in small amounts by the filter, were pervious to the anion column, and were removed mainly by the cation column indicating their cationic

nature. Co^{60} and Cs^{137} were removed mainly by the filter and that which passed through was retained on the cation column. Y^{88} and Ce^{144} were also retained mainly by the filter, but that which passed through was removed by the anion column.

Air Concentrations of Short-Lived Radionuclides Resulting from 1964 Chinese Detonation - C. W. Thomas

Fission products resulting from the Chinese detonation in October, 1964, were measured in samples of atmospheric debris, rain water, and material collected in fallout trays. Concentrations of Np^{239}, $Ba\text{-}La^{140}$, $Te\text{-}I^{132}$, Mo^{99}, $Zr\text{-}Nb^{95}$, Ce^{144}, Ru^{106}, Cs^{137}, and Mn^{54} were measured using multidimensional gamma ray spectrometry.

Four days after the Chinese detonation of October, 1964, fallout debris was detected in ground level air samples taken at Richland, Washington. These samples showed the presence of short-lived fission products in addition to the normal fallout spectrum which was concurrently being measured. The concentration of $Ba\text{-}La^{140}$ was used to follow the passage of the radioactive cloud resulting from this detonation. These data are presented in Figure 3.24, and indicate that the radioactive cloud required 11 days to circumnavigate the globe. By the third passage the cloud had become so diffuse as to be barely recognizable. To overcome the counting interference from thoron and short-lived daughters at ground level, an air sample was taken by airplane at 12,000 ft on October 22, 1964, and analyzed by multidimensional gamma ray spectrometry. The results are presented in Table 3.10.

During collection of this air sample the air flow gage was somewhat erratic so that activity measurements per unit volume of air cannot be presented with certainty. The sampling period was 2 hr, and under normal conditions the volumes of air filtered should be near 6000 ft^3/min.

Since June, 1964, fallout radionuclides have been collected in fallout trays bimonthly. The two samples collected in October, 1964, on this program afforded a direct comparison of the Chinese contribution to the worldwide fallout. The results from these fallout trays are presented in Table 3.11.

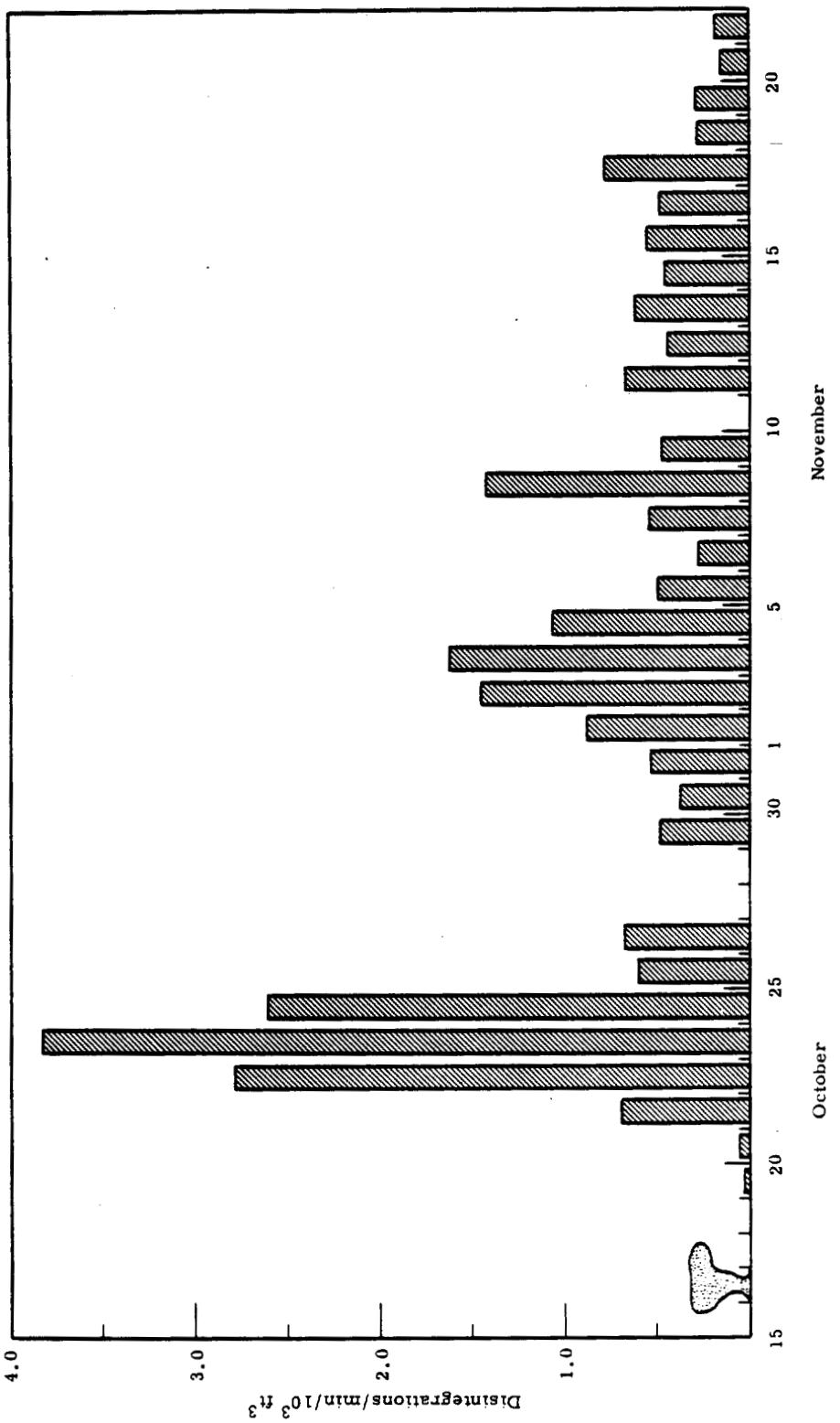

FIGURE 3.24

$Ba\text{-}La^{140}$ Concentrations in Air Samples

TABLE 3.10

CONCENTRATIONS OF RADIONUCLIDES COLLECTED AT 12,000 ft ALTITUDE DURING PASSAGE OF CLOUD FROM CHINESE TEST DETONATION

Radionuclide	Disintegrations/min/sample
Np^{239}	8700
$Ba\text{-}La^{140}$	3600
$Te\text{-}I^{132}$	3000
Mo^{99}	1400
$Zr\text{-}Nb^{95}$	211
Ce^{144}	134
Ru^{106}	64
Cs^{137}	30
Mn^{54}	4.1
Ru^{103}	(a)
Ce^{141}	(a)
Na^{22}	Not detected
Co^{60}	Not detected
Y^{88}	Not detected
Sb^{124}	Not detected
Cs^{134}	Not detected

(a) Significant photopeaks occurred at these energies, but quantitative values have not yet been determined.

TABLE 3.11

DEPOSITION OF RADIONUCLIDES NEAR RICHLAND, WASHINGTON DURING OCTOBER, 1964

	Disintegrations/min/ft^2	
Radionuclides	10/1/64 to 10/15/64[a]	10/15/64 to 10/28/64[b]
$Ba\text{-}La^{140}$	0	237
Ru^{106}	50	32
Ce^{144}	97	30
Cs^{137}	25.7	15
$Zr\text{-}Nb^{95}$	2.3	23.3
Mn^{54}	9.9	7.1
Sb^{124}	0.15	0.22
Co^{60}	0.13	0.14
Na^{22}	0.083	0.04
Y^{88}	0.078	0.047
Cs^{134}	0.067	0.04

(a) Represents the activity corrected to 10-7-64.

(b) Represents the activity corrected to 10-21-64.

Weather conditions during the two sampling periods were nearly identical except that the sample collected during the first part of October contained 0.11 in. of precipitation while the sample collected during the latter part of the month contained 0.07 in. of precipitation. The most notable change in radionuclide concentration was the marked increase in $Zr\text{-}Nb^{95}$ which before the detonation had reached the lowest concentration since the moratorium on nuclear testing. The reduction in the concentrations of the other isotopes was predictable and was due to seasonal trends that have been noted in 1962 and 1963.

Measurement of Airborne Radionuclides in Alaska - R. W. Perkins and H. G. Rieck

A high volume air filtering pump has been installed at the Arctic Research Laboratory, Point Barrow, Alaska. A comparison of several airborne radionuclides at Point Barrow and Richland, Washington, is presented.

In conjunction with studies of the fallout rates and mechanisms of airborne radionuclides it has been possible to measure 13 long-lived radionuclides on air filters by direct counting[3.66, 3.67] and to show the distribution in the stratosphere of several of the radionuclides as a function of latitude.[3.68] Although measurements of this large group of radionuclides have been made at a few latitudes in stratospheric samples they have been measured only at one location (Richland, Washington) at ground level. To improve our knowledge of the relative behavior of airborne radionuclides, high volume air sampling pumps are being located in Alaska and in the Southern Hemisphere. The Alaskan sampler was installed in November, 1964, at the Arctic Research Laboratory, Point Barrow, Alaska. The location for the Southern Hemisphere sampler has not yet been determined. The air sampler consists of a 100 ft^3/min vacuum pump that pulls air through an 8 by 10 in. membrane filter (5 μ pore size). The pump, plus its 8 ft cubical housing (Figure 3.25), is located 25 ft above ground level on a meteorology tower at the Arctic Research Laboratory.

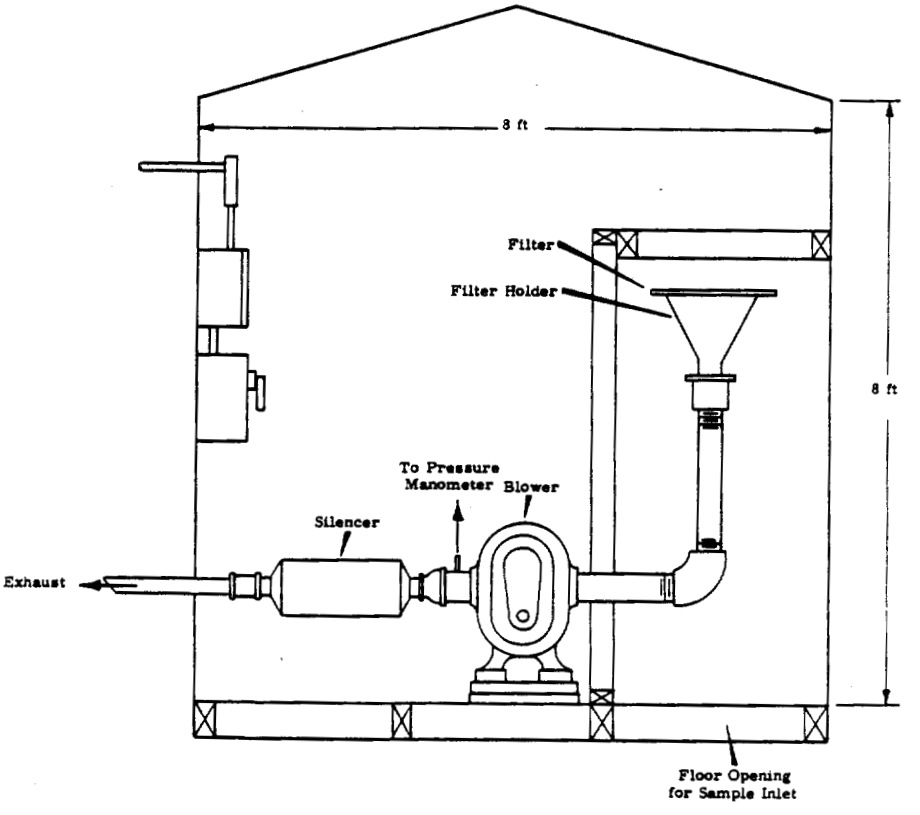

FIGURE 3.25

Air Filtering Installation at Point Barrow, Alaska

The radionuclide concentrations observed during December, 1964, on the Alaskan air filters and those from Richland, Washington, are compared in Table 3.12. Their ratios normalized to their respective Cs^{137} concentrations are included to permit a comparison of the relative radionuclide concentrations. It is apparent that in addition to the generally lower radionuclide concentrations in Alaska there are rather large differences in the relative compositions. Although a single comparison of these locations is of limited value it does serve to show the magnitude of the variations, and over a 1 yr period this type of information should prove

extremely valuable in understanding the independent behavior of the various airborne radionuclides.

TABLE 3.12

COMPARISON OF RADIONUCLIDE CONCENTRATIONS IN AIR FILTERS FROM POINT BARROW, ALASKA, AND RICHLAND, WASHINGTON

(December, 1964)

Radionuclide	Concentrations, disintegrations/min/10^6 ft^3		Ratio of Concentrations Normalized to Cs^{137}, $\left(\frac{\text{Point Barrow}}{\text{Richland}}\right)$
	Richland	Point Barrow	
Be^7	3380	2820	1.63
Na^{22}	1.89	2.20	2.28
Mn^{54}	172	189	2.14
Co^{60}	13.3	2.12	0.312
Y^{88}	0.97	1.43	2.87
$Zr\text{-}Nb^{95}$	465	192	0.807
Ru^{106}	1300	885	1.33
Sb^{124}	2.37	1.86	1.53
Sb^{125}	322	347	2.10
Cs^{134}	23.7[a]	0.50	0.0410[a]
Cs^{137}	824	422	1.00
Ba^{140}	157	55.0	0.681
Ce^{144}	2020	1770	1.71

(a) The Cs^{134} concentration at Richland, Washington during the last half of December was more than ten times higher than usual.

Na^{22} and Cs^{134} in Fallout, Foods, and People* - R. W. Perkins and J. M. Nielsen

The air concentrations of Na^{22} and Cs^{134} and their movement through the biosphere to man have been studied and compared with the behavior of Cs^{137}. The major food sources by which Na^{22} enters man appear to be the same as those by which Cs^{137} is taken into the body. The air concentrations of the "cosmic ray produced" Na^{22} during 1962-1963 were more than ten times higher than reported values before the 1961-1962 test series suggesting that a large addition to the atmospheric Na^{22} occurred then. The ratio of Na^{22} to Cs^{137} in Alaskan caribou flesh taken after the atomic tests (July, 1963) was ten times higher than in samples taken just before the tests, while the Cs^{134} to Cs^{137} ratio was four times lower. This provides further evidence that a considerable amount of Na^{22} was generated during the past test series. It also indicates that the major Cs^{134} injection into the atmosphere occurred in tests before the 1961-1962 series.

* Accepted for publication in Nature.

0028267

Air Concentrations of 12 Radionuclides from 1962 Through Mid-1964* - R. W. Perkins, J. M. Nielsen, and C. W. Thomas

The air concentrations of the 12 radionuclides Be^7, Na^{22}, Mn^{54}, Co^{60}, Y^{88}, Zr-Nb^{95}, Ru^{106}, Sb^{125}, Cs^{134}, Cs^{137}, and Ce^{144} are reported for the 2 1/2 yr period, 1962 through mid-1964. This study provided the world's most complete and comprehensive study of the absolute and relative behavior of many of these radionuclides. The measurement, concentrations, origin, and atmospheric movement and behavior of these radionuclides are discussed.

Ag^{110m} in the Atmosphere - R. W. Perkins

The activation product Ag^{110m} has been measured in the atmosphere for the first time. It was produced during nuclear testing operations and was present at a concentration of about 0.001 of that of Cs^{137} during mid-1963.

The testing of atomic weapons above ground results in the production of numerous radionuclides in addition to the fission products. Actually, every radionuclide that is produced by neutron irradiation of natural materials will result to some extent when a detonation occurs near the ground. Measurement of many airborne radionuclides in the atmosphere which result from both atomic weapons testing and from cosmic ray interactions with the atmosphere has been possible in the past by use of multidimensional gamma-ray spectrometry.[3.69] With this spectrometry technique Ag^{110m} has been identified and measured in the atmosphere for the first time. Ag^{110m} ($T_{1/2}$ = 253 days) is produced by the reaction $Ag^{109}(n, \gamma)$ Ag^{110m} and decays by emission of several gamma-rays in cascade. On carefully studying the multidimensional spectra of the air filter samples from which 12 airborne radionuclides were reported for the period 1962 through 1964,[3.66] Ag^{110m} was observed. A few samples which were collected during the peak fallout period of 1963 contained sufficient Ag^{110m} to allow its reasonably precise measurement. The measurement is based on the coincidence counting rate of several coincidence gamma ray combinations which produce a characteristic and unique photopeak in the energy-energy plane. This peak is due mainly to 0.885 and 0.656 MeV gamma rays

* Science, vol. 146, pp. 762-764. 1964.

0028268

being observed in one detector while total gamma ray energies of 2.036 and 2.266 respectively, due to more than one gamma ray, are observed by the second detector. The observed concentrations of Ag^{110m} in the atmosphere are included in Table 3.13 and are compared with the Cs^{137} concentration in the atmosphere.

TABLE 3.13

Ag^{110m} CONCENTRATIONS IN THE ATMOSPHERE AT RICHLAND, WASHINGTON, COMPARED WITH THE Cs^{137} CONCENTRATIONS

(disintegrations/min/10^6 ft^3 of air)

Date[a]	Cs^{137}	Ag^{110m}	$\frac{Ag^{110m}}{Cs^{137}} \times 1000$
4-A-63	5,130	2.85	0.556
4-B-63	5,080	1.61	0.317
5-A-63	6,550	3.27	0.499
5-B-63	13,400	8.93	0.666
6-A-63	5,010	2.47	0.493
6-B-63	7,390	5.45	0.737
7-A-63	5,990	6.91	1.15
7-B-63	6,910	7.54	1.09
8-A-63	6,980	7.56	1.08
8-B-63	5,030	5.58	1.11
9-A-63	3,820	3.92	1.03
9-B-63	3,890	6.09	1.566
10-A-63	3,010	1.98	0.658

(a) A and B signify approximately the first and second half of each month, respectively.

The source of Ag^{110m}, whether due to activation of inert silver in an atomic device or activation of the silver in soil or sea water, is not known. It has been observed that on neutron activation of sea water Ag^{110m} is a major constituent, and nuclear detonation in or above the ocean may have carried a significant portion of the activated sea water into the atmosphere. T. R. Folsom of Scripps Institute of Oceanography[3.70] had previously observed Ag^{110m} in marine organisms and had suggested that it may be detectable in the atmosphere.

Determination of Columbia River Flow Times Using Radioactive Tracers Introduced by the Hanford Reactors* - J. L. Nelson, R. W. Perkins, and W. L. Haushild**

A study of flow time of the Columbia River between Pasco, Washington, and the Pacific Ocean has been made using radioactive tracers introduced into the river in cooling water from the Hanford reactors. Two tracer methods were used. One used the decay of Na^{24} (15 hr) as an index of travel time to various points downstream while the other measured the time required for a "peak" of I^{131} activity to reach these locations. The methods were also used simultaneously and showed good agreement. Data at four river discharges indicate that the flow time from Pasco to Vancouver, Washington, varies from 3.2 days at high flow to 13.6 days at low flow.

Behavior and Transport of Radionuclides in the Columbia River Between Hanford and the Ocean - R. W. Perkins, J. L. Nelson, and W. L. Haushild**

Cooling of the Hanford reactors with Columbia River water and the subsequent disposal of this water to the river introduces many radioactive tracers to the river. The usefulness of many of these tracers has been limited in the past by their extremely low concentrations; however, through recent developments in multidimensional gamma ray spectrometry it is possible to make direct measurements of eleven of the longer lived radionuclides at locations between the Hanford reactors and the ocean. Through this multiple tracer technique it has been practicable to obtain vast amounts of information on the behavior of these elements in relation to their adsorption by and movement with the sediments of the river. During the past year transport of these radionuclides has been observed on a weekly basis at various locations between the Hanford reactors and the ocean. These measurements include a quantitative study of transport of radionuclides at the sampling points, and also measurement of the fraction of each radionuclide which is in solution. From this study the depletion and the changes in form of the radionuclides on transport by the river have been obtained. The study has also provided the information for estimating many important factors such as the inventory of these radionuclides in the river bottom sediments at any given time and the removal of these radionuclides due to scouring during the spring freshet.

---

* To be published in Water Resources Research.
** U. S. Geological Survey, Portland, Oregon.

0028270

Scouring of Radionuclides Deposited with Columbia River Sediments During the Spring Freshet - J. L. Nelson

A study was made of the scouring of deposited sediments from the McNary Reservoir of the Columbia River during spring high flows. Scouring, as determined by the Zn^{65}/Cr^{51} ratio in water and suspended sediment at Umatilla, Oregon, was approximately proportional to the increase in river discharge. About one third of the annual deposition of sediment was estimated to be scoured. Estimates of depletion and inventory of Zn^{65} in the McNary Reservoir were also made.

It is of interest in the study of reactions of reactor-produced radionuclides with Columbia River water, sediment, and organic material to define ways in which nuclides that are deposited in the river may be released or moved. One of the ways that this may occur is for fine sediments that retain radionuclides to be physically picked up by water of increasing velocity and carried to other points downriver or into the ocean. Previous data[3.71] have indicated that this, in fact, does occur to some extent during spring high water in the Columbia River. Theoretical considerations and studies on other rivers also indicate that some degree of scouring should be expected.

Since a large fraction of the deposited radionuclides in the river is in the McNary Reservoir,[3.71] scouring from that reach is of major interest. Samples of river water were obtained from about mid-river at the Umatilla, Oregon, bridge which is 1.5 mi downstream from the McNary Dam. There should be little or no opportunity for resettling of suspended sediment in this short reach of fast water. Weekly samples starting April 3, 1964, before the spring runoff started, and continuing to late fall, when water levels were back to low flow, were analyzed for Zn^{65} and Cr^{51}. The 1 gal samples were filtered through a 300 mμ millipore filter and then evaporated to 13 ml for counting in a 5 in. well crystal. More consistent data were obtained by adding the activities found on the filters to those in the water, so later samples were not filtered. With the sampling arrangement used, filtering was done 2 to 6 hr after the samples were taken and it is likely that a variable amount of sorption by particles occurred between sampling and filtering.

0028271

The parameter used to measure degree of scouring was the Zn^{65}/Cr^{51} ratio in the water and suspended sediment. Since the half-life of Zn^{65} is long (245 days) in relation to that of Cr^{51} (27.8 days), a relatively high ratio would indicate that aged sediment was being scoured. In Figure 3.26 the Zn^{65}/Cr^{51} ratio is plotted over a period of several months, and the Columbia River discharge at McNary Dam is plotted on a similar scale. It can be seen that the two curves follow each other very closely indicating that scouring is very nearly proportional to discharge.

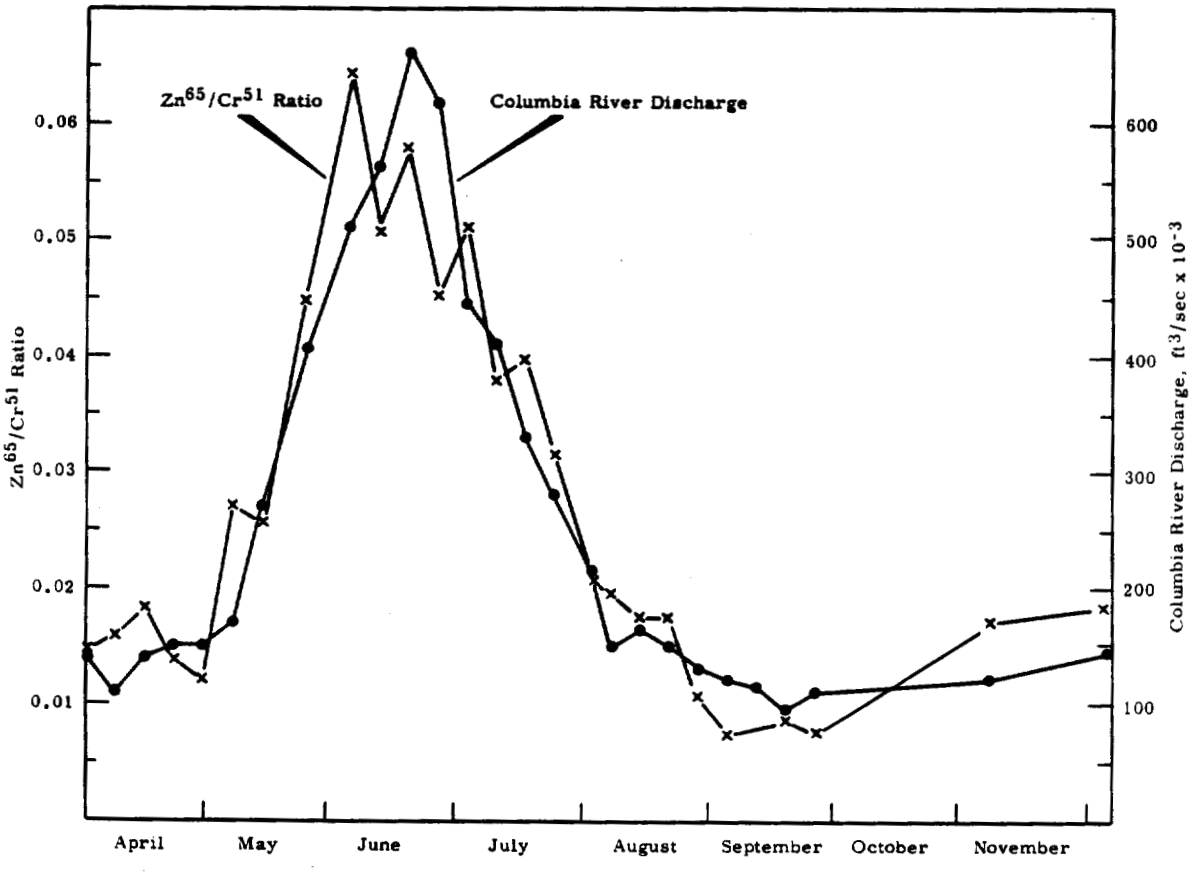

FIGURE 3.26

Zn^{65}/Cr^{51} Ratio of Columbia River Water in Relation to River Discharge at Umatilla, Oregon

The picture in Figure 3.26 is clear-cut as long as the Zn^{65}/Cr^{51} ratio in reactor effluent remains constant. However, over the period of this study,

it was changing considerably. Figure 3.27 shows the Zn^{65}/Cr^{51} ratio at each point divided by that in reactor effluent. The period used for reactor effluent data allowed time for flow from the reactors to Umatilla. The scouring as depicted in Figure 3.27 is even more accentuated than in Figure 3.26.

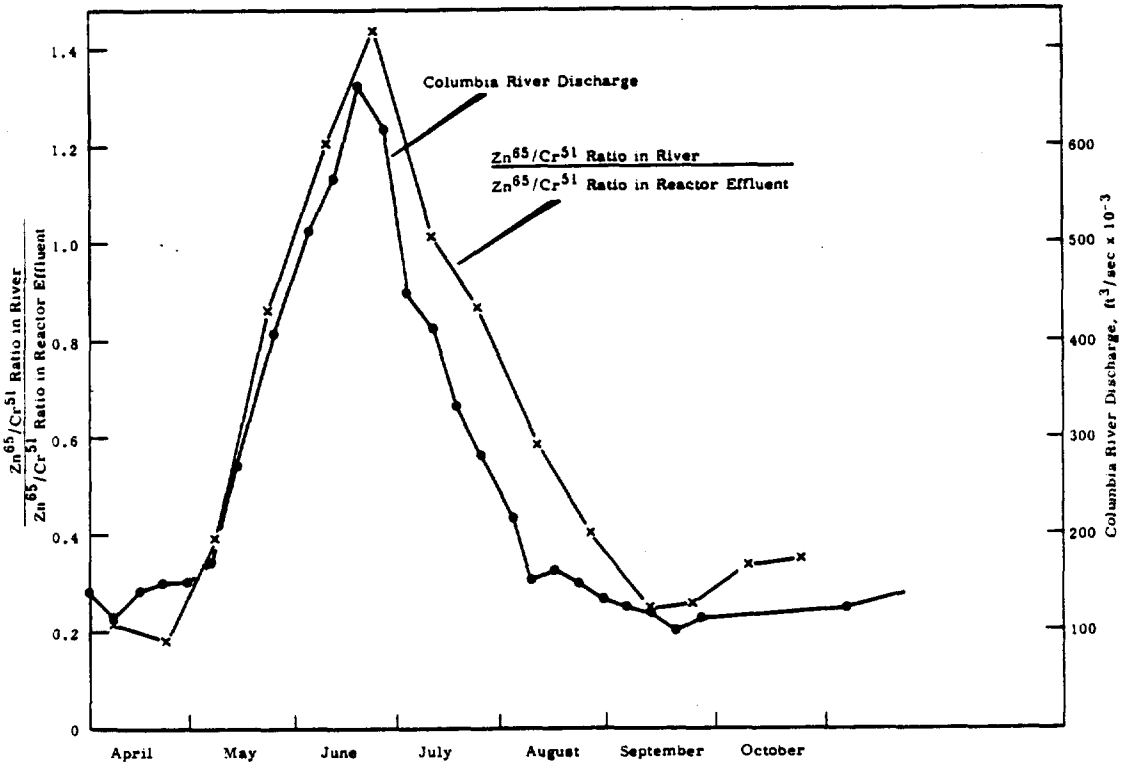

FIGURE 3.27

Scouring of Columbia River Sediments as Shown by Changes in Ratios of Zn^{65} to Cr^{51} in Relation to River Discharge at Umatilla, Oregon

From the analyses of the river water samples taken at Umatilla and of reactor effluent, it is also possible to calculate numbers for depletion, inventory, and curies scoured from McNary Reservoir. This has been done for Zn^{65}; depletion was about 65% from the reactors to Umatilla. If other years were similar to 1964, the inventory of Zn^{65} after decay corrections was estimated to be 5500 Ci. This was for a date soon after

the spring scouring period. About 1200 Ci were scoured during the 1964 freshet and this represents about a third of an annual deposition of Zn^{65}. These numbers are only estimates, but they agree fairly well with previous estimates based on analysis of core samples of bottom sediments.

Studies of Radionuclides in Columbia River Sediments* - J. L. Nelson, R. W. Perkins, and J. M. Nielsen

This is a brief summary of a status report published on studies in progress on the amounts, forms, and reactions of radionuclides in the Columbia River and especially in river sediments. The fallout isotopes $Zr\text{-}Nb^{95}$ were measured in Columbia River water over a period of about a year both above and below the Hanford reactors and in Snake River water before it enters the Columbia River. Since the levels of $Zr\text{-}Nb^{95}$ were not appreciably higher in the Columbia River below the reactors than at the other sampling sites, it was concluded that a large portion of the fission products in the Columbia River comes from fallout.

Transport rates of reactor-produced radionuclides in the Columbia River were obtained over a period of a year in cooperative study with the U. S. Geological Survey. The data indicate that large amounts of Zn^{65} and Cr^{51} that were in river water at Pasco, Washington did not reach Vancouver, Washington. The Zn^{65} transport rates at Vancouver were relatively high in June indicating that scouring of sediments was occurring. The fraction of radionuclides classed as particulates by filtration through a 300 mμ filter varied widely through the year but Zn^{65} was consistently more in the particulate form at Vancouver than at Pasco.

A coring device, 6 in. diam, was constructed and has been used to obtain several cores of Columbia River bottom sediments. Data from a core taken near McNary Dam in December, 1963, show relatively rapid sedimentation during the last 3 mo and slower sedimentation to the 20 in. depth which was about 5 yr old.

Particle size separations have been made on sediment from McNary Reservoir. Small clay-size particles contain a much greater concentration

---

* Published as HW-83614

of radionuclides than coarser particles, but the coarser particle size was also somewhat higher than the medium sizes. This has been shown to be due to organic matter which made up over 10% of the coarser fraction and only about 3% of the silt particles.

As a step in the understanding of the mechanisms involved in the sorption of radionuclides by river sediments, determinations were made of the chemical and physical form of reactor-produced radionuclides in the reactor effluent stream and in the Columbia River at various points downstream to Vancouver. This was done by passing filtered water samples through cation and anion exchange resins. It was found that Zn^{65}, Sc^{46}, and Mn^{54} became largely particulate as they moved down the river, and Cr^{51} remained mostly in solution. Of that in solution, Cr^{51} remained nearly all anionic, and Zn^{65} remained cationic.

Studies of the Mechanisms of Retention of Radionuclides in Columbia River Sediments - J. L. Nelson and N. H. Cutshall*

Experiments are reported in which Columbia River bottom sediments were treated with various reagents to learn the chemical forms of Co^{60}, Sc^{46}, Zn^{65}, Mn^{54}, and Cr^{51}. None of the nuclides except about 10% of the Mn^{54} were exchangeable as determined by extraction with neutral, normal solutions of ammonium acetate. A gradient density separation with bromoethanol indicated that about half of each of the nuclides except Sc^{46} may be in an organic phase. An oxidation of the remaining organic matter present with hydrogen peroxide removed a sizable portion of Cr^{51}. Following this, reduction by sodium hyposulfite with citrate present removed most of the Sc^{46} and appreciable, but smaller amounts of the other nuclides. A treatment with 0.01M HCl removed further small amounts. At this point over 80% of each of the nuclides had been removed from the sediment. In a reaction rate study of Cr^{51} with Columbia River sediments, trivalent chromium ions were sorbed very rapidly. However, hexavalent chromium ions reacted more slowly and for a sediment that had been oxidized with H_2O_2, sorption was only 60% complete after 180 hr. It was hypothesized that hexavalent chromium sorption occurs by prior reduction to the trivalent state by reducing constituents of the sediment. Electrodialysis of Columbia River bottom sediments indicated that Co^{60}, Zn^{65}, and Mn^{54} could be largely removed from the sediment and were cationic. Only about 1% of the Cr^{51} and Sc^{46} could be removed.

---

* Oregon State University

A knowledge of the mechanism of retention of radionuclides by bottom sediments of the Columbia River is of interest, because it allows predictions to be made of amounts and variation of sorption with changing conditions and of possible desorption mechanisms.

A series of chemical treatments was designed to attempt to separate the nuclides Cr^{51}, Mn^{54}, Zn^{65}, Sc^{46}, and Co^{60} into recognizable fractions. The steps were

(1) Removal of the exchangeable fraction by repeated equilibration with neutral, normal, ammonium acetate solution
(2) Treatment with pH 3 acetic acid to remove the weak acid soluble ions
(3) Removal of an "organic" fraction by density gradient separation with bromoethanol[3.72]
(4) Destruction of the remaining organic matter with H_2O_2 in the presence of ammonium acetate to prevent resorption of nuclides by inorganic particles
(5) Removal of reducible forms (perhaps associated with iron oxides) by sodium hyposulfite with citrate present to keep iron in solution[3.73]
(6) Extraction of additional acid-soluble nuclides by treatment with 0.01 M HCl.

The results of application of this series of chemical treatments of the Columbia River samples are presented in Table 3.14.

The data in the last column are for a bottom sediment from the Columbia River above the Hanford reactors equilibrated for 3 days with a solution of Cr^{51}. The data for all of the samples are sums of three or four equilibrations for each step and means of data for four depths in a sediment core (there were no discernible trends with depth in the core). Following equilibration for 30 min, the samples were centrifuged and decanted, and the supernatant solutions were evaporated to 13 ml for counting in a well crystal with anticoincidence shielding.

0028276

TABLE 3.14

DISTRIBUTION OF RADIONUCLIDES IN VARIOUS CHEMICAL FRACTIONS

(% of Nuclide in Each Fraction)

	Co^{60}	Sc^{46}	Zn^{65}	Mn^{54}	Cr^{51}	Priest Rapids Reservoir Sediment Traced with Cr^{51}
Ammonium Acetate	0	0	1.6	10.5	0	0.3
Acetic Acid	32.5	0.2	19.0	22.7	1.0	--
Bromoethanol	43.9	2.4	65.0	33.3	21.4	63.6
Hydrogen Peroxide	0	0.4	0.5	--	28.2	26.6
Sodium Hyposulfite	6.0	87.0	9.4	22.4	41.5	8.7
0.01M HCl	0	2.3	0.6	1.0	0.7	0.4
Not Removed	17.5	6.5	4.4	10.1	7.2	0.3

The only nuclide that had an appreciable exchangeable fraction was Mn^{54}. Acetic acid removed significant portions of Co^{60}, Zn^{65}, and Mn^{54}. The bromoethanol separation of organic matter removed large amounts of all but Sc^{46}, and the H_2O_2 treatment removed additional Cr^{51}. Sodium hyposulfite removed most of the nuclides that were left on the sediment at this point which involved nearly all of the Sc^{46}, and 0.01M HCl removed only very small amounts of the radionuclides.

The high apparent association of nuclides with organic matter was somewhat surprising and doubt was cast on the conclusions by a further experiment. In this experiment, the sodium hyposulfite reduction was conducted both before and after the organic removal steps. The data are given in Table 3.15.

These data indicate that a part of the Co^{60}, Zn^{65}, Mn^{54}, and Cr^{51} can be removed by either bromoethanol or sodium hyposulfite. One possible reason for this is that the bromoethanol may be acting as an extractant *per se* rather than serving merely to float off organic particles. This possibility was supported by an experiment in which Priest Rapids Reservoir sediment was first treated with hydrogen peroxide to destroy organic material present then spiked with Cr^{51} and put through the regular steps of separation. There was still as high a proportion of radionuclides in the bromoethanol fraction as there had been without prior organic

destruction. It is also likely that the citrate ion present in the sodium hyposulfite solution complexed and removed some organic matter along with associated nuclides when this step was done first. Further work is needed to understand all of the reactions involved.

TABLE 3.15

COMPARISON OF ORDER OF OXIDATION AND REDUCTION

(% of Total Nuclides in Each Fraction)

	Co^{60}	Sc^{46}	Zn^{65}	Mn^{54}	Cr^{51}
	Organic Removal First				
Bromoethanol	76.4	2.6	80.8	32.7	21.1
Hydrogen Peroxide	8.0	20.1	4.4	5.3	17.6
Sodium Hyposulfite	2.6	54.8	7.3	19.3	37.8
	Reduction First				
Sodium Hyposulfite	67.3	58.8	48.8	68.6	66.6
Hydrogen Peroxide	3.5	5.9	7.2	3.3	19.8

Cr^{51} in Columbia River water has been shown to be nearly all hexavalent rather than trivalent,[3.74] but the oxidation state of that associated with sediment is not known. However, the energy with which it appears to be held would suggest it to be in the trivalent state, and it is hypothesized that as the oxidation state slowly changes from hexavalent to trivalent the newly formed trivalent chromium is immediately sorbed out of solution and thus chromium associated with sediment would be trivalent. To check this hypothesis, samples of sediment were electrodialyzed. Samples used included both sediment from McNary Dam below Hanford and sediment from near Hanford that had been equilibrated with solutions of hexavalent and trivalent chromium. Only about 1% of the Cr^{51} could be removed from the sediments by electrodialysis, and it was not possible to draw conclusions concerning the oxidation state of chromium on the sediment. Co^{60}, Mn^{54}, and Zn^{65} could be largely removed from sediment by electrodialysis, but Sc^{46} could not. The three ions that were removed were found mostly in the cathode compartment. That the ions that could be removed by electrodialysis have a normal oxidation state of two while that of scandium is three supports the possibility of chromium being trivalent in the sediment.

An experiment was conducted on the reaction rate of Cr^{51} with river sediment from above the reactors. Both trivalent and hexavalent chromium were used, each with and without prior H_2O_2 oxidation of the sediment. The results of rate studies are shown in Figure 3.28. The trivalent chromium was sorbed very rapidly and completely both with and without oxidation of the sediment. However, the hexavalent chromium reaction was much slower especially with the sediment that had been oxidized. This again suggests that sorption of hexavalent chromium may proceed by a prior reduction to trivalent chromium by reducing constituents of the sediment. Oxidation of the sediment by H_2O_2 left few reducing constituents and thus a much slower reduction and sorption of hexavalent Cr^{51}.

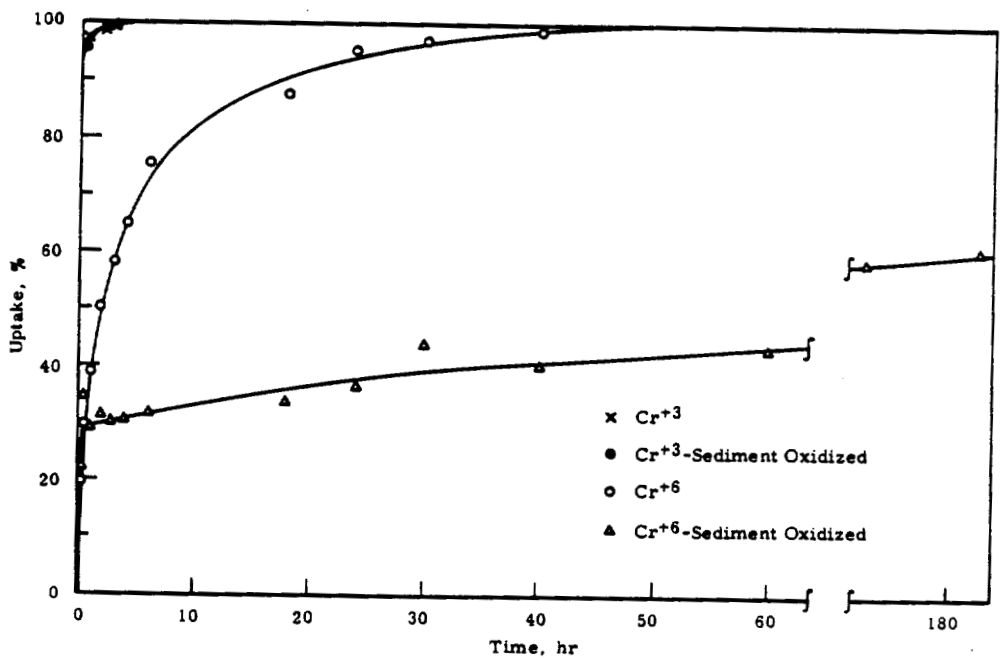

FIGURE 3.28
Rate of Uptake of Cr^{51} on Columbia River Sediment

Distribution of Sediments and Associated Radionuclides in the Columbia River Below Hanford - J. L. Nelson

Radionuclides in bottom sediments of the Columbia River are being inventoried. The principal method used is by water analyses at various points along the river to determine deposition, but it is also necessary to obtain core and other samples of various types of sediment to determine where, between water sampling points, the radionuclides are mostly deposited. Data are presented here on the distribution with depth of radionuclides in several general types of sediments. It is shown that biological samples concentrate radionuclides but estimated that they are relatively small in total mass in the river. Fine deposited sediments from McNary Reservoir are rather high in activity and thus contribute heavily to a total inventory. Shoreline, clay bank, and mud flat core data indicated rather low contributions of nuclides from these sources. Concentrations of radionuclides in the coarse sand, gravel, and rock that make up the largest part of the Columbia River bottom were low but penetrated to relatively greater depths than in other sediment types. Due to its large extent, contributions to isotope inventories from this type of sediment are significant but smaller than from reservoir sediments.

An inventory of the radionuclides held in bottom sediments is an important phase of the Columbia River studies. The inventory of Zn^{65} in bottom sediments, for example, is at least twenty times the amount that is in transit in water and suspended sediment at any particular time.

There are several ways to obtain an inventory. Extensive core sampling of the river bottom is the most direct way, but to be comprehensive, hundreds of core samples would be required. Also, tests with many types of coring devices have indicated that it is very difficult to obtain cores from large areas of the river bottom that are coarse sand, gravel, and rocks. Therefore, a somewhat different approach is being used that promises better data with less difficulty. This approach is to use analyses of river water and suspended sediment from various points along the river over extended periods of time to calculate the loss from the water and thus the deposition from point to point. Along with this, a limited number of core and hand samples are taken to locate areas of deposition in various reaches of the river. Preliminary data on inventory from water and suspended

sediment analysis are presented in other sections of this report. In this section, data are presented on bottom sediment samples from various typical types of sediments and locations in the river. Only a few such samples have been obtained, so that data should be considered as only indicative of average conditions that must be defined by more extensive sampling.

There are several types of sedimentation areas in the Columbia River bottom. One possible listing of these is:

- Coarse sand, gravel, and rock which is typical of the largest part of the river bottom where there is swift current
- Sand pockets in eddying areas such as below islands, in coves, on the inside of bends, and in sizable parts of the estuary
- Fine grained deposited sediments in slack water areas as behind dams
- Silty areas of slow moving shallow water in broadened parts of the river with highly variable particle sizes between sands and clays
- Clay banks of original parent material in nondepositing areas of the river
- Shore line soil and areas that are flooded during the spring freshet
- Biological material of various types and amounts in all parts of the river bottom.

Data obtained recently on radionuclide distributions in samples from each of these types of sediment are given below.

Coarse Sand, Gravel, and Rock

Ordinary gravity type coring equipment will not penetrate or retain sediment of this type. Therefore, helmet divers were sent to the river bottom near Richland, Washington, with a drive barrel corer in November, 1964. Driving the core barrel into the sediment was not possible because rocks lodged in the barrel. Some samples were obtained, however, by the divers digging a hole in the river bottom and taking samples by hand at various depths. These samples were separated into various particle sizes by wet screening and were counted directly in a well crystal. The results are presented in Table 3.16.

TABLE 3.16

RADIONUCLIDES IN PARTICLE SIZE SEPARATES OF COARSE SAND AND GRAVEL BOTTOM SAMPLES-COLUMBIA RIVER

Particle Size, mm	% by Weight of Whole Sample	Disintegrations/min/g				
		Co^{60}	Sc^{46}	Zn^{65}	Mn^{54}	Cr^{51}
			0 to 3 in. Depth			
<0.074	0.096	641	2906	15,286	1900	35,970
0.074-0.35	4.0	43	43	840	73	431
0.35-0.84	9.6	44	40	685	60	330
0.84-2.38	1.7	25	25	266	16	432
2.38-10	47.1	20	5	159	10	196
Estimated >10	37.4	15	5	85	6	100
Whole Sample	--	22	13	225	18	220
			6 to 8 in. Depth			
<0.074	0.042	287	1145	5567	802	20,710
0.074-0.35	4.1	15	14	280	24	231
0.35-0.84	6.3	15	10	217	18	131
0.84-2.38	2.4	5	3	78	4	102
2.38-10	51.2	2	2	27	3	70
Estimated >10	36.0	1	1	14	2	35
Whole Sample	--	3	3	48	5	77
			12 to 14 in. Depth			
<0.074	0.023	222	696	3268	326	12,469
0.074-0.35	3.1	9	7	159	14	155
0.35-0.84	4.4	9	5	120	10	<10
0.84-2.38	1.4	3	2	33	2	86
2.38-10	54.2	3	1	27	2	65
Estimated >10	37.0	2	1	20	1	35
Whole Sample	--	3	1	31	2	56

The < 0.074 mm silt and clay particles contained by far the highest concentration of nuclides, but the mass of this material was so small that only a small part of the total radioactivity was found in this fraction. Over 80% of the sediment was gravel and rock >2.38 mm in size. Activity decreased with depth but not as rapidly as deposited sediments and not in relation to half-life.

Sandy Bottom

A 2 in. driven core was obtained by divers during November, 1964, in a sandy bottom area on the lee side of an island just below Pasco, Washington. The core was sectioned and the variation of radionuclides with depth is shown in Table 3.17.

TABLE 3.17

RADIONUCLIDE CONCENTRATIONS AT VARIOUS DEPTHS IN A SANDY BOTTOM–COLUMBIA RIVER

Depth, in.	Disintegrations/min/g				
	Co^{60}	Sc^{46}	Zn^{65}	Mn^{54}	Cr^{51}
0-1	59	61	888	56	1014
1-2	47	27	601	40	435
2-3	44	40	672	72	768
3-4	45	21	549	38	348
4-5	46	11	519	29	133
5-6	45	7	497	22	52
6-8	46	7	486	21	50
8-10	45	8	487	21	47
10-12	40	7	423	20	67
12-14	51	9	617	27	55
14-16.5	81	37	1404	46	214

The concentration of the radionuclides, especially of Co^{60} and Zn^{65}, is considerably higher than in the coarser sand and gravel. Decrease of activity with depth is not so great in this core as might be expected. The activity actually increased significantly at the greatest depth. The reason for this is that more silt and clay was present in deeper samples.

McNary Reservoir Fine Sediment

Fine grained sediment is being deposited in reservoirs behind most of the dams on the Columbia River. McNary Reservoir is the first downstream from Hanford and also probably has more sediment deposition than any of the others. Data from a core taken in December, 1963, are given in Table 3.18.

Silty Areas of Slow Moving, Shallow Water

A rather extensive area that typifies this sediment is found between the mouth of the Snake River and the mouth of the Walla Walla River near Wallula Gap, Washington. The river here is very broad with large areas of shallow, slow moving water, especially along the east shore. This is still a part of the backwaters of McNary Reservoir or Lake Wallula. The

sediments are more highly organic and not as fine as those near McNary Dam. A core was taken about 4 mi below the mouth of the Snake River in water about 12 ft deep in November, 1964.. Radionuclide concentrations are shown in Table 3.19.

TABLE 3.18

RADIONUCLIDE CONCENTRATIONS AT VARIOUS DEPTHS OF SEDIMENT IN McNARY RESERVOIR–COLUMBIA RIVER

Depth, in.	Disintegrations/min/g				
	Co^{60}	Sc^{46}	Zn^{65}	Mn^{54}	Cr^{51}
0-1	137	293	4566	131	4123
1-2	149	212	3982	120	913
2-3	151	126	3041	85	569
3-4	137	26	1886	43	417
4-5	112	19	1239	24	200
5-6	88	15	549	12	40
6-8	93	3	475	10	27
8-10	70	<1	360	9	<10
10-12	30	<1	185	7	<10

TABLE 3.19

RADIONUCLIDE CONCENTRATIONS AT VARIOUS DEPTHS OF SEDIMENT NEAR FINLEY, WASHINGTON–COLUMBIA RIVER

Depth, in.	Disintegrations/min/g				
	Co^{60}	Sc^{46}	Zn^{65}	Mn^{54}	Cr^{51}
0-1	18	85	1040	51	2685
1-2	15	18	426	13	88
2-3	15	5	326	8	26
3-4	12	1	165	5	28
4-5	9	<1	46	3	25
5-6	5	<1	18	2	15
6-8	2	<1	8	1	<10
8-10	2	<1	7	1	<10
10-12	1	<1	3	<1	<10
12-13.5	<1	<1	3	<1	<10

The considerably lower level of radionuclides here than at McNary Dam may be partially caused by unmixed waters and sediments from the Snake River at this location. A very slow rate of sediment deposition is indicated here by the rapid decrease in radioactivity with depth. Little activity was found below 6 in.

0028284

Clay Banks of Original Parent Material

These are probably very few and small in the Columbia River; but, due to their very high exchange capacity, it may be possible for them to be quite high in radionuclides. A drive core was obtained from a bank of Ringold blue clay in about 50 ft of water between Richland and the mouth of the Yakima River. Radionuclide data from this core are given in Table 3.20.

TABLE 3.20

RADIONUCLIDE CONCENTRATIONS AT VARIOUS DEPTHS OF A CLAY BANK NEAR RICHLAND, WASHINGTON–COLUMBIA RIVER

Depth, in.	Disintegrations/min/g				
	Co^{60}	Sc^{46}	Zn^{65}	Mn^{54}	Cr^{51}
0-0.5	4	7	278	6	173
0.5-1.0	<2	<2	<5	<2	39
1-2	<2	<2	<5	<2	10
2-4	<2	<2	<5	<2	<10
4-6	<2	<2	<5	<2	<10
6-8	<2	<2	<5	<2	<10
8-11	<2	<2	<5	<2	<10

The clay in this bank was so "tight" that it appeared quite free of water after the first few inches. The very rapid decrease in radioactivity with depth in the top inch may be due to very low permeability of the clay for river water. Net water movement in the clay during relatively low water is probably upward into the river bottom from surrounding ground water. No deposition of sediment is occurring here and Cr^{51} is found the deepest in the clay because it is sorbed less rapidly by the clay from river water that penetrates the clay during high water periods.

Shoreline and Floodplain Sediment

Even though most of the bottom of the Columbia River is composed of coarse sand, gravel and rock, some parts of the shoreline are soil. During the spring freshet, the high water inundates much larger areas of fine sediment. This "floodplain" area could be one of the places where significant amounts of radionuclides are held. On July 9, 1964, cores were taken on shore about 6 in. above the water level and in the edge of the water near the old Hanford townsite inside the Hanford area. The place

where the first core was taken had been under water for about 3 wk during the spring freshet, but water had subsided about a week before the sample was taken. The data of the first core are given in Table 3.21. Data of the second core were not significantly different.

TABLE 3.21

RADIONUCLIDE CONCENTRATION AT VARIOUS DEPTHS OF A FLOODPLAIN CORE NEAR THE HANFORD TOWNSITE–COLUMBIA RIVER

Depth, in.	Disintegrations/min/g				
	Co^{60}	Sc^{46}	Zn^{65}	Mn^{54}	Cr^{51}
0-0.5	8	15	170	9	343
0.5-1.0	7	7	62	4	123
1.0-1.5	4	<1	16	1	44
1.5-2.0	2	<1	5	<1	<10
2-3	3	<1	5	<1	<10
3-4	<1	<1	<2	<1	<10
4-6	<1	<1	<2	<1	<10
6-8	<1	<1	<2	<1	<10
14-17.5	<1	<1	<2	<1	<10

Radioactivity measured in this core was not high, but it had penetrated about 2 in.

Biological Material

It is well known that river biota can concentrate some radionuclides to a great extent. When a core is taken from the bottom of the river, biota in and on the core, both living and dead, are sampled and analyzed with the sediment. Other biota are sampled with water samples and are found mostly on the filter. However some biota clinging to rocks, growing on the bottom, and in the larger pieces in the river environment may not be adequately sampled in these ways. Data on biota samples of three types are given in Table 3.22.

The algae scrapings contained some sediment and thus the figures are not entirely accurate for algae *per se*. It is obvious that biological material, on the basis of dry weight, can be higher in radionuclide concentration than even silt and clay separates such as those in Table 3.16.

TABLE 3.22

RADIONUCLIDE CONCENTRATIONS
IN SOME BIOLOGICAL SAMPLES FROM THE COLUMBIA RIVER

	Disintegrations/min/g				
	Co^{60}	Sc^{46}	Zn^{65}	Mn^{54}	Cr^{51}
Tree bark found in sediment near Richland	135	147	1,920	900	4,690
Algae scraped from rocks below Pasco	730	4830	21,800	12,000	76,000
Sponge growing on river bottom below Richland	162	1720	6,050	555	25,100

Discussion and Conclusions

With new and improved radioanalytical techniques, concentration data are now quite accurate and dependable. However, in trying to arrive at conclusions on total inventory of various isotopes and the relative importance of the different types of materials contributing to it, a more difficult problem is to determine the total amount of each type of sediment. Figures for total weights must be multiplied by concentration figures to obtain inventories. Core sampling in place of earlier grab samples solves the problem in the vertical dimension but determination of the extent of each type of sediment is not easy. One of the ways in which this problem is being attacked is by under water closed circuit television examinations of the river bottom.

Probably the most difficult material for which to obtain mass data is the river biota. The scraping of several large rocks that were relatively high in algae cover were needed to yield about one third of a gram dry weight of the algae listed in Table 3.22. Estimates at this time would indicate that there would be only a few grams of living biota per square foot average while there are several tens to hundreds of pounds of radionuclide-containing sediments per square foot.

Sediments such as the coarse sand, gravel, and rock in Table 3.16 are relatively constant in weight per unit volume, and the extent can be estimated with fair accuracy. With an assumed density of 1.65 and if the samples of Table 3.16 are representative of most of the river bottom from

the Hanford reactors to the mouth of the Snake River, it was calculated that there are about 70 Ci of Zn^{65}/mi^2 or about 1500 Ci of Zn^{65} in the whole reach. This can be compared with about 800 Ci of Zn^{65}/mi^2 calculated from McNary Reservoir samples in Table 3.18. A good estimate of the extent of this sediment is not available yet.

Many more samples and observations are needed before the distribution of nuclides is well understood. There is also a need for data on other isotopes such as P^{32} and on samples further downstream and into the estuary.

Measurement of a Large Group of Radionuclides in Columbia River Aquatic Organisms - R. W. Perkins

Evaluation of multidimensional gamma-ray spectrometry has shown that 20 radionuclides can be measured in aquatic organisms from the Columbia River by direct counting. The long-lived radionuclides in fish flesh are compared with their concentrations in river water.

The routes by which man is exposed to the radionuclides that enter the Columbia River in reactor cooling water is a problem of continuing study. Of particular interest is the factor by which radionuclides are concentrated in going from water through the river's aquatic food chain to fish. During 1957 a careful study of the radionuclides that decay by gamma ray emission was made using the then modern multichannel analyzers and the gamma-gamma coincidence counting techniques.[3.75] With the availability of multidimensional gamma-ray spectrometry[3.76] a more careful examination of the radionuclide spectrum present in fish and the other river organisms was made. An initial measurement of the radionuclide concentrations in flesh samples from a bass and a channel catfish that were taken from the river below the Hanford project are included in Table 3.23. The concentrations of the radionuclides present in river water at the same time of the year are also presented to allow a direct estimate of the concentration factor.

TABLE 3.23

CONCENTRATIONS OF THE LONG-LIVED RADIONUCLIDES IN COLUMBIA RIVER FISH AND IN RIVER WATER

	Disintegrations/min/kg		
	Water	Bass[a]	Channel Catfish[a]
Na^{22}	0.02	8.3	0.83
Sc^{46}	20	66	12
Mn^{54}	24.5	50	15
Co^{58}	12.7	30.8	4.48
Co^{60}	3	136	105
Zn^{65}	200	36,500	26,300
Cs^{134}	0.05	120	10.9
Cs^{137}	1	2,400	190

(a) Collected April, 1964

Further studies have shown that from a spectrum measurement shortly after sample collection plus one taken after a few weeks decay period it is possible to make a direct measure of 20 radionuclides in various aquatic samples. These include Na^{22}, Na^{24}, Sc^{46}, Cr^{51}, Mn^{54}, Mn^{56}, Co^{58}, Fe^{59}, Co^{60}, Cu^{64}, Zn^{65}, Ga^{72}, As^{76}, Zr-Nb^{95}, Ru^{106}, Sb^{124}, La^{140}, Ba^{140}, Cs^{134}, and Cs^{137}. Only some of the radionuclides are present in fish tissue; however, most of them are present and can be measured in plankton and algae samples. Whereas our previous studies[3.76] have required a combination of normal and coincidence gamma-ray spectrometric techniques to measure only part of these radionuclides, their direct measurement is now possible with multidimensional gamma-ray spectrometric techniques. Sample preparations normally involve drying, but for large bulk samples a low temperature ashing (400 C) followed by pressing the ash into a standard geometry for counting is performed.

A joint project is presently underway[3.77] with Battelle-Northwest Biology Department personnel to evaluate and apply this technique in studying the radionuclide distribution in several river organisms and in the various organs of fish.

I^{131} Measurement in Large Volumes of Columbia River Water -

R. W. Perkins

A rapid method for the extraction of I^{131} from large volumes of river water or rain water has been devised and tested. The extraction is direct from a 3 gal sampling jug with a yield of 82.4%

In considering methods for studying the flow time of the Columbia River[3.78] between Hanford and the Pacific Ocean it was apparent that the I^{131} that may be released to the river by a reactor fuel element failure could serve as a tracer. The reactor effluent water that is discharged to the river is monitored continuously both to signal reactor shutdown if a fuel element failure occurs and to allow the effluent water to be "cribbed" if the level exceeds predetermined operating limits. The very small amounts of I^{131} that are released to the river during a fuel element failure could serve as a tracer if a method for its measurement at a few disintegrations per minute per gallon were available. Because of normal reactor effluent water radionuclides in the river, a procedure was required that would selectively remove I^{131}.

The procedure has been devised for the separation of I^{131} from 3-gal river water samples. It is also satisfactory for washout studies that require a measurement of gaseous (inorganic) I^{131} washed from air by rain. The procedure involves preliminary reduction to iodide followed by oxidation to iodine, solvent extraction into CCl_4, reduction and back extraction into dilute acid, and precipitation as AgI for counting. The yield for the procedure is 82.4% with a measured standard deviation of less than 3%.

Procedure:

1. To 3 gal of water add 100 ml of concentrated H_2SO_4, iodine carrier (2 ml of 0.1N NaI), 2 g of sodium sulfite and stir for 1 min. NOTE 1.
2. Add 12 g of $NaNO_2$ and extract by stirring 5 min each time with three 150 ml portions of CCl_4. NOTE 2.
3. Combine the three 150 ml CCl_4 portions in a 1 liter separatory funnel, add 100 ml of 2.4N HNO_3, and shake for 1 min.

4. Drain the CCl_4 layer into a second 1 liter separatory funnel containing 1 ml of 5% Na_2SO_3, shake 1 min and discard the organic layer.
5. Drain the aqueous layer into a 150 ml beaker containing 5 ml of 0.1N $AgNO_3$ in 8N HNO_3, bring to a boil, cool 5 min and filter through a 0.45μ membrane filter.
6. Measure the I^{131} on the filter from the counting rate of its 0.36 MeV photopeak with a sensitive gamma-ray spectrometer.

Notes:

1. A 3 gal glass jug filled to within about 500 ml from the top is used for the extraction. Stirring is performed with a variable speed 0.02 hp stirring motor using a 1/8 in. diam stainless steel stirring rod that extends to 1 in. from the bottom of the jug with a 90° bend and a 2 in. horizontal section for an impeller.
2. The CCl_4 layers are drained through a rubber stopper that contains a glass stopcock and a Tygon® tube. On inverting the jug the CCl_4 drains through the stockcock and the tube serves as an air pressure release.

Ultra Sensitive Measurements of Radionuclides and Trace Element Constituents in the Ocean by Multidimensional Gamma-Ray Spectrometry -

R. W. Perkins and D. E. Robertson

Methods for the measurement of numerous natural and artificial radionuclides and trace elements in the ocean have been developed which provide greater sensitivity and selectivity than was previously available. The trace radionuclides are measured by direct counting of the sample while the inactive trace elements are measured from a direct count of a neutron activated sea water sample.

The complex chemical composition of the oceans and the many chemical reactions occurring, together with the physical and biological processes, make a study of the ocean physical chemistry very complicated. The rates and mechanisms of the ocean chemical processes are therefore difficult to determine and little studied. To describe the chemical equilibria and to determine the reaction rates and mechanisms, the concentrations of the constituents of the oceans must be known and their forms determined. Our

recent developments in extremely sensitive radionuclide analysis by multidimensional gamma ray spectrometry[3.76] provides a means whereby the ocean constituents may be studied with sensitivities increased by several orders of magnitude over those previously and currently used.

The presence in the oceans of many radionuclides from fallout, cosmic ray spallation, reactor waste disposal, and natural radionuclides, although at extremely low concentrations, nevertheless provide tracers for physical chemical studies provided techniques with sufficient sensitivity are available. When combined with neutron activation analysis, sensitive radionuclide measurement techniques make possible studies of the trace elements in oceans and of their reactions.

Preliminary studies on ocean water constituents indicate that direct measurement without chemical separation is possible for at least 10 radionuclides (K^{40}, Mn^{54}, Co^{60}, Ru^{106}, Ag^{110m}, Sb^{125}, Cs^{137}, Ce^{144}, Tl^{208}, and Ra^{226}) with the probability that several more can be determined. Sample preparations for such measurements have involved filtration of the sea water for particulate radionuclide counting and evaporation to the salts for soluble radionuclide counting. In addition, following neutron irradiation of 0.1 ml samples of sea water and a sufficient period for the Na^{24} (15 hr) to decay, multidimensional gamma ray spectrometry has allowed the direct simultaneous determination of the trace elements strontium, rubidium, iron, zinc, cobalt, cesium, antimony, silver, scandium, and uranium. Calculations show that sulfur, calcium, potassium, iodine, indium, magnesium, molybdenum, and copper should also be determinable by this technique if the irradiation is optimized for short-lived daughter determinations and Na^{24} is removed before spectrometric analysis.

Filtration-precipitation techniques[3.79] are being explored which will allow the removal of essentially all the dissolved elements from sea water except the alkali metal ions and the halide ions on an anion exchange precipitation column. Then, both the trace radionuclides can be removed from sea water for direct counting, and the radiosodium and radiohalides can be removed from irradiated sea water samples where the measurement of the induced short-lived radionuclide daughters is of interest.

0028292

Collection of Radioisotopes from River and Sea Water by Various Materials - W. B. Silker

The ability of various materials to concentrate selected radioisotopes from natural waters was investigated. Results obtained from collectors exposed in the Columbia River and the Pacific Ocean are reported.

Samples of several different materials were suspended in the Columbia River at Richland, Washington, to measure their relative effectiveness in concentrating radioisotopes discharged from the Hanford reactors. These materials were exposed for approximately 24 hr at a depth of $2\frac{1}{2}$ to 5 ft below the water surface and in a flowing portion of the river. At the end of this period they were removed and placed in 500 ml polyethylene bottles. The amount of radioactive isotopes retained by each was measured by gamma spectrometry using a 3 by 5 in. NaI(Tl) crystal. Although a constant counting geometry was maintained for all samples, the counting efficiency for the different radionuclides was not ascertained. Thus the results are presented as counting rates rather than disintegration rates. The sensitivity of the detection system permitted determination of the four long-lived isotopes given in Table 3.24.

TABLE 3.24

RELATIVE AMOUNTS OF RADIOISOTOPES ON EXPOSED COLLECTORS, counts/min/g

	Cr^{51}	Zn^{65}	Sc^{46}	Fe^{59}
Cheesecloth	219	36.9	54.8	9.7
Sponge, Coarse Paper	121	19.0	22.4	4.3
Sponge, Fine Paper	124	16.7	24.4	5.2
Sponge, Synthetic	113	15.7	22.6	4.7
Excelsior, Fine	51.9	13.5	10.7	2.1
Excelsior, Coarse	38.4	5.8	9.4	1.6
Steel Wool, Grade 0	56.0	5.9	12.4	2.1
Tea Bags	23.5	10.0	3.6	0.8
Charcoal Briquettes	3.9	1.5	0.8	0.1
Aluminum Turnings (degreased)	9.4	1.2	1.9	0.1
Aluminum Turnings (degreased and immersed in boiling water)	30.3	8.5	6.3	1.2

0028293

The constancy of the ratio of the nuclides collected by all media suggests that the collection process was not directly dependent on chemical reaction between the collector and the radioisotope. The appearance of the collectors suggested that they could have acted as collectors of algae and plankton which themselves could have been the primary concentrators of the radioisotopes.

The factors by which these materials concentrated Cr^{51} and Zn^{65} from the river water are presented in Table 3.25. These values are based on the dry weight of the collectors.

TABLE 3.25

CONCENTRATION OF RADIOISOTOPES BY COLLECTORS

	Concentration Factors, $\frac{\text{counts/min/g collector}}{\text{counts/min/ml water}}$	
	Cr^{51}	Zn^{65}
Cheesecloth	6200	22,800
Sponge, Coarse Paper	3200	9,800
Sponge, Fine Paper	3600	10,200
Sponge, Synthetic	3300	7,000
Excelsior, Fine	1500	6,400
Excelsior, Coarse	1200	4,400
Steel Wool, Grade 0	1700	5,400
Tea Bags	500	2,000
Charcoal Briquettes	100	600
Glass Cloth	400	2,000
Aluminum Turnings (degreased)	300	800
Aluminum Turnings (degreased and immersed in boiling water)	900	3,800

Samples of cheesecloth and fine paper sponge were suspended in the Columbia River below Bonneville Dam and from the U. S. Coast Guard lightship Columbia which is anchored in the Pacific Ocean southwest of the mouth of the Columbia River. Analysis of these samples was made by multidimensional gamma-ray spectrometry, which provided the results shown in Table 3.26.

The cheesecloth and sponge collected similar amounts of the various radionuclides at each location. Note that the zinc concentration

factors measured in collectors exposed at Bonneville decreased by a factor of 10 to 20 from those exposed at Richland, Even more striking is the great difference found in the concentration factor of Cr^{51}, which varied by three orders of magnitude between the two locations. This decrease in the fractional amount of the radioisotopes available for collection could reflect a change in either the chemical or physical form of the radioisotope.

TABLE 3.26

CONCENTRATION FACTORS FROM UPTAKE STUDIES WITH CHEESECLOTH AND SPONGE IN THE COLUMBIA RIVER AND THE OCEAN

	Columbia River (Bonneville)				Pacific Ocean (Lightship Columbia)	
	Cheesecloth		Sponge		Cheesecloth	Sponge
Isotope	Disintegrations/ min/g	Concentration Factor	Disintegrations/ min/g	Concentration Factor	Disintegrations/ min/g	Disintegrations/ min/g
Cr^{51}	37.5	3.2	46.7	4.0	32.5	58.5
Zn^{65}	62.5	763	83.6	1020	5.51	11.2
Fe^{59}	3.13	- -	2.11	- -	1.33	1.78
Sb^{124}	0.16	- -	- -	- -	- -	- -
Ba^{140}	1.19	- -	2.38	- -	- -	- -
Co^{60}	0.54	135	0.57	140	0.06	0.17
Sc^{46}	3.00	150	4.09	200	0.72	1.30
Co^{58}	0.11	- -	0.19	- -	- -	0.08
Ru^{106}	0.28	- -	0.81	- -	1.89	4.29
Mn^{54}	1.78	- -	1.71	- -	0.71	1.38
$Zr\text{-}Nb^{95}$	1.53	- -	2.95	- -	1.87	3.33

It becomes apparent that, although these materials are capable of concentrating the radioisotopes from both river and ocean water, knowledge of the concentration factor at each particular location would be required before meaningful results could be obtained. With the advent of more sensitive counting systems, which can measure low concentrations of radionuclides, the use of such collectors and the associated problems seems unwarranted.

A Comparison of the Ratios of Cs^{136} to Cs^{137} and Ba-La^{140} to Cs^{136} from U^{235} and Pu^{239} Fission - C. W. Thomas

The fissionable material used in nuclear devices may be determined by comparing the different ratios of certain fission products. This report presents ratios of fission products Cs^{137} and Cs^{136} and Ba-La^{140} and Cs^{136} measured by multidimensional gamma ray spectrometry on fission product mixtures from U^{235} and Pu^{239} fission.

Although the fissionable material responsible for fission products is generally measured directly by alpha energy analysis for the U^{235}, Pu^{239}, etc., it can also be determined from certain fission product ratios. Large differences between fission product yields from different fissionable nuclei occur on the shoulders of the fission yield curves. These differences are greater for fission from thermal neutrons than from fast neutrons. In nuclear explosive devices fast neutrons are largely responsible for the fission and the number of fission product ratios which can be used to determine the fissioning material is reduced and the resulting accuracy diminished. With the development of multidimensional gamma ray spectrometry the sensitivity for measurement of many radionuclides was enhanced. One such isotope was Cs^{136} where the complex decay scheme containing many gamma-gamma coincidences permitted its identification in fission product mixtures in spite of its low fission yield. The mass distribution curves for Pu^{239} and U^{235} place Cs^{136} at a position where the fission yield maxima occur. Due to the shielding by stable Xe^{136} the fission yield of Cs^{136} is very low, but much lower for U^{235} than for Pu^{239}. The yields from thermal fission given in the Handbook of Nuclear Research and Technology edited by Katcoff are 0.0068 for U^{235} and 0.11 for Pu^{239}.

To obtain the gamma ray spectrum of Cs^{136}, samples of U^{235} and Pu^{239} were irradiated in the Hanford reactors. The cesium radionuclides were chemically separated from the fission product mixture as cesium silicowolframate after repeated basic carbonate scavenge steps and were measured by multidimensional gamma ray spectrometry. The ratios of the various Cs^{136} photopeaks to the Cs^{137} photopeak were then obtained for both the Pu^{239} and the U^{235} fission. The ratios are related as shown in Table 3.27.

TABLE 3.27

RATIOS OF Cs^{136} TO Cs^{137} FROM U^{235} AND Pu^{239} FISSION

Cs^{136} Photopeak Energy	Pu^{239} Ratio / U^{235} Ratio
0.81	12.2
1.04	13.1
1.18	13.3
1.38	13.0
1.86	13.6

The gross fission product mixtures from these samples were examined directly by multidimensional gamma ray spectrometry. The interferences (mainly Ba-La^{140} and Te-I^{132}) masked the Cs^{136} coincident peaks, but measurements were possible by using selected channels where the Cs^{136} coincident peaks were maximized and the interferences from Ba-La^{140} and Te-I^{132} were minimized. These results showed a factor of 4 difference between the Ba-La^{140} to Cs^{136} ratios for U^{235} and Pu^{239}. Although this was much less than the separated Cs^{136} to Cs^{137} value of 13, it was sensitive enough to distinguish between the two different fission product mixtures without a chemical separation. The fission product mixture scan of the Chinese bomb fallout which had been taken 2 mo earlier was reevaluated using this method and the results were similar to the mixed fission products from U^{235}.

The above results indicate that by using either chemical separation and conventional gamma ray spectrometry and measuring the Cs^{136} to Cs^{137} ratio or multidimensional gamma ray spectrometry on mixed fission products and measuring the Ba-La^{140} to Cs^{136} ratio, the difference between U^{235} and Pu^{239} fission products can be determined.

<u>Cl^{38} and S^{38} Produced by Cosmic Radiation</u> - R. W. Perkins, C. W. Thomas, M. W. Hill, and J. M. Nielsen

Cl^{38} and S^{38} have been found as cosmic-ray spallation products of atmospheric argon for the first time. The concentrations of Cl^{38}, S^{38}, Cl^{39}, and Na^{24} in seven rain samples collected during the summer are reported.*

Previous attempts to obtain information regarding cloud formation and the washing of the atmosphere by rain have been based upon the relative concentrations of such relatively long-lived radionuclides as Be^{7} (53 d), P^{32} (14 d), P^{33} (25 d), and S^{35} (87 d) which are produced by cosmic-ray spallation of atmospheric gases. Information regarding short-term effects of atmospheric circulation and rainout would best be provided by nuclides

---

* Parts of this report are in <u>Nature</u>, vol. 205, no. 4973, pp. 790-791. February 20, 1965.

that have half-lives of the order of that required for a rain cloud to form. Attempts to use shorter-lived nuclides for such studies have been complicated by low concentrations and by insufficient sensitivity of the detection equipment.

Estimates were made of the expected production rates of possible spallation products of argon by using spallation systematics developed by Rudstam[3.80] and by Baranovskii and Murin.[3.81] These estimates indicated that Cl^{38} (37.3 min) should be present at concentrations comparable with Cl^{39} (55 min) which was first detected in rain water in 1956[3.82] and that S^{38} (2.9 hr) should be present at about an order of magnitude lower concentration. The concentration of Na^{24} (15 hr) was estimated to be still another order of magnitude lower.

The very high sensitivity of the anticoincidence-shielded multidimensional gamma-ray spectrometer[3.76] was utilized in our search for these radionuclides. Gamma-ray cascades are present in the decay of each, and coincidence techniques were utilized to provide very high sensitivity and low background.

The observed concentrations of Cl^{38}, S^{38}, Cl^{39}, and Na^{24} are in Table 3.28. The samples were collected by placing a 100 to 200 ft^2 plastic sheet on the ground during summer showers. The Cl^{38} and Cl^{39} were precipitated as AgCl, washed, dissolved, reprecipitated as AgCl, and counted directly. The residues were evaporated, placed on a standard counting dish, and counted for S^{38} and Na^{24}. The rain collection periods ranged from 5 to 50 min, and the concentrations shown were calculated to be those present at the time the rain first struck the ground by assuming that the deposition rate of the radionuclides was constant during the sampling period.

Plans are currently underway to look for Mg^{27}, Mg^{28}, Al^{29}, and Si^{31} which should all be more abundant than Na^{24} and for F^{18} which is expected to be less abundant than Na^{24} but perhaps observable. The samples already collected will also be counted for Na^{22} which has been detected in rain water.[3.83]

TABLE 3.28

CONCENTRATIONS OF THE COSMIC-RAY PRODUCED RADIONUCLIDES Cl^{38}, S^{38}, Cl^{39}, AND Na^{24} IN RAIN WATER[a]

Date	Volume, liters	Collection Time, min	Disintegrations/min/liter			
			Cl^{38}	S^{38}	Cl^{39}	Na^{24}
7/29/64	5.10	50	147 ± 15	13 ± 5	200 ± 17	1.5 ± 0.2
7/30	6.64	15	~18	4 ± 2	~10	0.59 ± 0.08
8/1	3.5	50	9 ± 5	(b)	15 ± 3	(b)
8/1	1.8	10	31 ± 12	(b)	28 ± 5	(b)
8/12	2.2	5	42 ± 13	~7	62 ± 12	1.7 ± 0.3
8/18	10.0	40	55 ± 9	(b)	53 ± 3	0.52 ± 0.11
9/2	45.5	45	18 ± 2	0.50 ± 0.26	21 ± 0.7	0.28 ± 0.04

(a) The plus or minus values are the standard deviations for the measurements.

(b) Not measured.

Washout Studies Using Natural Tracers from Radiochemical Separations Plant Stacks* - R. W. Perkins

The washout of gaseous and particulate material from air can be precisely measured by use of the natural tracers present in radiochemical plant stack gases. Methods for measuring some of these tracers in stack gas and in precipitation deposited in a sampling arc downwind have been developed.

The efficiency with which gaseous and particulate material in the air is removed during cloud formation and subsequent washing of the air by precipitation is not well known. Although theoretical rainout coefficients (removal of material from air during cloud formation) and washout coefficients (removal of material from air during the falling of precipitation) have been calculated, no actual measurements of these parameters have previously been reported. In conjunction with our fallout studies interests, an evaluation has been made of the use of the radioactive tracers present in nuclear-plant stack-gas effluents for rainout coefficient measurements. During the normal operation of a nuclear chemical separations plant, small amounts of I^{131} both in the elemental and organic bound form are released. In addition, very minute amounts of $Ru^{103-106}$ are present as particulate material, and the noble gas Kr^{85} is also released. A measurement of the washout coefficient for these

* The measured values of the washout coefficients and the theoretical considerations are included in "Precipitation Scavenging Studies," by R. J. Engelmann, Section I, Atmospheric Physics.

materials requires a measure of the emission rate at the stack and a measure of their concentration in rain (or snow) in an arc (which includes the stack plume) at some distance downwind. Radiochemical methods of analysis have been developed for the measurement of inorganic and organic bound I^{131} and Kr^{85} at the stack and for these plus $Ru^{103-106}$ particles in rain or snow collected at the sampling arc. The stack gas sampling is performed in the series of traps shown in Figure 3.29. The inorganic iodine (I_2 + HI) is collected in the NaOH scrubber; organic bound iodine is collected in the charcoal trap at room temperature. The Kr^{85} is retained almost completely by the first of the two charcoal traps which are held at dry ice-acetone temperature. The second trap detects any breakthrough of Kr^{85}. The membrane filter prevents any particulate material from entering the system, and does not collect a significant amount of I^{131} or Kr^{85}. The $Mg(ClO_4)_2$ trap serves to dry the gas but removes less than 1% of the I^{131} or Kr^{85}. This system is operated at a flow rate of 0.4 liter/min during the collecting of precipitation in the sampling arc. The sample collectors in the arc are 4 ft diam rings of plastic irrigation tubing with 4 mil plastic sheet stretched across. Immediately following a rain (or snow) collection, a 500 g sample is placed in a plastic bottle and sealed for the direct gamma-ray counting of Kr^{85}. The remaining sample is filtered through a 0.3 μ membrane filter to remove $Ru^{103-106}$ particles. Three-gallon samples are then analyzed for organic and inorganic I^{131}. The organic iodine is extracted, after the sample is made 0.1N in NaOH, by stirring three times with 150 ml portions of CCl_4 in the same manner as that used for our standard inorganic I^{131} extraction.[3.84] The combined organic layers are then counted in a plastic bottle in a large well crystal. The inorganic I^{131} is then extracted from this 3 gal sample,[3.84] precipitated as AgI and counted for 30 min in a high sensitivity gamma-ray spectrometer.

Successful measurements of the washout coefficients for inorganic I^{131} have been made, and field evaluations indicate that measurements of the washout coefficients for organic I^{131}, Kr^{85}, and particulate $Ru^{103-106}$ can be made also by this technique.

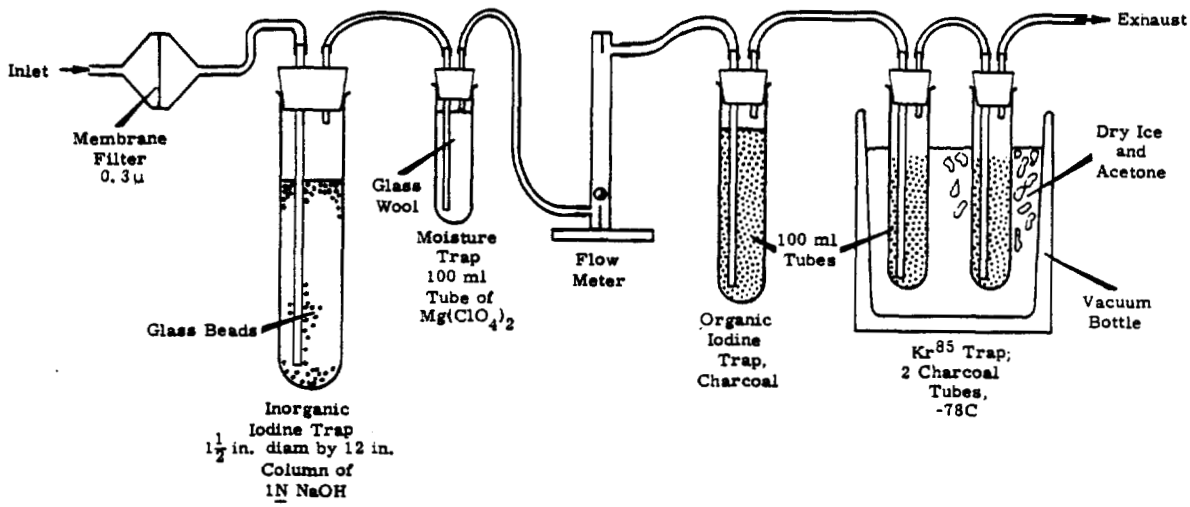

FIGURE 3.29

Stack Gas Sampling Train

Fluorescein as a Dual Atmospheric Tracer - J. D. Ludwick

The emission of fluorescein as an atmospheric tracer was found to be suitable in dual tracer tests with particulate zinc sulfide. Excellent results were obtained when certain experimental controls were placed on fluorescein generation. The physical behavior in the atmosphere of the resulting tracer material was very similar to that of zinc sulfide. Investigation of certain atmospheric diffusion parameters can now be accomplished using the two tracer technique.

A program for distribution, collection, and analysis of fluorescein atmospheric tracer, in conjunction with zinc sulfide, has been underway for several years.[3.85, 3.86] The simultaneous generation and emission of two tracers, whose behavioral characteristics in the atmosphere are identical, or nearly so, enables one to investigate atmospheric parameters in a single experiment that might be only approximately derived by repetitive single tracer dispersions. Information gathered from analysis of such tracers provides insight into the diffusion processes within the atmosphere and such related problems as air pollution.

The techniques for use of fluorescein in conjunction with zinc sulfide have progressed from the analytical laboratory procedures through the

limited field testing stage and finally to the massive field utilization step. The analytical procedures used have been adapted for use with the increased number of required analyses and with the more improved instrumentation available.

This report describes the large scale analysis system as modified from previous work and, more significantly, a quantitative appraisal of results from the last two of the four field tests. Techniques which were employed for fluorescein analysis permitted as little as 1×10^{-11} g to be detected; however, this lower limit of sensitivity was dependent upon the level of other atmospheric pollutants during field test conditions and the method of handling. Generally only about 2×10^{-10} g could be consistently distinguished from background levels. Prior zinc sulfide analysis was conducted by the Battelle-Northwest meteorological group* using fluorescence measurements, and as little as 2×10^{-9} g was detectable.

If necessary, a more involved measurement of the zinc sulfide may be made utilizing phosphorescence techniques. This latter technique is useful if fluorescein analysis should be required before zinc sulfide determination. Utilizing these techniques there was no cross tracer interference, and each tracer was readily handled independently.

Experimental

Although zinc sulfide, which is already particulate, was dispersed to the atmosphere as a particulate slurry, fluorescein was dissolved in water and emitted through the standard generator as a solution. Difficulty arose, due to the dependence of the final atmospheric fluorescein particulate product upon the concentration of the mother solution and the generator nozzle settings. Early field results led to the proper selection of concentrations and nozzle settings for the particular arrangement. Each tracer solution was emitted from adjacent generators and carried downwind to the awaiting Millipore filter collectors, arranged in ground arcs and towers.

* This project was conducted in collaboration with P. W. Nickola and the Battelle-Northwest Atmospheric Physics Section.

Fluorescence measurements of the zinc sulfide quantity were made, and then the individual filters were placed in 2-dram screw cap glass vials, and 4 ml of water was added to each vial. It is suggested that the daily capacity number of samples be treated in one batch (100 to 200) and that an automatic dispensing pipet be used to aliquot the water into the vials. For samples know to contain larger quantities of the fluorescein tracer, 8 ml of water was added. Each vial was briefly shaken and then readied for analysis. The daily capacity for analysis was largely determined by the number of quartz vials available for analysis work since, after use, a decontamination procedure was necessary. Due to cost, a limited number must be used and it is suggested that perhaps 25 to 30 quartz vials will provide a capacity of up to 200 samples in an 8 hr period.

Unless a definite green-yellow solution color was observed after dissolving the fluorescein from the filter in the glass vial, an aliquot of 2 ml was transferred into the quartz analysis vial. With experience, one is able to judge the proper aliquot to add to the quartz analysis vial. The instrumental analysis was very sensitive and one can add too much fluorescein for fluorescence measurements. All that was required here was that the final dilution be within the range of about 10^3 factors of concentration. As an example of treatment of higher concentration samples, one might take a 50 λ aliquot of the original solution and dilute it with 2 ml of water. In calculations, this dilution would then be noted.

Just before analysis, 100 λ of a 20 g/liter Na_3PO_4 solution was added to each sample. This increased and stabilized the fluorescence intensity. All fluorescence measurements were made with a previously calibrated spectrophotofluorometer. A secondary type interference filter, having peak response at 531 mμ was inserted into the emission section of the instrument to further refine the monochromator analysis system. The fluorescein was excited with 490 mμ light. The instrumental analysis for a small batch of 13 samples was completed within 3 min. Every batch analysed was accompanied by a standard and blank sample vial. The standard was measured at the beginning and end of each batch. The blank vials indicate any contamination from a prior batch.

It was found that decontamination was effective and rapid using the following method. All quartz vials were emptied and rinsed with water. They were placed in hot (not boiling) 8N HNO_3 for 5 to 10 min and then rinsed with distilled water and acetone before air drying. If the acid was allowed to boil while the vials were present, the slight bumping action would break many vials. Another precaution in analysis was to be sure that all the acetone had evaporated before introducing a new sample into the vial. Very high fluorescence readings will result with acetone present.

Results

This study was undertaken to develop a sensitive tracer whose presence would not interfere with the existing zinc sulfide analysis and would itself act in a manner nearly identical to that of zinc sulfide in atmospheric transport. Results of the fluorescein study have satisfied these criteria and provided an acceptably rapid mass analysis procedure.

Figures 3.30, 3.31, 3.32, and 3.33 illustrate results from ground position samples from the two latest field test experiments. The quantity of each tracer found was normalized for small differences in the relative amounts dispersed. The excellent quantitative results observed will then allow the use of these tracers for investigation of other atmospheric phenomena.

Investigation of Inert Atmospheric Tracers; Xe^{133} - J. D. Ludwick

A program was developed for emission, collection, and analysis of the radioactive rare gas Xe^{133} as an atmospheric tracer. The value of this type of tracer lies in its inert characteristics and its ability to follow the diffusion processes without regard to many of the factors influencing other tracers. The first field test of this tracer was carried out and progress to this time is discussed.

Considerable information has been gathered concerning atmospheric diffusion processes using many different types of gaseous and particulate tracers. In addition, a limited number of tracer deposition studies over various types of terrain and vegetation indicate qualitatively and semiquantitatively the scavenging effects from these factors. Complications arise from the turbulent diffusion processes in the atmosphere (as well as from

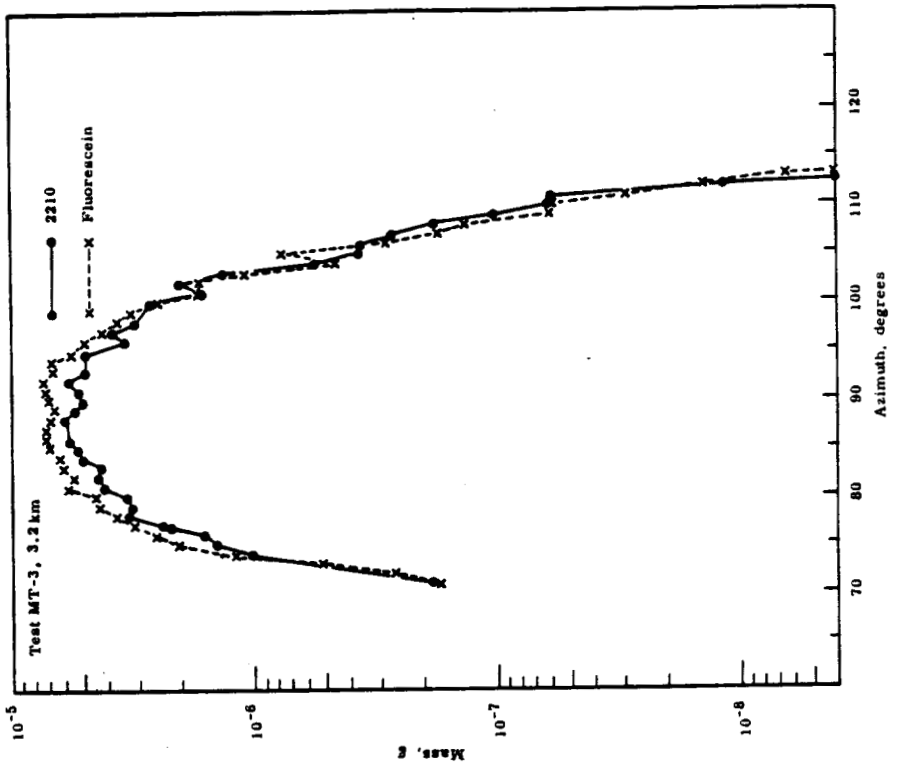

FIGURE 3.31
Crosswind Distribution of Tracers at 3.2 km from the Source

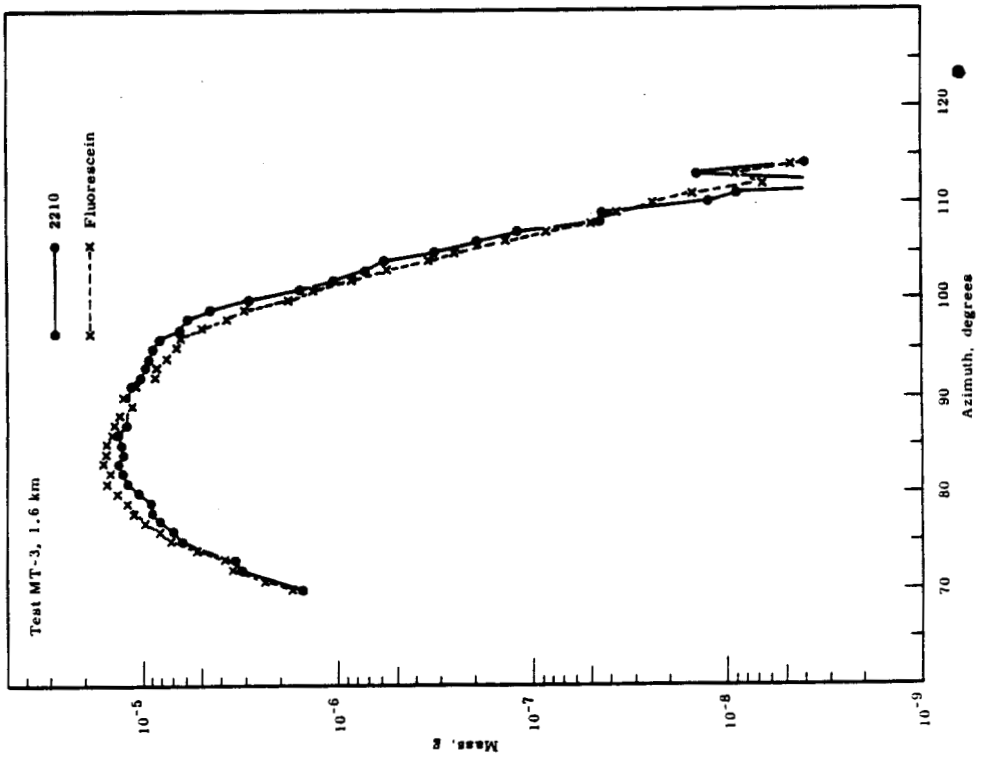

FIGURE 3.30
Crosswind Distribution of Tracers at 1.6 km from the Source

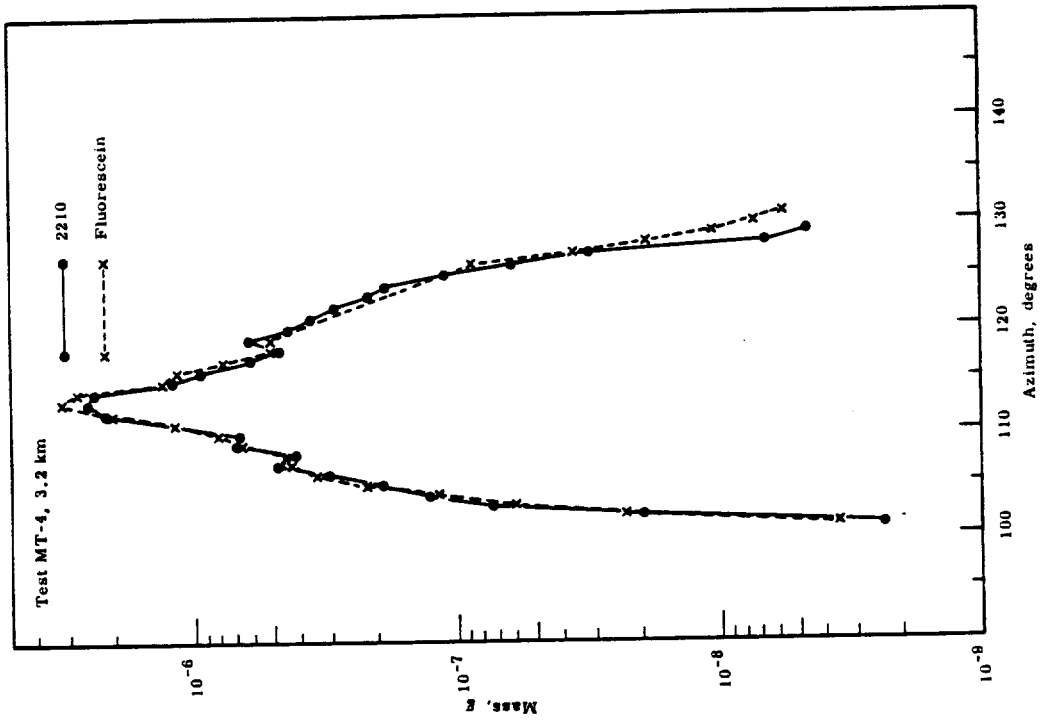

FIGURE 3.33
Crosswind Distribution of Tracers at 3.2 km from the Source

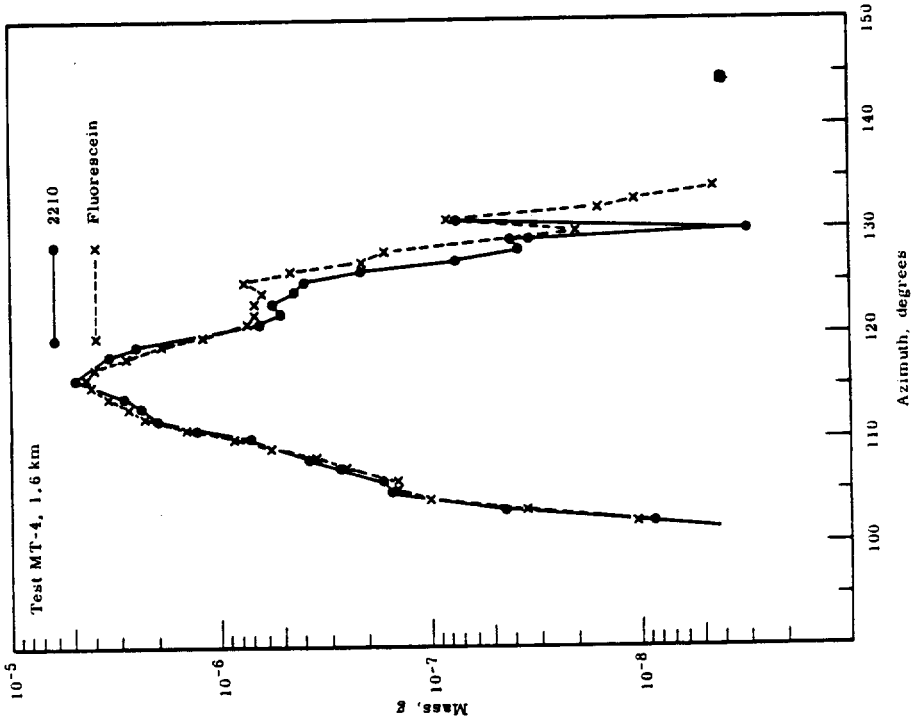

FIGURE 3.32
Crosswind Distribution of Tracers at 1.6 km from Source

gravitational effects) where tracers are thrust groundward and may or may not reenter their downwind course. One would desire a tracer whose characteristics are such that no processes other than diffusion and solution were taking place as travel downwind progressed.

Consideration was given to several of the rare gases as possible tracers. Argon, with its atmospheric abundance of almost 1% was precluded except as a radioactive tracer in the form of Ar^{41}. The short half-life (1.8 hr) and difficulty in selective trapping makes this unattractive even though the high energy gamma ray emitted is readily detected. The possibility of its use as a tracer in a transient detection system for less sensitive experiments should not be ruled out. A limited containment collection system with a pressurized cylinder would also lend itself to Ar^{41} detection.

Large quantity emission of the gases krypton and xenon remains a possibility, with the more sensitive and expensive (due to its much lower natural abundance) being xenon. Analysis possibilities would be the chromatographic process or mass spectrometry.

In considering the radioisotopes of krypton and xenon, the possibilities are greatly reduced when one takes into account such factors as half-life, health hazard, availability, and analysis. Although Kr^{85} would satisfy many requirements, its long half-life (10.6 yr) makes large source strength dispersals undesirable. The short half-life of Xe^{135} and the lack of availability of large quantities of Xe^{131} led us to select the 5.3 day Xe^{133} which can be obtained radiochemically pure and at a reasonable cost per curie. The required purification and analysis problems remained as formidable obstacles to the use of this radioisotope.

Low level internal gas counting techniques are available for detection of the weak beta emission (0.35 MeV) from Xe^{133}; however, a more rapid, less tedious method was needed.

It was known that some rare gases under the proper conditions are somewhat soluble in certain oils and organic materials. One of the best methods of low level beta detection at present is that of liquid scintillation counting. Here the solvent material may be varied to some extent;

however, it was found that a reasonable amount of xenon would dissolve in some of the best primary liquid scintillator solvents, toluene and xylene. With the possibility of dissolution of the Xe^{133} directly into the liquid scintillator, consequently allowing close to 100% counting efficiency of the dissolved portion, work to develop this procedure was undertaken and completed.

With a unique analysis advantage, equipment and procedures were developed and tested for use in the field dispersal and measurement of radioxenon. At present one field test has been conducted, dispersing about 1 Ci of Xe^{133} to the environs on the stable course of the meteorology grid. Simultaneously with the xenon emission, an adjacent zinc sulfide generation was made in an effort to determine behavioral differences between that normally used tracer and the inert rare gas.

Experimental

Xe^{133} was obtained in 0.5 in. glass ampoules which were introduced into a 20 ft^3 steel pressure cylinder. The regulator and cap were then sealed onto the vessel, and the cylinder was pressurized with argon carrier gas to the equivalent of 600 psi at 0 C. After it had been determined that the pressure seal was secure, the cylinder was shaken and the ampoules were shattered by 0.75 in. steel balls included in the cylinder. Breakage of the ampoules was determined by radiation survey instruments which registered homogeneous activity throughout the containment vessel. The cylinder was placed in a shielded stand (Figure 3.34) and moved directly adjacent to the zinc sulfide tracer dispersal point with the flexible copper tubing allowing exact positioning. A flow rate meter, which was previously calibrated to deliver 95% of the contents in 30 min, controlled the constant rate of radioxenon emission.

Final design in the development of an efficient trapping system for xenon is illustrated in Figures 3.35 and 3.36 which are front and rear views of the collection system. Thirteen such systems were located in the field, one upwind for background level measurements. Air and xenon enter the system through the front face filter which collects the zinc sulfide particulates. An alternate path of entrance utilizing a three-way valve is through

the flowmeter with filter by which the rate of flow is measured. The flow control (black knob to the right) is located at the extreme exit of the system connecting to a vacuum pump when in use. A glass vacuum vial and bubbler system containing a known quantity of inactive xenon gas carrier was located near the air entrance. This carrier gas and entrance air flows through a large bottle containing first magnesium perchlorate for moisture removal and Ascarite for moisture and carbon dioxide removal. The dried gases flow through two precooling glass bead traps housed in the large insulated vessel containing a mixture of dry ice and acetone. Then the cold gases are introduced into a large activated charcoal trap with charcoal flow path length of about 20 in. where xenon is efficiently collected.

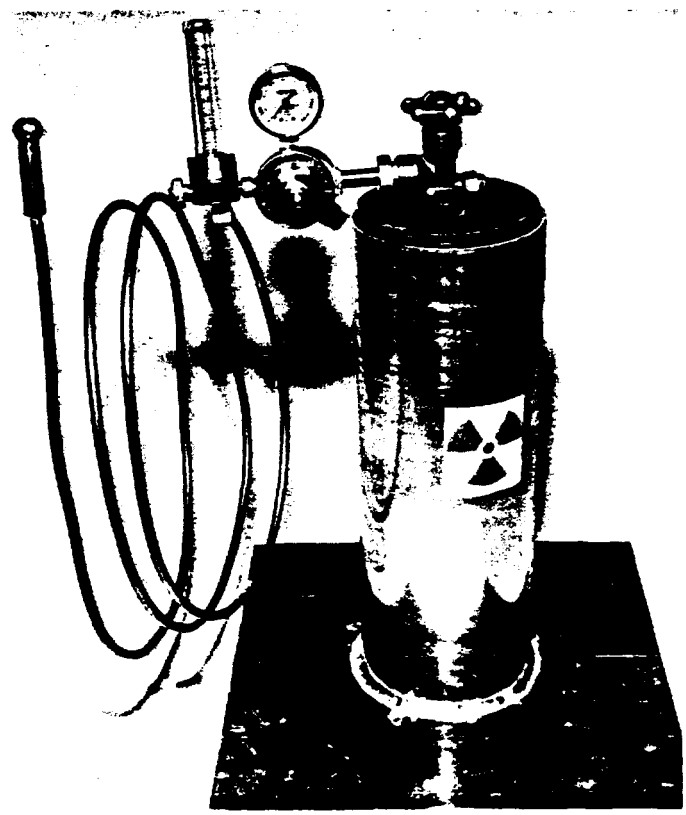

FIGURE 3.34
Xe^{133} Emission Vessel

Neg. No. 0650317-3

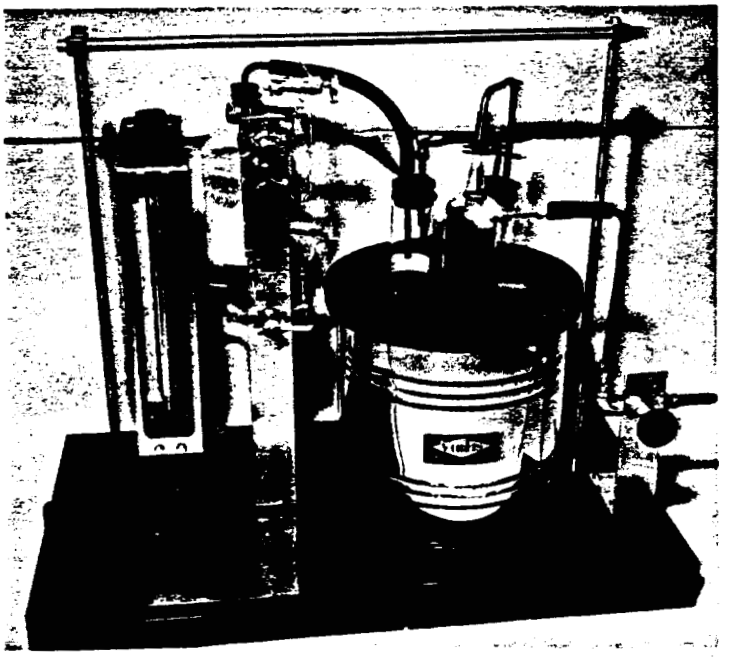

FIGURE 3.35
Xe^{133} Collection Apparatus
(Front)

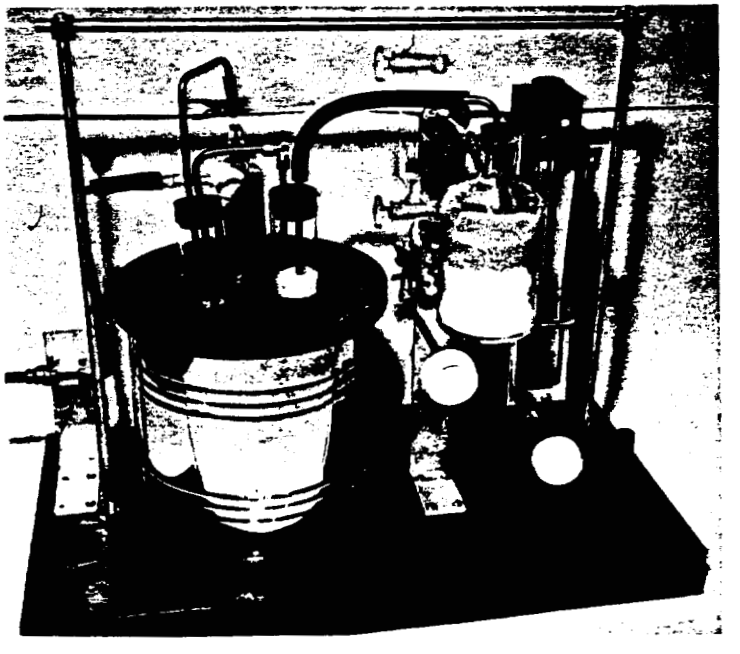

FIGURE 3.36
Xe^{133} Collection Apparatus
(Rear)

Neg. No. 0650317-2; 0650317-1

The charcoal traps are collected and maintained at -80 C while transporting from field to laboratory for analysis. Figure 3.37 shows the position, at the extreme right, of the charcoal trap mounted on the vacuum system. A large volume of other gases is collected; these are bled off through the two U-traps immediately to the left of the charcoal. These traps are maintained at -195 C, and the xenon collection trap was slowly warmed from -80 to 175 C. This process takes about 3 hr and the xenon was collected in the U-traps. In addition, a great deal of carbon dioxide and some other condensibles were collected and transferred to a small vacuum flask half filled with Ascarite and allowed to stand overnight; this cleared the vacuum line for another sample. There were two vacuum lines available for processing, allowing two samples to be processed in about 3 hr. Chromatographic separation over charcoal was then conducted for the reamining xenon sample. The xenon was loaded onto the charcoal U-trap seen at the center of Figure 3.37 and eluted at 35 C. The xenon fraction was collected on a second charcoal trap at the exit of the chromatographic unit, also illustrated.

This purified xenon was vacuum distilled into a quartz vial containing a previously degassed liquid scintillator maintained at -195 C. The scintillator solution contained 1.0 g/liter dimethyl-POPOP and 6.0 g/liter PPO dissolved in toluene. The vial was sealed under vacuum and warmed thus allowing xenon dissolution into the liquid scintillator. Very high detection efficiencies had been observed in previous work with this scintillator. As the vial warms one is concerned with the possibility of the xenon carrier building high pressures within the sealed quartz ampoule before the toluene melts; however, no mishap of this nature has occurred and it is suspected that the xenon is somewhat dissolved by the solid scintillator as the pressure rises. A maximum of 10 ml STP of xenon gas was utilized as carrier gas in these experiments. The volume of liquid scintillator was 3 ml.

After warming, the quartz vials were placed in a special light pipe contained as the detection unit of a liquid scintillation spectrometer. This is shown in Figure 3.38. Samples were counted for 1 hr intervals and rechecked to verify half-life characteristics about 5 days later.

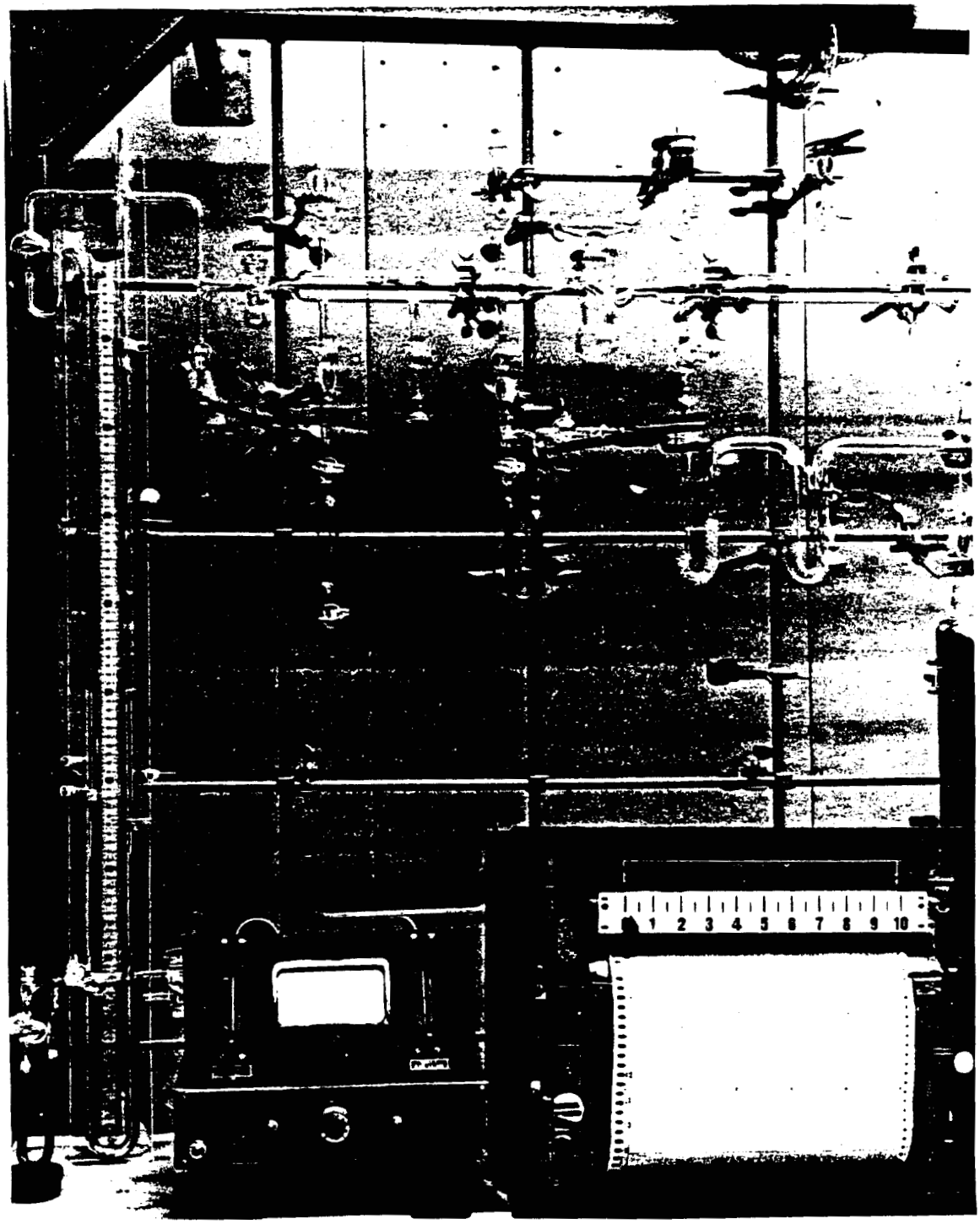

FIGURE 3.37

Xenon Purification and Analysis System

Neg. No. 0650317-4

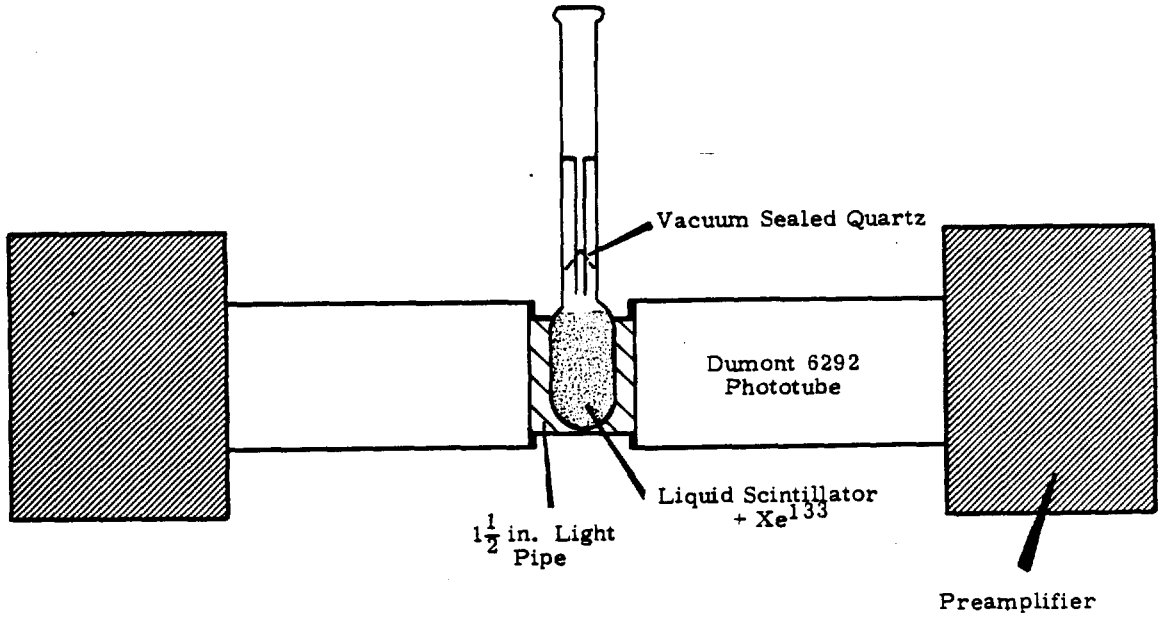

FIGURE 3.38
Xe^{133} Beta Detection System

Results

Experimental results from chromatographic purification are illustrated in Figure 3.39. Some air was loaded and reeluted from the charcoal each time a new trap was introduced into the system. A small amount of krypton was present in our carrier gas and also as an atmospheric component. The quantity of purified xenon was measured in a calibrated section of the vacuum line and is indicative of the overall field collection and chemical purification efficiency. Typically, from 50 to 85% yields were obtained from the purified product.

Results from tests on the liquid scintillator system have shown that large quantities of xenon gas can be dissolved within the liquid scintillator with little decrease in counting efficiency. The quenching effect was observed; however, if one works with less than 2×10^{-4} mole of xenon for this system, it is negligible. The counting efficiency of the gas dissolved within the scintillator was essentially 100%. A small amount of gas was found in the vapor phase above the liquid, depending upon the liquid-vapor partition coefficient. This vapor phase component was minimized by

limiting the amount of free volume in the sealed ampoule using a capillary tube neck. Results using standardized samples of Xe^{133} supplied by Oak Ridge showed about 94% of the radioisotope disintegrations being detected in the counting arrangement.

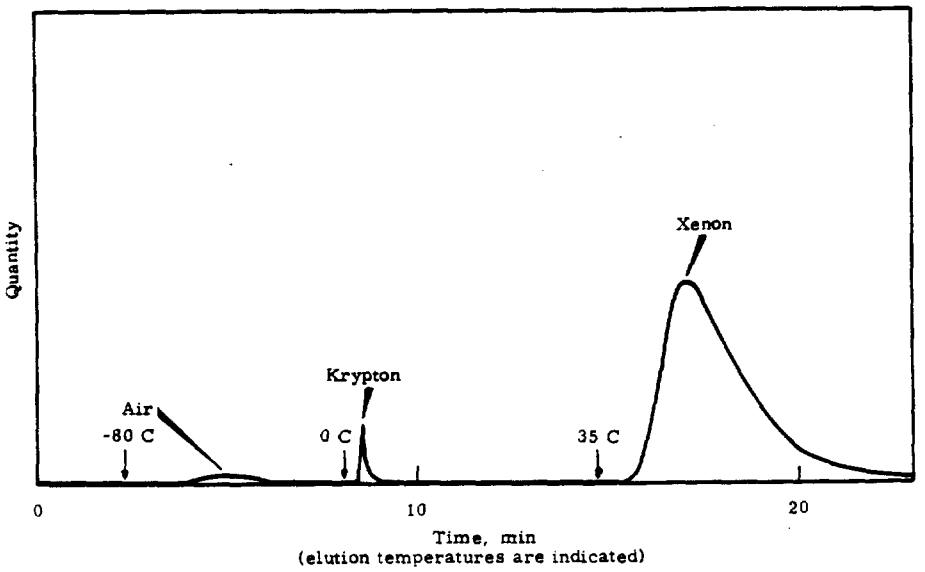

FIGURE 3.39

Xenon Purification Chromatograph

The Xe^{133} activity emitted during the first experimental field test was about 1.04 Ci as calculated from Oak Ridge data. The amounts collected at several sampling stations 200 and 800 m downwind Arcs 1 and 3, respectively, are represented in Table 3.29. Difficulty with some sampling stations developed in the field due to certain operational procedures, and not all samples were collected. It is anticipated that future field tests will be even more successful; however, the results clearly demonstrated that Xe^{133} can be used as an atmospheric tracer with sufficient sensitivity for many applications.

TABLE 3.29

DOWNWIND Xe^{133} CONCENTRATION

Sample	Xenon Recovery, %	Disintegrations/min
1-114	44	750
1-106	85	18220
1-098	60	18552
3-114	67	71
3-106	10	364
3-098	62	616

TABLE 2.4

Fe^{55} IN FOOD

	Sample	mg Stable Iron per 100 kg Sample	nCi Fe^{55} per kg Sample
Whole Wheat Flour	1	29	0.31
	2	46	0.27
Bleached White Flour	1	30	0.065
	2	31	0.036
	3	33	0.049
	4	31	0.026
Wheat Flakes	1	56	0.25
40% Bran Flakes	1	48	0.37
Quaker Oats	1	41	0.15
Beef Liver	1	--	0.95
	2	--	1.2
Beef Round Steak	1	22	0.86
	2	--	0.92
Eggs	1	25	0.54
	2	20	0.055
	3	23	0.16
Lettuce	1	--	0.017
	2	--	0.0066
	3	--	0.0069
Carrots	1	--	0.034
	2	--	0.041
	3	--	Not Detectable

Radioactivity in an Individual Eskimo - H. E. Palmer

The visit of an Eskimo to Battelle-Northwest, permitted a more detailed study of Cs^{137} burden, distribution, excretion, and search for other isotopes than had been possible under field conditions.

During October, 1964, it was possible for an Eskimo from Anaktuvuk Pass, Alaska, to spend 2 wk at our laboratory to help us study his body burden of Cs^{137} (1300 nCi). This paper reports the results of these studies.

Intercomparison of the Hanford Whole Body Counters

The subject was measured in the three whole body counters used at Hanford: the shadow shield, the mobile counter, and the iron room. The results were in very close agreement: 1300, 1290, and 1290 nCi of Cs^{137}, respectively. The counting rates were high enough to give a standard

deviation of ± 0.3% for a 20 min count. The subject was also counted with the NaI crystal used in Alaska. During the preceding year this crystal had cracked. The crack caused a change in the resolution and in the calibration factor. The comparison with the other crystals showed that the calibration changes we made were correct. It was also possible to obtain a better calibration of our simplified whole body counter.*

Differential Whole Body Scan

A differential scan with a 2 in. wide slit collimator on a $9\frac{3}{8}$ by 4 in. crystal was made over the entire length of his body. This scan showed that the parts of the body containing the most muscle had the highest Cs^{137} concentration. Figure 2.8 shows the counting rate obtained along the body and shows the shoulders, liver, thighs, and calves to have much more Cs^{137} than the bony section of the head, pelvic region, knees and ankles.

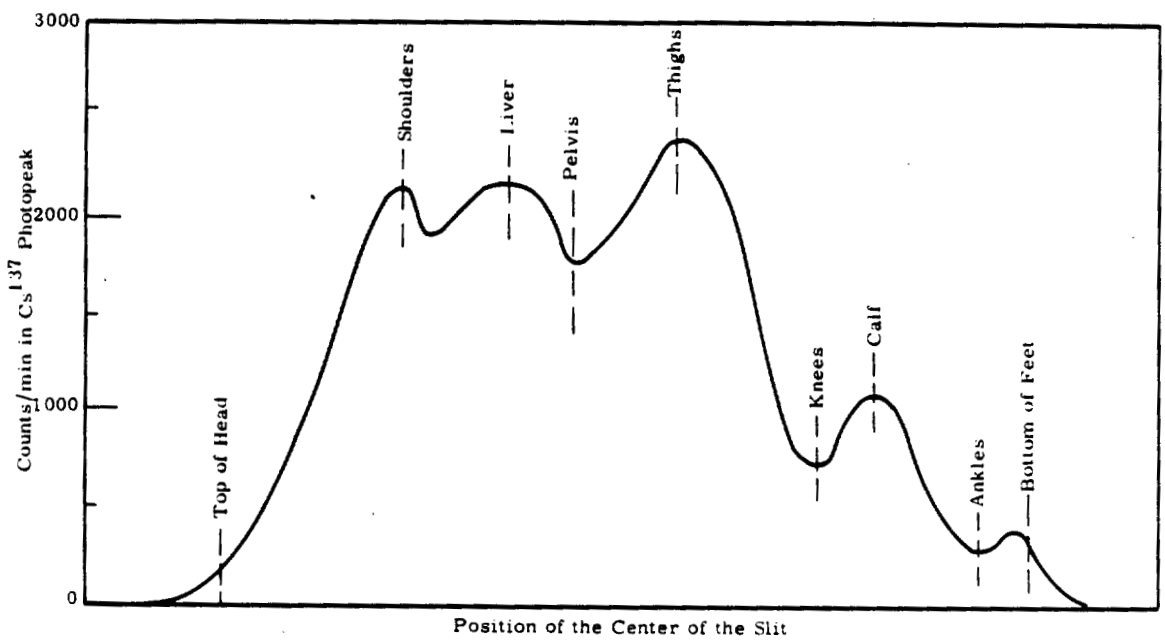

FIGURE 2.8
Differential Scan of an Eskimo
(2 in. Wide Collimator Slit)

* See "Simplified Whole Body Counting," p. 2.16.

Cs^{137} Excretion

Daily whole body counts gave a biological half-life for Cs^{137}. The body burden decreased from 1310 nCi to 1160 nCi in a 14 day period. This corresponds to 0.87% of the body burden per day or an 80 day half-life. Total urine collections were made over several 24 hr periods, and analysis of the urine showed the excretion by this route to range from 0.47% to 0.55% of the body burden per day with an average of 0.50%. This indicates that about 40% of the daily Cs^{137} loss from the body goes by some route other than urine excretion. If this 40% is excreted in feces this gives a urinary to fecal ratio of 1.3 which is much lower than the ratio of 4 to 10 reported by others.[2.10, 2.11]

Other Isotopes in the Body

No other isotopes were detected in the subject in the regular whole body counts. However, Na^{22} was detected by coincidence counting of the subject's arms between two large crystals. The coincidence spectrum is shown in Figure 2.9. The Na^{22} present was probably the small fraction deposited in the bones where it has a relatively long residence time compared to the 11 day half-life of the isotope in soft tissues. Fe^{55} was detected in a blood sample taken from the subject. From the concentration in the blood, the total body burden was estimated to be 75 nCi. The source of the Na^{22} and Fe^{55} and other studies of these two isotopes are discussed elsewhere in this report.*

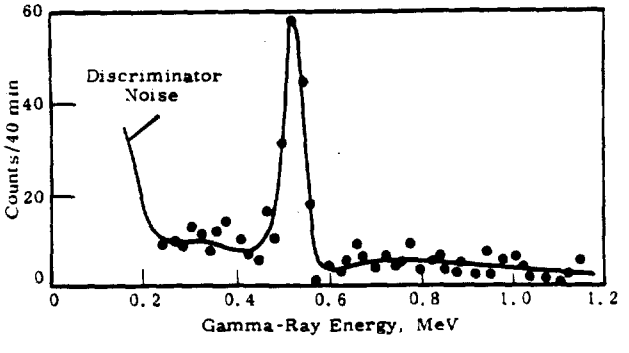

FIGURE 2.9
Gamma-Ray Coincidence Spectrum Due to Na^{22} in the Arm of an Eskimo

* Na^{22} in People and Food," p. 2.8 and "Fe^{55} in Humans and Their Food," p. 2.9.

Miscellaneous Studies

An estimate was made of the Cs^{137} interference in the background of the *in vivo* plutonium counter. The barium X-ray resulting from the decay of Cs^{137} in the subject's body was easily detected.

Dose rates at the surface of the Eskimo's body were determined with sensitive ion chambers in a low background, lead-shielded room. A dose rate of about 5 μR/hr was found. Because of the statistical uncertainties in these data, it is not possible to estimate how much of this came from the Cs^{137} in his body.

Simplified Whole Body Counting - H. E. Palmer

A small scintillation counter can be used without shielding to measure the Cs^{137} body burdens of Alaskan natives.

Several years ago we began to explore how much the shielding of whole body counters could be reduced while retaining as much counter versatility as possible. This work produced the Shadow Shield Counter[2.12] which provides nearly the sensitivity of an iron-room counter but weighs only 5 tons. Naturally we have been interested in what could be done with no shielding at all. Our studies of Cs^{137} in Alaskan natives permitted the whole body counting of people who contained enough activity to make shielding unnecessary.

Twenty Eskimos who had been counted on the Shadow Shield Whole Body Counter were also counted with a 3 x 3 in. NaI crystal. This was done by placing the crystal on top of their thighs at the crotch and then having them bend over the crystal so that the body almost completely surrounded the crystal. Some shielding against background radiation was provided, and as much of the body as possible was close to the crystal. The counting rate from the *in vivo* Cs^{137} and the background rate under the Cs^{137} photopeak for the 3 in. crystal with no shielding were almost identical to those of the 4 by $9\frac{3}{8}$ in. crystal in the shadow shield.

The counting rate per nanocurie of Cs^{137} in the body decreased as the length and thickness of the subject's body increased. Since weight is

proportional to both length and thickness, the counting rate per unit activity was plotted against body weight (Figure 2.10). All the points were within ± 10% of the line shown. This is the accuracy with which the body burden can be determined when this line is used to give the calibration factor. The equation of the line -0.034 W + 11.2 count/min/nCi of Cs^{137}, where W is the weight of the subject. A person having a low body burden of Cs^{137} can be counted to determine the background. This background is subtracted from the total count of a subject having a higher body burden, and then the Cs^{137} content of the background subject is added to the burden calculated for the difference count.

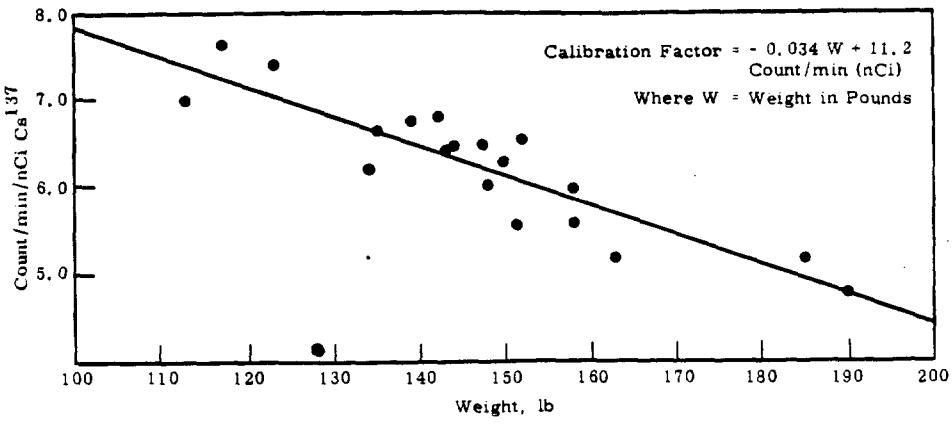

FIGURE 2.10

Dependence of Counting Rate on Weight when Measuring Cs^{137} Body Burdens with 3 in. Crystal

This method was used this summer to measure Cs^{137} in 14 men at Point Hope, Alaska, who were not also counted with the Shadow Shield Counter. They had an average of 64 nCi. They were counted for 4 min each. A small airplane containing a gasoline motor generator, multichannel analyzer, high voltage supply, and the 3 in. crystal was flown to Point Hope and the men were counted at the airstrip. Figure 2.11 shows one of the Eskimos being counted. Since that time, our instrument development laboratory has built us a battery powered transistorized single channel analyzer, with built-in high voltage supply, which weighs only 17 lb and can operate more than 100 hr on four 6 V lantern batteries.[2.13] With this instrument no village

is too isolated to be studied for Cs^{137} body burdens. We plan to use this instrument extensively in the future.

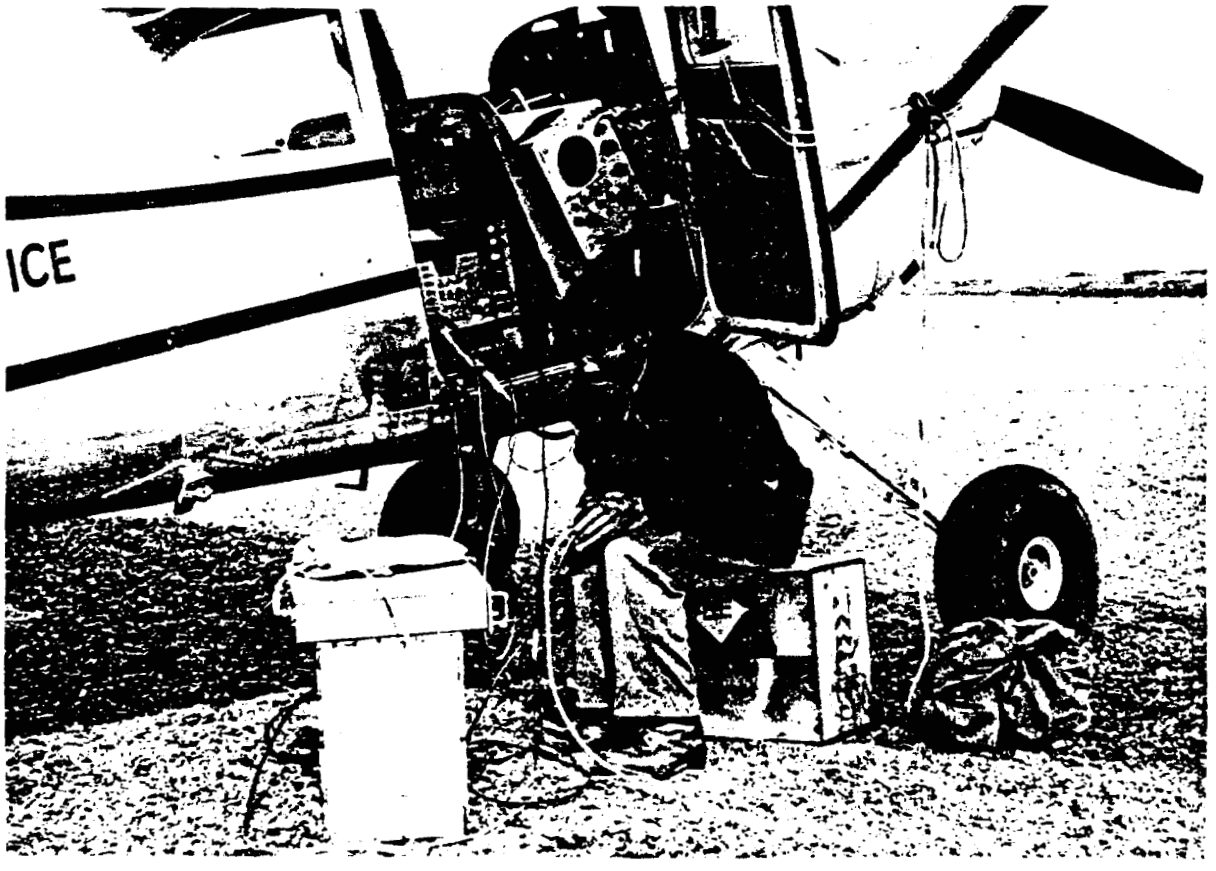

FIGURE 2.11

Field Application of Simplified Whole Body Counter

So far the 3 in. crystal has only been calibrated for Cs^{137} in adult men. However, this is sufficient for the Alaskan studies since our work shows that the average body burden of the women is consistently about 2/3 that of the men and that of the children under 14 yr is about 1/4 that of the adult men. With these relationships, it is only necessary to measure the male members of a village.

The sensitivity of the method is much better than we first expected. Body burdens down to a few nanocuries can be determined without any

Neg. No. 642245-1CN

shielding. The error in matching the subject's background becomes significant at these low body burdens and the background must be measured more accurately than is necessary for the high burdens. Development of other applications of this technique are planned. The method is best suited for those internally deposited radionuclides such as sodium, potassium, cesium, etc. that are distributed throughout the body. The measurement of a radionuclide in the lung would be more difficult with the crystal in the position we are now using it.

Cs^{137} in Trappist Monks - R. A. Jalbert* and H. E. Palmer

An attempt to measure the body intake of Cs^{137} through meat failed but gave interesting data on other sources, particularly whole wheat flour.

As a result of nuclear weapons tests, people in all parts of the world now contain small amounts of the radionuclide Cs^{137}. Its presence in humans was first reported by Miller and Marinelli[2.14] in 1955. Since that time many investigators have studied the Cs^{137} body burdens of people. Although many foods contain Cs^{137}, milk and meat are the largest contributors to human body burdens. Meat contributes almost all of the Cs^{137} to the diet of Alaskan Eskimos.[2.1] Comar[2.15] has estimated that for people in the rest of the United States 60% comes from milk and milk products, 25% from meat, and the remainder from flour, cereals, vegetables, and fruits.

To see what effect the absence of meat in the diet had on the Cs^{137} body burden, we made a whole body counting study of a group of Trappist monks at Our Lady of Guadalupe Abbey at Lafayette, Oregon. The Hanford mobile whole body counter was used for the study. We measured the body burden of Cs^{137} in 50 monks. Forty-two of them had not eaten any meat during the preceding year. Their average body burden was 36 nCi. This value is about 50% higher than the average Cs^{137} body burden (20 nCi) in adult males living at Richland, Washington, at the same time.

---

* University of Alaska and Summer Professor at Battelle-Northwest.

0028321

To find out why the Cs^{137} in the monks was so much higher than that in Richland people, we measured the Cs^{137} in their food and in another group of people living in the same area but eating an average diet including meat. Diet information obtained from the monks showed that whole wheat bread is the food that they substitute for meat. The average consumption of the whole wheat bread by each monk is 6.5 slices per day; they eat no white bread. Their average milk consumption is about 1.5 pints per day. The rest of their diet is similar to the average American diet except that they have very few desserts. The Cs^{137} content of the whole wheat flour they used was 0.22 nCi/lb and that of white flour was 0.071 nCi/lb. Whole wheat and white flour from several other sources showed this same difference. The Cs^{137} content of their milk and other food items was very similar to that of food from elsewhere in the area. The activity of the whole wheat flour and the monks' high consumption of the bread account for their high body burdens.

To compare the Cs^{137} in the monks with that in other people from the same area, we counted 30 young men at a Jesuit novitiate just 25 mi from the monastery. Their average body burden of Cs^{137} was 30 nCi. These men eat a typical American diet. Their average body burden is also significantly higher than that of the people at Richland. The climate of the two locations is very different. The monastery and novitiate are located in an area of high rainfall, and therefore probably high fallout, while Richland is located in an arid region.

Humans Exposed to Uranium Mine Atmospheres* - H. E. Palmer, R. W. Perkins,** and B. O. Stuart***

Measurements of the deposition and distribution of radon daughters in individuals exposed to uranium mine atmospheres were made using a mobile whole body counter. These measurements showed that 20% of the radioactivity was in the head, 10% in the neck region and 70% in the chest immediately following exposure.

---

* From Health Physics, vol. 10, pp. 1129-1135. 1964.

** Chemistry Department

*** Biology Department

Subsequent measurement showed very little transfer of the radon daughters from one region of the respiratory system to another. A comparison of these measurements with air sample measurements indicates that nearly 100% of the inhaled radioactivity was deposited. Dust particle analysis showed that about all of the radioactivity is associated with particles less than 0.5 μ, with particles smaller than 0.1 μ carrying the bulk of the activity.

Standardization of Whole Body Counters - R. A. Jalbert* and W. C. Roesch

A modification of Evan's one-meter-arc method gave results consistently about 15% too high for Cs^{137} but quite adequate for many purposes.

Attempts at this laboratory to use phantoms filled with liquids containing radionuclides to calibrate whole body counters have been unsuccessful.(2.16) It has been necessary to use people who have been given known amounts of a radionuclide for tracer studies or therapy. This is unsatisfactory because people usually are not available who contain new nuclides of interest. This paper reports the first work on development of a method of measuring activity in people that does not require comparison with another person containing a known amount of the activity.

Our technique is an adaptation of one introduced by Evans(2.17) known as the one-meter-arc method. Evan's method was to obtain four counts of a person containing radioactivity: C_1 was obtained with the person lying as nearly as possible along an arc of a circle of 1 m radius with the detector at the center of the circle, C_2 was obtained with the person facing the other way on the arc, C_3 was the net increase due to a known source of the radionuclide placed on the arc with the person between it and the detector, and C_4 was due to the source alone on the arc. Evans showed that under certain simple assumptions the activity in the person, N, was related to that of the known source, N_o by

$$N = N_o\sqrt{C_1C_2/C_3C_4} \qquad (1)$$

correct to terms of first order in the ratio of the thickness of the person to the radius of the circle. In the work described below we substituted

* University of Alaska and Summer Professor at Battelle-Northwest.

for C_4 a count obtained with the known source on the person on the side toward the detector. Then Equation (1) is correct to terms of second order in the ratio of the thickness to the distance.

Trials of the one-meter-arc method itself in this laboratory were not very successful. The difficulty was found to be a change in sensitivity of the big NaI crystal with direction of incidence of the photons. The theory assumes a detector equally sensitive in all directions.

Our adaptation of the one-meter-arc technique is to obtain the four counts in a Shadow Shield Whole Body Counter.[2.12] The purpose of placing the person on the arc of a circle in the original technique was to have every part of his body in approximately the same position relative to the counter. The resulting equal sensitivity of the detector to all parts of the body is achieved in the Shadow Shield by having the body move completely through a relatively narrow opening before a NaI scintillator. The sensitivitiy varies with position within this opening, but each part of the body moves through approximately the same sequence of positions so that each is counted with the same average sensitivity. To reduce the thickness-to-distance ratio and thus improve the applicability of Equation (1), we raised the NaI crystal so that it was about twice as far from the subject as before. The iron plate of the Shadow Shield then blocked some photons emitted near the edge of the body from reaching the NaI crystal in this raised position, so we enlarged the hole in the plate in the direction perpendicular to the direction of motion of the subject.

With this apparatus we confirmed that inverse square and exponential absorption attenuation, assumed in the theory, held for Cs^{137} gamma rays. Theory similar to Evans' shows that the counts C_a and C_b for a given source at depths a and b in a phantom are related to the count C_c for the source at a depth $c = \frac{1}{2}(a + b)$ by

$$C_c = \sqrt{C_a C_b} \tag{2}$$

to terms of second order in the ratio of the phantom thickness to the source-to-detector distance. Tests of Equation (2) with Cs^{137} proved

accurate to within 5%, but there was about 15% variation between the center of the phantom and the edge. Table 2.5 shows the results of measurements with a Remab phantom when known amounts of Cs^{137} were added. The calibration technique gives results systematically 15 to 20% too high. So far we have not been able to find out why.

TABLE 2.5

TEST OF CALIBRATION METHOD WITH PHANTOM

	Cs^{137}, nCi	
	Activity in Phantom	Calibration Technique
Whole Phantom	244	284
Head, Arms, and Legs	191	226
Arms and Legs	170	192
Torso	74.2	97.5

We chose to test the method on people by studying Cs^{137}, since "normal" body burdens of 20 to 40 nCi were common. Raising the crystal had reduced the sensitivity to about one-fourth the usual shadow shield value, so even these relatively high burdens gave us rather poor counting statistics. The statistics on the K^{40} and Zn^{65} determinations for the same subjects, which were necessary for correcting the Cs^{137} counts, were even poorer. We estimate that there is a standard deviation of about 15% in a typical body burden determination in this experiment. We compared our results with the body burden determined in the Hanford iron room whole body counter. To reduce the amount of time our subjects had to spend being counted, we determined C_3 and C_4 with a masonite phantom as thick as the subject. Tests on a few subjects showed this was sufficiently accurate. Two subjects made duplicate counts.

The results are shown in Table 2.6. The body burdens determined by our technique are systematically about 15% higher than those determined in the iron room. Their scatter is consistent with the statistical uncertainty we expected. The results show that the technique is capable of at least enough accuracy for health physics purposes for gamma ray energies comparable to that of Cs^{137}.

TABLE 2.6

TEST OF CALIBRATION METHOD WITH PEOPLE

Subject	Cs^{137}, nCi Iron Room	Calibration Technique
1	18.5	22.4
	--	23.2
	19.9	25.0
2	24.5	30.6
3	26.4	32.9
4	27.0	31.0
5	31.7	30.7
	--	31.1
6	32.0	33.3
7	36.6	41.0
8	37.0	40.5

Progress in Plutonium Whole Body Counting - K. L. Swinth and B. I. Griffin

Correlation with regular whole body counting and use of of an anticoincidence shield have been studied as ways of predicting or controlling the background rate of people in the plutonium counter.

The paper following this one* describes studies with the plutonium whole body scintillation counter(2.18) performed on dogs and aimed at the problems associated with the plutonium. This paper describes our studies on the background rate for people in the counter. This rate is due to radionuclides other than plutonium and its daughters in their bodies and to normal background as affected by absorption and scattering in their bodies. Knowledge of this normal background will determine how much plutonium we can detect in a person.

A correlation exists between the count rate of an individual in the Shadow Shield Whole Body Counter(2.12) and in the plutonium counter. Figures 2.12 and 2.13 show the results for eight people who contained no plutonium. The first shows the counts from the band of channels of the plutonium counter that contain the X-ray peak versus the count from all channels of the Shadow Shield Counter; the second includes both X-ray and 60 keV peaks. Using only those counts from the Shadow Shield Counter from a low energy region (40 to 400 keV) did not improve the correlation.

* "Counting Plutonium in Animals and Excreta," p. 2.27.

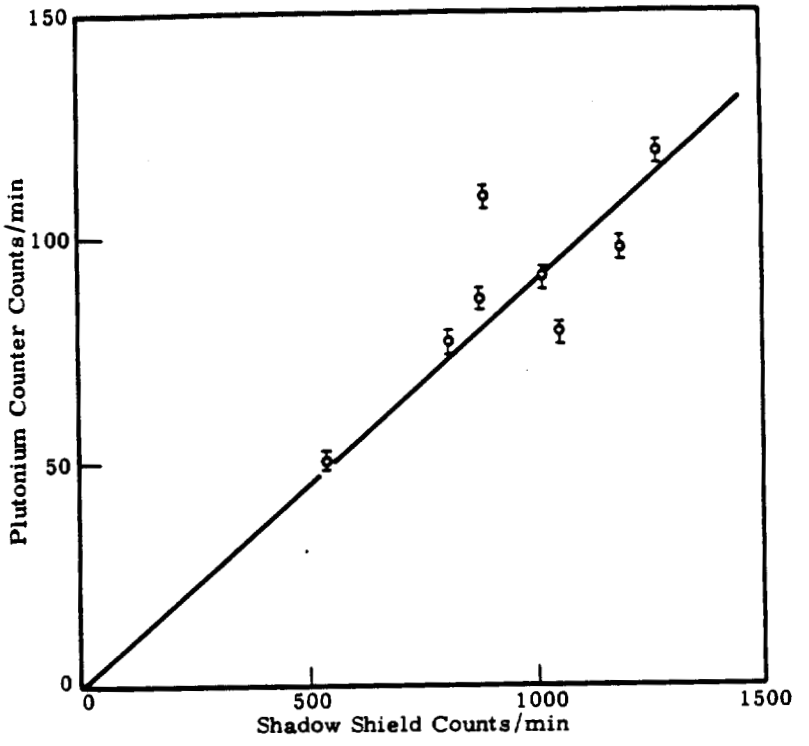

FIGURE 2.12

Count Rate of Unexposed People in the Plutonium Counter
(X-ray Channels 17 to 32)

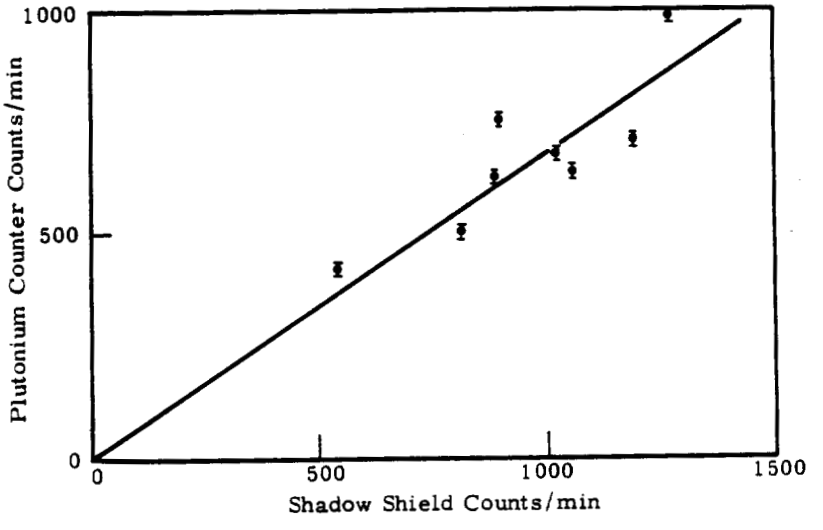

FIGURE 2.13

Count Rate of Unexposed People in the Plutonium Counter
(X-ray Channels 17 to 83)

0028327

Figures 2.12 and 2.13 suggest a linear correlation, but this must not be true for higher nonplutonium body burdens. An Eskimo who gave more than 20 times the Shadow Shield count of other subjects gave only one-third the count on the plutonium counter predicted by linear extrapolation of Figures 2.12 and 2.13.

Studies of this correlation are continuing. We have had difficulty in reproducing results and think it may be due to variable amounts of Cr^{51} in our subjects. Also we plan to limit the length of scan of the Shadow Shield to the part of the body included in the plutonium counter.

Many of the background counts from the plutonium counter are due to high energy photons that scatter only slightly in the NaI(Tl) scintillator so as to produce pulses mistaken for X-rays or 60 keV gamma rays. We placed a 6 in. thick plastic scintillator around one of the units of the plutonium counter to see if we could detect enough of these high energy rays to influence the background. Using the plastic counter in anticoincidence with the plutonium unit reduced the background rate to one-seventh for the empty counter but to only two-thirds when a person was present. The variation in background between people was about the same as that in Figures 2.12 and 2.13.

Figure 2.14 shows the pulse height spectra from the plutonium counter unit when one-half of the multichannel analyzer records pulses that are not coincident with ones in the plastic scintillator while the other half records pulses that are coincident. The coincident pulses must have been caused by high energy photons rather than by any from plutonium, otherwise they would not have been observable in the plastic. Counts of six people indicated that the ratios between the two spectra were the same within about 10% over at least the X-ray part of the spectrum. This indicates that the coincident spectrum might be a good predictor of the noncoincident spectrum when the latter is not observable because the man contains plutonium.

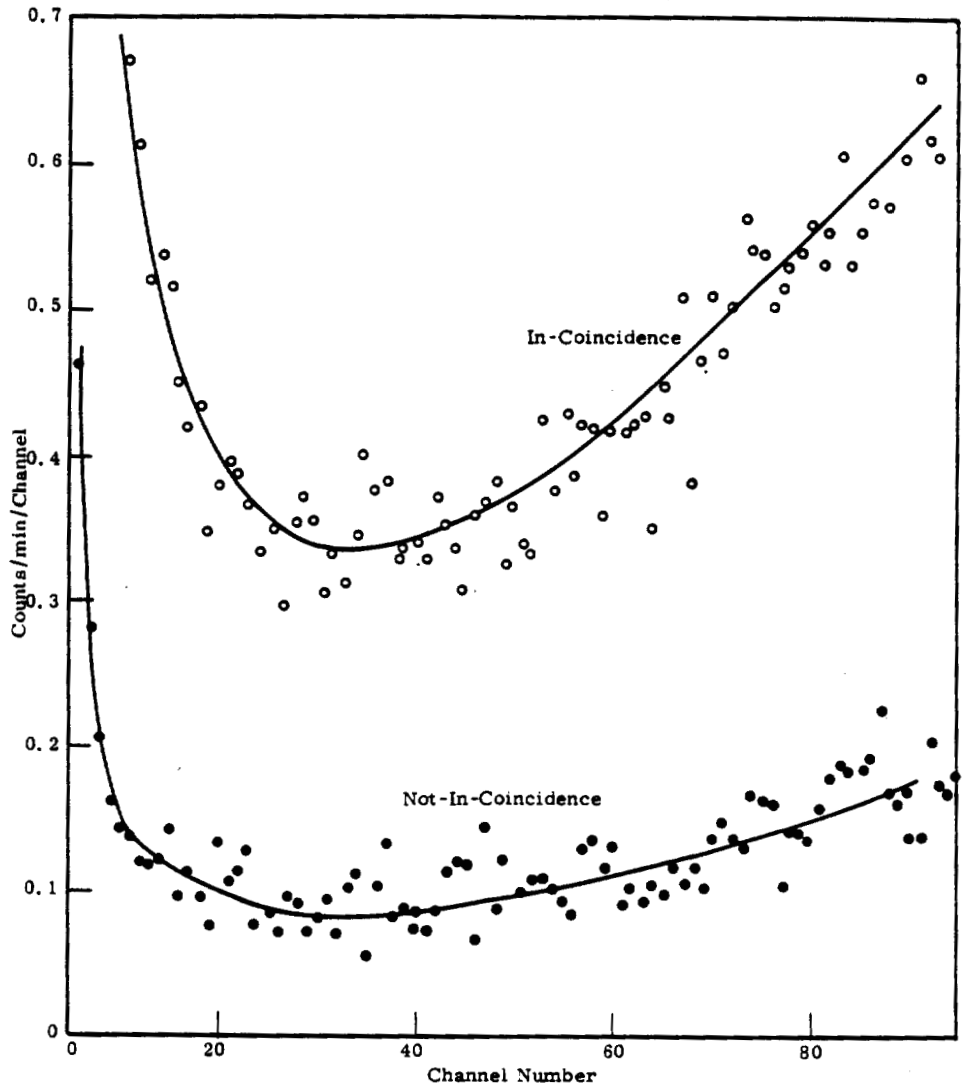

FIGURE 2.14

Simultaneous Plutonium Counter Spectra
In-Coincidence and Not-In-Coincidence with a Plastic Scintillator Shield
(Empty Counter; 300 min count; 0.8 keV/channel)

Counting Plutonium in Animals and in Excreta - K. L. Swinth and B. I. Griffin

The plutonium whole body scintillation counter was used to count dogs (containing 0.25 to 3.2 μCi of plutonium) and rat feces and urine specimens.

The following experiments were performed to learn more about the problems of counting plutonium *in vivo* and to determine the usefulness of X-ray counting of biological samples.

Dog Counting

The counting of dogs is especially interesting because it presents problems similar to those expected in counting humans. The dogs had been exposed to a plutonium aerosol consisting primarily of $Pu^{239}O_2$, but with small amounts of other plutonium isotopes. The dogs had been exposed about 4 yr previously, and three of them have since died from the effects of the plutonium. Figure 2.15 shows the pulse height spectrum from the plutonium whole body scintillation counter[2.18] of a dog estimated to contain 0.6 μCi and the spectrum from a dog containing no known plutonium. The first peak is due to the 17 keV X-ray from the plutonium isotopes. The second is due mostly to the 60 keV gamma ray from the decay of Am^{241}, a daughter of Pu^{241}.

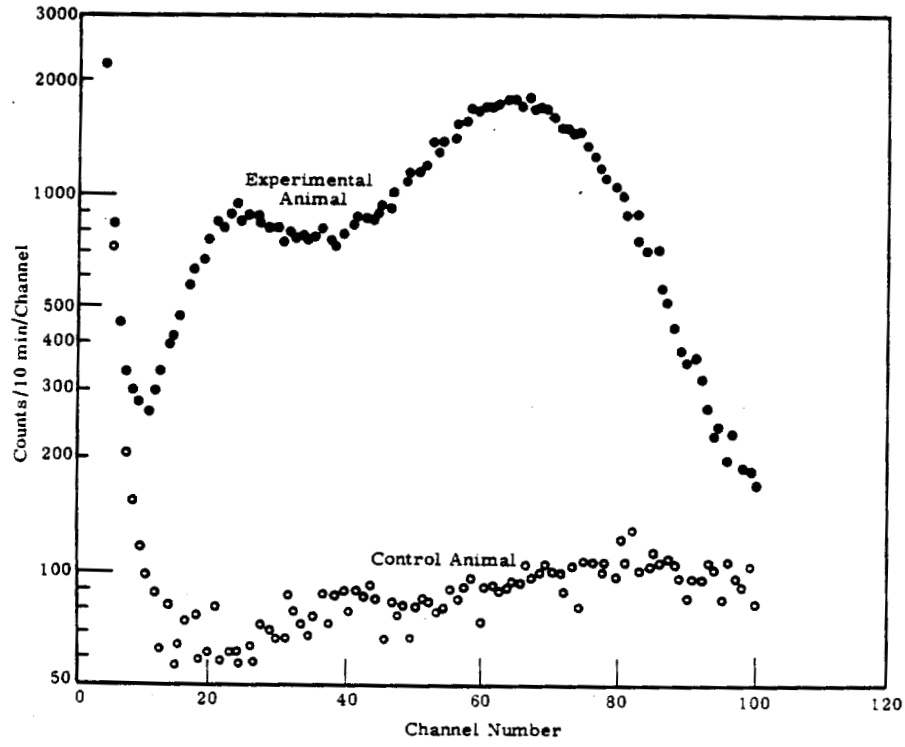

FIGURE 2.15

Pulse Height Spectra
from Experimental and Control Dogs

The first problem was to determine the optimum relative orientation of the dog and the counter units. We performed an experiment with a phantom of a dog for this purpose. The results are given in Table 2.7. Two sets of channels of the multichannel analyzer were used; the first covers only the X-ray peak while the second included both the X-ray and 60 keV peaks.

TABLE 2.7

EXPERIMENT WITH A DOG PHANTOM

Condition	Relative Counts	
	Channels 17 to 32	Channels 17 to 83
1.5 μCi Plutonium "evenly" distributed		
Phantom on Back	1.000	1.000
Phantom on Sternum	0.90	0.94
About 1 cm of tissue-equivalent material added	0.50	0.68
About 1 cm of fat-equivalent material added	0.64	0.63
Same sources centrally located	0.87	0.91
Same sources peripherally located	1.52	1.31

We finally decided to count the dog on its back with a counter unit below its back, another above its chest, and one on each side. The dog is usually anesthetized to make handling easier. On the back is not the easiest position to hold a dog, but it gives the maximum sensitivity. We found that the counting rate for the X-rays decreased by about 13% when a dog was turned to lie on its sternum. The results with the phantom, given in Table 2.7, show a 10% change when the phantom is turned over. Thus, it is not likely that the change was due to movement of internal organs. Some of the change may be due to unequal sensitivities of different counter units.

The phantom was made to have the same volume as a 10 kg dog, but its weight is 8.75 kg. In the back position it gave a count about one third that of a live dog containing the same amount of plutonium. We believe, however, that most of the difference results from different isotopic compositions of the plutonium in the dogs and that used in the phantoms.

The background counting rate of the empty counter is 55 ± 2.7 (standard deviation) and 212 ± 7.9 count/min in the two sets of channels of Table 2.7. The dogs change this rate by scattering and absorbing background radiation and by contributing radiation from radionuclides in their bodies. We used 20 dogs that had no known exposure to plutonium and that had been kept in similar facilities and on the same diet as exposed dogs to determine the background rate. The results were 116 ± 10.4 and 607 ± 52 count/min, respectively. The uncertainty in the background rate was not large enough to interfere significantly with the measurements reported below.

Due to the rapid attenuation of low energy photons even in tissue, one expects the count rate for a given amount of plutonium to vary with the size of the dog. To investigate how much variation there is, we counted 13 dogs, that had not been exposed to plutonium, with and without 0.24 μCi Pu^{239} inserted down to the bifurcation of the trachea. The counting rates in the X-ray channels showed a standard deviation of 31% of the average, but the range was 110%. Inclusion of the 60 keV channels reduced these to 19 and 69%. Using only the 60 keV channels was only slightly better than the latter. We have not found any parameter that correlates well enough with these variations to permit correction of measured counting rates. When the same source was placed in the dog phantom, the counting rate was the same as that of a live dog of the same weight, not of the weight the phantom was supposed to represent.

Three dogs have died since being counted in the whole body counter. Portions of these dogs were ashed and counted in an alpha ray counter. The body burden of plutonium was determined from these results; for this purpose it was assumed that only one isotope of plutonium was present. We used these data to calibrate the counter as shown in Table 2.8.

These results agree fairly well among themselves. However, the first two dogs were counted just a few days before they died while the last was counted 4 mo before death. The dogs lose weight rapidly just before death so the calibration factors for the last dog are probably better ones to use for the dogs still in reasonable health.

TABLE 2.8

CALIBRATION OF COUNTER BY POSTMORTEM SAMPLING

Body Burden Plutonium μCi	Whole Body Counter			
	Counts/min		Counts/min/nCi	
	Channels 17 to 32	Channels 17 to 83	Channels 17 to 32	Channels 17 to 83
1.4	2895	15,683	2.1	11.2
0.9	1863	12,521	2.1	14.0
1.2	2757	17,669	2.3	14.7

We have counted 30 dogs containing plutonium. Their body burdens ranged from 0.25 to 3.2 μCi. We made no correction for body size variation.

The experiences described above illustrate the difficulties that easily absorbed radiation cause in counting, background, calibration, body-size correction, simulation with phantoms, and (for plutonium) correcting for isotopic composition.

Rat Excreta

Urine and feces of rats exposed to Pu^{238} were counted in the plutonium whole body scintillation counter. Normally they are ashed and counted in an alpha-ray counter. It was simpler to count the 17 keV X-rays because no sample preparation other than drying was required. Counting sensitivity was enough that 3 min counts were adequate; large numbers of samples were counted quite easily.

The urine was absorbed on paper which was folded to 1 x 6 x 11 in. Feces (and liver) were contained in plastic bags 1/2 x 4 x 6 in. These were placed between two of the counting units, which are about 6 by 12 in. Pulses in the range 10 to 30 keV were counted. Five urine and seven fecal standards each of 59.5 nCi gave the calibration data in Table 2.9. Alpha-energy analysis showed that the plutonium was more than 99% Pu^{238}.

TABLE 2.9

CALIBRATION FOR EXCRETA COUNTING

Type	Average X-ray Counting Efficiency	Alpha Rays Per X-ray Counted
Feces	37%	26 ± 0.8
Urine	30%	32 ± 1.0

Low Energy Fast Neutron Spectroscopy - W. A. Glass

Development is nearly complete of a He^3 filled proportional counter neutron spectrometer for the energy range 0.1 to 1.0 MeV.

It is expected that the neutrons encountered where people work around reactors, plutonium separations facilities, fuel fabrication facilities, etc. contain an appreciable fraction with energies below about 1 MeV.[2.19] A study was begun last year to determine the feasibility of developing a neutron spectrometer to operate in the region of energies between 0.1 and 1.0 MeV to demonstrate the presence of these neutrons and to help assess their dose rate. The difficulties of measuring continuous neutron spectra at energies below 1 MeV are compounded by the nature of the radiation fields in which they are found. The typical field is characterized by:

- Being anisotropic to an unknown degree
- Containing a very high percentage of thermal neutrons, but also having neutrons with energies as high as 10 MeV
- Containing a large quantity of gamma radiation
- Having neutron fluxes corresponding to a few millirad per hour.

These conditions dictate the following criteria for a spectrometer.

- It must have essentially isotropic response.
- It must be adequately sensitive to neutrons in the 0.1 to 1.0 MeV range to collect data in a reasonable time from weak fields.
- Its response to gamma radiation must not interfere with the neutron response.

An appropriately designed proportional counter filled with He^3 as the active gas should be able to meet these requirements. Several papers

have described He^3 proportional counter neutron spectrometers.[2.20, 2.21] He^3 detectors use the $He^3(n,p)T$ reaction which has a positive Q of 760 keV. The smooth behavior of the cross section in the region between 0.1 and 10 MeV and the low positive Q make He^3 an ideal gas for spectrometers. Monoenergetic neutrons produce pulse height spectra that are constant from zero up to a height corresponding to the maximum energy He^3 nuclei can receive in an elastic collision with a neutron: 3/4 of the neutron's energy. The spectrum is then zero except for an isolated peak at a height corresponding to 760 keV plus the energy of the neutron. If a continuous energy spectrum contains no neutrons above about 1.1 MeV, the pulses due to recoils will be less than 760 keV and the pulse spectrum above 760 keV gives the energy spectrum directly. If neutrons above 1.1 MeV are present, some correction for the part of their recoil spectrum above 760 keV is needed. Detectors described in the literature either have been limited to measurement of nearly monoenergetic neutrons or have required collimated neutrons and a computer program to unfold the recoil response.

Figure 2.16 shows the detector developed to operate in the intermediate neutron energy range. The sensitive volume is defined by 18 peripheral counters and two end counters. These counters operate in anticoincidence with the main counter and define a 2 by 2 in. cylindrical volume from which signals are accepted for pulse height analysis. Only if the entire track of an event is contained within the sensitive volume will its signal be accepted. A short cylindrical volume was chosen to make the counter as isotropic as possible and yet maintain a cylindrical electrical field for the proportional counting action. The detector was filled with 14.5 psia He^3, 29 psia Kr, and 1 psia CO_2. Figure 2.17 shows typical pulse spectra for monoenergetic neutrons. The spectra show peaks at 760 keV due to thermal or very low energy neutrons. The full width at half maximum of this peak is 40 keV or 5.3%. The somewhat poorer resolution of the other peaks is due to spread in neutron energy caused by target thickness, Van de Graff beam energy spread, and the finite solid angle subtended by the detector (about 20 cm from the target) with consequent spread

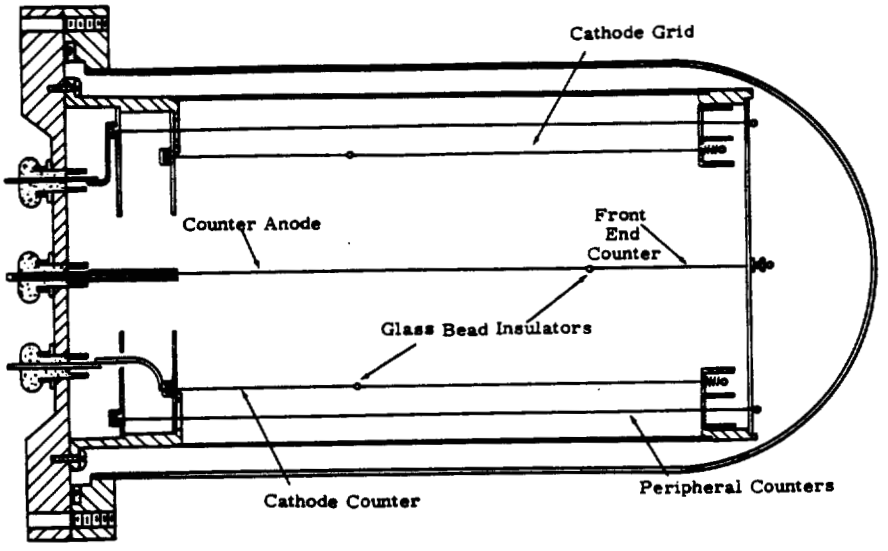

FIGURE 2.16

He^3 Neutron Spectrometer

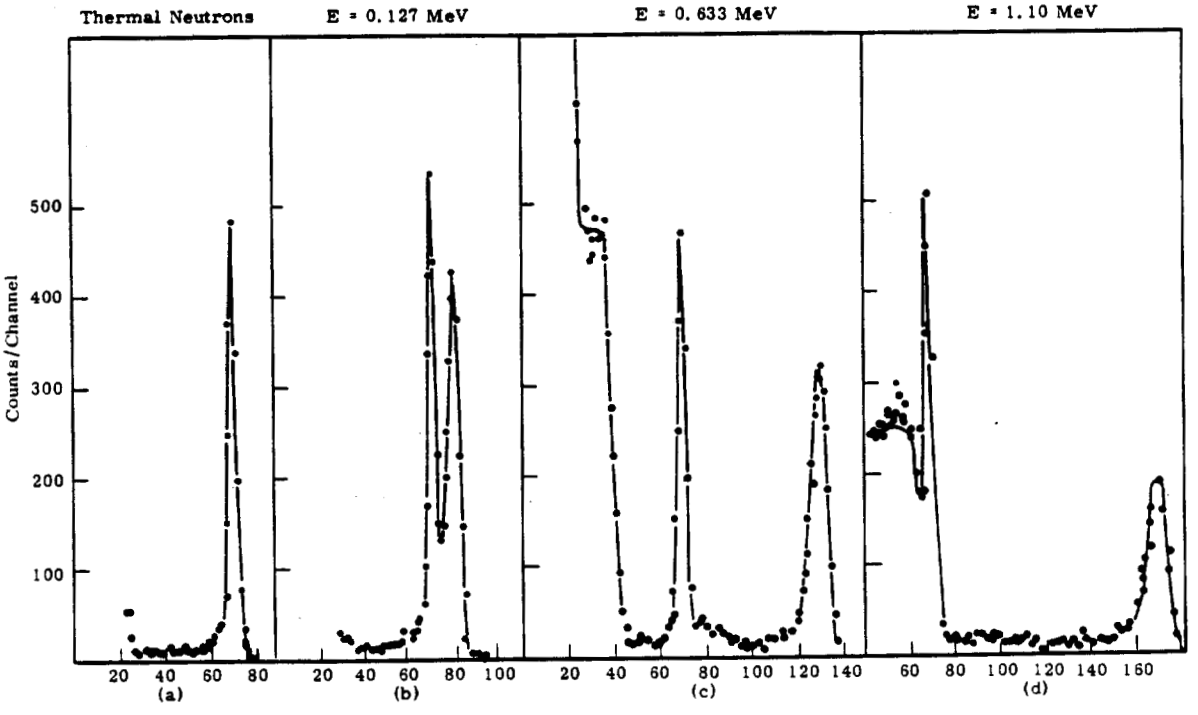

FIGURE 2.17

Typical Pulse Height Spectra for Monoenergetic Neutrons

002833b

in neutron energy. Figures 2.17 c and 2.17 d show the He^3 recoil edge at an energy equal to three-fourths the neutron energy. The effect of these recoil events on the measurement of a continuous spectrum that contains neutrons with energies above 1.1 MeV is obvious.

The volume in which an event can originate and still have no part of its track extending into the anticoincidence counters decreases with increasing energy. Figure 2.18 shows the results of an experiment to determine this geometrical efficiency as a function of neutron energy. The linearity of the efficiency of the counter as a function of energy is a result of the approximate linear relation between track length and reaction energy.[2.21] These data indicate that the spectrometer has a very easily corrected response to neutrons in the energy range of interest and will have zero sensitivity to high energy neutrons, except for their recoils.

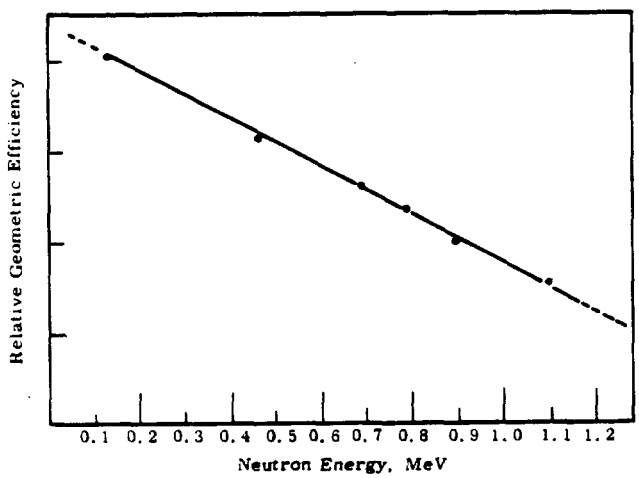

FIGURE 2.18
Geometric Efficiency of the He^3 Detector

The response of the detector to He^3 recoils produced by neutrons with energies in excess of about 1.1 MeV must be subtracted from the response due to the $He^3(n,p)T$ reaction for lower energy neutrons. As indicated earlier, other experimenters have unfolded the recoil response by computer codes. These methods require knowledge of the incident neutron direction. We have no such knowledge, so another method is being tried. This is a substitution method wherein He^4, which has a similar elastic scattering cross section, is substituted for He^3. The gas pressures are adjusted so that the track length distribution produced is the same for

both types of helium recoils. This adjustment of the track length distribution assures that the effective volume is the same for both He^3 and He^4 recoils. Preliminary results with neutrons having energies of 2.1, 2.6, and 3.5 MeV indicate that this method will produce adequate data for the subtraction of the recoil response of the detector.

A check of the sensitivity of the detector for different angles of incidence of the neutrons was made by turning the counter through an angle of 90°. The results are shown in Figure 2.19. They indicate that any anisotropy of the detector is negligible, at least for neutrons near 0.5 MeV.

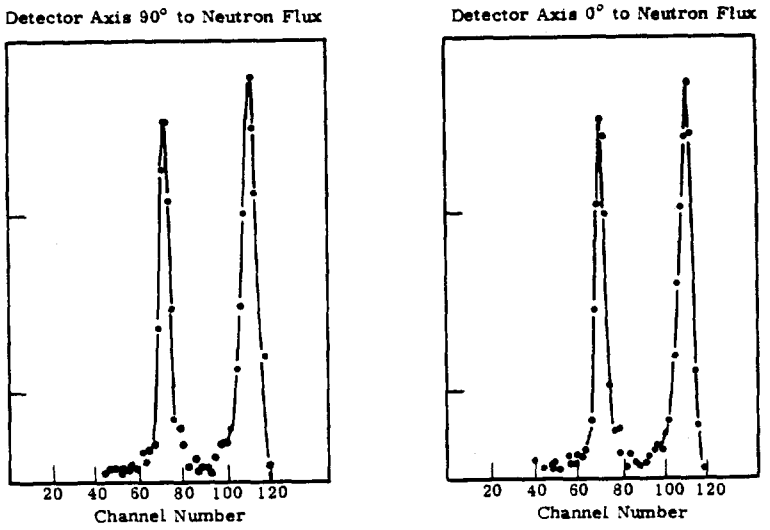

FIGURE 2.19

Anisotropy of He^3 Detector (E = 0.466 MeV)

The Secular Change of Pu-Be Neutron Sources - L. L. Nichols

The change in neutron yield of three Pu-Be sources with time was determined by comparison with the yield of a Pu^{238}-Be source of known isotopic composition.

The plutonium in most Pu-Be neutron sources is mostly Pu^{239}, but there are enough other isotopes to result in the neutron yield changing appreciably with time. Most of the change is due to 13.2 yr Pu^{241}. It is a beta emitter so it does not produce neutrons. However, it yields 458 yr Am^{241}, an alpha emitter that does. Increasing amounts of Am^{241} result

0028338

in increasing neutron outputs for Pu-Be sources. Since we and others use Pu-Be sources for reference sources in many experiments, it is essential to know how the output changes.

The output changes with time in several of our neutron sources were studied by comparing the count rates of a BF_3 tube for the sources and for a Pu^{238}-Be source of known isotopic composition. The plutonium in the Pu^{238}-Be source was principally Pu^{238}. The change in neutron emission rate of the Pu^{238}-Be source was calculated from the isotopic composition and from known half-lives and neutron-per-alpha yields. It is decreasing 0.78%/yr. The BF_3 tube was embedded in paraffin. The sources were placed, one at a time, in a hole in the paraffin. The gain of the counting system was adjusted as described earlier.[2.22] Since, however, ratios of counting rates are used below, errors in gain setting should have little effect on the results.

Table 2.10 gives the ratios of the counting rates for the three sources studied to the counting rate of the Pu^{238}-Be source corrected for decay. The ratios are decreasing about 1.8%/yr. We had expected them to increase by roughly this amount.[2.23] We do not know why they are decreasing and are continuing our observations.

TABLE 2.10

VARIATION IN OUTPUT OF Pu-Be SOURCES

	Ratios		
Date	Source 246	Source 710	Source 596
4-6-64	1.8754	2.3512	2.2460
5-7-64	1.8860	2.3577	2.2532
5-25-64	1.8858	2.3650	2.2570
7-7-64	1.8805	2.3605	2.2536
7-27-64	1.8828	2.3572	2.2499
8-17-64	1.8861	2.3611	2.2550
9-30-64	1.8785	2.3561	2.2516
10-29-64	1.8751	2.3500	2.2454
11-17-64	1.8703	2.3408	2.2311
11-19-64	1.8676	2.3408	2.2339
1-4-65	1.8686	2.3408	2.2373
Standard deviation due to statistics of counting	±0.0027	±0.0033	±0.0032

0028339

Fast Neutron Medical Research Facility - K. L. Swinth

The University of Washington facility was set up and the shield leakage and the dose distribution measured. Paraffin in the shield is being replaced by water to reduce fire hazard.

The medical facility described last year[2.24] was set up. The lithium stearate did not arrive in time to be incorporated in the shield. Figure 2.20 shows the results of a survey with a double-moderator neutron dosemeter[2.25] around the shield. The numbers are mrem/hr of fast neutrons when a small BF_3 tube inside the shield to monitor the generator output was giving 2000 count/min. The results indicate satisfactory shielding because:

- The facility will be in a concrete room which will give additional shielding.
- The lithium stearate will further reduce the rates.
- Operation will be infrequent.
- A monitor count rate of 2000 was obtained only with a new target.

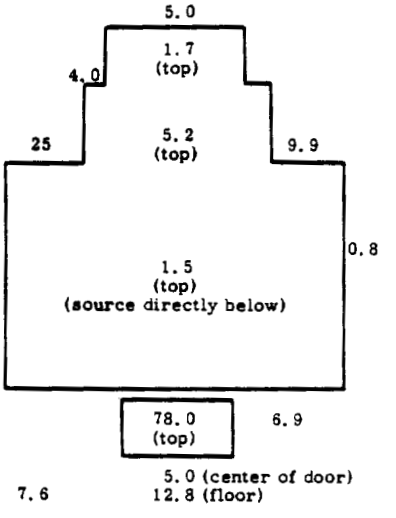

FIGURE 2.20

Fast Neutron Dose Equivalent Rates
Around the Fast Neutron Medical Research Facility
(Numbers are mrem/hr)

Surveys with a bare BF_3 tube for thermal neutrons gave dose rates of less than 1 mrem/hr except near the door where there were some small cracks. Here values as high as 5 to 10 mrem/hr were measured. The addition of lithium stearate should reduce the thermal neutron fluxes.

The double moderator indicated average neutron energies of 1 to 1.6 MeV around the shield. The lowest averages were near parts of the shield that were mostly concrete.

The equipment was moved to the University of Washington laboratory. It was decided that the paraffin shield presented too great a fire hazard to be permitted in a hospital so we are replacing it with water tanks.

The volume to be irradiated is contained in a 5 by 7 by 10 cm plastic cup. Dose distributions were measured in the cup with thermoluminescent dosimeters and copper foils and compared with earlier calculations. The scattering of the neutrons and the production of gamma rays in the shield material led to departures from the calculated values. There was a ±17% variation in neutron dose rate when the front of the cup was 2 cm from the target; calculation gave ±25%. The average gamma ray dose rate was 7.8% of the neutron dose rate. The average dose rate was 2.3 rad/min. There was a ±20% variation when the cup was 10 cm from the target. This is in agreement with calculation. In this case it is possible to reduce the variation by irradiating first from one direction then the other.

Instrumentation for Local Dose Measurement - W. A. Glass, L. L. Nichols, and D. N. Samsky

> A circuit was designed and built which converts the Nuclear Data Pulse Height Analyzer to a device that will perform a summation of the amplitudes of pulses arriving over a preset period of time. The time interval over which the summation takes place can be varied from approximately 100 μsec to 10^5 sec.

Rossi, Biavati, and Gross[2.26] have developed techniques to measure the local deposition of energy in small tissue equivalent spheres exposed to ionizing radiation. The measurement required the summation of the signals from a spherical proportional counter exposed to a constant and

known flux density of radiation for a time interval corresponding to the desired dose. This sum is then stored as a single data point. Repetition of this process over the same time interval and in the same radiation field yields the desired distribution of energies delivered to as many sites as time intervals used. This paper describes the circuit modifications necessary to convert a Nuclear Data Series 130 A Pulse Height Analyzer into a device that performs the summation and storage of signals described above.

A simplified discussion of the analyzer logic will suffice to permit description of the modifications made. Its analog to digital converter (ADC) gates a 2 Mc oscillator into a channel scaler for a time proportional to the pulse height. After the channel scaler has scaled to the appropriate channel an "initiate storage" cycle is triggered which adds one count to the selected memory position and resets the channel scaler to zero; the analyzer is again ready to accept the next pulse. As it is desired to sum the incoming pulse heights for a preset time (some given exposure) before storage in the memory, it is necessary to alter the analyzer's normal logic in two ways.

- The channel scaler must not be reset to zero after each incoming signal, but must remain "open" and retain the total number of ADC pulses until the preset time has elapsed.
- The cycle which adds one count to the appropriate memory channel must be blocked until the last signal of the time interval has arrived.

Alteration of the analyzer logic was accomplished by the circuitry in Figure 2.21. The time flip-flop provides a -4 V level at T and a +8 V level at $\overline{T}$ during the "on cycle"; this blocks the RCSO gate (reset channel scaler to zero gate) and alters the "add one" circuit so that no count will be stored in the memory. After the timing circuit (the oscillator, the schmitt trigger, and the RIDL preset scaler) has indicated that the preset time interval has elapsed, the input trigger is fired. This trigger produces a pulse that initiates a storage cycle (IS pulse) in the analyzer. At the same time it reverses the time flip-flop so that there is a +8 V level at T, thus unblocking the RCSO gate and also allowing a count to be added to the

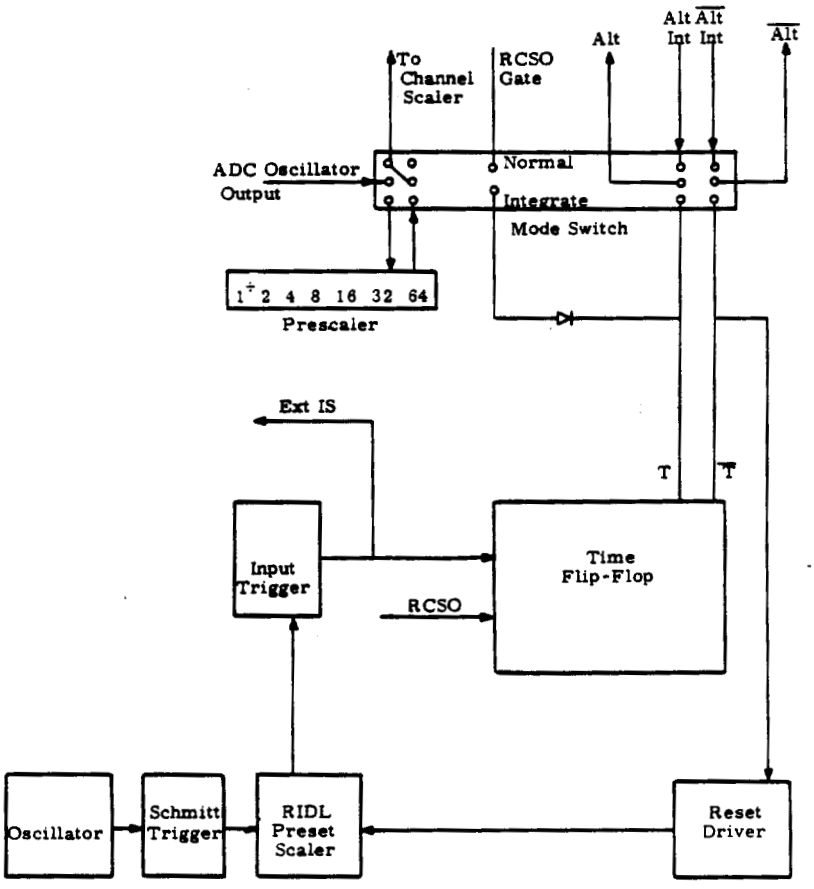

FIGURE 2.21
Local Dose System

memory in the channel at which the channel scaler has stopped. The -4 V level appearing a $\overline{T}$ resets the RIDL scaler and holds it in a "no count" state until the analyzer storage cycle has finished and produced a pulse that resets the channel scaler to zero and switches the time flip-flop back to its "on cycle." The time interval of the "on cycle" can be varied from 10^{-4} to 10^{5} sec in units of 10 μsec. Since the summation of more than a few input signals would normally overflow the 512 channel capacity of the memory, a prescaler was inserted between the ADC oscillator and the address scaler. The prescaler, in effect, expands the range of the memory by factors of 1, 2, 4, 8, 16, 32, and 64 depending on the position of a selector switch. The circuit modifications are contained in a single RIDL designer series module

and are connected to the analyzer through a 5 pole switch. When the switch is in the "normal" position the analyzer logic is unaltered; with the switch in the "integrate" position the analyzer logic is altered as described above. This convenience frees the analyzer for general laboratory use when not in use for local dose measurements.

If the signals to be summed and stored are randomly spaced in time (as events in a proportional counter) and have a pulse height distribution $\varphi(E)$, then the distribution $\Phi(E)$ resulting from the summation of the pulse heights in many equal time intervals becomes

$$\Phi(E) = \sum_{n=1}^{\infty} \frac{m^n e^{-m}}{n!} \varphi_n(E) \tag{1}$$

where m is the average number of pulses arriving during the summation time and

$$\varphi_n(E) = \int_0^E \varphi(X)\, \varphi_{n-1}(E - X)\, dx. \tag{2}$$

To test the operation of the modified analyzer, a source of signals was obtained by using a very narrow range of pulse heights centered on the Cs^{137} peak in a NaI crystal. This constitutes a source of signals that can be represented approximately by a delta function. With $\varphi(E) = \delta(E - E_o)$ the integral of Equation (2) is easily evaluated and

$$\Phi(E) = \sum_{n=1}^{\infty} \frac{m^n e^{-m}}{n!} \varphi(E - nE_o) \ . \tag{3}$$

With m small (i.e. the average number of pulses arriving during the summation time being small) we would expect $\Phi(E)$ to be enclosed in an evelope representing a Poisson distribution. As m becomes large we expect the discrete points of $\Phi(E)$ to be enclosed in a Gaussian envelope as demonstrated by approximating n! by the first term of Stirling's expansion which gives

$$\Phi(E) = \sum_{n=1}^{\infty} \frac{1}{\sqrt{2\pi m}} e^{-\frac{(n-m)^2}{2m}} \delta(E - nE_o) \quad . \tag{4}$$

For large m the probability function is nearly zero except for n = m and represents a normal distribution about $E = mE_o$ with a percent standard deviation that decreases as the inverse square root of m. Figures 2.22b through 2.22e present the results of summing the near delta function source spectrum (Figure 2.22a) for various time intervals. The expected transition from a Poisson envelope to a Gaussian envelope with its center at mE_o is evident as m becomes large.

A Helium Ion Separator for the Positive Ion Accelerator

L. W. Seagondollar* and L. L. Nichols

A helium ion separator was built and used in the high voltage terminal of the Hanford 2 MV positive ion accelerator. The ions are separated according to their charge-to-mass ratio. Focussed beams of H^+, He^+, and He^{++} were obtained.

The ratio of He^{++} to He^+ ions emerging from a standard rf ion source is of the order of a few tenths of a percent.[2.27, 2.28] Acceleration of several hundred microamperes of total beam would be required, therefore, to get a useable quantity of He^{++} ions for experimental work. Present limitations on the Hanford 2 MV Van de Graaff allow only 50 μA of beam without appreciable accelerator tube loading. An ion separator was designed and built that allows acceleration of the He^{++} ions without any appreciable He^+ beam.

The separator is located in the high voltage terminal of the Van de Graaff between the ion source and the entrance to the accelerator tube. The ion separation is accomplished by passing the beam through crossed electric and magnetic fields mutually perpendicular to the axis of the entering beam. Two Alnico V horseshoe magnets create the fixed

---

* University of Kansas, Summer Professor at Battelle-Northwest.

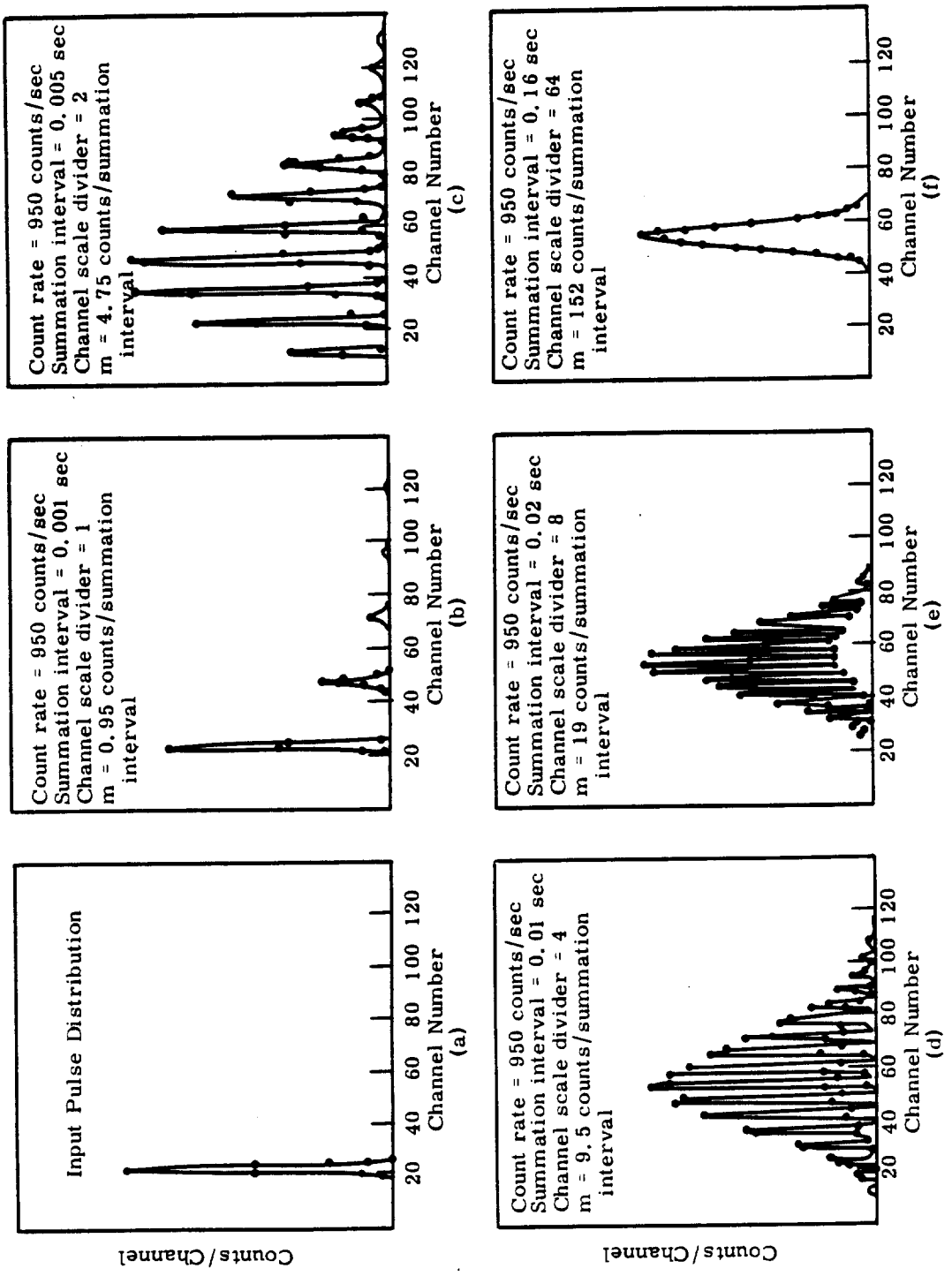

FIGURE 2.22

Tests of the Local Dose System

0028346

magnetic field. The electric field is created by 5-in. long, parallel plates. The electric field can be varied over a 10 kV range from the accelerator control console. For an ion of given charge-to-mass ratio, the electric field deflection is adjusted to compensate the magnetic field deflection so that the ion enters the accelerator tube through a small aperture in the end of the separator housing. All other ions are deflected onto a beam stop.

The Hanford 2 MV generator is a short column (33 in.) horizontal accelerator. Because of this, the design of the separator was influenced by weight, size, and power limitations in the high voltage terminal. The total weight and length of the ion separator are $38\frac{1}{4}$ lb and $12\frac{3}{4}$ in. A 1 ft tank and a 1 ft terminal extension were required to accommodate the ion separator in the terminal. Figure 2.23 shows a cross-section view of the ion separator. The dc power supplies for operation of the ion source probe and focus and the electric field of the separator were modified to increase their current and voltage outputs.

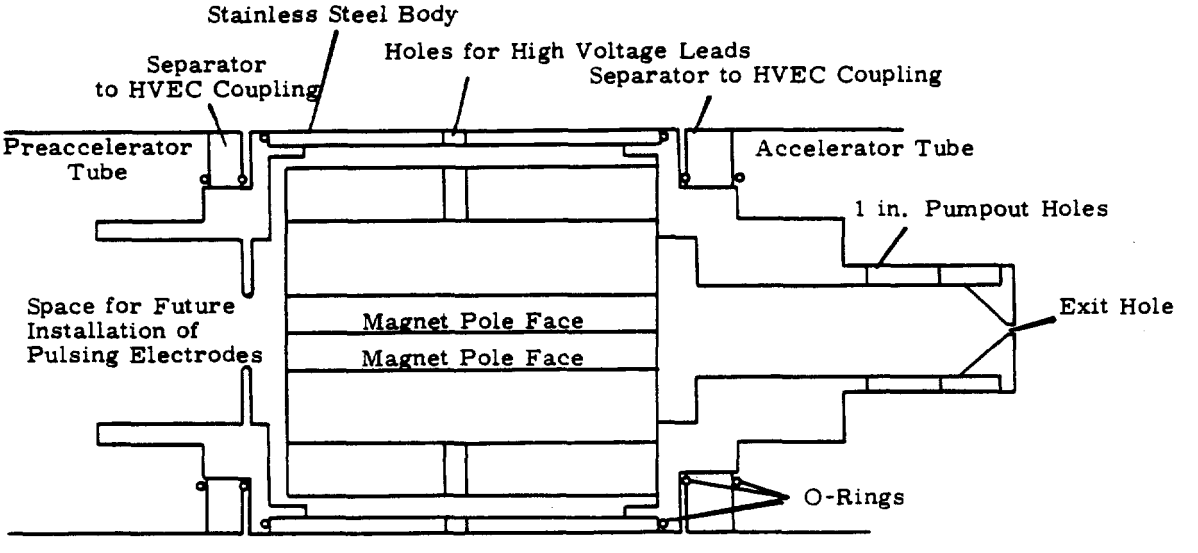

FIGURE 2.23

Cross Section of Separator Case with B-Field Magnets in Place (E-Field Assembly is not Shown)

0028347

The performance of the ion separator was checked by using the main analyzing magnet and a solid state charged particle detector located near the target. Tests indicated that the separator performed satisfactorily. A focussed, 0.5 μA beam of ions (e/m = 1/2) was obtained at the target.

The charge-to-mass ratios for He^{++} and HH^{+} ions are essentially the same. Consequently, a considerable amount of the HH^{+} ions contaminates the He^{++} beam. The presence and identity of the HH^{+} beam was easily verified by scattering the ions into the solid state monitor with a thin nickel foil. Present development work is directed toward eliminating or allowing for the hydrogen beam.

Pulse Reader for Ion Chambers - L. A. Braby

An ion chamber reader was developed that can read pocket pencils to ± 0.02 mR for small exposures.

When using condenser ion chambers, one would like to measure directly the difference in potential across the chamber before and after exposure. This can be done by observing the voltage pulse over a resistor in series with the charging voltage supply.[2.29]

The present device charges pencil ion chambers (about 4 pF) through a 1 MΩ resistor. An emitter-follower with input capacitance of about 4 pF is in parallel with this resistor. Its output is measured by a pulse-height voltmeter. In this device, the pulse charges a capacitor which is made to discharge at a constant rate. The resulting ramp voltage turns a 100 kc oscillator on and off, and the number of cycles counted by a sealer gives the ramp length. There are three such circuits connected by 10X amplifiers. The largest on-scale voltage is presented to be read. Accuracy is 2% from 10 mV to 10 V.

The switch that connects the ion chamber to the charging voltage must have a high leakage resistance and a low contact potential and generate little voltage due to mechanical impact of the switch elements. Contact bounce and other effects that occur after the chamber is charged are not important. Dry reed switches proved the best from among many tried.

Applying the magnetic field that closes the switch slowly (about 1 sec) minimizes mechanical impact effects.

The jig into which the chamber is inserted must be made of the same material as the chamber to minimize contact potentials. It must make good contact without applying enough force to the chamber center electrode to strain the insulators and cause spurious voltages. Finally, the electrical field where the chamber makes contact should be the same with the chamber in or out. Otherwise, the change in field would require charge to flow out (or off) the contact when the chamber was removed from charging, and this would produce a false reading when the chamber is reinserted.

Neither the switch nor the jig of the present device is ideal, but the error that each contributes is reasonably constant and can be corrected for. If a 4 pF pencil is left in the jig and the charging voltage changed, the change can be measured to the nearest millivolt. However, if the chamber is removed and then returned to the jig, errors of about 3 mV result. This corresponds to a dose of about 0.02 mR.

Fast-Pulse Averaging - W. C. Roesch

Averaging of repetitions of pulses as short as a few nanoseconds can be done with a sampling oscilloscope together with a digital storage oscilloscope. The intervals between repetitions need not be constant.

A common method of obtaining the true shape of a signal that is obscured by noise is to average many repetitions of the signal. Since the noise is random, its relative contribution to the average decreases as the number of repetitions increases. Averaging is also useful in studying signals that are inherently variable. Steingraber and Berlman developed equipment that can average signals that last only a few nanoseconds.[2.30] The purpose of this note is to describe a different system for averaging fast pulses. The components for this system are unaltered, commercial equipment.

In this system (as in Steingraber and Berlman's) a sampling oscilloscope (SO) takes samples of successive fast pulses. The output of the SO

at the terminals used to drive chart recorders is a signal that is a series of steps. The height of each step is proportional to the size of the sample it represents. The interval between steps equals the interval between the fast pulses that are sampled. Each step represents a different phase of the fast pulse. If the phase changes uniformly with time throughout the series of steps during a sweep of the SO, then the series of steps is a facsimile of an (unaveraged) fast pulse. The duration of the facsimile is much greater than that of the fast pulse. The facsimiles are measured with a digital storage oscilloscope (DSO). The DSO measures and averages repetitions of these facsimiles and thus effectively averages the fast signal.

If the time interval between fast pulses is constant, the interval may be used to establish the regular change of phase with time. This is done by using the horizontal sweep mode of the SO that advances the phase by a fixed increment for each pulse. The length of the facsimile equals the time between pulses times the number of samples per sweep of the SO. This length will probably not equal the length of the DSO sweep. The DSO is triggered by the return of the SO horizontal sweep. If the duration of the facsimile is greater than that of the DSO sweep, then the DSO will trigger on every SO sweep; if not, it will trigger on every other (or every third, or fourth, etc.) sweep and much time may be wasted. Regularly spaced fast pulses are usually generated in some way that provides a convenient triggering signal for the SO. For example, in studying fluorescence, the device exciting the fluorescence will usually provide a large, regular signal suitable for this trigger.

If the time intervals between repetitions of the fast pulses are not constant (or if they are), the regular change in phase with time can be established by driving the horizontal sweep of the SO with the (amplified) horizontal sweep of the DSO. The duration of the facsimile is then exactly equal to that of the DSO sweep, which is nice because none of the signal is missed. The horizontal sweep of the DSO is triggered internally.

This last method of pulse averaging can be applied, for example, to the randomly-spaced pulses from a scintillation counter. Figure 2.24 shows an average made this way of the pulses in a NaI(Tl) counter due to Co^{60} gamma rays. The SO was triggered by the pulses themselves. To obtain this trigger at as nearly the same place as possible early in each pulse, the pulses were amplified about 100 times and the trigger set at a low level on this amplified pulse. The samples were taken from unamplified pulses. The unamplified pulses had to be delayed about 100 nsec by passing them through a long coaxial cable to give the trigger time to take place.

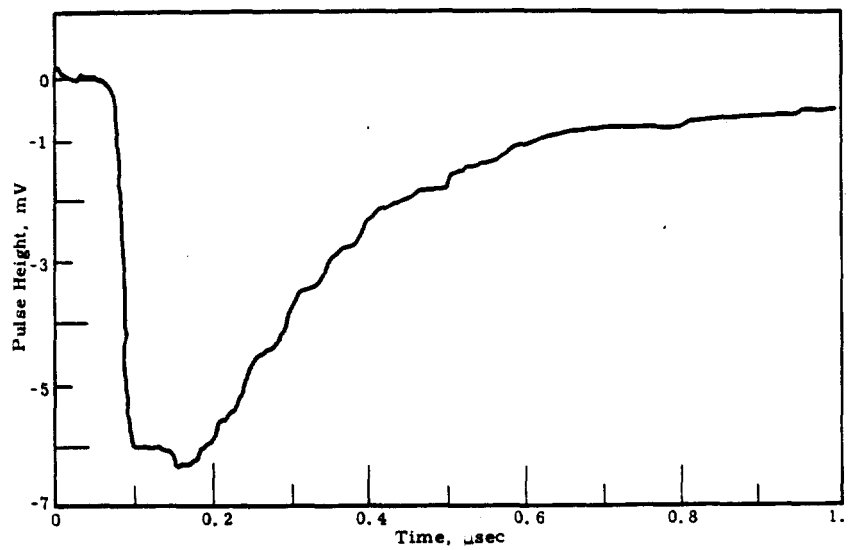

FIGURE 2.24

Average of the Pulses from a NaI Scintillation Counter due to Co^{60} Gamma Rays

An Alpha- and Beta-Ray Calorimeter - D. M. Fleming

A sensitive calorimeter suitable for measuring the energy output of small alpha- and beta-ray sources was designed and assembled. Preliminary tests indicate a sensitivity of about 5×10^{-7} W.

Previous work in calorimetry at this laboratory has been with a total-absorption gamma-ray calorimeter.[2.31] We wanted to apply calorimetry to dosimetry, but we felt that construction of a calorimeter of

small mass for alpha- and beta-ray measurements first would permit working out of details of jacket temperature control, temperature measurement, etc. A twin calorimeter was chosen to take advantage of the high sensitivity available in a thermopile and to permit constant calibration of the system while a measurement is in progress.

A top view of the calorimeter with the lids removed is shown in Figure 2.25. Each cell in the calorimeter consists of a graphite sample holder inserted in a lucite sleeve. The lucite sleeve is used to thermally connect the ends of the thermopile to the cells. The cells and thermopile are cast in styrofoam. Surrounding the styrofoam is a 1/8 in. thick copper heat baffle followed by more styrofoam and an isothermal jacket. The jacket is made of 0.030 in. copper, and its entire outside surface is covered uniformly with a layer of insulated manganin wire. The jacket is surrounded by a layer of styrofoam.

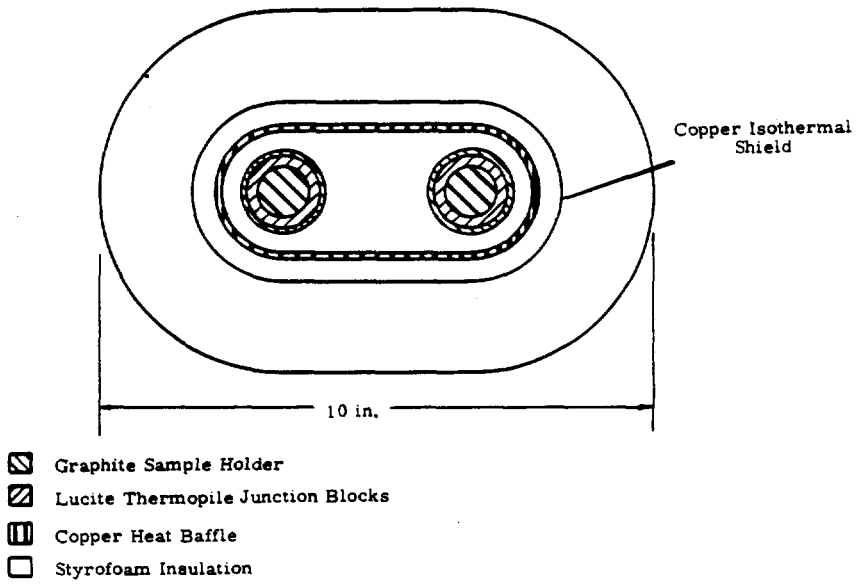

FIGURE 2.25

Top View of Calorimeter with Lids Removed

The thermopile connecting the two cells has 32 junctions of iron-constantan wire. This number was chosen to give optimum sensitivity when the thermal conductivity and electrical resistivity of the wires, the thermal

conductivity of the styrofoam insulation, and the input impedance of the galvanometer were considered. Sensitivity is about 5×10^{-7} C.

The manganin wire on the outer surface of the isothermal jacket is used as a heater to maintain the temperature of the jacket.

Two thermistors are mounted inside the jacket to provide a temperature reference. The thermistors are in one leg of a wheatstone bridge. The output of the bridge is amplified and operates a controller that supplies the proper current to the heating coil. Jacket control with this system is about $\pm 2 \times 10^{-5}$ C.

When the system was assembled the temperature difference between the cells fluctuated several thousandths of a degree. This fluctuation was eliminated by installing the copper heat baffle shown in the drawing.

To operate the calorimeter, the sample is placed in one cell and a calibrating coil in the other. The power in the calibrating coil is then adjusted until the output of the thermopile remains zero, indicating that the two cells are at the same temperature.

Calorimetric Determination of the Mean Beta Energy and Half-Life of Pm^{147}* -

E. J. Wheelwright,** D. M. Fleming, and F. P. Roberts**

The mean beta energy of the Pm^{147} decay has been calorimetrically measured at periodic intervals for 1 yr. Two independently prepared 1000 Ci sources of highly purified Pm_2O_3 were examined. The results obtained are selfconsistent and are in excellent agreement with measurements made on the same sources by an independent scientist using a second calorimeter. Values of 0.3330 ± 0.0005 W/g Pm^{147} and 2.620 ± 0.005 yr for the beta decay energy and the half-life, respectively, are believed to be the most reliable values yet published.

---

* Accepted for publication by Journal of Physical Chemistry.

** Chemistry Department

A Pulsed X-Ray Machine - D. M. Fleming and N. E. Mutka

Field Emission Corporation developed a 600 kV, 1200 J, pulsed X-ray machine for the AEC Division of Biology and Medicine. The machine was delivered to Hanford in 1964 to be tested and introduced into the Biology and Medicine program. We installed the machine in our laboratory and provided it with an ac-to-ac motor-generator set to provide isolation from other electrical equipment. We operated the machine successfully several times and began calibrating it with an erioglaucine dosimeter. A transient noise began to appear during the early part of the pulse on the oscilloscopes monitoring the machine current and voltage. We eliminated it by cleaning the high voltage connections. Before we could finish the calibration, a relatively low resistance ($3 \times 10^6\ \Omega$) path developed to ground and prevented further operation. The damaged component is being repaired.

Stopping Power Ratios for Radiation Nonequilibrium - K. G. Pailthorp*

Stopping power ratios measured or calculated for radiation equilibrium spectra should be accurate enough for use in an experiment being planned where nonequilibrium will exist.

The usual derivation of the Bragg-Gray principle assumes that electronic equilibrium exists at the cavity.[2.32] If the primary charged particles are generated at the rate of one per unit mass per unit time in the wall and are monoenergetic, and if one assumes that the degradation in energy of the particles is a continuous process, the spectral distribution of the flux density is given by the reciprocal of the mass stopping power of the wall material, $1/S_m(T)$.[2.33] I am planning to measure the dose distribution near the plane interface between two half-spaces of different material, one of which contains a beta or gamma emitter. Electronic equilibrium will not exist in this region. Hence, the spectrum of the flux density will not equal the inverse of the stopping power.[2.34] I have represented the spectrum by $f(T)/S_m(T)$ to see what effect the spectrum has on the stopping power ratio used in the Bragg-Gray principle.

---

* Oregon State University graduate student, Richland Fellowship program.

I investigated three such weighting functions:

$$f(T) = 1$$

$$f(T) = T_o - T$$

$$f(T) = 1 - \mathrm{erf}\,(x/\sqrt{4t_o})$$

The first is the spectrum for the case of radiation equilibrium. The third is the spectrum given by the age diffusion theory[2.35] at depth x in the nonemitting medium. The second is a radical weighted spectrum examined to demonstrate the range of variation of the resulting stopping power ratio. The general expression for the stopping power ratio in the Bragg-Gray principle is

$$\frac{E}{D} = \frac{\int_o^{T_o} \left[f(T)/S_m(T)\right] S_c(T)dT}{\int_o^{T_o} f(T)\, dT}$$

where

E = energy deposited per unit mass in the cavity

D = dose rate in the wall material

$f(T)/S_m(T)$ = spectral distribution of the flux density of charged particles in the wall material

$S_c(T)$ = mass stopping power of the cavity gas

$S_m(T)$ = mass stopping power of the wall material

T_o = maximum energy of the electron spectrum.

I employed the stopping power values from NBS Circular 577[2.36] in carrying out the numerical evaluation of the right side of the above equation. I examined two cases: an air-filled cavity in walls of aluminum and an air-filled cavity in walls of lead for 0.5 MeV primary electrons. The results are given in Table 2.11.

TABLE 2.11

BRAGG-GRAY STOPPING POWER RATIOS

Cavity-Wall	f(T) = 1	$T_o - T$	$1 - \mathrm{erf}\,(x/\sqrt{4t_o})$*
Air-Aluminum	1.11	1.11	1.11
Air-Lead	1.77	1.89	1.82

* At 0.4 cm

For the aluminum walls, the difference in the ratio E/D for the different spectra was less than could be shown by the accuracy of the numerical evaluation. For the lead-wall chamber the greater variation with energy of the ratio of the stopping power of air to that of the wall material increases the importance of the shape of the spectral distribution. However, the variation from the equilibrium value is less than 3% for the age diffusion spectrum in a rather extreme case.

REFERENCES

2.1 H. E. Palmer, W. C. Hanson, B. I. Griffin, and W. C. Roesch. "Cesium-137 in Alaskan Eskimos," Science, vol. 142, pp. 64-66. 1963.

2.2 H. E. Palmer, W. C. Hanson, B. I. Griffin, and D. M. Fleming. "Radioactivity Measurements in Alaskan Eskimos in 1963," Science, vol. 144, pp. 859-860. 1964.

2.3 H. E. Palmer. "Determination of the Average Cs^{137} Body Burden of a Population by Urinalysis," Hanford Radiological Sciences Research and Development Annual Report for 1963, HW-81746. January 1964.

2.4 H. E. Palmer. "Determination of Average Cs^{137} Body Burden in a Population by Urinalysis," Proceedings of the Ninth Annual Conference on Bio-Assay and Analytical Chemistry, TID-7696, pp. 111-119. 1963.

2.5 E. P. Hardy, J. Rivera, and W. R. Collins. Fallout Program Quarterly Summary Report, HASL-146. July 1964.

2.6 J. M. Nielsen. The Radiochemistry of Iron, NAS-NS 3017, Office of Technical Services. 1960.

2.7 C. J. Maletskos and J. W. Irvine, Jr. "Quantitative Electrodeposition of Radiocobalt, Zinc, and Iron," Nucleonics, vol. 14, no. 4, pp. 84-93. 1956.

2.8 International Commission on Radiological Protection. Report of Committee II on Permissible Dose for Internal Radiation, Pergamon Press, New York, 1959.

2.9 W. C. Hanson, H. E. Palmer, and B. I. Griffin. "Radioactivity in Northern Alaskan Eskimos and Their Foods, Summer, 1962," Health Physics, vol. 10, pp. 421-429. 1964.

0028357

REFERENCES (Contd.)

2.10 J. Rundo, J. I. Mason, D. Newton, and B. T. Taylor. "Biological Halflife of Calcium in Man in Acute and Chronic Exposure," Nature, vol. 200, pp. 188-189. 1963.

2.11 C. R. Richmond, J. E. Furchner, W. H. Langham. "Long Term Retention of Radiocesium by Man," Health Physics, vol. 8, pp. 201-205. 1962.

2.12 H. E. Palmer and W. C. Roesch. "A Shadow Shield Whole Body Counter," Health Physics, in press.

2.13 E. M. Sheen. Gamma Spectrometer for Use in Dosimetry Studies, HW-84250. October 1964.

2.14 C. E. Miller and L. D. Marinelli. "Measurement of Gamma Ray Activities from the Human Body," Radiological Physics Division Semiannual Report, July through December, 1955, ANL-5518, pp. 52-56. 1956.

2.15 C. L. Comar. Fallout from Nuclear Tests, U.S. AEC Division of Technical Information Extension, Oak Ridge, Tennessee. 1963.

2.16 W. C. Roesch, R. C. McCall, and H. E. Palmer. Hanford Whole Body Counter 1959 Activities, HW-67045. December 1960.

2.17 R. D. Evans. "Radium Poisoning: II. The Quantitative Determination of the Radium Content and Radium Elimination Rate of Living Persons." Am. J. Roentgenol., vol. 37, pp. 368-378. 1937.

2.18 B. I. Griffin and W. C. Roesch. "A Scintillation Counter for In-Vivo Detection of Plutonium," Hanford Radiological Sciences Research and Development Annual Report for 1963, HW-81746. January 1964.

2.19 L. L. Nichols, W. C. Roesch, and J. G. Pengra. "Low Energy Fast Neutrons," Hanford Radiological Sciences Research and Development Report for 1963, HW-81746. January 1964.

0028358

REFERENCES (Contd.)

2.20 R. Batchelor, R. Aves, and T. H. R. Skyrme. "Helium-3 Filled Proportional Counters for Neutron Spectroscopy," Rev. Sci. Instr., vol. 26, pp. 1037-1047. 1955.

2.21 W. K. Brown. A Helium-3 Neutron Spectrometer with Extended Energy Range: Part II. Method of Energy-Range Extension, UCRL 6811, Pt. II. May 1962.

2.22 J. DePangher. "A Reproducible Precision Polyethylene Long Counter for Measuring Fast Neutron Flux," Research and Development Activities in the Radiological Sciences, HW-70050, pp. 51-57. January 1961.

2.23 J. DePangher. "Secular Variations in Neutron Emission from Plutonium-Beryllium Sources," Research and Development Activities in the Radiological Sciences, HW-73337, pp. 54-58. January 1962.

2.24 W. C. Roesch, K. L. Swinth, and L. L. Nichols. "Fast Neutron Medical Research Facility," Hanford Radiological Sciences Research and Development Annual Report for 1963, HW-81746. January 1964.

2.25 J. DePangher. "Double Moderator Neutron Dosimeter," Nuclear Instr. & Methods, vol. 5, pp. 61-74. 1959.

2.26 H. H. Rossi, M. H. Biavati, and W. Gross. "Local Energy Density in Irradiated Tissues," Radiation Research, vol. 15, pp. 431-439. 1961.

2.27 ORTEC RF Ion Source Instruction Manual, p. F-1. 1961.

2.28 S. K. Allison. "Experimental Results on Charge Changing Collisions of Hydrogen and Helium Atoms and Ions at Kinetic Energies Above 0.2 keV," Rev. Mod. Phys., vol. 30, pp. 1137. 1958.

2.29 W. C. Roesch, R. C. McCall, and F. L. Rising. "A Pulse Reading Method for Condenser Ion Chambers," Health Physics, vol. 1, pp. 340-344. 1958.

0028359

REFERENCES (Contd.)

2.30 O. J. Steingraber and I. B. Berlman. "Versatile Technique for Measuring Fluorescence Decay Times in the Nanosecond Region," Rev. Sci. Instr., vol. 34, pp. 524-529. 1963.

2.31 I. T. Myers, and W. H. LeBlanc, and D. M. Fleming. "Precision Adiabatic Gamma-Ray Calorimetry Using Thermistor Thermometry," Rev. Sci. Instr., vol. 32, pp. 1013-1015. 1961.

2.32 Stopping Powers for Use with Cavity Chambers, National Bureau of Standards Handbook 79, p. 19. 1961.

2.33 L. V. Spencer and U. Fano. "Energy Spectrum Resulting from Electron Slowing Down," Phys Rev., vol. 93, pp. 1172-1181. 1954.

2.34 H. E. Johns, J. E. Till, and D. V. Cormack. "Electron Energy Distributions Produced by Gamma Rays," Nucleonics, vol. 12, no. 10, pp. 40-46. 1954.

2.35 W. C. Roesch. Age Diffusion Theory for Beta Ray Problems, HW-32121. 1954.

2.36 A. T. Nelms. Energy Loss and Range of Electrons and Positrons, National Bureau of Standards Circular 577. 1956.

0028360

RADIOLOGICAL CHEMISTRY

Radiation Chemistry

Radiation-Induced Swelling and Hemolysis of Red Blood Cells - D. R. Kalkwarf and W. D. Felix

The importance of possible sites for hemolytic damage in irradiated erythrocytes was investigated by simultaneous measurement of cell volume and hemoglobin release with time after irradiation.

Human erythrocytes are readily available subjects for studying effects of ionizing radiation on living cells and methods for their chemical protection. Previous work has shown that these cells hemolyze after irradiation and that this effect can be inhibited by a variety of hydroxyl-radical scavengers.[3.1] As there are many different cell sites for hydroxyl radical attack, the question naturally arises as to which type of site is most critical for the maintenance of cell integrity. Knowledge of these locations would simplify the selection of chemical additives to exert more efficient protection.

Damage to at least three types of sites could lead to hemolysis: Type A, macromolecular components of the red cell's interior whose decomposition into smaller aggregates would raise the osmotic-pressure gradient across the cell membrane and produce osmotic hemolysis; Type B, ingredients required for active transport of sodium ion whose decomposition would allow this ion to accumulate within the cell and cause osmotic hemolysis; Type C, structural components of the red cell membrane whose decomposition would provide holes through which hemoglobin could escape.

The simultaneous measurement of cell volumes and extracellular hemoglobin provides one way of determining the relative importance of these three sites in the hemolytic process induced by irradiation. Osmotic

0028361

hemolysis, as experienced by cells immersed in a hypotonic medium, is characterized by retention of hemoglobin until the cells have swollen to 154 to 175% of their initial volume.[3.2] After hemolysis, the cells regain their original shape and volume.[3.3] If osmotic hemolysis occurs in irradiated cell suspensions, the importance of Type A and Type B sites is indicated. On the other hand, release of hemoglobin without swelling would support the importance of Type C sites. Variation in the shape of the cell volume distributions with time is another criterion for judging the relative importance of the cell sites. If only Type A sites were damaged, one would expect a congruence in successive cell volume distributions since an equal increase in osmotically active particles would probably have occurred in all cells. If Type B sites were damaged, however, the shape of successive distributions would probably change due to the more complicated relationship between damage to the sodium pump and osmotic swelling.

To test these ideas, human red blood cells were drawn by venipuncture and washed three times with equal volumes of sterile, isotonic, saline solution. They were then diluted to 3×10^7 cells/ml with sterile 0.15M sodium chloride solution containing 1% dextrose by weight and buffered at pH 7.4 with phosphate. Ten milliliter portions of this suspension were placed in sterile, glass ampoules with rubber puncture-seals and irradiated at 75 C in an A.E.C.L. Gammacell-200 with a dose-rate of 3.30×10^3 rad/min. After irradiation, the suspensions were kept at 37 C with gentle agitation; and periodically, samples were removed with a 100 μliter Hamilton syringe. Hemolysis was followed colorimetrically at 409 mμ on the supernatant solutions from centrifuged samples. The distribution of cell volumes in a 10^5 cell sample was measured, after an appropriate dilution with isotonic saline, on a Coulter Counter, Model B, to which was attached an R. C. L., 256-channel, pulse-height analyzer. The linearity between cell volume and channel number was established by calibration with spherical particles whose diameters were measured microscopically.

Figure 3.1 shows the change in distribution of cell volumes with time after irradiation. At least the majority of cells are seen to swell, although

the distributions are far from congruent. There is also some indication of cell shrinkage after maximum swelling. A useful parameter of these distributions is the modal cell volume, i.e., the most frequently occurring volume. This parameter together with the extent of hemolysis is plotted in Figure 3.2 as function of the time after irradiation. It is interesting to note that the modal cell volume increased to 168% of its initial value, but substantial amounts of hemoglobin had been released before that condition was attained.

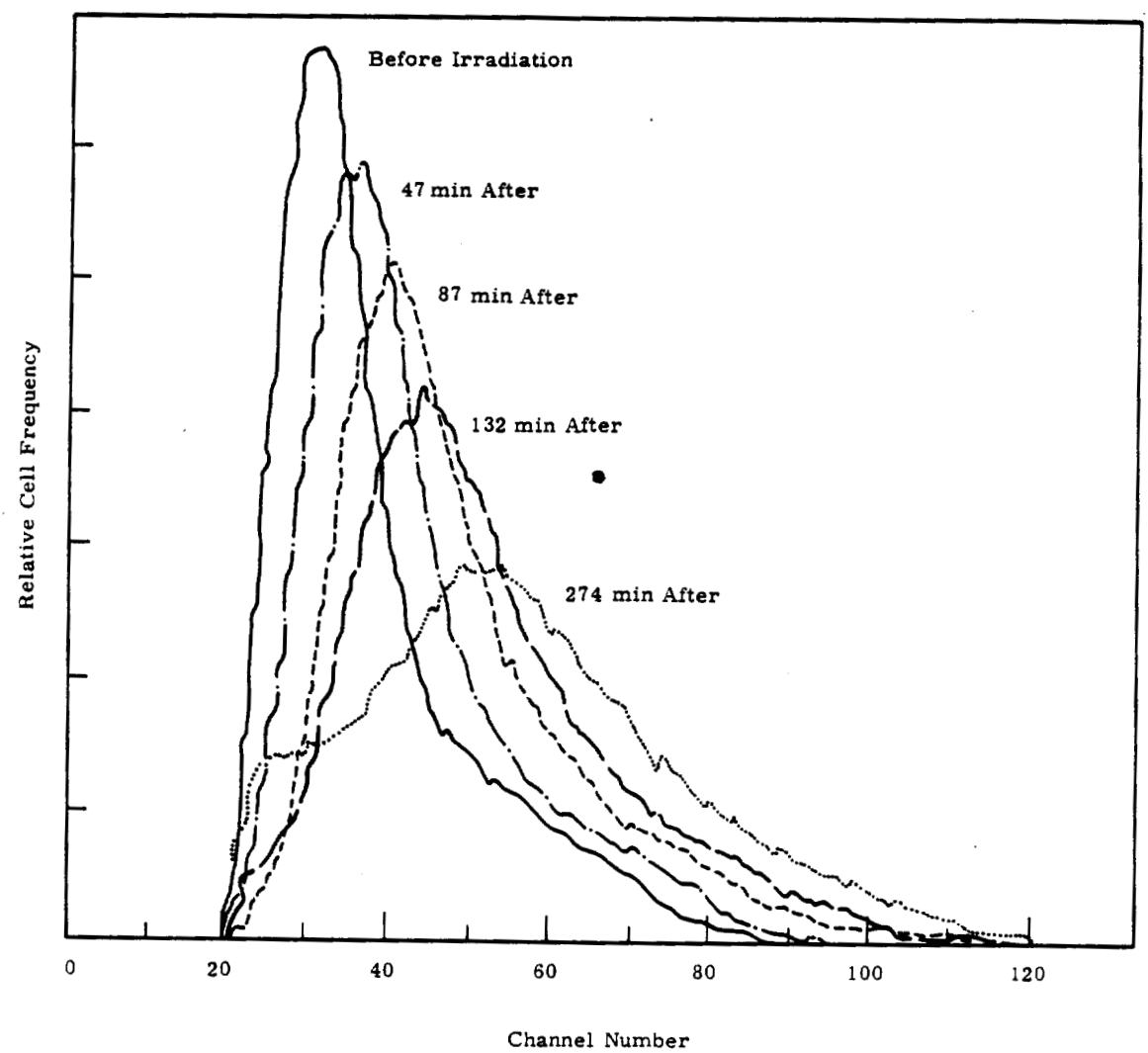

FIGURE 3.1

Size Distribution of Human Red Blood Cells in Isotonic Saline Before and After 1.2×10^5 Rads, Gamma Radiation

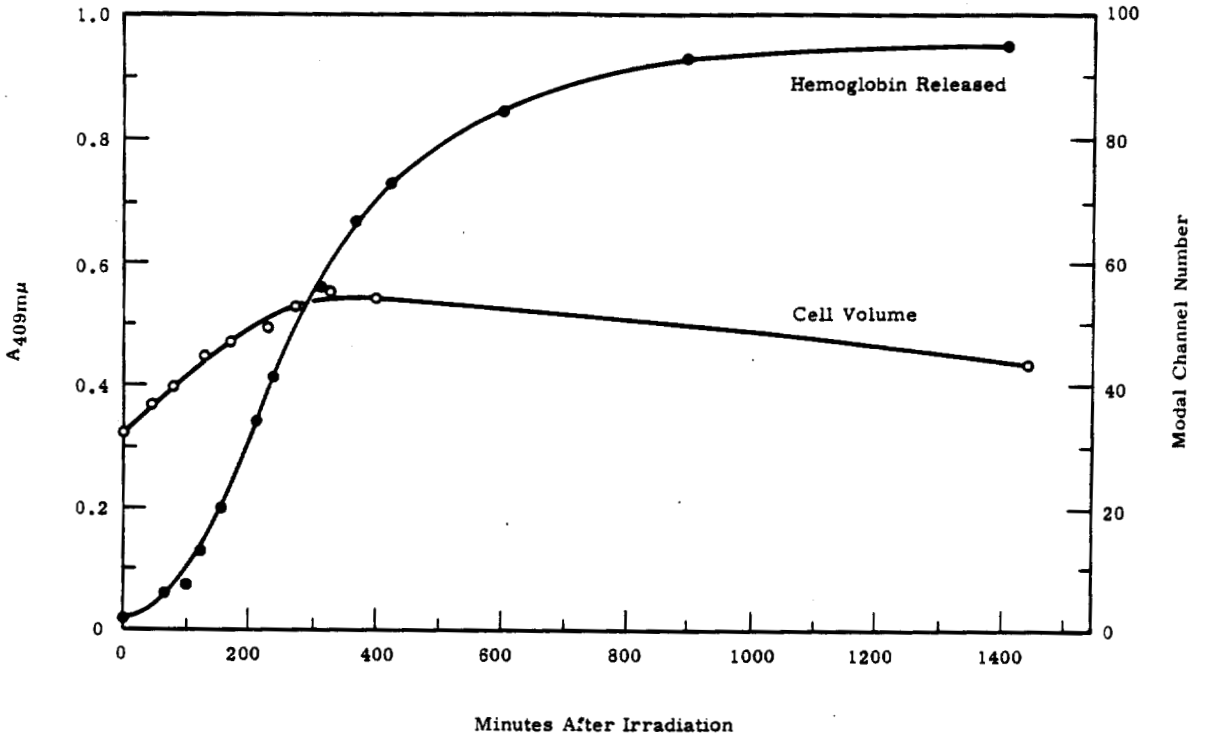

FIGURE 3.2

Volume Changes and Hemoglobin Loss from Human Red Blood Cells Following 1.2×10^5 Rads, Gamma Radiation

Attempts to evaluate the relative importance of damage to the three types of sites are hampered by the broad initial distribution of cell volumes. Except for the early appearance of hemoglobin, the present evidence indicates that Type B sites are most important. The apparent early release of hemoglobin may well be due to the initial presence of cells in greatly different stages of swelling and hence with different sensitivities to radiation induced hemolysis. Future experiments on more homogeneous cell populations should provide evidence for deciding this issue.

Radiation Protection of Aqueous Jellies - D. R. Kalkwarf

Evidence is presented that the radiation-induced collapse of intermolecular structure in aqueous agarose jellies is due to hydroxyl radical attack. Liquefaction occurred after megarad radiation doses, but jellies could be protected by small amounts of erioglaucine to withstand an order-of-magnitude-greater dose.

0028364

In many regions of living tissue, the physical state of the components resembles that of an aqueous jelly, i.e., an elastic gel which is very rich in water. Jellies are distinguished by their low energy of formation, their sensitivity to additives, even inorganic ions, and their ability to immobilize large quantities of liquids at temperatures well above the normal melting point. By their formation, an organism can chemically control the rigidity within its regions and the diffusion of metabolites between them. Jelly structures could easily be critical sites for radiation damage within an organism, and it thus seems important to consider methods for protecting them by chemical means.

Aqueous jellies prepared from commercial agarose were used as prototypes in studying the effects of irradiation and their inhibition. Agarose is a linear polysaccharide whose proposed structure is shown in Figure 3.3.[3.4] It forms firm jellies with water at room temperature in concentrations as low as 0.10% by weight. The simplicity of the intramolecular structure of agarose suggests that these jellies result from hydrogen-bonding between hydroxyl groups on the intertwined strands of the polymer. As evidence for this intermolecular structure, it was found that 0.20% agarose solutions would not form firm jellies in the presence of > 0.80M NH_4SCN or > 0.90M $Ca(NO_3)_2$. Both SCN^- and Ca^{2+} ions are known to bind water strongly and inhibit the formation of tertiary structure in proteins.[3.5]

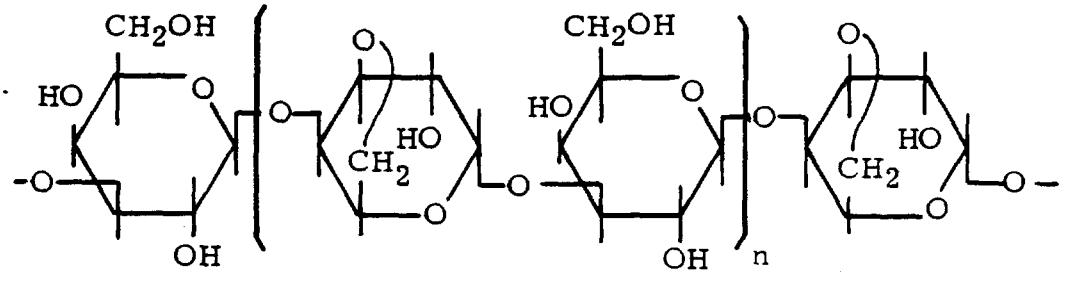

FIGURE 3.3
Proposed Structural Formula for Agarose

When jellies of agarose are irradiated in closed containers containing an air space, they develop gas pockets and eventually liquefy. This latter transition is fairly sharp; Figure 3.4 shows the radiation doses required to liquefy various concentrations of agarose. Solutions containing less than 0.1% agarose were also irradiated to test for possible jelly formation due to crosslinking, as is found in aqueous solutions of polyvinyl alcohol and other polymers. No radiation-induced jelly formation was detected, and it was concluded that only degradation of the polymeric structure of agarose occurs during irradiation.

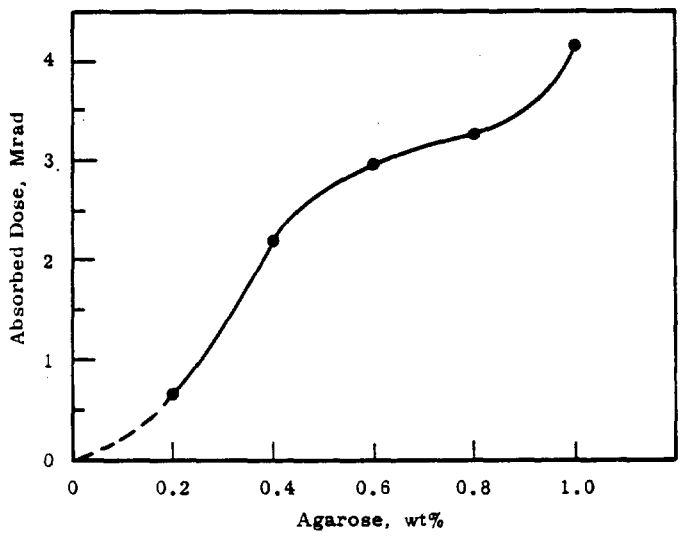

FIGURE 3.4
Absorbed Dose of Co^{60} Gamma Radiation Required to Liquefy Aqueous Agarose Jellies

Chemical protection of irradiated agarose jellies was achieved by incorporating the hydroxyl-radical scavenger, erioglaucine, into the jelly before irradiation. Figure 3.5 shows the extension in radiation stability which various concentrations of this additive afford a 0.20% agarose jelly. The ability of small amounts of erioglaucine to extend the irradiation lifetime of this jelly by significant factors, e.g., a factor of 11 by addition of 0.6% erioglaucine, suggests that agarose jelly structure is degraded by hydroxyl radical attack. Additional evidence for this conclusion was found by preparing a 0.20% agarose jelly in D_2O and irradiating it to the liquefaction point. If hydroxyl radicals or their deuterium-substituted counterparts are the active intermediates in destroying jelly structure, the heavy-

water jelly should liquefy at 0.89 times the dose required for the light water analogue, since the irradiation yield of OD radicals in D_2O is reported[3.6] to be 1.12 times the yield of OH radicals in H_2O. The liquefaction dose actually found was 5.5×10^5 rads or 0.81 times the dose required for the light-water jelly.

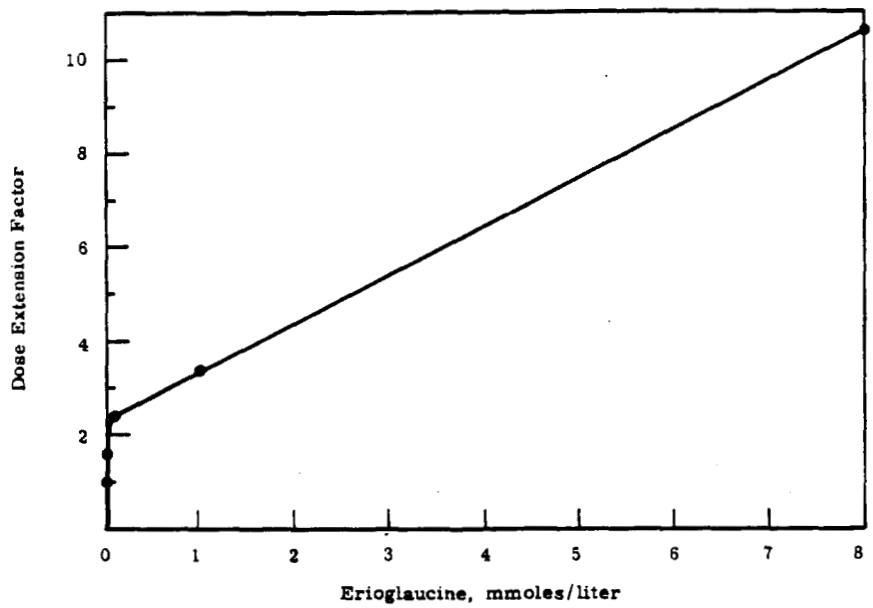

FIGURE 3.5

Factors by Which Various Concentrations of Erioglaucine Extend the Dose Required to Liquefy a 0.20% Agarose Jelly

Although agarose jellies are relatively resistant to biologically important doses of radiation, this demonstration of their protection suggests that damage to more radiation-sensitive jellies could also be inhibited by radical scavenging. More efficient protection with chemical additives may be possible if they can stabilize particular intermolecular structures to radical attack. Future work with aqueous jellies will explore these possibilities.

Radiation Chemistry of Erioglaucine in Frozen Aqueous Solution - D. R. Kalkwarf

The radiation sensitivity of erioglaucine in ice is 0.7% of its sensitivity in liquid water. Possible explanations for this behavior are proposed.

Erioglaucine has been shown to react rapidly with hydroxyl radicals in the liquid phase, but it is less able to compete with other solutes for these radicals as the temperature is lowered. Two explanations have been presented for this phenomenon. One is that the activation energy of the reaction between erioglaucine and the radicals is greater than that for any of the competing reactions.[3.7] The other suggests that hydroxyl-radical reactions can occur more rapidly through sheaths of organized water surrounding the solutes than by diffusion of reactants through the liquid.[3.8] If true, the second explanation would be of particular importance in understanding the relative radiation-sensitivities of constituents in biological systems. For this reason, measurements of the radiation-sensitivities of erioglaucine solutions were extended to temperature below the ice point.

Solutions of 6.0×10^{-6} M erioglaucine were brought to the test temperature in closed polyethylene containers and then irradiated* at a close rate of 3.30×10^{3} rads/min. A polystyrene-foam jacket around the container kept the temperature of the solutions from rising more than 0.02 C/min during the irradiation. The measured effect was the decrease in optical absorbance of the sample at 631 mμ after irradiation and warming to 25 C. Figure 3.6 shows this effect at -7 ± 2 C and at 25 C. Comparison of the initial slopes of these curves indicates that erioglaucine is 150 times more sensitive at the higher temperature. Figure 3.7 shows the fraction of the initial absorbance remaining after 1 min irradiations of solutions at various temperatures. The decreased radiation-sensitivity of erioglaucine in ice is seen to extend slightly into the liquid state.

The substantial increase in radiation stability of erioglaucine solutions with freezing is heuristic. Hydroxyl radicals are quite reactive in irradiated ice, as has been shown by the rapid decrease in their ESR signal intensity even at 77 K.[3.9] Their inability to bleach erioglaucine in ice suggests that other reactions are competing more favorabily for the radicals. During irradiation at 25 C, hydroxyl radicals can disappear by a variety of reactions, e.g.:

* In an AECL Gammacell-200

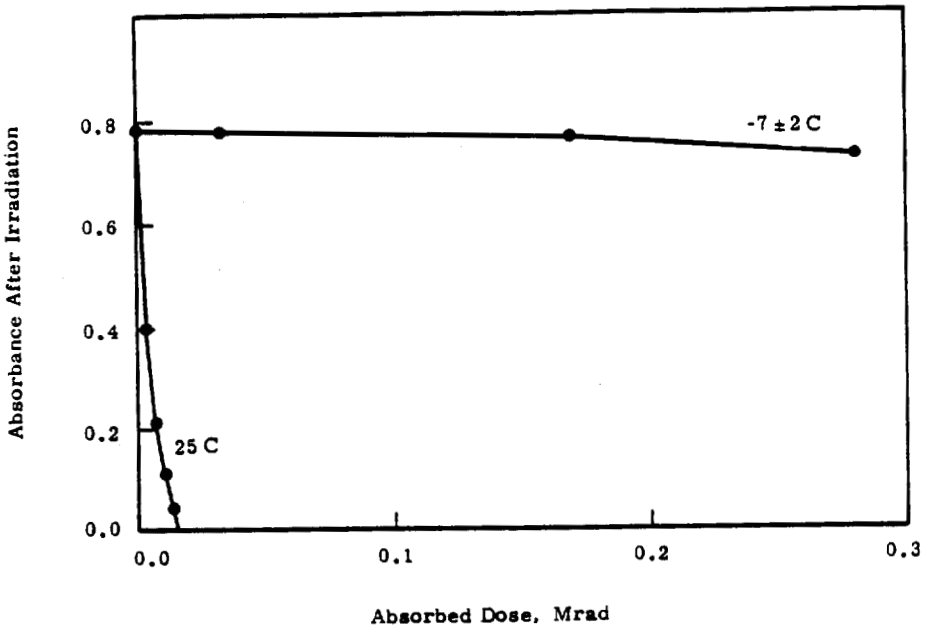

FIGURE 3.6

Effect of Temperature on the Radiation-Induced Bleaching of 6.0×10^{-6} M Erioglaucine Solutions

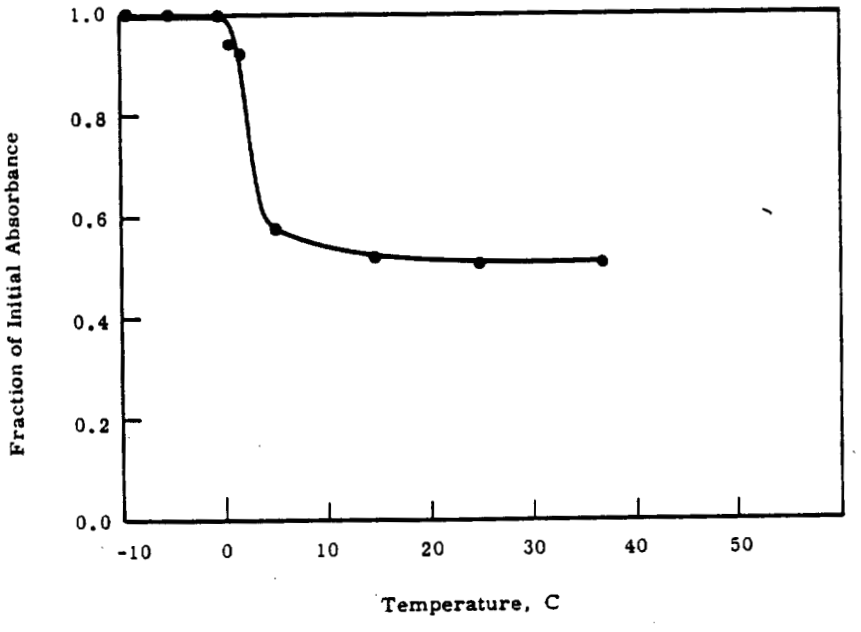

FIGURE 3.7

Fraction of Initial Absorbance Remaining in 6.0×10^{-6} M Erioglaucine Solutions After Absorbing 3800 Rads at Various Temperatures

0028369

- $OH + e^-_{aq} \rightarrow OH^-$, $k_1 = 3.0 \times 10^{10}$ liters/mole–sec[3.10]
- $OH + OH \rightarrow H_2O_2$, $k_2 = 6 \times 10^9$ liters/mole–sec[3.10]
- OH + Erioglaucine → Products, $k_3 = 4.5 \times 10^9$ liters/mole–sec.[3.8]

A shift in the relative values of these rate constants in ice solutions could account for the greater stability of erioglaucine there; but at present, there is insufficient evidence to decide whether this shift is due to a relatively larger activation energy for Reaction (3) or whether Reaction (1) is accelerated by the ease of electron transfer in ice.

Yield of p-Nitroaniline Radicals Formed in Irradiated Aqueous Solutions-

R. N. Diebel and D. R. Kalkwarf

The concentration of radicals produced by gamma irradiation of 2×10^{-3}M p-nitroaniline in water at pH 13 was measured by electron spin resonance. The yield was evaluated to be 4.1 radicals per 100 eV in the presence of ethanol and formate.

Continuation of our previously reported work[3.11] has now enabled us to ascertain the yield of radicals in gamma irradiated p-nitroaniline (PNA) solutions. Determination of the G value (number of radicals produced per 100 eV of absorbed dose) may be of value in working out the radiation chemistry of organic solutes and in devising means for preventing radiation damage in living tissue.

The experimental system for circulating solution through the Co^{60} irradiator and into the electron spin resonance (ESR) cell was much the same as previously described.[3.11] Polyethylene tubing and containers were used where feasible. The pump, the tubing in the irradiation zone, and the cooling coil were of Type 316 Stainless Steel. Two-way greaseless stopcocks (Teflon® core; glass bodies) were placed at the inlet and outlet of the ESR aqueous sample cell to facilitate calibration with solutions of diphenylpicrylhydrazyl (DPPH) in benzene.

A dual sample ESR cavity (V4532), modified to form a TE 015 cavity by addition of the optical transmission accessory, was used in measuring

the concentration of the radicals. The front sample position was used for the aqueous solution cell while a sample of powdered coal was used in the rear position as a standard for monitoring the cavity Q and detector efficiency.

Standard solutions of DPPH* in benzene were prepared by weighing. Their concentrations were checked photometrically and by titration with hydroquinone in ethanol. The concentrations evaluated by these three methods agreed within 1%.

Solutions of PNA were prepared by weight using freshly boiled water. Carbonate-free NaOH was added to bring the solution to approximately 0.1M in NaOH while the PNA concentration was nominally 2×10^{-3}M.

The solution was purged with helium and then degassed by slowly admitting it to an evacuated glass storage vessel which was connected to the circulating system. Usually the circulation system was operated with a helium atmosphere, but it was also reasonably vacuum tight. Some irradiation experiments with PNA were carried out at the vapor pressure of the solution with no results obviously different than when using the helium atmosphere.

The ESR spectra used for quantitative measurements were made using a large value for the 100 kc modulation field at the aqueous sample cell. This broadened the radical spectrum into three lines by smearing out the proton hyperfine structure. Spectra of DPPH were obtained at the same value of modulation amplitude and input microwave power as used with the PNA. The amplitude of the signal from the coal standard increased a factor of 1.34 when changing from aqueous solutions in 0.1M NaOH to the benzene solutions of DPPH. The quantitative comparisons were made using the first moments as obtained on a moment balance.[3.12]

To determine the yield of PNA radicals, the dose received by the solution during passage through the irradiator was evaluated using erioglaucine. We could determine the dose absorbed by the solution from measurements of the change in absorbance of the dye upon passage through irradiator

---

* Aldrich Chemicals

at constant flow rate. After performing a series of measurements at different flow rates we determined that the dose received by our PNA solution was 3.50×10^{20} eV/liter. During this particular experiment, we used a flow rate of 3.9 ml/sec and the time delay between the irradiator and ESR cell was then 12 sec. Since the radical signals decay exponentially with a 15 sec half-life, this flow rate did not introduce too large a correction for decay but still permitted most of the radicals to decay before being recirculated through the irradiator.

The measurement of radical concentration yielded a value of 2.41×10^{-5} M or 1.45×10^{19} PNA radical per liter at the outlet of the irradiation zone. Combining this value with the dose mentioned yields G = 4.1 PNA radicals per 100 eV. Having G = 4.1 seems possible since Allen[3.14] has pointed out that the total yield of reducing equivalents may be as high as 4.3 with $G(e^-aq.) = 2.85$, $G(H) = 0.55$, and $G(H_2) = 0.45$. At the same time Allen also indicates that other experiments have yielded a total of only 3.6 oxidizing equivalents in the radiolysis of water. It would be more satisfying to us to take the effective reducing equivalents in basic solution as $G(e^-aq.) + G(H)$ to give a total of 3.4 for the G (reduction) which would affect PNA.

We are pursuing this study further by looking at other nitrobenzene derivatives. Also we expect to look at the effect of adding competitors for hydrated electron and the related reducing species present in irradiated water.

Comparison of Radicals Formed by Gamma Irradiation and Dithionite Reduction of Aromatic Nitro-Compounds in Water - D. R. Kalkwarf and R. N. Diebel

A long-lived radical produced by gamma irradiation of aqueous p-nitroaniline solutions was determined to have the structure $[H_2N\text{-}\bigcirc\text{-}\dot{N}O_2]^-$ and to be produced by reduction with hydrated electrons. A radical with considerably greater stability under similar conditions was detected in irradiated solutions of p-nitrobenzoate. The structure of this radical is uncertain, although it was shown not to be $[O_2C\text{-}\bigcirc\text{-}\dot{N}O_2]^=$, the radical formed by dithionite reduction.

Electron-spin-resonance spectrometry is not only a means for detecting free radicals; but, due to the fine detail in many spectra, it is a powerful method for determining chemical structure. Radiolysis of p-nitroaniline in water has been shown to produce a radical with a quite-detailed ESR spectrum and a half-life of 15 sec at room temperature.[3.15] It was of considerable interest to determine the chemical structure of this and other radiation-produced radicals to understand their modes of formation and the relationships between radical structure and chemical reactivity.

Aqueous solutions of p-nitroaniline and p-nitrobenzoate ion were irradiated in the flow system described previously;[3.15] and, in both cases, characteristic ESR spectra were detected at the sample cell placed downstream from the irradiator. These spectra are shown in Figures 3.8 and 3.9 and were obtained at room temperature in deoxygenated solutions containing 0.1M NaOH. The spectrum of the radical from the p-nitroaniline solution was found to consist of three groups of thirteen lines each; although at the amplification used in Figure 3.8, the end lines in each group are barely discernible. The centers of these groups are separated by 15.3 G, while the individual members are separated by 1.1 G. The spectrum of the radical from the p-nitrobenzoate solution was also found to consist of three groups of lines, but there are eighteen lines per group. The centers of these groups are separated by 13.1 G while the individual members are separated by 0.6 G.

In irradiated water at pH 13, hydrated electrons are currently considered to be the predominant reducing species while hydroxyl radicals are the predominant oxidizing species. Considerable controversy still exists, however, concerning which predominates at this pH.[3.16] Several types of secondary radicals could be produced by reaction of these species with p-nitroaniline, e.g.:

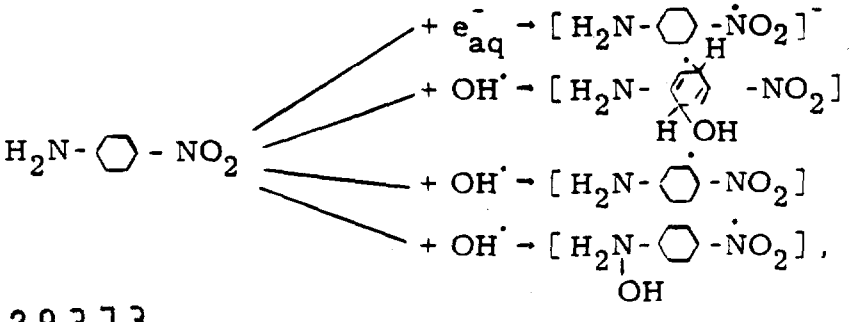

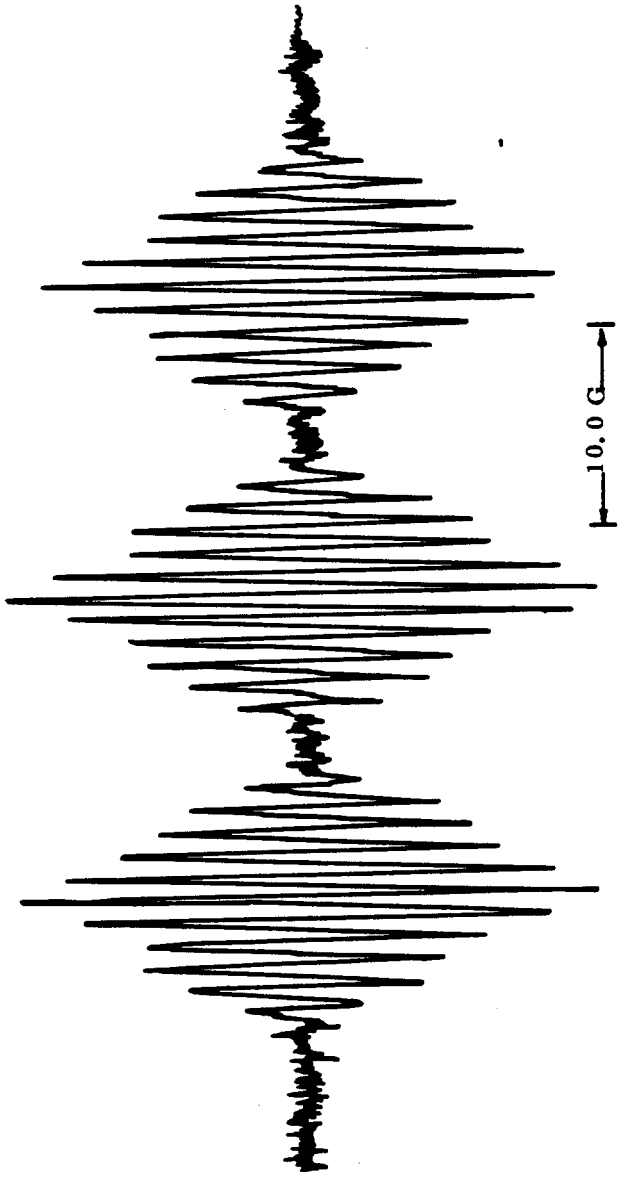

FIGURE 3.8

ESR Spectrum of Irradiated p-Nitroaniline Solution in Deoxygenated Water at pH 13.0

FIGURE 3.9

ESR Spectrum of Irradiated p-Nitrobenzoate Ion in Deoxygenated Water at pH 13.0

0028374

and analogous structures could be produced from p-nitrobenzoate. The problem, then, is to select the structures of the radicals actually observed from among several possibilities.

Two methods for identifying the chemical structures of the observed radicals were available: comparison with sythetic spectra and comparison with spectra obtained from products of other chemical reactions with the nitro compounds. The ESR spectrum of a proposed radical structure can be synthesized by considering the contributions to hyperfine splitting by each of the atoms in the radical with nonzero nuclear spin. The actual ESR spectrum of irradiated p-nitroaniline suggests that the splitting of 15.3 G is due to the nitro-nitrogen atom. If this value is applied to Structure (1) together with assumed splittings of 3.3 G for the two ortho hydrogens and 1.1 G for the remaining hydrogen and nitrogen atoms, the spectrum shown in Figure 3.10 can be synthesized. The heights of the lines are proportional to signal intensity, and the spectrum is a good approximation to that obtained from the actual radical. It is also a good approximation to the spectrum obtained by electrolytic reduction of p-nitroaniline.[3.17]

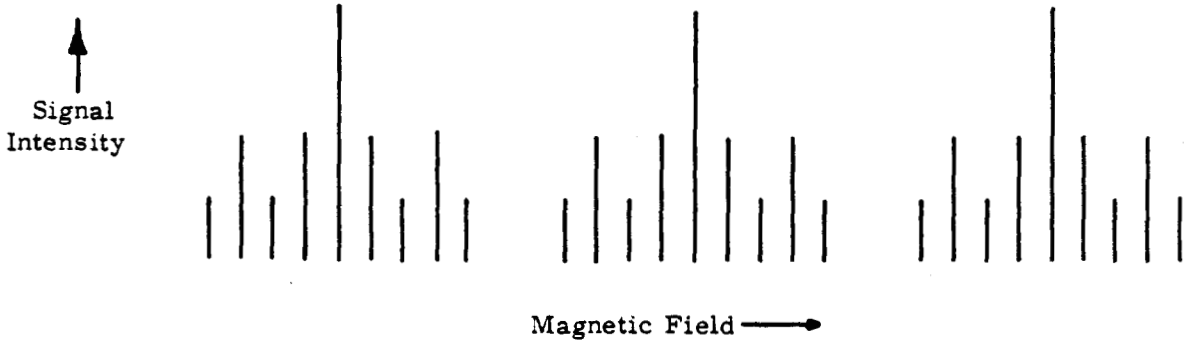

FIGURE 3.10

Synthetic ESR Spectrum for the $[H_2N\text{-}\bigcirc\text{-}\dot{N}O_2]^-$ Radical

None of the other structures considered above, except perhaps, (4) could give such a spectrum.

If the radical in irradiated p-nitrobenzoate solution is assumed to have the structure:

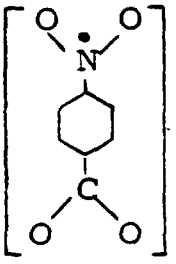

(5)

with spectral splittings of 13.1 G for the nitro-nitrogen, 3.3 G for the two ortho hydrogens and 1.1 G for the two meta hydrogens, the structure shown in Figure 3.11 can be synthesized. This bears little resemblance to that obtained from irradiated p-nitrobenzoate solutions, although it does resemble the spectrum of the radical formed by reduction of p-nitrobenzoate with dithionite.[3.18]

To obtain comparison spectra of radicals obtained by other chemical reactions, a second flow system was constructed so that the samples could be examined in the same sample cell used in the irradiation experiments. Two solutions, each stored in a 1 gal polyethylene reservoir, were allowed to move by gravity into a mixing cell and then immediately into the sample cell of the spectrometer. Molecular oxygen was removed by a continuous stream of helium through the reservoirs.

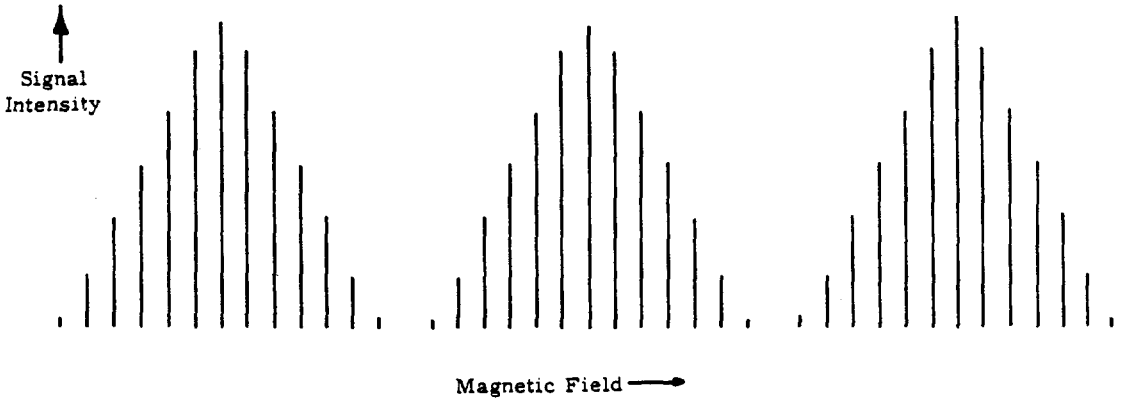

FIGURE 3.11

Synthetic ESR Spectrum for the $[O_2C\text{-}\bigcirc\text{-}\dot{N}O_2]^{=}$ Radical

Figure 3.12 shows the spectrum obtained by mixing 1.0×10^{-2} M sodium dithionite (at pH 13) with 2.0×10^{-2} M p-nitroaniline (at pH 13) in water containing 14% acetone by weight. It closely resembles that obtained during the radiolysis experiment with three groups of lines separated by 15.1 G between groups and 1.1 G between lines. Higher resolution of the signals from both solutions showed further similarities in fine structure as indicated by arrows in Figure 3.13. This figure compares the low-field group in each spectrum under instrumental conditions which sacrifice intensity for resolution. As a result, the end lines disappear into the noise level, but the lines indicated by arrows are resolved. Since these lines appear in both spectra, they probably are due to traces of other nitroaniline isomers in the starting material rather than indicating the presence of structures such as (2) through (4). It seems very unlikely that sodium dithionite could produce any of these other structures since it is clearly a reducing agent, i.e.

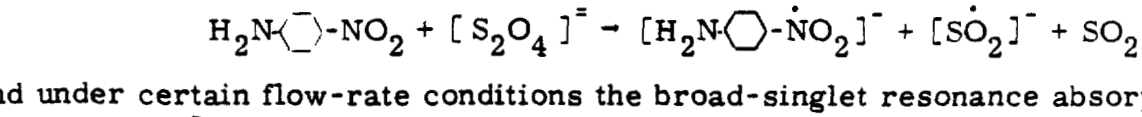

and under certain flow-rate conditions the broad-singlet resonance absorption of the $[\dot{SO}_2]^-$ radical was superimposed on the spectrum.

Figure 3.14 shows the spectrum obtained by mixing 1.0×10^{-2} M sodium dithionite at pH 13 with 1.0×10^{-2} M p-nitrobenzoate. This resembles the spectrum obtained during the radiolysis experiment only in the strong triplet splitting due to the nitro-nitrogen atom. It does, however, correspond quite exactly to the synthetic spectrum for Structure (5). After ruling out this structure for the radical produced during radiolysis, spectra based on other possible structures were synthesized; however, as yet, a good fit has not been found.

One of the purposes of this study is to determine structural features of free radicals which increase their stability, since long-lived radicals might be used to hold dormant some damaging processes in irradiated tissue. The half-life of the radical from irradiated p-nitrobenzoate was found to be 8 min at room temperature or 32 times the half-life of the radical

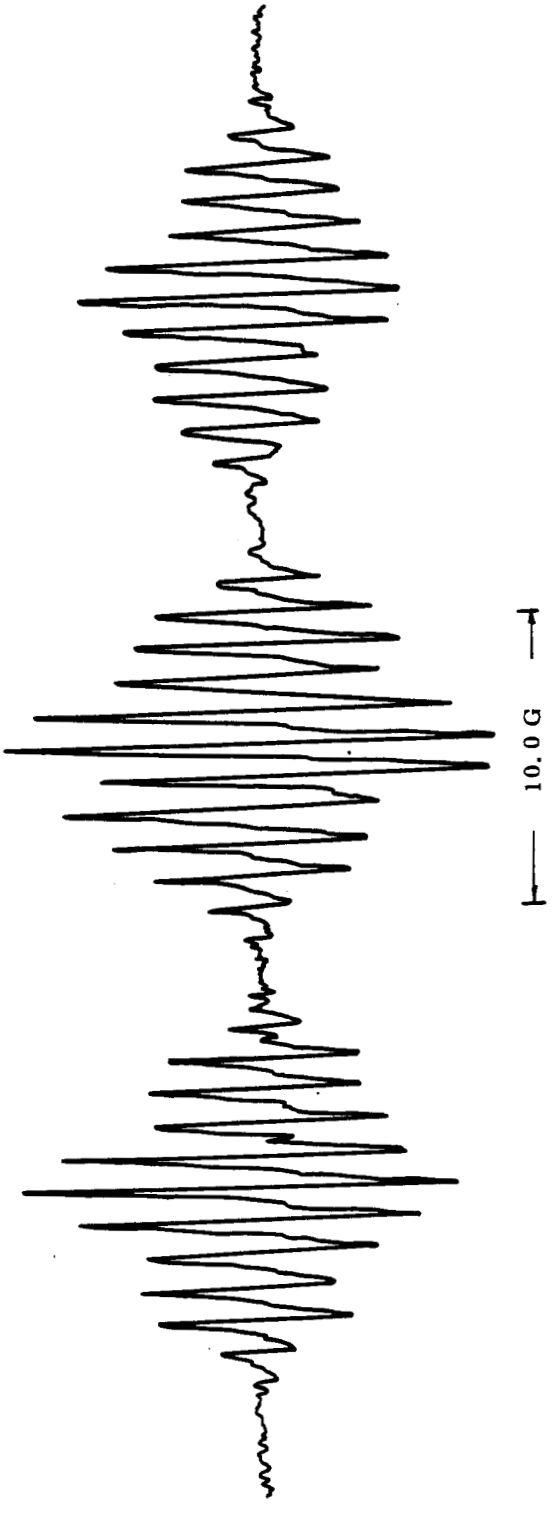

FIGURE 3.12

ESR Spectrum of Product Formed by Reducing p-Nitroaniline with Sodium Dithionite

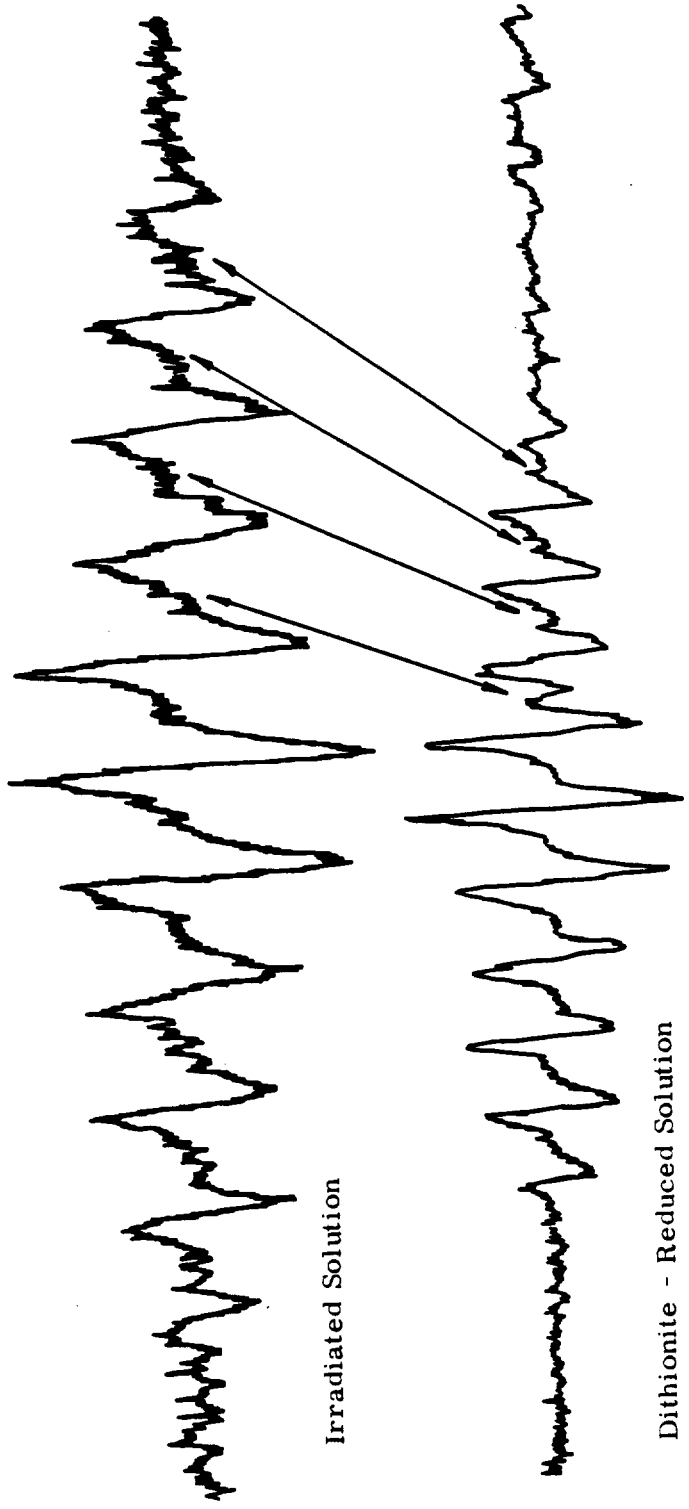

FIGURE 3.13

High Resolution ESR Spectra of Radicals Produced from p-Nitroaniline

0028379

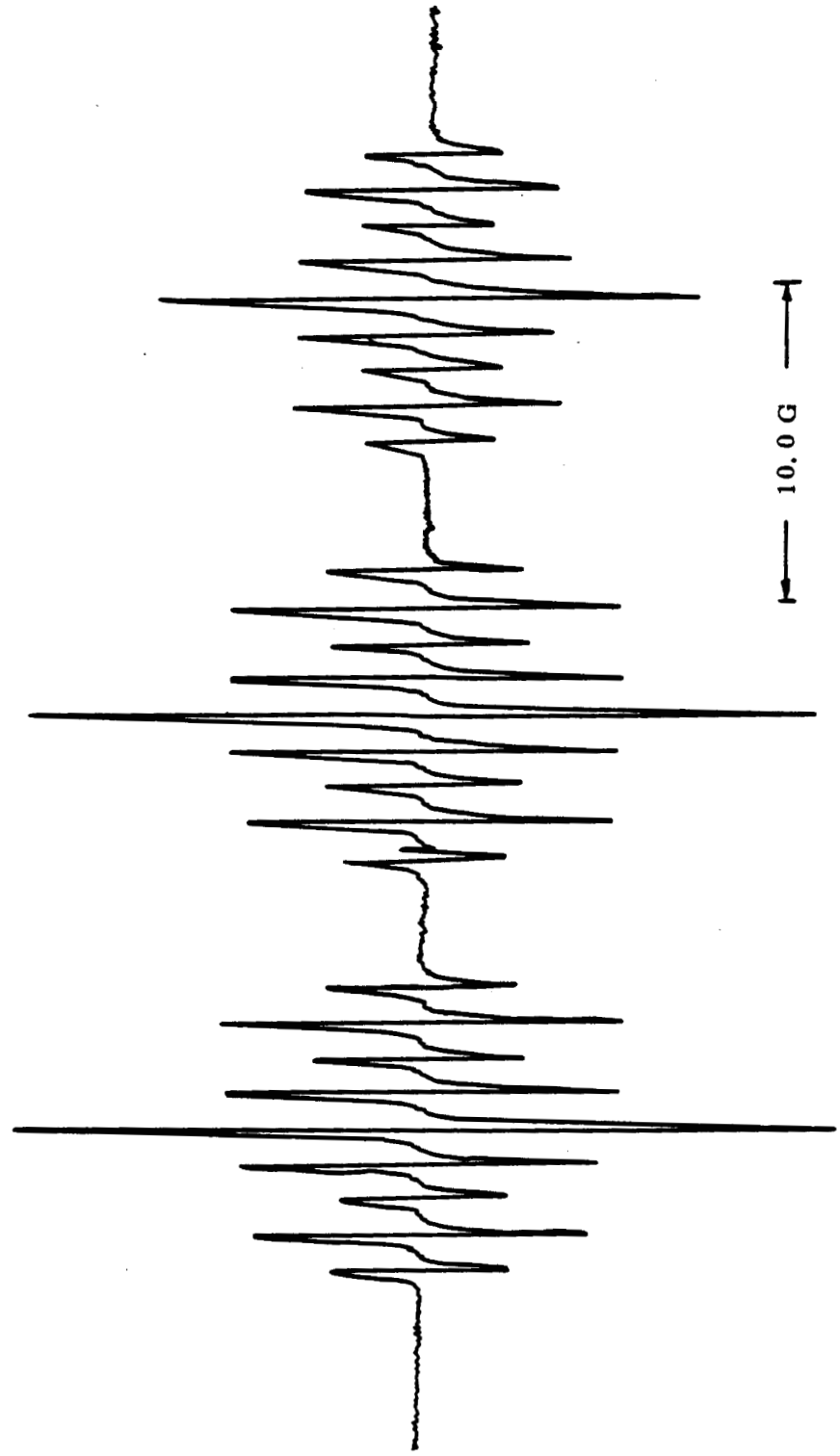

FIGURE 3.14

ESR Spectrum of Product Formed by Reducing p-Nitrobenzoate Ion with Sodium Dithionite

0028380

from p-nitroaniline under identical conditions. Such a dramatic increase in radical lifetime with a fairly slight alteration in parent solute provides added impetus for determining the structures of radiation-produced radicals.

Kinetics of Diffusion Through Human Erythrocyte Membranes -

W. D. Felix

A model for the radiation-induced hemolysis of human erythrocytes is discussed in which the controlling rate step is the diffusion of Na^+ and K^+ ions through damaged or blocked active transport sites. The apparent diffusion coefficient (5.0×10^{-7} cm^2/sec) for ions diffusing through an average of 2.90 effective holes having average radii of 4.0 Å per cell was calculated by fitting the model to experimental cell swelling data.

Irradiation of human erythrocytes suspended in isotonic media results in swelling, spherocytosis, and eventual hemolysis. Hemolysis may be considered as occurring by the rapid loss of macromolecular intracellular constituents through a tear or break in the membrane, or by leakage through the membrane that has been stretched to the point of absolute permeability.[3.19] Two general theories of osmotic hemolysis may well be applied to radiation induced hemolysis. The first considers osmotic hemolysis to be the direct result of the continuous distribution of differing cell resistances throughout the cell population, whence the reactions between cell and lysin are irreversible. The second proposes that hemolysis is the result of random sequential competition of the lysins for certain sites on the cell membrane: lysis resulting when certain numbers of critical sites have been occupied.[3.20]

Except under extreme stress, osmotic hemolysis is believed not to occur as a rupture at one point, but rather as a relaxation of the restraints or stabilizing forces responsible for the maintainance of semipermeability.[3.21, 3.22] That is, "functional holes" are induced in the membrane thereby leading to the disruption of ionic equilibria, an increase in osmotic pressure, the influx of water, and the stretching of the membrane until macromolecules leak out.

The present paper considers the cellular membrane as the location of sites for that radiation damage responsible for red cell hemolysis. It is

0028381

assumed that the primary function of these sites is in maintaining the differences in ionic concentration across the thin barrier. Specific enzymatic or metabolic processes will not be discussed nor will other forms of radiation damage be considered, notwithstanding that such forms may in themselves be capable of inducing erythrocyte death, were not hemolysis to occur. The general development depends heavily upon similarities in the processes occurring during osmotic and radiolytic hemolysis and upon hypotheses embodied in the ionic transport model.

Recent investigations of the red cell have led to rudimentary, but functional, concepts on ionic transport through the cell membrane. The integral part occupied by lipids in the membrane suggests that the chemical composition of the lipids may take part in determining permeability properties of the membrane. However, extensive studies are still required to complete the map of erythrocyte lipids for comparison with experimental data.[3.23] Erythrocytes are highly permeable to anions (Cl^- half exchange time: 0.24 sec) and to water such that anionic concentration and thermodynamic equilibrium is maintained across the membrane at all times.[3.24] Although the ratio of intra- to extracellular ionic concentration is 28.6 for K^+ and 0.090 for Na^+, the total intra- and extracellular cationic concentrations are approximately equivalent. The concentration of protein, particularly hemoglobin, within the cell is sufficient to bring to balance the osmotic pressure gradients across the cell membrane.[3.25-3.27] Glycolysis is necessary within the cell to furnish the energy needed to maintain the potassium and sodium ionic concentration gradients.[3.28]

Compared to chloride exchange, diffusion of Na^+ and K^+ is very slow (K^+ half exchange time: 31 hr). Since the electrophoretic mobilities of the Cl^- and K^+ ions are nearly equivalent, the difference in permeability is commonly interpreted in terms of positively charged channels passing through the membrane, the effective channel diameter being on the order of the hydrated ionic diameter. Positively charged ions are thus screened out while small, negatively charged and neutral species are allowed free access. Entrance of K^+ (exit of Na^+) to the cell involves transport up an electrochemical potential

barrier whereas exit (entrance of Na^+) through the positive channels is predominately down the concentration gradient requiring little or no energy. Solomon[3.11] found that the membrane pores had equivalent radii (those radii which would be exhibited by an ideal membrane whose permeability to ions is the same as that of the red cell) of 3.5 to 4.2 Å, that the major route of entrance of K^+ into the cell was different from that taken by water, and that the major exit route was different from the entrance.

The normal red cell is a biconcave disk, 8.4 μ in diameter, 2.4 μ thick at the widest section, and 1 μ thick at the narrowest.[3.29] Attack by lysins whereby the cation impermeable membrane is disrupted results in swelling as noted by the gradual loss of the discoid shape. The resistance to deformation is the same at the rim as at the saddle region of the cell and is also the same as that of the membrane of the swollen cell. The changes in curvature during the shape transformation require an increase in internal pressure of less than 1 mm of water. However, on becoming spherical there is an abrupt increase in rigidity or tension of the membrane with commensurate rise in internal pressure occurring as resistance to stretching deformation.[3.30] The cell then rapidly loses hemoglobin in all directions and hemolysis is complete.[3.19] The gross changes in molecular organization occurring during the tangential stressing period are apparently reversible.[3.31]

Thus, damage to the cell can occur as a result of acts which tend to disrupt the delicate ionic equilibrium. For example, hemolytic agents such as straphanthin and digitonin block active transport, perhaps by displacing K^+ from carrier sites, but have little effect on glucose metabolism. Moreover, other agents such as n-ethylmaleimide, which is fully permeable throughout the cell, react with intracellular glutathione, thus stifling glycolysis resulting in disrupted cation gradient, leading to spherocytosis and hemolysis. Nonpermeable p-mercuribenzoate exhibits a similar effect except that glycolysis is not disturbed. Both of the latter agents are sulfhydryl inhibitors, the sulfhydryl groups apparently being involved in ion transport, red cell shape, and viability.[3.32]

0028383

Similarly, radiation exposure may be expected to cause hemolysis by disruption of glycolysis, sulfhydryl inhibition, or by otherwise attacking the transport ferries, and/or blocking the pores by attacking or replacing charged groups in the channels. The end result of interest in free radical attack is that the concentration balance of Na^+ and K^+ is upset. As these ions leak through the cell an equivalent ionic concentration of both species is gradually approached on both sides of the membrane, the slight osmotic pressure gradient due to intracellular hemoglobin causes water to flow in, resulting in gradual sphering of the cell. The remaining functional transport sites are at the same time working to maintain the original sodium-potassium balance. The overall effect is to maintain a system only slightly removed from equilibrium, thereby creating the slight osmotic potential sufficient to deform the cell membrane. Final hemolysis occurs as in the normal osmotic hemolytic mechanism. The rate controlling step is thus the diffusion of Na^+ and K^+ through the leaky sites under the combined driving force of the concentration gradients of these ions across the cell membrane.

The model used in this presentation was selected on the basis of preliminary experimental evidence from the three models discussed in the previous paper.[3.33] Thus, although the actual radiation hemolysis phenomenon may include some contribution from the other two mechanisms, such interactions have been neglected. Assuming the quasi-stationary state, that is, that the concentration gradient within the membrane may with sufficient accuracy be assumed constant, Jost[3.34] writes for the general diffusion equation

$$J = q(c - c')\, D/\delta \qquad (1)$$

where c is the concentration above and c' below the membrane, q is the effective cross section of the membrane, and δ its thickness. Now consider the diffusion current for a system of two diffusion components in solution,

$$J = q(c_1' - c_1)\, D_1/\delta + q(c_2' - c_2)\, D_2/\delta \ . \qquad (2)$$

Let c_1 and c_1' be the intra- and extracellular concentrations of Na^+, and c_2' and c_2 of K^+. Assuming that the two species have equal mobilities,

$D_1 = D_2$, and since the concentration of intracellular Na^+ (K^+) is approximately equivalent to the extracellular concentration of K^+ (Na^+), the subscripts may be dropped, whence

$$\frac{dc'}{dt} = \frac{J}{V'} = 2\,q\,(c' - c)\,D_1/\delta V' \quad .$$

For unequal volumes, where V and V' are the intra- and extracellular volumes respectively, one may write two equations for the rate of change of diffusion current

$$V'dc' + 2\,Dq/\delta\,(c' - c)\,dt = 0 \tag{3a}$$

$$V\,dc + 2\,Dq/\delta\,(c - c')\,dt = 0 \quad . \tag{3b}$$

Since the apparent holes through which the ions pass are tortuous, the diffusion coefficient gives a measure of the effect of impedances from interaction with lipid and protein of the cell membrane.

Combining Equations (3a, b)

$$\frac{d(c' - c)}{(c' - c)} + \beta\left(\frac{1}{V'} + \frac{1}{V}\right)dt = 0$$

and integrating we have

$$\frac{c' - c}{(c' - c)_o} = \exp\left[-\beta t\left(\frac{1}{V'} + \frac{1}{V}\right)\right] \tag{4}$$

where

$$\beta = 2qD/\delta \tag{5}$$

and where the subscript o refers to the initial state. The concentration term in Equation (4) may be written

$$\frac{c' - c}{c'_o - c_o} = \frac{\frac{n'}{V'} - \frac{n}{V}}{\frac{n'_o}{V'_o} - \frac{n_o}{V_o}} \tag{6}$$

where n and n' are the number of moles of intra- and extracellular Na^+, and V and V' are the respective volumes in liters. Since

$$V' >> V \tag{7a}$$

$$V' \simeq V_o' \tag{7b}$$

and defining a swelling ratio, b

$$V = V_o(1 + b) \tag{8}$$

and relating the extracellular volume to the original cellular volume

$$V' = aV_o \tag{9}$$

Equation (7) becomes

$$\frac{c' - c}{c_o' - c_o} = \frac{n'(1 + b) - an}{n' - n_o a} \left(\frac{V_o}{V}\right) \quad . \tag{10}$$

Since the initial concentration gradient of Na^+ is large, the $n_o a$ term in Equation (9) is negligible compared to n'. Finally, since the ratio of change in the total moles of intra- to extracellular Na^+ should closely parallel the swelling ratio, that is, $na/n' = b$, we can rewrite Equation (5)

$$\frac{V_o}{V} = e^{-\beta t/V} \tag{11}$$

where from Equation (7a)

$$\left(\frac{1}{V'} + \frac{1}{V}\right) \simeq \frac{1}{V} \quad .$$

Now consider the case of the cell with more than one hole (or blocked site). Integration of Equation (3) for more than one hole will result in

$$\frac{V_o}{V} = e^{-\beta jt/V} \tag{12}$$

where j is the number of damaged sites in that cell. The average concentration gradient, $\bar{g} = (c' - c)$, within all the cells is

$$\bar{g} = \frac{\sum_{j=1}^{N} g_i}{N} \tag{13}$$

where the summation extends over all N cells. Now if the holes in the cells may be considered equivalent, the summation in Equation (13) may be replaced by

$$\bar{g} = \frac{\sum_{j=1}^{K} N_j g_i}{N} \tag{14}$$

where N_j is the number of cells having j holes. The summation extends over all concentrations of holes per cell. Assuming that the number of cells having any given number of holes, j, is related to a Poisson distribution, any number of cells, N_j, may be written

$$N_j = N \cdot P(x_j) \tag{15}$$

where $P(x_j)$ is the Poisson probability term,

$$P(x_j) = \frac{e^{-\lambda} \lambda^j}{j!} \tag{16}$$

where λ is the average number of damaged sites per cell. Thus Equation (14) may be written

$$\bar{g} = \sum_{j=0}^{\infty} P(x_j)\, g_i \;;$$

$$\frac{\bar{g}}{g_o} = \frac{V_o}{V} = \sum_{j=0}^{\infty} P(x_j) e^{-\beta_j t/V} \quad . \tag{17}$$

As written, Equation (17) would imply that cells would swell indefinitely as would indeed be the case were the membrane infinitely stretchable and were pore sizes never expanded enough to allow macromolecular constituents to leak out. Spherocytosis occurs, however, at a volume approximately 154 to 176% of the original discoid cell volume[3.2, 3.35] at which point hemoglobin leaks out rapidly and the cell shrinks back to its original discoid shape. This effect must then be included in the model.

The change in volume whereby a cell swells to about 160% of its original volume corresponds to a concentration gradient ratio, $\bar{g}/g_o = 0.625$. All cells for which the diffusion term in Equation (17) has exceeded the dimensions of the maximum permissible volume ratio, that is for which

$$e^{-\beta_j t/V} < 0.625 \quad , \tag{18}$$

will have released their internal hemoglobin and the stroma will have returned to the original shape. Since the diffusion parameter, β, is constant for all cells, the critical factor which will determine the rate of becoming ghosts will be the number of psuedo-holes or leaky sites, j, per cell. At any given time, all cells which have more than a certain number of leaky sites, M_c, (all leaky sites assumed equivalent) will have become ghosts. M_c is then directly dependent upon the radiation dose received. At infinite time,

$$\lim_{t \to \infty} \frac{V}{V_o} = 1 \quad ; \tag{19}$$

that is, all cells will either have hemolyzed, the resulting ghosts being at the original cell volume, or the cells will have undergone no radiation damage and will have retained their initial size and volume throughout. The latter condition neglects aging effects, since at infinite time in the actual physical system all cells will have hemolyzed.

This observation will not affect the results, however, since over the time interval experimentally examined, aging effects will be negligible. Thus, Equation (17) must be written

$$\frac{V_o}{V} = \sum_{(j=0)}^{M_c} \frac{\lambda^j e^{-\lambda} \cdot e^{-\beta t j/V}}{j!} + \sum_{(j=M_c+1)}^{\infty} \frac{\lambda^j}{j!} e^{-\lambda} \quad . \tag{20}$$

To facilitate the fitting of the derived equation to the experimental results, a nonlinear fitting procedure was used. This procedure, entitled NELLY, as programmed for use on the IBM 7090 computer employs a truncated Taylor's expansion to fit any nonlinear equation having finite and continuous first derivatives. Input information includes the data points, equations for the partial derivatives with respect to the undetermined parameters, and initial estimates for the parameters. Equation (20) may not be differentiated such that an explicit expression for the partial derivative with respect to the

parameter, M_c, may be written. Thus to use NELLY, it is necessary to determine the best fit parameters, λ and β, using an arbitrary value for M_c. From the first set of parameters, a new value for M_c is calculated and another fit is tried. Iteration continues until successive values of M_c are equal. Equation (20) was fitted to cell swelling data reported in the preceding paper.[3.33] The results are plotted in Figure 3.15. Fitted parameters were

$$\lambda = 2.90 \pm 0.05$$
$$\beta = 0.00127 \pm 4.9 \times 10^{-5} \quad .$$

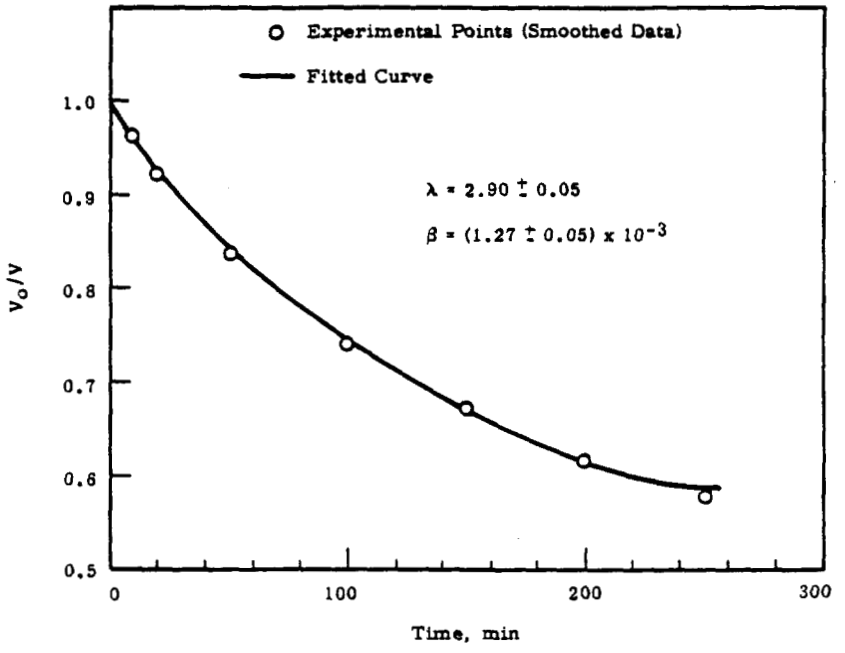

FIGURE 3.15

Rate of Swelling of Cells Exposed to Co^{60} Gamma Radiation (1.22×10^5 rads total dose)

Measurements of cell membrane thickness have been reported of 50 to 1000 Å, the 100 to 500 Å range presently considered to be the most accurate.[3.36, 3.37] Assuming then, a 250 Å membrane thickness, a pore radius of 4.0 Å,[3.29] and a cell volume of 90 μ^3,[3.32] the apparent diffusion coefficient, D, calculated from the value of β is 5.0×10^{-7} cm^2/sec. In the present case, diffusion occurs through an average of 2.9 damaged transport sites per cell. The

parameters required for a proper curve fit are significant. The calculated diffusion coefficient, 5×10^{-7} cm^2/sec, may be compared with diffusion coefficients of 1.5×10^{-5} cm^2/sec for KCl in the giant axon of Sepia and 5.3×10^{-9} cm^2/sec for the mutual diffusion coefficients of some proteins in water.[3.38] The average range of mutual diffusion coefficients for protein-water systems is between 10^{-7} and 10^{-10} cm^2/sec.[3.39]

It is difficult to make further comparisons because of the large uncertainties in the values used to calculate D. The average number of holes per cell, λ, may not be considered an absolute number, but instead is the apparent number of damaged sites or the number of functional holes caused by irradiation. It would be anticipated that: (1) many transport sites would be only partially damaged, and (2) that other undamaged sites would tend to distribute the resulting heavier pumping load such that the effective number of blocked sites would be less than the actual number. It has been calculated that the density of ferry terminals on the outer surface of human red cells is only one per 10^6 $\mathring{A}^2$ of cell surface.[3.40] Thus, it is not surprising that the erythrocyte is relatively radiation resistant.

It is of interest to compare the present model with another by Dick[3.38] appearing recently. In the latter model, osmotic driving forces were weighted more heavily than in the model presented here. Consequently diffusion boundaries were treated as if fixed. The osmotic model gave the equation for cell swelling.

$$\frac{V_e - V_t}{V_e - V_o} \cdot \frac{V_o}{V_t} = \sum_{n=1}^{\infty} Q \cdot \exp\left[-\theta_n^2 \; Dt/(\delta/2)^2\right]$$

where Q is a function of a permeability coefficient and the osmotic pressure; V_t is the total volume of the cell at various times, t, where t = 0 for initial time and t = e for the time when the cell reaches equilibrium with the external solution; δ is the membrane thickness; and D is the mutual diffusion coefficient. Dick's model was derived for normal osmotic swelling and did not consider the effect of attack upon transport sites by lysins.

The present results do not allow the identification of any one unique mechanism for free radical initiated inhibition of active transport; it is probable that the total effect is due to a combination of many related primary and secondary events.

Development of Apparatus and Techniques for Pulsed Radiolysis - W. D. Felix

To permit the study of individual fast reactions in the radiation chemistry of biochemical systems, pulsed radiolysis apparatus capabilities have been developed for use with a 2 MeV electron accelerator. A detection system consisting of light source, spectrophotometer, and oscilloscope was used to investigate the time dependent variation of concentration of optically absorbing species produced by the radiation or by intermediate reaction. Modifications in accelerator operation from pulsing by beam sweep to pulsing from the source are also described.

The theories of chemical reactions apply to every rate process. In living cells, however, processes which were once thought to be simple reactions have been shown to involve a series of consecutive and cyclic reactions.[3.41] Inasmuch as the very complicated processes occurring during irradiation of a biological species undoubtedly depend upon a multitude of individual, consecutive, and interlinked reactions, it would seem logical before undertaking any analysis of the whole as an overall rate process, first to consider individual, isolated systems of reactions.

The principal problem in the radiation chemistry of an isolated biological system becomes that of determining absolute rates and mechanisms of the reactions of primary and intermediate radicals with each other and the solute. Classical methods of kinetic research normally permit the study of reactions with half-times of minutes or at least a few seconds. In the last decade this situation has rapidly changed with the advent of instrumentation and techniques for examining reactions with half-times down to 10^{-9} second.[3.42] The fast detection of the changes involved in these reactions is accomplished with electronic aids having a time resolution commensurate with the specific elementary reaction. In radiation chemistry the determination of absolute rate constants has been most effectively done with

pulsed linear accelerators capable of delivering radiation intensities of up to 100 krads/pulse. Pulse lengths are generally kept shorter than or of the order of the life of the radicals being investigated. Thus, very short exposures in the micro- or millisecond range are generally required.[3.43] Radical reactions which are thereby induced in a small liquid sample may then be monitored by high speed spectrophotometry. Various arrangements for pulsed radiolysis have been described.[3.44-3.46]

The apparatus described here was designed to complement a Van de Graaff 2 MeV, electron accelerator. The physical arrangements of the irradiation room are shown in Figure 3.16. The electron beam passed through a small irradiation cell; a light beam passed through the cell perpendicular to the electron beam. An optical system using front surface mirrors and quartz lenses was used to focus the light beam onto the slit of a monochromator located behind a lead brick shield.

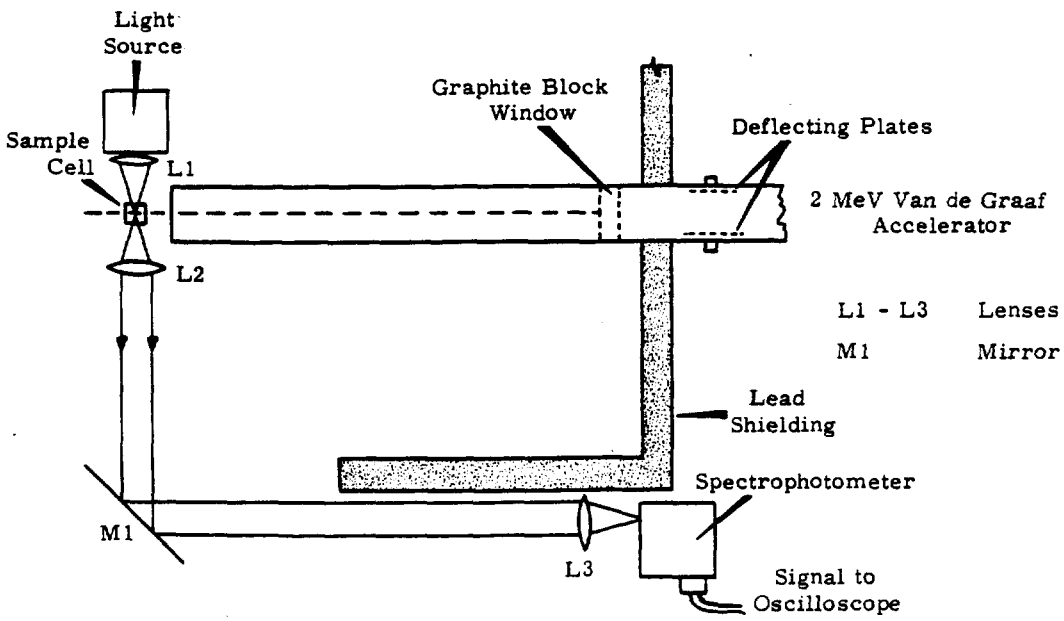

FIGURE 3.16

Physical Arrangement of Pulse Radiolysis Laboratory

Pulsing was effected by sweeping the beam past a 6 mm window in a graphite block in the evacuated beam tube. The beam which emerged from the accelerator terminal passed between a set of parallel deflection plates

located approximately midway along the evacuated tube. Impressing a 4 kV positive charge on one plate while holding the opposite plate at 4 kV negative caused the beam to be deflected away from the slit and onto the graphite block. The switching circuitry that controlled the beam deflection plate charge was designed to eliminate bounce or flutter in the sweep. With this arrangement it was possible to get 0.1 msec burst of 2 MeV, 200 μA electrons, where 1 msec beam sweep corresponds to approximately 1 krad total dose. The shape of the pulse is shown in the oscilloscope trace in Figure 3.17.

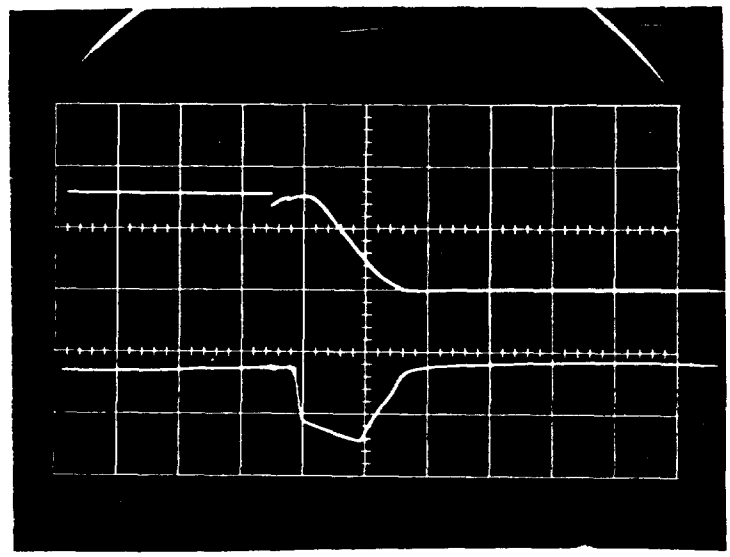

FIGURE 3.17

Upper Signal: Single Oscilloscope Trace Showing the Decay of the Optical Absorption Signal of Erioglaucine in Aerated Water at 631 mμ
Lower Signal: Time-Profile of the Electron Pulse
(Horizontal: 1 division = 1 msec/cm; vertical: 1 division = 0.5 V/cm.)

To investigate the dose distribution in the irradiation cells, stacks of polyvinyl chloride coverslips (0.22 mm thick, 2 by 2 cm) were exposed to the electron beam at various distances from the aluminum exit window. Relative density distributions both parallel to and in the plane perpendicular to the beam were determined from photometric measurements of the plastic discoloration. Since this dosimeter is temperature sensitive, it was necessary to cool the stack uniformly during irradiation. Cooling was effected

by alternating the plastic plates with sheets of aluminum foil, the entire stack being attached to an aluminum block immersed in a cold bath (-80 C). Density variation along the plane perpendicular to the beam and 9 cm from the beam exit port was less than 7%. Density variation within the stack was less than 5% for an equivalent liquid sample at least 7 mm deep using 2 MeV electrons.

Transient species are detected photometrically. The analyzing light was from a xenon (150 W) or xenon-mercury (200 W) high pressure lamp. Automobile storage cells were used as the power supply for the lamp to avoid the ac ripple usually associated with high current rectification circuits. For lamp ignition and for the first few milliseconds of sustained operation, the batteries were connected in series with a 75 W power supply. The monochromator was a low resolution, high aperture, grating instrument.* The signal from a 1P28 photomultiplier tube at the exit slit of the monochromator was fed to a dual beam oscilloscope through a dc differential amplifier. Immediately before the pulse, the signal was zeroed with the internal dc standard voltage. The zero signal was then compared with the signal level following the pulse. Light fluctuation over the short time interval involved was minimal. The oscilloscope display was photographed on high speed Polaroid® film. A double beam, scanning spectrophotometer is presently being modified for use with the accelerator. With this secondary detection facility, it will be possible to directly scan and quantitatively record steady state concentrations of transient species under conditions of continuous irradiation.

An example of an oscilloscope trace is shown in Figure 3.17 for the radiolysis of a solution of erioglaucine (6.0×10^{-6} M) monitored at the major visible absorption peak (631 mμ). The decay of the dye occurred within a much shorter half-life than could be determined with the pulse width used. During the preliminary pulsed irradiation experiments, it became apparent that background radiation was contributing significantly to the total dose that a sample received. In the few seconds required to ready the accelerator for pulsing and for following the decay, the sample received

* Farrand Optical 103420

approximately as much dose from the background (i.e., leakage through the graphite block and down the tube) as from a single millisecond burst. Even with wider beam deflection and better shielding, similar accelerator systems which use the beam sweep method have also shown considerable background dose.[3.46]

To eliminate background radiation, to increase the dose per pulse and to decrease the pulse width, the accelerator is presently being modified whereby pulsing is effected at the high voltage end. With this modification it will be possible to obtain pulses as short as 1 μsec at 30 mA beam current.[3.47] Since the only electrons to reach the sample are contained in the burst, there is no background dose. The pulsing circuit is repetitive for variable on-off periods. With this capability it will be possible to examine a large spectrum of radiation induced reactions from the very rapid reactions with half lives on the order of a few microseconds to the decay of very long lived species with half lives of seconds or minutes. Thus, it will be possible to study individual free radical reactions over a continuous range of eight powers of ten with respect to time.

Radioanalytical Methods

Cs^{137} in Alaskan Eskimo Hair* - T. M. Beasley and H. E. Palmer**

The measurement of Sr^{90} in the hair of rats injected with various quantities of this isotope has stimulated interest in the analysis of hair as a possible means of estimating radioisotope concentrations in the body.[3.48] Cs^{137} has been measured in the hair of Alaskan Eskimos whose Cs^{137} body burdens were determined by whole body counting techniques.

Twenty hair samples showed detectable amounts of Cs^{137}. Male hair samples gave concentrations ranging from 3 to 8 disintegrations/min-g of hair/μCi Cs^{137} in the body while values for the female hair samples showed less consistence and ranges of 1 to 20 disintegrations/min-g of hair/μCi Cs^{137} in the body. Since the hair sample did not represent the hair formed at the time which the whole body count was made and undoubtedly contained hair which was not all the same age since its formation, the range in values is not surprising.

---

* Accepted for publication in Health Physics.

** Physics and Instruments Department

Separation of Sr^{90} from Hair - T. M. Beasley

The analysis of hair as a method of determining Sr^{90} body burdens[3.48, 3.49] requires a method of isolating the isotopes in a form suitable for beta ray counting and subsequent determination of the Sr^{90} daughter, Y^{90}. Numerous schemes have been devised for separating radiostrontium from a variety of matrices,[3.50] but nothing has been published concerning the analysis of hair for strontium.

Spectrochemical analyses of hair elsewhere[3.51] and in this laboratory[3.52] have shown the following inorganic constituents to be present: Ca, Mg, Al, B, Fe, Mn, P, Pb, Si, Zn, and Ti. Also present in a rather large amount (47.7 ± 5.5 mg/g) is sulfur.[3.53] The presence of both calcium and sulfur as major constituents in hair complicates its analysis for strontium in that both wet chemical and dry ashing procedures used for digesting the hair lead to the formation of acid insoluble $CaSO_4$ that carries the trace amounts of strontium present in the sample.

The presence of sulfate in the hair residues was determined on a sample obtained by wet ashing hair with a mixture of concentrated nitric and perchloric acid, and on a similar hair sample dry ashed in an atomic oxygen furnace. The ash resulting from the atomic oxygen furnace was dissolved in 6M HNO_3 and barium ion, as the chloride, was added to the solution. The white precipitate that formed was subsequently identified by X-ray diffraction as $BaSO_4$. Identical results were obtained where barium ion was added to the perchloric acid residue.

Since sulfate cannot be eliminated in the analysis, precipitation of strontium sulfate from the acid digest can be used in isolating the radiostrontium. The mixed $CaSO_4$-$SrSO_4$ precipitate can then be converted to the carbonate by fusion with sodium carbonate and dissolved in acid; any one of several standard radiochemical methods can then be employed to isolate the strontium.[3.50]

0028396

REFERENCES

3.1 D. R. Kalkwarf and R. W. Henkens. "Kinetics of Radiation-Induced Hemolysis of Human Red Blood Cells," Hanford Radiological Sciences Research and Development Annual Report for 1962, HW-77609, p. 3.82. January 1963.

3.2 J. F. Hoffman, M. Eden, J. S. Barr, and R. H. S. Bedell. "The Hemolytic Volume of Human Erythrocytes," J. Cellular Comp. Physiol., vol. 51, p. 405. 1958.

3.3 J. T. Dodge, C. Mitchell, and D. J. Hanahan. "The Preparation and Chemical Characteristics of Hemoglobin-Free Ghosts of Human Erythrocytes," Arch. Biochem. Biophys., vol. 100, pp. 119-130. 1963.

3.4 C. Araki. "Seaweed Polysaccharides," Proc. Fourth Intern. Cong. Biochem., 1958, Vienna, vol. I: 15. 1959.

3.5 P. H. von Hippel and K.-Y. Worg. "Neutral Salts: The Generality of Their Effects onthe Stability of Macromolecular Conformations," Science, vol. 145, pp. 577-580. 1964.

3.6 A. O. Allen. Radiation Chemistry of Water and Aqueous Solutions, D. Van Nostrand, Princeton, New Jersey, 1961. pp. 43-48.

3.7 D. R. Kalkwarf. "The Effect of Temperature on Radical-Capturing Reactions in Irradiated Aqueous Solutions," Hanford Radiological Sciences Research and Development Annual Report for 1963, HW-81746, p. 3.105. January 1964.

3.8 D. R. Kalkwarf. "The Effect of Temperature on Radical-Capturing Reactions in Irradiated Aqueous Solutions," Hanford Radiological Sciences Research and Development Annual Report for 1962, HW-77609, p. 3.75. January 1963.

3.9 T. Henriksen. "ESR Studies on Irradiated Frozen Aqueous Solutions of Sulfur Compounds," J. Chem. Phys., vol. 38, pp. 1926-1933. 1963.

0028397

REFERENCES (Contd.)

3.10 H. Fricke and J. K. Thomas. "Pulsed Electron Beam Kinetics," Radiation Res. Suppl., vol. 4, pp. 35-53. 1964.

3.11 R. N. Diebel and D. R. Kalkwarf. "Kinetic Studies of Organic Radicals Formed in Irradiated Aqueous Solution," Hanford Radiological Sciences Research and Development Annual Report for 1963, HW-81746, pp. 3.113-3.119. January 1964.

3.12 W. Köhnlein and A. Müller. Phys. Med. Biol., vol. 6, pp. 599-604. 1962.

3.13 D. R. Kalkwarf. "Erioglaucine as a Chemical Dosimeter," Radiological Chemistry Annual Report, January - December 1960, HW-68533. pp. 57-59.

3.14 A. O. Allen. "Radiation Yields and Reactions in Dilute Inorganic Solutions," Radiation Res. Suppl., vol. 4, p. 57. 1964.

3.15 R. N. Diebel and D. R. Kalkwarf. "Kinetic Studies of Organic Radicals Formed in Irradiated Aqueous Solution," Hanford Radiological Sciences Research and Development Annual Report for 1963, HW-81746, p. 3.113. January 1964.

3.16 A. O. Allen. "Radiation Yields and Reactions in Dilute Inorganic Solutions," Radiation Res. Suppl., vol. 4, p. 54-73. 1964.

3.17 L. H. Piette, P. Ludwig, and R. N. Adams. "Electron Paramagnetic Resonance and Electrochemistry. Studies of Electrochemically Generated Radical Ions in Aqueous Solution," Anal. Chem., vol. 34, p. 916-920. 1962.

3.18 P. L. Kolker and W. A. Waters. "The Radical-Anions of Para-Substituted Aromatic Nitro-Compounds," J. Chem. Soc. (London) p. 1136-1141. 1964.

3.19 D. Danon. "Osmotic Hemolysis by a Gradual Decrease in the Ionic Strength of the Surrounding Medium," J. Cellular Comp. Physiol., vol. 57, p. 111. 1961.

REFERENCES (Contd.)

3.20 T. A. J. Prankerd. The Red Cell, An Account of its Chemical Physiology and Pathology, Blackwell Scientific Publication, Oxford, 1961. p. 87.

3.21 A. K. Parpart and R. Ballentine. "Molecular Anatomy of the Plasma Membrane," Modern Trends in Physiology and Biochemistry, edited by E. S. G. Baron, Academic Press, New York. 1952.

3.22 H. Green, et al. "Effects of Antibody and Complement on Permeability Control of Ascites Tumor Cells and Erythrocytes," J. Exp. Med., vol. 110, p. 699. 1959.

3.23 L. L. M. van Deenen and J. de Gier. "Chemical Composition and Metabolism of Lipids in Red Cells of Various Animal Species," The Red Blood Cell, edited by C. Bishop and D. M. Surgenor, Academic Press, New York. 1964.

3.24 J. W. Harris. The Red Cell. Production, Metabolism, Destruction: Normal and Abnormal, Harvard University Press, Cambridge, Mass., 1963. p. 215.

3.25 A. K. Solomon. "Permeability of the Human Erythrocyte to Sodium and Potassium," J. Gen. Physiol., vol. 36, p. 57. 1952.

3.26 D. H. P. Streeten and A. K. Solomon. "Effect of Adrenocorticotropic Hormone (ACTH) and Adrenal Steroids on Potassium Transport in Human Erythrocytes," J. Gen. Physiol., vol. 37, p. 643. 1954.

3.27 G. L. Gold and A. K. Solomon. "Transport of Sodium into Human Erythrocytes in Vivo," J. Gen. Physiol., vol. 38, p. 389. 1955.

3.28 E. T. Dunham and I. M. Glynn. "Adenosinetriphosphatase Activity the Active Movements of Alkali Metal Ions," J. Physiol., vol. 156, p. 274. 1961.

3.29 A. K. Solomon. "Red Cell Membrane Structure and Ion Transport," J. Gen. Physiol., vol. 43, p. 1. 1960.

REFERENCES (Contd.)

3.30 R. P. Rand and A. C. Burton. "Mechanical Properties of the Red Cell Membrane. I. Membrane Stiffness and Intracellular Pressure," Biophysical J., vol. 4, p. 115. 1964.

3.31 J. F. Hoffman. "Physiological Characteristics of Human Red Blood Cell Ghosts," J. Gen. Physiol., vol. 42, p. 9. 1958.

3.32 J. W. Harris. The Red Cell. Production, Metabolism, Destruction: Normal and Abnormal, Harvard University Press, Cambridge, Mass., 1963. p. 127.

3.33 D. R. Kalkwarf and W. D. Felix. "Radiation Induced Swelling and Hemolysis of Red Blood Cells," p. 3.1, this report.

3.34 W. Jost. Diffusion in Solids, Liquids, Gases, Academic Press, New York, 1960. pp. 436-444.

3.35 W. B. Castle and G. A. Daland. "Susceptibility of Mammalian Erythrocytes to Hemolysis with Hypotonic Solutions," Arch. Inter. Med., vol. 60, p. 949. 1937.

3.36 J. W. Harris. The Red Cell. Production, Metabolism, Destruction: Normal and Abnormal, Harvard University Press, Cambridge, Mass., 1963. p. 200

3.37 T. A. J. Prankerd. The Red Cell, An Account of its Chemical Physiology and Pathology, Blackwell Scientific Publication, Oxford, 1961. p. 14.

3.38 D. A. T. Dick. "The Permeability Coefficient of Water in the Cell Membrane and the Diffusion Coefficient in the Cell Interior," J. Theoret. Biol., vol. 7, p. 504. 1964.

3.39 J. T. Edsall. The Proteins, edited by H. Neurath and K. Bailey, Academic Press, New York, 1963. vol. I, pt. B, p. 549.

3.40 A. K. Solomon, T. J. Gill, and G. L. Gold. "K Transport in Human Erythrocytes: Evidence for a Three-Compartment System," J. Gen. Physiol., vol. 40, p. 327. 1956.

REFERENCES (Contd.)

3.41 F. H. Johnson, H. Eyring, and M. J. Polissar. The Kinetic Basis of Molecular Biology, John Wiley and Sons, New York, 1954. p. 123.

3.42 E. F. Caldin. Fast Reactions in Solution, John Wiley and Sons, New York, 1964. p. 3.

3.43 H. Fricke and J. K. Thomas. "Pulsed Electron Beam Kinetics," Radiation Res. Suppl., vol. 4, p. 35. 1964.

3.44 R. L. McCarthy and A. MacLaughlin. "Transient Benzyl Radical Reactions Produced by High Energy Radiation," Trans. Faraday Soc., vol. 56, p. 1187. 1960.

3.45 L. M. Dorfman, I. A. Taub, and R. E. Buhler. "Pulse Radiolysis Studies. I. Transient Spectra and Reaction-Rate Constant in Irradiated Aqueous Solutions of Benzene," J. Chem. Phys., vol. 36, p. 3051. 1962.

3.46 J. P. Keene. "Pulse Radiolysis Apparatus," J. Sci. Instr., vol. 41, p. 493. 1964.

3.47 H. A. Schwarz. Unpublished Data, Brookhaven National Laboratory, December 1964. (Personal Communication).

3.48 B. J. Hopkins, L. W. Tuttle, W. J. Poiver, and W. H. Strain. "Sr-90 in Hair," Science, vol. 139. March 15, 1963.

3.49 R. J. Della Rosa and G. Peterson. "Strontium-90 in Beagle Hair," 9th Annual Meeting of Health Physics Society, to be published.

3.50 D. N. Sunderman and C. W. Townley. The Radiochemistry of Barium, Calcium, and Strontium, NAS-NS-3010, Office of Technical Services. 1960.

3.51 Unita Silvestri. "Ricerche Spettrografiche Sulla Composizione Chimica dei Capelli," Rendiconti delle Adunanze della Societa Medica Chirurgica di Bologna, vol. 127, pp. 66-72. 1955.

0028401

REFERENCES (Contd.)

3.52 D. F. Petersen, V. E. Mitchell, and W. H. Langham. "Estimation of Fast Neutron Doses in Man by $S^{32}(n,p)P^{32}$ Reaction in Body Hair," Health Physics, vol. 6, pp. 1-5. 1961.

3.53 T. M. Beasley. Unpublished Data, Pacific Northwest Laboratory, Richland, Washington.

3.54 R. Ko. Electrodeposition of Plutonium from Acid Solution, HW-32673. 1956.

3.55 R. W. Perkins. "The Direct Measurement of Radionuclides in Bioassay Samples by Multidimensional Gamma-Ray Spectrometry," Proceedings of the Tenth Annual Conference in Bioassay and Analytical Chemistry, October 8-9, 1964, Cincinnatti, Ohio.

3.56 R. W. Perkins. An Anticoincidence Shielded-Multidimensional Gamma-Ray Spectrometer, HWSA-3726. September 22, 1964.

3.57 R. W. Perkins, C. W. Thomas, and J. M. Nielsen. Air-Borne Radionuclide Measurements and Physical Characteristics Determination, HWSA-3742. October 15, 1964.

3.58 L. J. Kirby, W. B. Silker, and R. W. Perkins. Determination of Radioactive Rare Earths in Reactor Effluent Water, TID-7568 PT2, pp. 214-229. 1959.

3.59 C. W. Thomas and W. B. Silker. The Estimation of Aluminum Corrosion from Reactor Coolant Activity Concentration, HW-81746. 1964.

3.60 Nucleonics, Margaret Beach Glos, asst. editor, vol. 22, no. 5, p. 50. 1964.

3.61 A. J. Tavendale, Nucl. Instr. Methods, vol. 26, p. 183. 1964.

3.62 C. R. Hill. "A Method of Alpha Particle Spectroscopy for Materials of Very Low Specific Activity," Nucl. Instr. Methods, vol. 12, pp. 299-306. 1961.

REFERENCES (Contd.)

3.63 R. V. Osborne and C. R. Hill. "High Resolution Alpha Spectroscopy at Very Low Specific Activities," Nucl. Instr. Methods, vol. 29, pp. 101-106. 1964.

3.64 C. R. Hill. "An α-Spectrometer for Normal Biological Levels of Activity," Health Physics, vol. 8, pp. 91-92. 1962.

3.65 C. R. Hill. "Identification of α-Emitters in Normal Biological Materials," Health Physics, vol. 8, pp. 17-25. 1962.

3.66 R. W. Perkins, J. M. Nielsen, and C. W. Thomas. "Air Concentrations of Twelve Radionuclides from 1962 through Mid-1964," Science, vol. 146, pp. 762-764. 1964.

3.67 R. W. Perkins. "Ag^{110m} in the Atmosphere," p. 3.68, this report.

3.68 R. W. Perkins, C. W. Thomas, and J. M. Nielsen. "Airborne Radionuclide Measurements and Physical Characteristics Determinations," Proceedings of the 2nd AEC Fallout Conference, Germantown, Maryland, November 3-6, 1964.

3.69 R. W. Perkins. "An Anticoincidence Shielded Multidimensional Gamma-Ray Spectrometer," Nucl. Instr. Methods, to be published.

3.70 T. R. Folsom. Unpublished Data, Scripps Institute of Oceanography, University of California, La Jolla. (Personal Communication).

3.71 R. W. Perkins. "Columbia River Sediment and Transport Studies," Hanford Radiological Sciences Research and Development Annual Report for 1963, HW-81746, pp. 3.86-3.94. 1964.

3.72 W. T. Lammers. "Density Gradient Separation of Organic and Inorganic Particles by Centrifugation," Science, vol. 139, pp. 1298-1299. 1963.

3.73 N. H. Aguilera and M. L. Jackson. "Iron Oxide Removal from Soils and Clays," Soil Sci. Soc. Am. Proc. vol. 17, pp. 359-364. 1953.

3.74 Jack L. Nelson, R. W. Perkins, and J. M. Nielsen. Progress in Studies of Radionuclides in Columbia River Sediments, HW-83614. August 1964.

REFERENCES (Contd.)

3.75 R. W . Perkins. "Gamma-Ray Spectrometric Systems of Analysis," Proceedings of the Second United Nations International Conference on the Peaceful Uses of Atomic Energy, vol. 28, p. 445, Geneva. 1958.

3.76 R. W. Perkins. "An Anticoincidence Shielded-Multidimensional Gamma-Ray Spectrometer," Nucl. Instr. Methods, to be published.

3.77 J. J. Davis, R. W. Perkins, R. F. Palmer, W. C. Hanson, and J. F. Cline. "Radioactive Materials in Aquatic and Terrestrial Organisms Exposed to Reactor Effluent Water," Proceedings of the Second United Nations International Conference on the Peaceful Uses of Atomic Energy, vol. 18, p. 423, Geneva. 1958.

3.78 J. L. Nelson, R. W. Perkins, W. L. Haushild. "Flow Time Measurements of the Columbia River Using Radioactive Tracers Introduced to the Columbia River," Limnology and Oceanography, to be published.

3.79 R. W. Perkins. Anion Exchange-Precipitation Procedure for the Separation of Na^{24} from Reactor Effluent Water, HW-38573. August 10, 1955.

3.80 S. G. Rudstam. Phil. Mag., vol. 46, p. 344. 1955.

3.81 V. I. Baranovskii and A. N. Murin, U.S.S.R. Bulletin, Physical Series, vol. 25, p. 893, 1961, Academy of Sciences. (English Translation).

3.82 L. Winsberg. Geochim. et Cosmochim. Acta, vol. 9, p. 183. 1956.

3.83 C. W. Thomas and R. W. Perkins. Unpublished Data, Pacific Northwest Laboratory, Richland, Washington. (Personal Communication).

3.84 R. W. Perkins. "I^{131} Measurement in Large Volumes of Columbia River," p. 3.90, this report.

3.85 J. D. Ludwick. Dual Atmospheric Tracer Techniques for Diffusion Studies Using Phosphorescence-Fluorescence Analysis, HW-70892, March 1961.

3.86 J. D. Ludwick and P. W. Nickola. A Fluorescein Analysis Technique for Use in Atmospheric Diffusion Studies, HW-77609. January 1963.

CHEMICAL EFFLUENTS TECHNOLOGY

Soil Chemistry and Geochemistry

Some Adsorption, Diffusion, and Dispersion Characteristics of Anions in Soils - B. F. Hajek

Adsorption, diffusion and dispersion characteristics of Cl^-, PO_4^{-3}, CrO_4^{-2} and $Cr_2O_7^{-2}$ were determined in a Hanford soil. Adsorption selectivity is $Cr_2O_7^{-2} > AsO_4^{-3} > PO_4^{-3} > CrO_4^{-2}$ and Cl^-. Diffusion coefficients ranged from 0.21×10^{-6} cm^2/sec to 1.2×10^{-6} cm^2/sec. Laboratory soil columns were used to determine dispersion and rate of anion movement through soil relative to flow rate.

Studies of some anion-soil reactions were conducted to further characterize simultaneous transfer of solutes and solvent through soil material. Phosphate, arsenate, chloride, chromate, and dichromate traced with P^{32}, As^{74}, Cl^{36}, and Cr^{51} were selected for study because of their presence in reactor effluent water; however, As^{74} was substituted for As^{76} because of its slower decay rate. Chloride was used to trace water movement.

Equilibrium distribution coefficients (ratio of the amount adsorbed per gram of soil to the equilibrium solution concentration) are given in Table 4.1. No positive adsorption of chloride or chromate was detected.

TABLE 4.1

ANION EQUILIBRIUM DISTRIBUTION COEFFICIENTS

Anion	Tap Water	Distilled Water	ppm 10	25	50	100
PO_4^{-3}	10.84	4.91	1.88	1.69	1.13	1.33
AsO_4^{-3}	12.97	9.96	6.78	6.07	5.54	5.28
$Cr_2O_7^{-2}$	34.39	14.50	30.70	24.83	25.89	29.68

However, negative chloride adsorption was noted which is easily explained by anion exclusion from the double layer and hydration of mineral surfaces. Increased adsorption of phosphate and arsenate from trace quantities in tap

water is probably due to salt effects. This so-called salt effect on anion adsorption is related to pH and other soil properties. The effect is large at high pH (>7), usually decreases with falling pH, and can become negative.[4.1]

The apparent large adsorption of the dichromate ion very likely does not involve anion retention. It is likely that dichromate oxidizes organic matter present in the soil. This reaction would cause chromium to be reduced from the VI to the III valence state and to be adsorbed as a cation.

From the limited data presented here it is not possible to designate some anion exchange capacity value for soils. Any small change in pH, ionic strength, accompanying ions, and equilibrium time will greatly change the amount of sorption.

When solutes are transferred through a porous medium, such as soil, some frontal dispersion is caused by diffusion. The fact that diffusion and hydraulic dispersion coefficients must be separated in dispersion equations has been verified.[4.2]

Diffusion coefficients, as defined by Fick's first law, of chloride, arsenate, and chromate are given in Table 2. The values were determined experimentally by using diffusion cells. Fick's law was solved for diffusion through a central plane from one half-cell to another. The half-cells were assumed to be infinite in length, that is, no concentration change occurs at the outer ends of each half-cell.

TABLE 4.2

DIFFUSION COEFFICIENT VALUES FOR CHLORIDE, ARSENATE, AND CHROMATE THROUGH SOIL

Volumetric Moisture Content	$D_p \times 10^6$, cm^2/sec		
	Cl^-	AsO_4^{-3}	CrO_4^{-2}
0.27	1.20	0.23	0.43
0.20	0.80	0.21	0.25

0028406

The diffusion coefficient is determined in the expression,

$$\frac{D_p}{\theta} = \left(\frac{\ell}{2}\right)^2 \frac{\pi}{t} \left(\frac{q}{q_\infty}\right)^2$$

in which

D_p = porous system diffusion coefficient

θ = volumetric moisture content

ℓ = length of each half-cell

t = time that diffusion was allowed to occur between half-cells

q = total quantity that diffused through the central plane between the half-cells

q_∞ = amount of material having diffused past the central plane when time is infinite. This quantity will be one-half the initial amount of diffusing ion added.

When ions, such as arsenate, that react with the porous medium are considered, θ is replaced by $\theta + K_d BD$ in which K_d is the equilibrium distribution coefficient, and BD is the bulk density.[4.3]

Anion breakthrough curves for soil columns 40 cm long and 1.9 cm diam are shown in Figure 4.1. These data are presented as a plot of C/C_o versus column throughput volume on log probability paper. Chloride breakthrough corresponds closely to water travel time since no adsorption occurs and the exclusion volume is small. The average travel time and hydraulic dispersion of chloride and chromate ions could be predicted by evaluating the expression,[4.4]

$$b \frac{\partial c}{\partial t} = D \frac{\partial^2 c}{\partial x^2} - v \frac{\partial c}{\partial x}$$

in which

c = concentration

t = time

D = dispersion coefficient (includes both hydraulic dispersion and diffusion coefficients).

x = distance

v = flow velocity

b = adsorption factor (b = 1 when no adsorption occurs).

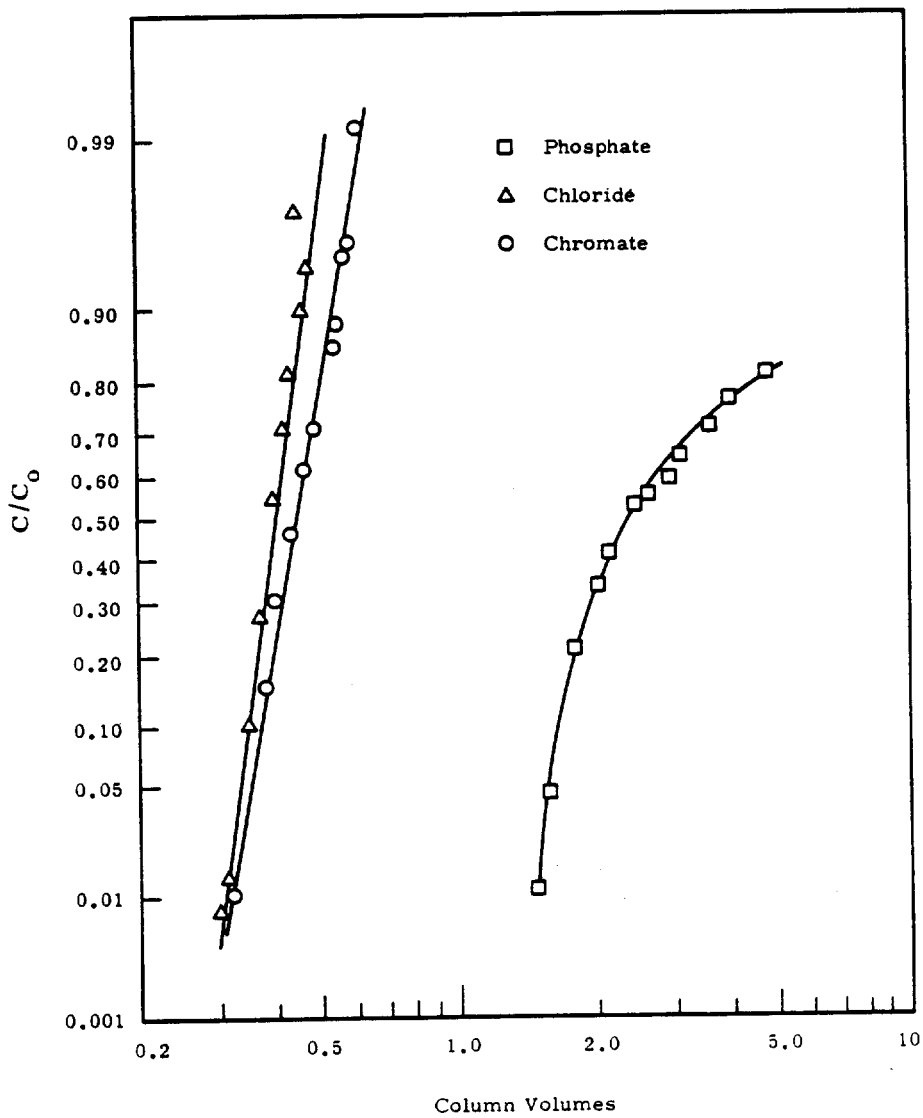

FIGURE 4.1

Phosphate, Chloride, and Chromate Breakthrough Curves

No equation was found that would satisfactorily predict phosphate (or arsenate with similar breakthrough characteristics) breakthrough. Slow reaction rates present the greatest problem.

Neg. No. 0650442

Clay Mineral Composition of Two Hanford Soils - B. F. Hajek

The clay portion (< 2μ) was fractionated from the surface horizon of two Hanford soils. Semiquantitative analysis of minerals made by X-ray diffraction analysis showed that montmorillonite is the dominant clay mineral. Vermiculite, mica, chlorite, and traces of kaolinite also were detected.

The mineralogical composition of the clay fraction from surface horizons of two Hanford soils was determined by X-ray diffraction analysis.

One soil represents surface soil material in the valley south of Gable Mountain on the Hanford project; the other was collected near the Columbia River in the vicinity of F-Reactor. Clay fractions were separated by a centrifuge procedure.[4.5] The fractionation followed treatments that removed exchangeable divalent cations, free carbonates, iron oxides, and organic matter.

The minerals detected are given in Table 4.3. Montmorillonite is the most abundant clay mineral in all fractions except the 2-0.2 μ fraction of the F-Reactor soil.

TABLE 4.3

MINERALOGICAL COMPOSITION OF CLAY FRACTIONS

	Montmorillonite	Vermiculite	Mica	Chlorite	Kaolinite
Valley soil 2 to 0.2μ	1	2	3	trace	--
<0.2μ	1	2	trace	--	--
F-Reactor soil 2 to 0.2μ	4	1	3	2	trace
<0.2μ	1	2	trace	3	--

Note: Amounts are ranked from 1 (most abundant) to 4 (least). Identification of trace quantities is not certain.

This study will be extended to include other Hanford soils, and more quantitative techniques will be employed in addition to X-ray analysis.

Clay minerals contribute most to the active portion of Hanford soils; for this reason a qualitative knowledge of the mineralogy is essential.

Furthermore, many studies have been made of radionuclide-clay mineral systems. Some of this basic knowledge can be applied to soil systems when the mineralogy is known.

Self-Diffusion Coefficients of Some Cations in Open Zeolites - L. L. Ames, Jr.

> Sodium, strontium, and cesium self-diffusion coefficients were determined in the natural zeolites erionite, phillipsite, and clinoptilolite and the synthetic zeolites Linde 4A and 13X. Cerium self-diffusion in 13X also was studied. Diffusion coefficients of from 1×10^{-9} to 1×10^{-6} cm^2/sec were obtained in aqueous systems at 50 C.

Self-diffusion values were obtained for several zeolites by loading a shallow bed with a nontraced solution. When equilibrium was reached between the bed and nontraced solution, a tracer was added and the increase of radioactivity on the bed noted as a function of time. These data were used to obtain an apparent diffusion coefficient by the method of Helfferich.[4.6] A typical diffusion curve is shown in Figure 4.2. Self-diffusion coefficients for two different grain size ranges are given in Table 4.4.

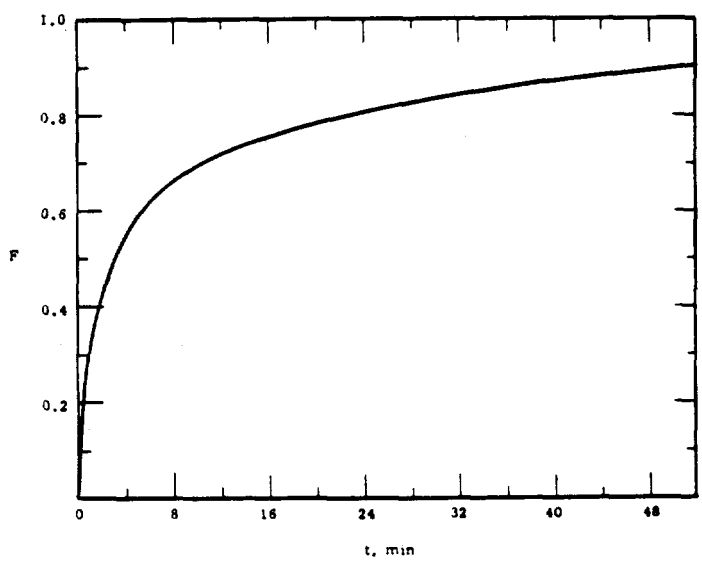

FIGURE 4.2

Corrected Curve for the Isotopic Diffusion of Sr^{85} in Type X at 50 C (Average particle radius was 1.85×10^{-2} cm, time to 50% exchange was 192 sec, and bed weight was 0.5 g.)

Neg. No. 0641928-4

TABLE 4.4

SELF-DIFFUSION COEFFICIENTS IN cm^2/sec AT 50 C IN TWO DIFFERENT ZEOLITE GRAIN SIZE RANGES

(Total equilibrium solution normality was 0.2)

Cation System	Erionite	Oregon Clinoptilolite	Phillipsite	Type X	Type A
			0.25 to 0.50mm		
Ce^{+3}–Ce^{144}	- -	- -	- -	2.46×10^{-9}	- -
Sr^{+2}–Sr^{85}	2.77×10^{-8}	1.17×10^{-8}	9.55×10^{-9}	5.37×10^{-8}	8.19×10^{-9}
Cs^{+}–Cs^{134}	1.43×10^{-6}	1.91×10^{-7}	4.30×10^{-7}	1.15×10^{-7}	1.23×10^{-7}
Na^{+}–Na^{22}	2.46×10^{-7}	7.83×10^{-8}	3.44×10^{-7}	1.56×10^{-7}	6.87×10^{-8}
			0.50 to 1.00mm		
Ce^{+3}–Ce^{144}	- -	- -	- -	2.33×10^{-9}	- -
Sr^{+2}–Sr^{85}	2.77×10^{-8}	1.03×10^{-8}	9.44×10^{-9}	5.65×10^{-8}	8.63×10^{-9}
Cs^{+}–Cs^{134}	1.42×10^{-6}	2.02×10^{-7}	4.72×10^{-7}	1.87×10^{-7}	1.18×10^{-7}
Na^{+}–Na^{22}	2.72×10^{-7}	8.85×10^{-8}	4.14×10^{-7}	1.68×10^{-7}	7.68×10^{-8}

TABLE 4.5

AVERAGE SELF-DIFFUSION COEFFICIENTS IN cm^2/sec

(Total solution normality was 0.2, with 0.1N solutions of each cation for mixed cation solutions; the radioactive cation is the measured cation in each case.)

Cation System	Erionite	Oregon Clinoptilolite	Phillipsite	Type X	Type A
			50 C		
Ce^{+3}–Ce^{144}	- -	- -	- -	2.40×10^{-9}	- -
Sr^{+2}–Sr^{85}	2.77×10^{-8}	1.10×10^{-8}	9.49×10^{-9}	5.51×10^{-8}	8.41×10^{-9}
Cs^{+}–Cs^{134}	1.43×10^{-6}	1.97×10^{-7}	4.51×10^{-7}	1.52×10^{-7}	1.21×10^{-7}
Na^{+}–Na^{22}	2.59×10^{-7}	8.43×10^{-8}	3.79×10^{-7}	1.62×10^{-7}	7.28×10^{-8}
Na^{+}-Ce^{+3}–Ce^{144}	- -	- -	- -	7.46×10^{-9}	- -
Na^{+}-Sr^{+2}–Sr^{85}	2.03×10^{-7}	4.71×10^{-8}	7.44×10^{-8}	8.40×10^{-8}	3.44×10^{-8}
Na^{+}-Cs^{+}–Cs^{134}	9.02×10^{-7}	1.66×10^{-7}	5.09×10^{-7}	1.46×10^{-7}	1.28×10^{-7}
			70 C		
Ce^{+3}–Ce^{144}	- -	- -	- -	3.82×10^{-9}	- -
Sr^{+2}–Sr^{85}	3.18×10^{-8}	1.67×10^{-8}	1.81×10^{-8}	1.15×10^{-7}	3.58×10^{-8}
Cs^{+}–Cs^{134}	2.58×10^{-6}	2.87×10^{-7}	5.70×10^{-7}	4.91×10^{-7}	2.58×10^{-7}
Na^{+}–Na^{22}	5.73×10^{-7}	9.55×10^{-8}	5.30×10^{-7}	4.30×10^{-7}	1.43×10^{-7}

Average self-diffusion coefficients for several zeolites at two different temperatures are shown in Table 4.5. Several mixed cation solutions also were used to obtain diffusion coefficients in mixed cation systems.

The higher valence cations were the slowest to diffuse, and univalent cations were the most rapid. Self-diffusion rates in the zeolites studied were, however, relatively rapid, being comparable to a highly cross linked organic resin. The effect of adding a slowly diffusing cation to a fast one is to slow the whole exchange system to an intermediate exchange rate.

Linde 13X Equilibria with Trivalent Cerium and Yttrium Cations - L. L. Ames, Jr.

Cation exchange equilibria of the zeolite Linde 13X with sodium-cerium, sodium-yttrium, and strontium-cerium systems were studied. A Linde 13X selectivity series of Sr > Ce ≈ Y > Na was found.

The zeolite cation exchange processes that are planned for use in the Hanford Waste Management Program[4.7] may be required to handle influent solutions containing rare earths. Only Linde 13X, of the several synthetic zeolites available for use, showed a significant trivalent cation capacity. The properties of Linde 13X are given in Table 4.6.

TABLE 4.6

LINDE 13X PROPERTIES, SODIUM-FORM

$\frac{SiO_2}{Al_2O_3}$	2.4
Binder, wt%	20.0
H_2O, wt%	25.0
Structural Type	Faujasite
Cerium Capacity, meq/g	3.6

A selectivity coefficient was determined at equilibrium and corrected for nonideal behavior of the cations in the solution and on the zeolite; this procedure resulted in a thermodynamic equilibrium constant. The methods used to correct for nonideality in the solution phase are given in the Appendix. The sodium-strontium correction method was given in a previous paper.[4.8] A typical isotherm for Linde 13X in a univalent-trivalent cation system is given in Figure 4.3. The thermodynamic data derived from the isotherms are given in Table 4.7. Note that the free-energy changes balance within ± 100 cal/mole, when rounded to the nearest 100 cal/mole. The free-energy change for the reaction $\frac{1}{3}(3Na_z + Ce_s \rightleftharpoons Ce_z + 3Na_s)$ plus the free-energy change for the reaction $\frac{1}{6}(3Sr_z + 2Ce_s \rightleftharpoons 2Ce_z + 3Sr_s)$ approximately equals the free-energy change for the reaction $\frac{1}{2}(2Na_z + Sr_s \rightleftharpoons Sr_z + 2Na_s)$ where the subscripts "z" and "s" refer to cations in the equilibrium solution, or on the zeolite. Linde 13X is highly selective for cerium in the presence of sodium but prefers strontium to both cerium and sodium.

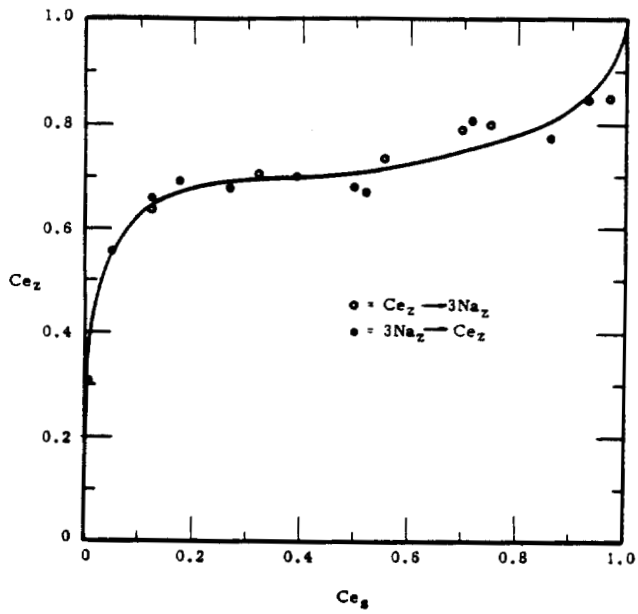

FIGURE 4.3

25 C Isotherm for the Reaction $3Na_z + Ce_s \rightleftharpoons Ce_z + 3Na_s$ with Type X

(Total equilibrium solution normality was constant at 0.5.)

Note: Ce_z = equivalent fraction of cerium on the zeolite.
Ce_s = equivalent fraction of cerium in the equilibrium solution.

TABLE 4.7

TYPE X THERMODYNAMIC DATA
DERIVED WITH BARRER AND MEIER'S EQUATION

$$\text{Log } \chi = \text{Log } \chi_{c_1} - \int_{\chi_{c_0}}^{\chi_{c_1}} B_z \, d\log \chi_c{}^{*}$$

(Log values are rounded to three places.)

$\text{Log } \chi_{c_1}$	$\int_{\chi_{c_0}}^{\chi_{c_1}} B_z \, d\log \chi_c$	Log χ	χ, 25 C	$\Delta G°$, 25 C
		$3Na_z \rightarrow Ce_z$		
-3.000	-4.695	1.695	45.6	-2300
		$2Na_z \rightarrow Sr_z$		
0.725	-0.574	1.299	19.9	-1800
		$3Sr_z \rightarrow 2Ce_z$		
-7.340	-7.220	-0.120	0.759	+200
		$3Na_z \rightarrow Y_z$		
-1.574	-2.394	0.820	6.61	-1100

* Reference 4.9.

Neg. No. 35853-3

Appendix

$NaCl-CeCl_3$ Mixed Electrolyte

Assuming that the mean activity coefficient is equal to

$$\left(f^{+v^+} \cdot f^{-v^-}\right)^{\frac{1}{(v^+)+(v^-)}}$$

where v^+ is the number of cations and v^- is the number of anions, and

$X_1 = Na^+$, $X_2 = Ce^{+3}$, and $Y = Cl^-$, then $f\begin{pmatrix}X_1Y\\X_2Y\end{pmatrix} = \left(f_{X_1} \cdot f_Y\right)^{1/2}$ and

$f\begin{pmatrix}X_2Y\\X_1Y\end{pmatrix} = \left(f_{X_2} \cdot f_{Y_3}\right)^{1/4}$.

Combining,
$$\frac{f_{X_1}^{\ 3}}{f_{X_2}} = \frac{\left(f_{X_1} \cdot f_Y\right)^{1/2}}{\left(f_{X_2} \cdot f_Y^{\ 3}\right)^{1/4}} = \frac{\left[f\begin{pmatrix}X_1Y\\X_2Y\end{pmatrix}\right]^6}{\left[f\begin{pmatrix}X_2Y\\X_1Y\end{pmatrix}\right]^4} \quad . \qquad (1)$$

Solving Equation (1) with Glueckauf's equation for a mixed electrolyte with a common anion, the result is:

$$\log \frac{\left[f\begin{pmatrix}X_1Y\\X_2Y\end{pmatrix}\right]^6}{\left[f\begin{pmatrix}X_2Y\\X_1Y\end{pmatrix}\right]^4} = \frac{r+3}{r+6}\left(3 \log f^{X_1Y} - 4 \log f^{X_2Y}\right) - \frac{3/2\,(r-3)}{I(1+I^{-1/2})} \cdot X_2,$$

where $f\begin{pmatrix}X_1Y\\X_2Y\end{pmatrix}$ = a mean activity coefficient for NaCl in the presence of $CeCl_3$

$f\begin{pmatrix}X_2Y\\X_1Y\end{pmatrix}$ = a mean activity coefficient for $CeCl_3$ in the presence of NaCl

f^{X_1Y} = a mean activity coefficient for NaCl

f^{X_2Y} = a mean activity coefficient of $CeCl_3$

X_1 = NaCl concentration in moles per liter

X_2 = $CeCl_3$ concentration in moles per liter

$r = X_1/X_2$

I = the total ionic strength

$SrCl_2$-$CeCl_3$ Mixed Electrolyte

If $X_1 = Sr^{+2}$, $X_2 = Ce^{+3}$, and Y = a common anion Cl^-, then by definition:

$$f^{X_1Y} = f\begin{pmatrix}X_1Y\\X_2Y\end{pmatrix} = \left(f_{X_1} \cdot f_Y{}^2\right)^{1/3}, \text{ and } f^{X_2Y} = f\begin{pmatrix}X_2Y\\X_1Y\end{pmatrix} = \left(f_{X_2} \cdot f_Y{}^3\right)^{1/4}, \text{ or}$$

$$\frac{\left(f_{X_1} \cdot f_Y{}^2\right)^{1/3}}{\left(f_{X_2} \cdot f_Y{}^3\right)^{1/4}} = \frac{\left[f\begin{pmatrix}X_1Y\\X_2Y\end{pmatrix}\right]^9}{\left[f\begin{pmatrix}X_2Y\\X_1Y\end{pmatrix}\right]^8} \quad . \tag{2}$$

Solving Equation (2) with Glueckauf's equation,

$$\log \frac{\left[f\begin{pmatrix}X_1Y\\X_2Y\end{pmatrix}\right]^9}{\left[f\begin{pmatrix}X_2Y\\X_1Y\end{pmatrix}\right]^8} = \frac{2r+3}{r+2}\left(\frac{9}{4}\log f^{X_1Y} - \frac{8}{3}\log f^{X_2Y}\right) - \frac{\frac{3}{4}(2r-3)}{I\,(1+I^{-1/2})} \cdot X_2$$

where

$f\begin{pmatrix}X_1Y\\X_2Y\end{pmatrix}$ = a mean activity coefficient for $SrCl_2$ in the presence of $CeCl_3$

$f\begin{pmatrix}X_2Y\\X_1Y\end{pmatrix}$ = a mean activity coefficient for $CeCl_3$ in the presence of $SrCl_2$

f^{X_1Y} = a mean activity coefficient of $SrCl_2$

f^{X_2Y} = a mean activity coefficient of $CeCl_3$

X_1 = a $SrCl_2$ concentration in moles per liter

X_2 = a $CeCl_3$ concentration in moles per liter

$r = X_1/X_2$

I = the total ionic strength.

Zeolite Cation Selectivity - L. L. Ames, Jr.

Previous study of the cation exchange characteristics of several natural and synthetic zeolites showed an apparent relationship between silica to alumina ratio and cation selectivity. Determination of cation exchange equilibria with high and low silica modifications of the same zeolite structure types confirmed that cation selectivity is a function of anionic site separation distance.

Cation specificity, according to Eisenman,[4.10] may be viewed as a result of interactions between (1) cations and water and (2) cations and anionic sites. Both the radii of the anionic sites and their distance apart on the zeolite structural framework influence the cation-zeolite interaction.

The anionic radii are approximately the same for all the zeolites (all have AlO_4 anionic sites), so anionic site separation distance becomes the controlling factor in cation selectivity. Data from previous selectivity work is summarized in Table 4.8. From a consideration on Table 4.8, the high silica zeolites, with larger anionic site separation distances, are the most cesium-selective from cesium-sodium systems, and the low silica zeolites, with lesser anionic site separation distances, are the most strontium-selective from strontium-sodium systems.

The zeolites shown in Table 4.9 were used to determine cation exchange equilibria with high and low silica to alumina modifications of the same structure. A typical exchange isotherm is given in Figure 4.4. The thermodynamic data derived from the isotherms is shown in Table 4.10. The relationship between cesium selectivity and silica to alumina ratio is apparently a straightforward one, but strontium selectivity is somewhat more complex. A probable cause of the anomalous strontium selectivity behavior is the nonhomogeneous nature of anionic site separation distances.

TABLE 4.8

RELATIONSHIP BETWEEN THE THERMODYNAMIC EQUILIBRIUM CONSTANT χ, AND SILICA TO ALUMINA RATIO FOR SEVERAL ZEOLITES AT 25 C

($Na_z \rightarrow Cs_z$ refers to the exchange of sodium on the zeolite to cesium on the zeolite, and $2\,Na_z \rightarrow Sr_z$ refers to the exchange of sodium on the zeolite to strontium on the zeolite.)

Zeolite	SiO_2/Al_2O_3	χ $Na_z \rightarrow Cs_z$	χ $2Na_z \rightarrow Sr_z$
Linde Type A (4A)	2.0	0.323	83.2
Linde Type X (13X)	2.4	0.355	19.9
Nevada Phillipsite	4	26.4	0.107
Linde AW-500	4 to 5	29.7	0.288
Nevada Erionite	6	32.9	0.794
Linde AW-400	6 to 7	39.0	0.363
Norton Zeolon	10	29.2	0.235
Hector Clinoptilolite	8 to 10	51.9	1.29

TABLE 4.9

COMPOSITIONS AND PROPERTIES OF THE SODIUM-BASED ZEOLITES USED IN THE STUDY

Zeolite	SiO_2/Al_2O_3	Structural Type	Anhydrous Unit Cell	Binder, wt%	Water, wt%	Measured Capacity, meq/g
Type X	2.4	Faujasite	$Na_{88}\,(AlO_2)_{88}(SiO_2)_{104}$	20	25	3.6
Type Y	4.6	Faujasite	$Na_{58}\,(AlO_2)_{58}(SiO_2)_{134}$	0	21	2.8
Type A	2.0	A	$Na_{12}\,(AlO_2)_{12}(SiO_2)_{12}$	10	30	3.9
ZK-4	3.3	A	$Na_{4.9}\,(AlO_2)_{5.6}(SiO_2)_{18.4}$	0	20	3.1

TABLE 4.10

THERMODYNAMIC DATA

($\Delta F°$ is the standard free-energy change for the exchange reaction indicated.)

Zeolite	SiO_2/Al_2O_3	χ, 25 C			$\Delta F°$, 25 C		
		$Na_z \rightarrow Cs_z$	$2Na_z \rightarrow Sr_z$	$3Na_z \rightarrow Ce_z$	$Na_z \rightarrow Cs_z$	$2Na_z \rightarrow Sr_z$	$3Na_z \rightarrow Ce_z$
Type X	2.4	0.355	19.9	45.6	+ 600	-1800	-2300
Type Y	4.6	6.46	19.5	91.2	-1100	-1800	-2700
Type A	2.0	0.323	83.2	--	+ 700	-2600	--
ZK-4	3.3	4.57	4.22	--	- 900	- 900	--

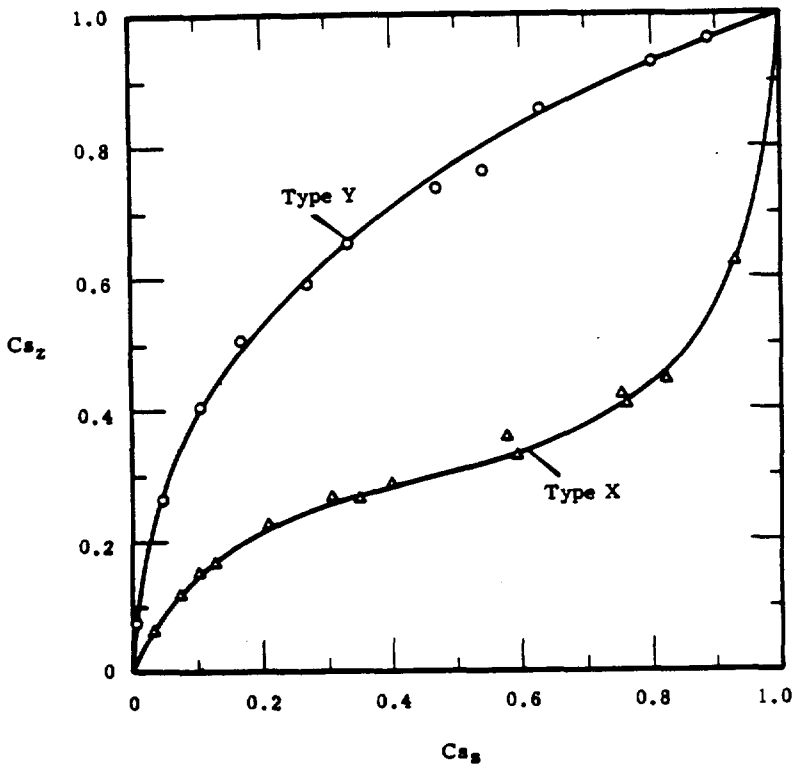

FIGURE 4.4

25 C Isotherm for the Reaction $Na_z + Cs_s \rightleftharpoons Cs_z + Na_s$ with Type X and Type Y

(Total equilibrium solution normality was constant at 1.0.)

Note: Cs_z = equivalent fraction of cesium on the zeolite.

Cs_s = equivalent fraction of cesium in the equilibrium solution.

Soil Physics

The Movement of Ground Waters in Confined Aquifers Beneath the Hanford Project - R. E. Brown

Regional recharge of a confined aquifer at seven possible sites near Hanford results in a general southeastward hydraulic gradient and flow path. Local irrigation and the recent Priest Rapids Dam pool impoundment appear to influence the flow of water and low-level wastes contained in the aquifer. The situation emphasizes the importance of knowledge of ground-water flow in three dimension and the geologic and hydrologic factors influencing flow paths, flow rates, and aquifer discharge areas.

Neg. No. 0643169-5

In 1960, proof of the gentle but progressively greater folding with depth of the Ringold Formation (up to angles of about 1°) permitted identification of aquifers in which low-level radiocontaminants could move to depth. Simultaneously the concept was recognized that ground waters could flow in confined aquifers beneath the Columbia River in directions locally not related to the river flow. Later, contaminants were identified as moving into an aquifer that becomes confined toward the Columbia River. In 1962, trace concentrations of radionuclides were detected in that highly confined aquifer in the upper part of the basalt series near and several hundred feet below the Columbia River. Stratigraphic studies confirmed that the wastes had entered the aquifer through an erosional window where the unfolded Ringold Formation silts and clays were eroded away, exposing the upper Beverly Member of the basalt series to recharge. Eastward the aquifer is confined first by the Ringold Formation silts and clays, then by the Elephant Mountain basalt flow that intervenes between the silts and clays and the upper Beverly Member aquifer. This confinement precludes ready entry into the Columbia River.

In 1963, geophysical seismic work confirmed the stratigraphy and location of the geologic units of interest near the Columbia River. Recently, piezometric gradients in the upper Beverly Member aquifer were determined for part of the Hanford Project area and sites of recharge were identified. Elsewhere, changes and rates of changes of piezometric head in wells to the same aquifer suggested other recharge sites. In total, seven areas of recharge surrounding the Hanford Project on all sides except to the southeast appear indicated. Altitudes of indicated areas of recharge of the aquifer and determined hydraulic gradient directions suggest that movement of ground waters in the confined aquifer are to the southeast toward Wallula Gap. Ultimate emergence of the ground waters from the confined aquifer will occur.

In addition to natural sources of recharge in the southwest, west, north and east, the upper Beverly Member aquifer evidently is recharged by water from the Priest Rapids Dam pool to the northwest, from the

Columbia Basin Irrigation Project to the northeast and east, and from the 200-East area vicinity where contaminants were earlier identified entering the aquifer. The newest increments identified may increase the gradients and rates of flow of the ground waters and locally at least alter their flow paths.

Geological studies suggest that some small anomalies in the unconfined water table gradients beneath the Hanford Project may be caused by local discharge of water from the upper Beverly Member aquifer into the water table aquifer. The volumes of water involved and the practical importance of this possible event remain to be determined. The importance of a full awareness of ground water flow in three dimensions, particularly between different aquifers, rather than the classical two-dimensional concept, is again clearly affirmed.

A Sequence for Predicting Waste Transport by Ground Water - R. W. Nelson

A sequence of steps for analyzing ground water flow and predicting rates and paths of movement is described. Three computer programs are used to yield data in forms useful for subsequent steps and definitive of the ground water behavior with respect to outflow paths and rates. Input data required for the computations include the distribution of potentials (fluid heads) throughout the region of interest, boundary permeability data, representative data on relative capillary conductivity versus capillary pressure head of the soils, and the configuration of flow system boundaries. Independent fitting functions are also required to supplement the derived mathematical computation and program.

Introduction

The analysis of the effects of ground water flow on waste transport in natural soils involves several steps. The sequence starts with rather simple and basic flow system concepts and characteristics and builds step by step toward providing realistic predictions of waste transport through soils.

The desired end result of such an analysis is a rational prediction of the concentration of wastes entering streams, rivers, or other potable

waters traversing the region under study. For Hanford, the waste transport analysis must provide the ability to predict the entry of wastes into the Columbia River and should include rates, entry points, and nuclide concentrations. The concentrations are dependent upon the travel times (i.e., time for decay of radionuclides), and these are governed by both the rate of water movement and the soil sorption retardation of the radionuclides. When the ground water flow time analysis is completed, the latter phenomenon can be introduced.

The water travel times and the resulting distribution of arrival times are the required results from the mathematical analysis of the flow system. Such travel times are obtained by integrating the ground water velocities along the flow paths. Both the velocities and the flow paths are available for the travel time calculations if the distribution of potentials and permeabilities is known for the flow regime of interest.

For an existing steady-state flow system, the potentials measured in wells, together with field measurements of soil permeabilities along a surface which intersects all streamlines, provide a basis for the unique determination of permeabilities (independent variables) everywhere in the flow system. If the flow system subsequently changes, due to changes in disposal practices or in environmental conditions (e.g., rainfall variations, a river dam, etc.), then the accompanying changes in ground-water potential distribution can be predicted accurately by solving the new flow system boundary value problem which interrelates all of the pertinent independent variables. Among these variables are the permeability distribution in the flow system (determined previously for the original flow system) and the physical configuration of and potentials along the flow system boundaries. In essence, the problem resolves to using potential data for an existing flow system to obtain the permeability distribution, and then using that permeability distribution and new boundary conditions to obtain values for the potentials which will exist when the system is altered.

Of the variables involved, the permeability distribution is the most difficult to obtain, and considerable research effort has been required to

achieve the capability for making unique permeability distribution determinations economically.

Analysis Sequence

The steps in the water transport analysis just briefly outlined above involve several types of basic data and computer programs to obtain the desired final results. The three major parts include:

- Determination of the in-place permeability distribution for heterogeneous soils
- Prediction of the new distribution of potentials through setting up and solving the boundary value problem
- Utilization of the new distribution of potentials to enable waste transport predictions.

Under these three major headings the required data and computer programs are schematically outlined in Figure 4.5. Each will be described briefly.

In-Place Permeability Measurement

The principle underlying the method for the determination of the relative permeability is that, through analyzing the energy dissipation (change in potentials) in an existing ground water flow system, the permeability distribution can be deduced. A general theory substantiating this principle and showing the conditions for a unique permeability distribution is available.[4.11, 4.12] The theory shows that the ground water potential must be known or measured as a function of space throughout the region of interest. Also a special boundary condition in permeability is needed in steady flow systems.[4.13]

The measurement of potentials at various locations in the field results in a tabular set of data as illustrated in the upper left corner of Figure 4.5. Such tabular data are most accurately and easily used in large systems through reduction to equation form. The "GENORO Computer Program" (Generalized Orthogonal Regression Program) is

OPERATIONS ON PREDICTED POTENTIAL TO ENABLE WASTE DISPOSAL ANALYSIS

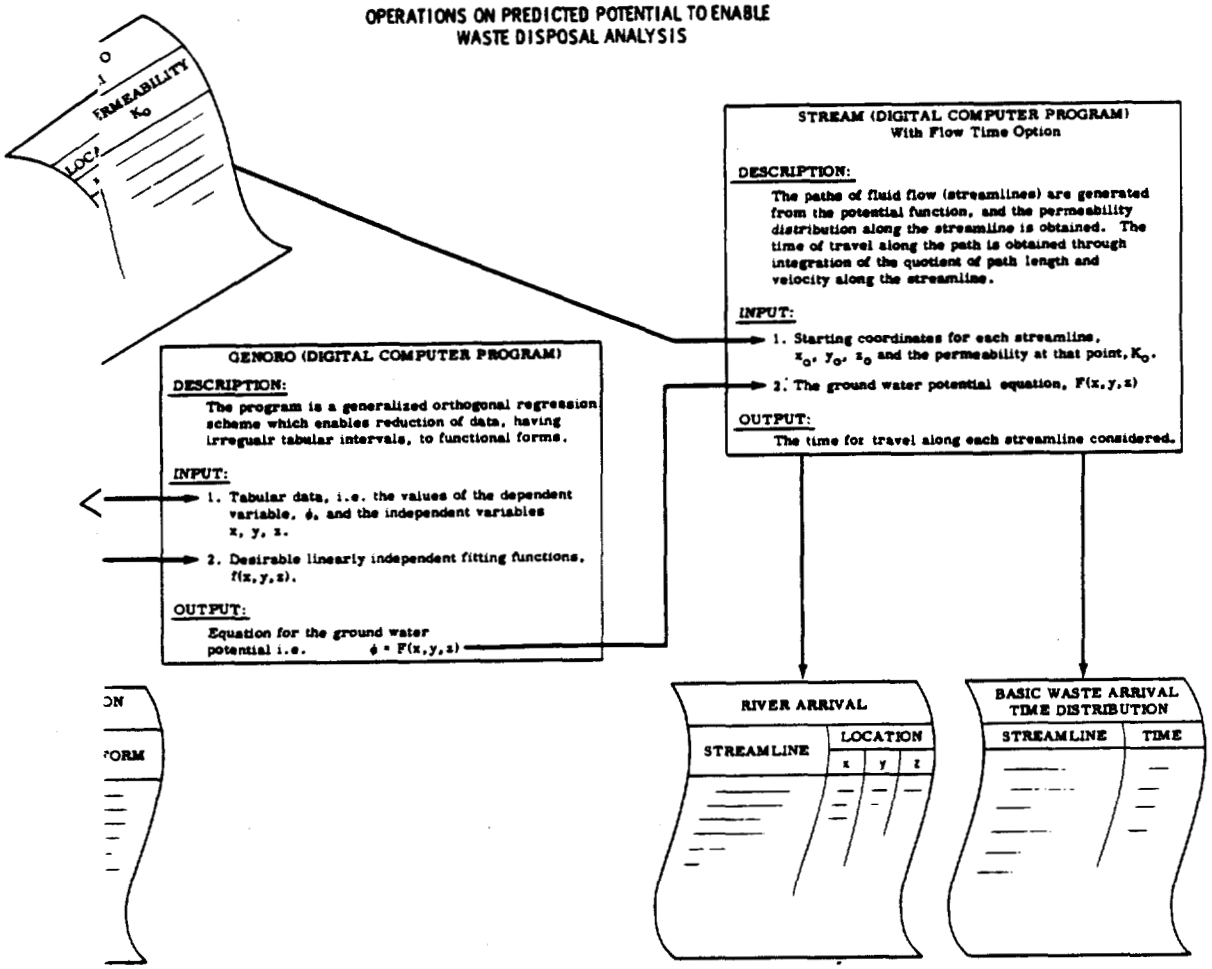

used to generate the equation for the potentials from the tabular data. The program requires input of the functional forms to be used in the data fitting. Those functional forms utilized to the present time include power, trigonometric, and logarithmic series. Such forms are satisfactory for smaller flow problems; however, better functionals are being sought for use on large multidimensional flow problems.

The GENORO program is a versatile tool limited only by the storage capacity and digit significance of the IBM 7090 computer. The program is written in Fortran II and can handle as many independent variables as desired. This enables fitting one, two, and three-dimensional problems with or without time dependence. The input potential data need not be regularly spaced since the methods in the program assume complete irregularity of the independent variables, the spatial locations of measurement points. The methods of orthonormal computation to handle the irregular data and conduct the fitting in the GENORO program are described in greater detail elsewhere.[4.14]

Once the equation representing the field potential data has been obtained, the permeability distribution is calculated by "STREAM," i.e., the Streamline Generation and Evaluation Program (Figure 4.5). The additional inputs to this program are the field measurements of permeability along a surface that intersects all streamlines.

The STREAM program carries on four sequential operations. The first two steps provide the desired permeability distribution and the last two give the water travel time and flow distribution needed for later waste transport calculations. The four operations, which begin for each streamline at the input initial points X_o, Y_o, Z_o, (Figure 4.5), are:

(1) The streamline is generated through solving the appropriate pair of differential equations containing the potential function.

(2) The permeability integral is evaluated along the streamline generated in Step (1) using again the potential function.

(3) The travel time integral, which uses the permeability from Step (2) and the potential function, is evaluated along the streamline found in Step (1).

(4) The flux or flow distribution between successively calculated streamlines is determined.

Careful evaluations of the numerical errors involved in the methods used in these steps have shown accuracies which far exceeded original expectations. The error analysis also showed the accuracy to be independent of the streamline length.

The underlying equations used in the STREAM program represent considerable original and fundamental work carried on at Hanford on the flow of fluids in heterogeneous porous media. Included in this work are derivations of the equations for stream functions in heterogeneous media,[4.15] the permeability integral,[4.16] and the three-dimensional flux indexing integrals. An AEC research and development report containing instructions for using the STREAM program and some background mathematics is in preparation.[4.17]

The distribution of permeabilities is the output of the STREAM program. As indicated in Figure 4.5, this distribution of permeabilities is required as data for use in the next step which involves setting up and solving the boundary value program representing the new flow system.

Set Up and Solution of the Boundary Value Program

The boundary value problem interrelates all the pertinent variables. When solved it gives the new potentials that would result from changes in the flow system. All of the variables enter in one of two ways to form a unique boundary value problem. Either the variable enters into the partial differential equation or into the boundary conditions. Accordingly, if a solution to the partial differential equations is found and each of the boundary conditions is satisfied, then the distribution of potentials so obtained is the one and only distribution that will occur.

Some characteristics in the region being studied enter the analysis as part of the partial differential equation. There are two groups of such soil data (Figure 4.5). The most extensive group comprises the spatial

distribution of permeability determined as already described. The other soil property needed is the capillary conductivity dependences upon capillary pressure characteristics of the media, i.e., the parameters for partially saturated flow.

The partial differential equation modeling the flow system is nonlinear and describes steady, partially saturated flow in porous media which are heterogeneous with respect to conductivity. Although the nonlinear model is far more complicated to solve, it is used here for the better description it provides and to eliminate the unwieldy free boundary surface arising from a saturated flow model. Specifically, the nonlinear model describes the partially saturated flow above the water table; whereas, the linear saturated flow model cannot. Further, in regions where the flow becomes saturated, the general nonlinear form automatically reduces to the special linear case describing saturated flow. Therefore, the need for the free surface (i.e., water table), which is a boundary only for the saturated model, is unnecessary for the nonlinear partially saturated flow model. Discussion of solution difficulties and methods for the nonlinear form will be deferred briefly.

The remaining requirement for a well-posed boundary value problem is a description of the actual boundary conditions. Such conditions are made up of two parts.

- The geometrical description of all the physical boundaries required to completely bound or isolate the flow region under study.
- The distribution of ground water potential along each of these boundaries.

The description of boundaries and the associated potential conditions are closely related and depend upon careful determinations. Usually the insight necessary for setting realistic boundaries comes through knowledge of the existing flow system.

With complete boundary conditions and the partial differential equations available, the boundary value problem is uniquely formulated. In

Figure 4.5 all of the input data and computer operations in the left half of the figure have been considered. Specifically, the four inputs (field data, boundary potential data, relative capillary conductivity, and permeability data) are available for input to a computer program for solution.

The present STEADY computer program (not shown in the figure) has been in use for the past 4 yr and has demonstrated considerable capability in solving the class of nonlinear boundary value problem arising in this work.[4.18] During this time experience has been accumulated in handling computational instabilities for the nonlinear equations. The result is three stability control procedures which very capably handle the instabilities arising in this class of problems.[4.19]

However, a limitation of the present STEADY program is the size of problems that can be solved. The solution is accomplished through reduction by finite differences of the partial differential equation to a very large set of simultaneous algebraic equations. The number of equations is then closely related to the size of the problem being solved. The present program has a maximum capacity of 8000 equations with the same number of unknowns. This capacity is adequate for many problems; however, it is restrictive for large three-dimensional problems.

The N-STEADY Computer Program, the envisioned replacement for the present STEADY program, is needed to obtain the new potentials resulting from changes in the present flow system. The new program will be designed to handle the much larger problems foreseen. Experience will form the basis for the new solution capability, but Diakoptics[4.20] probably will be used to enable piece by piece solution of the much larger set of equations. Once the problem is broken into pieces, the smaller parts can be solved individually using the methods of current experience. Later, through the interconnection matrix, the pieces will be reconnected to solve efficiently the very large problems. The proposed development of N-STEADY will involve considerable time and effort in formulating, programming, and testing. Yet, through this development, the requirement for a much expanded solution capability for very large problems will be realized.

0028427

The completed result or output from using the present STEADY or N-STEADY programs, as shown in Figure 4.5, is the predicted distribution of ground water potentials. In other words, the setting up and solution of the boundary value problem has interrelated all the conditions of fluid inflow on some boundaries, outflow along others, no flow across still others, and potential variations of still other boundaries. The predicted potential distribution is the unique result everywhere in the region of interest resulting from these many interactions. Such a prediction is the result needed to enable consideration of water transport.

Waste Transport Analysis

A consideration of the transport of a mass of contaminated water by a ground water flow system involves the same methods and steps that have already been discussed. The predicted potentials are again a tabular set of data as a result of the finite difference solution method rather than a functional form. Therefore, as before, the function fitting is carried out by the GENORO program using the predicted potential data and desirable function forms as input. The result is the functional equation describing the potentials over the system as needed for input to the STREAM program.

The primary purpose of the STREAM program in this part of the sequence is to determine the travel paths and times of flow. Those points (i.e., corrdinates) where waste is introduced to the flow system and the permeability at each point are used as starting conditions for the paths of flow. The program generates the paths of flow, determines the velocities along each path, and evaluates the appropriate integrals to give the travel time. After enough paths (and associated times) have been generated to form the general flow pattern, the flow distribution between successive streamlines is calculated by the STREAM program. Such flux figures (flow distributions), when indexed properly with the streamline shortest travel time, provide the data needed to plot the distribution of water arrival times at a given outflow surface.

Basic Water Arrival Distribution

The water arrival distribution is basic in the analysis of the transport characteristics of steady ground water flow systems. The arrival distribution is the history of arrival at some ground-water outflow surface (e.g., a river) of an instantaneous flow increment which left a given site at zero time. Such an arrival distribution is shown in Figure 4.6 where the cumulative fraction of the instantaneous flow pulse, q/Q, is plotted against the travel or arrival time, T. For example (from Figure 4.6) at about 11.5 yr after the water flow left the disposal site, one-half (q/Q = 0.5) of the flow pulse Q would have reached the river, entered and would have been swept downstream. Similarily, at about 15.5 yr, three-fourths of the initial pulse leaving at zero time would have entered the river and moved downstream. The basic water arrival curve is described in more detail elsewhere.[4.21]

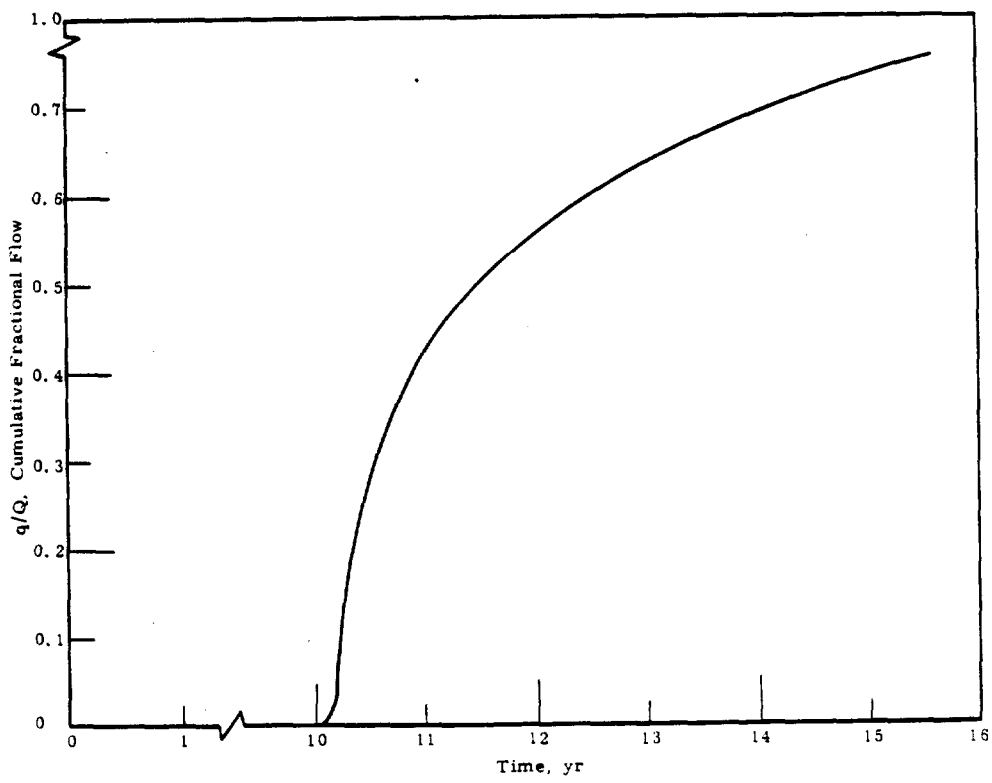

FIGURE 4.6

Distribution of Water Arrival Times

0028429

If the retarding effects of soil sorption of contaminants are neglected, the water arrival distribution is useful in predicting contamination levels of water entering the river. For intermittent release of contaminated water at a disposal site, Figure 4.7 shows the arrival curves for a release period of 0.25 yr. The curve on the left is the arrival distribution of the first contaminated water; whereas, the curve on the right shows the last contaminated water arriving. Accordingly, the area between the two arrival curves represents all the contaminated water reaching the river. Further, a measure of the volume of water containing contaminants at any time is the difference in ordinates between the two curves for that time. The differences in ordinates, plotted as the low-peaking curve in Figure 4.7, is the relative rate of release to the river of contaminated water as a function of time. Such results are precisely those sought as the goal of the analysis sequence described here.

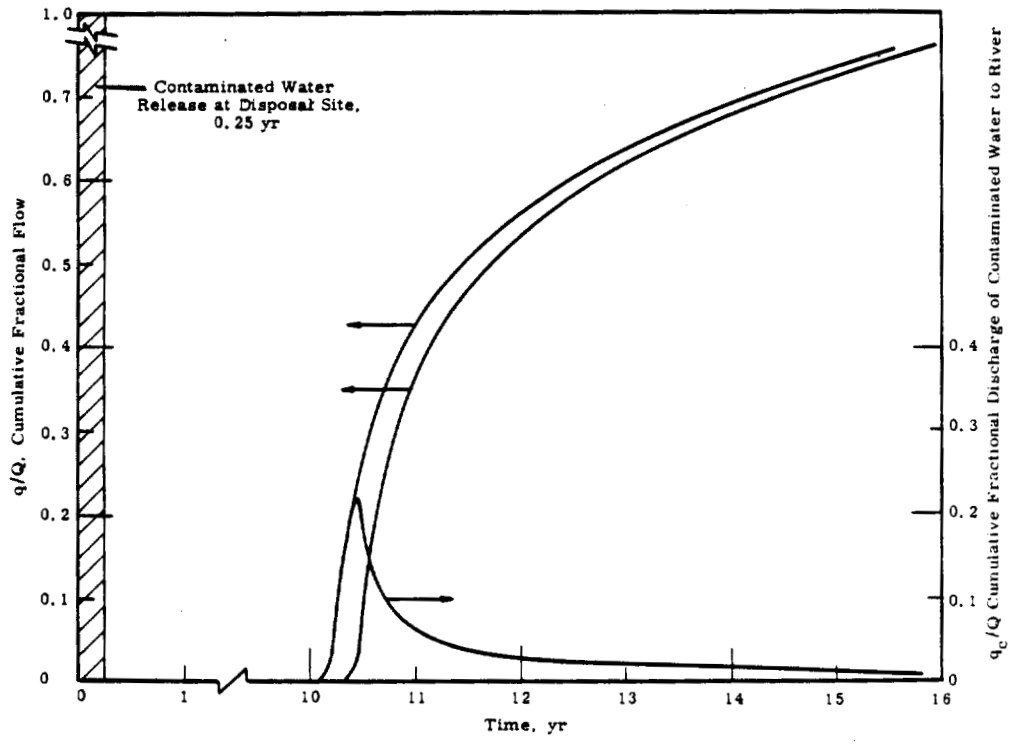

FIGURE 4.7

Predicted Arrival Time of Contaminated Water

The Permeability Integral: A Key to Measurement in Heterogeneous Porous Media - R. W. Nelson

A sequence of analysis is presented that enables the efficient solution of the partial differential equation defining permeability distributions for heterogeneous porous media. The solution method is simplified to the simultaneous solution of a pair of ordinary differential equations, followed by integration of the derived permeability integral. Such a procedure has been shown to be efficient and provides excellent accuracy.

In preceding papers[4.11, 4.15, 4.22, 4.23] theoretical considerations were given to the more basic theory for steady flow in heterogeneous porous media. In-place measurement of permeability was shown to be possible by utilizing the theory. Effective solution methods for deducing permeability distributions from observed potential data, however, were not found immediately.

The permeability integral, which was obtained by using the original measurement theory,[4.11, 4.22] the recently derived stream functions for heterogeneous media,[4.15] and the complete differential of the potential have overcome the solution problem. With these three results, it is possible to reduce the solution procedure to the simultaneous solution of two ordinary differential equations followed by direct integration to obtain the permeability.

Background Equations for Heterogeneous Media

Permeability Measurement Equation:[4.11]

$$\frac{\partial\varphi}{\partial x}\frac{\partial K}{\partial x} + \frac{\partial\varphi}{\partial y}\frac{\partial K}{\partial y} + \frac{\partial\varphi}{\partial z}\frac{\partial K}{\partial z} + \left(\frac{\partial^2\varphi}{\partial x^2} + \frac{\partial^2\varphi}{\partial y^2} + \frac{\partial^2\varphi}{\partial z^2}\right) K = 0 \qquad (1)$$

where

K is the hydraulic conductivity or permeability distribution for heterogeneous media

φ is the hydraulic potential or potential function

x, y, z, are the space coordinates with z oriented parallel to the gravitational vector.

Equation (1) is a first order partial differential equation that can be reduced to the system of ordinary differential equations:

$$\frac{dx}{\frac{\partial\varphi}{\partial x}} = \frac{dy}{\frac{\partial\varphi}{\partial y}} = \frac{dz}{\frac{\partial\varphi}{\partial z}} = -\frac{dK}{\left(\frac{\partial^2\varphi}{\partial x^2} + \frac{\partial^2\varphi}{\partial y^2} + \frac{\partial^2\varphi}{\partial z^2}\right)K} \quad . \tag{2}$$

Stream Function Equations:[4.22]

$$\frac{dx}{\frac{\partial\varphi}{\partial x}} = \frac{dy}{\frac{\partial\varphi}{\partial y}} = \frac{dz}{\frac{\partial\varphi}{\partial z}} \tag{3}$$

The Permeability Integral

The substitution of Equation (3) into the equation for the total differential of potential gives:

$$d\varphi = \frac{\partial\varphi}{\partial x}\,dx + \frac{\left(\frac{\partial\varphi}{\partial y}\right)^2}{\frac{\partial\varphi}{\partial x}}\,dx + \frac{\left(\frac{\partial\varphi}{\partial z}\right)^2}{\frac{\partial\varphi}{\partial x}}\,dx, \tag{4}$$

and on rearranging and using one of Equations (2)

$$\frac{dK}{K} = -\frac{\left(\frac{\partial^2\varphi}{\partial x^2} + \frac{\partial^2\varphi}{\partial y^2} + \frac{\partial^2\varphi}{\partial z^2}\right)}{\left(\frac{\partial\varphi}{\partial x}\right)^2 + \left(\frac{\partial\varphi}{\partial y}\right)^2 + \left(\frac{\partial\varphi}{\partial z}\right)^2}\,d\varphi, \tag{5}$$

which on integrating gives

$$\ln\frac{K}{K_o} = -\int_{\varphi_o}^{\varphi}\frac{\nabla^2\varphi}{|\nabla\varphi|^2}\,d\varphi \tag{6}$$

where

K_o is the permeability at some starting point x_o, y_o, z_o

φ_o is the potential at the starting point x_o, y_o, z_o

K is the permeability at any point x, y, z with which the upper limit of the integral, φ, is associated.

The solution procedure involves solving the equation pair (3) simultaneously to define the streamline or path for steady flow. The permeability integral, Equation (6), is then evaluated along the streamline so defined to yield the permeability distribution along the streamline commencing at the location x_o, y_o, z_o. The entire permeability distribution is obtained by considering successive streamlines in a like manner.

The numerical methods for carrying out these solution steps are quite straight-forward, and excellent accuracy has been found through use of this solution method.

Earth Material Sampling by Coring Techniques - J. R. Raymond

Methods and techniques are described and equipment shown for small diameter hole core sampling of consolidated and unconsolidated materials. Both rotary and drive coring methods have been used at Hanford for sampling in a wide variety of situations.

Core sampling techniques have particular applicability for indirect or undisturbed material sampling. Core sampling is done by cutting, washing, abrading, or displacing material away from a cylindrical central sample core. The core feeds into a hollow barrel or tube that protects and retains the sample. The core barrel is advanced into the material by rotational and/or compressive and impact forces applied through a drill rod to a bit or drive shoe mounted below the core barrel. Although coring techniques are used extensively to sample earth materials, the same methods may be successfully used to sample almost any material ranging from fluid mud and clay to solid steel.

Core Sampling Methods

Core samples may be obtained by drive sampling or rotary sampling. The method used depends on the physical properties of the sampled material. The same basic equipment components are used with both methods. In the drive sampling method, the core barrel is driven into the sample material by impact of a heavy weight. In rotary sampling, the core barrel is drilled into the material by rotating the bit and core barrel while cuttings are flushed

from the hole by flow of a fluid under pressure. The drive sampling equipment and techniques are much simpler than those used for the rotary coring method.

Drive Coring Equipment and Techniques

Figure 4.8 is an exploded view of a typical drive sampling core barrel. The sampler consists of a drive shoe, core lifter, sample barrel, and sampler head. The drive shoe or bit is hardened tool steel and is tough enough to break small rocks and pebbles. The inside diameter of the bit is slightly smaller than the core barrel, and the core will pass into the barrel without undue friction or compaction. The core lifter or retainer has a number of spring fingers that allow easy passage of the core into the barrel but prevent return flow of the sample out of the core barrel. The core barrel in this illustration is a split tube type that is held together by the drive shoe and the core barrel head. The sample is easily removed by unscrewing the drive shoe and head and "splitting" the core barrel. The head, in addition to clamping the core barrel together, provides a rod coupling and contains a ball check valve to vent fluid from the barrel. The check valve also assists in retaining the core. This sampler takes a $1\frac{5}{8}$ in. by 2 ft long core.

Figure 4.9 shows operation of the drive sampling equipment. A length of heavy wall drive rod or casing is attached to the core barrel head. The drive head (a heavy steel collar) is attached to the drive rod and a short section of rod that serves as a drive hammer guide is screwed into the top of the drive head. The drive hammer is a heavy steel weight with a guide hole through the center. A jar-back collar is attached to the top of the guide rod. In operation, the drive hammer is repeatedly lifted by a winch and dropped against the drive head. The core barrel progresses downward as the sharpened steel drive shoe compresses and displaces the sample media. The sampling is completed when the core barrel has been driven its full length into the material. The weight is then raised against the jar-back collar and the core barrel is jarred or lifted from the hole. The sampler may be rerun in the hole for progressive depth sampling as long as the material does not cave. When caving takes place, a separate casing may be driven in the hole to provide core barrel access.

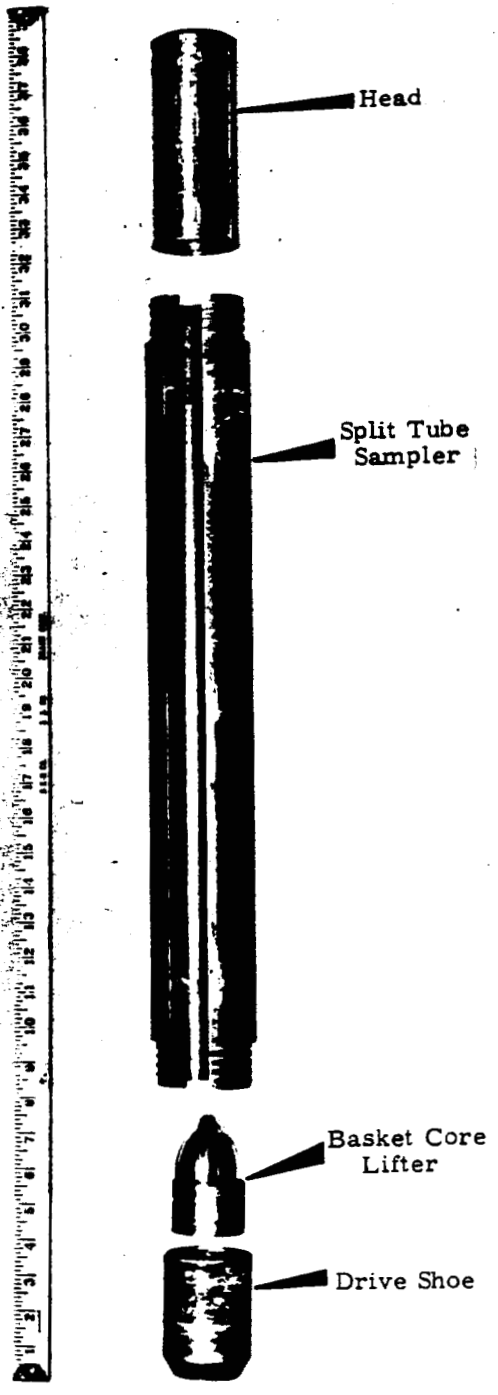

FIGURE 4.8

Split-Tube Drive Sampler

Neg. No. 33326-1

0028435

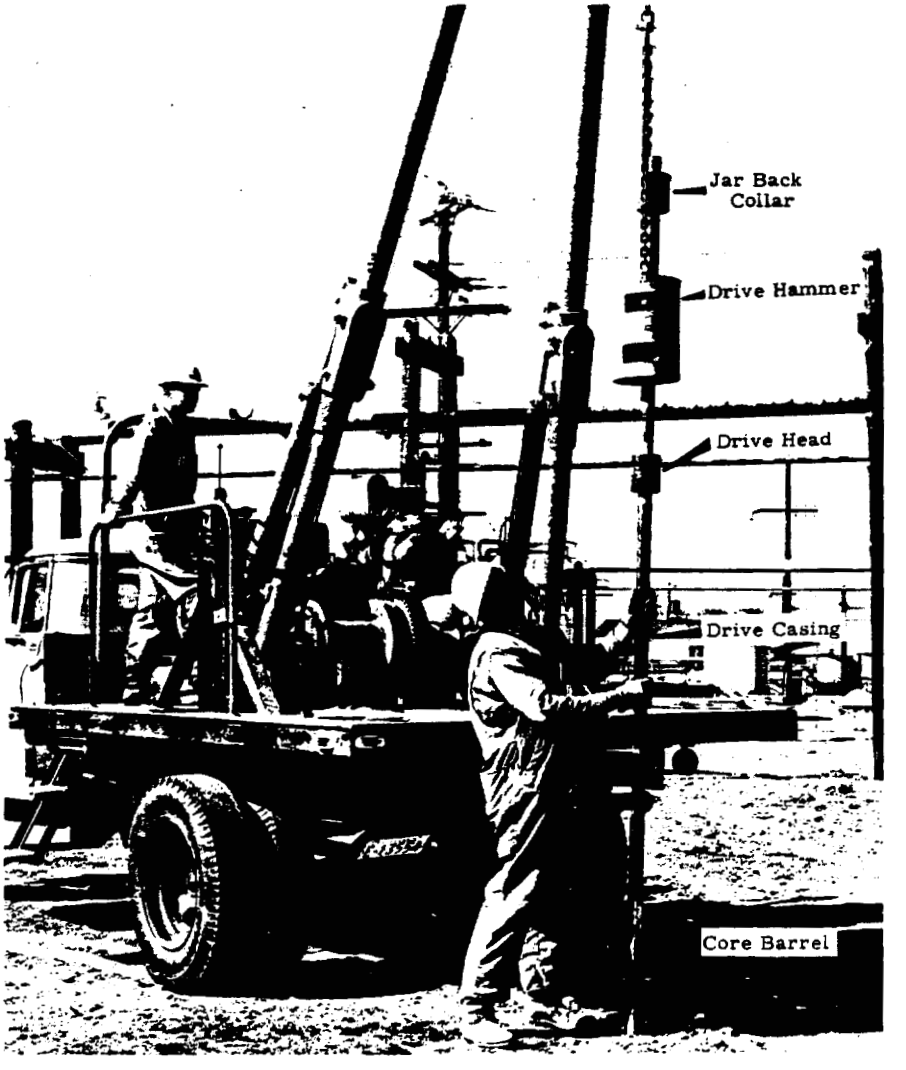

FIGURE 4.9

Drive Sampling Operation

The drive sampling technique is usually successful only with soft or unconsolidated porous media where the drive shoe can compress or displace the material. With proper use, nearly undisturbed samples may be taken by the drive method.

The drive coring method has been successfully used at Hanford to sample earth materials ranging from sand and gravel to mud in waste disposal crib bottoms and shallow wells.

Neg. No. 0641992-3

Rotary Coring Equipment and Techniques

Rotary core sampling equipment consists of a drill bit screwed to the end of a core retaining barrel, drill rods attached to the upper end of the core barrel, and a power source to rotate the rods and apply compressive pressure on the bit. Generally a high pressure fluid pump and a source of water or other drilling fluid are also required. Many different types of rotary core bits are available for sampling a great variety of materials. The core barrel may be simply a section of drill rod or it may be a more complex double tube assembly.

Almost any material can be cored using the rotary method but it is important, particularly with unconsolidated material, that proper techniques and equipment are used. Factors that affect coring are: bit, core lifter and core barrel design, rotary speed, bit pressure, and drilling fluid type, viscosity, flow rate, and pressure.

Figure 4.10 is an exploded view of a typical small diameter, double-tube core barrel. A clay-type bit for soft material coring is pictured with this particular sampler. The double-tube barrel consists of two concentric tubes; the drilling fluid is diverted to the bit between the outer tube and inner (sample) tube. The bit is mounted on the outer tube with minimum clearance between the inside bit shoulder and the lifter case. The swivel, in theory, permits the inner sample barrel to remain stationary while the outer barrel and bit rotate. Strips of copper brazed to the end of the inner barrel provide a lower bearing. The double tube barrel and swivel arrangement prohibits excessive fluid flow either up or down the inner core barrel and prevents core washout. Soft porous material is always disturbed to some extent in the rotary coring process. Some fluid invasion and contamination of the sample also occurs.

Figure 4.11 shows a small rotary drill assembly used at Hanford. The equipment has been used to obtain core samples of waste tank bottom sludge and earth material. It is also used to drill small diameter non-cored special test wells. A modified chain-saw engine provides power for

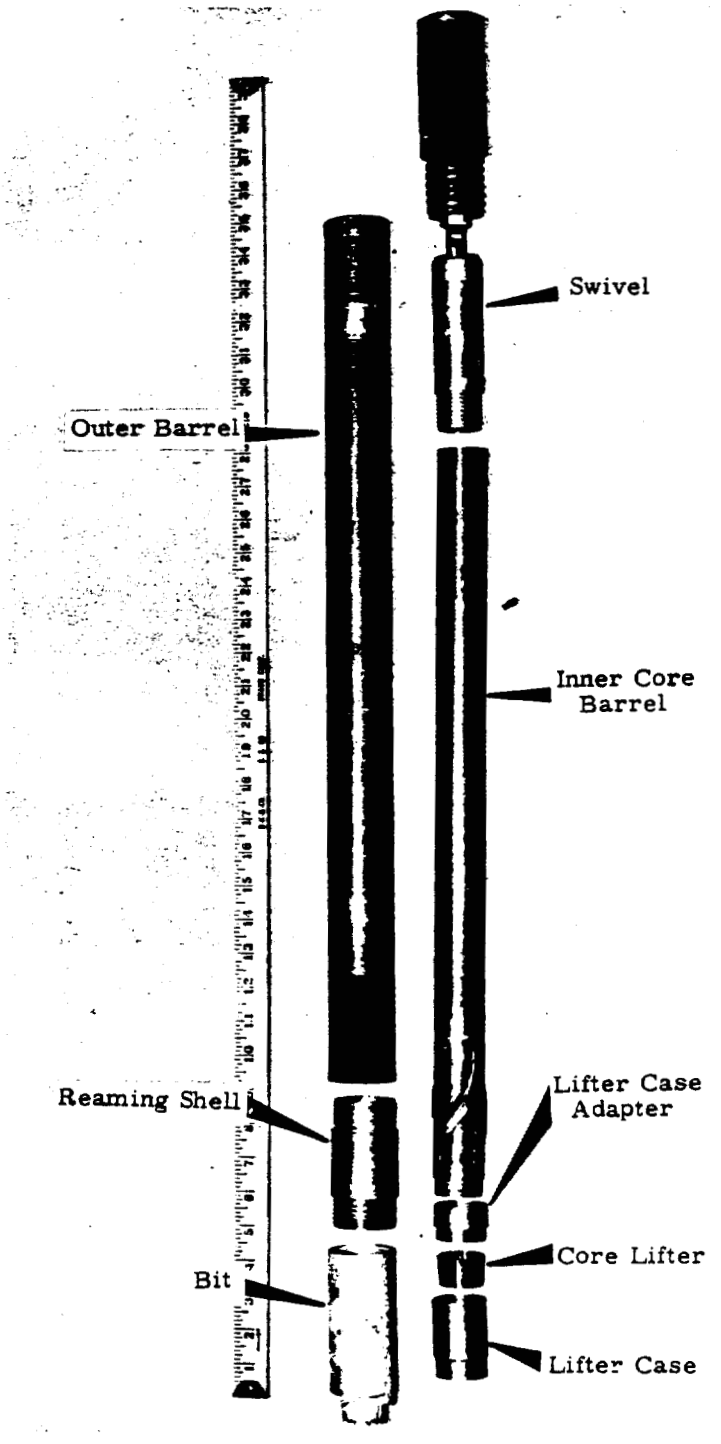

FIGURE 4.10

Double-Tube Rotary Core Barrel

Neg. No. 33326-3

rotating the drill rod, and a hydraulic ram is used to apply compressive force to the bit. A small gasoline engine driven progressive cavity pump supplies drilling fluid pressure. The drill is mounted on the front of a 3/4-ton truck. The truck provides the necessary hold down weight and permits operation mobility.

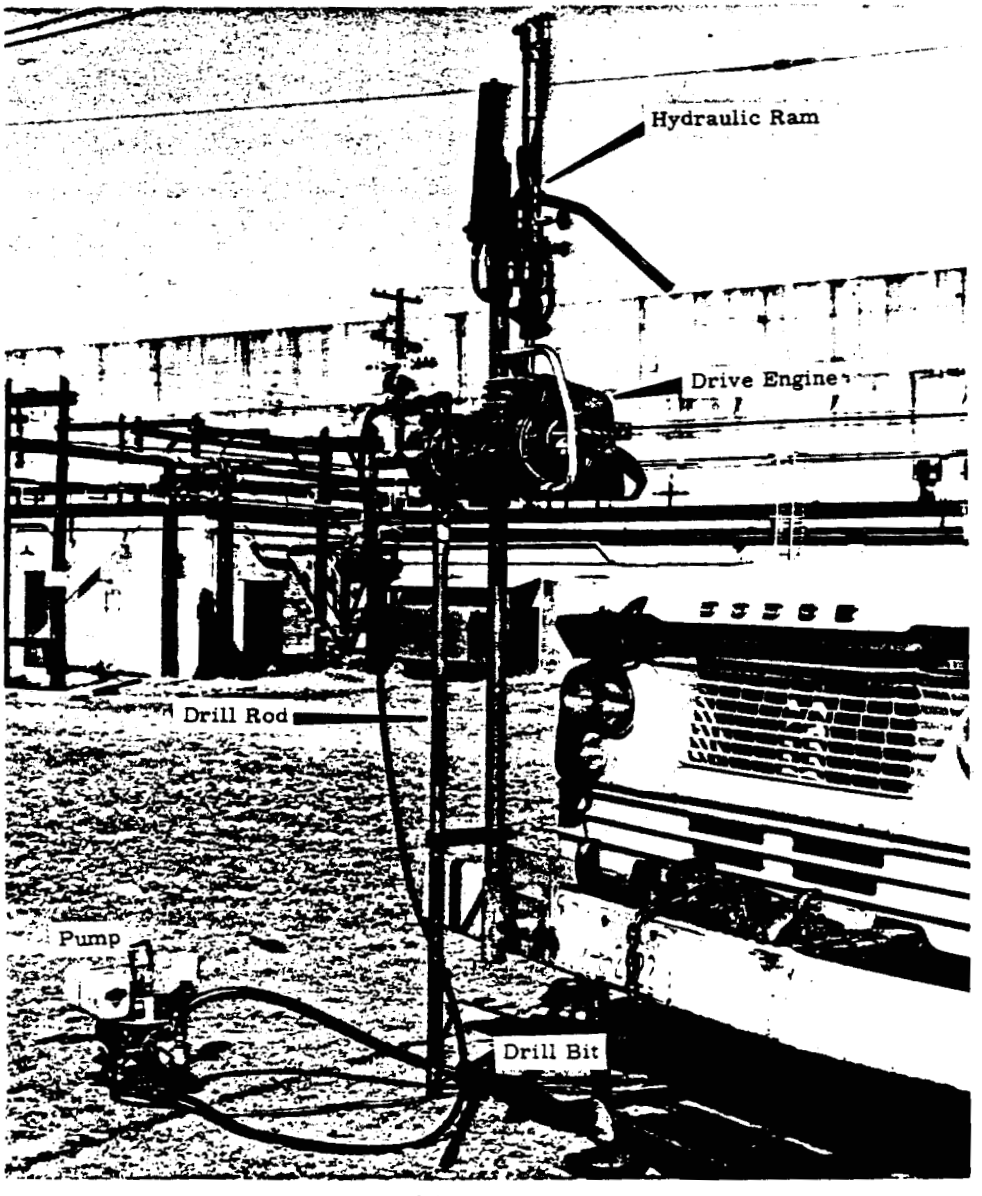

FIGURE 4.11

Rotary Core Drill

Neg. No. 0641992-5

Use of a Neutron Well Probe - J. R. Raymond

Response of a neutron well probe was correlated with subsurface stratigraphic breaks where such breaks were also associated with changes in particle size of sedimentary earth materials. Cross correlation with other radioactivity and drilling logs is useful for full evaluation of the neutron log.

The neutron probe is a well logging tool that responds directly to moisture in the sediments adjacent to a well. The neutron logging system basically consists of a probe containing a fast neutron source, a slow neutron detector, and associated high voltage supply and signal amplifier. An armored wire line provides probe support and signal conduction. Surface equipment consists of a hoisting system, count-rate meter, and a strip chart recorder.

Fast neutrons emitted from the source move into the earth materials adjacent to the probe. Light element nuclei (such as hydrogen, helium, or carbon) moderate the neutrons to thermal energies by elastic scattering. A portion of these "slow" neutrons is scattered back to the detector. The degree of thermalization and scattering is proportional to the amount of light element nuclei present. Hydrogen in soil moisture and ground water is the major moderating element present in the ground. Thus, for most cases, the neutron probe response is directly and uniquely related to soil moisture.

Discussion

The neutron probe was designed primarily for measuring moisture content of the soil adjacent to buried high-level, radioactive waste storage tanks to assist in evaluating soil thermal conductivity. The probe may also be used to study subsurface moisture in the aeration zone above the water table and to determine degree of saturation in the capillary fringe. Such studies provide information on unsaturated water flow through porous media. The probe may also be used in the subsurface water-saturated zone to determine total porosity for use in estimating ground-water flow rates.

0028440

Geologic stratigraphic changes may be indicated by neutron well logging in certain cases where the stratigraphic discontinuities are associated with changes in the particle size of sedimentary earth materials. Fine-grained sediments with small pore size (silts and clays) retain more moisture against the force of gravity than do coarse-grained materials with large pore size (sand and gravel). The assumption is made that the materials have in the past been water saturated; this assumption is generally valid with regard to sedimentary earth materials.

Figure 4.12 shows the neutron and scintillation logs of a well that penetrates a fine sandy-silt zone described as the Palouse Formation. Coarser sands and gravels lie above and below the Palouse. The drilling log shows entrance into the silt at about 50 ft below ground surface. The scintillation log, which indicates the presence of naturally occurring gamma radiating isotopes, shows an increase in count rate starting at about the same depth due to the increased natural radioactive material content in the fine sediments. The moisture content increase is noted at about 50 ft by a count rate increase on the neutron log. The drilling log records the bottom of the silt at 140 ft, and a corresponding decrease in count rate is noted on the scintillation log. The stratigraphic break is evident on the neutron log when comparison is made with the scintillation trace. However, the lower boundary would be difficult to define from the neutron log alone. The top of the saturated zone (water table) is noted by a sharp rise in neutron count rate at 202 ft. The lenticular nature of the silt and fine sand is noted on both logs by the sharp variations in count rate. This shows that the material is not homogeneous.

Figure 4.13 shows the neutron and scintillation logs of another well that penetrates the Palouse Formation at a different location. This well goes through a zone of perched water above the normal water table. The Palouse Formation is well defined by comparison of both logs. The top of the perched water zone is noted by a sharp rise in neutron count rate at 196 ft. The normal water table is encountered at 210 ft where an additional increase in neutron count rate occurs. The scintillation log gives little

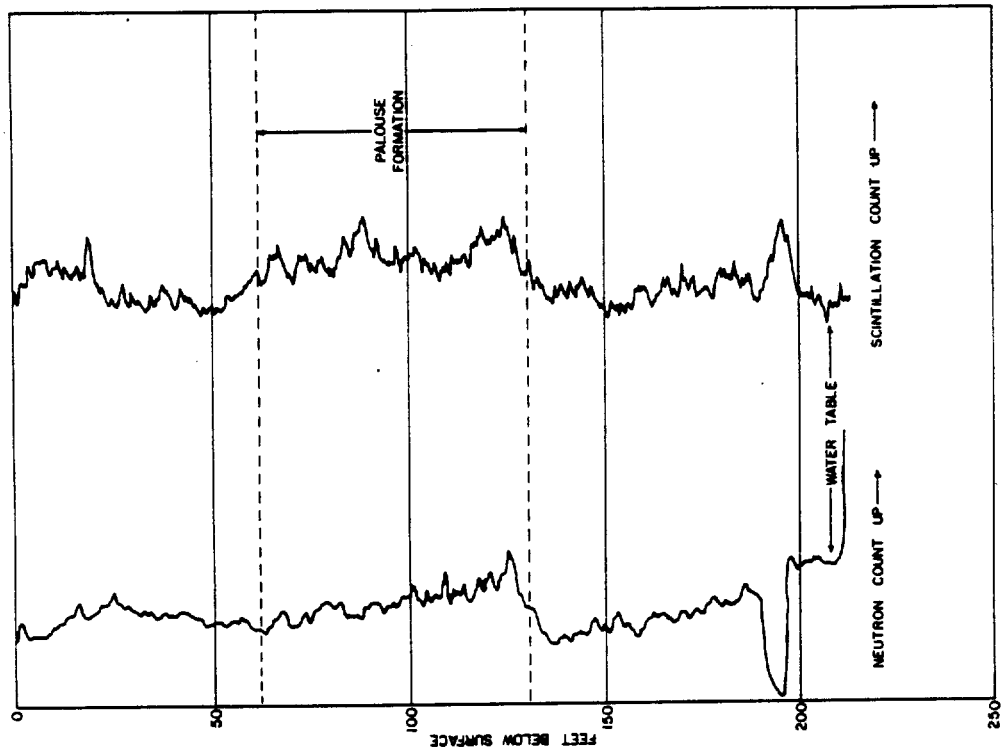

FIGURE 4.13
Neutron and Scintillation Logs of the Palouse Formation (Second Location)

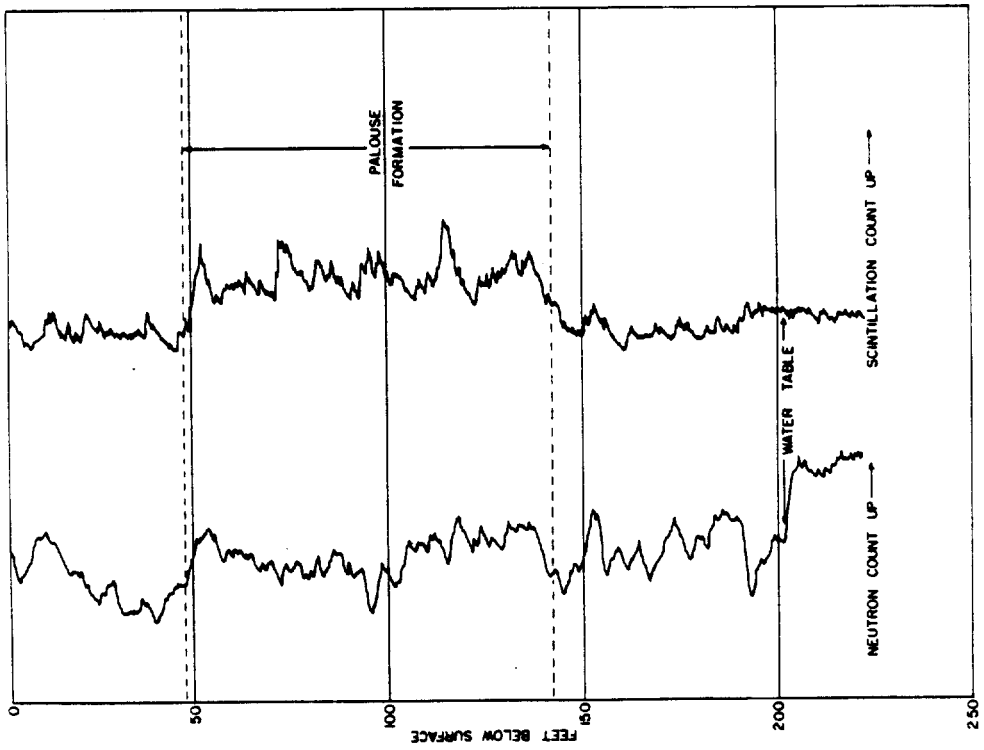

FIGURE 4.12
Neutron and Scintillation Logs of the Palouse Formation (Sandy-Silt Zone)

Neg. No. 0650561-1; 0650561-3

indication of either the perched zone or the water table. The nature of the aquiclude that separates the perched water from the water table is not shown by either the radioactivity logs or the drilling log. A significant change in material characteristics is noticeable above the perched zone at 190 ft where the neutron count rate shows a sharp decrease and the scintillation count rate increases; the drilling log indicated no change in composition. The change is probably caused by cementation of the sand and gravel by calcium carbonate. The cementation would decrease the porosity and thus lower the moisture content and the natural radioactivity content would probably be increased.

The examples shown support the belief that the neutron log, when used with other information such as scintillation and drilling logs, supplies valuable data on subsurface geology and hydrology in a sedimentary environment.

Analytical Description of Soil Characteristics for Partially Saturated Flow - L. G. King

Two empirical equations are described for relating relative permeability to capillary pressure. Of the two, Gardner's equation appears to fit the experimental data better and is certainly easier to use because of its simple form. An equation is also presented for representing saturation as a function of capillary pressure. This equation can be differentiated. Hence, the equation can be used to calculate relative permeability and diffusivity as functions of saturation in computer programs for solution of both steady and transient partially saturated flow problems involving radioactive liquid waste. The main utility of the equations appears to be in simplifying the handling of input data and programming for digital computers. They may also prove useful in studying wide ranges of possible soils in that a wide range is covered by changing a small number of parameters.

In 1958, Gardner[4.24] presented an equation of the form

$$k = \frac{a}{p_c^{\tau} + b'} , \qquad (1)$$

where k is the permeability, p_c is the capillary pressure, and a, b', and τ are parameters depending on the liquid, the soil, and the capillary pressure history of the system. Equation (1) is dimensionally inconsistent but can be rewritten[4.25] in dimensionless form as

$$k_r = \frac{1}{(p_c/p_1)^{\tau} + b} , \tag{2}$$

where p_1 is a parameter having the same dimensions as capillary pressure, and τ and b are dimensionless. All three parameters are positive. The relative permeability, k_r, is defined as the ratio of permeability at any given saturation to the permeability at complete saturation.

As p_c approaches zero, the limit of relative permeability from Equation (2) becomes

$$\lim_{p_c \to 0} k_r = 1/b, \tag{3}$$

and as p_c becomes large, k_r approaches zero. Also as p_c becomes large,

$$\lim_{p_c \to \infty} \left[\frac{d(\log k_r)}{d(\log p_c)} \right] = -\tau \quad ; \tag{4}$$

i.e., for large p_c, Equation (2) approaches a straight line with slope equal to $-\tau$ on a logarithmic plot.

The following equation was presented last year[4.26]

$$k_r = \sigma \left[\frac{\cosh \left[(p_c/p_2)^{\eta} \right] - 1}{\cosh \left[(p_c/p_2)^{\eta} \right] + 1} \right] \tag{5}$$

where p_2, η, and σ are parameters which depend on the liquid, the soil, and the capillary pressure history and are such that $\eta > 0$, $p_2 > 0$, and $0 < \sigma \leq 1$. The parameter, p_2, also has the same dimensions as capillary pressure while the other parameters are dimensionless. For Equation (5), the limits corresponding to Equations (3) and (4) are

$$\lim_{p_c \to 0} k_r = \sigma \tag{6}$$

and

$$\lim_{p_c \to \infty} \left[\frac{d(\log k_r)}{d(\log p_c)} \right] = 2\eta \quad . \tag{7}$$

Figures 4.14 and 4.15 show Equations (2) and (5) fitted to experimental imbibition data[4.28] for "Soltrol C"* as the wetting liquid. Both equations describe a plateau[4.26] for small p_c and approach a straight line quite rapidly as p_c increases. Equation (2) fits the data better than Equation (5). For these comparisons, σ was held equal to $1/b$ so as to match the equations in the plateau region. [See Equations (3) and (6)].

The equation presented last year[4.26] for describing saturation as a function of capillary pressure may be rewritten in the form

$$S = \delta \left\{ \frac{\cosh \left[(p_c/p_o)^{\beta} + \epsilon \right] - \gamma}{\cosh \left[(p_c/p_o)^{\beta} + \epsilon \right] + \gamma} \right\} \tag{8}$$

where S is saturation (ratio of volume of liquid occupying the pores to the total volume of pores) and p_o, β, γ, δ, and ϵ are parameters, depending upon the liquid, the soil, and the capillary pressure history. In Equation (8), p_o has the same dimensions as capillary pressure while the other four parameters are dimensionless. The parameters are such that $p_o > 0$, $\beta < 0$, $0 < \gamma \leq \cosh \epsilon$, $0 < \delta \leq 1$, and $\epsilon \geq 0$. As p_c approaches zero, the limit of saturation from Equation (8) is

$$\lim_{p_c \to 0} S = \delta \tag{9}$$

and as p_c becomes large,

$$\lim_{p_c \to \infty} S = \delta(\cosh \epsilon - \gamma)/(\cosh \epsilon + \gamma) \; . \tag{10}$$

---

* A core test fluid obtained from Phillips Petroleum Company.

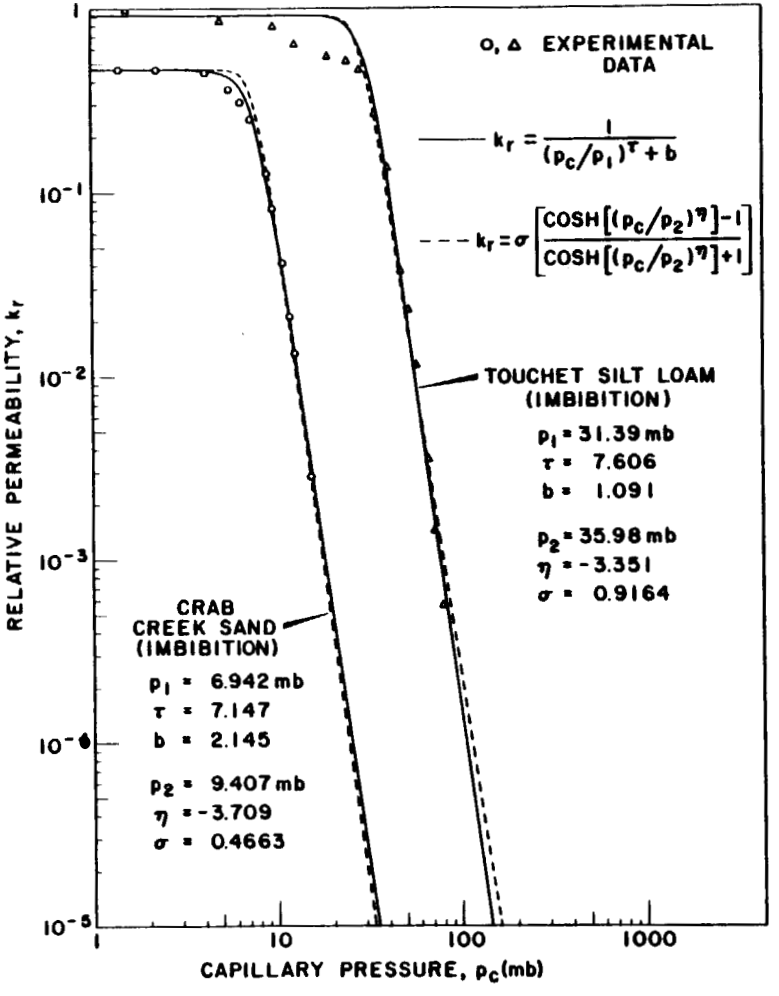

FIGURE 4.14

Comparision of Equation (2) and (5) Fitted to Experimental Imbibition Data of Relative Permeability Versus Capillary Pressure for Crab Creek Sand and Touchet Silt Loam

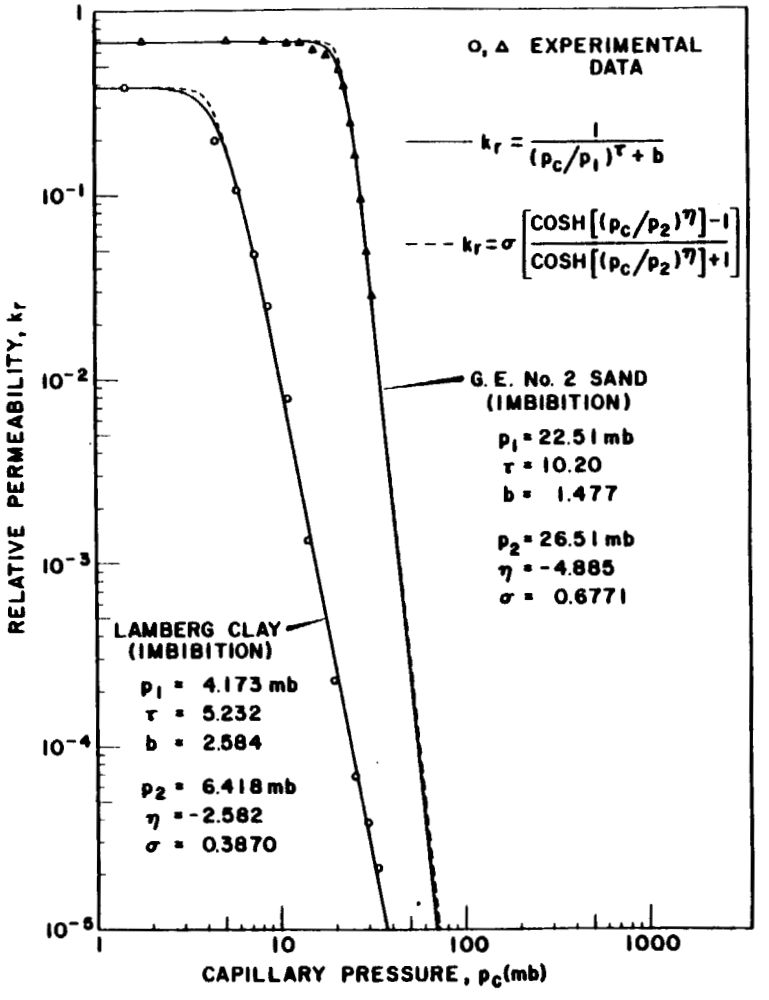

FIGURE 4.15

Comparison of Equation (2) and (5) Fitted to Experimental Imbibition Data of Relative Permeability Versus Capillary Pressure for G. E. No. 2 Sand and Lamberg Clay

Neg. No. 0643055-3; 0643055-4

0028446

Thus, the values of S given by Equation (8) are in the range $\delta \geq S >$ $\delta(\cosh \varepsilon - \gamma)/(\cosh \varepsilon + \gamma)$. This lower limit of S should correspond closely to the "residual saturation" used by Brooks and Corey.[4.27]

Figures 4.16 and 4.17 show Equation (8) fitted to experimental data[4.28] for both imbibition and drainage. The equation describes a plateau for small values of capillary pressure and appears to describe both imbibition and drainage equally well.

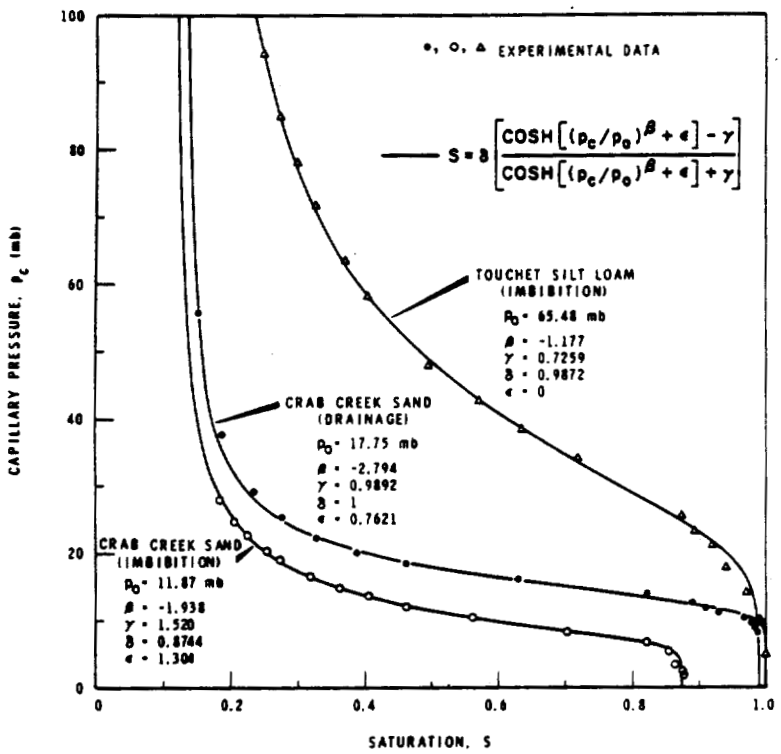

FIGURE 4.16

Equation (8) Fitted to Experimental Data of Saturation Versus Capillary Pressure for Crab Creek Sand and Touchet Silt Loam

Equation (8) and either Equation (2) or Equation (5) may be used to obtain the relative permeability and diffusivity as functions of saturation. Solving Equation (8) for p_c gives

$$p_c = p_o \left\{ \ln\left[\gamma \left(\frac{\delta + S}{\delta - S}\right) + \sqrt{\gamma^2 \left(\frac{\delta + S}{\delta - S}\right)^2 - 1} \right] - \varepsilon \right\}^{1/\beta} \tag{11}$$

Neg. No. 06430551-1

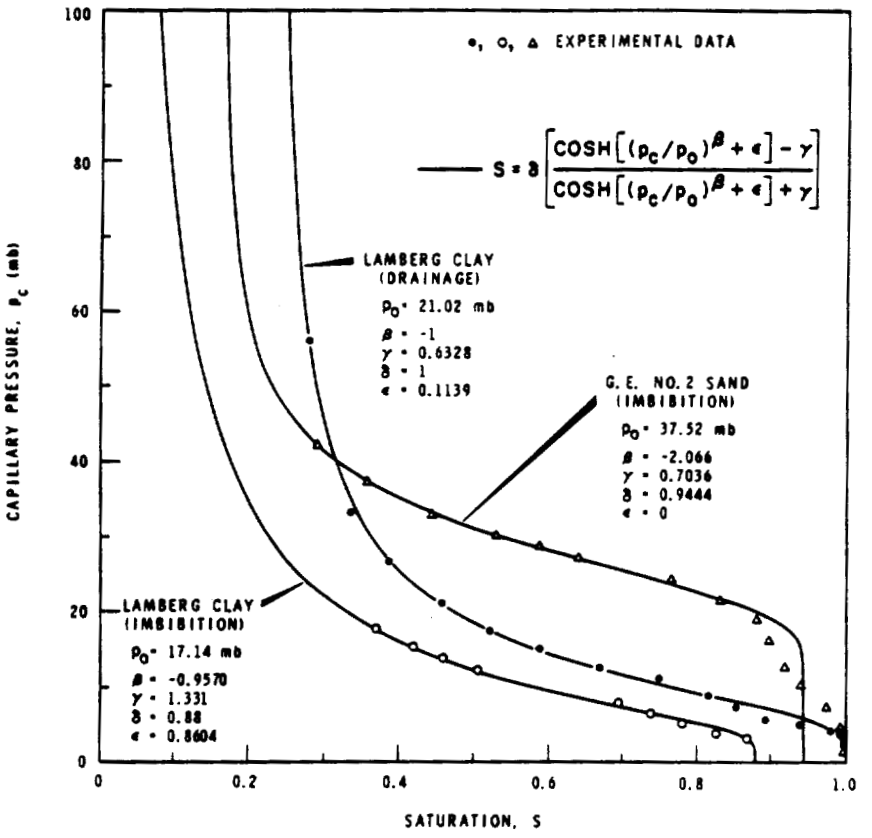

FIGURE 4.17

Equation (8) Fitted to Experimental Data of Saturation Versus Capillary Pressure for G. E. No. 2 Sand and Lamberg Clay

Results of using Equation (11) together with either Equation (2) or Equation (5) to calculate relative permeability as a function of saturation are presented in Figure 4.18. Differentiating Equation (8) with respect to p_c gives

$$\frac{dS}{dp_c} = \frac{(2\beta\gamma\delta/p_o)\ (p_c/p_o)^{\beta-1}\ \sinh\left[(p_c/p_o)^{\beta} + \epsilon\right]}{\left\{\cosh\left[(p_c/p_o)^{\beta} + \epsilon\right] + \gamma\right\}^2} \quad . \qquad (12)$$

Neg. No. 0643055-2

The diffusivity, D, is given by[4.28]

$$D(S) = -\frac{k_r k_s}{\mu f \frac{dS}{dp_c}} \tag{13}$$

where k_s is the saturated permeability (length-squared dimensions), μ is fluid viscosity, and f is the porosity of the medium. The steps for calculating D(S) are: (1) for a given value of S compute p_c from Equation (11), (2) use this value of p_c to calculate k_r from either Equation (2) or Equation (5), (3) use the value of p_c to calculate $\frac{dS}{dp_c}$ from Equation (12), (4) use these results in Equation (13) to calculate D(S). Results of these calculations are shown in Figure 4.19.

The choice of parameter values in Equations (2), (5), and (8) can be simplified for given experimental data by using some of the properties discussed earlier. Very good estimates of τ and b of Equation (2) and of σ and η of Equation (5) can be easily made. Values of the relative permeability in the plateau region give 1/b and σ.* Values of the slope of the straight line for larger values of capillary pressure give $-\tau$ and 2η.** Thus, the first attempt to find the value of either p_1 or p_2 can be carried out in a one-parameter space. Note that the equations should fit experimental data for drainage from complete saturation equally well. For this last case, both b and σ should be held equal to 1, and the fitting is accomplished in a two-parameter space.

The fitting with Equation (8) is more difficult. The only good estimate is for δ which is 1 for drainage from complete saturation and is equal to the value of S in the plateau region for imbibition. By adopting $\varepsilon = 0$ as a first estimate, the initial fitting must still be accomplished in a three-parameter space.

---

* See Equations (3) and (6)

** See Equations (4) and (7)

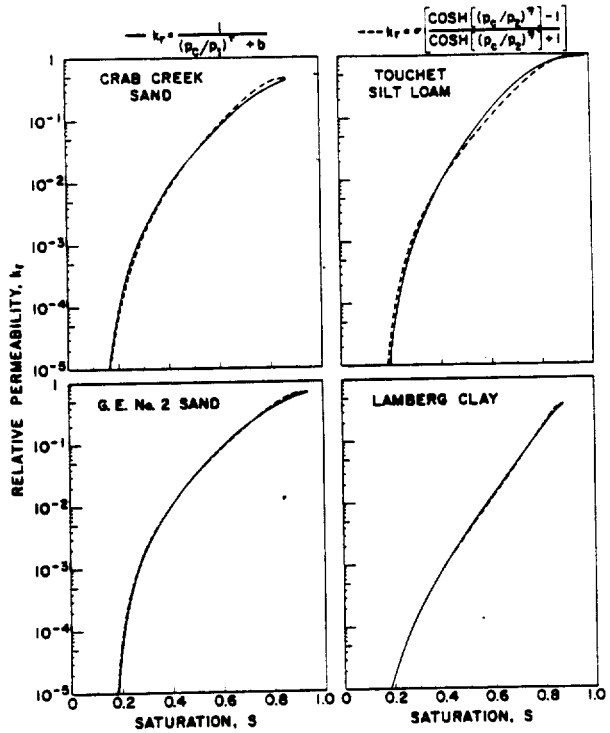

FIGURE 4.18

Comparision of Equations (2) and (5) Used Together with Equation (11) to Calculate Relative Permeability as a Function of Saturation for Imbibition

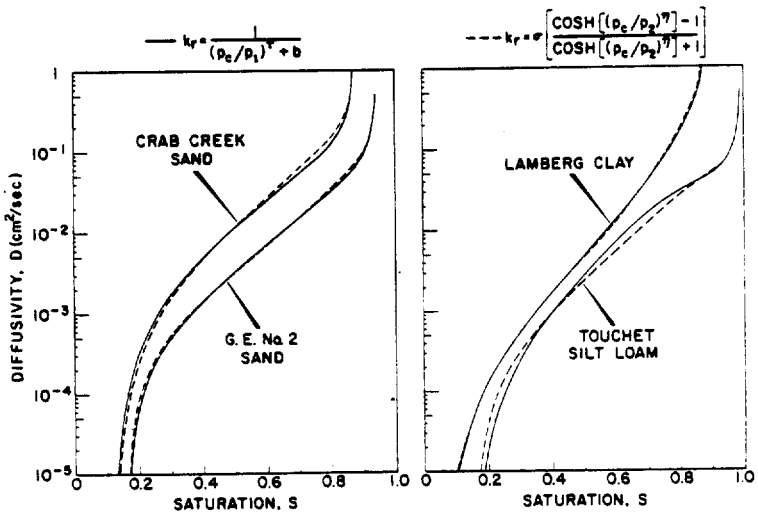

FIGURE 4.19

Comparision of Equations (2) and (5) Used Together with Equations (11), (12), and (13) to Calculate Diffusivity as a Functionn of Saturation for Imbibition

Neg. No. 0643106-2; 0643106-1

Measurement of Soil Characteristics for Partially Saturated Flow - L. G. King

Methods are described for obtaining and analyzing data for simultaneous laboratory measurement of liquid permeability, saturation, and capillary pressure of partially saturated porous media. The attenuation of gamma rays from an Am^{241} source was used to measure saturation of a column of soil. A typical set of results is shown. Results of this type are needed as input data for solution of partially saturated flow problems related to waste disposal analysis.

Methods of measuring soil characteristics have been explained in detail elsewhere.[4.28, 4.29] Briefly, when the inflow and outflow pressures of the liquid were properly controlled, steady flow was established and there was a zone of constant permeability, capillary pressure, and saturation within the column. In this zone, the capillary pressure was measured with tensiometers;[4.28, 4.29] the permeability was calculated from outflow and potential gradient determinations; and the saturation was calculated from gamma ray attenuation. Then, the inflow and outflow pressures were changed to give a new steady flow condition.

For a sand from central Washington, Figures 4.20 and 4.21 show results for a particular hysteresis loop.[4.25] The sand was completely saturated with "Soltrol C"* and then drained to a certain point after which it was allowed to imbibe liquid as indicated by the arrows on the figures. Each point, obtained for a steady flow condition, represents the average of measurements at six points.

All sections of the plastic soil-column container were machined, both inside and outside, to give identical geometries regardless of where the gamma ray source was positioned along the column. Thus, for a given soil material, the only variables affecting the count rate measured at the detector crystal were the bulk density and the amount of liquid filling the pores of the sample (i.e., the saturation). The absorption equation for a

* A core test fluid obtained from Phillips Petroleum Company

0028451

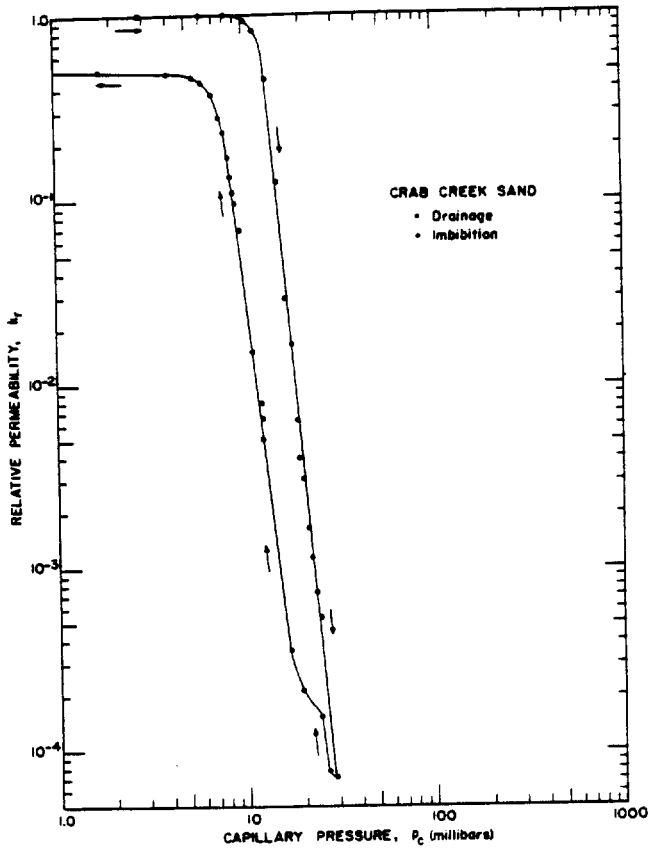

FIGURE 4.20

A Particular Hysteresis Loop for the Relative Permeability-Capillary Pressure Relationship

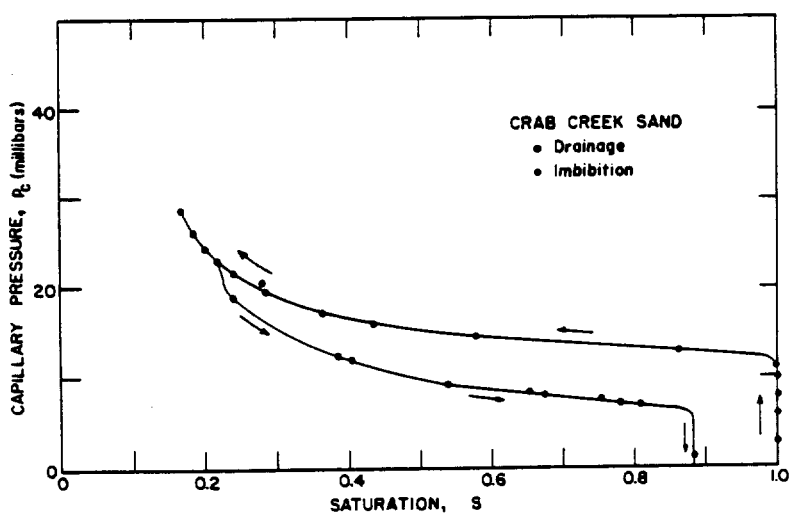

FIGURE 4.21

A Particular Hysteresis Loop
For the Saturation-Capillary Pressure Relationship

Neg. No. 0650561-2; 0650561-4

dry column of soil may be written

$$I_d/I_0 = e^{-D\mu_s\rho_s + N} \tag{1}$$

where I_d is the intensity transmitted through the dry column, I_0 is the incident intensity, D is the diameter, μ_s is the mass absoprtion coefficient for the soil, ρ_s is the bulk density of the soil, and N involves all the other values which are constant throughout the measurements. Likewise, for the column at any particular saturation,

$$I_w/I_0 = e^{-D(\mu_\ell\rho_\ell Sf + \mu_s\rho_s) + N} \tag{2}$$

where S is the saturation and f is porosity.

Dividing Equation (1) by Equation (2) gives

$$I_d/I_w = e^{D\mu_\ell\rho_\ell Sf} \tag{3}$$

or

$$\ln(I_d/I_w) = D\mu_\ell\rho_\ell Sf \quad . \tag{4}$$

For a given column, liquid, and porosity, D, μ_ℓ, ρ_ℓ, and f are constant. Hence, Equation (4) becomes

$$S = C \ln(I_d/I_w) \quad , \tag{5}$$

subject to the conditions: (1) when $I_w = I_d$, S = 0; (2) when $I_w = I_{w_0}$ (completely saturated column), S = 1. Using the second condition, C = $1/\ln(I_d/I_{w_0})$, and Equation (5) becomes

$$S = \frac{\log (I_d/I_w)}{\log (I_d/I_{w_0})} \quad , \tag{6}$$

where I_d is the count rate when the soil is dry, I_w is the count rate at any particular saturation, and I_{w_0} is the count rate when the soil is completely saturated.

Each time the column was counted, a standard was also counted to check for possible instrument drift. All count rates were adjusted by using the average of the standard count rate as a base. The adjusted count rates were used in Equation (6) to plot Figure 4.21.

Prediction of One-Dimensional, Transient, Partially Saturated Imbibition - L. G. King

Reasonable corrections have been applied to steady flow input data to calculate a transient boundary value problem. Calculations are compared to experimental transient data. The agreement leads to the conclusion that the equations give a reasonable description of the flow provided the boundary conditions are accurately specified and the soil characteristics are properly measured. These results support the current program of laboratory measurement of soil characteristics for partially saturated flow problems.

Consider a horizontal column of uniform dry soil to which is supplied liquid at a constant capillary pressure after time, t = 0. The problem may be formulated mathematically as the partial differential equation,

$$\frac{\partial S}{\partial t} = \frac{\partial}{\partial x}\left(D(S)\frac{\partial S}{\partial x}\right) \quad , \tag{1}$$

subject to the conditions,

$$S = S_o, \; x = 0, \; t \geq 0, \tag{2}$$

and

$$S = S_n, \; x > 0, \; t = 0, \tag{3}$$

where S is saturation, x is the horizontal distance measured from the end where liquid enters the column, t is time since liquid was applied, and D is diffusivity which is a function of S and is given by

$$D(S) = -\frac{k}{\mu f \frac{dS}{dp_c}} \tag{4}$$

In Equation (4), k is permeability (length-squared dimensions), μ is liquid viscosity, f is porosity of the soil, and p_c is capillary pressure.

A study was conducted which had as one of its objectives to determine if curves of k_r versus p_c and S versus p_c measured during steady flow conditions could be used to predict accurately the transient horizontal flow described above. Since reporting results of this study,[4.28] a very probable error was found in p_c of the k_r versus p_c relationship. This error was caused by the oil dissolving the plasticizers from the plastic tubing leading from the tensiometer ring to the glass manometer tube (Figure 4.22).

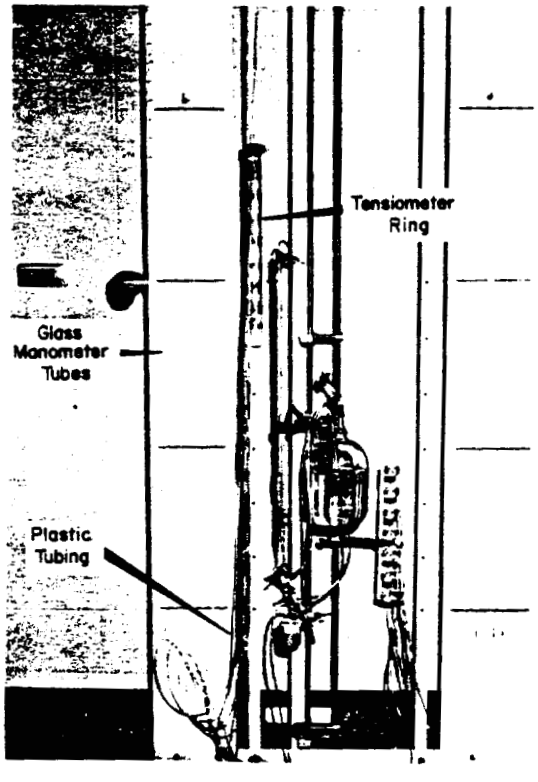

FIGURE 4.22

Permeability-Capillary Pressure Column During Initial Filling For Steady Imbibition Data

The oil in the plastic became more dense than that in the glass tube. This type of manometer can cause the measured capillary pressure to be as much as 1.8 millibars smaller than the actual capillary pressure. The transient data were predicted quite well when the p_c was corrected.

The corrected data were used as input to a computer program* for numerical solution of Equation (1) subject to Conditions (2) and (3). Results

* A. E. Reisenauer. "Iterative Calculation of One-Dimensional, Transient, Partially Saturated Flow," p. 4.53.

Neg. No. 0642552-3

are shown in Figure 4.23 where the input data were corrected as follows: (1) for Crab Creek Sand, 1.1 millibars was added to each p_c value of the k_r versus p_c relationship;[4.~~27~~ 28] (2) for GE No. 2 Sand, 1.4 millibars was

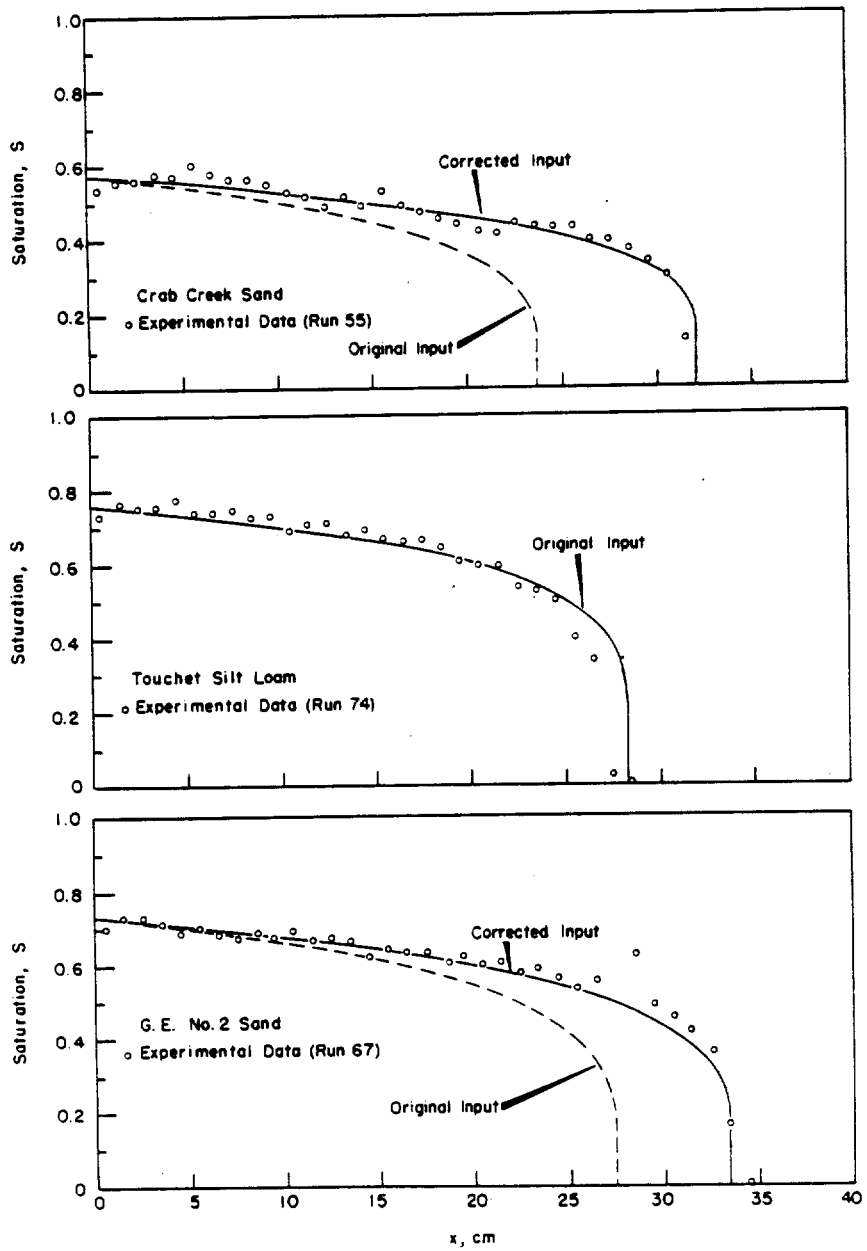

FIGURE 4.23

Effects of Correcting Capillary Pressure of the Steady Permeability-Capillary Pressure Data on Prediction of Transient, Horizontal Imbibition

Neg. No. 0650589

0028456

added; and (3) the Touchet Silt Loam data were not corrected. The Touchet Silt Loam data required no correction since almost all oil which was later in the glass manometer tube had been in contact with the plastic tube for some time. The other soils were started at a capillary pressure such that considerable fresh oil began in the glass manometer tube and remained there throughout the gathering of data. The "original input" on Figure 4.23 is the data reported earlier.[4.28] The "graphical computer input"[4.28] has been compared with the use of equations to describe the input data. The agreement was satisfactory; hence, the equations* were used for preparing Figure 4.23.

Results shown in Figure 4.23 further substantiate the general conclusion reached earlier:[4.28] "It is concluded that Equation (1) gives a reasonable description of the flow provided the boundary conditions are accurately specified and the diffusivity is measured properly."

Iterative Calculation of One-Dimensional, Transient, Partially Saturated Flow - A. E. Reisenauer

An iterative procedure based on Philip's method[4.30] for the numerical solution of the equation

$$\frac{\partial S}{\partial t} = \frac{\partial}{\partial x}\left(D \frac{\partial S}{\partial x}\right)$$

was programmed for a high-speed computer. Several significant improvements and additions to the method were made. The immediate application of this work is in formulating methods for predicting the transient development of the flow pattern beneath a waste storage tank or pipeline.

Horizontal, one-dimensional, transient, partially saturated flow in porous media is described by the equation

$$\frac{\partial S}{\partial t} = \frac{\partial}{\partial x}\left(D \frac{\partial S}{\partial x}\right) \quad , \tag{1}$$

subject to the conditions

$$S = S_n, \; t = 0, \; x > 0 \tag{2}$$

$$S = S_o, \; t \geq 0, \; x = 0 \tag{3}$$

* L. G. King. "Analytical Description of Soil Characteristics for Partially Saturated Flow", Equations (2) and (8), p. 4.39.

where S is saturation, t is time, x is horizontal distance and D, the diffusivity is

$$D = -\frac{k}{\mu f}\frac{dp_c}{dS} \quad . \tag{4}$$

In Equation (4), k is permeability, μ is liquid viscosity, f is soil porosity, and p_c is capillary pressure. Through the substitution,

$$\omega(S) = xt^{-1/2} \quad , \tag{5}$$

the solution of Equations (1), (2), and (3) reduces to the numerical solution of

$$\int_{S_n}^{S} \omega dS = -2\,D\,\frac{dS}{d\omega} \tag{6}$$

subject to the conditions

$$S = S_o,\ \omega = 0. \tag{7}$$

The numerical solution of Equations (6) and (7) given by Philip[4.30] was programmed for the IBM 7090 computer. The program provides flexibility in the method and adds several new features.

Hand tabulation of the values of D was eliminated by using either of two input methods. Since $S(p_c)$ and $k(p_c)$ data can be successfully fitted with equations,[4.25] the parameters of the equations are used as input to the program. From these functions the values of $\bar{D}$ are calculated at up to 100 increments in S. An integration with a capacity of 1000 increments is used in calculating the $\bar{D}$ needed for the initial estimates.

A means of using graphical data for the D(S) may also be used in place of the functional forms. The graphical method is described by King.[4.28]

During the iteration process the complimentary error function needs to be evaluated several times. Instead of Philip's function, A(x), the following methods of calculation are used.

The product, $f(\xi) = \sqrt{\pi}\, e^{\xi^2}$ erfc ξ, where $\xi = \varphi_{n-1}/2\sqrt{\bar{D}_{n-1/2}}$, is computed rather than erfc ξ alone. For $0 \le \xi \le \sqrt{2}$, the approximation used is

$$f(\xi) = 2\left(a_1 w + a_2 w^2 + a_3 w^3 + a_4 w^4 + a_5 w^5\right) \quad ,$$

where $w = 1/(1 + \bar{p}\xi)$ and a_1, a_2, a_3, a_4, a_5, and $\bar{p}$ are constants, the values of which are given by Hastings.[4.31]

For $\sqrt{2} < \xi \le 4$, $f(\xi)$ is approximated by an exponentially weighted polynomial of degree 8, the coefficients of which involved the Hermite orthogonal polynomials. The range of ξ is divided into 24 intervals of approximately equal length. A polynomial is obtained for the end points of each interval. For a given ξ, the interval end point nearest to ξ is used to determine the polynomial used for $f(\xi)$.

For $4 < \xi < \infty$, the asymtotic expansion,

$$\frac{1}{\xi}\left[1 + \sum_{p=1}^{N} (-1)^p \frac{(1)(3)(5)\ .\ .\ .\ (2p-1)}{\left(2\xi^2\right)^p}\right]$$

is used for $f(\xi)$. This asymptotic series is truncated either when the absolute value of the next term is greater than the absolute value of the last term or when the absolute value of the next term is smaller than 10^{-8} times the accumulated sum of terms.

The program requires as input the initial saturation, the final saturation, the porosity, and the column area in addition to the parameters of the equations or the graphical data for the internal calculation of the $\bar{D}$ values.

The program results include a list of $\bar{D}$ and φ values as a function of S for each iteration (all but the final values may be suppressed) as well as a listing of the moisture profile, S(x), for various input times.* These profiles are integrated to give the accumulated volume inflow for each time.

---

* L. G. King. "Prediction of One-Dimensional, Transient, Partially Saturated Imbibition, p. 4.50.

0028459

Comparison of Approximate Solution for Flow in Heterogeneous Soil with an Exact Solution - A E. Reisenauer

A statistical comparison between the results of an exact solution and a finite difference solution of the same boundary value problem showed a standard error of difference of 2.56×10^{-5}, due entirely to the approximation of the continuous derivatives with discrete increments. The combined error of the derivative approximation and averaging of the permeability, as done to solve for flow through heterogeneous soil, showed a standard error of difference of 8.88×10^{-4}.

The solutions of problems involving incompressible flow through porous media are generally obtained through finite difference methods.[4.18] Such methods usually ignore the error in the approximation of the continuous derivatives with discrete segments. An estimate of this error can be obtained by comparing a boundary value problem solved both analytically and by finite differences.

In problems involving the equations which apply to saturated flow through heterogeneous porous media, stability during the finite difference iteration may be a problem. Stability can be maintained in such cases by averaging the permeability about the point and substituting this number for the value at the central node, as called for by the point pattern of the equations.[4.19, 4.32] This practice introduces an added error of unknown magnitude into the resulting solution. A closed form solution for a specific boundary value problem provided a means of investigating the magnitude of each of the errors.

The physical model described in the boundary value problem is a rectangular soil volume of length L, width ℓ, and height λ. There is no component of flow through the sides or bottom; all flow is in the horizontal direction, entering from one end.

The boundary conditions in the directions of flow are:

$$\psi(0, y, z) = 0.0 \tag{1}$$

$$\psi(L, y, z) = \left(\cos \frac{\pi y}{\ell} + \frac{b\ell}{2\pi} \sin \frac{\pi y}{\ell}\right)\left(\cos \frac{\pi z}{\lambda} + \frac{d\lambda}{2\pi} \sin \frac{\pi z}{\lambda}\right) e^{-\frac{by}{2} - \frac{dz}{2}} \tag{2}$$

where a, b, and d are constants.

The partial differential equation used to describe the flow is:

$$\frac{\partial^2 \varphi}{\partial x^2} + \frac{\partial^2 \varphi}{\partial y^2} + \frac{\partial^2 \varphi}{\partial z^2} + a \frac{\partial \varphi}{\partial x} + b \frac{\partial \varphi}{\partial y} + d \frac{\partial \varphi}{\partial z} = 0 \quad . \tag{3}$$

Two cases were solved with the permeability, K, being varied:

$$K = 1.0 \tag{4}$$

$$K = e^{ax + by + dz} \quad . \tag{5}$$

Each case was solved on a three-dimensional grid, and the results were used as the initial estimate to the answer of the finite difference solution. The values at the ends of the model (through which flow moved) were not iterated but were used as fixed boundaries. Thus from Equation (4) we get results in which the difference between the closed form solution and the finite difference solution was due entirely to the difference approximation. Also, from Equation (5) we get a flow system which provides a basis for evaluating the error associated with averaging the permeability values.

A statistical comparison between the finite difference solution of the boundary value problem having a constant permeability (Equation 4) and the closed-form solution showed a mean difference of -7.6×10^{-8} and a standard error of difference of 2.56×10^{-5}. This result reflects only the error of using discrete segments in the finite difference approximations.

The combined error of the derivative approximation and the averaging of the permeability, as done when solving the finite difference method with varying permeability (Equation 5) is shown by a mean difference of 3.27×10^{-4} and a standard error of difference of 8.88×10^{-4}. Both of the comparisons were based on matrices containing 7380 node points.

Neutron Soil Moisture Monitor - E. M. Sheen, W. L. Bunch, and M. R. Wood*

---

* Reported in Section 5, Instrumentation

0028461

Atmospheric Radioactivity and Fallout, Aerosol Studies

Analysis of Particle Size Frequency Distributions - G. A. Sehmel

A method has been developed to fit particle size distributions if the size frequency distribution does not fit one of the standard forms. By application of the method, an analytical expression is obtained which smooths the experimental data. The method is based on a least squares technique to fit a partial distribution function that extends over the limits of the experimentally determined size range.

An accurate knowledge of the particle size frequency distribution is required for fundamental studies in mass and heat transfer in micromeritics in which the aerosol transport properties are a function of particle size. For example, inertial impaction of particles on a surface is proportional to the square of the particle size, the deposition of particles from a turbulent air stream onto the surfaces of a conduit is proportional to the fourth power of the particle size, and the errors associated with anisokinetically sampling aerosols from an air stream are a function of particle size. Since most aerosols include particles of nonuniform sizes, a problem is to separate the behavior of each size. Only for nearly uniform aerosols from the LaMer generator or spinning disc generator, from pollens, or from dispersed polystyrene latex spheres is the problem averted. Nevertheless, nonuniform aerosols are almost a prerequisite for some studies in which certain aerosol physical properties are required. In some experiments, even when a uniform aerosol could be used, eventual contamination of the equipment with particles of the several sizes may ultimately require the use of particle sizing and size distribution analysis.

Much work has been done on the development of automatic devices and instrumental aids to increase the accuracy and the rapidity with which particle size distributions can be made. In general, the output from each method is the same as that obtained through the use of a calibrated graticule in the eyepiece of a microscope. Particles are sized and recorded as being within a series of size ranges. The data must then be processed by some method of interpolation to determine the number of particles of any required size.

0028462

Several methods have been developed to assist in determining size distributions from the numbers determined in each size range. Except for two (the log normal and the Weibull distributions which may have theoretical significance for some types of distributions) the methods consist of using empirical equations to represent the data.

To represent a true size distribution, the fraction of the total number of particles having radii between r and r + dr can be written,

$$df = f(r)dr,$$

with the normalizing condition,

$$\int_0^\infty f(r)dr = 1 \quad .$$

The function, f(r), is the frequency distribution curve or the differential curve of the particle size distribution. In practice, analytical expressions for size distributions are used which may not satisfy the normalizing criteria. Nevertheless, at times the aerosol research worker must choose between several models to represent the data. The models include:

- Mixed exponential[4.33]
- Normal[4.33, 4.35]
- Log-normal[4.33, 4.35]
- Weibull[4.34]
- Nukiyama-Tanasawa[4.33, 4.35]
- Mugele-Evans upper-limit function[4.35]
- Rosin-Ramler.[4.33, 4.35]

Even within this wide range of models, some size distributions cannot be adequately represented.

In a recent study[4.36] the particle size distribution was observed to change rather drastically between experimental runs. The previously mentioned models did not fit the size distributions, and a systematic method of representing the data was required.

A method was developed to yield an expression for the particle size distributions between the limits of the experimentally determined size range. The method is based on a first estimation of the size frequency distribution, integration to determine the calculated number of particles in any size range, comparisons with the experimentally determined number of particles, and iteration until the size distribution as determined by least squares techniques converges. Computer processing facilitates the calculations.

In developing the method of calculation, we observed that the logarithm of the quotient of the percentages of particles in any size increment divided by the width of the size increment in microns, was nearly linear with the particle size at the midpoint of the increment or at most could be represented by a cubic expression on semilog paper. The cubics approximated the true size distributions. The goal was to determine the best cubic (or lower power) expression for the size distribution.

From the previously mentioned quotients for each size increment, a least squares curve was calculated through the average particle size in each size increment. The analytical least squares curve was integrated to obtain the calculated number of particles in each size increment. Next, the calculated, CALC, and experimental percentage, EXP, in each size increment is compared and the comparison used as a basis for the first iteration. That is for each average size, $\bar{X}$, in an increment, ΔX, the next estimate of the frequency distribution, f, at $\bar{X}$ is

$$f_{i+1} = f_i + \frac{\text{EXP-CALC}}{\Delta \bar{X}} .$$

The calculation is repeated, and by the fifth iteration a well defined curve is obtained.

Using this technique a wide range of size distributions was successfully represented by analytical methods. Representative fits with experimental data are shown in Figure 4.24.

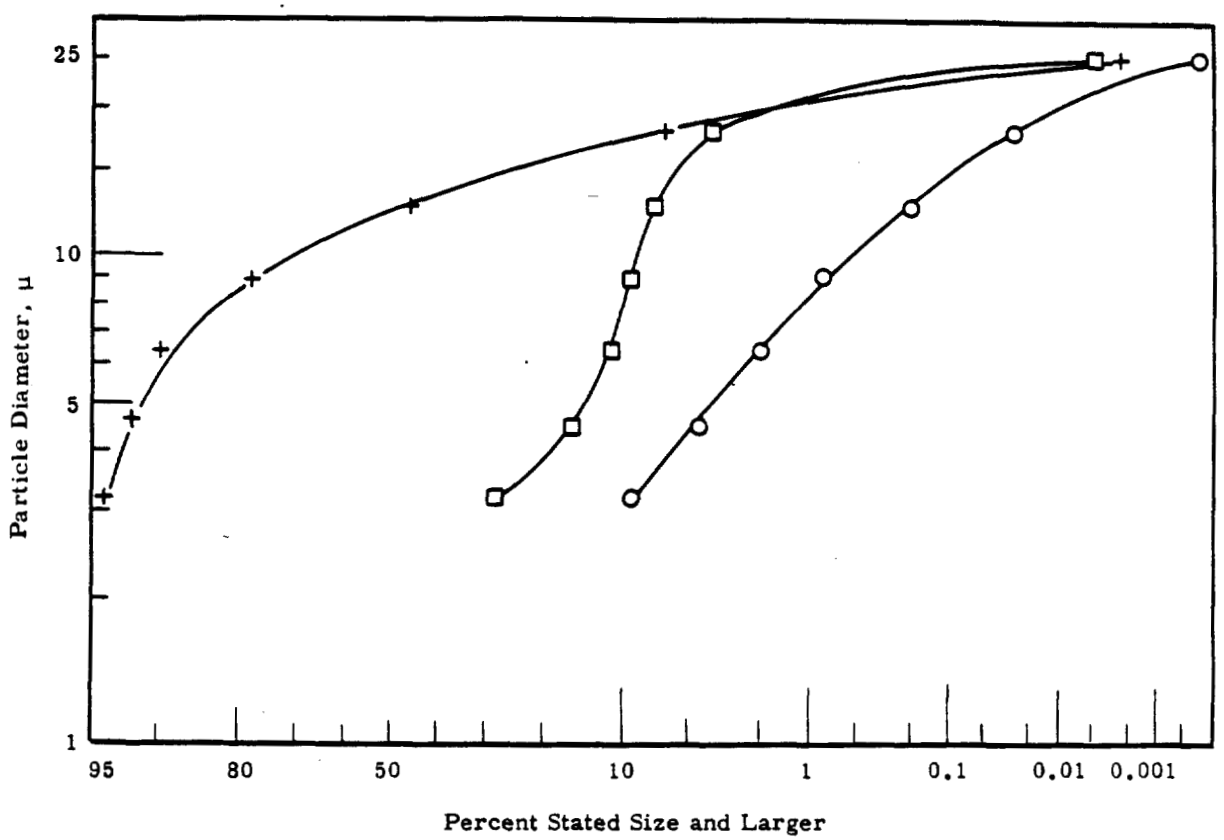

FIGURE 4.24

Calculated and Experimental Size Distributions

The method should have application to orders greater than cubic if more than seven size increments are measured.

Theoretical Expressions for the Motion of Particles in a Temperature Gradient - A. K. Postma

An analysis of the aerodynamic and thermal forces acting on a particle in a temperature gradient was made without the simplifying, although unrealistic, assumptions made in earlier derivations. Expressions were derived for the net force on a particle and the velocity with which the particle will move in a thermal gradient. The derived equation for particle velocity agrees with equations of Brock,[4.37] a surprising result in light of the unrealistic assumptions. The velocity of thermal repulsion from the more realistic model used in this study does not agree with velocity calculated from the more familiar Epstein equation for thermal force.

Neg. No. 0650186-1

The phenomenon of thermal repulsion of particles suspended in fluids has received extensive theoretical and experimental investigation. The theoretical calculations of the thermal forces for particles large compared to the gas mean free path have been made under the assumption that the particle remained stationary with respect to the fluid far from the particle.[4.37, 4.38]

In reality, the observed phenomena, e.g., thermal diffusion, thermal deposition, etc., result from the motion caused by the thermal force. Schadt and Cadle[4.39] have pointed out that the velocity of thermal repulsion has heretofore been calculated by equating the thermal force exerted on a stationary particle to Stokes Law force arising from the particle motion. Mathematically written, this is

$$\text{thermal force} + \text{viscous force} = 0. \qquad (1)$$

Since Equation (1) applies to the steady motion of the particle through the fluid, both of the forces must be calculated for the condition existing when the particle moves uniformly through the gas. Neither the thermal force calculated from present theories, nor the Stokes' Law viscous force satisfy this requirement. As noted above, the thermal force has been calculated for a particle stationary with respect to the fluid stream, and it is not self-evident that the force does not depend on the gas flow which will result if the particle moves. The Stokes-Cunningham equation for viscous force is based on boundary conditions which require that the tangential velocity at the wall depends only on the rate of shear at the wall. For thermal motion this condition is not even approximated. It can be shown that there is an additional velocity at the surface of the sphere, the magnitude of which varies from zero to a value greater than the velocity of thermal repulsion.

Experimentally, Schadt and Cadle[4.39] found reasonably good agreement between the thermal force obtained from Stokes' Law and the thermal force measured statically by balancing it with an electrical force. This observed agreement rightly raised doubts in the minds of these investigators regarding the validity of the theory of thermal forces.

0028466

The object of the present work is to resolve the questions raised above regarding the velocity of thermal repulsion. This involves a rederivation of the thermal force equation, including the effect of a relative velocity, U, between the particle and the gas stream. The velocity of thermal repulsion will be the value of U for which the net force vanishes.

The net aerodynamic force acting on a particle may be obtained by integrating the normal and tangential stresses acting on the surface. The value of these stresses depends on the velocity profile, which was obtained from Stokes' solution for flow around a sphere, allowing for a nonzero fluid velocity, U. The arbitrary constants in the velocity profile equations were determined from the conditions at the surface of the sphere, which required a solution for the temperature distribution. The final equation for the net force on a sphere is

$$F = \frac{4\pi\mu a}{\left(1 + 3C_m \frac{\ell}{a}\right)} \left\{ -\frac{9}{4}\frac{\mu g}{\rho T} \frac{\left(\frac{k_f}{k_s} + C_t \frac{\ell}{a}\right)}{\left(1 + \frac{2k_f}{k_s} + 2C_t \frac{\ell}{a}\right)} + U\left(\frac{3}{2} + 3C_m \frac{\ell}{a}\right) \right\} \qquad (2)$$

where

F = net force on particle
μ = gas viscosity
a = particle radius
g = temperature gradient
ρ = gas density
T = average absolute temperature near particle
k_f = thermal conductivity of fluid
k_s = thermal conductivity of particle
U = relative velocity between particle and distant fluid
C_t = thermal accommodation coefficient
C_m = momentum accommodation coefficient
ℓ = mean free path in fluid.

The velocity of thermal repulsion can be obtained from Equation (2) by setting the net force, F, equal to zero. This gives for the velocity of thermal repulsion:

$$U = \frac{3}{2}\frac{\mu g}{\rho T}\frac{\left(\frac{k_f}{k_s} + C_t\frac{\ell}{a}\right)}{\left(1 + 2C_m\frac{\ell}{a}\right)\left(1 + \frac{k_f}{k_s} + 2C_t\frac{\ell}{a}\right)} \quad . \tag{3}$$

It is interesting to compare this velocity with that obtained by equating the thermal force predicted by earlier equations (based on U = 0), to the Stokes-Cunningham viscous force. The result depends on the equation used to obtain the thermal force. From Brock's[4.37] equation for thermal force, the velocity calculated in this manner is identical to that given in Equation (3), which is surprising in light of the discussion above. If Epstein's[4.38] equation for thermal force is equated to the viscous force, we get

$$U = \frac{3}{2}\frac{\mu g}{\rho T}\frac{k_f\left(1 + C_m\frac{\ell}{a}\right)}{\left(k_s + 2k_f\right)} \quad . \tag{4}$$

Aside from the difference in the effect of thermal conductivity, this equation predicts an increase in U as the particle size decreases, for all particle and stream parameters. This is in contrast to Equation (3) which predicts that the velocity may either increase or decrease with particle size, depending on the relative magnitudes of k_f, k_s, C_t, C_m, and $\frac{\ell}{a}$.

The velocity of thermal repulsion obtained by equating the thermal force on a stationary particle with the Stokes-Cunningham viscous force has been compared to the velocity obtained by a rederivation of the thermal force allowing for a relative velocity, U, between the particle and the fluid. Agreement is obtained if, in the former method, the thermal force is calculated using Brock's[4.37] equation. If the thermal force is calculated according to Epstein's[4.38] equation, the velocity of thermal repulsion is predicted to increase with increasing $\frac{\ell}{a}$ values, for all particle and stream

parameters. This is not in agreement with the results of the analysis based on the more realistic model in which the particle motion is taken into account. The latter predicts that the velocity of thermal repulsion may either increase or decrease with $\frac{\ell}{a}$, depending on the relative magnitudes of k_f, k_s, C_t, C_m, and $\frac{\ell}{a}$.

The experimentally observed agreement[4.39-4.41] between the thermal force measured statically with that calculated from Stokes' Law is explained theoretically.

Electrical Charges on Particles Produced by a Spinning Disc - A. K. Postma

A brief study was made of the sign and magnitude of charge per particle prepared with a spinning disc aerosol generator. Virtually all particles had a positive charge of from 300 to 1000 electronic units. Static charges on the spinning disc were found to be unimportant in influencing the charge carried by the particles. Disc speed, disc composition, and dye concentration were also examined to determine their effect.

To evaluate electrical effects on the behavior of an aerosol, it is necessary that the magnitude of the particle charge be known. For aerosols produced by evaporation of an atomized liquid, the initial particle charge should be equal to the charge on the liquid drop. According to the accepted theory of statistical fluctuations in ion concentration,[4.42] the drop charge is symmetrically distributed about zero charge, with the average number of elementary charges being dependent upon the ionic concentration and the drop size. Initial experiments were conducted to determine the applicability of this theory to the charging of particles produced by a spinning disc generator. The liquid aerosolized was a dilute solution of uranine and methylene blue in ethanol. The charge on the test aerosol was determined by depositing the particles in an electric field maintained between two parallel plates. Since the aerosol stream was introduced midway between the planes, the particle charge could be calculated by determining the point at which deposition occurred on the plate. The amount of

0028469

material deposited as a function of the distance downstream was obtained by cutting the plates into 1-in. sections, which were subsequently washed in distilled water. The dye content of the water was then measured fluorometrically.

Although the experiments to date cannot be considered complete, the following observations are worth noting.

- All of the particles collected had a positive charge. This is in contrast to theoretical prediction that 50% of the drops would have a negative charge.
- The average charge varied from 300 to 1000 electronic units, depending on the dye concentration and the disc speed. For a particular operating condition, the charges were log-normally distributed, with a standard deviation of approximately 20%.
- For the same disc speed, the charges were larger for the lower dye concentrations.
- Static charges on plastic parts of the apparatus were not important in determining drop charge. This was demonstrated by the observation that the charging was the same after exposed plastic parts were covered with a grounded aluminum foil. Thus the charging does not appear to be produced by induction in an externally applied electric field.
- The charges produced were the same for a glass disc as for a stainless steel disc, implying that the composition of the disc is unimportant.

From these observations the following tentative conclusions may be drawn.

- The charges on particles produced by a spinning disc generator cannot be accurately predicted from the statistical ion fluctuation theory.
- Highly charged particles are formed, requiring neutralization if electrical effects are to be made negligible.

- Since the charges are all of the same sign, it may be possible to effectively neutralize the charge by impressing a potential gradient between the disc and the surrounding cage, which would considerably simplify the apparatus.

Particle Deposition and Retention in Vertical Conduits - G. A. Sehmel

All available experimental data relating to turbulent deposition of particles in vertical conduits were empirically correlated using least squares techniques. A single semi-dimensionless equation presented accounts for 92% of the experimental data scatter. A new term is introduced into the correlation which allows for deviations from Stokes' Law behavior of the particle drag coefficient.

Representative samples from gaseous streams containing fine particles of radioactive materials are commonly required in plants which process nuclear materials. Since the sample delivery lines are usually unavoidably long, information on the impaction and deposition of these particles is required to interpret the sample results in terms of the concentration in the gaseous streams Identification of the parameters controlling deposition on surfaces will also contribute to a better understanding of deposition of airborne particles on terrain and vegetation. The retention of particles on surfaces is also of interest in evaluating contamination spread and the degree of hazard from unusual incidents releasing appreciable quantities of radioactive aerosols.

It is the purpose of this study to determine the quantitative relationships among the variables governing particle deposition in conduits and to establish deposition models which are supported by the data.

Particulate deposition during turbulent flow has been measured by Friedlander and Johnstone,[4.43] and by Postma and Schwendiman.[4.44] In both studies, the deposition velocity, K, cm/min, was determined from the average concentration of particles in the gas stream and the number of particles deposited on the tube wall.

To improve upon the semi-theoretical equations[4.43] for predicting the deposition velocity, Sehmel and Schwendiman;[4.45] Schwendiman, Sehmel, and Postma;[4.46] and Epstein and Evans[4.47] have developed empirical equations or correlations to represent the existing deposition data. In all cases, one significant parameter may have been neglected. This is the non-dimensional drag coefficient, C_d. The drag coefficient should be important in deposition since the particles must be stopped from the main air stream velocity and deposited through the rather thin layer of the hypothetical quiescent boundary layer.

The drag coefficient is defined for a falling sphere as the ratio of the drag resistance to the product of the cross-sectional area and the dynamic pressure,

$$C_d = \frac{(\text{drag force})}{\frac{1}{2}\rho_g v^2 \frac{\pi d^2}{4}}$$

where ρ_g is the air density, v is the terminal settling velocity, and d is the particle diameter. For a spherical particle which obeys Stokes' Law,

$$\text{Drag force} = 3\pi\mu\, vd = \frac{\pi}{6} d^3 \left(\rho - \rho_g\right) g$$

where μ is the air viscosity, ρ is the particle density, and g is the gravitational acceleration. The drag force is $3\pi\mu$ vd; hence, the equations reduce to

$$C_d = \frac{24}{Re_p} .$$

For particle Reynolds' numbers, Re_p, greater than about one,

$$C_d = \frac{24}{Re_p}\left[1 + f\left(Re_p\right)\right]$$

where f is a function. The deviations from Stokes' Law behavior can be given by the expression,

$$\psi = 1 + f\left(Re_p\right) .$$

Thus $\psi > 1$ is an indication of the deviations of the air wake around a particle from ideal behavior. To represent analytically the deviations presented by Fuchs,[4.48] the following expression was developed to represent the drag coefficient dependency upon the particle Reynolds' number:

$$C_d = \frac{24}{Re}\left[1 + \left(a + b\,Re + c\,Re^2 + d\,Re^3 + e\,Re^4\right)\left(Re^f\right)\right]$$

where

$$a = -1.1205 \times 10^{-3}$$
$$b = 1.2009 \times 10^{-1}$$
$$c = -2.0444 \times 10^{-4}$$
$$d = 2.9734 \times 10^{-7}$$
$$e = -1.2782 \times 10^{-10}$$
$$f = -2.1210 \times 10^{-1}$$

All coefficients are statistically significant and the equation is applicable for particle Reynolds' numbers of 1 to 1000.

In the particle deposition work, the experimental particle Reynolds' numbers based on the main stream air flow were as high as 24. This corresponds to ψ values of from 1.0 to 2.4. To evaluate the statistical significance of ψ, least squares techniques were used to calculate empirical logarithmic transformed equations to correlate the data of Friedlander and Johnstone[4.43] and Postma and Schwendiman.[4.44] Of the equations developed to date, the best empirical fit is the following semi-dimensionless equation:

$$K = 6.60 \times 10^{-21}\, \rho^{1.24771} \left(\frac{d}{D}\right)^{4.11174} \left(\frac{Re^{4.95818}}{\psi^{7.18737}}\right)$$

in which

K = deposition velocity, cm/min
ρ = particle density, g/cm^3
d = particle diameter, μ
D = tube diameter, cm
Re = tube Reynolds' number.

All coefficients are statistically significant and the multiple correlation coefficient is 0.9615. Thus, 92.5% of the variation in the data is accounted for by the correlation. The correlation is applicable to the following range of experimental data:

K = 0 003 to 1500 cm/min
ρ = 2.2 to 7.8 g/cm^3
d = 0.8 to 30 μ diameter
D = 0.5 to 2.6 cm diameter
Re = 2000 to 30,100.

The correlation may be interpreted to suggest that the deposition constant, K, increases as the fifth power of the air velocity and the fourth power of the particle diameter. These same power dependencies were predicated theoretically by Friedlander and Johnstone for reduced stopping distances of less than about one.

The suggested correlation is in agreement with theoretical power dependencies and introduces the statistically significant parameter ψ. While refinements in the correlation are in progress, considerable refinements in experimental techniques are needed to determine more accurately the functional dependency of the deposition constant on physical parameters.

Improved Aerosol Generators and Applications - A. K. Postma

Performance parameters of a spinning disc aerosol generator were determined. Aerosols were prepared with very narrow size distribution from colloidal suspension of iron and silica as well as from several soluble salts. The generator has proved to be of considerable worth in studying the behavior of particles 2 to 10 μ.

A spinning disc aerosol generator designed and fabricated locally was operated using various solutions and colloids for generating particles. The operating parameters of disc speed, feed solution concentration, and delivery rate, satellite withdrawal air volume, and particle transport air were investigated to establish how these parameters affected particle characteristics and generation rates. The generator was described and the operating parameters discussed in Reference (4.49) and will not be repeated here.

Very nearly uniform particles can be prepared from various compounds. Methylene Blue, Rhodamine B, sodium chloride, and lead nitrate were the soluble materials used. Colloidal suspensions were also investigated and were very promising. Iron oxide sols and silica sols available commercially gave spherical, uniform aerosols.

The use of minute amounts of intensely colored dyes and fluorescent organic compounds as tracers for soluble salts and sols used to generate aerosols was investigated. Tracers of Methylene Blue and Rhodamine B could be leached from insoluble particles of iron oxide and silica, hence these organic dyes can serve as a measure of the quantity of aerosol generated. They are easily measured colorimetrically or fluorometrically.

Photomicrographs of particles generated by the spinning disc generator are shown in Figure 4.25 and an elevation drawing of the generator is shown in Figure 4.26.

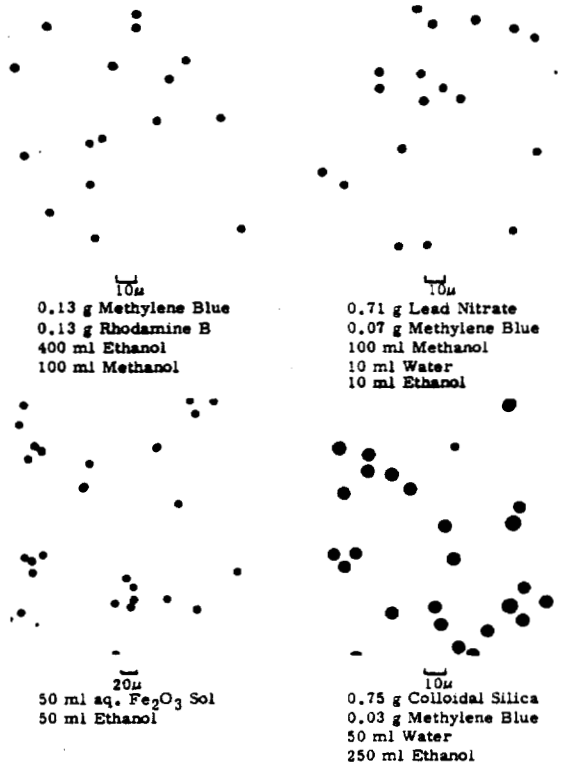

FIGURE 4.25

Photomicrographs of Particles Generated

Neg. No. 0650186-2

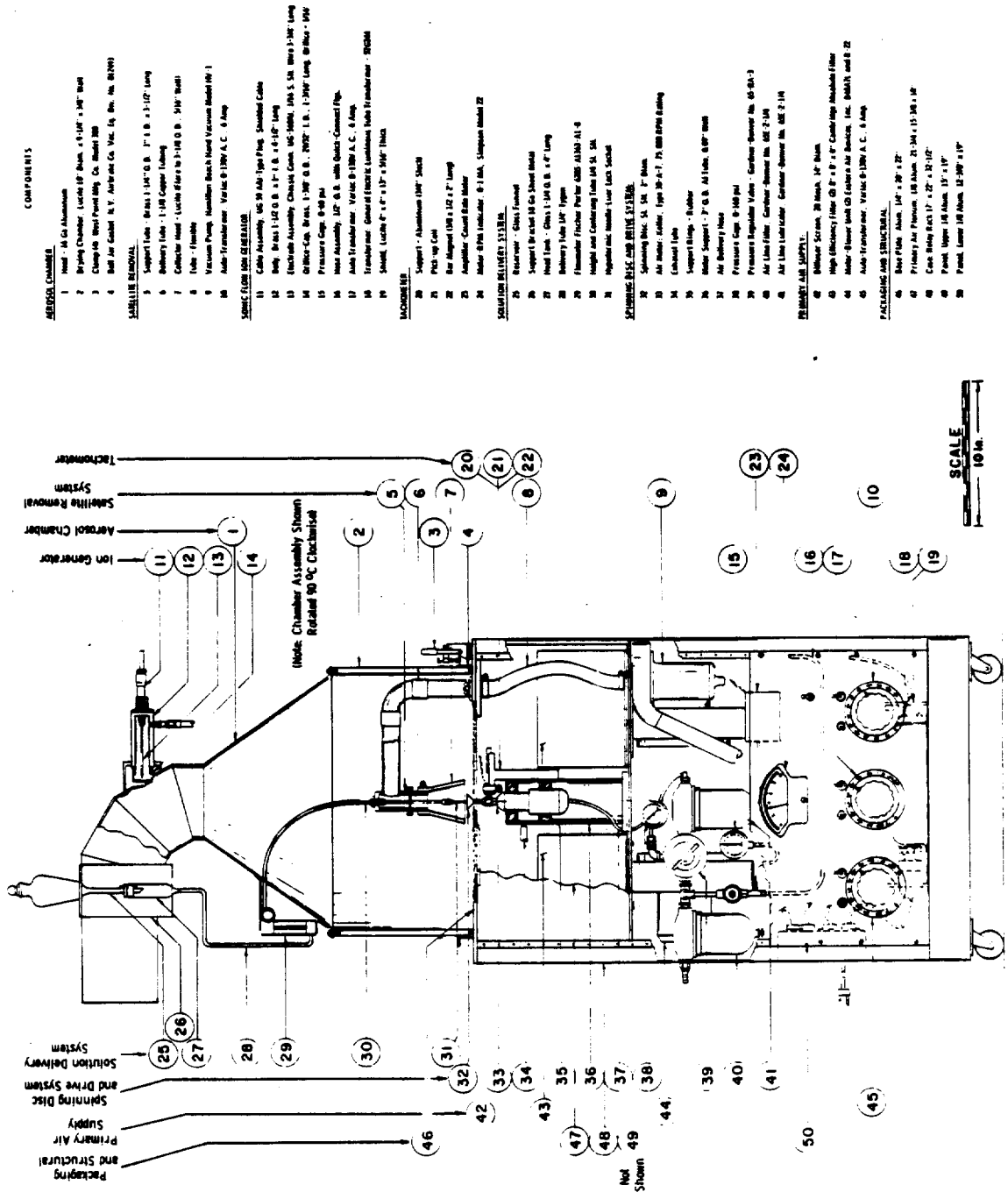

FIGURE 4.26

Improved Aerosol Generator

Neg. No. 0641580

REFERENCES

4.1 F. E. Bear. Chemistry of the Soil, Reinhold Publishing Corporation, New York, 1964. 2nd Ed., pp. 200-202.

4.2 D. R. Nielsen and J. W. Biggar. "Miscible Displacement: IV, Mixing in Glass Beads," Soil Sci. Soc. Am. Proc., vol. 27, pp. 10-13. 1963.

4.3 L. K. Porter, W. D. Kemper, R. D. Jackson and B. A. Stewart. "Chloride Diffusion in Soils as Influenced by Moisture Content," Soil Sci. Soc. Am. Proc., vol. 24, pp. 460-463. 1960.

4.4 A. Ogata. Dispersion in Porous Media, Northwestern University, August 1958. (Ph. D. thesis).

4.5 M. L. Jackson. Soil Chemical Analysis-Advanced Course. Mimeograph, published by the author, Madison, Wisconsin, pp. 31-164. 1956.

4.6 F. Helfferich. Ion Exchange, McGraw-Hill, New York, p. 260. 1962.

4.7 R. E. Tomlinson. The Hanford Program for Management of High-Level Waste, HW-SA-2515. 1962.

4.8 L. L. Ames, Jr. "Some Zeolite Equilibria with Alkaline Earth Metal Cations," Am. Mineral, vol. 49, p. 1099. 1964.

4.9 R. M. Barrer and W. N. Meier. "Exchange Equilibria in a Synthetic Crystalline Exchanger," Trans. Faraday Soc., vol. 55, p. 130. 1959.

4.10 G. Eisenman. "Cation Selective Glass Electrodes and Their Mode of Operation," Biophys. J., vol. 2, no. 2, p. 259. 1962.

4.11 R. W. Nelson. "In-Place Measurement of Permeability in Heterogeneous Media I. Theory of a Proposed Method," J. Geophys. Res., vol. 65, no. 6. June 1960.

4.12 R. W. Nelson. "In-Place Measurement of Permeability in Heterogeneous Media I. Experimental and Computational Considerations," J. Geophys. Res., vol. 66, no. 8. August 1961.

0028477

REFERENCES (Contd.)

4.13 R. W. Nelson. "Conditions for Determining Areal Permeability Distributions by Calculation," Journal of the Society of Petroleum Engineers. September 1962.

4.14 C. A. Oster. GENORO, A General Data Fitting and Linear Functional Evaluation Computer Code for the IBM 7090, HW-76692. May 1963.

4.15 R. W. Nelson. "Stream Functions for Three-Dimensional Flow in Heterogeneous Porous Media," Proceedings of XIII General Assembly, International Union of Geodesy and Geophysical Section of International Association of Scientific Hydrology, Pub. No. 64, p. 290, Berkeley. 1963.

4.16 R. W. Nelson. The Permeability Integral - A Key to Measurement in Heterogeneous Porous Media, cf. The following paper.

4.17 R. W. Nelson, C. A. Oster, and A. B. Schubert. Unpublished Data, Battelle-Northwest.

4.18 R. W. Nelson. "Steady Darcian Transport of Fluids in Heterogeneous Partially-Saturated Porous Media," Part 1, Mathematical and Numerical Formulation, HW-72335, Pt. 1. June 1962.

4.19 A. E. Reisenauer, R. W. Nelson and C. N. Knudsen. "Steady Darcian Transport of Fluids in Heterogeneous Partially-Saturated Porous Media," Part 2, The Computer Program, HW-72335, Pt. 2. October 1963.

4.20 Gabreal Kron. Diakoptics - The Piecewise Solution of Large-Scale Systems, Macdonald and Co., London, England. 1963. p. 166.

4.21 R. W. Nelson. Unpublished Data, Battelle-Northwest. April 1964.

4.22 R. W. Nelson. "Flow in Heterogeneous Porous Media I. Darcian Description of Two-Phase Systems," To be published in J. Geophys. Res.

0028478

REFERENCES (Contd.)

4.23 J. E. Warren and H. S. Price. "Flow in Heterogeneous Porous Media," Journal of the Society of Petroleum Engineers, vol. 1. no. 3. 1961.

4.24 W. R. Gardner. "Some Steady-State Solutions of the Unsaturated Moisture Flow Equation with Application to Evaporation from a Water Table," Soil Sci., vol. 85, pp. 228-232. 1958.

4.25 L. G. King. "Description of Soil Characteristics for Partially Saturated Flow," To be published in Soil Sci. Soc. Am. Proc.

4.26 L. G. King and A. E. Reisenauer. "Analytical Description of Soil Parameters for Partially Saturated Flow," Hanford Radiological Sciences Research and Development Annual Report for 1963, HW-81746, pp. 4.42-4.47. January 1964.

4.27 R. H. Brooks and A. T. Corey. Hydraulic Properties of Porous Media, Hydrology Paper No. 3, Colorado State University. 1964.

4.28 L. G. King. Imbibition of Fluids by Porous Solids, Colorado State University, 1964. (Ph. D. dissertation).

4.29 L. G. King. "Measurement of Soil Parameters for Partially Saturated Flow," Hanford Radiological Sciences Research and Development Annual Report for 1963, HW-81746, pp. 4.39-4.42. January 1964.

4.30 J. R. Philip. "Numerical Solution of Equations of the Diffusion Type with Diffusivity Concentration-Dependent," Trans. Faraday Soc. vol. 51, no. 391, pt. 7. July 1955.

4.31 Cecil Hastings, Jr. Approximations for Digital Computers (Princeton, New Jersey).

4.32 A. E. Reisenauer. "Methods of Solving Problems of Multidimensional Partially Saturated Steady Flow in Soils," J. Geophys. Res. vol. 68, pp. 5725-5733. 1963.

0028479

REFERENCES (Contd.)

4.33 H. L. Green and W. R. Lane. Particulate Clouds: Dusts, Smokes and Mists, D. Van Nostrand Company, Inc., Princeton, New Jersey. pp. 229-232. 1964.

4.34 J. H. K. Kao. "A Graphical Estimation of Mixed Weibull Parameters in Life Testing of Electron Tubes," Technometrics, vol. 1, no. 4, pp. 389-407. November 1959.

4.35 R. A. Mugele and H. D. Evans. "Droplet Size Distributions in Sprays," Ind. Eng. Chem., vol. 43, no. 6. pp. 1317-1324. June 1951.

4.36 G. A. Sehmel. Subisokinetic Sampling of Particles in an Air Stream, cf p. 4.58.

4.37 J. R. Brock. "On the Theory of Thermal Forces Acting on Aerosol Particles," J. Colloid Sci., vol. 17, p. 768. 1962.

4.38 P. S. Epstein. "Zur Theorie des Radiometers," Z. Physik, vol. 54. p. 437. 1929.

4.39 C. F. Schadt and R. D. Cadle. "Thermal Forces on Aerosol Particles," J. Phys. Chem., vol. 65, p. 1694. 1961.

4.40 P. Rosenblatt and V. K. LaMer. "Motion of a Particle in a Temperature Gradient; Thermal Repulsion as a Radiometer Phenomenon," Phys. Rev., vol. 70, p. 385. 1946.

4.41 R. L. Saxton and W. E. Ranz. "Thermal Force on an Aerosol Particle in a Temperature Gradient," J. Appl. Phys., vol. 23, p. 917. 1952.

4.42 T. T. Mercer. "Aerosol Production and Characterization: Some Considerations for Improving Correlation of Field and Laboratory Derived Data," Health Physics, vol. 10, pp. 873-887. 1964.

4.43 S. K. Friedlander and H. F. Johnstone. "Deposition of Suspended Particles from Turbulent Gas Streams," Ind. Eng. Chem., vol. 49, pp. 1151-1156. 1957.

REFERENCES (Contd.)

4.44 A. K. Postma and L. C. Schwendiman. Studies in Micromeritics, I. Particle Deposition in Conduits as a Source of Error in Aerosol Sampling, HW-65308. May 1960.

4.45 G. A. Sehmel and L. C. Schwendiman. The Turbulent Transport and Deposition of Particles Within Vertical Tubes, Eighth AEC Air Cleaning Conference, Oak Ridge, Tennessee, October 22-25, 1963. HW-SA-3183. 1963.

4.46 L. C. Schwendiman, G. A. Sehmel, and A. K. Postma. Radioactive Particle Retention in Aerosol Transport Systems, International Conference on the Radioactive Pollution of Gaseous Media, Saclay, France, November 12-16, 1963, HW-SA-3210. October 1963.

4.47 L. F. Epstein and T. F. Evans. Deposition of Matter from a Flowing Stream, GEAP-4140, General Electric Company. December 1962.

4.48 N. A. Fuchs. The Mechanics of Aerosols, translation edited by C. N. Davies, The MacMillan Company, New York, p. 32. 1964.

4.49 L. C. Schwendiman, A. K. Postma, and L. F. Coleman. A Spinning Disc Aerosol Generator," Health Phys., vol. 10, p. 947-953. December 1964.

0028481

INSTRUMENTATION

Radiological Measurement Methods and Instrumentation

Alpha Energy Analysis Plutonium Air Monitoring - D. P. Brown and N. S. Porter

Detection of low level concentrations of airborne plutonium is hampered by the simultaneous collection of naturally-occurring alpha emitters (radon and thoron) on the filter. A method for discriminating between the natural background and plutonium has been realized using alpha energy analysis techniques.[5.1, 5.2] This report describes an alpha air monitor, that uses energy analysis, developed for use at the Inhalation and Toxicology Laboratory at Battelle-Northwest. Three identical detectors, made with 3-in. multiplier phototubes and 1 mil thick CsI(Tl) crystals are employed to monitor for airborne alpha contamination in three separate locations in the laboratory. Signals from the preamplifiers are mixed in a 3-channel pulse mixer circuit, inverted, and coupled to the amplifier-discriminator. The amplifier-discriminator output drives a count-rate-meter to provide an indication of the natural (radon-thoron) alpha activity. The amplifier output drives a pulse height analyzer, which in turn drives a second count-rate-meter to indicate total alpha activity, which can be recorded. The count-rate-meter currents are compared and the difference is used to actuate alarm circuitry. The monitor has a sensitivity of about 9 MPC-hr for the detection of airborne Pu^{239}.

Discussion

A system for detecting airborne plutonium at three different locations in the Biology Inhalation Toxicology Laboratory was desired. Earlier work with alpha energy analysis[5.1] had indicated that an increase in detector size and air flow rate would result in greater sensitivity than was realized in the prototype instrument. Accordingly, 3-in. diam detectors were specified. Due to economic considerations, it was desired to utilize available equipment to the degree possible and still meet the

---

*. A sensitivity of 9 MPC-hr means that the instrument can detect no less than one maximum permissible concentration in 9 hr or nine maximum permissible concentrations in 1 hr.

requirement to monitor three separate locations simultaneously. This required the development of special mixing circuitry and switching capability.

A system block diagram is shown in Figure 5.1. The high voltage

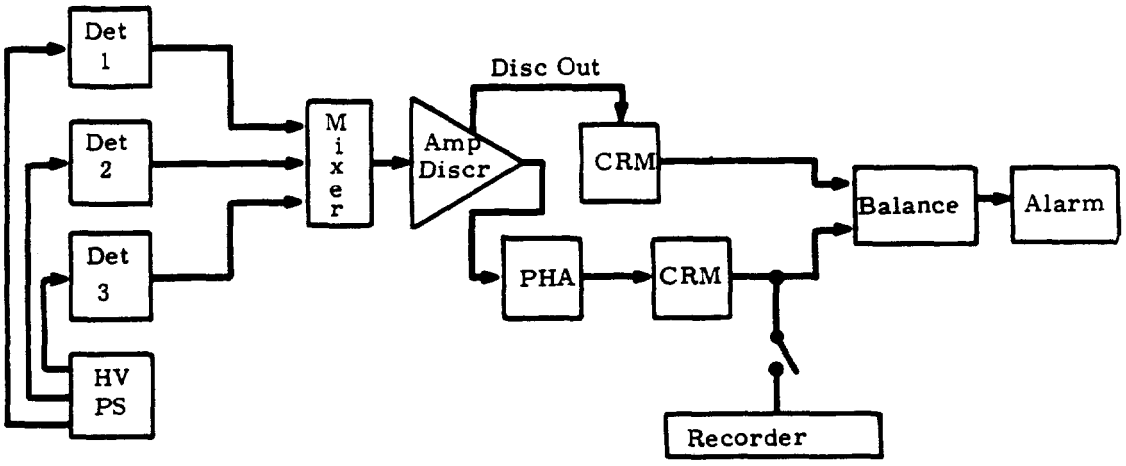

FIGURE 5.1

Alpha Air Monitor

supply, amplifier-discriminator, and pulse-height analyzer are "Designer Series" modules of Radiation Instrument Development Laboratory, as are the preamplifier designs. The two count rate meters are Technical Measurements Corporation type RM-1B. A perforated aluminum can, which surrounds the multiplier phototube in each detector, is adjustable in height and holds the filter holder approximately 1/4 in. from the crystal. Building vacuum is used to draw room air through the filter at about 6 ft^3/min for the asbestos filters and 4 ft^3/min for the membrane filters. The crystals are 1 mil thick [CsI(Tl)] and mounted on 1/8 in. light pipes, which are optically coupled to the phototubes. Three layers of 0.2 mg/cm^2 aluminum dutch leaf and one layer of 0.9 mg/cm^2 double-aluminum coated Mylar® cover each crystal to prevent light leaks. A magnetic shield is also provided. The dynode resistor voltage divider, voltage adjustment potentiometer, P1, and preamplifier are located in the base of the assembly. The transistorized preamplifier, mounted on a single printed circuit board, features a positive pulse output, single cable for signal and power input, and employs charge integration and pulse shaping within a stabilized feedback circuit to minimize distributed capacitance effects. Power supply voltage measured

at the UHF output connector is approximately -10 V dc under full load. The high voltage must be of positive polarity.

A channel selector module contains the decoupling circuits for the three detectors, a signal mixer, and an inverter stage. The schematic diagram is shown in Figure 5.2. The signals from the detectors pass to the mixer through a selector switch that is wired to allow the operator to monitor any one or all of the signals simultaneously. The three separate inputs are directed to the bases of three transistors. Since the collector current is relatively independent of the collector-to-emitter voltage, the three transistors have their collectors connected in common through a single resistor. Signal gain through the mixer is approximately four for each channel. Because the commercial amplifier requires a positive pulse input, the mixed signal is inverted through unity gain amplifier, Q4. Additional gain is possible from this stage by increasing the collector resistor appropriately. These circuits use a supply voltage of 10 to 15 V dc.

Output pulses from the amplifier vary up to a maximum of +10 V, while the discriminator output provides uniform pulses of 10 V magnitude with 0.5 μsec duration for all input pulses above the discrimination level. The discriminator output drives the count-rate-meter, which monitors alpha activity due to natural emitters. The amplifier output goes to the pulse height analyzer.

The heart of the system is the pulse height analyzer, since it discriminates between those pulses due to collected Pu^{239} and those caused by natural emitters. In operation, the threshold window voltage and window width are adjusted to view the peak Pu^{239} energy spectrum. Figure 5.3 shows typical Pu^{239} and natural emitter spectra. It is seen that some background from the natural emitters will fall within the window and will be counted. These are balanced out by subtracting the natural emitter contribution, as monitored on the upper CRM, from the total alpha count, as monitored on the lower CRM. The difference is the count due to Pu^{239}. To accomplish this, two meter currents are "bucked" against one another in a balance circuit, and the difference is used to actuate the alarm circuitry.

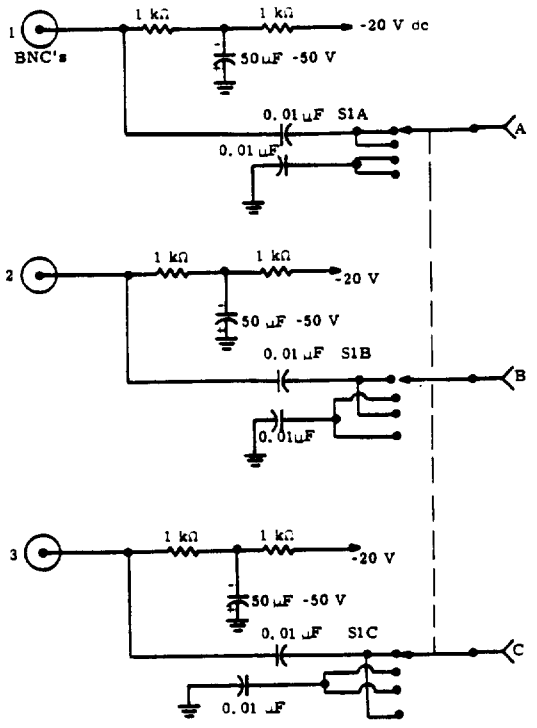

a. Detector Selection and Decoupling Circuits

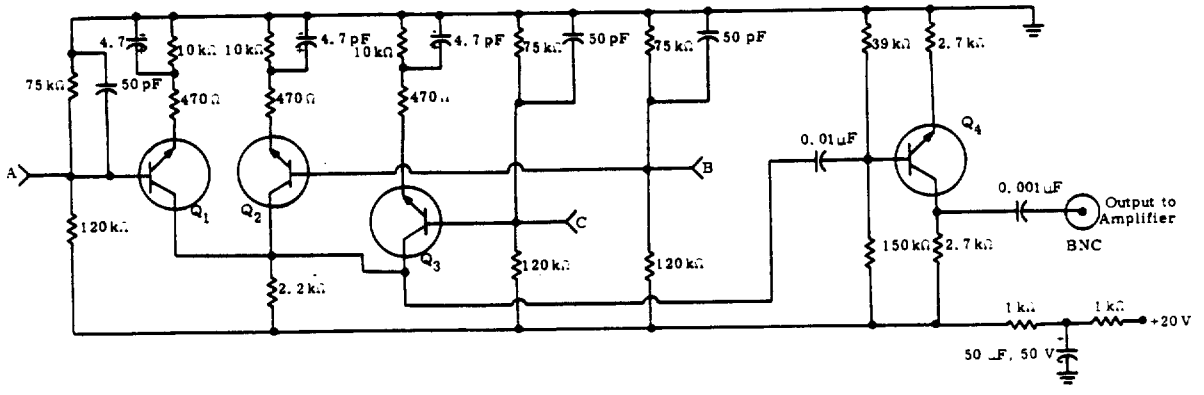

b. Mixer-Inverter Circuits

FIGURE 5.2

Channel Selector Module
($Q_1 \ldots Q_4$ = 2N2219
Whole Values = pF, Others μF)

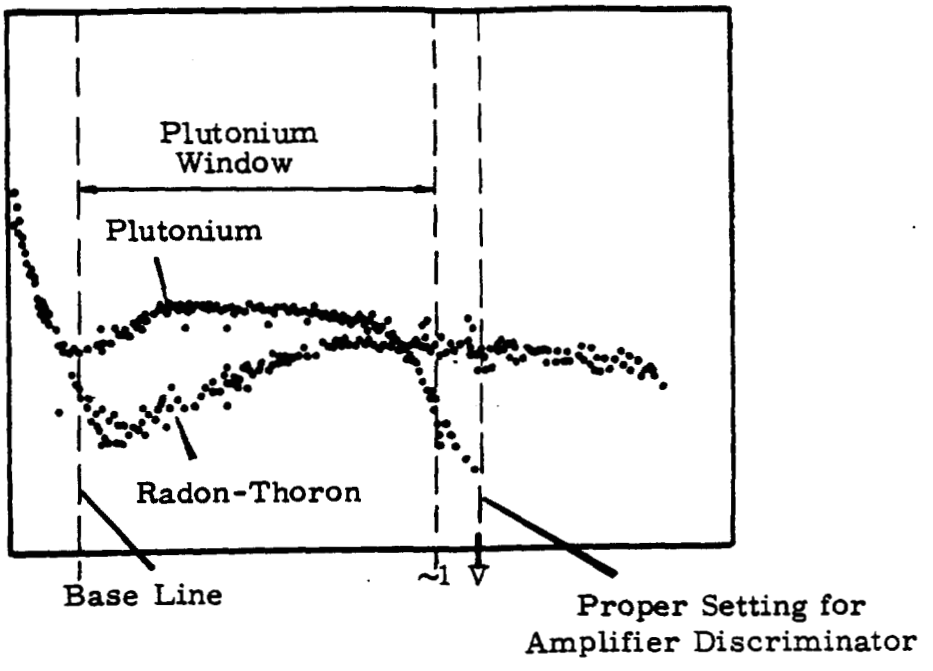

FIGURE 5.3
Typical Energy Spectra

The alarm system uses a "Versatrol" assembly to perform the alarm function. Upper and lower alarm limits can be set at the meter-relay front face. Alarm indicators are the front panel lights and the bell. Secondary alarming is provided from the count-rate-meters by adjusting their alarm points at each front panel to a desired percent of full scale. When this set-point is reached by the CRM pointer, the CRM will energize the alarm unit.

The sensitivity of this system depends on the air flow rate through the filter since the rate of contamination buildup on the filter is directly proportional to the flow. The time required for 400 disintegrations/min to accumulate and cause alarm, at a flow rate of 6 ft^3/min in an environmental Pu^{239} concentration of 1 MPC (2×10^{-12} $\mu Ci/cm^3$), is 529 min or about 9 hr. This yields a sensitivity of 9 MPC-hr. For other concentrations and flow rates, the time to alarm is given by

$$T_a = \frac{Pu}{(Q)(MPC)}$$

where

T_a = time to alarm

Pu = disintegrations/min to cause alarm (400 disintegrations/min)

Q = Flow rate in ft^3/min

MPC = 2×10^{-12} $\mu Ci/cm^3$ or 12.57×10^{-2} disintegrations/(min)(ft^3) for Pu^{239}.

The completed instrument, shown in Figure 5.4 with one of the three detectors, has operated successfully for several months at the Inhalation Toxicology Laboratory.

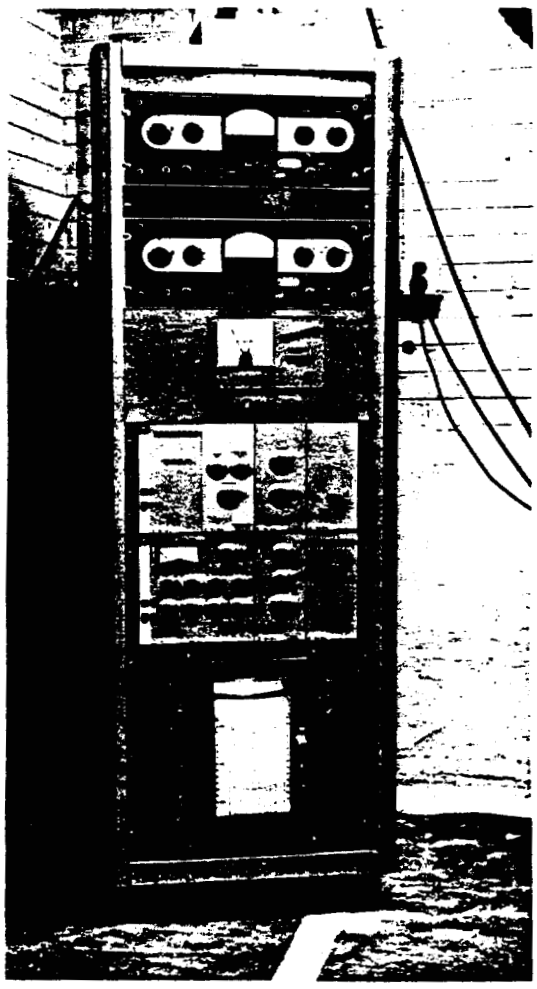

Neg. No. 0641600

FIGURE 5.4
Alpha Air Monitor in Cabinet

Detection of Low Energy Beta Particles - C. A. Ratcliffe and E. M. Sheen

During surveys for radioactive contamination, many types of radiological instruments are used. The detection of low energy beta particles, as from Pm^{147}, is difficult because the particles are not sufficiently energetic to penetrate the usual detector wall or window. Three physical probe configurations and two companion solid-state preamplifier designs presented in this paper are suitable, in particular, for the detection of low energy beta particles as from Pm^{147}. The designs include a large area probe for rapid monitoring of large surface areas, a similar small probe for personnel monitoring, and a wedge-shaped probe for monitoring in corners and other places in which the other two would not be suitable. Two preamplifiers allow up to 500 ft of coaxial cable to be used between the probes and the amplifying count-rate, and/or annunciating instrumentation, such as a "Scintran."(5.3) One preamplifier, which has a low current requirement, is powered at all times, with battery life estimated to be in excess of 1 yr. The other preamplifier, also requiring only a small current, is switched on and off automatically with the multiplier phototube dynode voltage divider current.

Discussion

Three probes for the detection of low energy beta particles will be described with notes on the preamplifier design.

The large area probe is shown assembled in Figure 5.5 and disassembled in Figure 5.6. The probe incorporates an EMI-9530 multiplier phototube, a low noise type with a 5 in. diam disk of 0.01 in. thick NE-102,* covered with two layers of aluminum "dutch leaf" and a layer of scintillation grade, double aluminized Mylar.® The total "thickness" of the covering is thus about 1.3 mg/cm^2. The phototube is covered (except for the photocathode) with black plastic electrical tape to eliminate light. The probe housing is a 10 in. length of 6 in. diam thin wall aluminum pipe, with a fitted end cover; a handle is attached for carrying convenience. The sensitive end of the probe is covered with 72% open area brass screen for mechanical protection. A small, wheeled dolly was fabricated to simplify monitoring of floor areas, and in operation, the probe is adjusted so the sensitive end is about 1/4 in. from the floor.

* Nuclear Enterprises, Ltd., Winnipeg, Canada.

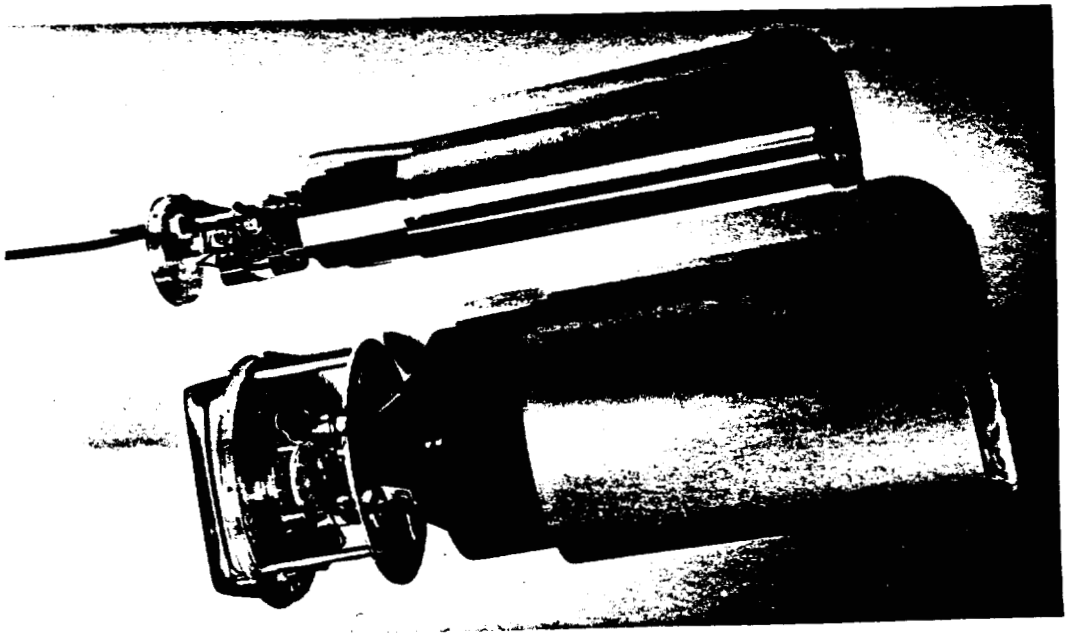

FIGURE 5.6
Detectors, Disassembled to Show Construction

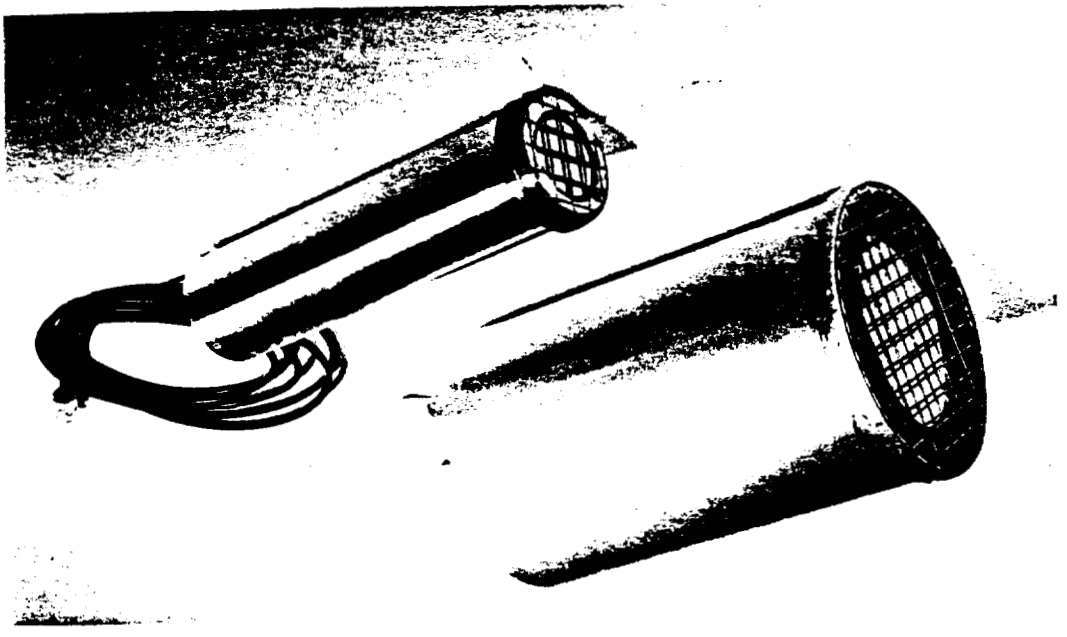

FIGURE 5.5
Detectors for Low Energy Beta Particles

Neg. No. 0640805-2; 0640805-1

0028489

The large area probe preamplifier, shown in Figure 5.7, is a Darlington-connected emitter follower with a power switch (Q3) controlled by current in the phototube dynode resistor voltage divider. When the main instrument, which contains the high voltage power supply, amplifiers, and other circuits is energized, the current in the dynode voltage divider switches on Q3, which had the preamplifier as a collector load. Transistor Q3 is a silicon transistor with low I_{CBO} so battery drain is negligible when the main instrument is not energized. Battery life should be about 3000 hr. The high voltage filter and pulse separator network ($R_F C_F$) has a sufficiently slow rise time to prevent destruction of Q1. A gain control is provided to adjust the voltage across the phototube; both large steps and vernier control are available.

A smaller probe, useful in personnel monitoring, uses an EMI-9536B multiplier phototube carefully mounted in a $2\frac{1}{2}$ in. diam thin-wall aluminum tube. This is also shown assembled in Figure 5.5 and disassembled in Figure 5.6, and the preamplifier is shown in Figure 5.7 and in schematic in Figure 8. The scintillator type, covering material, and mesh screen are as described for the large area probe. Preamplifier 2, which is powered by a single mercury cell with an estimated life of 12,000 hr, uses the bias resistors for Q1 as the phototube load resistor, and the 1 kΩ emitter resistor also forms part of the high voltage filter and pulse separator network. A Zener diode protects the emitter-base diode of the transistor during the "turn-on" transient. This preamplifier, and the one described previously, is capable of driving at least 500 ft of coaxial cable to the main instrument. The battery and preamplifier, mounted between the phototube base and the probe end cap, are insulated since they "float" at the potential of the high voltage supply. No gain control is provided on this preamplifier.

The third probe is shown in Figure 5.9 and (in section) in Figure 5.10. No preamplifier is included as it is intended for use close to the main instrument. The preamplifier of Figure 5.8 could be added easily, however, for use with cables longer than about 10 ft. If the cable is to be long, a preamplifier is mandatory, as the signals are small and the added

0028490

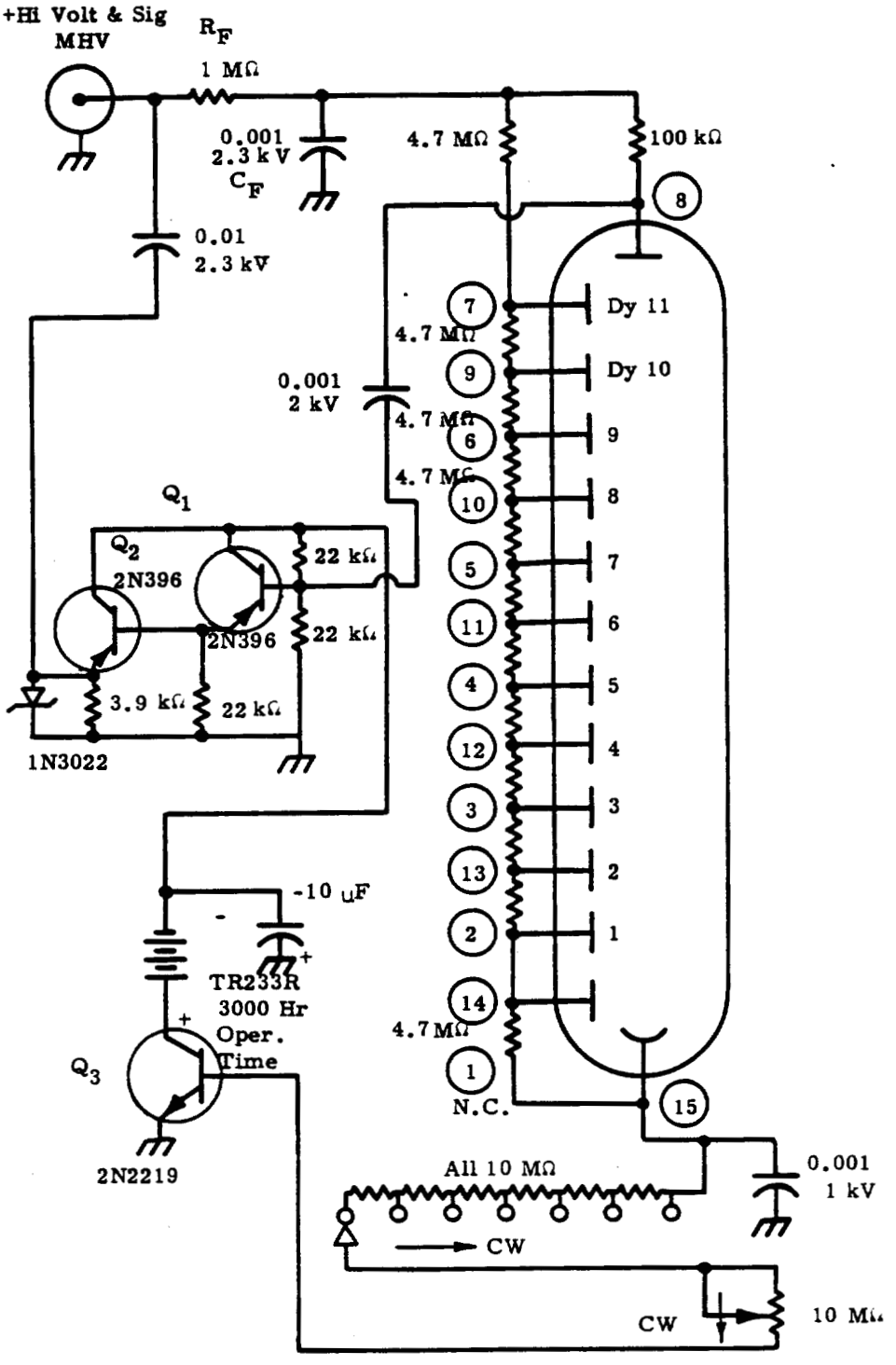

FIGURE 5.7

Preamplifier with Power Switching

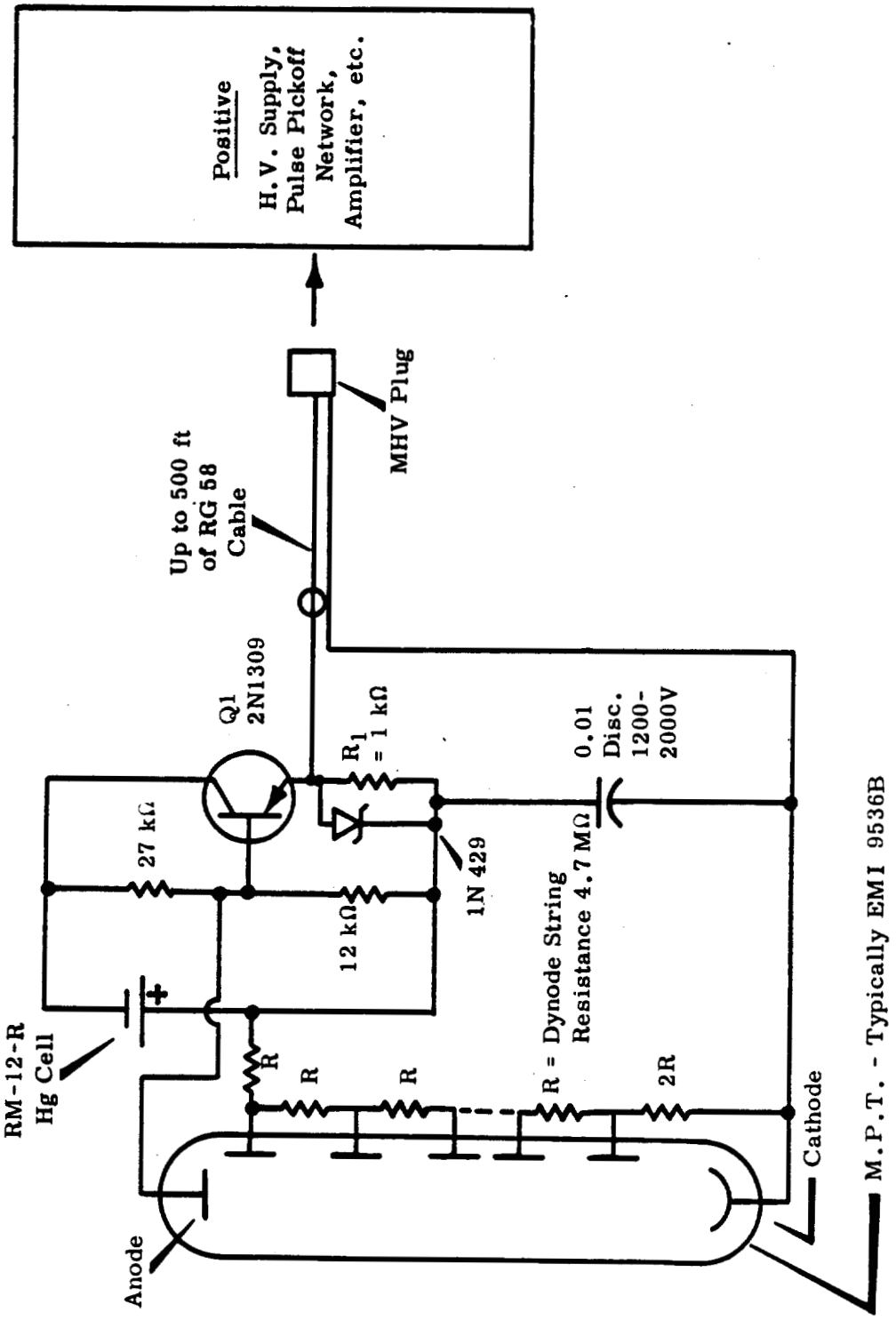

FIGURE 5.8
Preamplifier Schematic

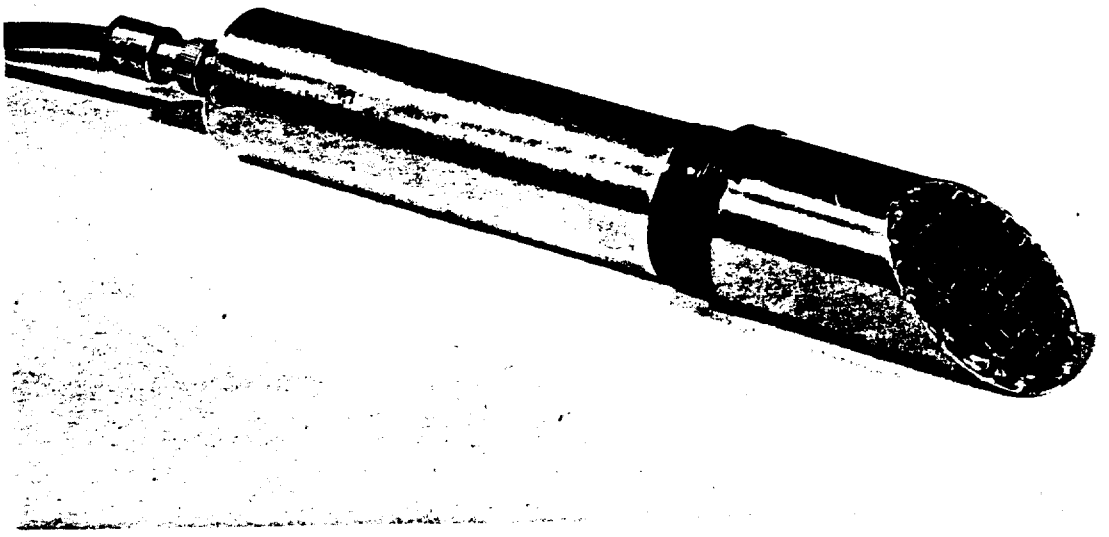

FIGURE 5.9
Wedge-Shaped Probe

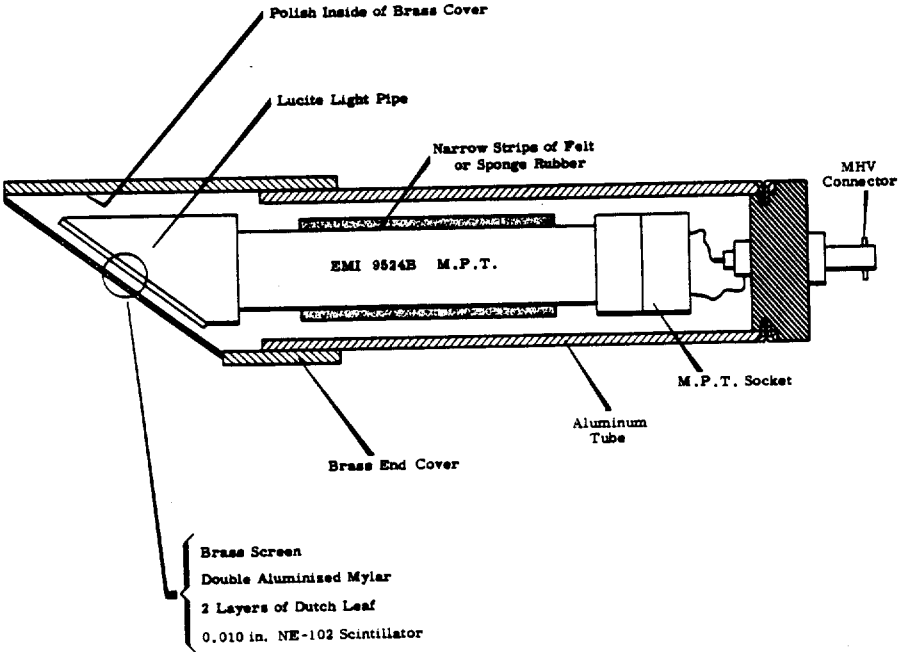

FIGURE 5.10
Section of Wedge Probe

Neg. No. 0642234-1

0028493

capacitance will degrade the signal below the noise level. A 1.5 in. diam, low-noise EMI-9524B multiplier phototube was chosen for the detector, as all possible noise must be suppressed. The scintillator was again 0.01 in. thick NE-102 with covering and screening as before. Since the scintillator, in this case, is not directly on the face of the phototube, a short piece of polished lucite was fitted to the aluminum tube and to the phototube. The inside of the brass tube was also polished near the light pipe, which is fastened to the aluminum tube with two short screws. The end cap, closely fitted to the aluminum tube, has a single MHV connector mounted on it.

Three probes of different configurations were designed and tested for the detection of low energy beta particles. In addition, two preamplifier designs have been shown, either of which may be fitted to any of the probes. These preamplifiers permit single cable operation and will drive up to 500 ft of cable to the main instrumentation.

The detectors were tested with Pm^{147} point sources of various activity levels and exhibited detection efficiencies of 3 to 10% with suitable background correction and discriminator adjustments. The large probe exhibited a 10% counting efficiency with a 7/8 in. diam plated source, and a 3% efficiency with the Pm^{147} deposited on blotter, where absorption caused a reduction in counting efficiency. Similar tests on the 2 in. diam probe yielded 8 and 3% efficiencies, respectively. The wedge probe yielded 3 to 9% depending on the position of the source relative to the counting window, high voltage employed, and the sensitivity adjustment of counting instrument. All three probes, particularly those containing the preamplifiers, exhibited adequate signal-to-noise ratios at all usable discriminator settings, making field adjustment and use easy. The units may be used over a temperature range from 10 to 120 F—suitable for most applications.

On some occasions, the Mylar® covering may have minute pin holes in it. The location of these holes may be ascertained by operating the probe and counting system and scanning the probe with light from a small, focused light. If a pin hole is found, it can be covered with either black acetate ink or silver paint.

Method for Beta-Gamma Hand and Shoe Counting Under Varying Background Conditions - W. G. Spear

Instrumentation for radionuclide detection and measurement is usually required and one instrument commonly used for personnel protection is the hand and shoe counter. Stringent beta-gamma emitting radionuclide detection requirements and varying background radiation levels at many Hanford locations preclude the usual techniques. Contamination detection requirements at Hanford for hands, shoes, and clothing cannot be met by standard hand and shoe counters when the gamma background exceeds about 50 μR/hr. Use of scintillation detectors and solid state circuitry was developed for detection of a 10 nCi Ra D-E-F standard test source under gamma background from a normal level of about 15 μR/hr up to 1mR/hr. An automatic method of compensating or subtracting the gamma background was used and the performance reflects a 20:1 improvement over usual beta-gamma hand and shoe counters. A prototype instrument has been successful in extensive field tests.

Advanced Alpha-Beta-Gamma Hand and Shoe Contamination Monitor - C. A. Ratcliffe and E. M. Sheen

Development of an advanced hand and shoe contamination monitor was based on the need to improve general performance of such instruments by increasing the counting signal-to-background ratio and by providing new solid state circuits. A desired unit cost reduction was an added incentive for development of the improved instrument and, in addition, it was desired to have essentially the same general design for alpha-beta-gamma, for beta-gamma, and for alpha only monitors. The monitor incorporates the low-noise multiplier phototubes, lucite light pipes, probe preamplifiers to provide the best signal to noise ratio, and new solid state circuits throughout. The design is basically for a combination alpha-beta-gamma monitor; however, the general design features are directly applicable to the manufacture of single purpose instruments, as for beta-gamma only or for alpha only monitors.

Discussion

Figures 5.11 and 5.12 are block diagrams of the monitor and pertinent electronic circuits. Many of the circuits are used in several channels; thus, in many cases, the circuits were assembled with two or more per printed circuit board with separation achieved by function and by channel to simplify signal tracing techniques.

0028495

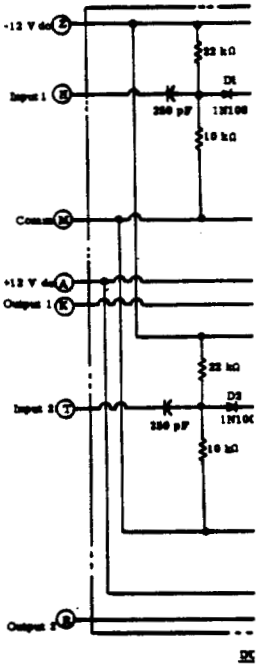

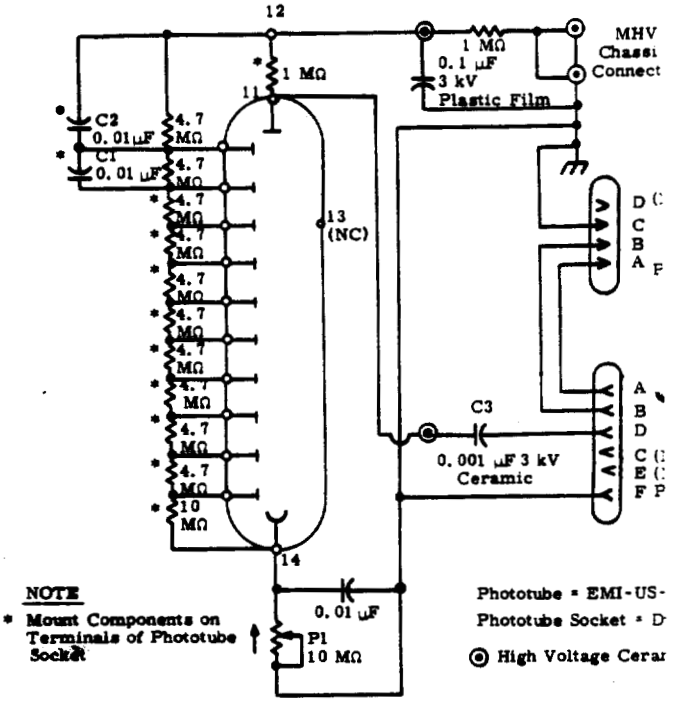

HAND AND SHOE PROBES

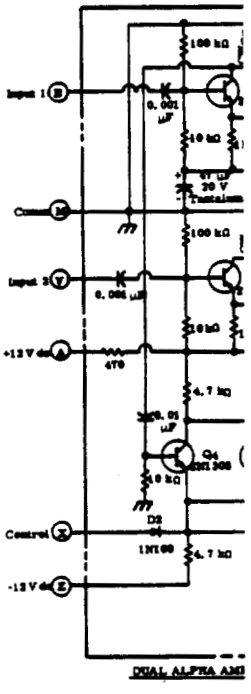

DUAL ALPHA AM

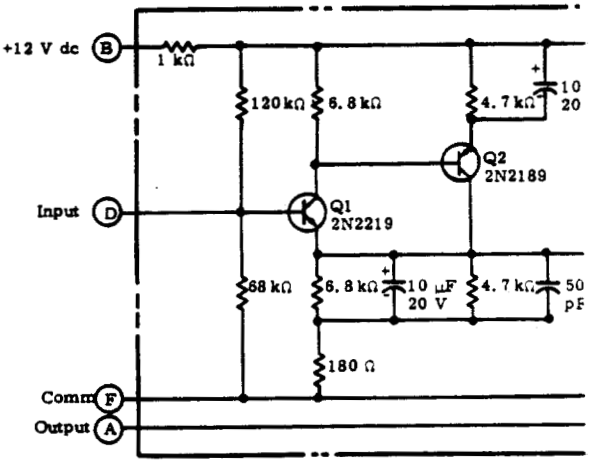

PREAMPLIFIER BOARD

Othe

0028496

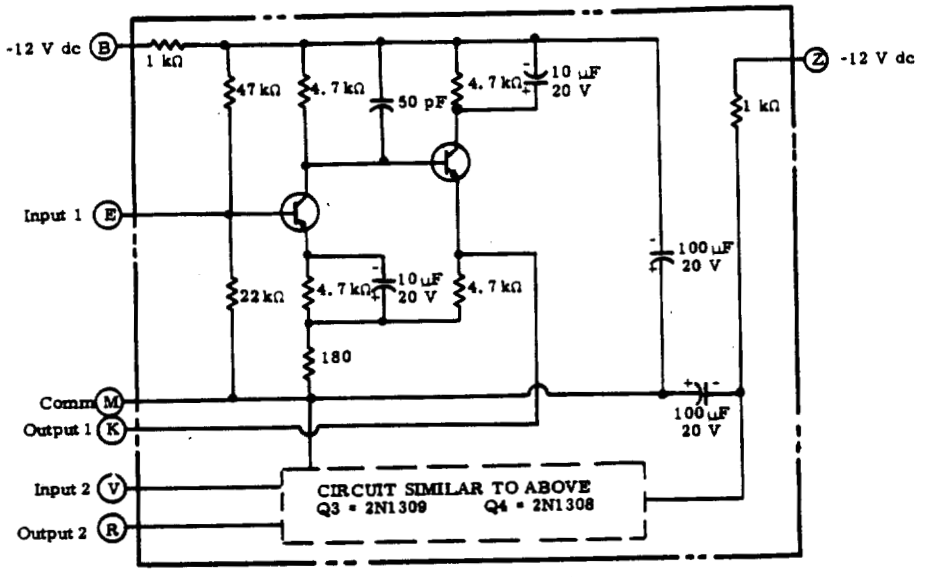

EXTERNAL AMPLIFIER BOARD

. SH. 1

. H-4-39270

3400161C

indoffs

47 µF
20 V

FIGURE 5.12

ircuits for Hand and Shoe Monitor

The scintillation detection probes are similar to those described by Spear.[5.4] These probes contain lucite light pipes and were modified by the substitution of low-noise multiplier phototubes (EMI-9536B), by the addition of solid state preamplifiers (voltage gain of 25), and by addition to each probe of a gain control to permit easy balancing of the gains of the probes incorporated in the instrument. An additional pulse height improvement is realized by a reduction in shunt capacitance. The amplification factor for each probe is adjusted by varying the phototube high voltage. This is accomplished by a 10 MΩ rheostat operating near ground potential; this allows individual probe gain adjustment without need for high voltage insulation of the rheostats. During initial adjustment, each phototube gain may be varied, along with adjustment of controls on the circuit boards to be described, to obtain equal sensitivities for several counting probes.

Detection and Indication Channels

The channels for monitoring the right hand comprise one probe for the back of the hand, one for the palm of the hand (with gain controls and preamplifiers in each probe), and main chassis electronics. The preamplifier outputs are connected to inputs of the "Dual Alpha Amplifier and Discriminator" circuit board. On this board, the input signals are amplified using adjustable-gain, inverting amplifiers, and the output signals are directed to the discriminator.

The dual-input discriminator has a common threshold-level adjustment and a single output, from which a signal is obtained if either applied pulse exceeds the threshold level. The discriminator output is connected to one portion of the "Alpha Register Driver" circuit board (the second portion is used for the "Left Hand" channel). The output of the register driver operates the register marked "Right Hand Alpha" on the monitor panel.

The output signals from the amplifiers also pass through gain controls marked "Beta-Gamma Gain" on the board and are directed to the "Dual Beta-Gamma Amplifier and Discriminator Board." The signals are

amplified by 20 and directed to another adjustable-threshold, dual input discriminator (as before). The discriminator output is scaled down by a factor of 32 (minor rewiring may change this to 16, 8, 4, or 2 if desired), and the scaler output signal is connected to the "Right Hand Beta-Gamma Register Driver" to drive the "Right Hand Beta-Gamma" register on the front panel.

The channels for monitoring the left hand are identical to those described above; however, the alpha register drivers for the right and left hands are on a common board, as are the beta-gamma register drivers for both hands.

The shoe monitoring channel is similar to the hand channels, but having one probe per shoe, and using the amplifiers and discriminator as described previously. Since the shoes are not monitored for alpha particles, the alpha discriminator portion is not used and the alpha register driver and register are omitted.

Capability for incorporation of external monitoring (clothing, etc.) probes is included. Such probes[5.5] may be fabricated for either alpha or beta-gamma detection, and they operate from positive high voltage and contain no preamplifiers. The "external probe" channel includes an amplifier ("External Amplifier"), another adjustable gain amplifier, a discriminator, and a gated oscillator (board marked "External Probe"). Aural output signals are provided by means of a small speaker.

Counting Interval Timer

The "Counting Interval Timer" controls the counting by removing cutoff bias on the discriminators during the counting interval; whereas, the phototubes and amplifiers remain energized and operating at all times. A switch is provided (rear of chassis) to bypass the timer, allowing continuous counting if desired. This feature should be useful during adjustment and maintenance work. Timer operation and counting is initiated by inserting the hands into the hand probes; this action operates the "Start" microswitch

and energizes the "Count" neon lamp. When the counting interval is completed, the "Count" lamp extinguishes and the "Reset" lamp is energized. The count cycle cannot be reinitiated until the circuitry has been reset (extinguishing the "Reset" lamp). The lamps are not energized when the timer bypass switch is used.

Use Register

An extra register was provided (rear or instrument) to record the number of users of the monitor. This "User Count" register is operated during the reset interval; thus, it actually tallies the number of times the instrument has been reset. Operation in this mode prevents electrical noise transients from entering the counting channels to possibly alter the displayed count.

General Assembly

The electronics portion of the monitor is contained on a 17 by 17 by 14 in. chassis with a 10.5 in. panel. Mounted on the panel are the readout registers and associated lamps, a power pilot lamp, the timer "Count" and "Reset" lamps, the "Reset" push button, and the speaker for use with the external probe. Mounted on the chassis are the components for the high voltage and register-driver power supplies, the "user" register, and a card file containing the printed circuit cards (boards). The main chassis is mounted on swiveled chassis slides for ease of maintenance.

For certain applications, it may be desirable to have an instrument for measurement of alpha contamination only. For this case, the shoe probes, the beta-gamma scintillator on the hand probes, several of the registers, and several circuit boards may be omitted.

Results

Prototypes of the various circuits were fabricated and tested satisfactorily for operation and counting efficiency. Eight units are now being fabricated offsite for use at Hanford. Sensitivities of the probes are easily adjusted to be equal as described. On the hand probes, alpha particles

(from a 500 disintegrations/min Pu^{239} source for example) may be detected with a counting efficiency of from 9 to 27% (averaging 16%) depending on the position of the source relative to the probe detection surface. Counting efficiency for Pu^{239} at the "finger end" of the probe averages about 20%. For beta particles (as from Pm^{147}), detection efficiency averages about 3%, and for Ra D-E-F, the efficiency averages about 7%.

Detection and Measurement of Airborne Plutonium - W. G. Spear

Measurement of low level concentrations of airborne plutonium, in particular Pu^{239}, is a difficult problem and is limited, in practice, to methods based on the detection of alpha particles. Since the associated radiation hazards arise principally from inhalation and ingestion, it becomes necessary to monitor continuously the air in areas where the potential contamination hazard exists. The valid assessment of the air concentration of plutonium is complicated not only by the minute maximum permissible concentrations (2×10^{-12} $\mu Ci/cm^3$ = 1 MPC for Pu^{239}) but also by the existence of the large and quite variable airborne background of alpha activity from the decay products of the natural emitters, radon and thoron. In comparison to the biological hazard imposed by the Pu^{239}, this background activity consitutes a minimal hazard in the concentrations normally encountered. The problem, then, is to discriminate against this background to provide meaningful Pu^{239} measurements to evaluate the hazard as rapidly as possible.

Several measurement techniques applicable to the problem include those of half-life, particle size, rate of change of activity, coincidence counting, and alpha spectrometry. Detection, instrumentation, and required time difficulties are encountered to various degrees with each of the techniques; however, considerable investigative and experimental effort over the past few years has demonstrated the most promising methods to be coincidence counting and alpha spectrometry. Considered during investigative work are such factors as the magnitude and rate of radon-thoron buildup, atmospheric dust entrainment and particulate size, maximum possible air flows, types of air filters, impaction methods, detection efficiency, counting statistics, compensation techniques, characteristics of various detectors, and electronic circuitry techniques. Developed experimental instrumentation has demonstrated that measurement sensitivities of 8 to 15 MPC-hr can be achieved for airborne Pu^{239} under quite nonideal conditions. With less difficult atmospheric and background conditions, better sensitivities are obtained.

Discussion

Several techniques are applicable to the problem of measuring airborne concentration of Pu^{239}; however, before considering these in detail, it might be appropriate to review[5, 6] the equations pertinent to particulate deposition on the collection medium.

Equations for Airborne Radionuclide Concentration Measurements

The radioactivity deposition rate on a filter depends on the air concentration, the air flow rate, and the decay factor as follows:

$$\frac{dQ}{dt} = \frac{CF}{m} - \lambda Q \tag{1}$$

where

Q = quantity (μCi) collected on the filter
C = concentration ($\mu Ci/cm^3$) of the radionuclide in the air
F = flow rate (ft^3/min) through the filter
λ = decay constant (min^{-1}) of the radionuclide
m = proportionality constant to convert ft^3 to cm^3 or $3.53 \times 10^{-5}\ ft^3/cm^3$.

For a varying concentration, the value of C would be a time-dependent function as determined by the concentration variation; however, for an essentially constant value of C and with Q being zero at time zero, the amount of radioactive material on the filter at the end of period t minutes is

$$Q = \frac{CF}{m\lambda}(1 - e^{-\lambda t}). \tag{2}$$

For the case where a delay, t_d, is encountered (as with sample counting) before the filter is counted, Equation (2) is multiplied by $e^{-\lambda t_d}$. Equation (2) can be rearranged, and the concentration becomes

$$C = \frac{m\lambda Q}{F(1 - e^{-\lambda t})}. \tag{3}$$

Since the instrument reading is, typically, in counts/min, the value of Q can be rewritten

$$Q = \frac{A}{GL} \tag{4}$$

where

A = observed net counting rate in counts/min

G = counting efficiency or $\frac{\text{standard source counts/min}}{\text{standard source disintegrations/min}}$

L = a constant or $2.2 \times 10^6 \frac{\text{disintegrations/min}}{\mu\text{Ci}}$

thus

$$C = \frac{(3.53 \times 10^{-5})\lambda A}{FGL(1 - e^{-\lambda t})}$$

or

$$C = \frac{(3.53 \times 10^{-5})\lambda A}{FG(2.2 \times 10^6)(1 - e^{-\lambda t})} = \frac{(1.60 \times 10^{-11})\lambda A}{FG(1 - e^{-\lambda t})}. \tag{5}$$

In addition, an "absorption factor" (f) is required depending upon the type of filter material, the porosity, etc. For the "typical" case, this factor might be as high as 0.3. Equation (5) is divided by (1 - f) or 0.7. The filter collection efficiency also appears in the denominator, typically 0.99. Thus, Equation (5) is written

$$C(\text{in } \mu\text{Ci/cm}^3) = \frac{(3.53 \times 10^{-5}\ \text{ft}^3/\text{cm}^3)(\lambda\ \text{min}^{-1})(A\ \text{counts/min})}{(F\ \text{ft}^3/\text{min})\left(G \frac{\frac{\text{counts}}{\text{min}}}{\frac{\text{disintegrations}}{\text{min}}}\right)\left(2.2 \times 10^6 \frac{\frac{\text{disintegrations}}{\text{min}}}{\mu\text{Ci}}\right)(0.7)(1 - e^{-\lambda t})}$$

or

$$C = \frac{(2.30 \times 10^{-11})\lambda A}{FG(1 - e^{-\lambda t})} \tag{6}$$

and expanding the term $(1 - e^{-\lambda t})$,

$$C = \left[\frac{(2.30 \times 10^{-11})A}{FG}\right]\left[\frac{\lambda}{1 - 1 + \frac{\lambda t}{1!} - \frac{(\lambda t)^2}{2!} + \ldots}\right]$$

or

$$C = \frac{(2.30 \times 10^{-11})A}{FGt} \tag{7}$$

where

A = net counts/min as readout indicated

t = exposure time (minutes) of filter to air flow

F = air flow in ft^3/min

G = counting efficiency of $\frac{\text{counts/min}}{\text{disintegrations/min}}$

2.30×10^{-11} = a constant with dimensions of $(ft^3/cm^3)\left(\frac{\mu Ci\text{-min}}{\text{disintegrations}}\right)$.

Thus, dimensionally

$$C\left(\frac{\mu Ci}{cm^3}\right) = \left[\frac{2.30 \times 10^{-11}\left(\frac{ft^3\ \mu Ci\ min}{\text{disintegrations}\ cm^3}\right)}{F\left(\frac{ft^3}{min}\right) G\left(\frac{\text{counts}}{\text{disintegrations}}\right)}\right]\left[\frac{A\ \frac{\text{counts}}{min}}{t(min)}\right].$$

Equation (7) applies for the continuous detection of long half-life radioactivity on a fixed filter. Since the filter buildup of material is indicated by the slope of the trace on the readout (recorder) chart, the average concentration over a buildup period can be ascertained by substitution of the chart-indicated rates (subtracting the normal or background rate to obtain the net counts/min increase), the time involved, the flow rate, and the counting efficiency into Equation (7).

For a short half-life radionuclide, such as radon, the filter-collected material reaches saturation and continued sampling results in no further increase in readout. If the concentration diminishes, the material

will follow its characteristic decay curve and the readout level will move back toward the normal background.

For this case, $e^{-\lambda t}$ approaches $e^{-\infty}$ or zero if t is long compared with the half-life, and Equation (6) can be simplified to

$$C = \frac{(2.30 \times 10^{-11})\lambda A}{FG(1 - e^{-\lambda t})} = \frac{(2.30 \times 10^{-11})\lambda A}{FG}$$

and

$$\lambda = \frac{0.693}{T_{1/2}}$$

where $T_{1/2}$ is in minutes (half-life).

Therefore,

$$C = \frac{(1.60 \times 10^{-11})A}{FG\,T_{1/2}} \tag{8}$$

where

A = net counts/min as readout indicated

F = air flow in ft^3/min

G = counting efficiency or $\frac{\text{source counts/min}}{\text{source disintegrations/min}}$

$T_{1/2}$ = half-life of the radionuclide in minutes

1.60×10^{-11} = a constant with dimensions $\frac{ft^3\ \mu Ci\ min}{cm^3\ disintegrations}$.

If there were a delay between filter exposure and counting (as in sample counting for example), Equation (8) would be multiplied by $e^{\lambda t_d}$; however, for a continuous monitor, t_d is zero and $e^{\lambda t_d} = 1$. Therefore, the concentration is directly proportional to the indicated counting rate above regular background.

Measurement Methods

Several techniques applicable to the problem of measuring airborne concentration of Pu^{239} include those of half-life, particle size, rate of change of activity, coincidence counting, and alpha spectrometry. Detection, instrumentation, required time, atmospheric dust concentrations, and airborne natural emitters all present difficulties which are encountered to various degrees with each technique; however, considerable experimental effort of late has demonstrated the most promising methods to be coincidence counting and alpha spectrometry. Factors considered in the investigations include the magnitude and rate of buildup of the natural alpha emitters, atmospheric dust entrainment and particulate size, maximum possible air flows, types of air filters, air impaction, detection efficiency, counting statistics, compensation or subtraction techniques, detector characteristics, and electronic circuitry.

The problem for airborne plutonium monitoring is to be able to detect as rapidly and reliably as possible Pu^{239} concentrations of 1 MPC levels (2×10^{-12} $\mu Ci/cm^3$) or greater when the background natural alpha emitters may be present in concentrations as high as 2×10^{-10} $\mu Ci/cm^3$, or 100 times the concentration of Pu^{239}. For continuous, fixed-filter, constant-detection monitoring, the filter buildup for a 1 MPC concentration of Pu^{239} is about 0.126 disintegrations/min/ft^3, and that for the natural emitters can be as high as 12.6 disintegrations/min/ft^3. Thus, for a typical air flow of 10 ft^3/min, the Pu^{239} buildup will be 1.26 disintegrations/min/min. At the end of one hour, the Pu^{239} on the filter will equate to 75.6 disintegrations/min or about 19 counts/min for a typical 25% counting efficiency for detection. At the same time under the "worst case" natural background conditions, the buildup of radon-thoron will be providing about 1900 counts/min. Obviously, normal gross counting methods are inappropriate, and some method of discrimination must be employed to achieve a reasonable Pu^{239} detection sensitivity.

The half-life technique is based on the fact that background alpha emitters (radon and thoron) have effective half-lives of about 30 min and 10.6 hr respectively; whereas, Pu^{239} has a half-life of about 2.5×10^4 yr. Thus, by allowing the filter-collected material to decay for a suitable time or by making two separate collections over an appropriate time interval, the radon-thoron contribution can be deduced and subtracted to provide a measurement of the collected plutonium. The obvious disadvantage is the time required for assessment of the possible problem; thus, this method is an after-the-fact type and is not useful for continuous air monitoring.

The rate-of-change or rate of activity buildup technique to distinguish between Pu^{239} and the radon-thoron background was investigated by Rankin at Hanford[5.7] in 1959-1960 and is apparently being used to some extent in commercial instruments. An equilibrium count rate is established when the rate of collection of the natural emitters on the filter equals the decay rate. Since the radon concentration in the atmosphere is about 50 times greater than the thoron concentration, this method is essentially controlled by the effective half-life of about 30 min for radon. By employing two count-rate-meters with appropriate and different time constants, a differential signaling unit connected between the outputs of the instruments can be used to signal for buildup of Pu^{239}. The time-to-alarm will, naturally, depend on whether the natural emitters are increasing, remaining constant, or decreasing when the airborne Pu^{239} concentration appears. The technique is limited, as determined by extensive testing, to a Pu^{239} detection sensitivity of about 25 to 50 MPC-hr.

In the past few years, Brown, Rankin, and Spear[5.8, 5.9] at Hanford have concentrated on the coincidence counting method and on alpha energy analysis (spectrometry) techniques. At Savannah River, Alexander[5.10] has investigated air impaction (rather than air filters) methods with associated gross alpha counting. The British investigators Iredale,[5.11] Gale,[5.12] and Allenden[5.13] have experimented with coincidence counting and with air impaction followed by alpha spectrometry. All of these methods are employed for continuous air monitoring.

Development of the coincidence counting technique resulted in a detection sensitivity of about 15 MPC-hr for Pu^{239} under "worst case" conditions for radon and thoron. The method employs beta-alpha coincidence counting to differentiate between natural alpha emitters and Pu^{239}. In the radon and thoron decay chains, shown in Figure 5.13, one notes that in the radon chain Bi^{214}(RaC) decays by beta emission to Po^{214}(RaC') which decays by alpha emission with a half-life of about 150 μsec. Similarly, in the thoron chain, Bi^{212}(ThC) decays by beta emission to Po^{212}(ThC') which decays by alpha emission with a half-life of about 0.3 μsec. Thus, in both chains, emission of a beta particle is followed by an alpha particle emission within the relatively short average time interval of approximately 150 μsec. This beta-alpha coincidence is used to identify the natural emitters through use of the relatively constant ratio of the coincidence events to total detected alpha activity. The alpha activity due to Pu^{239} is then determined by subtracting the natural emitter contribution from the total detected alpha activity on the collecting filter. Thus, by detection and electronic circuitry manipulations, the natural emitter contributions can be compensated, to a degree, to provide a net readout signal for the Pu^{239} alphas.

The alpha spectrometry approach employs either scintillation (CsI crystals) detectors or solid state junction or surface barrier diodes in an effort to provide Pu^{239} versus natural emitters discrimination by high-resolution energy analysis and appropriate electronic circuitry, typically one or two single-channel pulse analyzers and/or balancing circuits. This method is effective to a measurement sensitivity of 8 to 15 MPC-hr as the Pu^{239} alphas have energies of 5.10, 5.13, and 5.15 MeV; whereas, the radon-thoron daughters emit alphas ranging from 5.3 to nearly 9 MeV.

Impaction methods, where high velocity air is directed through a special aperture, provide, under some circumstances, a degree of separation of Pu^{239} particles from those of the natural emitters. Following the impaction, either gross alpha counting or alpha spectrometry can be employed to yield the information relative to Pu^{239} concentrations. From the experiments carried out by many investigators, it appears that a

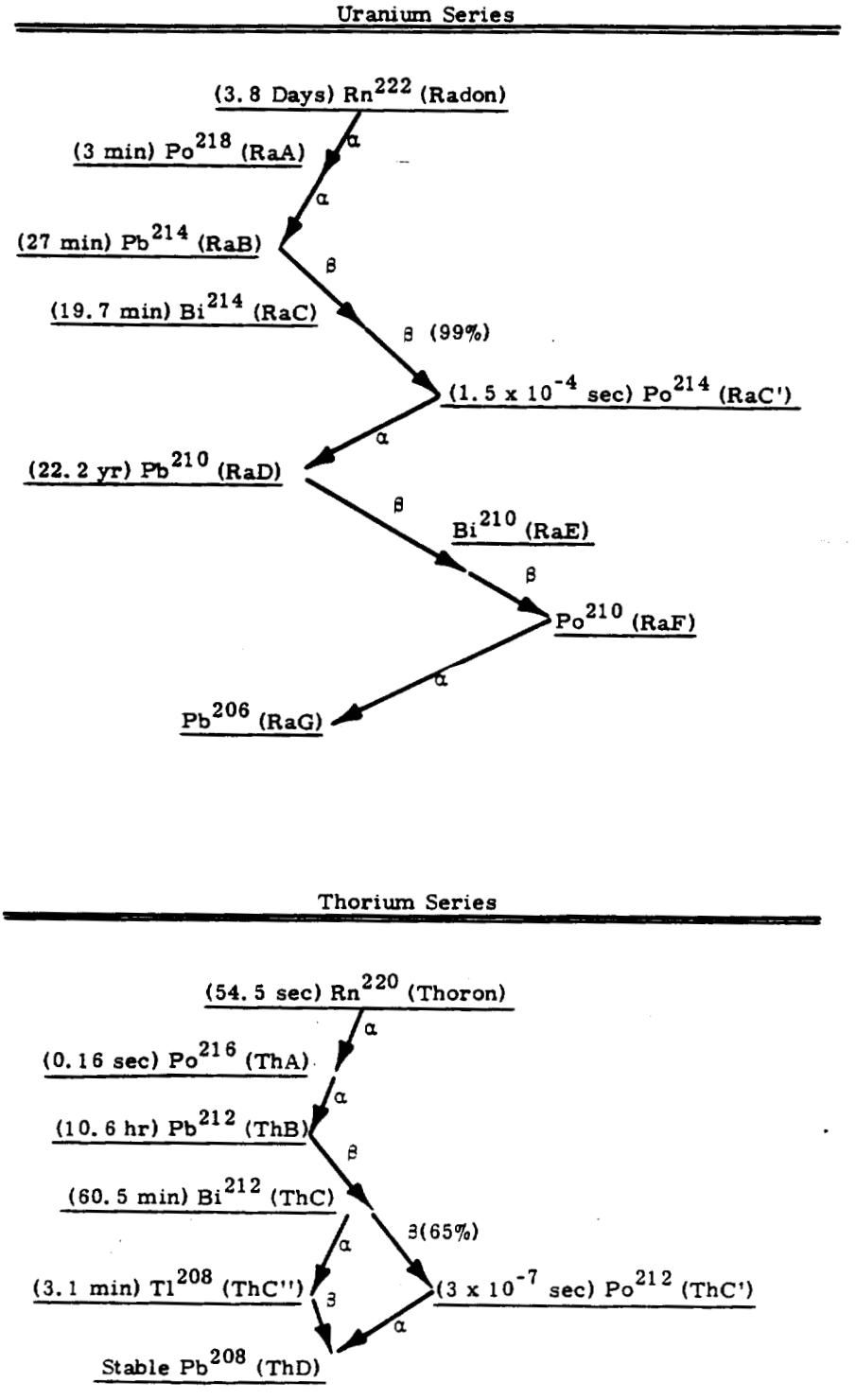

FIGURE 5.13

Radon-Thoron Decay Chain

majority of the Pu^{239} particles have diameters from 0.3 to 10 μ; whereas, a majority of the natural radioactivity is carried by particles less than 0.1 μ in diameter. Dust particles may have diameters extending through both of these ranges; therefore, dust collection is a problem. It is important to note that Pu^{239} particles to 0.2 μ or even less are possible. Bair, et al.[5.14] at Hanford described animal inhalation experiments with PuO_2 particles from 0.2 to about 7.5 μ in diameter. The results of the investigations indicated that both chemical form and particle size drastically affect lung deposition and subsequent translocation. The particle size appeared to be particularly important for PuO_2. The data indicated that inhalation of aerosols with diameters of 5 to 6 μ is more hazardous than for the range 0.2 to 2 μ. In any case, various investigators have indicated that impactors, especially of the annular type, can effect a separation with stated Pu^{239} collection efficiencies varying up to 90% and with natural emitter collection efficiencies of 5 to 10%. In general, the collection ratio or separation factor will be proportional to the ratio of the particle sizes involved; however, because of the very wide range of particle sizes, the chances for concentration measurement errors would appear to be large.

Figure 5.14 shows the improvement over the past 8 yr in the measurement of airborne Pu^{239}. In 1956, a sensitivity of about 500 MPC-hr was being achieved, and by 1964 the sensitivity had been improved to a value of 1 to 6 MPC-hr, depending upon the method, the airborne dust problems, and the natural emitter concentrations. Figure 5.15 shows a comparison of specific monitors developed at Hanford.

Compact Solid State High Voltage Supply - E. M. Sheen and C. A. Ratcliffe

Scintillation gamma spectrometers require high voltage power supplies of exceptional stability, low temperature coefficient, and low noise output. In addition, the design of compact portable spectrometers requires the high voltage supply to be small and light weight and to be capable of moderate current output at stable and adjustable voltages. A high voltage supply meeting these general requirements for portable spectrometers was developed using solid state components and miniature transformers. A voltage range from 600 to 1500 V dc at 0.25 mA was achieved with a voltage temperature coefficient of about 0.01%.

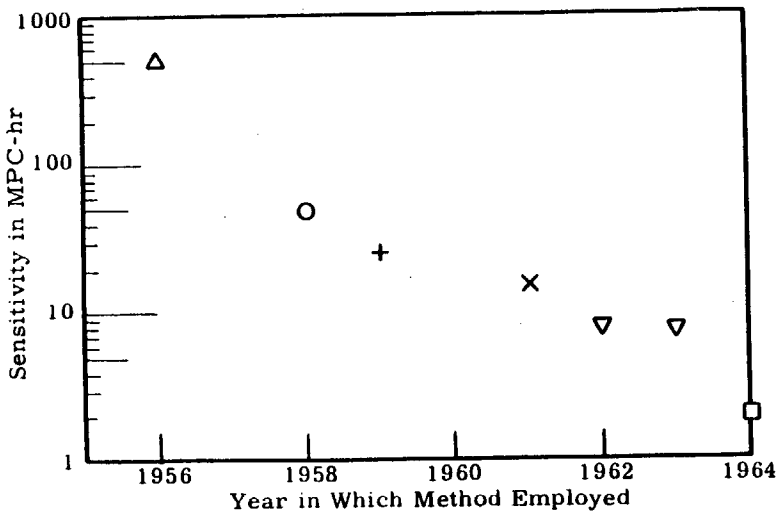

△ = Straight high level method (500 MPC-hr)

○ = Two separated detectors plus differential circuitry (50 MPC-hr)

+ = Rate-of-change measurement (25 MPC-hr)

× = Coincidence-counting technique (15 MPC-hr)

▽ = Scintillation and solid state detectors plus spectrometry (6 to 8 MPC-hr)

□ = Impaction on planchet plus gross alpha detection (1 to 2 MPC-hr) (for dust-free, air conditioned atmosphere)

FIGURE 5.14

Improvements in Airborne Pu^{239} Measurement

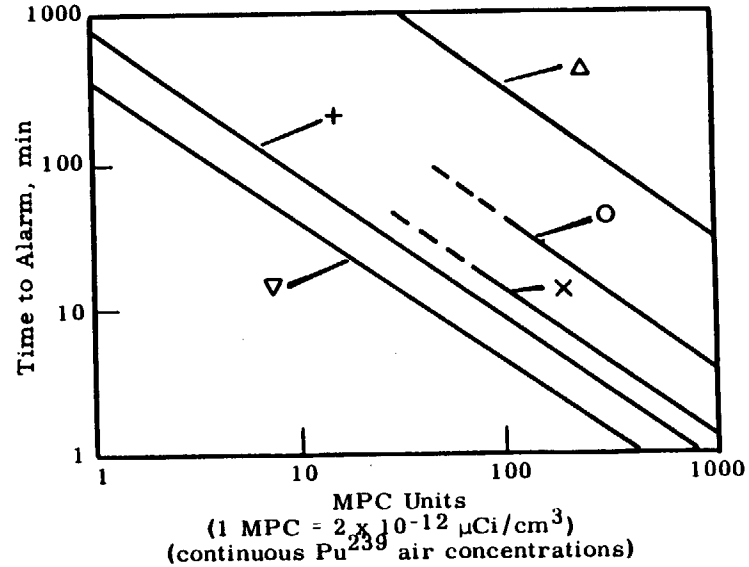

△ = Gross counting high level monitor

○ = Dual-detectors and differential amplifier

+ = Rate-of-change monitoring method

× = Coincidence-counting technique

▽ = Alpha spectrometry method

FIGURE 5.15

Comparison of Specific Hanford Monitors for Airborne Pu^{239}

0028511

Discussion

A compact solid state high voltage supply, shown schematically in Figure 5.16, was developed for use in experimental battery-powered and compact line-powered gamma spectrometer instruments.

A small meter is employed to indicate the approximate high voltage magnitude and a 10-turn potentiometer is provided for adjustment of the voltage in sufficiently small increments to permit use of the one control for gain of the gamma spectrometer instrument. The circuit is not complex and comprises an oscillator-amplifier, miniature transformers, rectifier, filter, voltage reference unit, and an operational amplifier. The operational amplifier compares a sample of the high voltage with the reference unit voltage and drives output emitter followers. The power emitter follower output sets the voltage amplitude from the oscillator-amplifier to provide the required power at high voltage from the rectifier-filter combination.

A Unijunction® transistor oscillator, Q1, is used to provide an adjustable-frequency pulse source to trigger a fixed pulse width monostable multivibrator, Q2 and Q3. Potentiometer P1 is used to adjust the frequency for maximum efficiency. Circuit power required is +15 V dc at 10 mA, -15 V dc at 17 mA, and an unregulated source of -15 to -25 V dc at 30 to 60 mA depending on high voltage output load. The monostable multivibrator output is direct-coupled to a power transistor switch, Q4, that connects two miniature transformers across a voltage level set by another power transistor, Q7, that is controlled by the operational amplifier output voltage.

High voltage pulses from the two transformers are rectified by small selenium stacks, and the charge is stored on Capacitors C6 and C7. Resistor R12 and Capacitor C9 filter the output voltage and R13 decouples the dc sample line from C9. Capacitor C8 provides an ac signal to the sample line to prevent C9 from causing instability. A fraction of the high voltage is connected to the positive input of the operational amplifier through R13, R15, R16, and P3, and is adjusted by the setting of P3. The negative

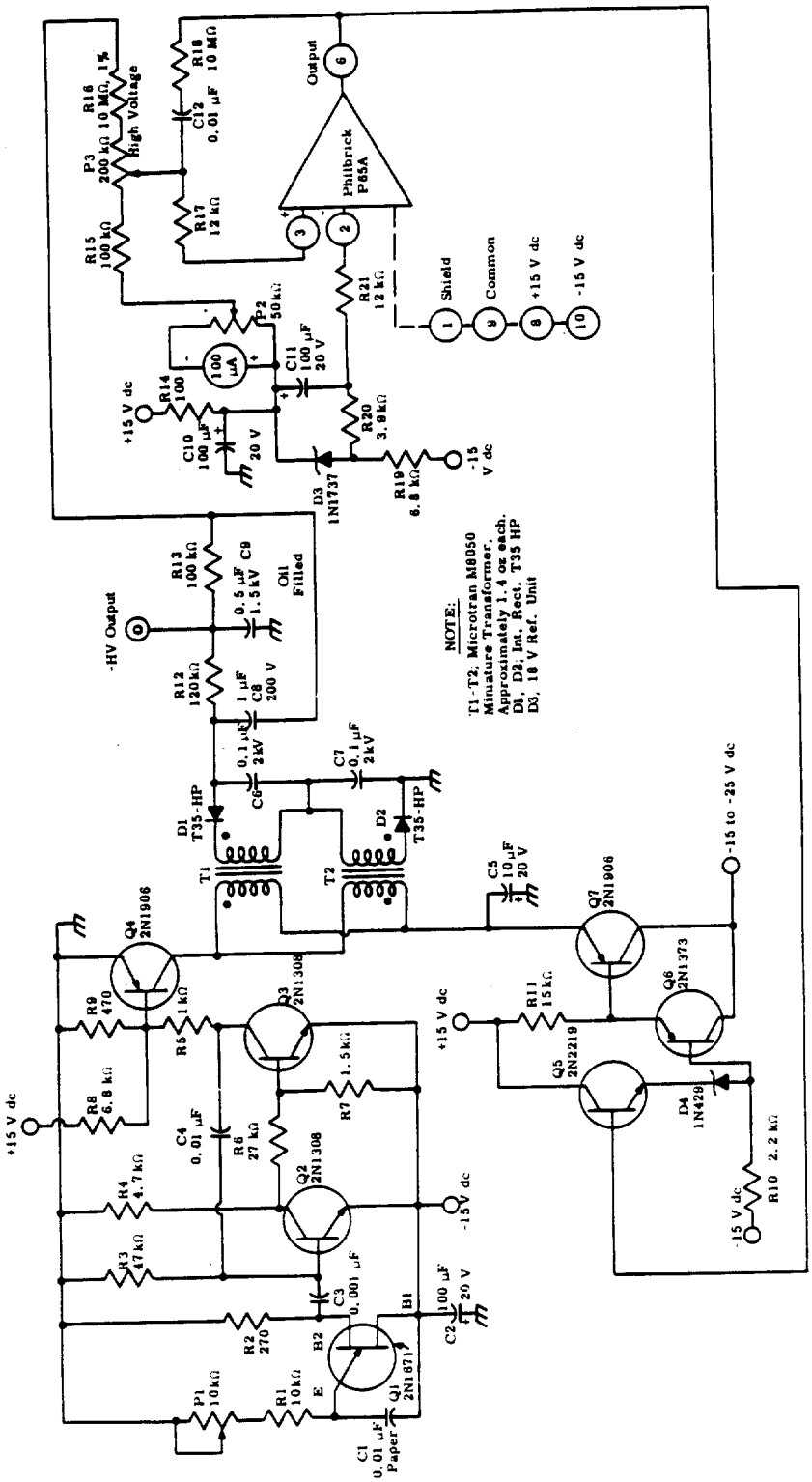

FIGURE 5.16

Compact Solid State High Voltage Supply

input of the operational amplifier is connected to D3, and 18.6 V dc reference diode. The difference voltage is amplified by the operational amplifier and the output voltage is applied to the base of emitter follower Q5. A Zener diode is used to offset the emitter follower voltage toward B- by 5 V dc. Additional current gain is provided by Q6 and Q7 to set the voltage across C5 and the transformers.

Power supply prototypes were fabricated to provide from -600 to -1500 V dc output at load currents up to 0.25 mA. The temperature coefficient at 1000 V dc was 0.007%/C°; this variation was approximately equal to the voltage variation with temperature of the particular reference diode used for the test. The ripple voltage measured was 10 mV, peak-to-peak. The supply promises to be useful for both portable battery-powered and line-powered scintillation spectrometer applications.

Integrator for a Portable Neutron Dose Rate Meter - E. M. Sheen and C. A. Ratcliffe

Neutron dose rates at Hanford are routinely established with portable survey instruments that use a small BF_3 proportional counter tube. The instruments, similar to those described in previous reports,[5.15, 5.16] comprise a high voltage supply, pulse amplifier, and a 3-decade count rate meter. A relationship between count rate and the neutron dose rate has been determined[5.17] for fast and slow neutrons. The purpose of this development effort was to provide miniature, economical pulse counting integrators for use with these survey instruments to indicate accumulated neutron dose. The integrator is sufficiently small to be mounted on the main instrument using headphone jacks to provide both mechanical support and electrical connections. The pulse rate from the survey instrument is divided by 1536 by the integrator circuitry, and the result is recorded on a 3-decade electromechanical register. Each registered event corresponds to 0.1 mrem of slow neutron dose, and the total integrator storage capacity is 99.9 mrem. Mechanical reset is provided on the register. Operating power for the integrator circuitry is obtained from the main instrument and a small internal 22.5 V battery.

0028514

Discussion

Investigation of the integrator problem revealed many conflicting requirements regarding suitable scaler circuits. Commercial binary or decade circuit modules of the various types investigated, such as micro-logic modules, were too large, too expensive, or both. Therefore, a solid state counter was developed to satisfy the requirements. A pulse rate division of 1536 provides one count to the register for each 0.1 mrem of slow neutron dose, as derived from the dose rates measured by the main instrument. This division is accomplished with 11 binaries in a permuted counter, and the incorporated 3-decade register can indicate 99.9 mrem neutron dose maximum.

Suitable driving and output circuitry was required to drive the register from the portable survey instrument. The circuit was required to be tolerant of changes in battery voltage and ambient temperature conditions, and in addition, power was to be obtained from the parent instrument on a minimal basis. A prototype was fabricated using silicon transistors (TO-5 can size), mica capacitors, and "cordwood" construction to use the available space. This prototype was discarded because the transistors were moderately expensive and the "cordwood" design was difficult to fabricate and maintain.

Investigation revealed the transistor type 2N2712 to be an inexpensive, small, silicon NPN transistor suitable for application in the instrument; consequently, the circuit was revised to employ these transistors and miniature ceramic capacitors in a design which could tolerate the normal component value variations. The circuits were mounted on 1.7 by 2.3 in. double-clad epoxy glass plug-in printed circuit cards for ease in maintenance and to provide redundant contact connections. The internal construction of the integrator and the exterior of the main instrument are shown in Figures 5.17 and 5.18. Circuit diagrams and internal wiring connections are shown in Figures 5.19 and 5.20.

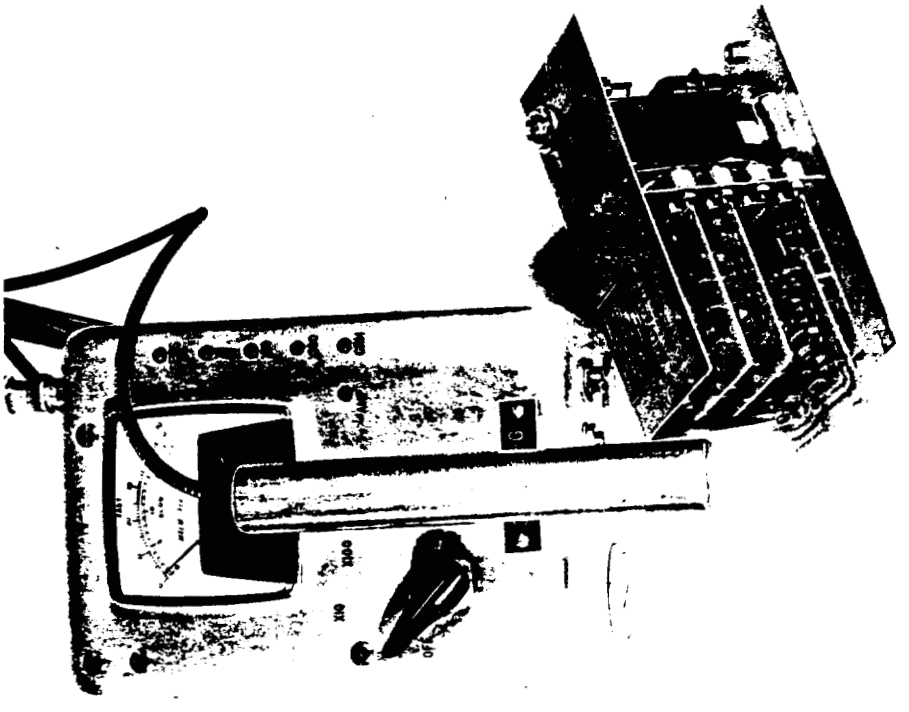

FIGURE 5.17
Integrator Components with Survey Instrument

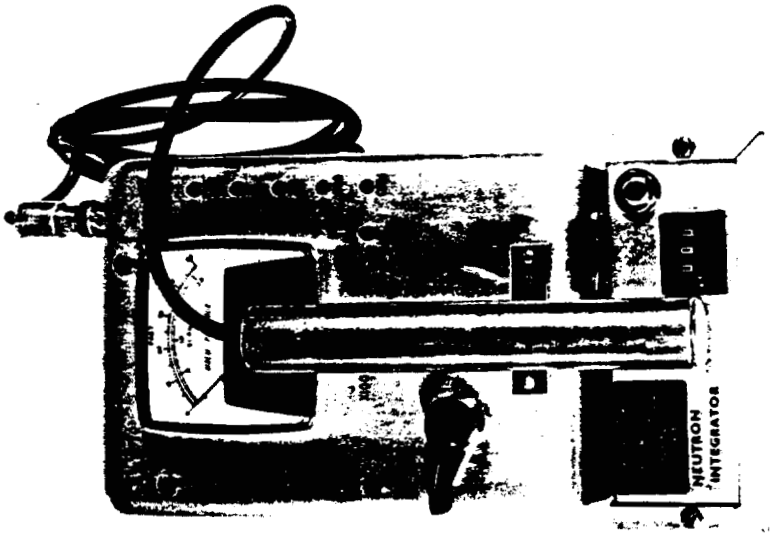

FIGURE 5.18
Integrator Assembled with Survey Instrument

Neg. No. 0640500-2; 0640500-1

0028516

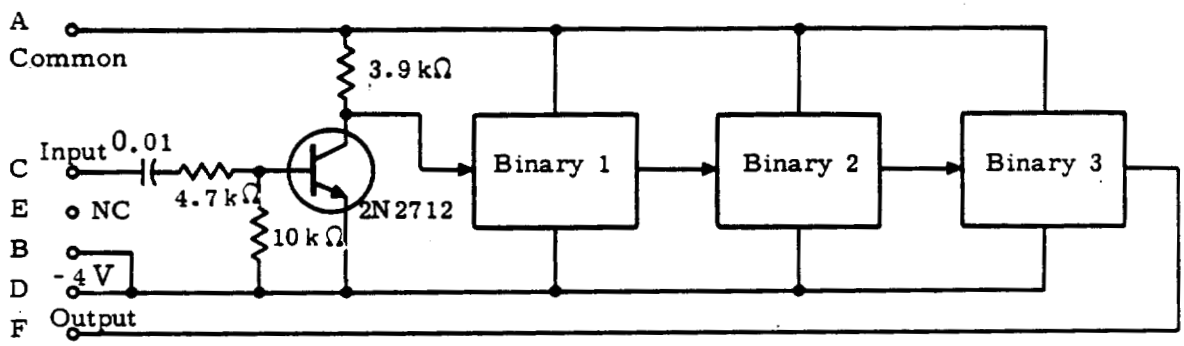

Board 1

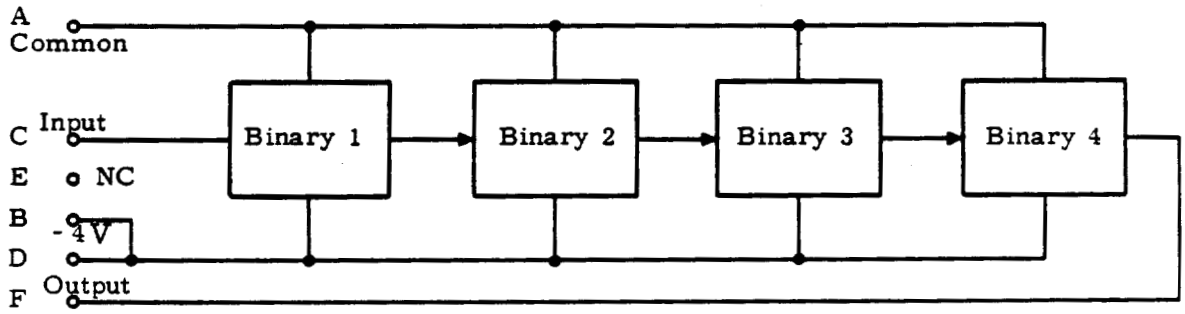

Board 2

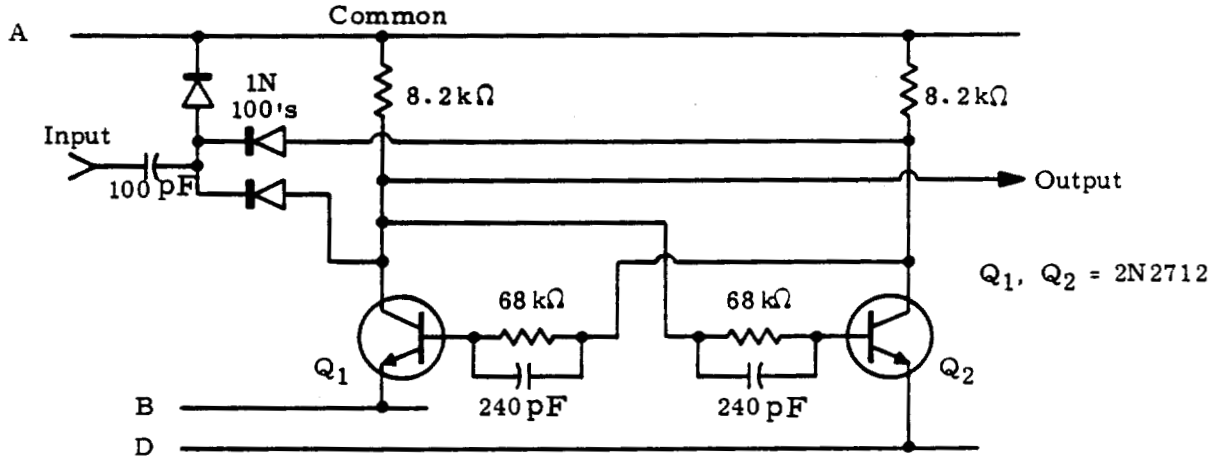

Typical Binary

FIGURE 5.19

Arrangement of Boards 1 and 2

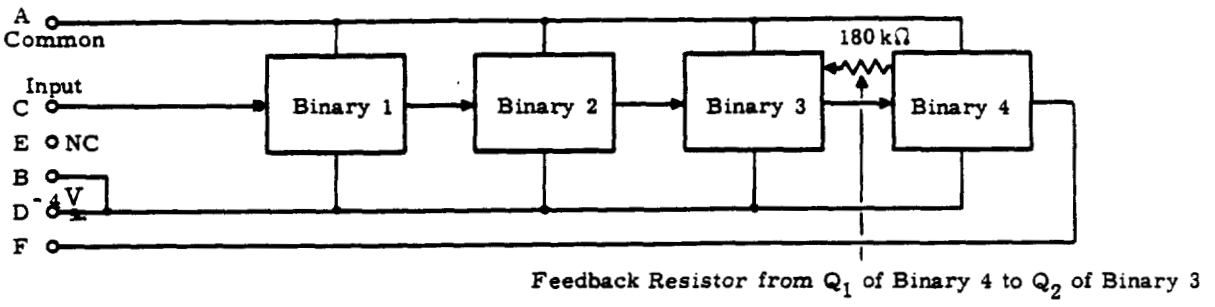

Board 3

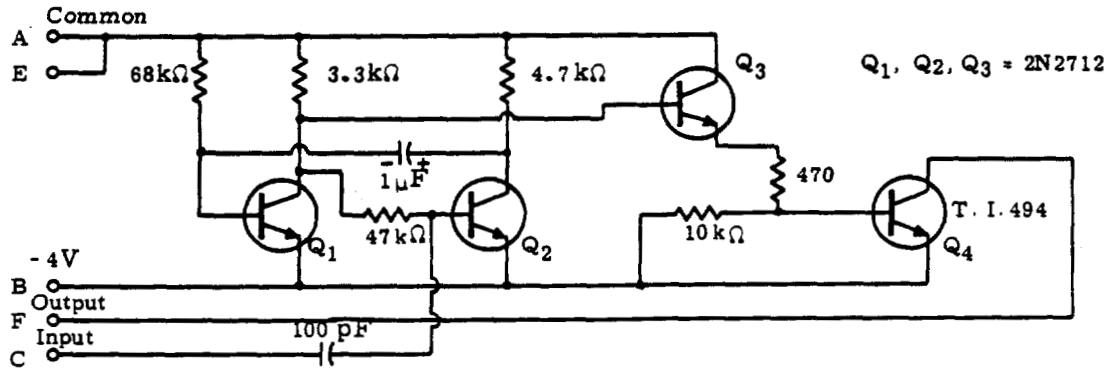

Board 4

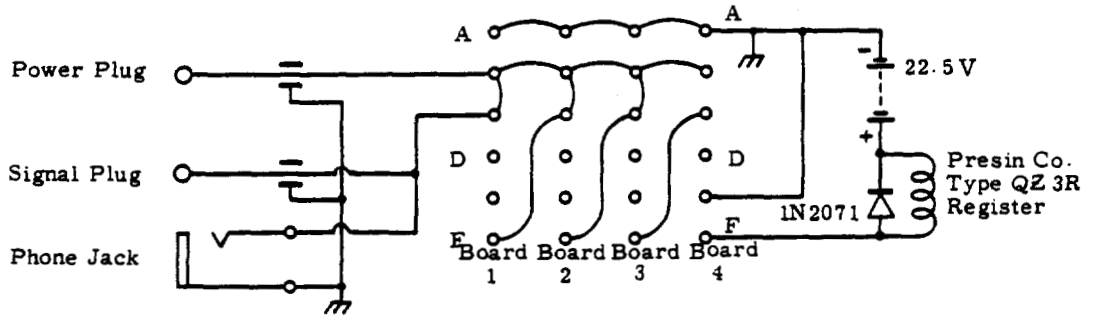

Integrator Wiring

FIGURE 5.20

Arrangement of Boards 3 and 4

Printed Circuit Board 1 contains an amplifier stage to adapt the output of the main instrument to the input of the counter stages. This amplifier is an off-biased saturating stage, which accepts positive input pulses and emits negative pulses suitable for operating the following counter stage. Three counter stages are incorporated. Each counter stage is a diode-triggered binary, providing a circuit with adequate speed and a reasonably small number and volume of components. Circuit Board 2 contains four binary counters, arranged in tandem to form a scale of 16. Board 3 also contains four binary counters, arranged in tandem to form a scale of 12 by permuting two of the binaries from a scale of 4 to a scale of 3. This permutation is accomplished by a 180 kΩ feedback resistor from the collector of Q1 in Binary 4 to the base of Q2 in Binary 3. Board 4 adapts the output of the counter stages to the mechanical register. This is done with a 40 msec monostable multivibrator and two switch transistors, which energize the register for 40 msec on receipt of each counter circuit output pulse.

Integrator power is applied by the main instrument switch; thus, no power switch is necessary on the integrator. The internal 22.5 V battery requires no switch since the register driving transistor is normally off and conducts a negligible amount. The integrator requires only 25 mW of power from the portable survey instrument, and the life of the small register battery is in excess of 3.5×10^5 events, equivalent to 35 indicated rem. The integrator outside dimensions are 2 by 3 by 5 in. The circuits were temperature tested and satisfactory operation was obtained from 0 to 150 F. The circuits are tolerant of normal component value variation and no component selection is necessary. In addition to the planned application with portable neutron survey instruments, the integrator could be adapted to count pulses from other sources in the range of 0 to 10^5 counts/min.

Neutron Soil Moisture Monitor - E. M. Sheen, W. L. Bunch, and M. R. Wood

At Hanford, heat dissipation from underground, radioactive-waste tanks is an important problem. Determination of soil thermal conductivity, used to evaluate the heat dissipation, generally requires measurement of the subsurface moisture. A soil moisture monitor was developed to aid in the studies. Other Hanford geologic and hydrologic applications of the monitor will include study of subsurface moisture in the aeration zone above the water table, especially in the capillary fringe; determination of the aquifer porosity in the saturated zone to aid in measurement of ground water flow rates; and study of stratigraphic discontinuities as associated with changes in the particle size of sedimentary earth materials.[5.19] The instrumentation system includes a probe that contains a fast neutron source, slow neutron detectors, and necessary solid state circuitry; a supporting and signal transfer cable; a cable drum and winch; a count rate meter; and a recorder. The probe contains five BF_3 proportional counter tubes, an amplifier, a high voltage supply, and a 1 Ci Pu-Be neutron source. A single coaxial cable supports the probe, returns signal information to ground-level instrumentation, and conveys low voltage power to the probe. A pulse height discriminator and a power supply are located at ground level. The probe signal pulses are decoupled from the low voltage power bus, integrally discriminated, and used to drive a conventional count rate meter and strip chart recorder combination.

Biological and Biomedical Instrumentation

Instrument for the Automatic Regulation of Inhaled Aerosols* - D. P. Brown and N. S. Porter

Beagle dogs were exposed to Fe^{59} during inhalation experiments at the Battelle-Northwest Biology Inhalation Toxicology Laboratory. Subsequently, the animals were made to inhale cigarette smoke in an effort to discover a possible relationship between smoking and the clearance rate of the isotope from the lungs. The smoking routine was conducted manually by a technician on a regular daily basis. Standardization of the smoking process would provide a more consistent and uniform application of smoke

* This paper was presented at the 17th Annual Conference on Engineering in Medicine and Biology. Cleveland, Ohio. November 16, 1964.

0028520

and provide more effective control for such a laboratory experiment. It was desired to duplicate the smoking process of man as closely as possible with air inhaled through the nose and smoke through the mouth. An instrument to control the number of fresh-air breaths for each smoke-filled breath was developed to aid in the experimental investigations.

Discussion

The instrument, depicted in the block diagram of Figure 5.21, is a controller that can selectively provide from 1 to 11 fresh-air breaths for each smoke-filled breath to three dogs simultaneously. Thermistor transducers are mounted at the air and aerosol intakes to provide signals used for counting. When the selected number of fresh-air breaths is reached, an air valve is closed and the dog must inhale through the cigarette whereupon the instrument is reset and air is again available.

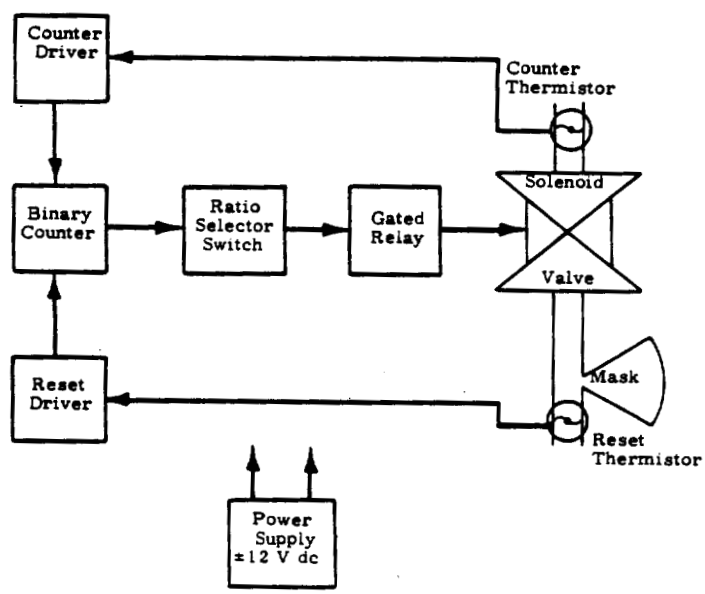

FIGURE 5.21
System Block Diagram

As the thermistor detects each inspiration, the voltage change across it is used to drive the comparator, triggering, and pulse-shaping circuits comprising the counter driver. The output pulses drive a binary counter through a selector switch that determines the cycling ratio. The

counter, in turn, activates a relay that closes a solenoid valve to control air flow. The next inspiration must pass air through the cigarette and the smoke-filled breath passes across a second thermistor used to reset the system and open the air valve. Solid state components are used throughout for reliability and ease of maintenance.

Figure 5.22 shows details of the nose mask. Note that the cigarette fits in the tee-tube above the reset thermistor. A flutter valve is used to prevent smoke from entering the dead space between the mask and the solenoid valve. A second flutter valve accommodates the exhaling of smoke from the tube and mask. The other thermistor is mounted on the external side of the solenoid valve.

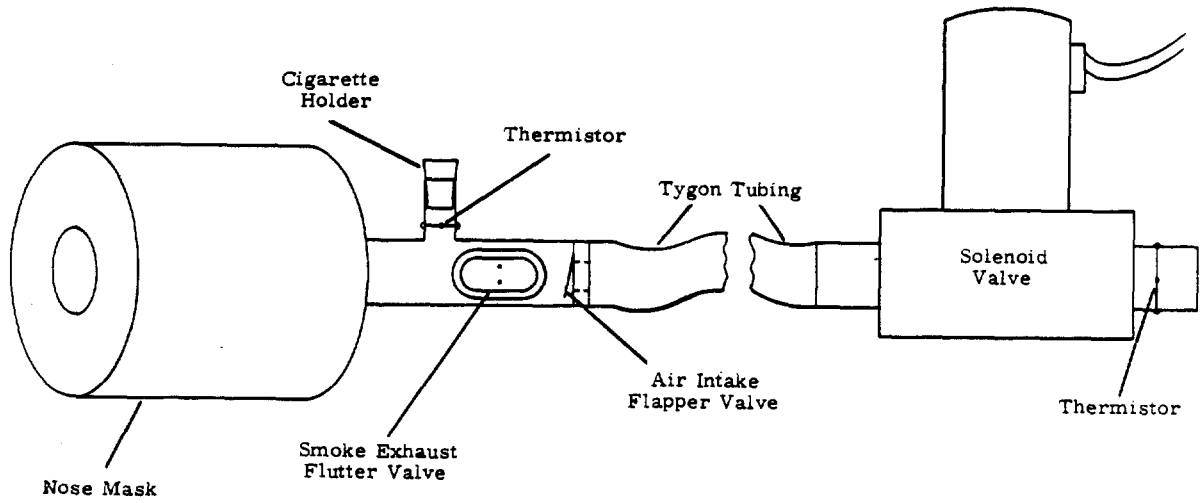

FIGURE 5.22
Nose Mask

The controller has been used daily for several months to facilitate the scheduled exposure of dogs to cigarette smoke. Changes have been made from time to time to improve the dog mask and the aerosol valving. Experience has shown that the smoke detecting thermistor becomes covered with smoke tars and tobacco residue. These materials are easily removed by washing the thermistor (in its holder) in warm, soapy water and then rinsing. Otherwise, the thermal time constant increases to a point which stops operation of the counting circuits. Certain of the dogs attempt to circumvent the system by breathing in a very shallow fashion; hence, the

time constants and thermistor heating current have to be carefully regulated. It should be noted that any other aerosol can be used with the controller by merely exchanging the cigarettes with lines to an appropriate aerosol generator through a two-way solenoid valve, which can be exchanged with the one used here.

Animal Physiological Function and Radionuclide Uptake Measurement and Telemetry Development - N. C. Hoitink and N. S. Porter

A system is being developed to provide a method for continuous monitoring of several animal physiological parameters without in any way confining the animal or requiring it to be connected to the readout instrumentation. The functions to be monitored are body temperature, respiration rate, blood pressure, and I^{131} uptake in the thyroid. A temperature telemetry system was developed and field tested, and a respiration rate channel was tested in the laboratory in previous work; these developments were reported last year[5.20] and will not be repeated. The development described in this paper include the thyroid uptake measurement channel and the progress on a reliable method for measuring blood pressure. With the exception of the blood pressure measurement channel, the transmission telemetry portions of the system are ready for final assembly and testing. It is expected that project completion will be achieved by mid-1965.

Discussion

Progress on the animal physiological function telemeter during 1964 was confined to development of methods and circuits in the laboratory to measure and telemeter the desired functions. As stated, the temperature and respiration channels were successfully completed late in 1963.

The major developmental accomplishments in 1964 included circuits to measure the thyroid uptake of I^{131} and experiments to establish a method for measuring animal blood pressure in a reliable fashion. The thyroid uptake channel, both the transmitting and receiving portions, was successfully bench-tested and is now ready for general field testing. The most difficult measurement to implement and the one on which the majority of future effort must be concentrated is that of blood pressure measurement. In an attempt to develop a suitable transducer, a designed device consisted of a

nonoccluding cuff which could be fitted over an artery and which contained a coil with a moving iron core. The coil was a part of the tuned tank circuit of an oscillator, and as the pressure varied in the artery, the frequency of the oscillator varied. The transducer was tested and a number of difficulties were observed. The frequency change was small and it did not seem to be dependably reproducible. The frequency of the oscillator was considerably higher than desired because of the small size of the coil.

Although more development effort might have improved the transducer, a commercial blood pressure transducer became available late in 1964 and one was obtained. The transducer is a slotted-cuff device with two attached strain gages, one active and a second for temperature compensation. The device is used by connecting two external resistors to the strain gages to form a bridge circuit, and the output signal of the bridge varies with the blood pressure. This signal is amplified sufficiently to obtain a dc signal adequate to control a voltage-controlled, sub-carrier oscillator. Since reliable low level dc amplification is inherently difficult to achieve, especially with a minimum amount of circuitry, it is necessary to use an ac signal to excite the bridge. This permits use of normal ac amplification but requires that the signal be demodulated (rectified) to obtain the dc signal necessary for the sub-carrier oscillator. The circuits to fulfill these requirements have been partially developed, and both the supply for the bridge and the amplifier are completed. The demodulator was designed and is being fabricated in miniature form. When satisfactory results are obtained from the blood pressure channel, it will be possible to combine all four channels and complete the system with inclusion of necessary filters and the finished signal recovery circuits for the receiver.

The circuit diagrams for the radionuclide uptake counting circuits are shown in Figures 5.23 and 5.24. The sub-carrier oscillator, which is tuned to 14.5 kc, is a transistor relaxation oscillator with a tuned tank circuit. The output of the oscillator is gated into the transmitter with each input pulse from the Geiger-Mueller (GM) tube by the remaining circuits. Receipt of an input pulse activates the flip flop comprised of transistors Q4 and Q5. This turns on (or off) the gate by biasing transistor Q7 off

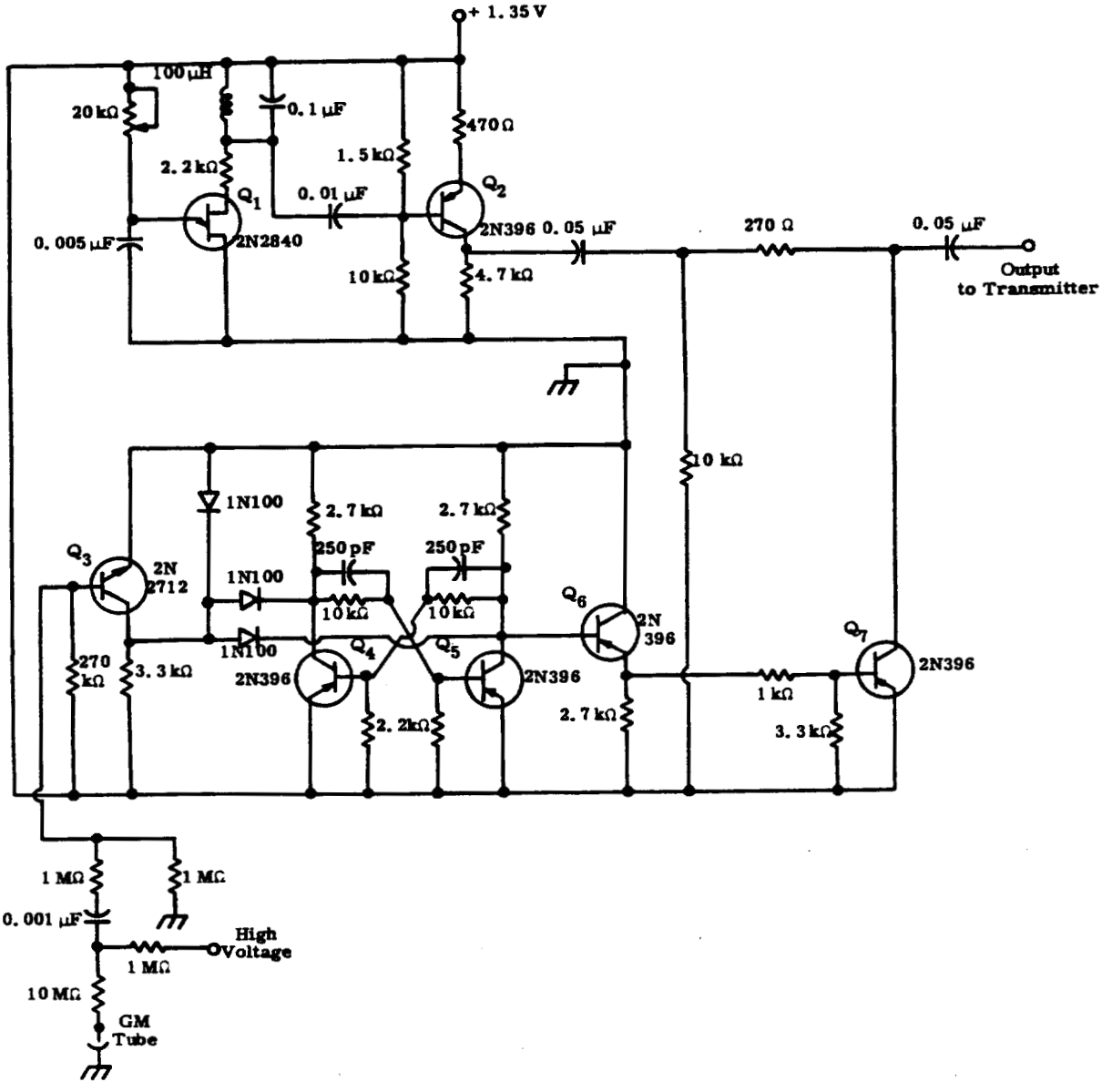

FIGURE 5.23

GM Tube Pulse Counting Channel
(Transmitter)

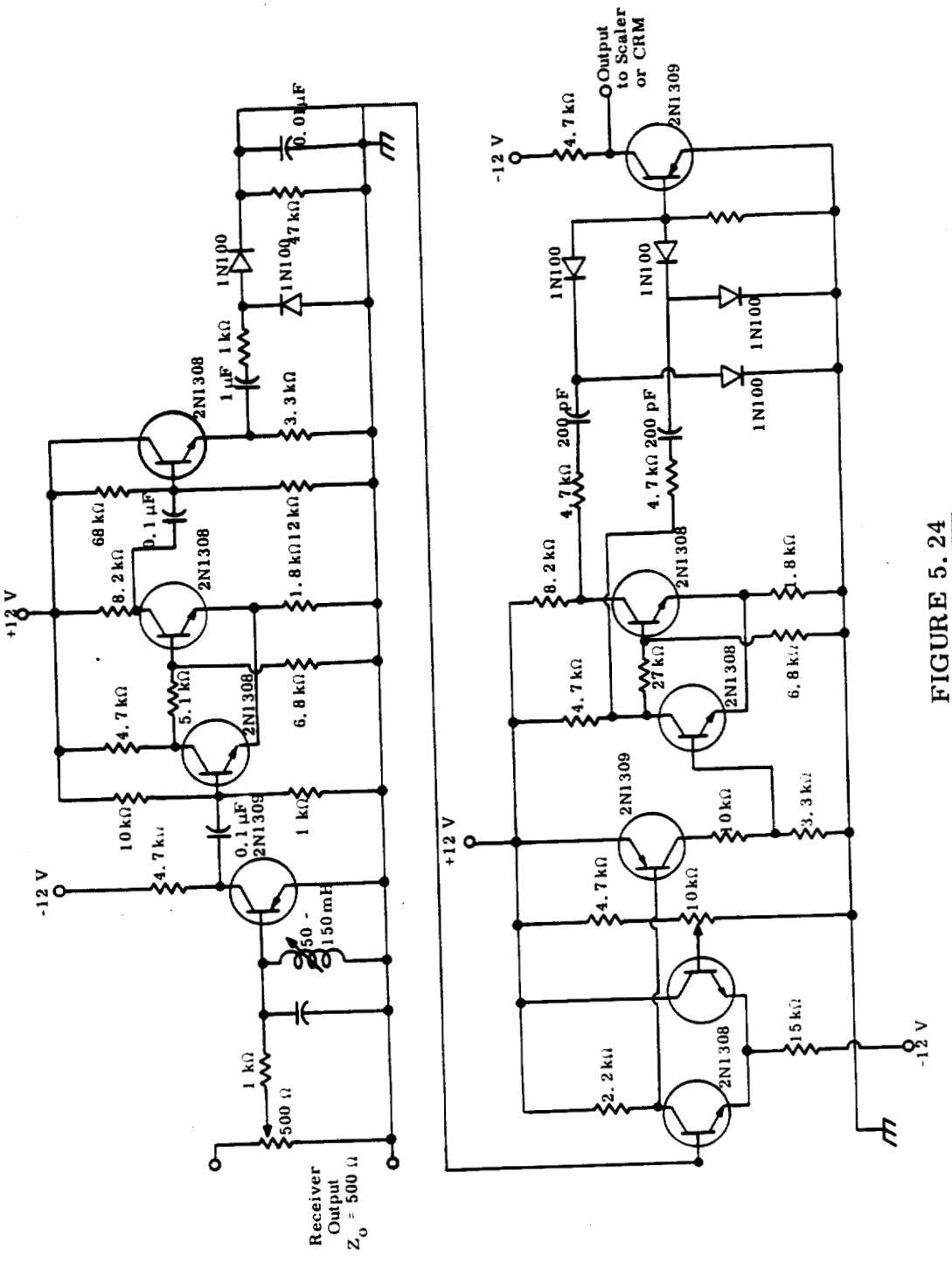

FIGURE 5.24

GM Tube Pulse Counting Channel (Receiver)

(or on). When Q7 is on, it effectively shorts the oscillator output to ground while in the off condition the oscillator output is allowed to proceed to the transmitter. The transmitter is modulated by pulses of the sub-carrier oscillator frequency, the beginning and end of each indicating a pulse received from the GM tube. The receiver and signal recovery circuits demodulate the sub-carrier frequency pulses to provide rectangular pulses which are then differentiated to obtain pulses at the beginning and end of each rectangular pulse. The original pulses are thus "recovered" and are used to drive a scaler or a count-rate-meter, as required.

The circuits for the blood pressure measurement channel are shown in Figure 5.25. A transducer oscillator provides excitation for the bridge circuit, which includes (as two arms) the strain gages mounted on the transducer. The other two arms of the bridge and the zero potentiometer are included in the transmitter portion. With an excitation of 0.3 V applied to the bridge, output of the bridge is about 0 to 100 μV for the blood pressure levels being measured. Since a dc voltage variation from 0 to 0.2 V is required to drive the voltage-controlled, sub-carrier oscillator, it is necessary to provide considerable gain for the bridge output signal. The amplifier shown has an open loop gain of about 10,000 and a gain of 1000 when used with feedback for stability. The output of the amplifier is 0 to 100 mV. At this time the demodulator to provide the necessary dc signal and the voltage-controlled oscillator have been designed and are being fabricated in miniature form. When these circuits are complete, tests will be conducted to determine the linearity.

In all of the circuits, miniature components and compact assembly methods are used so the entire transmitter (including batteries) will be in a package of 3 by 5 by 1 in. in size. This may seem large; however, it should be pointed out that a four channel system requires bandpass filters between channels to reduce interchannel interference and to insure low harmonic content in the sub-carrier signals to facilitate signal separation and recovery at the receiving station. These filters are relatively large (typically 0.75 by 0.75 by 0.5 in.) and prevent achieving extreme miniaturization.

0028527

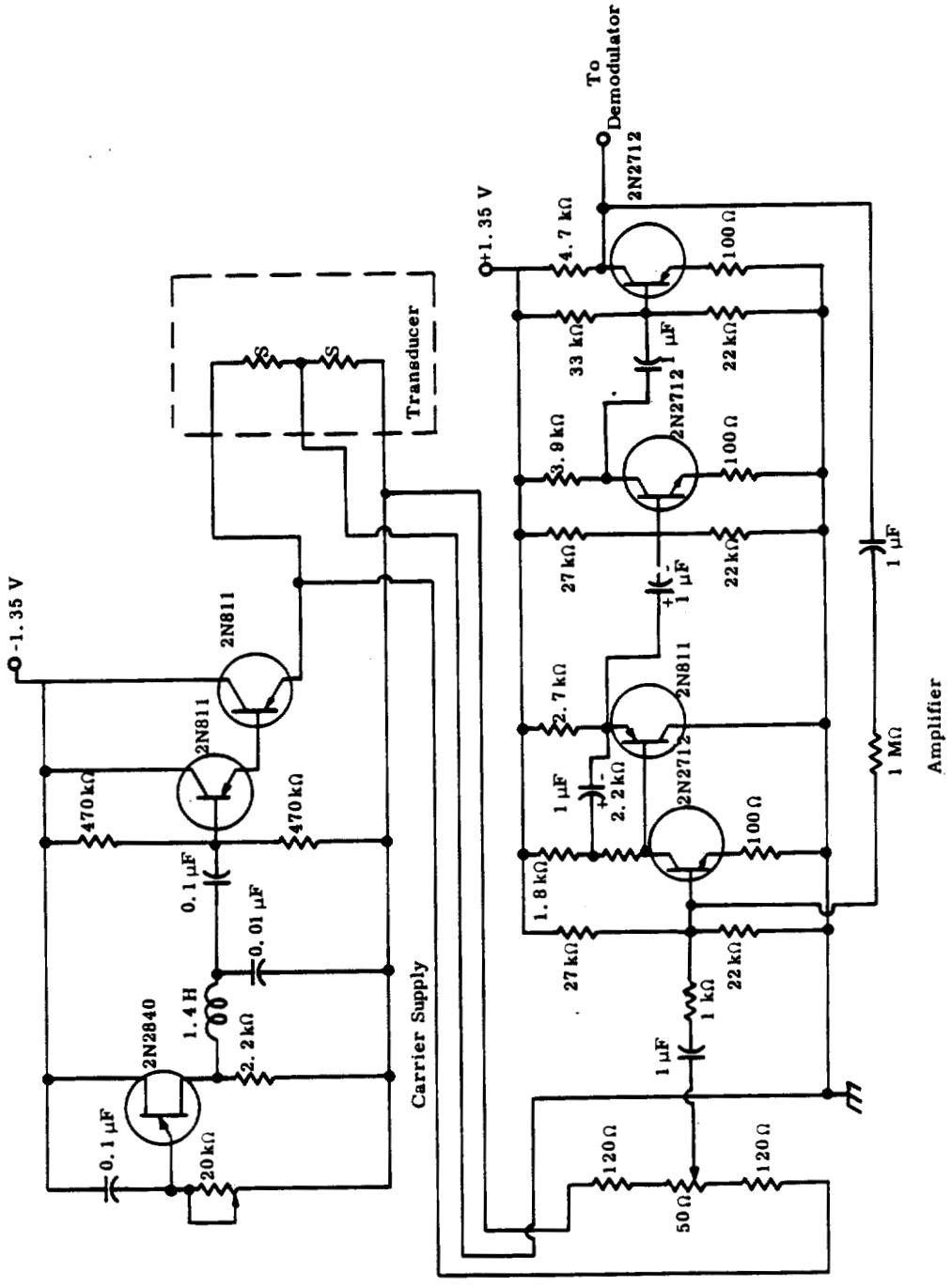

Note: The carrier supply must be floating with respect to the amplifier and the rest of the transmitter. It must have a separate, ungrounded battery supply.

FIGURE 5.25

Carrier Bridge Amplifier

All of the transducers intended for use at this time are shown in Figure 5.26. The blood pressure transducer was described. Both the temperature and the respiration rate transducers are thermistors. The thyroid uptake transducer is a small GM tube. It is intended that the GM tube on the left be placed outside of the animal; however if necessary, several more miniature GM tubes are available and are shown in the photograph. The miniature tubes can be implanted if desired by the biologists. The temperature transducer can be implanted or employed in a natural opening. The thermistor used for respiration rate measurements will be clipped inside the nostril of the animal. The blood pressure transducer will be fitted over a vessel with a 3.5 to 4 mm outside diameter.

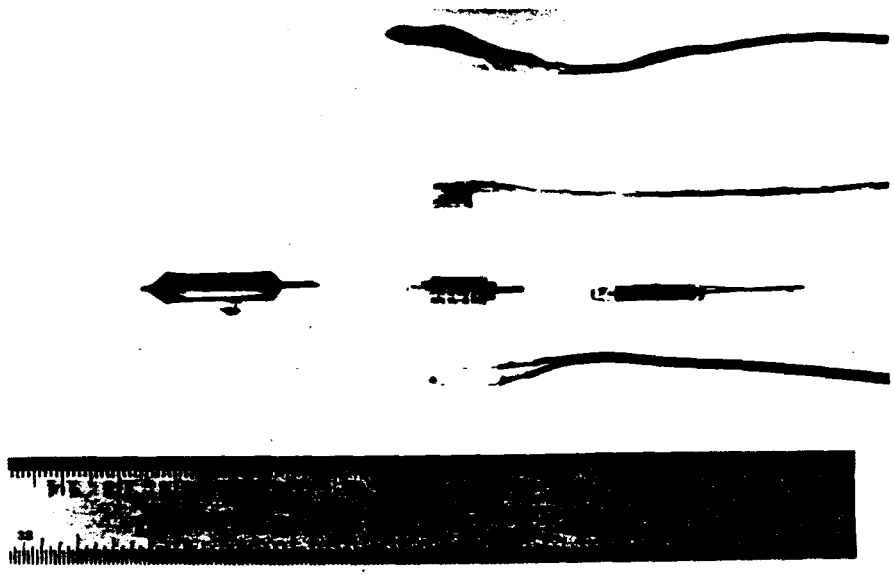

FIGURE 5.26

Transducers (from the top) Include Temperature, Blood Pressure, Thyroid Uptake, and Respiration Rate

Detection of Pu^{239} in Human Wounds - D. P. Brown and N. S. Porter

The exact location of Pu^{239} in wounds and the assurance of surgical removal are two difficult problems. Conventional alpha detectors are hampered by the high absorption of alpha particles in body tissue. A wound probe of small diameter was desired for use during wound surgery at Hanford. Such

Neg. No. 0650252

0028529

a probe is described in this paper. The completed Pu^{239} detecting probe is 10 in. long and 1 7/16 in. in body diameter with a 1/2 in. diameter frontal extension, 1 5/16 in. long, for wound probing. The crystal detector for the 17 keV X rays from Pu^{239} and a suitable light pipe are contained in the extension, and a multiplier phototube is housed in the main portion of the probe. The entire probe assembly is housed in stainless steel which is easily cleaned after use and is cable-connected to the laboratory counting instrumentation. Positive high voltage must be applied to the phototube and -20 V dc is required for the solid state preamplifier. The positive signal pulses from the phototube are coupled to an amplifier for counting. The measured counting efficiency for Pu^{239} is typically 20% for test sources of 1.6×10^3 and 1.95×10^5 disintegrations/min.

Discussion

Pu^{239} can be detected by special detectors sensitive to either the alpha particles or the X rays emitted during radioactive decay. In a flesh or puncture wound, the body fluids and tissue readily absorb the emitted alpha particles; however, the 17 kev X rays have more relative penetrating ability and can be detected through as much as 1/4 in. of body fluid and tissue. If the detector is a thin (2 mm) NaI(Tl) crystal with a very thin "entrance window" (covering), the counting efficiency for photon energies above about 100 keV is so small that the crystal effectively acts as a high energy photon filter; thus, the signal-to-background ratio is enhanced.

The accurate location of Pu^{239} within a wound requires a probe with a small sensing volume while retaining adequate detection sensitivity. The probe length has to be such that medical personnel can observe the wound during examination. Since a relatively long light pipe was needed for probing, light attenuation posed a problem in securing an adequate signal-to-noise ratio. Laboratory experiments, using an EMI-9524-B multiplier phototube, showed that a $1\frac{1}{4}$ in. long by about 5/16 in. diameter quartz light pipe provided a satisfactory compromise in achieving an adequate signal-to-noise ratio.

Following extensive laboratory tests for determining the optimum mechanical configuration for detection of the 17 keV X rays, a probe assembly, shown in Figure 5.27, was designed and then procured as an integral unit. The sectioned view shows a 0.005 in. thick by 5/16 in. diam beryllium window covering a 2 mm thick, cleaved NaI(Tl) crystal of the same diameter. The crystal is optically coupled to a quartz light pipe, which is coupled to the $1\frac{1}{8}$ in. diam EMI-9524-B photomultiplier tube. The crystal detector and light pipe are contained in a thin stainless steel shell $1\frac{5}{16}$ in. long and 1/2 in. diam, which is an extension to the main housing. The rest of the probe was designed and fabricated to form a housing for the phototube voltage divider, the tube base, and the preamplifier. To join the units, the phototube is inserted into the tube base and the sleeve is screwed onto the threaded collar of the detector to form a single unit as shown in Figure 5.28.

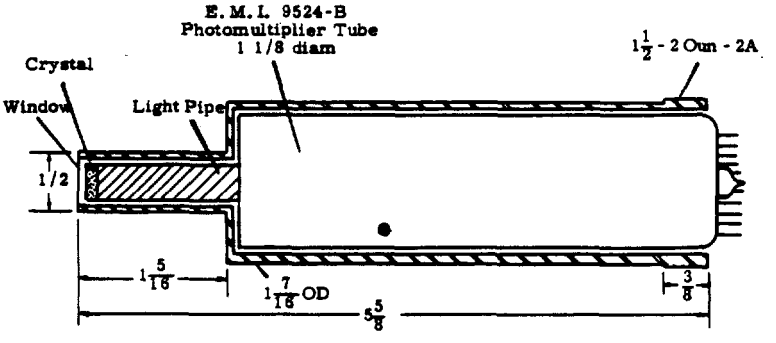

FIGURE 5.27
Probe Assembly Diagram
(Dimensions in Inches)

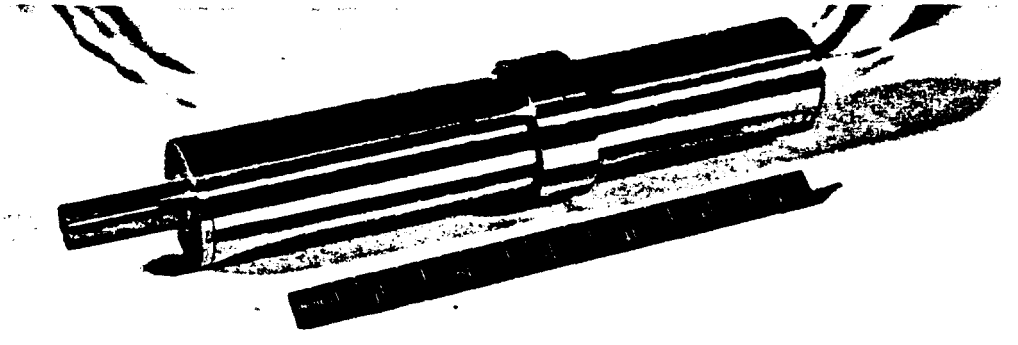

FIGURE 5.28
Assembled Wound Probe

Neg. No. 0643469-2

A schematic diagram of the electronic circuitry is shown in Figure 5.29. The preamplifier is a modified, miniaturized version of a charge-sensitive preamplifier. To alleviate noise and stability problems, the phototube cathode and the probe housing are operated at ground potential. The probe assembly can be chemically sterilized before and after use. Care is taken not to contaminate the probe window with radioactive materials during wound examination. This is best done by using a thin plastic or rubber cot over the extension.

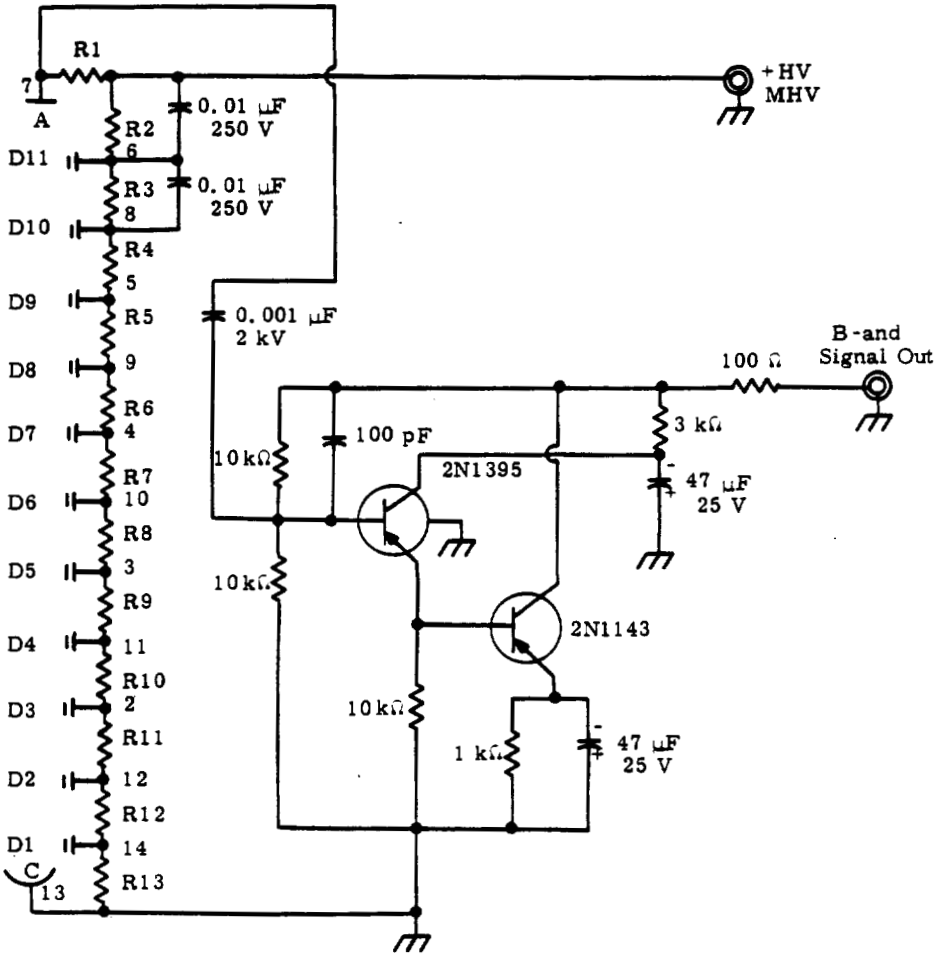

R1 and R5 through R12 = MΩ
R2, R3, R4 = 2.2 MΩ
R13 = 1.8 MΩ

FIGURE 5.29
Probe Electronic Circuitry

Initial results, using the probe with an amplifier and scaler, demonstrated a counting efficiency of 20% for Pu^{239} sources of 1.6×10^3 and 1.95×10^5 disintegrations/min. The "background" was about 20 counts/min which was reduced to about 5 counts/min by shielding the detector with 2 in. of lead. In addition, it was determined that an unshielded background rate of about 6 counts/min could be achieved by using a single channel pulse height analyzer with its base line set below 17 keV and with the window width adjusted to accept contributions caused by 60 keV photons. This improved operation was achieved since most of the background counts were caused by higher energy photons. Hence, it is recommended that the probe be used, whenever possible, with a single-channel analyser. It is noted, in addition, that by including the pulses caused by the 60 keV photons from Am^{241} (present with the Pu^{239}) probe sensitivity can be increased somewhat.

Improvements to the Biology Animal Scanning Counter - N. S. Porter and D. P. Brown

The Inhalation Toxicology dog counter,[5.21] as originally developed and fabricated in 1958, was designed to monitor dogs, *in vivo*, for Pu^{239}, Sr^{90}, Ru^{103}, Ru^{106}, and Cs^{137}. The original steel-shielded sytem provided a mechanical scanning mechanism which transported the dogs, at selected rates, past the detector heads. Biology interest was renewed as better dog phantoms became available and more intensive investigations initiated. Consequently, it was desired to incorporate an improved scanning capability in the counter and to effect other modifications to automate the system and improve operational capabilities. The modifications included a scanning capability continuously variable from 0 to 10 in./min reproducible under varying loads from 0 to 50 lb, switching to synchronize the strip chart recorder with the carriage, a signal control also operated by the carriage, and improvement of the adjustment capability of the lower offset detectors through counter balance. In addition, new ball-bushings were installed to provide smoother operation. Collected data using the system have proven to be useful in delineating internal radionuclide depositions in beagle dogs.

Discussion

During the postexposure studies of beagle dogs, which have previously inhaled quantities of such radionuclides as Pu^{239}, Sr^{90}, Ru^{103}, Ru^{106}, and Cs^{137}, it is desirable to obtain deposition data by scanning the animals. Scanning rates must be adjustable, as determined by the deposited activity in the animals, from 0.5 to 2 in./min. At the same time, the platform speed must be constant without regard to differences in weight of the animals, where this weight can vary from 25 to 45 lb. In addition, the system has to accommodate the plastic dog-carrying boxes being used for counting purposes. The boxes, approximately 12 by 30 by 18 in., restrain the animals during counting. Simplicity of design and ease of operation are also factors to be considered in the design of the new system.

The location of the heavy steel counter dictated that the unit be partially dismantled when not in use to prevent congestion at the Whole Body Counter vault door. The supporting member for the carriage is plywood (18 by 2.75 by 90 in.) with 24 in. of one end being removable (attached with quick disconnect clamps). Steel "C" rails are attached to the support member with a butt-joint at the disconnect point. A Graham reversible, variable speed drive unit (attached to a 4 ft long screw) is used to obtain a continuously variable scanning rate of from 0 to 10 in./min. The assembly is attached to the supporting member, parallel to the rails, with appropriate support bearings. The carriage is constructed of plywood with steel axles and roller-bearing wheels. An aluminum arm is attached to the tray with the extended end attaching to the drive-nut on the screw. As the motor turns the drive-screw, the drive-nut propels the platform back and forth along the rails. End and side stops are attached to the platform to reference the dog boxes. Cams are provided to operate limit switches at both ends of the tray run. All wooden surfaces are epoxy finished. Electrical connections are made to provide remote reversing with a three-pole, double-throw switch and to provide signal and recorder (start-stop) control to synchronize data collection with scanning. The entire assembly is bolted to the

steel shell of the counter. The extreme ends of the support member are supported by 0.5 in. carriage bolts from the concrete floor and the system is leveled to insure that the midline of the dogs passes through the center of the counter assembly during scanning. Construction and mounting details are shown in Figure 5.30 and 5.31. The longer, counterbalanced lower detector supports are also seen in the figures. This addition greatly improved the adjustability of these detectors.

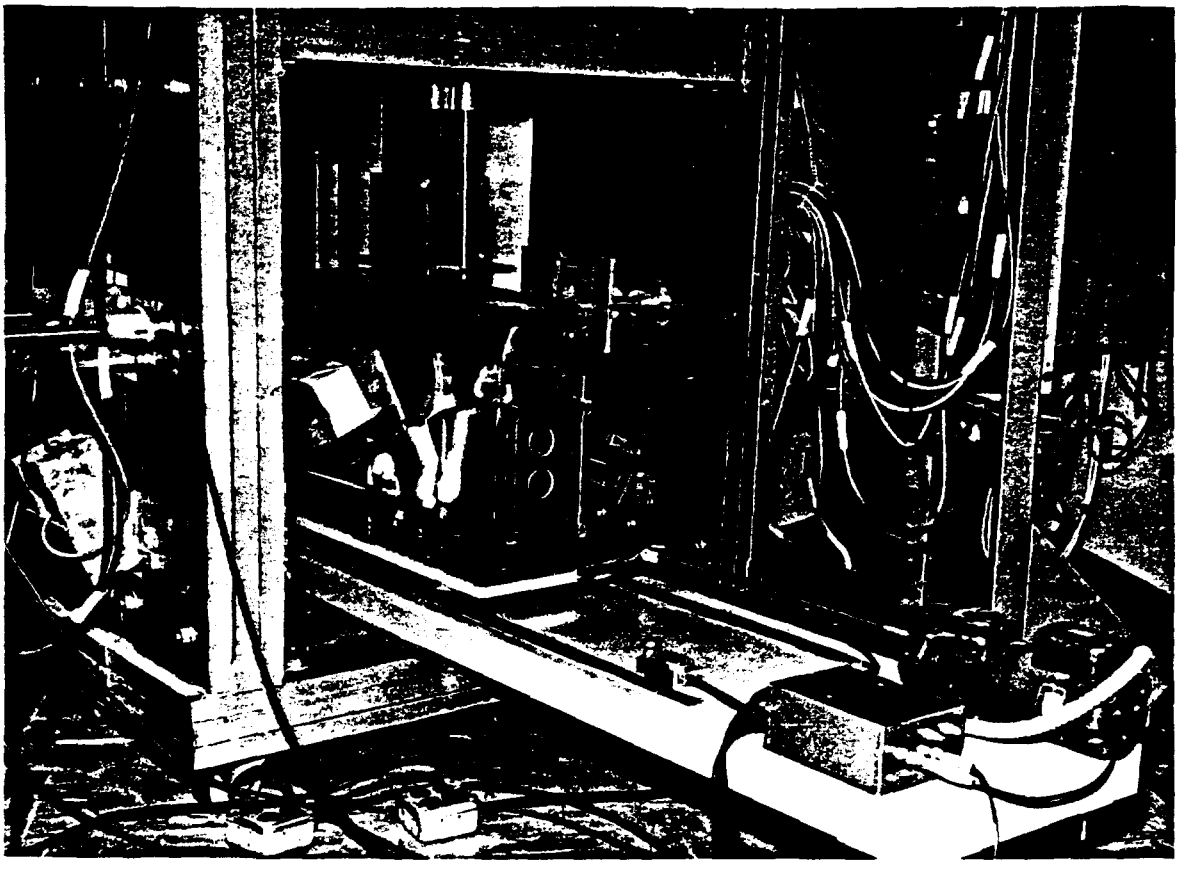

FIGURE 5.30

Scanning Counter
with Beagle Being Counted

Neg. No. 0650024-1

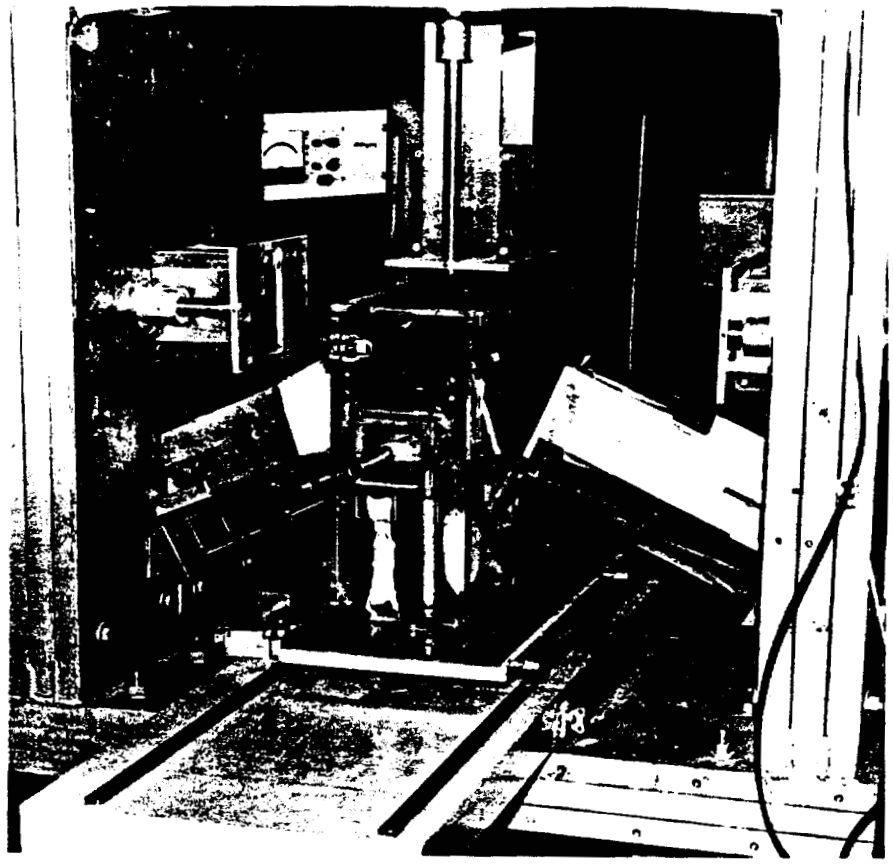

FIGURE 5.31

Reverse View
of the Scanning Counter

Biological Spectrometer and Analyzer - N. S. Porter and E. M. Sheen

During radiobiological experimentation with animal subjects of the Battelle-Northwest Biology Experimental Animal Farm, a need arose for a portable field instrument for the measurement of alpha, beta, and gamma emitting radionuclides. The biology spectrometer and analyzer instrument was developed to meet the requirements of the experimental investigations. The circuitry comprises a high voltage supply for the detectors, a pulse amplifier, single channel analyzer, count-rate-meter, five decade scaler, power supply, and the required testing and logic circuits. During operation, data presentation is made either on the count-rate-meter or on the scaler as selected by the operator. All circuitry is solid

Neg. No. 0650024-2

state and designed for efficient, maintenance-free operation for extended periods of time, and provision is made for both battery and 110 V ac operation. The battery pack, which includes a charger for recharging the Ni-Cd batteries after 8 hr of use, is contained in a separate cabinet as a convenience feature. Portability is such that one man can transport and easily handle both units simultaneously. Satisfactory operation has been demonstrated during several months of field use, and the versatility permits operation in the laboratory or field with equal success.

Discussion

The biology spectrometer and analyzer was developed to fill the needs of radiobiological investigations with alpha, beta, and gamma emitting radionuclides. As a variety of different detector-probes was already in use with various laboratory instruments, it was desirable that the new instrument be compatible with them. Portability was an important requirement as much of the laboratory work is done in the field where conventional 110 V ac power is not available. The instrument, shown in Figure 5.32, meets the requirements.

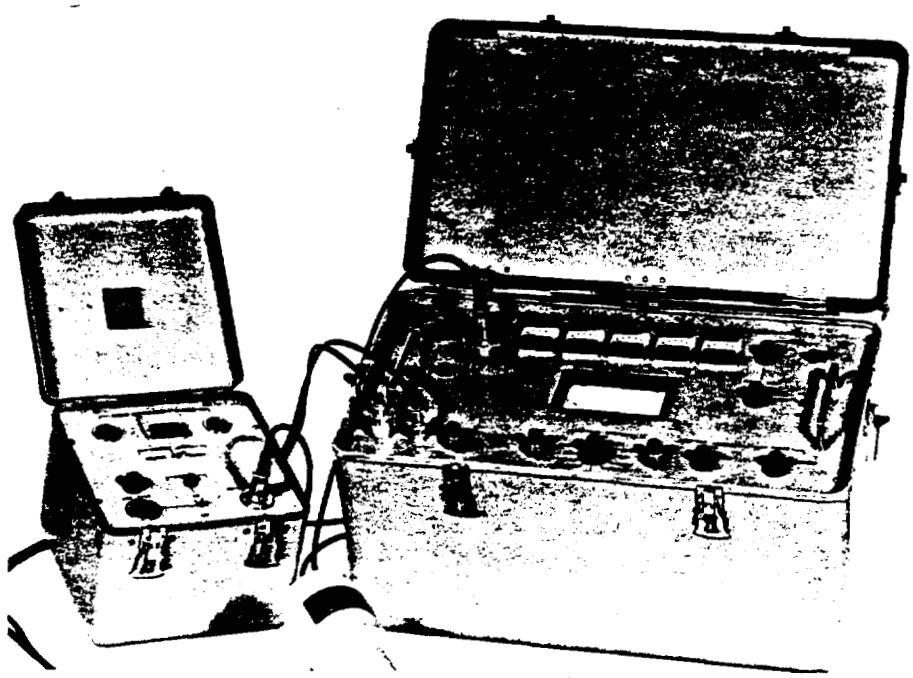

FIGURE 5.32
Biology Spectrometer and Analyzer

Neg. No. 0642401-1

Figure 5.33 is a block diagram of the complete instrument. As indicated, all features of spectrometer and analyzer use are utilized including a high voltage supply, pulse linear amplifier, single channel analyzer, count-rate-meter, multi-decade scaler, low level power supply, and required testing and logic circuitry.

The high voltage for the scintillation probes is obtained from a compact, electronically-regulated, solid state supply that is continuously variable from -600 to -1500 V dc with a 10-turn potentiometer on the front panel. Preamplifier operating voltage is obtained over the signal line. The negative scintillation pulses are amplified in an RC-clipped amplifier to levels from -1 to -5 V. A voltage gain of 50 is available from the amplifier, which has a linearity of ± 1%, and amplifier gain is adjusted to avoid saturation with the largest expected pulses. The overall instrument gain is controlled by varying the high voltage to the detectors.

The single channel analyzer is of conventional design with window-width and baseline adjustments. It operates in differential or integral mode, selectable at the front panel, and drives the 7-range count-rate-meter up to 10^6 counts/min full scale maximum. To facilitate scaling, an electronic timer with preset times of 6 sec, 30 sec, 1 min, 5 min, and 10 min is provided. The timer is a relaxation oscillator with suitable dividing and logic circuits to open a gate for the specified time intervals. Scaling is accomplished with a 5-decade, 200 kc scaler with meter readout to facilitate reading in sunlight.

To test circuitry operation, a test oscillator was included to provide pulses at approximately 600/sec for checking the count-rate circuits and scaler. When the instrument is powered by 110 V ac, the circuitry operating voltages are obtained from a suitable unregulated power supply.

The circuitry of the instrument was designed using solid state components and techniques to provide reliable, efficient, and maintenance-free operation over extended periods of time. Commercial modules are used to the extent possible. Provision was made for both battery and 110 V ac line

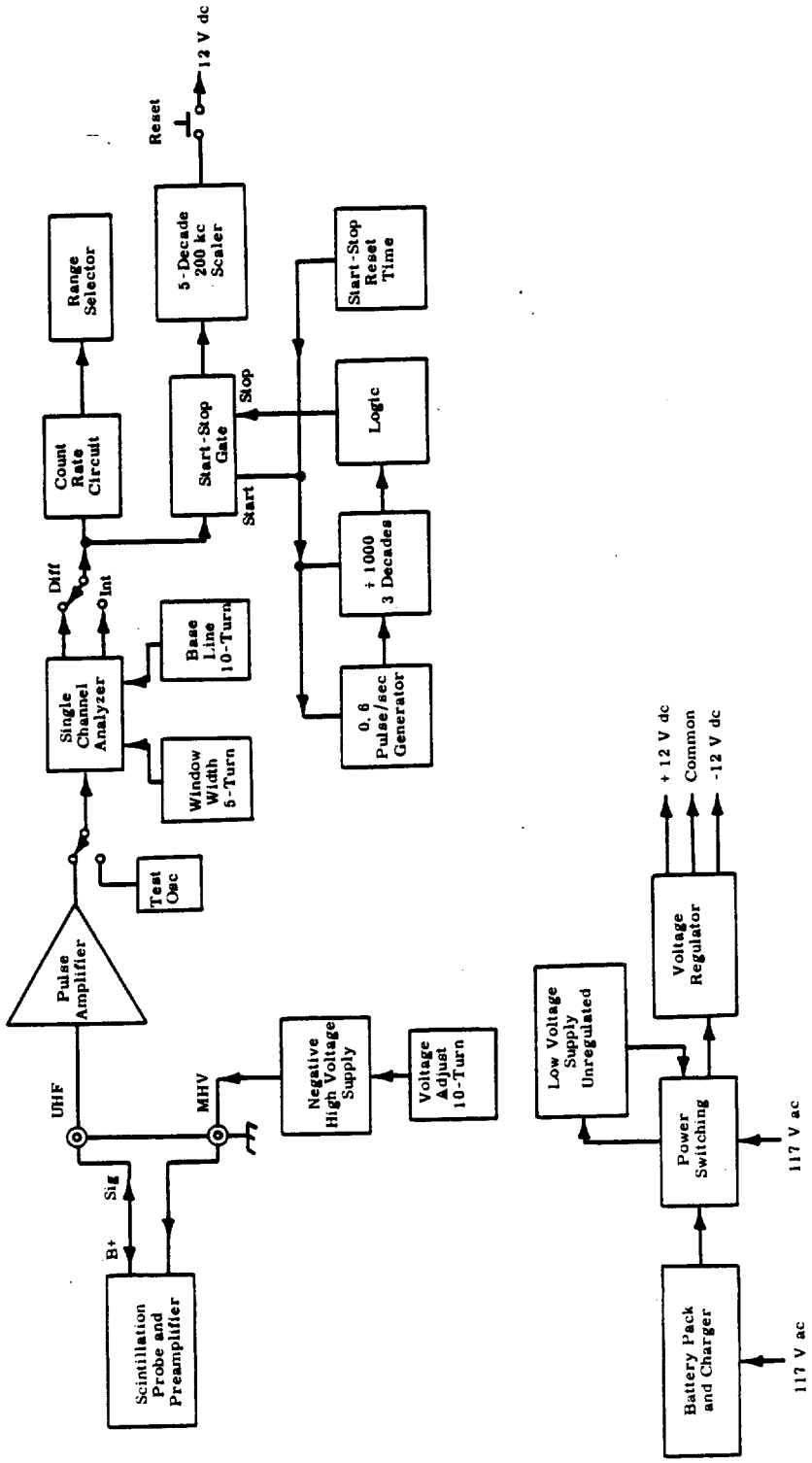

FIGURE 5.33
Block Diagram
of the Biology Spectrometer and Analyzer

operation. The battery pack, which includes a charger for recharging the Ni-Cd batteries, is contained in a separate cabinet as a convenience feature. The pack can provide normal spectrometer power requirements (4 W) for approximately 8 hr before recharging is necessary. Portability is such that one can easily transport and handle both units simultaneously, as the pack weighs 15 lb and the spectrometer approximately 35 lb.

Dosimetry and Atmospheric Physics Instrumentation

Peak Pulse Measuring Instrumentation for Use with Ion Chamber Dosimeters - N. C. Hoitink

An instrument, capable of reading the peak voltage of a pulse from ionization chamber dosimeters, was needed for use in dosimetry studies. The instrument had to be able to measure pulses from 10 mV to 10 V in amplitude with rise-times from 50 to 100 nsec. Since it is not possible to determine even the approximate size of the pulse before measurement and since the measurement of the pulse during the recharging of the ionization chamber destroys the information "stored" in the chamber, it was necessary that the instrument select the proper range for each pulse during the readout process. The instrument provides a digital output of from 1 to 10 V with an appropriate indicator lamp supplying the proper multiplying factor. The instrument performs the necessary logic to select the correct channel for processing the input pulse and for energizing the indicator. Successful operation is being achieved in the intended experimental application.

Discussion

A peak pulse measuring instrument was developed to fulfill the need for a device capable of measuring the peak voltage of a pulse resulting from the charging of a small ionization chamber dosimeter. The pulses to be measured are available as the output from an emitter follower that serves as a low input capacitance, high impedance preamplifier. The pulses are, typically, several microseconds in duration with risetimes of 50 to 100 nsec.

The method used to measure the pulse height requires that a capacitor be charged to the peak voltage of the input pulse and then the time

required to discharge the capacitor be measured. This discharge time is proportional to the input pulse height. Before describing the functions performed in the measurement process, several of the problems will be mentioned.

To cover the pulse height ranges required, it was necessary to provide pulse amplifiers that were linear within ±1% and that had voltage gains of approximately 10 each. For convenience, it was necessary to design the instrument so the output would continue to indicate the correct measurement until the reading had been recorded. Since it is not possible to determine before the measurement how large the pulse will be, it was necessary that the instrument "select" the proper gain channel for the pulse to provide an output of 1 to 10 V along with an appropriate indication of the power of 10 multiplier, which describes the decimal point location.

Figure 5.34 is a block diagram of the instrument. Briefly, the instrument generates a negative ramp signal, the discharge time of which is proportional to the maximum voltage of the input pulse. Two trigger pulses are generated; the first is provided at the start of the ramp and the second when the ramp returns to zero. These two trigger pulses are used to "set" and "reset" a flip-flop circuit that gates a 100 kc crystal-controlled oscillator into a scaler. The scaler display is then a digital representation of the input pulse height.

The input to the instrument is low impedance and must be driven by a preamplifier to accommodate 300 Ω. A risetime "spoiler" is connected to the input to stretch the risetime of the pulse sufficiently to allow the remainder of the instrument to function properly. This method reduces the pulse height somewhat; however, the reduction is a constant percentage of the input pulse height, providing the shape of the pulse is the same as it is for this application. The output of the risetime spoiler is connected to the input of the first measurement channel and to the first gain-of-ten amplifier. The output signal from the amplifier is connected to the second measurement channel and the second gain-of-ten amplifier, which is connected to the third measurement channel. The amplifiers employ voltage feedback and are

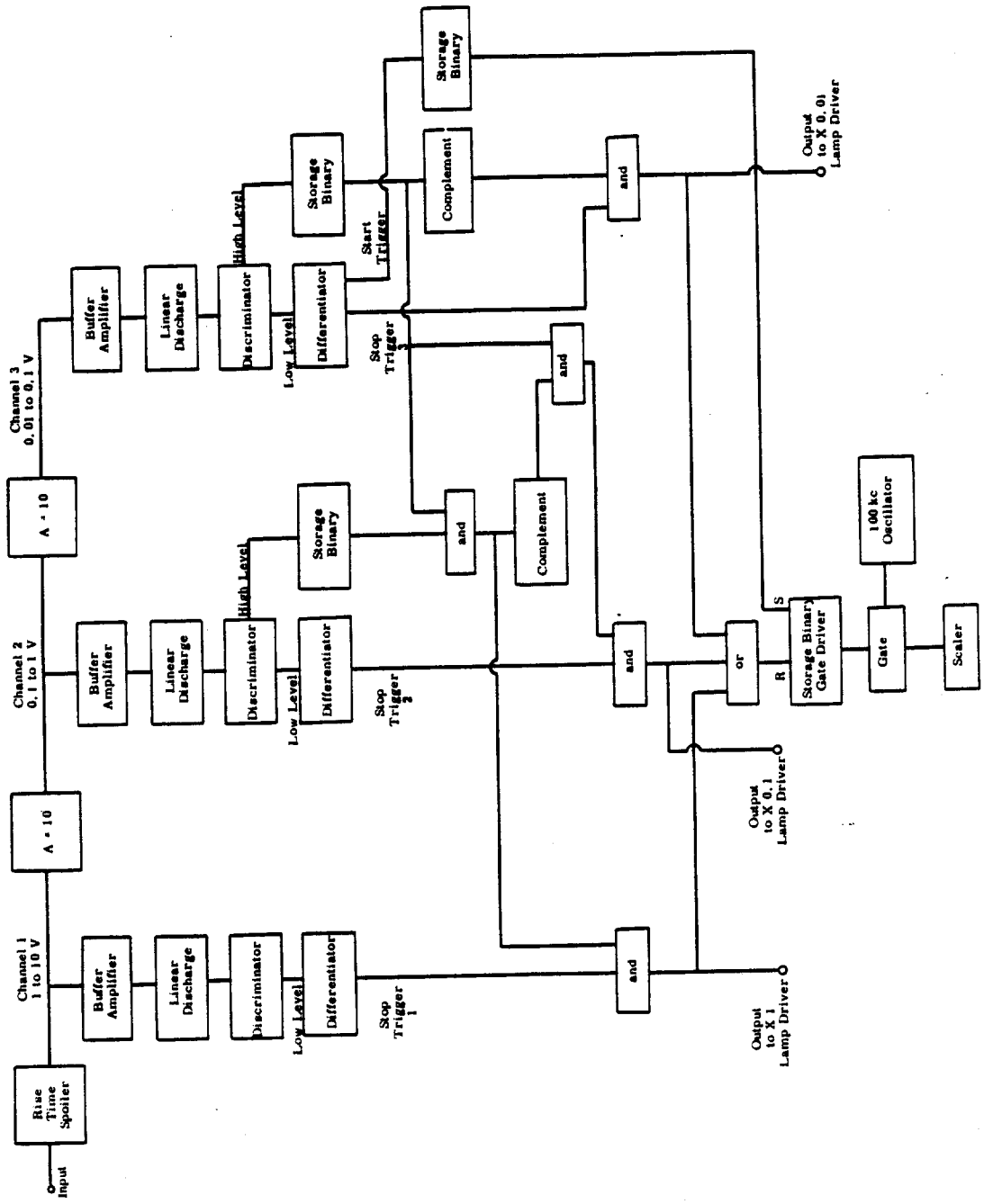

FIGURE 5.34

Peak Pulse Measurement Instrument

linear to an output level of about 11 V. The amplifier saturates with input pulses greater than 1 V, but this does not affect the proper operation of the instrument. The input stage to each measurement channel is a unity gain buffer (isolation amplifier) that drives the linear discharge circuit while isolating it from the input and from the gain-of-10 amplifiers.

The next stage of the measurement channel is the heart of the instrument, the linear discharge circuit. This circuit is shown in Figure 5.35.

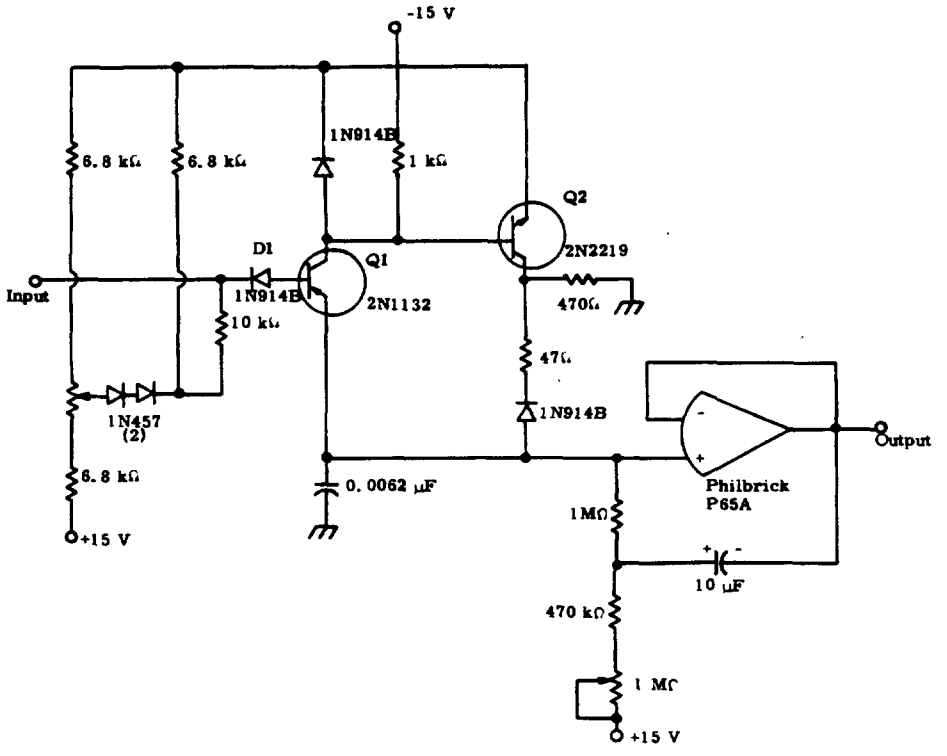

FIGURE 5.35

Linear Discharge Pulse Height-to-Time Converter

The capacitor in the emitter circuit of Q1 charges to a voltage equal to the voltage of the input pulse while the input increases, but when the pulse reaches its peak value and begins to decrease, the transistor and the diode in the base circuit become reverse biased so the capacitor must discharge through the bootstrapped operational amplifier and resistance circuit. This requires a constant current and therefore a linear discharge. A typical

linear discharge waveform, along with the input pulse, is shown in Figure 5.36. The two signals shown have different time bases as noted below the figure.

The output of the operational amplifier is monitored by two level discriminators, one of which provides an output when the linear discharge voltage exceeds 10 V and the other provides an output when the input is greater than about 0.1 V. The low-level discriminator is turned on for a time very nearly equal to the time required for the input linear discharge signal to return to zero. Figure 5.37 illustrates the low-level discriminator output signal along with the linear discharge from which it is derived. The output of the low-level discriminator is differentiated to obtain trigger pulses, which are available for selection as the correct pulses to set and reset the signal that gates the oscillator into the scaler. The high-level discriminator output signal indicates by its presence that the input has exceeded the allowable 10 V. The output of this discriminator, as shown in Figure 5.38, is used in the logic portion of the instrument to select the correct channel to be used to gate the oscillator.

The logic portion of the instrument is shown in the block diagram wherein the logic circuits are shown individually. It is the purpose of the logic to select the gate trigger pulse from that channel which will provide the largest reading that does not exceed 10 V. An output signal from a high-level discriminator "sets" a storage binary. The binary remains set thereby providing a logical "1" to indicate that this particular channel has exceeded the permitted 10 V level. It can be seen by diagram reference that the logic function just described is thus properly implemented. The oscillator is gated on by only the third channel (the channel which measures 10 to 100 mV). This approach simplifies the logic by requiring that only the correct "stop" pulse be selected. For input signals large enough to produce trigger pulses from more than one channel, the first (or start) triggers occur essentially coincidentally in each channel. For this reason, it is permissible to use only the one signal generated in the third channel.

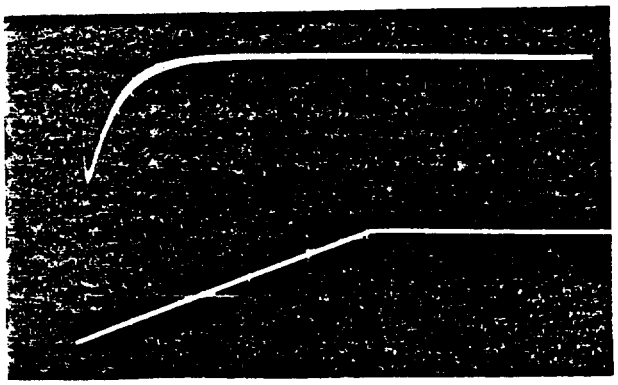

FIGURE 5.36

Input Pulse and Linear Discharge Waveform
(Top, 10 V input pulse, 10 μsec/division, 5 V/division; bottom, linear discharge characteristic, 2 msec/division, 5 V/division)

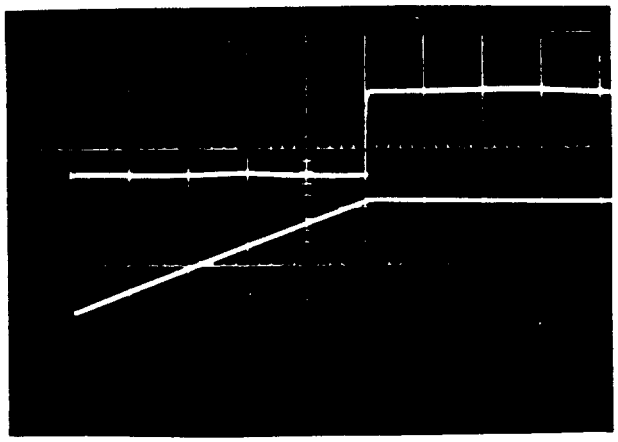

FIGURE 5.37

Low Level Discriminator Output
(Top, 2 msec/division, 5 V/division; bottom, linear discharge, 2 msec/division, 5 V/division)

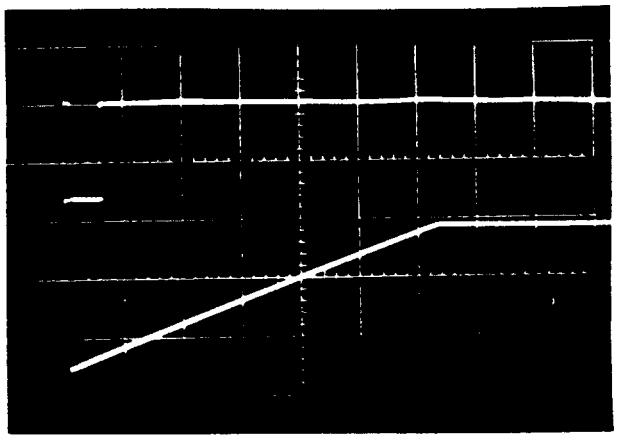

FIGURE 5.38

High Level Discriminator Output
(Top, 2 msec/division, 5 V/division; bottom, linear discharge, 2 msec/division, 5 V/division)

0028545

So that the instrument may ignore any pulses received after the first pulse, the "start" trigger pulse does not activate the gate binary, but rather it activates a storage binary, which in turn, triggers the gate binary to the "on" condition. Since the storage binary must be reset manually, it is impossible for an unwanted pulse to activate the scaler (thereby destroying the reading) until after the reset switch on the instrument has been manually engaged.

Additional circuits not included in the block diagram, but which are necessary, include a calibrate pulse generator, lamp drivers, and power supplies. The pulse generator is provided for use in calibrating and checking the performance of the instrument. The generator uses a mercury-wetted relay to provide pulses from 10 mV to 10 V in amplitude and accurate to about 0.25%. The lamp drivers consist of a binary for each decade which is set if that decade is so selected by the logic circuits. The binary drives another transistor, which in turn, drives the indicator lamps on the front panel. An unfiltered, full-wave-rectified 24 V dc power supply provides power to operate the indicator lamps. The power supply for the remainder of the instrument is an adjustable, series-regulated type and provides a nominal ± 15 V dc at 50 and 150 mA, respectively.

The performance of the instrument has been acceptable, and performance information is shown in Figure 5.39. The percentage error is plotted versus the input pulse height. The data were taken shortly after the instrument had been calibrated; and, with the exception of three points, the readings are well within ± 1%. With more careful calibration, the accuracy was improved. The instrument is calibrated by adjusting the slope of the linear discharge so input signals of 5, 0.5, and 0.05 V produce scaler readings of 500. The adjustment is made by increasing or decreasing the resistance of potentiometer P2 of the linear discharge circuit (shown in Figure 5.35). The adjustment is made on the front panel of the instrument.

002854b

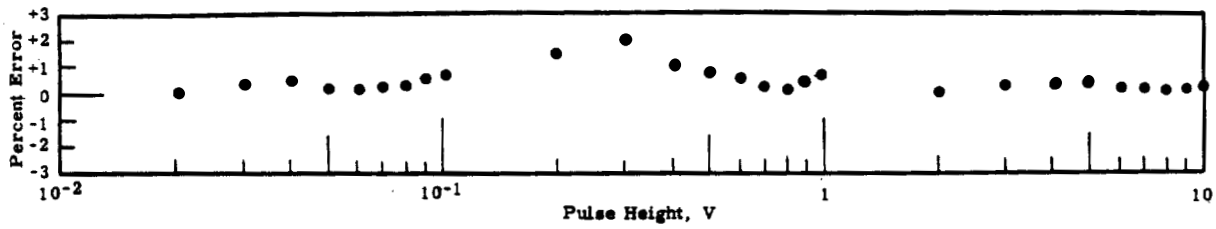

FIGURE 5.39
Instrument Performance

The completed instrument is shown in Figure 5.40. The instrument requires that a scaler be used as the readout device as shown in the figure. If desired, a suitable scaler may be included within the instrument package.

FIGURE 5.40
Peak Pulse Measuring Instrument

Neg. No. 0650166-2

Gamma Spectrometer for Use in Whole Body Counting - E. M. Sheen

Studies of the Cs^{137} body burdens of Alaskan natives have been conducted by members of Battelle-Northwest since the summer of 1962.[5.22, 5.23] These studies were conducted using a Hanford-developed shadow-shield whole body counter that employs 5 tons of lead shielding, a multichannel analyzer, large NaI(Tl) scintillation crystal, high voltage supply, and a gasoline-engine-driven power supply. During the studies, it was determined that body burdens above about 100 nCi (Cs^{137}) could be measured to about ± 10% with a 3 by 3 in. NaI(Tl) crystal held in the lap of the subject, with his body bent forward over the detector.[5.24] No shielding is necessary, other than that provided by the body of the subject. This capability created the need for a compact, solid state, battery-powered spectrometer comprising a single-channel pulse height analyzer, count-rate meter, high voltage supply, and scaler. An instrument of of this type would permit easy access to remote Alaskan areas by airplane with a minimum amount of instrumentation and with no lead shielding required. The instrument, which is also directly applicable to general field problems, operates from ± 8 V dc supplied by an electronically-regulated, battery supply using standard 6 V dc lantern batteries. The complete instrument, including power supply, weighs 17 lb, and approximately 100 hr of operation can be obtained from a set of batteries.

Discussion

A photograph of the completed spectrometer is shown in Figure 5.41 and the comprehensive block diagram is provided in Figure 5.42.

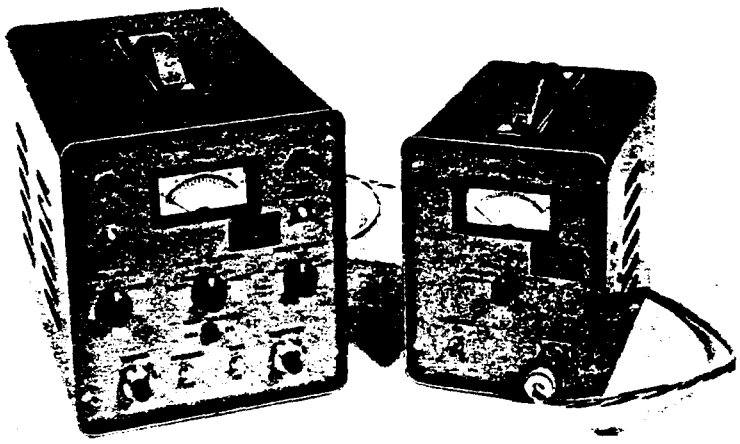

FIGURE 5.41
Complete Gamma Spectrometer

Neg. No. 064314-2

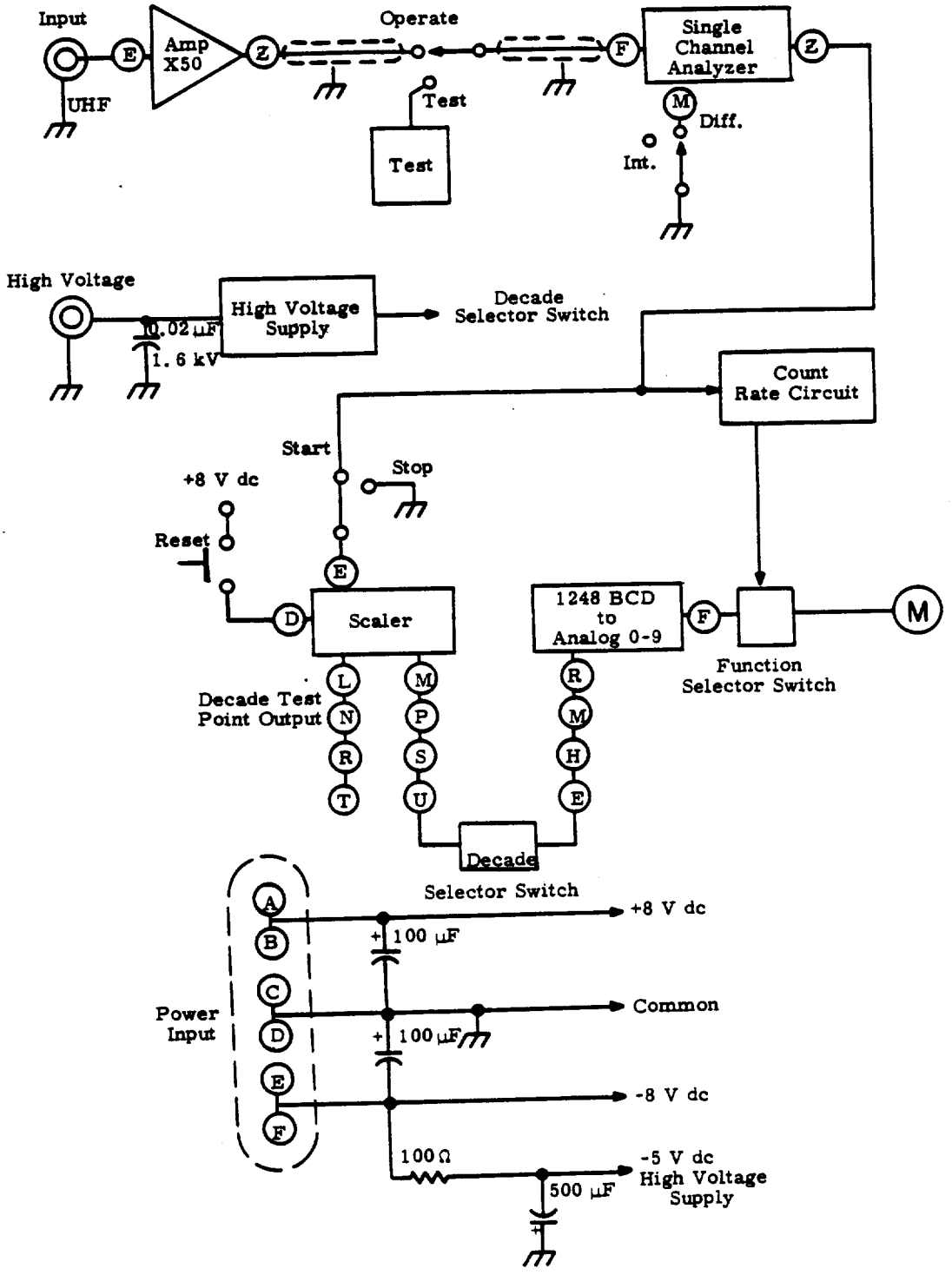

FIGURE 5.42

Spectrometer Block Diagram

In operation, an RC-clipped linear pulse amplifier amplifies negative pulses from the scintillation probe, and the "Operate-Test" switch selects either these pulses or pulses from a test-pulse generator and connects them to the single-channel pulse height analyzer. The pulse height range is from 0 to -5 V peak. Output pulses from the analyzer are gated to the scaler by the "Start-Stop" switch and are direct-coupled to the count-rate circuit. A selector switch connects the meter to the count-rate circuit, to the scaler decade 10-level analog output, or to the high voltage corona regulator tube. Monitoring the regulator current permits adjustment to the proper value and provides a test to indicate supply operation.

Integral linearity of the combined pulse amplifier and analyzer is ± 1%. The analyzer window width can be varied from zero to the maximum energy level using a 10-turn dial potentiometer. A toggle switch is provided to permit integral counting without the necessity of major window width adjustment, and a 10-turn locking base line control is also provided. The count-rate meter is used to facilitate gain adjustment to a desired radionuclide photopeak at the appropriate base line energy level. Normally, the data are obtained from the 5-decade scaler for accuracy.

The number of pulses stored in the scaler is measured by switching the binary-coded-decimal (BCD) numbers to a 10-level analog current circuit and reading the equivalent number on a 0 through 9 scale on the meter. This method results in a definite saving in both components and power, as compared with conventional low-voltage decade indicators. Following a modest amount of practice, the operator can quickly read all five decades (sequentially) and record the numbers.

A circuit diagram for the linear pulse amplifier is shown in Figure 5.43. Transistors Q1 and Q2 form a complementary feedback pair with a stable voltage gain of 10. The output pulse is coupled to a second complementary feedback pair designed to provide a gain of 5 and a linear (0 to 5 V peak) output signal pulse. The differential linearity of the complete amplifier is approximately ± 1%. Output pulses from the noninverting amplifier are capacitively coupled to the lower-level discriminator portion of the single channel analyzer.

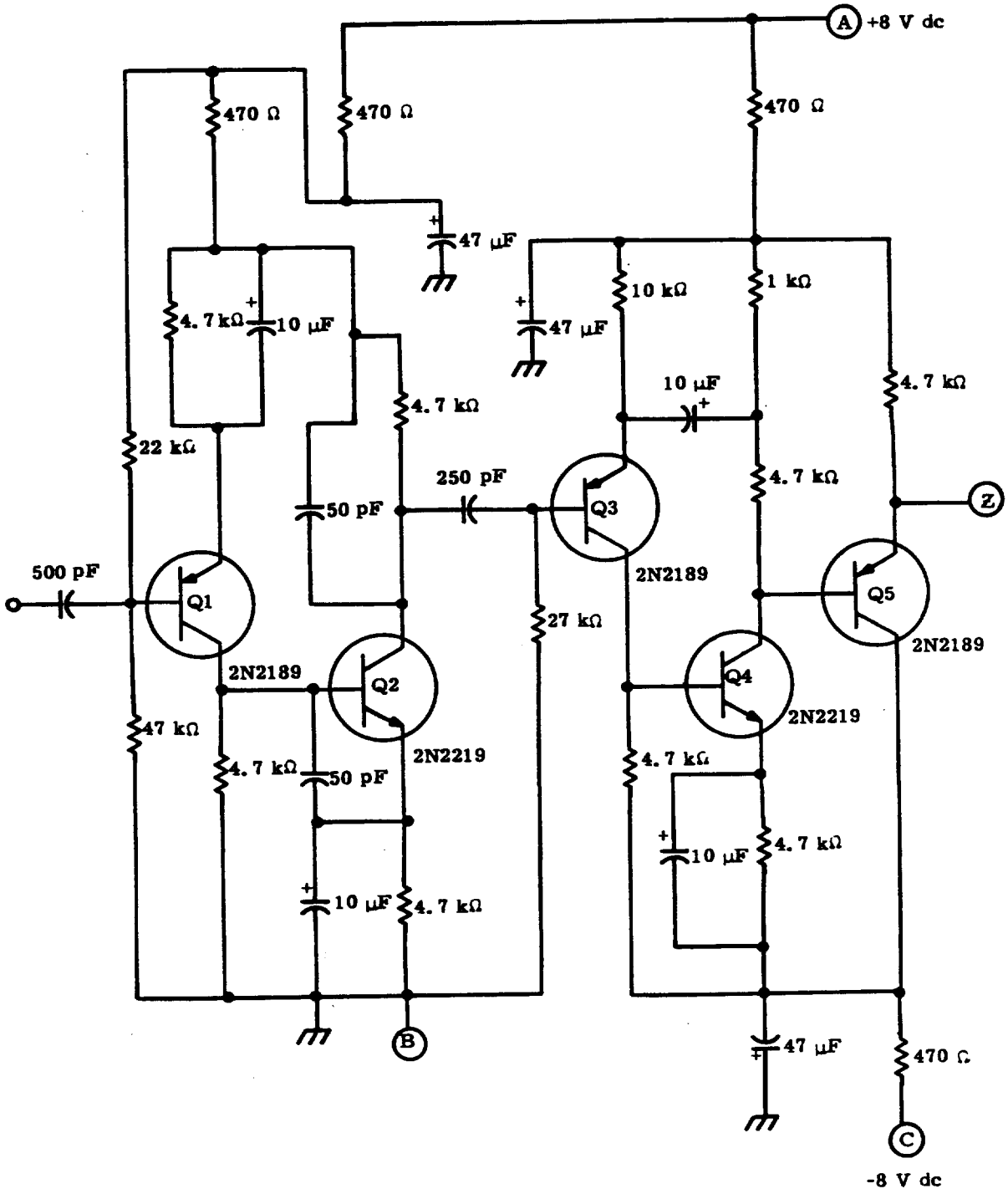

FIGURE 5.43

Linear Pulse Amplifier

Figure 5.44 details the lower-level discriminator circuit. The input pulse connects to a 1N916 diode, which is reverse biased by the

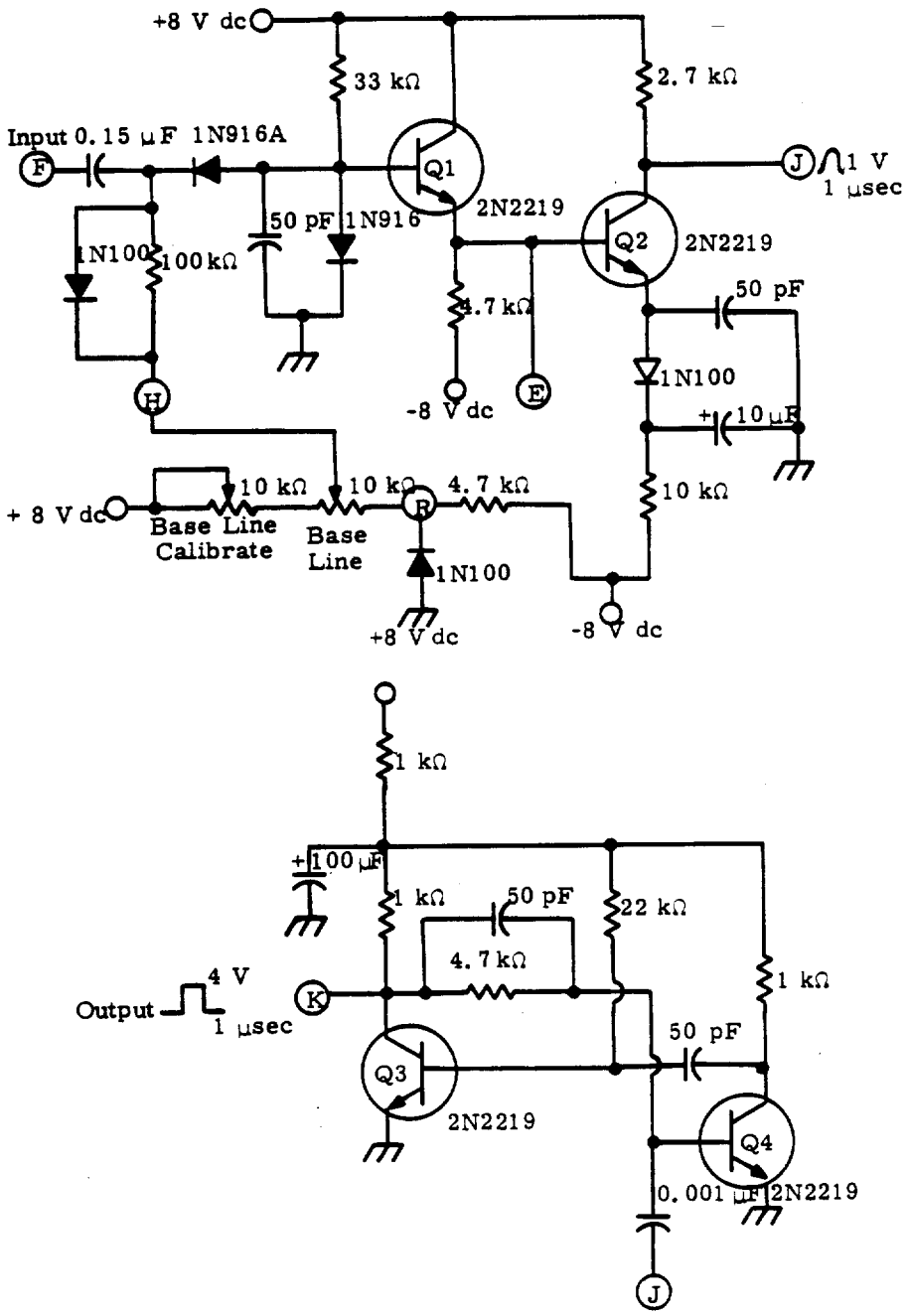

FIGURE 5.44

Lower Level Pulse Discriminator

amount of base line voltage setting. As the pulse voltage magnitude exceeds this bias, current is switched from the second 1N916 to the input. This current magnitude is nearly constant, removing much of the nonlinearity normally associated with the diode forward characteristic. Transistor Q1 is an emitter follower with the output pulse equal to the input pulse height minus the base line voltage setting. Transistor Q2 is a cross-over detector that triggers a monostable multivibrator if the input pulse exceeds (significantly) the base line setting. The monostable multivibrator (Q3 and Q4) provides a time delay to permit logical comparison of the trailing edge of this pulse with the output pulse from the upper-level discriminator.

Figure 5.45 shows the circuits for the upper-level discriminator, including a voltage comparator (Q5 and Q6) that drives a monostable multivibrator (Q8 and Q9). The pulse from Q9 inhibits the output pulse of the single channel analyzer. The output gate circuit (Figure 5.46) consists of a differentiator from the lower-level discriminator, which drives the base of Q10. Presence of an upper-level discriminator pulse clamps the base of Q10, thereby inhibiting the output pulse. For pulses within the window width, Q10 is switched on and drives an inverter (Q11) to provide a -8 V, 2 μsec pulse to operate the scaler and count-rate circuits.

The count-rate meter is shown in block diagram form in Figure 5.47 and is detailed in Figure 5.48. The count-rate circuit consists of a binary with a complementary pair, an emitter follower, and an output stage driving a linear diode-transistor charge pump circuit. Incremental charge, independent of the output voltage, is transferred to the capacitor at the base of Q5 and is removed through one of the several calibrating shunt resistor and potentiometer combinations. The count-rate circuit provides a 0 to 5 V peak output voltage integrally linear with counting rate to within ± 1%. For this instrument, the count-rate meter is employed only to "peak" the single channel analyzer; thus, only three decades of range are provided. However, if count-rate output data are desired, a 1, 3, 10 range sequence is available

0028553

and can be obtained with the same fundamental circuit by switching input capacitors in the stated sequence. Transistor Q6 charges the long-time-constant capacitor to the voltage of the shorter time-constant capacitor to permit switching with minimum disturbance to the reading of the counting rate.

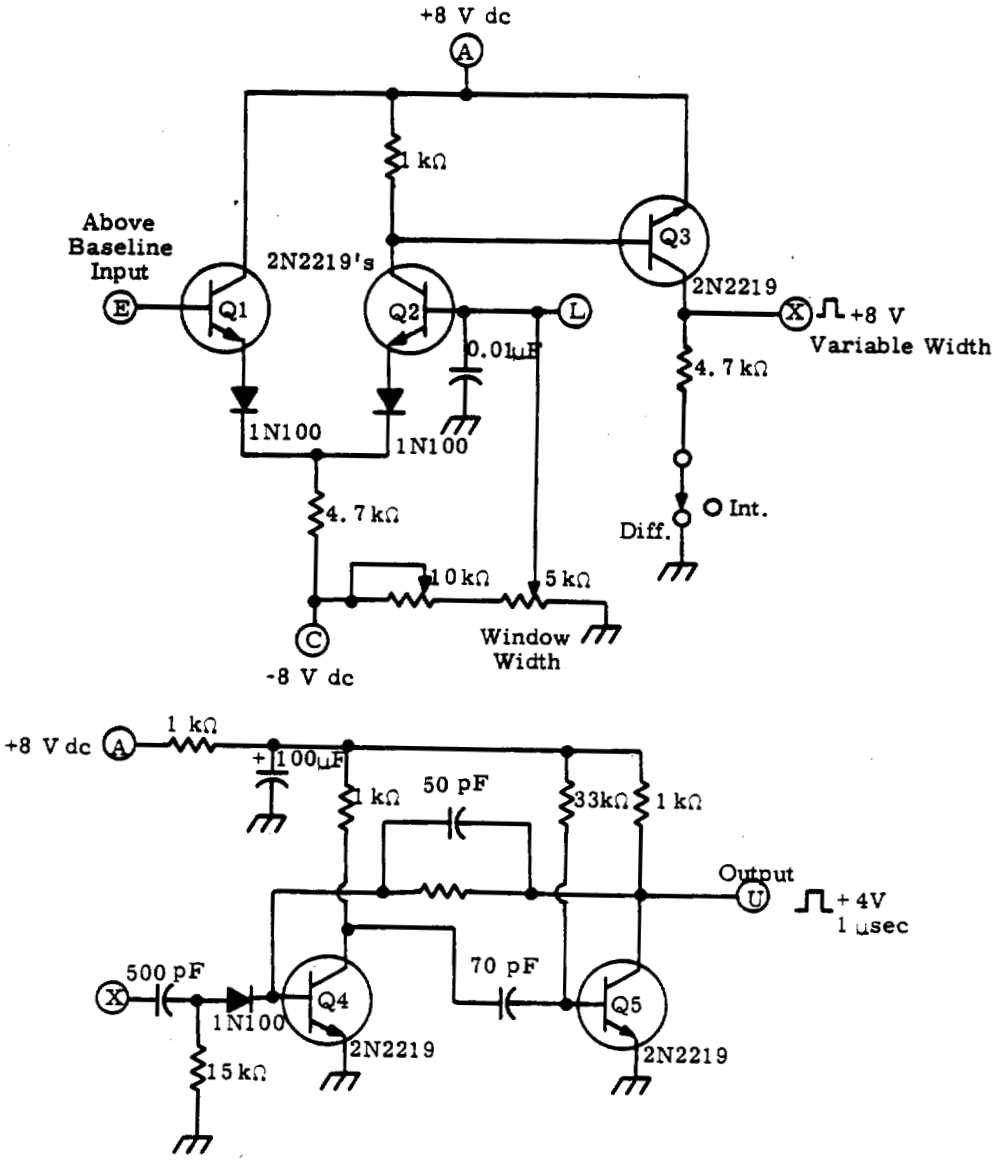

FIGURE 5.45

Upper Level Pulse Discriminator

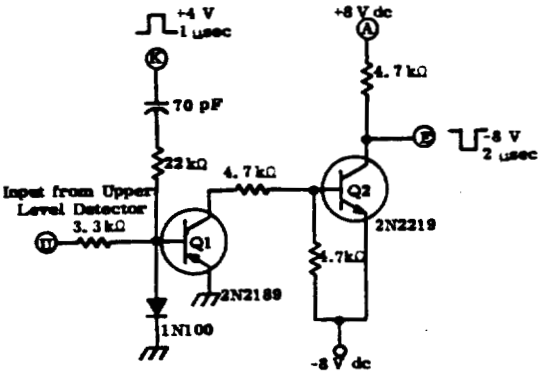

FIGURE 5.46

Single Channel Analyzer
Output Gate Circuit

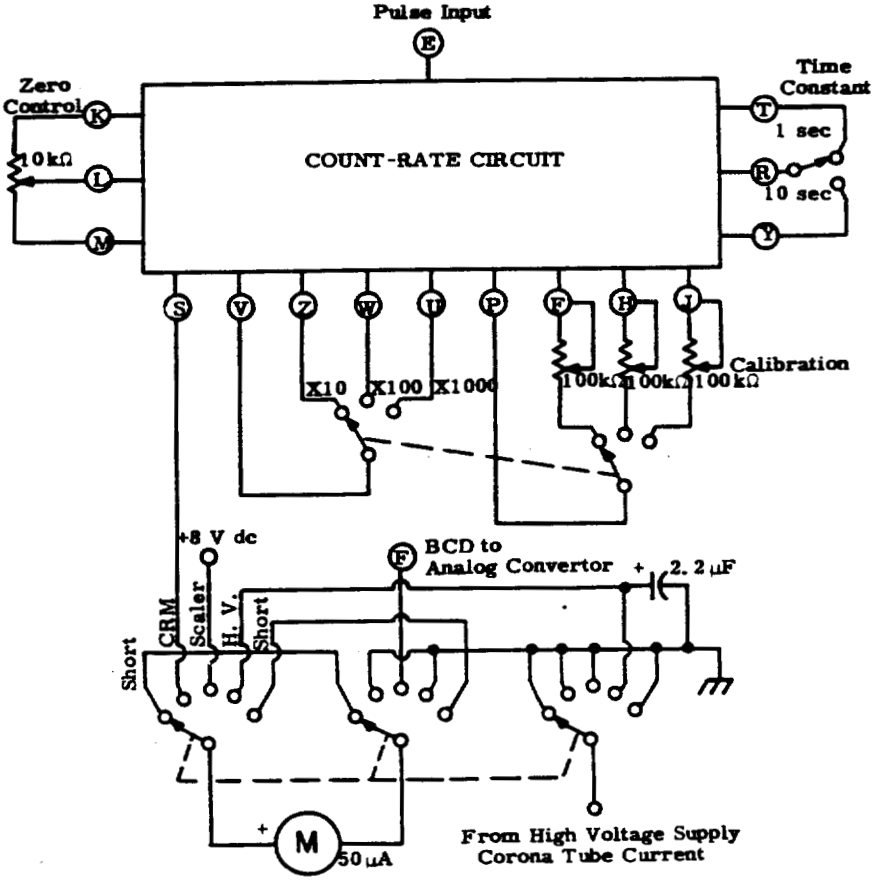

FIGURE 5.47

Count-Rate-Meter

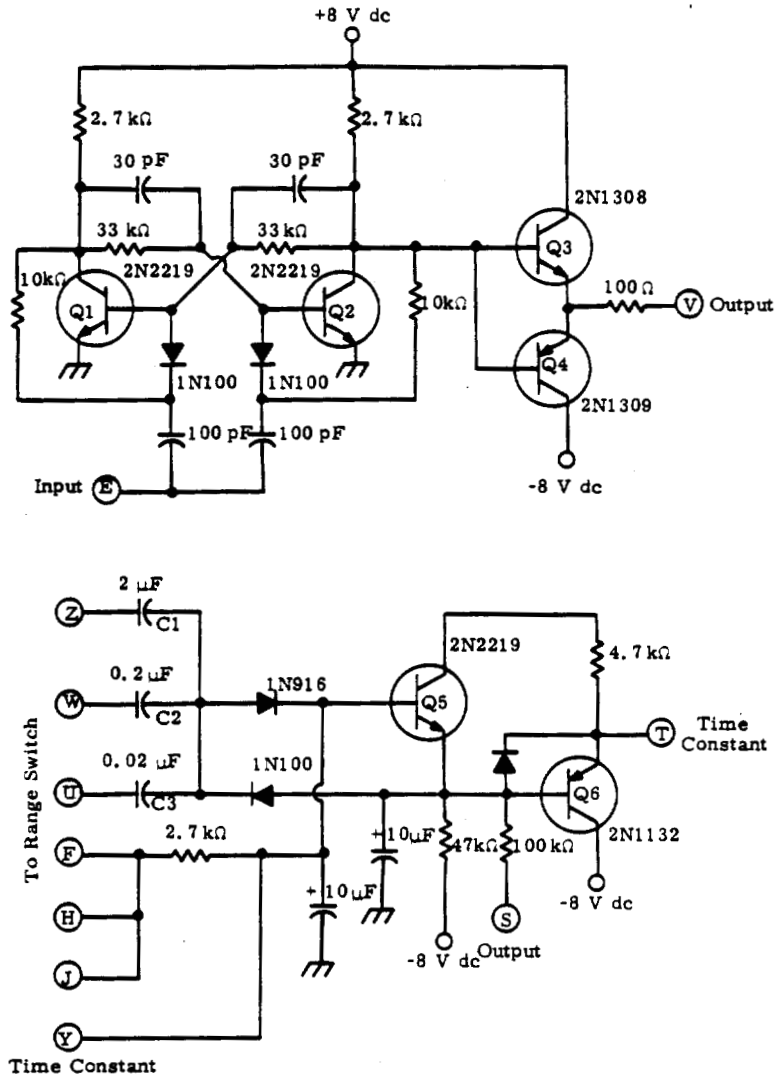

FIGURE 5.48

Count-Rate-Meter

The 5-decade scaler (Figure 5.49) uses decade circuits comprising four binaries with a feedback "AND" gate to the input of the second binary to provide a 1, 2, 4, 8 binary-coded-decimal (BCD) output. The binary outputs are filtered to prevent switching transients of the BCD-to-analog converter from changing the scaler count. The BCD-to-decimal converter (Figure 5.50) consists of four saturating inverters that switch currents of 5, 10, 20 and 40 μA through the 50 μA meter to correspond to the BCD 1, 2, 4, and 8 "weight" numbers.

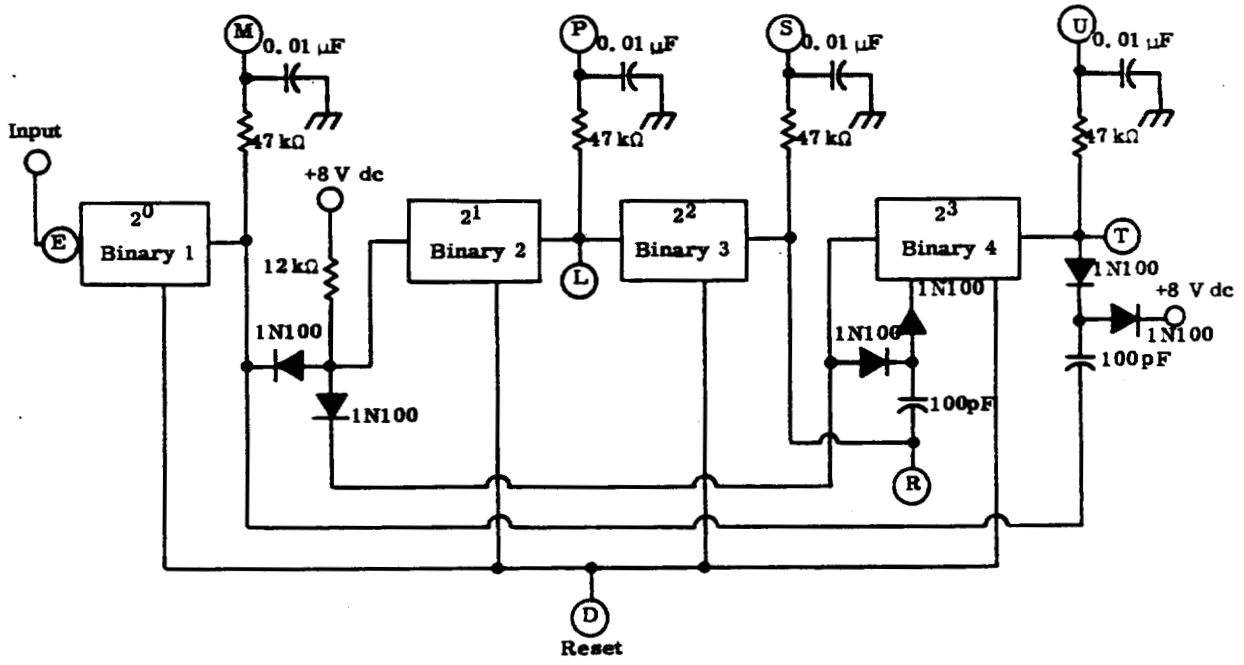

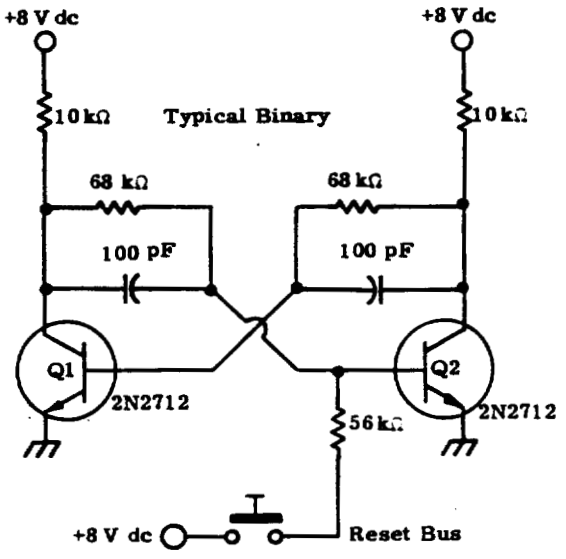

FIGURE 5.49

Scaler

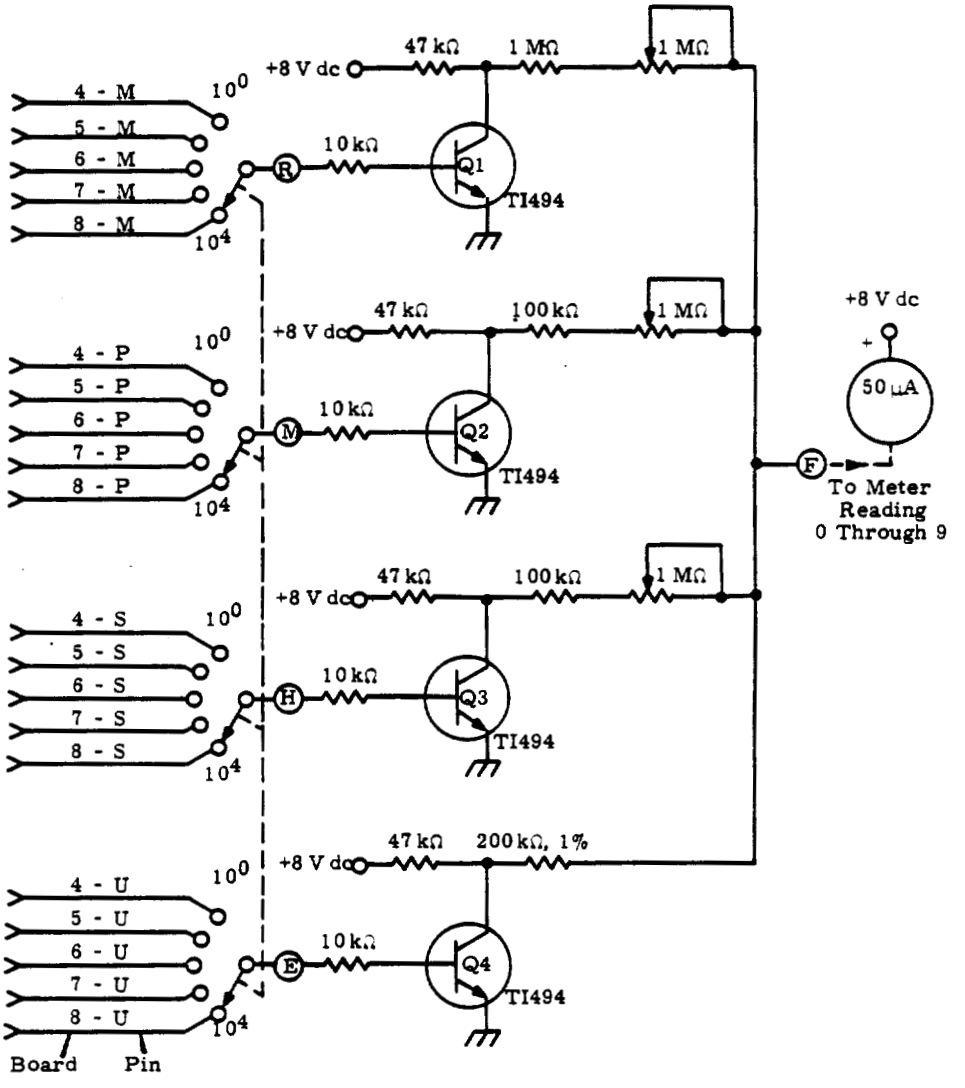

FIGURE 5.50

BCD to Decimal Converter and Meter Driver

A test pulse generator is provided (Figure 5.51) to generate -4 V pulses for use in testing and calibrating the single channel analyzer and count-rate portions of the instrument. A transistor pulse generator (Q1) drives a "double saturator" (Q2 and Q3) to provide the required pulses.

High voltage is provided by a transistor blocking oscillator, corona-regulated circuit (Figure 5.52) that is powered from the -8 V dc bus and requires approximately 30 mA of current. This supply is similar

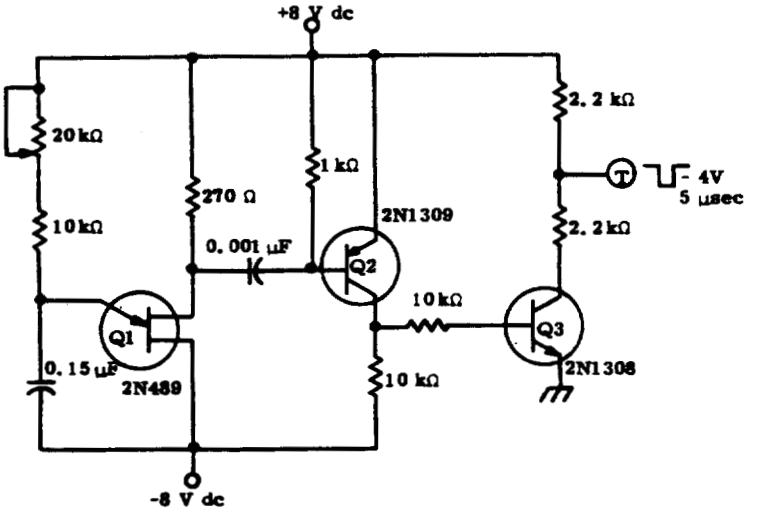

FIGURE 5.51

Test Pulse Generator

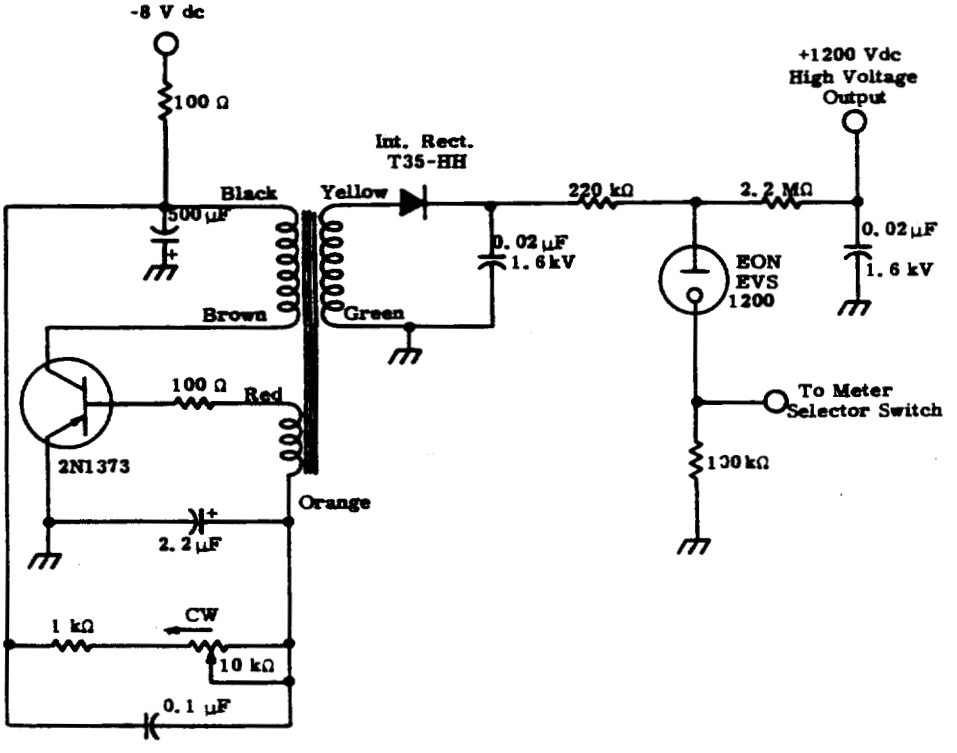

FIGURE 5.52

High Voltage Supply

to those used in Hanford portable radiological instruments and was chosen for simplicity, small size, and reliability.[5.25] The low voltages (+8 V dc and -8 V dc) are provided by a battery pack and regulator combination, shown in Figure 5.53, and all of the circuits operate from these two voltages. The regulator circuit (Figure 5.54) performs properly with 9.5 to 12 V dc input, as provided by two 6 V dc lantern batteries (in series) for each regulator.

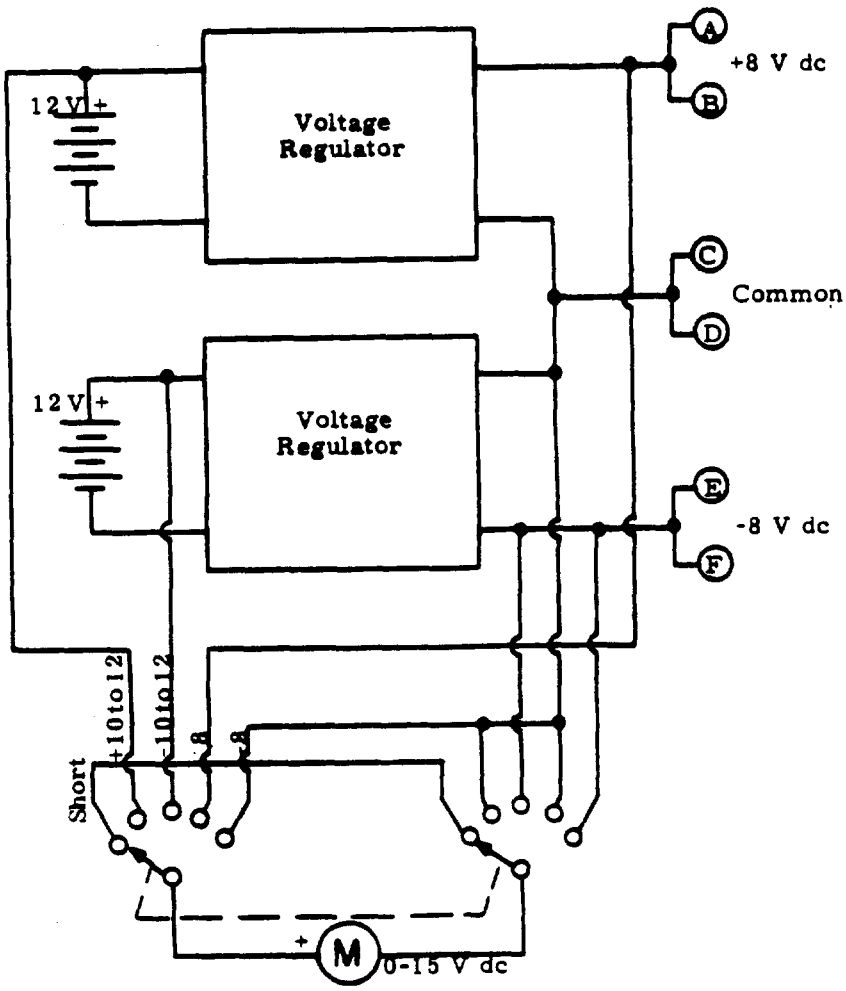

FIGURE 5.53
Low Voltage Power Supply

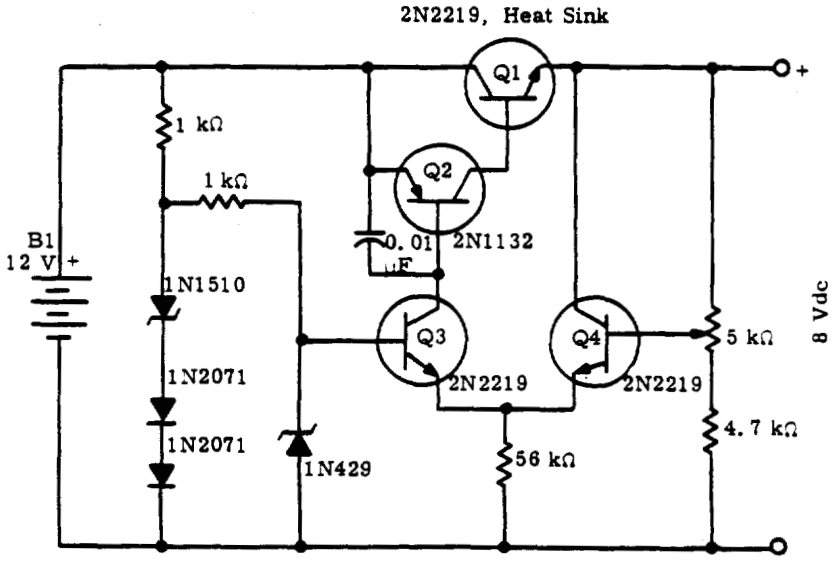

FIGURE 5.54
Voltage Regulator

Signaling Radiation Dosemeters - D. P. Brown

The problem of measuring dose to personnel continued to receive active investigative and experimental attention. Development was conducted on personally carried, miniature, signaling radiation dosemeters which employ a recharging type of ionization chamber as a sensor. The objective was to develop a dosemeter of a reliable nature with uniformity of response that would provide a readily apparent audible signal following accumulation of a predetermined dose. The effort centered around a single signal-activation point, typically 50 to 200 mR. Solid state circuits were developed along with a method of charging the center rod of the "pencil" type ionization chamber before use. Work was directed at developing the recharging fiber and center rod mechanical assembly to achieve reliable performance. Several experimental dosemeters were assembled and tested with promising results. One dosemeter was adjusted to cause alarm signal activation following a dose accumulation of about 50 mR, and the second was adjusted for a 200 mR level. Testing indicated that alarm signal activation repeatability values of ± 4% and ± 3% were obtained for the 50 mR and 200 mR units respectively, and a simple mechanical adjustment within the chamber can provide dose value alarm trip points as desired. Each experimental dosemeter weighs about 8 oz and can easily fit into a shirt pocket.

0028561

Discussion

The ionization chamber, shown in Figure 5.55, is an "automatic recharging" pencil-type ionization chamber.[5.26] The small 2.5×10^{-4} in. diam fiber is attracted to the center rod as the chamber is discharged by ionization; when contact is made, the chamber is recharged through the fiber. A pulse developed during "recharge" can be used to activate specific circuitry. The "initial charge" switch is used to assure that the chamber is fully charged before use in a radiation field. Energy for recharging is supplied by a storage capacitor. The equivalent circuit of the "ionization chamber" is shown in Figure 5.56.

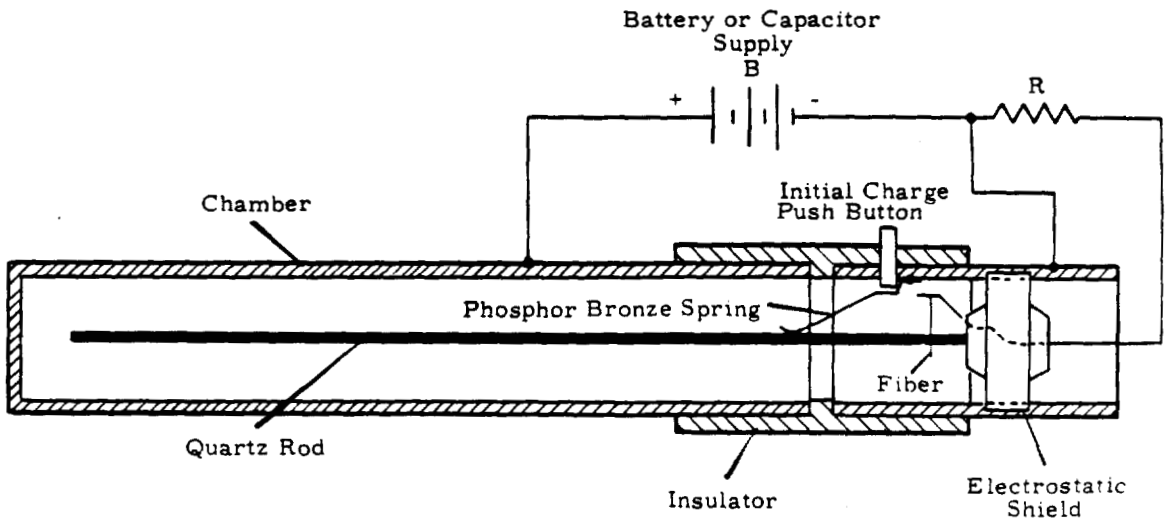

FIGURE 5.55
Modified Ion Chamber Details

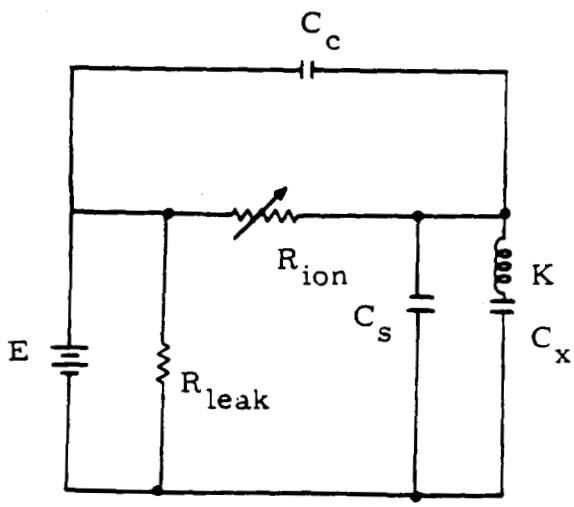

FIGURE 5.56
Equivalent Circuit

The active chamber capacity is C_c; C_s is the capacity from center rod to shield; C_x is the capacity from center rod to the fiber; K represents the restoring force spring-constant of the fiber tending to return it to a normal "rest" position; R_{ion} represents the conductive path produced by the ions within the chamber; and R_{leak} is the leakage resistance. Initially, before the voltage source is connected, the fiber is in its rest position, approximately 1×10^{-2} in. from the center conducting rod. The position of the fiber and its relative flexibility determine the dose required to cause appropriate signaling. When voltage is applied, capacitors C_s and C_x (in parallel) are charged with capacitor C_c in series. Since one "plate" (the fiber) of C_x is free to move, the fiber, which is under the influence of the attractive force between opposite charges, is attracted until it contacts the center rod (the other "plate"). This contact discharges both C_s and C_x and leaves C_c charged to the supply voltage. As ionizing radiation causes current to flow through R_{ion}, capacitors C_s and C_x will begin to be charged once more. The fiber will again be influenced by the attractive force and will move slowly toward the center rod.

Considering the equivalent circuit,

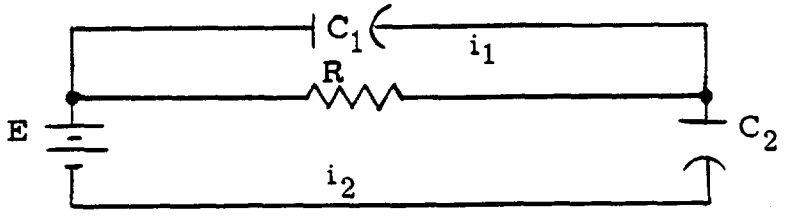

loop equations are

$$R(i_1 + i_2) + \frac{1}{C_1} \int i_1 \, dt = 0$$

and

$$R(i_1 + i_2) + \frac{1}{C_2} \int i_2 \, dt = E \ .$$

With initial conditions being $E_{C_1} = E$ and $E_{C_2} = 0$, the matrix equations are

$$\begin{pmatrix} I_1 \\ \\ I_2 \end{pmatrix} \begin{pmatrix} R + \frac{1}{C_1 S} & R \\ \\ R & R + \frac{1}{C_2 S} \end{pmatrix} = \begin{pmatrix} \frac{E}{S} \\ \\ \frac{E}{S} \end{pmatrix}$$

and it follows that

$$e_{C_2} = E\left[1 - \exp\left(-\frac{t}{T}\right)\right]$$

and

$$e_{C_1} = E\left[\exp\left(-\frac{t}{T}\right)\right]$$

where

$$T = R(C_1 + C_2) \ .$$

Now for any voltage e_{C_1}, the time t can be solved for, giving

$$t = T \ln \frac{E}{e_{C_1}} \ .$$

Substituting this term into the equation for e_{C_2} gives

$$e_{C_2} = E\left[1 - \frac{1}{\exp\left(\ln \frac{E}{e_{C_1}}\right)}\right] = E\left[1 - \frac{e_{C_1}}{E}\right] = E - e_{C_1} \ .$$

As the capacitor C_1 is discharged by ionization, its voltage changes by Δe. Thus $e_{C_1} = E - \Delta e$ giving

$$e_{C_2} = \Delta e.$$

Thus the voltage rise on C_2 is equal to the voltage drop on C_1.

Since

$$\Delta e = \frac{\Delta Q}{C} ,$$

and since for this detector, for alarm at 100 mR, $\Delta Q = 2.59 \times 10^{-10}$ coulombs, then

$$\Delta e \cong 90 \text{ V} .$$

The fiber must be positioned physically so it recharges the chamber and causes alarm activation when the voltage between fiber and center rod, C_2, is 90 V.

Sensor Operation

As the fiber is gradually attracted closer to the center rod, it reaches a point, after a movement of distance x = 0.6 d (d is the perpendicular distance from the center rod to the fiber), where the fiber rapidly moves to touch the center rod, thereby recharging C_c. Figure 5.57 is a graph of attractive force for various values of charge on C_s and C_x; also plotted is the restoring force of the fiber. Under typical operation, there are two crossing points, A and B. As long as the fiber position, x, is to the left of point B, it will come to rest at point A. This follows because as long as the attractive force is greater than the restoring force (left of point A), the fiber moves toward the center rod. When the restoring force is greater, the fiber will move away from the center rod. As the charge on C_x increases, a point will be reached where the restoring force curve is tangent to the attractive force curve. Any further increase in attractive force will cause instability.

Assuming the attractive force is

$$F = \frac{f(Q)}{g(d - x)}$$

where f(q) is a function of the charge on C_x, d is the distance between the rest position of the fiber and the edge of the center rod, and x is the deflection distance of the fiber; and since the restoring force on the fiber can be expressed as

$$F_r = K_r x$$

where K_r is related to moment of inertia, the modulus of elasticity, and to the fiber length. Then, the point of instability is

$$x_1 = \frac{g(d - x)}{g'(d - x)} \quad .$$

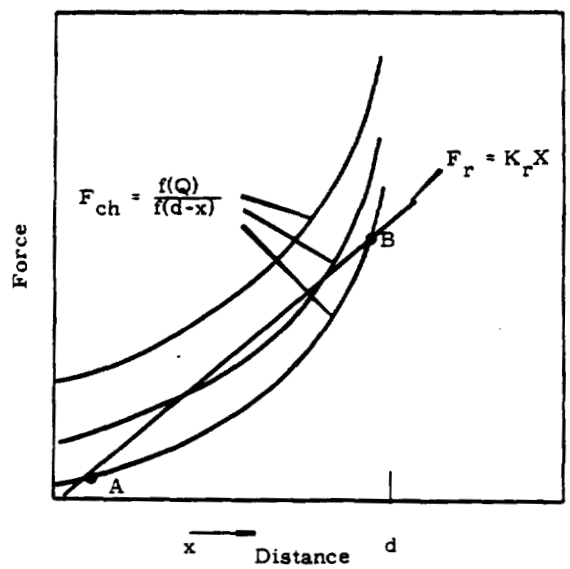

FIGURE 5.57

Attractive Force Versus Distance for Several Values of Charge on C_s and C_x

Figure 5.58 is a graph of fiber deflection versus voltage between the fiber and the center rod. Note that the point of instability occurs where

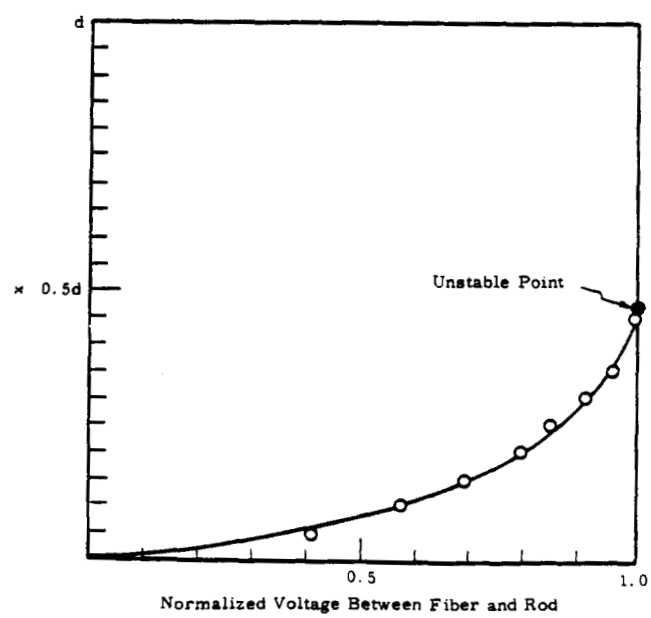

FIGURE 5.58

Fiber Deflection Versus Voltage Difference

$x \approx d/2$. Since the voltage between the fiber and the rod causes the attraction, the voltage (V) at the point of instability is independent of the supply voltage (E_{bb}) as long as $E_{bb} > V$. In practice, E_{bb} was chosen to be 300 V to assure adequate collection efficiency in the ion chamber and to assure the charging of C_x to V. Voltage (V) is typically 90 V but can be lower (or higher) depending on the dose-to-signal point desired. To reduce the size of the instrument, a 0.1 μF low-leakage capacitor is used as a "source" of E_{bb} instead of a battery.

Mechanical and Leakage Considerations

As the two curves of Figure 5.57 approach being tangential, the point of instability moves very close to the point of stability and excessive mechanical shock can move the fiber beyond the unstable point. In the units tested, however, this condition was not a problem.

A second point of consideration is the limitation imposed by the leakage resistance (R_{leak}) which tends to discharge the storage capacitor shown in Figure 5.56. The drop in voltage across the capacitor appears as "negative dose." This sets a lower limit on the dose rate at which the unit will function; thus, leakage should be reduced to the minimum possible amount by rigorous cleaning procedures.

One difficulty encountered is the tendency of the fiber to stick to the center rod after repeated cycling. Typically, the fiber begins to adhere to the rod following about 1.2×10^4 operations, and for the usual adjustment setting of 100 mR/pulse (or cycle), this equates to a dose of 1.2×10^3 R. Many different materials were tried for the fiber and for the center rod. Materials investigated for fibers included platinum, stainless steel, metallic-coated quartz, and tungsten. For the center rod, the tested materials were platinum, stainless steel, tungsten, metallic-coated quartz, conductive plastic, conductive-coated (Aqua-dag®) quartz, and conductive Teflon®. The best combination was a platinum fiber and a conductive Teflon® center rod, giving 2×10^5 operations before sticking occurred. However, the considerable difficulties involved in fabricating the conducting

Teflon® rod make its use impractical at this time. The second-best combination was either a platinum or a metallic-coated quartz fiber and a conductive-coated (Aqua-dag®) quartz center rod. This method provides about 1.2×10^4 operations before the fiber starts adhering to the rod.

For those cases where a metal fiber and either metal rod or metalized quartz rod were used, the adherence difficulty seemed to be caused by micro-welding. Observation, using a microscope in a darkened room, revealed arcing at the point of contact. Further, after many operations, the fiber and rod appeared discolored at the point of contact.

The adherence phenomenon for the conductive-coated (Aqua-dag®) center rod appeared to be from a different cause. The conductive coat was damaged at the point of contact with some material being removed from the coat, leaving a small pit the size of the fiber. It is possible that the irregular sides and bottom of the formed pit, which contained many relatively sharp and jagged edges, caused the fiber to attach. Readjustment of the fiber to a new location on the rod starts the process over again in the same manner as for a new assembly.

Evaluation tests on the completed dosemeter (Figures 5.59 and 5.60) indicated the dose required to cause signal activation was within ±10% of the preselected level for dose rates up to 3.6 R/hr and for temperatures to 60 C. For dose rates above about 6 R/hr, the signal point accuracy was typically ±25%. Approximately 1.2×10^4 cycles or operations (equating to about 1.2×10^3 R) can be achieved before the recharging fiber begins adhering to the chamber rod. The sensor is gamma energy independent, to ±10%, from 120 keV to 2 MeV. Mechanical shock problems proved to be negligible and the angular response was deemed adequate for the purposes intended. The complete dosemeter weights about 8 oz.

Since the sensitive portion of the dosemeter is an ion chamber, the chamber could be made sensitive to neutrons by incorporation of an appropriate coating material. The output pulse could also be used to control a

FIGURE 5.59
Opened Complete Dosemeter

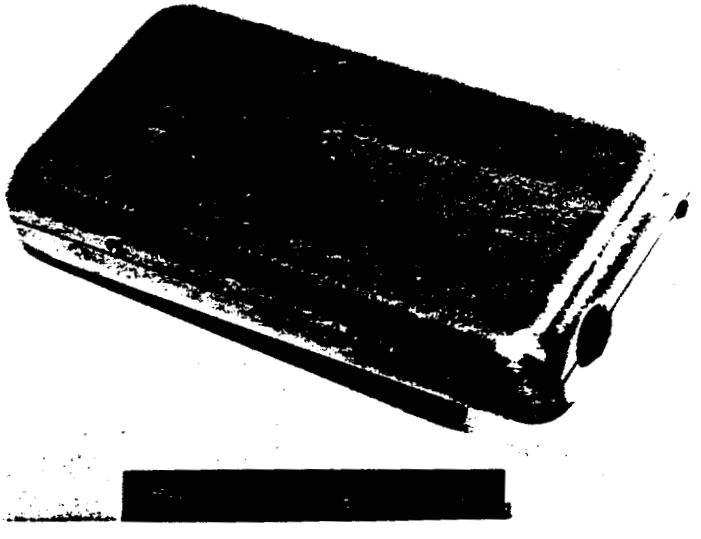

FIGURE 5.60
Complete Dosemeter

Neg. No. 0640406-2; 0640406-1

0028569

miniature transmitter for the telemetering of dose information to a central station.

Further information, including all details of the solid state circuits used in the dosemeters, can be found in a completed report.[5.27]

Wind Component Analyzer Development - C. A. Ratcliffe and E. M. Sheen

Atmospheric diffusion studies, as performed by Atmospheric Physics*, include the necessity of measuring wind components. It was determined that correct performance was not being attained with the employed instrumentation; thus, further developmental effort was necessary to correct the deficiencies. In addition, it was desired that the improved instrumentation be compatible with a recently acquired recording and data reduction system. Electronic circuitry development work was conducted to provide correct operation and full compatibility with available equipment. The improvements included amplifiers, filters, and offset and readout circuits. General field testing carried out has been satisfactory and the instrumentation is now fully operational.

Discussion

The originial wind component meter (WCM) system, employed at Hanford in atmospheric studies, was commercially fabricated a number of years ago. It was desired to improve general operation and to provide compatibility with a tape recording system, where the use of a tape recorder permits data from all three of the WCM channels to be continuously entered into an analog computing facility without loss of frequency response or of relative timing information. This is a vast improvement over the original system of recording on an oscillograph and then transcribing the data manually for computation. The input characteristics of the tape recorder electronics are ±1 V for maximum excursion, and to preserve and utilize this capability and dynamic range, amplification of the millivolt level input signals was required. This was accomplished by installing some instrumentation quality dc amplifiers. The increased gain and bandwidth of these units, over the system previously used, exposed problems of interfering carrier

* See Section I.

voltages from the WCM and power line frequency interference because of "pickup" and ground loops. A beat-frequency effect also occurred because of the proximity of the carrier frequency in the WCM to the chopping frequency in the dc amplifiers. This last effect was removed by changing the oscillator frequency from about 470 Hz to about 610 Hz.

Figures 5.61, 5.62, and 5.63 show the revised circuitry, the amplifier circuitry, and the revised transducer head. The modifications required to change the oscillator frequency are shown in Figure 5.64, the circuit diagram of the developed oscillator.

As the wind speed and inclination transducers of the WCM are powered by the 610 Hz carrier generator in a partially balanced Wheatstone bridge, the output signals, which are functions of the wind speed and inclination, contain, as noise, varying amounts of carrier frequency signal. Measurements of these values compared with output noise requirements indicated that at least 80 dB of rejection was required at the carrier frequency. This rejection was implemented by installing two filters on each channel. The input filters consist of balanced twin-H filters at a moderate impedance level, and the output filters are twin-T in tandem with L-section, low pass, RC sections. These used small value components to avoid raising the effective output impedance. With commercial components and one potentiometer adjustment per filter, ample rejection of carrier noise was attained.

The problem of power line frequency interference was definitely not trivial, as long cables and minuscule valid signals were involved. In essence, the solution was to use valanced differential type circuits when possible, balancing adjustments, careful shielding and layout, and the elimination of ground loops. Some attenuation of 60 Hz signals was also obtained in the filtering. Additionally, a new cable was added to transmit the 610 Hz power from the laboratory equipment to the field transducer; this avoided a considerable amount of interaction. The field transducer mounting head was modified both electrically and mechanically.

0028571

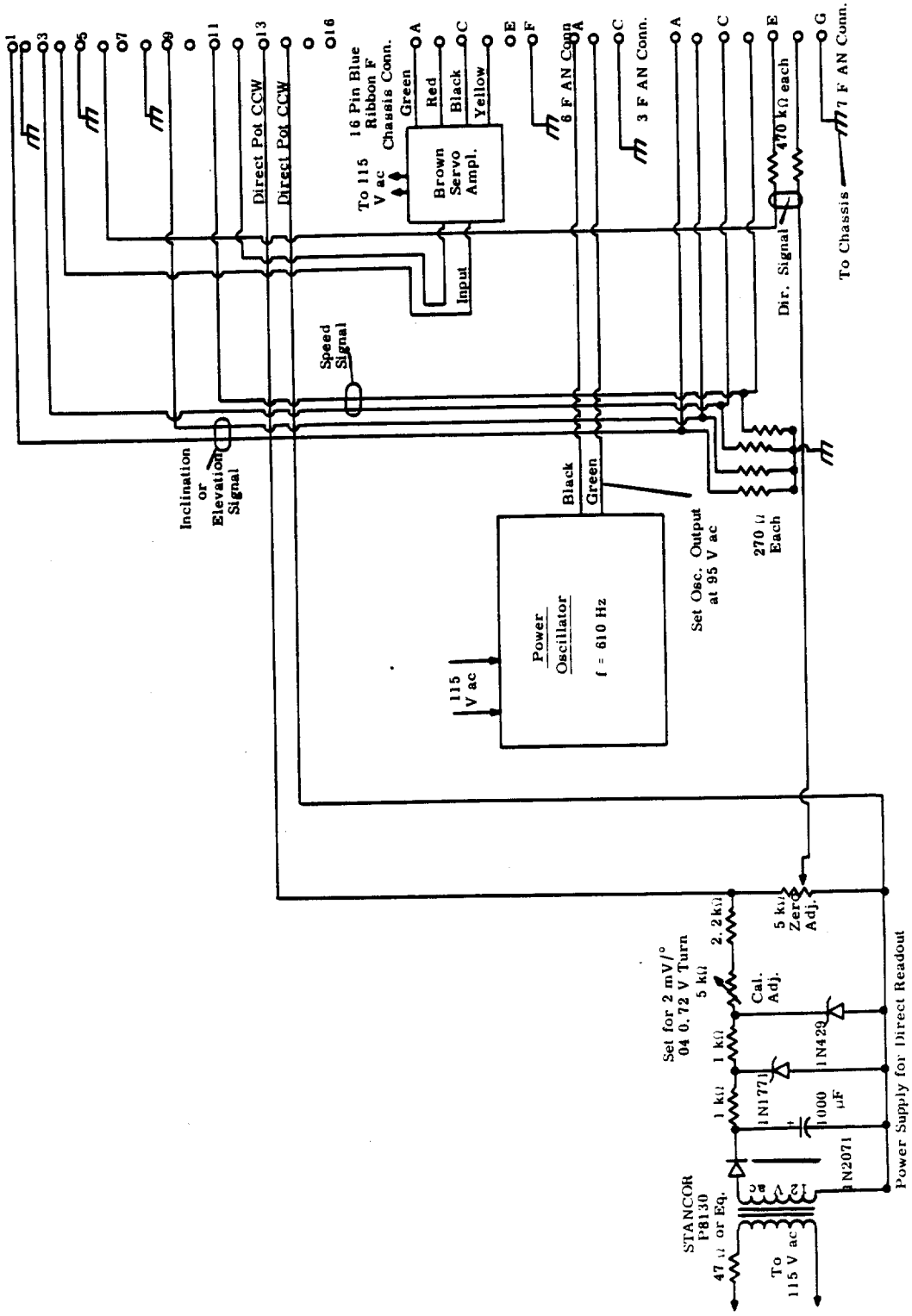

FIGURE 5.61
Revised Original Chassis

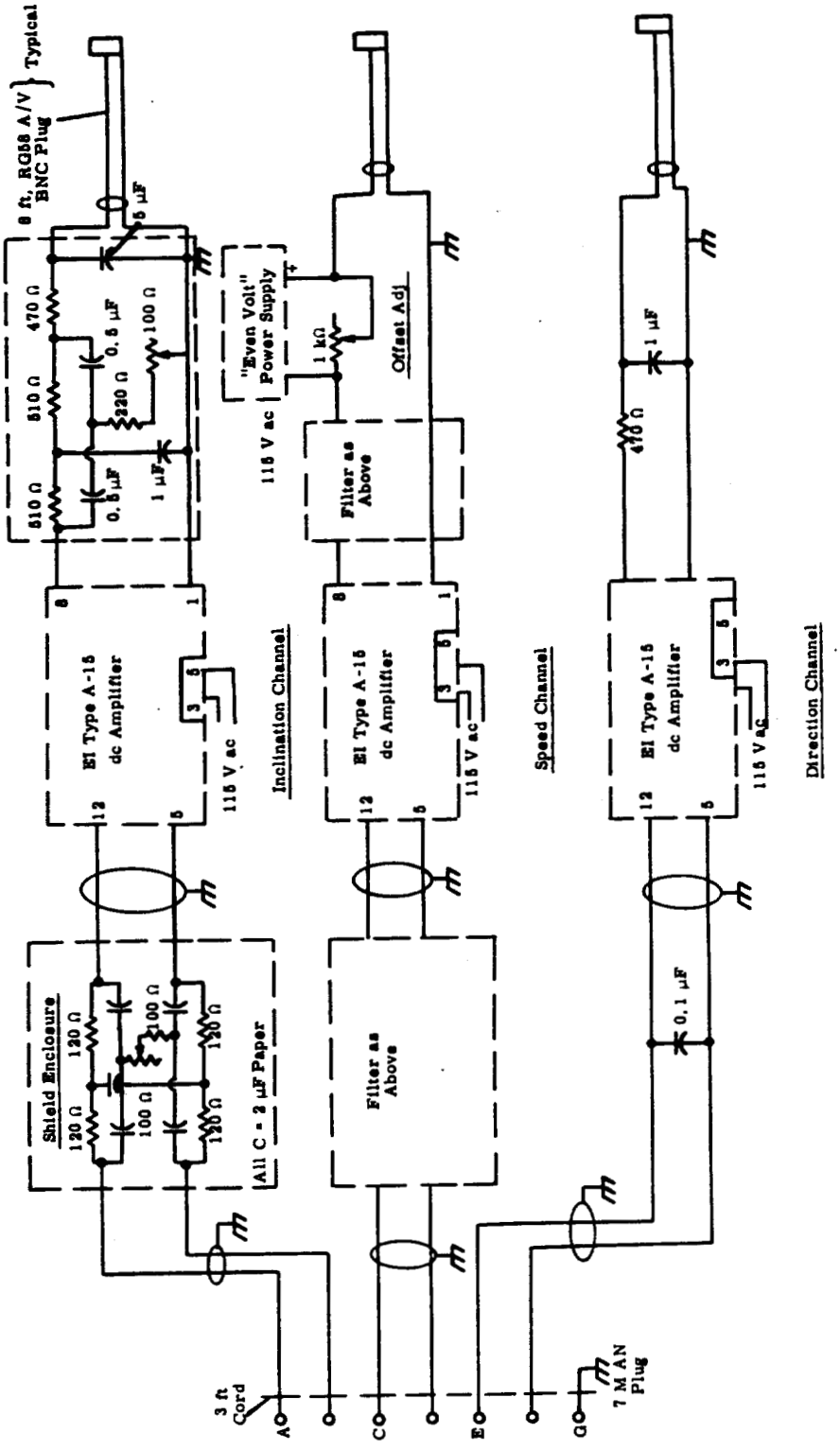

FIGURE 5.62
Amplifier Chassis

0028573

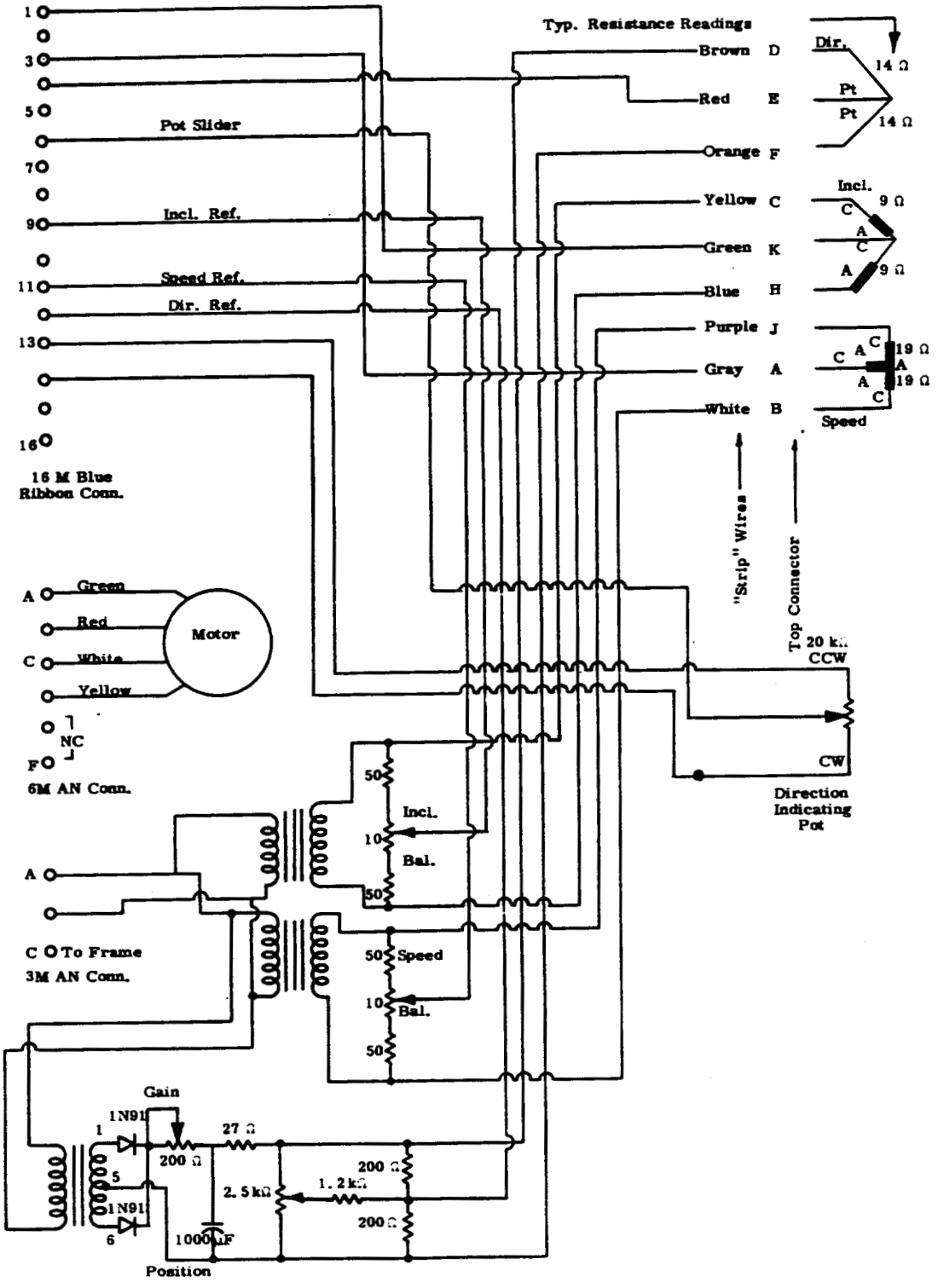

FIGURE 5.63

Revised Transducer Head

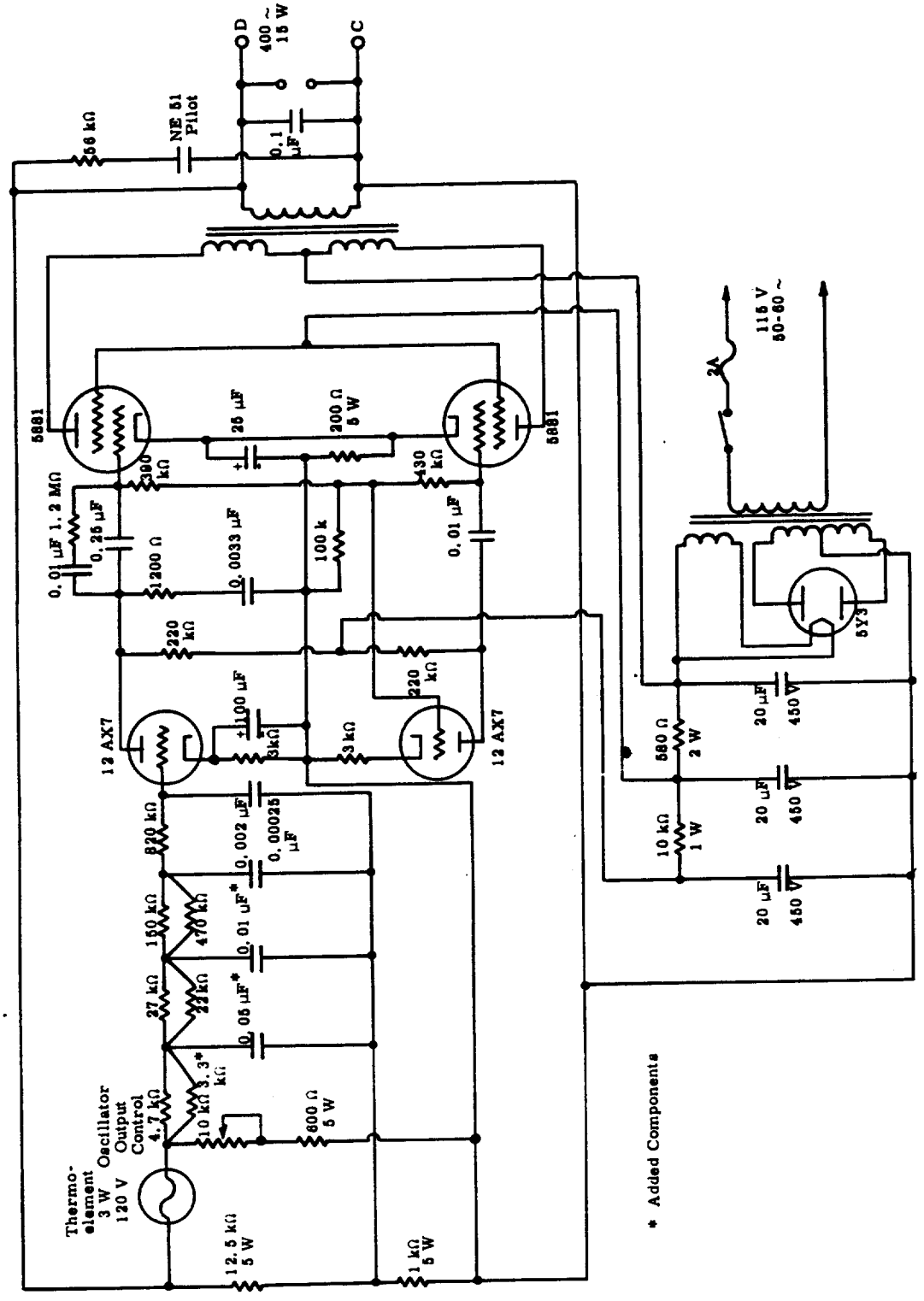

FIGURE 5.64
Revised Oscillator

A new power supply system was added to the direction readout apparatus. This is double Zener diode regulated to avoid sensitivity to line voltage or temperature, and is at high level, suitable for driving the direction channel amplifier. The amplifier is used to eliminate potentiometer loading error which would otherwise exist.

A variable voltage offset supply was added to the output of the "Speed" channel. This is required to permit full use of the tape recorder input range of ± 1 V since the amplifier output signal is always negative. The voltage is variable and closely resetable, allowing the user considerable latitude in recording and magnifying the desired results.

Following development and installation of the improvements stated, considerable laboratory testing was conducted with satisfactory results obtained. The system was delivered to the field for testing, and the results to date indicate that performance is satisfactory.

Automatic Data Collection System for Meteorological Tower Investigations - C. A. Ratcliffe and E. M. Sheen

This paper presents further developmental and achieved measurement accuracy information, in supplement to a previous paper.[5.28] Micrometeorological studies require rapid scanning and recording of data from wind direction, wind speed, and temperature transducers at six elevational levels on a portable tower. A wind direction vane, an anemometer with frequency output, and a thermocouple were used at each of the six levels. During each 5 sec scanning period, all direction and speed measurements are recorded on both printed and punched paper tape. Additionally, the six temperatures are recorded sequentially over a 30 sec period on the same record as the speed and direction data. The punched paper tape record is compatible with data reduction equipment. The data system uses solid state components for long life and high reliability. The portable field tower can be located 500 ft from the instrumentation mobile van to avoid aerodynamic interference. Successful field operation is being achieved with the system.

Discussion

The completed, tested, and in-use automatic data system for use in meteorological studies is shown in brief block-diagram form in Figure 5.65. A field photograph of the instrument is shown in Figure 5.66. The system, which uses all solid state circuitry for reliability and stability, is described in general terms in lieu of a detailed discussion of the various individual electronic circuits. Major features described are transducers, analog to digital conversion, paper tape printing and punching, time programming, and signal conditioning and gating. Figure 5.67 is a close-up view of the portable tower with mounted sensors on three arms.

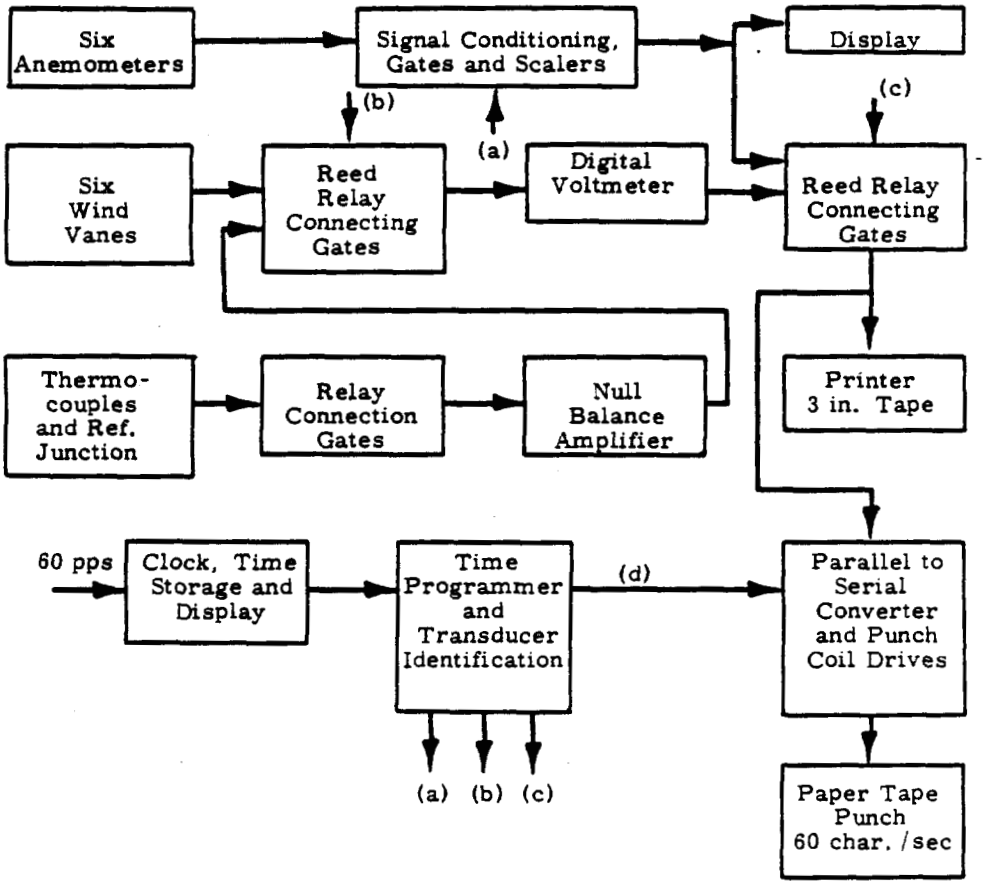

FIGURE 5.65

Automatic Data Collection System for Meteorological Investigations

0028577

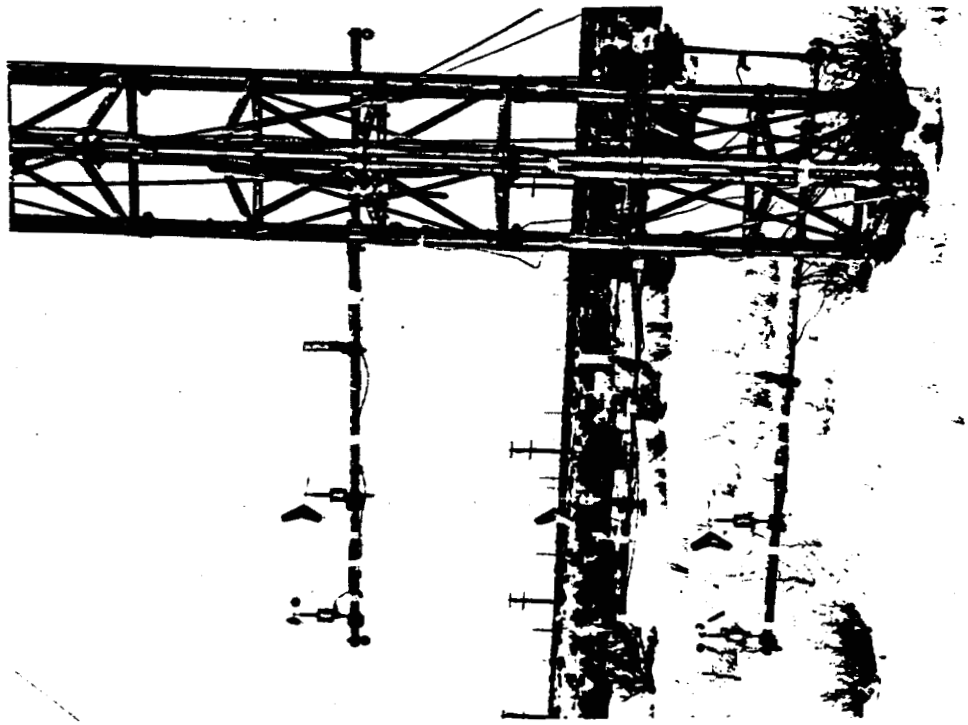

FIGURE 5.67
Portable Tower
Showing Three Arms with Mounted Sensors

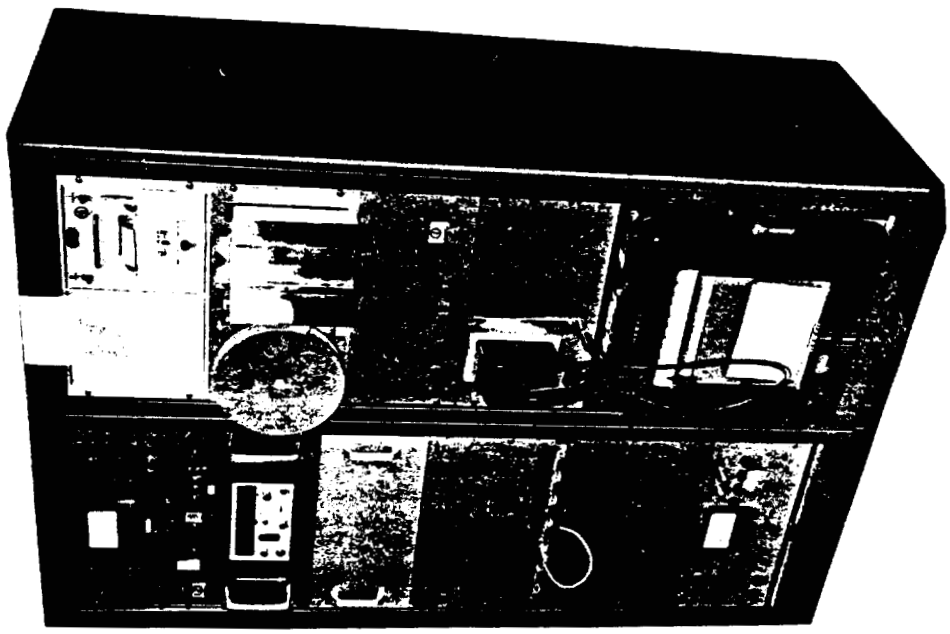

FIGURE 5.66
Automatic Data Collection
System Instrumentation

0028578

Transducers and Date Conversion

The wind speed transducers are Beckman and Whitley Model M1564 with linear preamplifiers added to drive 500 ft of terminated cable. The preamplifiers were designed to provide stable linear gain over the expected ambient temperature range. Anemometer outputs are sinusoidal voltages with the frequency linearly related to wind speed. At the data logging instrumentation, the voltage signals are connected to noise discriminators and signal-shaping amplifiers to convert the sinusoids to square wave signals. These are connected through time-programmed control gates to digital scaler storage units. The scaling period is 3.5 sec to provide the output wind speed directly in mph with a correction factor near unity. Binary coded decimal (BCD) outputs from the wind speed scaler connect through reed-relay gates to the printer and paper tape punch.

Beckman and Whitley Model M1565 wind direction transducers were calibrated to provide an output voltage of 0.02 V per degree of rotation. This analog voltage is connected through reed-relay gates to a commercial solid state digital voltmeter, digitized, and presented as BCD signals to the printer and paper tape punch. Resulting printed wind directions are divided by two to obtain the direction angle in degrees.

The output signals from the wind vane transducers are smoothed by a filter having a 3.5 sec time constant to remove most of the effect of "flutter," yet allow valid changes in wind direction to be recorded. The time constant is varied by changing accessible resistors. During the recording interval, the filter output is sampled for 60 msec, digitized by the digital voltmeter, and printed and punched.

The six temperature transducers are copper-Constantan thermocouples. Each thermocouple signal is selected in turn, compared to a heated (130 F) reference junction, and amplified by a null balance amplifier. The mechanical output of the amplifier is changed to an electrical output by a potentiometer and digitized by the digital voltmeter. Recording proceeds as before.

0028579

Timing Functions

Timing functions are derived from the 60 cps power line by shaping the power supply output voltage and dividing the frequency to obtain both 4 and 60 pulses/sec and 1 pulse/min. These signals connect to sequencer circuits that provide both experiment running time and internal programming information. The 1 pulse/min rate is scaled as experiment running time, and the scaler (BCD) outputs are recorded. A time programmer comprises three separate sequencers, a 20 point unit for speed and direction programming, a 6 point unit for temperature programming, and a 15 point unit used in the paper tape punch serial converter. The sequencers use scalers and diode logic to energize the appropriate "1 out of n" points. The sequencers are normally operating but may be turned off or manually advanced by single steps for testing. The 20 point sequencer advances at the rate of 0.25 sec per step, or 5 sec per complete cycle. The 6 point sequencer operates temperature gates and advances at the rate of one step per 5 sec or 30 sec per complete cycle. Thus, one temperature measurement is made each 5 sec. The 15 point unit advances at the rate of 60 steps/sec.

The sequencer outputs are combined to provide time programming for the signal gates, timed print command and digital voltmeter control pulses, and transducer identification signals.

Economic considerations and convenience of fabrication led to the use of commercially available transistor logic modules for many of the individual circuits. For example, the wind speed scaler storage unit consists of 6 scalers, 4 decades each, as available from several manufacturers. Special circuits such as the wind speed signal conditioning circuits, anemometer preamplifiers, paper tape punch coil drivers, etc., were developed.

System Readout

The system readouts consist of a printed record and a punched paper tape. Transducer data and identification and time information are all

presented in parallel, or at once on many wires, to the digital printer. For recording by the paper tape punch, this information must be presented to the punch in a serial fashion, and this time translation is performed by the parallel-to-serial converter which accepts all the data to be recorded and releases it sequentially to be punched. The heart of this converter is the 15 point sequencer, which performs the required function by controlling connection gates, a punch command generator, and the driving circuitry for the paper tape punch.

Operational Experience

The system operated in the laboratory for many months during development and fabrication and in the field for several months. Stability of calibration has been excellent, with no appreciable drifts. Maintenance requirements are predicted to be small and should concern mainly the transducers, printer, and paper tape punch. Automatic data logging system readout accuracies attained are ± 0.1 mph for speed, ± 0.5° static accuracy for direction (not including transducer errors), and ± 1 F° for temperature. With the six thermocouples in a constant temperature bath, the recorded temperature is constant to within ± 0.2 F° at any temperature within the range of the instrument, which is from 0 to 120 F. Power consumption for the complete system is less than 350 W from a 115 V ac source. The system can be operated from either an electric utility line or a small portable generator and is located in a field laboratory mobile van.

REFERENCES

5.1 D. P. Brown. Detection of Airborne Plutonium Using Alpha Energy Analysis Techniques, HW-78734. September 1963.

5.2 D. P. Brown. "Airborne Plutonium Detection," Hanford Radiological Sciences Research and Development Annual Report for 1963, HW-81746, pp. 5.59-5.67. January 1964.

5.3 W. G. Spear. Transistorized Line-Operated Radiation Detection Instrumentation, HW-65553. January 1961.

5.4 W. G. Spear. Method for Beta-Gamma Hand and Shoe Counting Under Varying Background Conditions, HW-78956. October 1963.

5.5 W. G. Spear. Transistorized Line-Operated Radiation Detection Instrumentation, HW-65553. January 1961.

5.6 G. L. Helgeson. "Determination of Concentrations of Airborne Radioactivity," Health Physics, vol. 9, pp. 931-942. 1963.

5.7 M. O. Rankin. "Medium Level Continuous Alpha Particulate Air Monitor," Health Physics, vol. 4, pp. 293-311. 1961.

5.8 D. P. Brown, M. O. Rankin, and W. G. Spear. Coincidence Count Alpha Particulate Air Monitor, HW-75384. January 1963.

5.9 D. P. Brown. Detection of Airborne Plutonium Using Alpha Energy Analysis Techniques, HW-78734. September 1963.

5.10 J. M. Alexander. Continuous Monitor for Prompt Detection of Airborne Plutonium, DPSPU-64-30-11, du Pont de Nemours & Co., Savannah River Laboratory. June 1964.

5.11 P. Iredale and G. Hinder. The Detection of Airborne Plutonium Hazards, AERE-R-3783, Atomic Energy Research Establishment, Harwell, Berks., England. January 1962.

5.12 R. J. Gale. Use of Simple Scintillation Alpha Spectrometry for Contamination Control in Laboratories, AERE-M-931, Atomic Energy Research Establishment, Harwell, Berks., England, November 1961.

REFERENCES (Contd.)

5.13 D. Allenden. "A Monitor for Uranium and Plutonium in the Air," AEI Engineering, vol. 2, no. 6. November 1962.

5.14 W. J. Bair, D. H. Willard, J. P. Herring, and L. A. George. "Retention, Translocation, and Excretion of Inhaled $Pu^{239}O_2$," presented at the Hanford Symposium on the Biology of Transuranic Elements, Richland, Washington, May 1962. Also in Health Physics, vol. 8, no. 6. December 1962.

5.15 W. G. Spear. Portable Radiation Instrumentation Standardization, HW-60404. September 1959.

5.16 E. M. Sheen and W. G. Spear. Portable Radiation Survey Instrument, HW-78872. September 1963.

5.17 J. DePangher. "Double Moderator Neutron Dosimeter," Nuclear Instr. & Methods, vol. 5, pp. 61-74. 1959.

5.18 J. R. Raymond. Unpublished Data, General Electric Company, Richland, Washington, January 1963. (Personal Communication).

5.19 E. M. Sheen, W. L. Bunch, and M. R. Wood. Neutron Soil Moisture Monitor, HW-82009. May 1964.

5.20 D. P. Brown, N. C. Hoitink, N. S. Porter, and J. Ryden. "Physiological Data Telemetry," Hanford Radiological Sciences Research and Development Annual Report for 1963, HW-81746. January 1964.

5.21 W. G. Spear and M. O. Rankin. Operation Manual for the Dog Counter, HW-55856. June 1, 1958.

5.22 H. E. Palmer, W. C. Hanson, B. I. Griffin, and W. C. Roesch. "Cesium-137 in Alaskan Eskimos," Science, vol. 142, no. 3588, pp. 64-66. October 4, 1963.

5.23 H. E. Palmer, W. C. Hanson, B. I. Griffin, and Dale M. Fleming. "Radioactivity Measurements in Alaskan Eskimos in 1963," Science, vol. 144, no. 1620, pp. 859-860. May 15, 1964.

REFERENCES (Contd.)

5.24 H. E. Palmer. "Studies of Radioactivity in Alaskan Eskimos by Urinalysis and by Non-Shielded Whole Body Counting Methods," Paper presented at the Fourth Symposium on Radioactivity, Riso, Scandinavia. October 5-6, 1964.

5.25 E. M. Sheen and W. G. Spear. Portable Radiation Survey Instrument, HW-78872. September 1963.

5.26 H. V. Neher. "An Automatic Ionization Chamber," Rev. Sci. Instr., vol. 24, no. 2. February 1953.

5.27 D. P. Brown. Miniature Signaling Radiation Dosemeters, HW-83868. November 1964.

5.28 E. M. Sheen and C. A. Ratcliffe. "Automatic Data System for Atmospheric Physics Studies," Hanford Radiological Sciences Research and Development Annual Report for 1963, HW-81746, pp. 5.6-5.10. January 1964.

0028584

INTERNAL DISTRIBUTION

Copy Number	
1	G. J. Alkire
2	F. W. Albaugh
3	W. J. Bair
4	C. A. Bennett
5	O. E. Boston
6	L. K. Bustad
7	I. B. Daer
8	R. F. Dickerson
9	S. L. Fawcett
10	R. F. Foster
11	P. A. Fuqua
12 - 61	J. J. Fuquay
62 - 66	J. K. Green
67	W. A. Haney
68	J. F. Honstead
69	F. P. Hungate
70 - 75	E. R. Irish
76	R. L. Junkins
77	A. R. Keene
78	H. A. Kornberg
79	M. Lewis
80	C. E. Linderoth
81	R. E. Nakatani
82	C. E. Newton
83 - 92	J. M. Nielsen
93	W. D. Norwood
94	R. F. Palmer
95	H. M. Parker
96	R. S. Paul
97	D. W. Pearce
98	I. C. Roberts
99 - 104	W. C. Roesch
105	L. C. Schwendiman
106 - 125	W. G. Spear
126	A. J. Stevens
127	F. Swanberg
128	R. C. Thompson
129	C. R. Tipton, Jr.
130	E. E. Voiland
131	M. T. Walling
132	W. K. Woods
133	D. C. Worlton
134 - 135	Biology Library
136 - 140	Technical Information Files
141 - 142	Technical Publications Files

0028585

ERNAL DISTRIBUTION (Special) ·36

Number of Copies

1	Johns Hopkins University Baltimore, Maryland Attn: W. A. Patrick
2	National Institute of Radiological Sciences 250, Kurosuna-Cho, Chiba-shi, Japan Attn: M. Saiki M. Suzuki
2	N. V. Belchim 200 Boeretang Mol, Belgium Attn: Paul Dejonghe Leo H. Baetsle
2	Oak Ridge National Laboratory Attn: K. Z. Morgan E. G. Struxness
1	Savannah River Operations Office Attn: K. K. Brown
1	U. S. Public Health Service Division of Health Mobilization, Washington, D. C. Attn: J. J. Lang, Research Branch
1	University of Arizona, Tucson Department of Geology Attn: E. S. Simpson
1	University of California, Berkeley Department of Civil Engineering Attn: W. J. Kaufman
1	University of North Carolina, Chapel Hill Department of Chemistry Attn: H. C. Thomas
1	University of Wisconsin Department of Chemistry Attn: H. Gladys Swope
1	University of Illinois Department of Agronomy Attn: M. B. Russell
1	World Health Organization Geneva, Switzerland Attn: R. L. Dobson, M. D.

·(2)

0028586